Vibrations non linéaires de structures élancées hautement flexibles : stratégies numériques efficaces dans le domaine fréquentiel

Marielle Debeurre

HESAM UNIVERSITÉ

Arts et Métiers Sciences et Technologies

ÉCOLE DOCTORALE SCIENCES ET MÉTIERS DE L'INGÉNIEUR
LISPEN - Campus de Lille

THÈSE

présentée par : **Marielle DEBEURRE**
soutenue le : **7 décembre 2023**

pour obtenir le grade de : **Docteur d'HESAM Université**

préparée à : **École Nationale Supérieure d'Arts et Métiers**

Spécialité : **Mécanique**

Nonlinear dynamics of highly flexible slender beams: efficient numerical strategies in the frequency domain

THÈSE dirigée par :
M. Olivier THOMAS

et co-encadrée par :
M. Aurélien GROLET

Jury		
M. Remco LEINE	PU, Universität Stuttgart	Rapporteur
M. Franck RENAUD	MCF, ISAE-Supméca	Rapporteur
M. Jean-François DEÜ	PU, CNAM	Président du jury
Mme Enora DENIMAL	Chargée de recherche, INRIA	Examinatrice
M. Olivier THOMAS	PU, ENSAM	Directeur de thèse
M. Aurélien GROLET	MCF, ENSAM	Co-encadrant
M. Ludovic RENSON	Senior lecturer, Imperial College London	Invité

THÈSE

To loved ones and loved ones lost;
you are missed, but never forgotten.

In memory of **Simon Benacchio**
1988 – 2023

He came like the wind, like
the wind touched everything,
and like the wind was gone.

The Wheel of Time

Never be so kind
you forget to be clever;
never be so clever
you forget to be kind.

---

marjorie

Acknowledgments

I have heard it said that if you can count the number of true friends on one hand, then you are indeed a lucky person. If that is the case, then I count myself among the luckiest. Although not many, I know that the people around me are true, that I can fall back on them whenever needed and for however long needed. I am thankful, then, to be presented with a timely opportunity to thank them, and to immortalize here my gratitude.

To begin, I must acknowledge the community that welcomed me when I arrived in Lille: to all the members of LISPEN, to those I had the pleasure of meeting while at ENSAM and especially to Emmanuelle, who kept up with the demands of my constant traveling with never a frustration expressed - thank you all. To my dear friends and colleagues of THREAD, though our meetings were sometimes few and far between, I was always warmed by your kindness and open hearts. And although the schedule was hectic, it was a true pleasure to connect with each and every one of you and to celebrate in the diversity of life and culture while pursuing the same end goals. It was an honor to be a part of THREAD.

Next, and not to be overlooked, to Olivier, the epitome of the tireless leader whose sole limitation is the minute hand of the clock, who showed me that even perfection can be improved, and to Aurélien, to whom "thank you" seems ridiculous in its simplicity, who let my superlatives run free from the very first day - thank you. The path we've walked together was certainly not always straight, but seeing the destination makes every long day, every late night, every tough week, every tear and every disagreement worth the toil. I hope you are as proud of the work we did together as I am.

Of course, what is life if not for the moments of camaraderie and laughter shared with friends? To the community, then, that I am blessed to have been a part of: to my friends and colleagues Arthur, Mathieu, Michel, François, Maxime, Guillaume, Hugo, Floriane, Shuhan, Santiago, Martin, Dorian, Tiphaine and Marine, who created an atmosphere of welcome and joy unlike any other. I take here a moment to mention in particular my dear friend Lei, who always knows what I like before I know it myself, and to "my generation" of the dynamics squad: to Marguerite, the most lovable and theatrical of Ravenclaws, to Vincent, who always knows how to have a good time, to Zein, the friendly and dependable "boy-next-door" genius, and above all to Eddy, whose care for others knows no bounds and whose constancy and reliability makes a mountain look unsteady by comparison.

Before leaving the European sphere, I feel obliged to express my gratitude to he who was present for Acts I and II of the play along with the intermission, and who missed only the final credits: Simon, any of us LISPENois would say that we wished we had more time with you, had gotten to know you better, had shared more bûches de Noël and Secret Santas, but to these I add my personal gratitude for the things we did together, for having had the opportunity to work with you on a project over the course of well-near two years and for having been given a smile, a nod, an "okay" but never an ounce of judgment. Thank you for your dependability, thank you for your kindness and thank you for your

inspiration. I hope that, in the end, we made you proud.

And finally, off to the USA I go to thank those whom words cannot compensate. To my family and friends, all of my grandparents, to friends and family lost but whose memories we cherish and carry on, and of course to the furrier friends of my family - in short, the list being too long (I leave you to identify yourselves, you know who you are!), for the sake of brevity I say only that you will never know hardship so long as I am breathing, or at least you will never know it alone. My love and gratitude for you knows no limits. Finally, above all, I am practically bound by a code of honor to acknowledge my parents, without whom I certainly (and quite literally) would not have come as far in life. My gratitude to them is such as can never be repaid and I spare the printer its ink in the security that they know how grateful I am to have the relationships with them that I do, and how much I love them.

Abstract

The study of highly flexible slender beam structures such as cables, wires, hoses, turbine, engine and rotor blades, ropes, flexible rulers and wings has been of great interest in recent years due to their widespread use in modern industry. These flexible structures are found extensively in automotive and aerospace manufacturing, public transportation, robotics, micro- and nano-electromechanical systems (MEMS/NEMS) and even bio-inspired and biomechanics. The unique geometry of these structures takes the form of a beam where one dimension, typically the length, is exceedingly large compared to the two others. This geometry leads to a very low bending stiffness while the axial stiffness remains relatively high, so that these so-called highly flexible beams are capable of reaching extreme amplitudes of displacement. At very large amplitudes, so-called geometrical nonlinearities tied to the rotations of the cross-sections of the beam enter into the equations of motion, nonlinearities that cannot be simplified with any accuracy at such large amplitudes. In such cases, the geometrically exact beam model is often used to model the mechanics of the structure since it exactly preserves the geometrical nonlinearities up to any amplitude of motion. In this work, we are interested in studying the periodic oscillations of these highly nonlinear systems at extreme amplitudes of vibration. To this end, a finite element discretization of the geometrically exact beam model is realized. The finite element model is solved entirely in the frequency domain to target periodic solutions with a strong focus on computational efficiency. The numerical strategy presented in this work is capable of modeling highly flexible beam structures both in 2D and in 3D. Also included in this work is an experimental validation of the numerical strategy involving dedicated experiments in vibration control.

Keywords: Nonlinear dynamics, Slender beams, Numerical strategies, Geometrically exact beam model, Geometrical nonlinearities, Finite element method, Periodic solutions.

Contents

List of Tables

List of Figures

Chapter 1

Introduction

The work of this thesis concerns the modeling, analysis and general mastery of the dynamics of slender one-dimensional (1D) beam-like structures, examples of which include wires and cables, hoses, ropes, threads and strings, flexible rulers and even in certain cases wings and blades (some examples are shown in Figs. 1.1 and 1.2). These structures represent examples of the mechanical beam, considered one of the cornerstone structures in solid and structural mechanics as well as finding widespread use in aerospace, civil, biomedical, electrical engineering and robotics. This thesis is organized within the framework of the THREAD European Training Network (THREAD-ETN) on the numerical modeling of highly flexible structures, funded by the European Union's Horizon 2020 research and innovation program under the Marie Skłodowska-Curie grant agreement No. 860124. The purpose of the THREAD-ETN is to bring together a new generation of engineers and mathematicians in order to develop appropriate models and numerical methods for the design of highly flexible slender structures capable of meeting the demands of modern industry. Within this framework, this particular thesis focuses on the development of efficient, fully numerical models able to capture the nonlinear dynamics of these flexible 1D structures up to any amplitude of vibration, thus allowing for a better understanding of their highly nonlinear behavior. The work of the thesis was carried out at the Laboratoire d'Ingénierie des Systèmes Physiques et Numériques (LISPEN) lab, part of the Lille campus of Arts et Métiers Institute of Technology.

In this introduction chapter, we seek to position the reader into the specific context of the thesis. The dynamics of beam structures encompasses a far-reaching body of work and for this reason efforts are made to focus the scope of this thesis to its topic of principal concern: the mechanics of *highly flexible, 1D beam structures*, nonlinear in nature due to the presence of geometrical nonlinearities in the equations of motion tied to very large rotations of the beam cross-sections. With this context in mind, an extensive review of the current state of the art is presented in § 1.2, complemented by an introduction to the so-called geometrical nonlinearities characteristic of these structures in § 1.3 and a global overview of the thesis in § 1.4.

Table of Contents - Chapter 1

1.1 Background and context

Within the context of the THREAD project, the work of this thesis was inspired by the perceived lack in the literature of numerical strategies (especially *efficient* numerical strategies) to model and characterize the dynamics of flexible 1D beam structures. These structures are capable of reaching very large amplitudes of displacement or rotation in vibration with only small to moderate excitations owing to their unique geometry. The geometry of these structures takes the form of a (deformable) beam where one dimension, in this case the length of the beam, is exceedingly large compared to its other dimensions (hence "one-dimensional"), so that the dimensions of the cross-section are small and the beam structure is characterized as thin (hence "slender"). Due to this particular geometry, the bending stiffness *i.e.* in the transverse directions (perpendicular to the longitudinal direction) is low, whereas the stiffness in the axial direction is very high. The result is an unusually large capacity for displacement in bending in the transverse directions (hence "flexible").

These features make flexible beam structures both interesting and unique in the field of solid and structural mechanics and yet very difficult to model physically. The behavior cannot be represented with any accuracy by linear beam models; nonlinear models incorporating the geometrical nonlinearities present in such systems (discussed in §1.3.2) are therefore necessary, along with appropriate numerical strategies for solving the nonlinear dynamic equations.

1.2 Motivation for the thesis

While accurate modeling and prototyping have for many years been indispensable steps in the engineering design process, numerical modeling and prototyping have only become prevalent in recent decades as technology has evolved. In particular, industry in general has increasingly come to rely on virtual prototyping as the associated cost of performing experiments or making design changes can increase drastically when moving from a virtual to a physical environment. The examples of slender 1D beam-like structures of §1.1 are found everywhere in modern engineering systems: a system with any electrical component naturally incorporates wires to carry electrical current; any system involving a fan or a turbine implies the presence of blades that are often slender; both people and objects are transported using systems hanging from or incorporating ropes and cables; the industrial applications of these types of structures are seemingly endless. Furthermore, these components are often grouped together (*e.g.* as a cable bundle or multi-material beam or rod) or integrated into complex engineering systems, increasing the associated computational cost, sometimes to a prohibitive level, of a fully exact, 3D numerical simulation of the system as a whole. For these reasons, the development of computationally-efficient and accurate numerical models of flexible beam structures represents an active subject of research.

Specific industrial examples are numerous, both in statics and dynamics, spanning many engineering disciplines. Examples of civil applications include the dynamics of cables and ropeway systems subjected to moving loads in cable cars or reeving systems [65], [172]. The drill string of a drilling rig represents another interesting industrial application of slender beams as it is noted in [174], [238] to

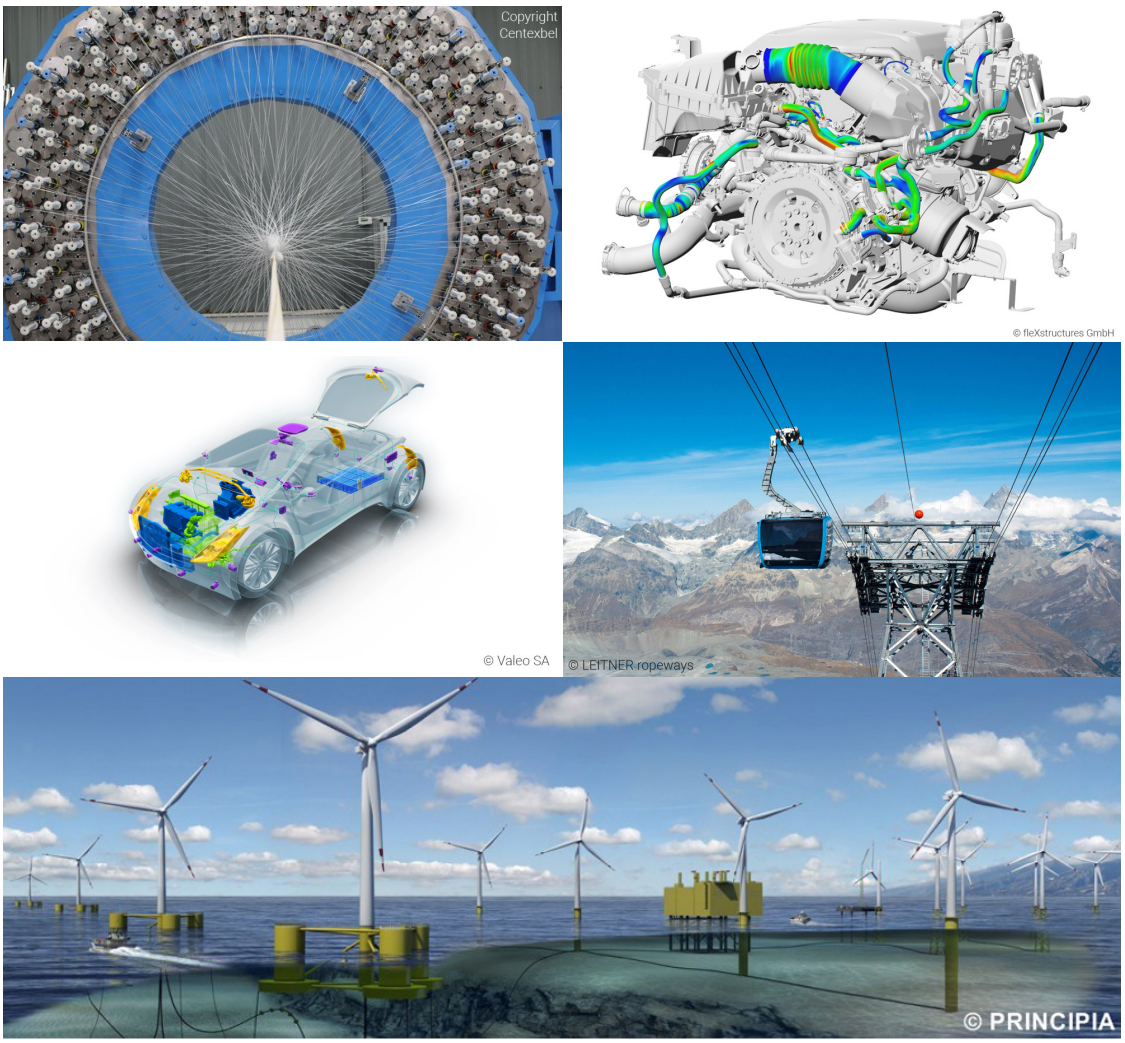

Figure 1.1: Industrial examples of slender 1D beam systems, clockwise from top left: fiber weaving machine (Centexbel), flexible hoses and cables in an automotive engine (fleXstructures GmbH), cable ropeway systems for cable cars (LEITNER ropeways), offshore wind turbines (PRINCIPIA), and flexible elements in automotives (Valeo).

have a length-to-thickness ratio even greater than a human hair. The rotating blades of wind turbines can also be modeled as slender beam structures whose rotational velocity changes as a function of the wind speed, and, in the case of offshore wind turbines, appropriate models for the mooring lines and power cables are needed in order to optimize the offshore performance [51], [52], [181]. Slender beam structures are also used in biomedical applications such as flexible medical equipment like endoscopes [222] or the supercoiling of DNA strands [90], [218], [256], in bio-inspired engineering for soft robotic applications [77], [259] or insect-like nanodrones [42], [72], [73], and in the modeling of woven fabrics and human hair [26], [63], among others.

Apart from these applications (and many more can be cited), flexible beam structures find a real home in automotive, aerospace and electrical engineering, and extensive research has been funded in this regard. In the automotive industry, efficient modeling of cables and cable bundles is of great im-

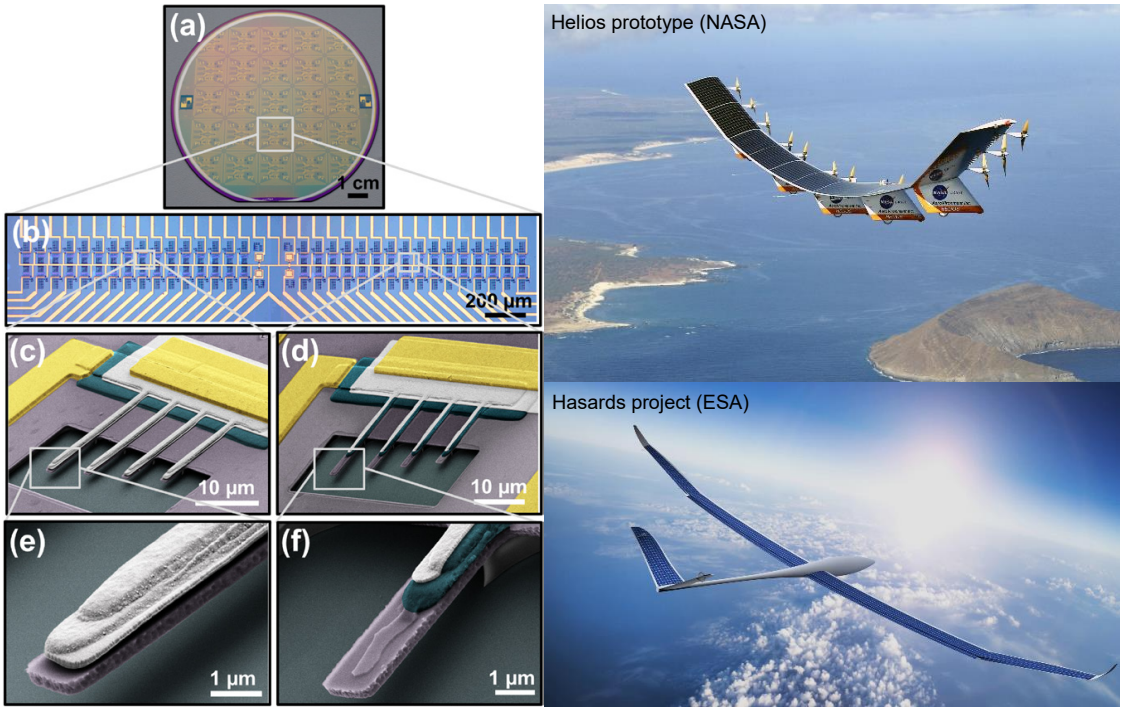

Figure 1.2: Additional industrial examples of slender 1D beam systems, clockwise from top left: piezoelectric NEMS cantilevers [61], Helios prototype (NASA), Project Hasards (ESA).

portance in finding the optimal layout of cabling in vehicles [45] and, moreover, their importance will only continue to increase in the global transition to electric vehicles. Optimization of placement and handling during manufacturing is also of importance in order to maximize the lifetime of the cables, since excessive or cyclic torsion/twisting of a cable can lead to fatigue and early failure [209]. Another subject of research tied to the optimization of cabling in vehicles is appropriate constitutive modeling of composite cables (recall that electrical cables are made up of a conductive wire, often made of copper, wrapped for protection in an elastomer shell; the cross-section is therefore not homogeneous or isotropic) [151]. Cabling is also heavily used in aerospace engineering so that the aforementioned research topics still apply, but other notable examples of flexible structures in aerospace applications can be cited. Rotating blades, such as the rotating blades of turbo engines or helicopter rotor blades, can be modeled as slender beam structures [13], [155], [183], [229]. Satellite antenna and the wings of flexible aircraft and satellites [3], [182], [223] all constitute examples in which the nonlinear modeling of slender beam structures is critical to the design and functionality of the system. On a smaller scale, slender beam structures can also be found in many electrical engineering applications. They are extensively used in nano and microelectromechanical systems (NEMS and MEMS, respectively) [61], [85], [137]. Some examples of slender beam structures in NEMS and MEMS that have recently appeared in the literature incude nanotubes and nanowires [244] and microcantilevers [148], [149] for various applications. Furthermore, electromechanical systems coupling large amplitude beam structures with piezoelectric elements are extensively studied for energy harvesting applications [61], [67], [85], [99], [139], [257].

Beyond strictly industrial applications, it is also of interest to the general field of mechanics to study the behavior of slender beam structures since they represent a highly nonlinear mechanical struc-

ture that manifests certain phenomena characteristic of nonlinear dynamics. The general study and analysis of these nonlinear phenomena can fuel better understanding of them and eventual industrial exploitation beyond the current state of technology. Some of these characteristic nonlinear phenomena include oscillation frequency dependence on the amplitude or energy of the system, interactions between nonlinear modes via transfers of energy (internal resonances), bifurcations, changes in stability and the existence of multiple solutions, jumps, discontinuities and eventual chaos. Many of these phenomena are discussed in textbooks on nonlinear vibrations, such as the classic *Nonlinear Oscillations* of Nayfeh and Mook [162] or Thomsen [231] and the reader is referred to the recent work [22] for a stability analysis compatible with large systems containing many degrees of freedom (such as large finite element systems). Some of these nonlinear phenomena are encountered in the work of this thesis and are examined in further detail in §2. Finally, the study of slender beam structures is useful in the development of nonlinear reduced order models. In situations where the solution is complex or computationally expensive, where reference solutions must be computed with a finite element (FE) software package, nonlinear reduced order models are of particular interest. A comprehensive review of model order reduction techniques for geometrically nonlinear structures is found in [236], but §2.4.2 expands on the topic of nonlinear reduced order models and particularly the nonlinear normal mode.

To model the nonlinear dynamics of slender beam structures, analytical approximations can be found in the literature (*e.g.* the Crespo da Silva model of § 2.1.4), but these are often limited in accuracy to moderate rotations at most. Fully numerical models capable of modeling the nonlinear dynamics of 1D slender beam structures up to any rotation amplitude are needed, especially efficient numerical models, since many existing methods come with a heavy computational cost. This gap in the literature, coupled with the plethora of applications heretofore cited, provides the motivation for this thesis.

1.2.1 State of the art and novelty

The literature concerning the mechanics of beam structures embodies a huge volume of modeling and solving strategies that far exceeds the scope of this thesis. Even when focusing the ambit to beam structures in large rotation, the literature remains vast. Many different models have been proposed in the literature and especially different approaches in deriving the governing equations. In particular, the differences lie in defining the strain measurement-constitutive law-stress measurement relationships. We here group together some of the most common families of approaches that help to position the work of this thesis in the literature.

In one group, geometrically nonlinear models whereby the constitutive law is imposed in order to relate the stress and strain measurements are grouped together. These number among them the models based on the well-known Cosserat rod theory of the Cosserat brothers [43] and the analytical inextensible elastica first developed by Crespo da Silva and Glynn [46], [47]. In the Cosserat rod model, assuming that one direction (called here axial or longitudinal) is much larger than the two others, the kinematics of the beam are written based on the displacement of the beam centerline and the motion of the cross-sections along the centerline, motion which is governed by a local reference frame called directors (see Fig. 2.3)). The constitutive relation relating stress resultants and strains is imposed, in some cases having been determined experimentally [151], [156], in order to find the forces and moments (see *e.g.* [132]). The Cosserat rod model captures the effects of extension and shearing as a generalization of Timoshenko beams, an extension of the Kirchhoff rod model, which captures only the effects of bending and torsion (and possibly extension, depending on if it is the *extensible* or *inextensible* Kirchhoff model [131], [254]). Another model, originally developed by Crespo da Silva

and Glynn for the nonlinear non-planar oscillations of beams up to moderate rotations [46], [47], uses the same strain measurement as that used in the Cosserat rod theory and the constitutive law is once again imposed. In [46], [47], the purpose was to develop governing equations suitable for a perturbation analysis and was used widely in the literature for the nonlinear analysis of beam dynamics up to moderately large rotations [24], [42], [53], [54], [229].

In another group, geometrically nonlinear models are collected together which are formulated organically from a 3D continuum mechanics perspective, either based on Euler-Bernoulli or Timoshenko kinematics for the beam. Here, the cross-section kinematics and the 3D nonlinear continuum mechanics equations guide the derivation of the model, such that the stress measurement is a priori determined based on the choice of the strain measurement (*i.e.* the one energetically conjugated to it). The proposed formulation of this thesis falls into this group. In our case, the formulation is based on a consistent linearization of the Green-Lagrange strain tensor, energetically conjugated to the second Piola-Kirchhoff stress tensor and a linear elastic constitutive law. Other works utilize Biot stresses and strains, which in certain conditions (as in the case of Euler-Bernoulli kinematics [229] or Timoshenko kinematics working under the assumption of small strains [107], [229]) are equivalent to the consistent linearization of the Green-Lagrange strains. The paper of Irschik and Gerstmayr [114] addresses these topics in an approachable way.

Although it can be difficult to sort through the various approaches to large rotation beam models, the final governing equations of each approach based on judicious selection of appropriate strain measurements and constitutive relations take the same final form. The differences are then tied to how the equations are solved or what simplifications are postulated. In this regard, one particular model called the *geometrically exact* or sometimes called the *Reissner-Simo* beam model based on the original formulation of Reissner [191], [192] and extended to 3D by Simo and Vu-Quoc [219], [220] is highlighted here. Within the umbrella of geometrically exact models, models called *Reissner-Simo* in the literature typically include the effects of shearing (based on Timoshenko beam kinematics), whereas models known as *Kirchhoff-Love* typically do not (based on Euler-Bernoulli beam kinematics) [131], [156], [242]. In general, in the geometrically exact model, no simplifications are made to the geometrical nonlinearities of the system, so that the behavior remains exact regardless of the extent of the rotation of the beam cross-sections. The geometrically exact model is at the heart of many recent works (*e.g.* [68], [69], [253] or see [135], [156]) concerning large rotations of flexible beam structures, and serves as the foundation of the approach taken in this thesis. Since the rotations in the geometrically exact model are arbitrarily large, another subject of research regards parametrization of the rotation terms (*i.e.* how the rotations are represented in the governing equations) [14], [135]. In this respect, the different approaches can be mathematically complex; some such approaches include rotation parametrization via rotation vectors, Euler angles, Rodrigues parameters (see *e.g.* [101]), unit quaternions [35], [45], [83], [100], [101], [132], [197], [261], [263] and Lie group methods [30], [33], [200], [221], but research is actively ongoing.

Finally, a strategy for solving the nonlinear equations of motion must be defined. In general, the nonlinear equations describing highly flexible structures cannot be resolved using straightforward, closed-form analytical methods. Alternate numerical strategies must then be proposed and here the approaches in the literature can vary. To carry out a spatial discretization of the model, finite element methods are popular [21], [27], [48]–[50], [66], [79]–[81], [116], [156], [198], [210], [211], or other numerical techniques such as finite differences [131], [132] or Galerkin techniques [69], [71] are found in the literature. Commercial finite element software can also be used, but for complex systems, the computational cost is sometimes prohibitively large and more efficient strategies are desired. Numerical

resolution of the discrete equations branches yet again when considering strategies for solving time-dependent dynamic systems (in contrast to static simulations, where the time-independent equations can be solved *e.g.* with continuation methods [45]). Time integration schemes are extensively used [30], [131], [142], [199], [200], [221], [262], but frequency domain strategies to solve periodic systems can also be advantageous. Frequency domain strategies directly target the steady state of the periodic solution and therefore can represent an efficient and attractive strategy for modeling the nonlinear dynamics of vibrating systems, yet the literature in this field is lacking. Some works involving frequency domain simulations of highly flexible beams have been published recently, but these are restricted to the dynamics of highly flexible cantilevers [69]–[71], [82].

The various numerical solving strategies found in the literature each have their advantages and disadvantages and the choice is generally made in light of certain numerical properties. For example, depending on the model's eventual application, certain numerical "choices" can be made, such as, among many others:

- the choice of interpolations in a finite element method, such as objectivity-preserving interpolations [50], [83], [104], [116], [142], [199] or the more simple polynomial interpolations [45], [229] (this subject is discussed in § 2.3.2),
- a numerical time integration algorithm that is energy-momentum conserving [50], [142], [264],
- frequency domain-based solving methods to compute periodic solutions [41], [97], [121].

Some of the most common solving techniques are presented in § 2.2.

The novelty of this thesis resides precisely in the solving of a finite element discretization of the geometrically exact beam equations *in the frequency domain*. In this case, we are interested primarily in the large amplitude periodic vibrations of slender, highly flexible beam structures. The frequency domain strategy is automated by the MANLAB solver [96] (discussed in more detail in § 2.2.4), which is based on a truncated Fourier series expansion of the unknowns in a process called the Harmonic Balance Method and solved using a scheme for the continuation of periodic solutions called the Asymptotic Numerical Method [37], [38], [41], [55], [121]. The solving procedure implemented in MANLAB is efficient, can be applied to a wide variety of nonlinear systems and allows for bifurcation and stability analysis during continuation [22], [97].

In conjunction with numerical simulations, experimental analysis is also of great importance in studying general mechanical systems, but especially highly flexible beam structures. The unique nonlinear phenomena exhibited by these structures in numerical simulations can be recreated and validated with dedicated experiments. Many works in the literature have investigated with experiments the dynamics of flexible beam structures, some of which include [11], [12], [53], [54], [70], [71], [150], [205], [226], [246]. Although recent works have been able to match experimental large amplitude dynamics of cantilever beams to numerical simulations [70], [71], more work is nevertheless needed to further understanding of the nonlinear behavior of flexible structures. In particular, we are interested in developing an experimental protocol that both agrees with numerical simulations and can also be extended to many different flexible systems. A more in-depth review of the literature is discussed in Chapter 6 with relation to the concepts involved in our experiments.

1.2.2 Research objectives

The research objectives of this thesis are next defined in order to demonstrate how the the thesis can respond to the industrial need of §1.2. Basing the work of this thesis on previous related work (finite

element modeling of fan blades in moderate amplitude vibration [225], static modeling of cables and cable bundles [44]), we elect to choose as our model the *geometrically exact beam model* where the dynamic equilibrium equations are derived naturally from a *nonlinear continuum mechanics perspective*, which is then discretized into *finite elements* and solved, as efficiently as possible, in the frequency domain to target *periodic solutions*. In addition, we are interested in an *experimental analysis* of flexible beam structures in order to better enrich our understanding of their unique dynamical behavior. Finally, we aim for a *general mastery of the nonlinear behavior of flexible beam structures* through investigation of nonlinear phenomena.

In summary, the principal research objectives of this work are to:

1. Develop a novel modeling strategy for the simulation of large amplitude nonlinear dynamics of slender 1D beam structures based in the frequency domain. The geometrically exact beam model is used in order to capture the geometrical nonlinearities of the system in large rotation and discretized into finite elements. The finite element equations of motion are solved in the frequency domain in order to directly target the steady-state periodic solutions of the system. The solving procedure consists of a Harmonic Balance (HBM) Fourier series expansion, which is then solved with a continuation strategy called the Asymptotic Numerical Method (ANM), all of which is automated by the MANLAB solver [96].

2. Validate the proposed numerical modeling strategy with dedicated vibration experiments involving flexible beam specimens subjected to periodic excitation. Experimental validation can add value to numerical models by confirming their capacity to predict physical reality. To this end, the experiments are used to investigate nonlinear phenomena predicted by the numerical model (experimentally-determined nonlinear modes, couplings between modes, instabilities, etc).

3. Characterize, investigate and otherwise generally explore the highly nonlinear dynamical behavior of slender 1D beam structures and the nonlinear phenomena they exhibit.

1.3 Nonlinearities in solid mechanics

First, we introduce the subject of nonlinearities in the field of solid mechanics, including a general definition of what it means for a system to be nonlinear and some common nonlinearities found in mechanical systems. In general, it is considered easier to define a nonlinear system as *one which is not linear* rather than beginning with a definition of nonlinear systems themselves. Linear systems are found in a variety of applications beyond mechanics, but often represent a mathematical idealization of something which in reality is nonlinear. From a mathematical perspective using a "black box" analogy, a linear black box system governed by the transfer function $H(s)$ (where the s indicates the transformation from the time domain to the Laplace domain) exhibits two fundamental properties, specifically that (1) scaling the input to the system leads to the output being scaled by the same factor, and (2) the addition of multiple inputs to a linear system results in the addition of the corresponding outputs. Taken together, these properties make up the principle of superposition, so that a system can be said to be linear if it obeys the principle of superposition.

In the context of dynamics, the linear system, then, fully preserves the harmonic content of the input signal. The classic example is that of a sinusoidal input of a certain frequency Ω: if the sinusoidal signal $x_1 = A\sin(\Omega t)$ is transmitted to the linear system governed by the transfer function $H(s)$, the output $y_1 = B\sin(\Omega t + \varphi)$ is also a sinusoid, thus preserving the harmonic content of the

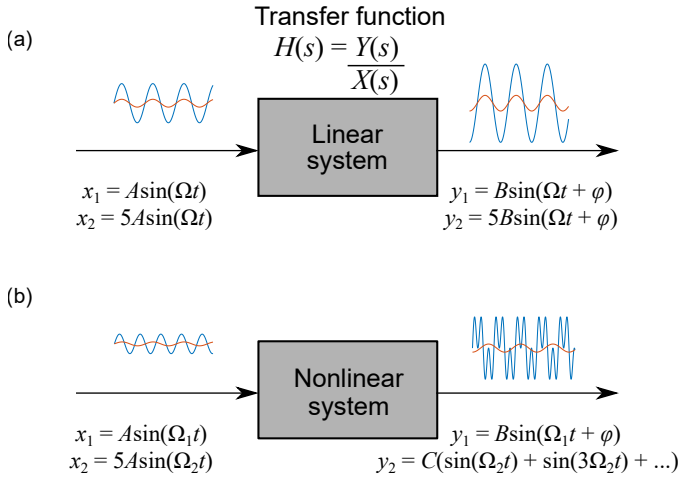

Figure 1.3: Linear and nonlinear representations of a "black box" system, (a) linear system, (b) example of a nonlinear system.

input x_1; the linear system induces a change only in the amplitude and/or phase of the sinusoidal signal. Furthermore, the linear system obeys the two aforementioned fundamental properties, so that if the input is scaled such that $x_2 = 5x_1 = 5A\sin(\Omega t)$, the output is scaled by the same factor $y_2 = 5y_1 = 5B\sin(\Omega t + \varphi)$ as shown in Fig. 1.3(a).

A dynamic system is said to be *nonlinear* then if it is not linear, that is, if it does not obey the above properties [Fig. 1.3(b)]. In this case, the harmonic content of the input signal is not preserved, which can lead to harmonic distortions present in the output signal or other nonlinear phenomena such as quasi-periodicity, discontinuities, bifurcations and chaos. In this case, the output of a nonlinear system is dependent on the input; an example of this, which is of particular importance in the applications studied in this thesis, is the dependence of the natural frequencies of a nonlinear system on the amplitude of vibration. This last phenomenon is especially important when characterizing a nonlinear dynamical system using the concept of the nonlinear normal mode (see §2.4.2).

1.3.1 Types of nonlinearities

Restricting the discussion to the types of nonlinearities encountered in solid mechanics, three major groups are identified:

Material nonlinearities Material nonlinearities indicate that the constitutive relation relating the mechanical stresses to the strains is itself nonlinear. Some common mechanical examples are mentioned here:

- Nonlinear (elastic/viscoelastic) materials: in some cases, even though deformations of certain materials are fully reversible, the relation between stress and strain (*i.e.* the constitutive law itself) is nonlinear. A famous example of this is the viscoelastic elastomer (*e.g.* rubbers).
- Plastic materials: many materials (notably metals) exhibit a region of elasticity (where the stress-strain relation is typically linear and the deformation is fully reversible) and a region of plasticity once the elastic limit on the stress-strain curve has been surpassed. Once reached, plastic deformation is irreversible and the relation between stress and strain becomes nonlinear.

- Smart alloys/shape-memory alloys: a unique set of materials are those termed "shape-memory alloys" or "smart alloys," whose crystalline structure transforms under certain thermo-mechanical influences (*e.g.* heating and cooling, applied mechanical loads). In these cases, often the transformation is reversible, but the material changes themselves introduce a hysteresis in the stress-strain relation, making it nonlinear.

Contact nonlinearities Contact nonlinearities arise in situations where different components or different bodies of a structure or system come into contact at an interface. The type of contact can vary: some common forms of contact between different components or surfaces include dry friction, which resists the motion of two solid surfaces in contact, sliding contact such as between two structures sliding relative to one another at a contact interface and intermittent contact, where objects in motion habitually come into contact with one another often at the same interface. Dry friction is most often represented by the simple Coulomb model. While the objects in contact may go through periods of sticking and slipping (and, therefore, the friction is irregular), in many cases the simple Coulomb model of dry friction suffices for useful applications in industry.

Geometrical nonlinearities Geometrical nonlinearities, which represent the main nonlinearities encountered in this work, define the types of nonlinearities considered when the motion of a mechanical system is of large amplitude. Examples can be given both for systems composed of rigid bodies in large rotation (*e.g.* the simple pendulum, where the nonlinear dynamic equation $\ddot{\theta} + \omega_0^2 \sin\theta = 0$ with $\omega_0^2 = g/L$ cannot be linearized using $\sin\theta \simeq \theta$ if the rotation θ is large) and mechanical structures undergoing large amplitude displacements (*e.g.* slender 1D beams or 2D plates and shells). The geometrical nonlinearities found in numerous industrial applications (§ 1.2) often are not encountered alone, but are coupled with other types of nonlinearities. For example, a flexible beam structure subjected to large displacements and made of an inelastic material [151] combines geometrical with material nonlinearities, or the contact between human hairs modeled as flexible beam structures joins together potential geometrical nonlinearities with contact [26].

Coupling and other nonlinearities Beyond these, there are, of course, other types of nonlinearities, such as those due to interactions between a mechanical system and its environment (*e.g.* fluid-solid interactions, nonlinear damping [42]) or couplings with other types of systems (*e.g.* electro-mechanical couplings [85]). Nonlinearities are also sometimes intentionally added into a system to be exploited for their behavior; a well-known example of this is nonlinear vibration absorbers (*e.g.* nonlinear energy sinks [212]) that make use of the interaction between nonlinear modes in order to attenuate vibrations. However, these latter types of nonlinearities are not discussed in this work.

1.3.2 Geometrical nonlinearities encountered in flexible beam structures

Recall from §1.1 that the hallmark of flexible, slender 1D beam structures is their extreme capacity for bending. In such systems, naturally the nonlinearities that arise are geometrical, tied to the large displacement amplitude of the transformation. Two principal types of nonlinear mechanisms are typically discussed in the study of flexible 1D structures, that of (i) an *axial-bending* or *membrane-bending* coupling, or of (ii) very large rotations of the beam fibers due to large displacement of the beam. In the case of 1D slender structures, it is typically the physical problem itself which determines the dominant nonlinear mechanism encountered:

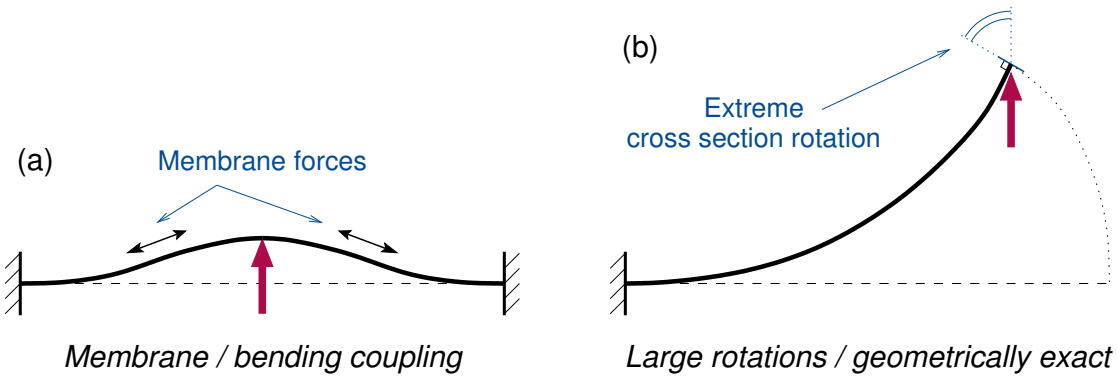

Figure 1.4: Geometrical nonlinearities encountered in flexible beam structures, (a) axial-bending coupling mechanism (von Kármán models), (b) large rotations mechanism (geometrically exact models).

(i) Axial-bending coupling (Fig. 1.4(a)): in cases where the longitudinal direction is fixed, transverse displacements cause the beam to stretch and the length of the beam to increase, generating tension or "membrane" forces in the length of the beam, forces which are nonlinearly related to the transverse displacement when it is on the order of the thickness of the beam. In order for this nonlinear mechanism to be activated in 1D structures, the longitudinal direction *must be blocked* by the boundary conditions of the problem (*e.g.* the clamped-clamped beam of Fig. 1.4(a)). This mechanism is also commonly found in flexible two-dimensional (2D) structures (*e.g.* flexible plates and shells). In such cases, the von Kármán model [36], [228], [229], first developed to model plates [122] and shells [154], proposes an efficient truncation of the nonlinear term of the Green-Lagrange strains.

The large rotations are not the principal mechanism of geometrical nonlinearity in this case as the rotations of the cross-sections with the longitudinal direction blocked do not reach the amplitudes of other conditions, like the clamped-free condition of the cantilever beam (compare the disaplacements of the centerlines between Figs. 1.4(a) and (b)). In fact, in the von Kármán model, the rotations are linearized, so that the definition of the curvature κ of the beam becomes:

$$\kappa = w'', \tag{1.1}$$

where w is the transverse displacement of the centerline of the beam (the derivation of the von Kármán model is shown in § 2.1.4). The curvature κ is related to the bending moment M according to the constitutive law of the material (see Eq. (2.15b): $M = EI\kappa$), so that the relationship between the bending moment and the displacements is linear. The source of the nonlinearity in the von Kármán model is the *axial-bending coupling* term, without which the model becomes linear.

(ii) Large rotations (Fig. 1.4(b)): in cases where the longitudinal direction is not fixed and the axial-bending mechanism is not activated, the geometrical nonlinearities are activated instead by the sheer amplitude of rotation of the beam cross-sections. We often cite the classical example of the cantilever beam: since one end of the cantilever is free, it can reach displacements on the order of the length of the beam, which translates to nonlinear rotation terms that become significant the more the beam is displaced. In this case, more nonlinear terms than what is proposed by the von Kármán model should be kept in the Green-Lagrange strains to accurately model the nonlinear

behavior. The geometrical nonlinearities engendered by the large rotations of the cross-sections are complex to resolve; alternate ways to parameterize the rotation terms and solve the nonlinear system comprise an active and prominent subject of research as discussed in § 1.2.

The geometrical nonlinearities in the large rotation models translate to two nonlinear mechanisms in the equations: nonlinearities tied to the curvature κ and nonlinearities related to inertia (in particular translational kinetic energy):

- In the former, the curvature itself is nonlinear (being defined as a nonlinear function of the displacements of the centerline), so that the bending moment is likewise a nonlinear function of the displacements. Based on Euler-Bernoulli kinematics, the curvature in the large rotation model is given by [130]:

$$\kappa = \frac{w''(1+u') - u''w'}{(1+u')^2 + (w')^2}, \tag{1.2}$$

  which is easily seen to be a nonlinear function of the axial u and transverse w displacements. This contrasts greatly with the aforementioned von Kármán model, where κ is linearly related to w''.
- In the latter, the terms governing the translational kinetic energy ($\rho A\ddot{u}$ and $\rho A\ddot{w}$ in Eqs. (2.16b) and (2.17)) translate to nonlinearities in the equations due to the extreme amplitude of the motion.

The analytical inextensible model of § 2.1.4 (restricted to in-plane motions) highlights these two mechanisms nicely due to the strong form of the beam equations being reduced to only a single equation in w; the nonlinear nature of the axial inertial term $\rho A\ddot{u}$ shows up clearly in Eqs. (2.21) and (2.22).

1.4 Outline of the thesis

Having introduced the motivation behind the work of this thesis, its relevance in modern industry, the anticipated challenges and specific research objectives of the thesis along with generalities on the field of nonlinear dynamics and nonlinear beam mechanics, we proceed to laying out in detail the work that was carried out in this regard. The work of this thesis is divided into several chapters on the basis of chronological order, so that the work of later chapters naturally builds on the work of earlier chapters. Chapter 2 aims to outline the basic tools and topics needed to understand the work of the thesis; the general governing equations involved in the modeling and solving of nonlinear beam dynamics are developed and an overview of several moderate-to-large rotation beam models commonly found in the literature is provided along with their assumptions, simplifications, advantages and limitations. The ideas, models and solving methods described in Chapter 2 make several appearances in later chapters of this thesis. Beyond this, Chapters 3 - 6 detail the scientific journey undertaken during the thesis:

- Chapter 3 outlines the full development and implementation of the finite element discretization of the geometrically exact beam model for the numerical modeling of beam structures in large amplitude vibration. In this chapter, the model is restricted to in-plane motions in two dimensions. The specifics of the model, discretization and solving procedure are described and assessed using several test cases.

- Chapter 4 represents an application of the two-dimensional (2D) model presented in Chapter 3 in order to study the effect of gravity and slenderness on the large amplitude dynamics of flexible vertical cantilevers. The nonlinear behavior of the vertical cantilevers is investigated with particular emphasis on using the results to better define the dedicated experiments of Chapter 6.
- Chapter 5 extends the 2D model of Chapter 3 into three dimensions (3D). An alternate method of parametrizing the rotation terms based on quaternions is presented and tested on simple test cases. In addition, the 3D formulation involving quaternions restricted to in-plane motions is derived in order to compare to the rotation parametrization of Chapter 3.
- Chapter 6 discusses experimental validation of the numerical model based on 2D in-plane motions. The numerical model of a cantilever vibrating at large amplitude on its first three nonlinear modes is compared to experiments involving a flexible ruler excited on the three nonlinear modes with a shaker table. The experiments make use of a technique in vibration control in order to measure the nonlinear modes experimentally.

Finally, a summary of the main results and final remarks are presented in the conclusion along with a vision on future studies that have as their foundation the work undertaken during this thesis.

Chapter 2

Modeling of flexible beam structures: modeling and resolution of geometrical nonlinearities

Sections 1.2 and 1.3.2 centered the focus of our study on the nonlinear dynamical analysis of flexible slender beam structures. Recall that, moving forward, the nonlinearities encountered in the flexible beam structures studied in this work are the geometrical nonlinearities described in §1.3.2. Other types of nonlinearities can of course be considered and often are in many industrial applications (recall § 1.3.1); here, however, the study is restricted to elastic isotropic materials where the constitutive law is linear and does not consider contact. Thus, the focus remains solely on the geometrical nonlinearities. Examples of the types of beam structures considered in this work are shown in Fig. 2.1.

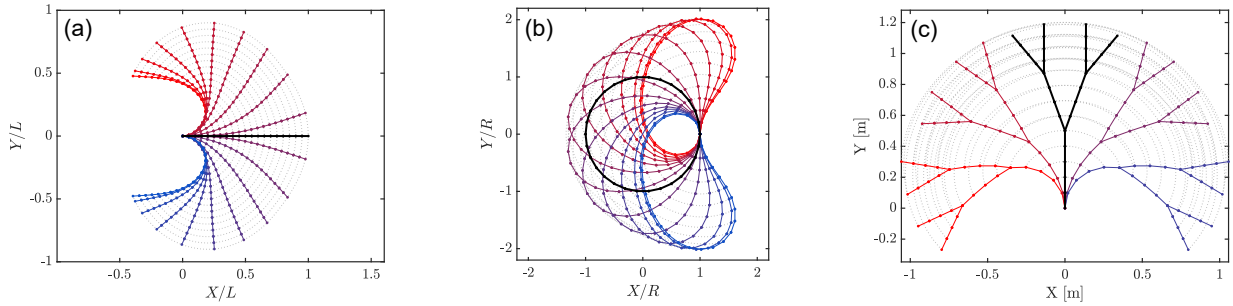

Figure 2.1: Deformed shapes of slender flexible beam structures, (a) first nonlinear mode of a cantilever beam, (b) first nonlinear mode of a flexible ring, (c) first nonlinear mode of a flexible tree.

The aim of this chapter is to present the most important modeling and solving strategies encountered in this work for the simulation of highly flexible slender beam structures. The topics of this chapter represent the main tools for understanding the work of this thesis.

In § 1.1, the flexible slender beam structure is defined as a deformable beam where one dimension of its geometry (usually the length of the beam) is exceedingly large compared to the other two dimensions, allowing the possibility for very large displacements. The geometrically exact beam model is in this case the ideal model as there is no simplification of the rotation terms, meaning that it accurately models the behavior of the beam at any amplitude of displacement. In § 1.2.1, it is

indicated that there are multiple ways of deriving the geometrically exact beam equations. In this chapter, we will show beginning in § 2.1 how the geometrically exact beam equations can be derived through a systematic reduction to 1D of the 3D nonlinear continuum mechanics equations. Kinematic distinctions and some "special case" models derived from simplifications of the geometrically exact model are also presented in § 2.1. Next, common methods used to resolve nonlinear differential equations are discussed in § 2.2, and a systemic overview of the solving procedure used in this thesis is outlined. Some considerations regarding numerical implementation of the geometrically exact model are addressed in § 2.3. The types of solutions that are sought in the work of this thesis are described in § 2.4, including the main concepts related to nonlinear normal modes which are important for understanding later chapters of the thesis. Finally, a summary of the main points of this introductory chapter to recall moving forward is provided in § 2.5.

Table of Contents - Chapter 2

2.1 Modeling of beam structures: generalities and some models

In this section, we lay the foundation for modeling highly flexible slender beam structures. The general procedure to systematically derive the 1D geometrically exact beam model beginning from the 3D nonlinear continuum mechanics equations is outlined. In addition, some particular cases, which are simplifications of the geometrically exact model through the introduction of additional assumptions, are described.

2.1.1 Mechanical modeling of the flexible beam

In order to derive the nonlinear dynamic equations of motion of the deformable beam structure, a continuum mechanics based approach is taken, deriving the beam equations following particularization of the equations for a nonlinear continuum undergoing large displacements. This contrasts with the rather straightforward method of writing the equations of motion for a system composed of a collection of discrete elements (pendulums, spring-mass systems, *etc.*), which are obtained directly via *e.g.* the Euler-Lagrange equations. Although the flexible slender beam structures may undergo very large displacements, the local strains remain small.

Many different models restricted to the motion of a 1D continuum exist for describing the nonlinear behavior of a flexible slender beam undergoing large displacements and in each the prudent definition of hypotheses and assumptions can be used to simplify the full (geometrically exact) model. The general procedure for deriving each 1D model, however, remains the same and is as follows:

1. The kinematics reduced to the displacements of the centerline of the beam, denoted here as $\mathbf{u}$, are written, with any point lying in the cross-section being related back to the displacement of the corresponding centroid of the cross-section,
2. the strain measurement is selected and the strains computed based on the displacements $\mathbf{u}$,
3. a constitutive law appropriate for the material under consideration is selected in order to relate the mechanical stresses to the strains,
4. the stress measurement is selected and related to the computed strains using the aforementioned constitutive relation, and the general stress resultants are computed,
5. the equations of motion are defined using the variational formulation based on the principle of virtual work, making use of the definitions of the general stress resultants and the variation of the displacements and the strains.

The global hypotheses, compatible with both Euler-Bernoulli and Timoshenko kinematics, can then be summed up as follows:

Assumption #1

> The cross-sections undergo a rigid-body motion with the displacement $\mathbf{u}$ governed by Eq. (2.6).

Assumption #2

> The normal stress in the directions perpendicular to the longitudinal direction (*i.e.* the two transverse directions $\mathbf{u}_y$ and $\mathbf{u}_z$) are neglected, being considered small in front of the principle direction $\mathbf{u}_x$, so that:
>
> $$S_{yy} = S_{zz} = 0. \tag{2.1}$$

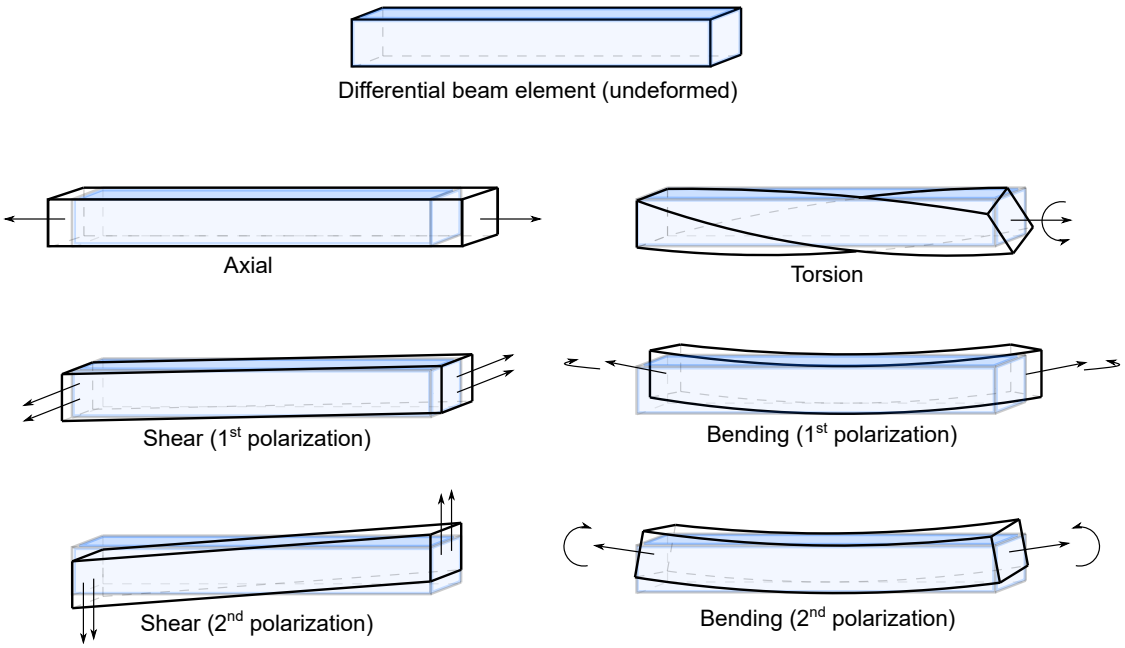

Figure 2.2: Deformation modes of a differential beam element in 3D.

Assumption #3

> Although the cross-sections of the 1D beam continuum are subjected to rotations of any given amplitude, the local strains of the continuum remain small throughout the motion.

Assumption #4

> The beam is homogeneous and made of linearly elastic and isotropic material, so that a linear constitutive law is valid.

2.1.2 Governing equations based on a total Lagrangian formulation: beginning from a 3D continuum

Variational formulation We seek to derive the dynamic equations of motion in the weak form using the principle of virtual work, which is written for all time t and for all virtual displacements $\delta\mathbf{u}$:

$$\delta W_e - \delta W_i - \delta W_a = 0, \tag{2.2}$$

with δW_i, δW_a and δW_e the virtual work of internal, inertial and external forces, respectively, defined as:

$$\delta W_i = \int_V \mathbf{S} : \delta\mathbf{E}\, \mathrm{d}V, \tag{2.3a}$$

$$\delta W_a = \int_V \rho\ddot{\mathbf{u}} \cdot \delta\mathbf{u}\, \mathrm{d}V, \tag{2.3b}$$

$$\delta W_e = \int_V \mathbf{f}_b \cdot \delta\mathbf{u}\, \mathrm{d}V + \int_{\partial V} \mathbf{f}_s \cdot \delta\mathbf{u}\, \mathrm{d}S, \tag{2.3c}$$

where V represents the domain of the reference configuration of the 3D continuum, ∂V its surface frontier and $\mathrm{d}V$ a differential volume of it, $\delta\mathbf{E}$ the variation of $\mathbf{E}$, the Green-Lagrange strain tensor, and $\mathbf{S}$ the second Piola-Kirchhoff stress tensor, energetically conjugated to $\mathbf{E}$, $\ddot{\mathbf{u}} = \partial^2\mathbf{u}/\partial t^2$ is the acceleration of the considered point, ρ the density of the material, $\mathrm{d}S$ a differential area of the surface, and $\mathbf{f}_b$ and $\mathbf{f}_s$ the external body and surfaces forces, respectively. The choice of the Lagrangian tensors $\mathbf{E}$ and $\mathbf{S}$ is tied to the description of the motion relative to the initial reference configuration at $t = 0$ since this configuration is known, whereas the current configuration of the continuum is unknown.

Strain measurement We consider that any differential element of the beam can deform in 6 different ways: three translational deformations comprising axial deformation and shear deformation in two polarizations, and three rotational deformations comprising a curvature due to torsion or twisting and bending curvatures in two polarizations. These modes of deformation are shown in Fig. 2.2. For movement fixed in the plane, naturally the number of deformation modes reduces to three: axial deformation, shear deformation in the in-plane polarization and curvature due to in-plane bending. The other polarizations of bending and shear and the twist due to torsion involve out-of-plane deformation and are not considered in plane motions.

The Green-Lagrange strain tensor $\mathbf{E}$ is used to describe the deformation of a continuum undergoing large displacements, as is the case here, and is written:

$$\mathbf{E} = \frac{1}{2}\left(\mathbf{F}^{\mathrm{T}}\mathbf{F} - \mathbf{I}\right) = \frac{1}{2}\left(\nabla\mathbf{u} + \nabla^{\mathrm{T}}\mathbf{u} + \nabla^{\mathrm{T}}\mathbf{u}\nabla\mathbf{u}\right), \tag{2.4}$$

where $\mathbf{F} = \mathbf{I} + \nabla\mathbf{u}$ is the deformation gradient tensor, $\mathbf{I}$ the identity matrix, $\nabla\mathbf{u}$ the gradient of the displacements $\mathbf{u}$ and $^{\mathrm{T}}$ indicates the transpose of a vector or matrix. Notice that the last term of Eq. (2.4) $\nabla^{\mathrm{T}}\mathbf{u}\nabla\mathbf{u}$ is quadratic with respect to $\mathbf{u}$. $\mathbf{E}$ remains valid for any amplitude of rotation of the beam continuum, even in cases where the rotation is extremely large.

Constitutive law Finally, the constitutive law relating $\mathbf{E}$ and $\mathbf{S}$ is indicated. Since, in this work, the study is restricted to continua of elastic isotropic (and homogeneous) material (Assumption #4), a linear Kirchhoff-Saint-Venant constitutive relation is used, which takes the general form:

$$\mathbf{E} = \frac{1+\nu}{E}\mathbf{S} - \frac{\nu}{E}\mathrm{tr}(\mathbf{S})\mathbf{I}, \tag{2.5}$$

with E the Young's modulus of the material and ν the Poisson's ratio.

2.1.3 Geometrically exact beam model (or large rotation model): reduction to a 1D continuum

Having selected the appropriate stress and strain measurements and constitutive relation, we can proceed with the 5-step procedure of §2.1.1 to derive the geometrically exact model based on the kinematics of the centerline of the beam. In what follows, for simplicity, the motions are restricted to 2D in-plane motions in order to more easily derive the beam equations. The geometrically exact model for motions in 3D is derived later in Chapter 5.

The structural model based on the 3D continuum occupying the domain V is now reduced to a 1D continuum whose kinematics are governed by (i) the displacement of the centerline curve on which each point C is defined by the curvilinear abscissa $x \in [0, L]$ with L the length of the beam, and (ii) the orientations of a collection of cross-sections, where each cross-section located at x is a plane

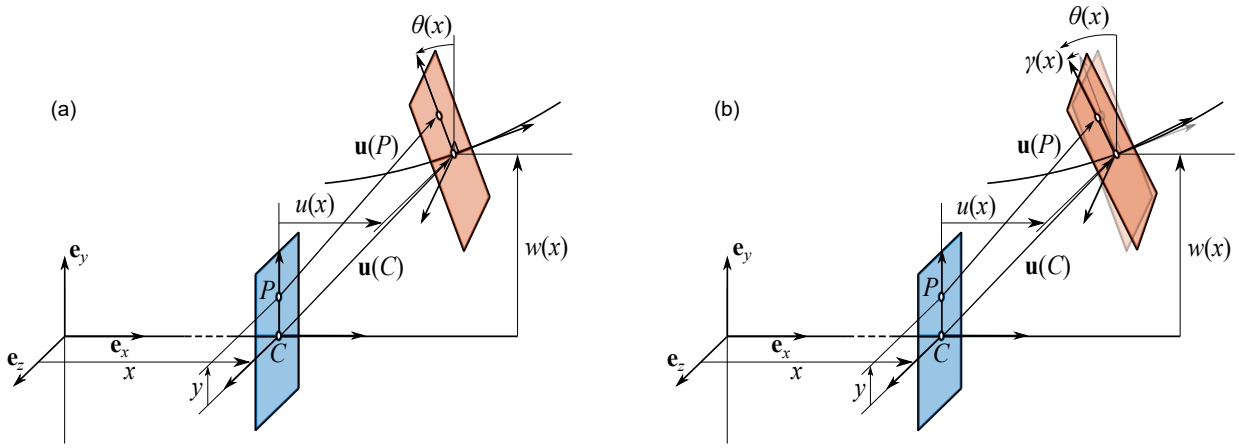

Figure 2.3: 2D beam kinematics, (a) Euler-Bernoulli, (b) Timoshenko.

(2D) surface whose centroid passes through C on the centerline. In the reference configuration, the cross-section plane at x is orthogonal to the centerline curve.

In the geometrically exact model, the geometrical nonlinearities tied to the large rotations of the cross-sections are kept exact without any truncation or simplification of the rotations (hence "geometrically exact"). This model, therefore, accurately describes the transformation of the beam *regardless of the amplitude of the rotation*. Even for cases of extreme rotation, such as a cantilever beam "bending backwards" beyond its fixed end [Fig. 2.1(a)], the geometrically exact model remains accurate. The difficulty of this model is then tied to how the rotation terms are modeled; in 2D, this is rather straightforward since there is only one rotation to be accounted for (θ). Different methods for rotation parametrization in 3D exist, however, and represent one of the main challenges of the geometrically exact model (see § 1.2.1).

Kinematics Referring to Fig. 2.3, we consider a cross-section of a beam of length L located at x. The displacement of any point P in the cross-section is written:

$$\mathbf{u}(P) = \mathbf{u}(C) + [\mathbf{R}(\theta) - \mathbf{I}]\,\mathbf{CP}, \tag{2.6}$$

where C is the point in the cross-section of P intersecting the centerline of the beam, $\mathbf{u}(C)$ is the displacement of C, $\mathbf{CP}$ is the vector governing the position of P in the cross-section and $\mathbf{R}(\theta)$ is the rotation operator defining the rotation of the cross-section, given here as the 2D rotation matrix:

$$\mathbf{R}(\theta) = \begin{bmatrix} \cos\theta & -\sin\theta \\ \sin\theta & \cos\theta \end{bmatrix}, \tag{2.7}$$

with θ the angle of rotation of the cross-section. The displacement, then, is written explicitly as:

$$\mathbf{u}(P) = (u - y\sin\theta)\,\mathbf{e}_x + [w + y(\cos\theta - 1)]\,\mathbf{e}_y, \tag{2.8}$$

where $(\mathbf{e}_x, \mathbf{e}_y)$ is the reference frame as defined in Fig. 2.3 and with u and w the axial and transverse displacements, respectively, of C.

In the study of beam mechanics, a distinction is made between two alternate methods of defining the kinematics of the beam. The distinction lies in the incorporation of shearing of the cross-sections

during deformation of the beam. Timoshenko-style kinematics takes into account the effect of shearing, while Euler-Bernoulli kinematics neglects any shearing of the cross-sections (so that the cross-sections always remain perpendicular to the centerline of the beam). This distinction is shown in Fig. 2.3. If using Euler-Bernoulli kinematics, an additional assumption is made, in addition to the previous four:

Euler-Bernoulli Assumption #1

> The cross-sections, perpendicular to the centerline of the beam in the initial configuration, remain perpendicular to the centerline throughout deformation of the beam (*i.e.* shearing is not considered).

It should be noted, however, that in the case of flexible 1D structures, shearing is in general small due to the slenderness of the beam (Assumption #3), meaning that the difference between the two kinematics styles is small. In what follows, the geometrically exact model is presented based on Timoshenko kinematics, but Euler-Bernoulli kinematics could also be used (see § 2.3).

Consistent linearization of the Green-Lagrange strains For the displacement $\mathbf{u}$ of any point P in the beam as defined by Eq. (2.8), the Green-Lagrange strains $\mathbf{E}$ are defined according to Eq. (2.4) without any simplification of the nonlinear terms (in contrast with the von Kármán model, which will be presented in § 2.1.4). It is fully possible to proceed with the full nonlinear Green-Lagrange strains, but, being complex, often a procedure called the "consistent linearization" of the Green-Lagrange strains is carried out to simplify $\mathbf{E}$ when the local strains are small without loss of accuracy [74], [229]. In the consistent linearization, the deformation gradient $\mathbf{F}$ is decomposed into two parts, a rotation tensor governing the rotation of the cross-section $\mathbf{R}(\theta)$ [Eq. (2.7)] and a stretch tensor (denoted here $\tilde{\mathbf{U}}$) independent of the rigid-body transformation:

$$\mathbf{F} = \mathbf{R}(\theta)\tilde{\mathbf{U}}, \tag{2.9}$$

with $\mathbf{R}^{\mathrm{T}}\mathbf{R} = \mathbf{I}$ recalling that $\mathbf{R}$ is orthogonal. Then, $\tilde{\mathbf{U}}$ can be rewritten:

$$\tilde{\mathbf{U}} = \mathbf{R}(-\theta)\mathbf{F} = \mathbf{I} + \mathbf{L}, \tag{2.10}$$

where:

$$\mathbf{L} = \begin{bmatrix} e - y\kappa & 0 \\ \gamma & 0, \end{bmatrix} \tag{2.11}$$

and:

$$\begin{cases} e = (1+u')\cos\theta + w'\sin\theta - 1, & \text{(2.12a)} \\ \gamma = w'\cos\theta - (1+u')\sin\theta, & \text{(2.12b)} \\ \kappa = \theta', & \text{(2.12c)} \end{cases}$$

where $\diamond' = \partial\diamond/\partial x$ is the spatial derivative in $\mathbf{e}_x$, e is the axial strain, γ the shear strain and κ the curvature.

According to this definition, the Green-Lagrange strain tensor $\mathbf{E}$ defined by Eq. (2.4) can be rewritten as:

$$\mathbf{E} = \frac{1}{2}\left(\mathbf{F}^{\mathrm{T}}\mathbf{F} - \mathbf{I}\right) = \frac{1}{2}\left(\tilde{\mathbf{U}}^{\mathrm{T}}\tilde{\mathbf{U}} - \mathbf{I}\right) = \frac{1}{2}\left(\mathbf{L} + \mathbf{L}^{\mathrm{T}} + \mathbf{L}^{\mathrm{T}}\mathbf{L}\right). \tag{2.13}$$

The consistent linearization procedure essentially states that, for cases where the local strains are very small, *i.e.* $e \ll 1$ (small axial strain), $\gamma \ll 1$ (small shear strain) and $y\kappa \ll 1$ (small *thickness*, which does not mean that the curvature κ must necessarily be small), the quadratic part of $\mathbf{E}$ as a function of $\mathbf{L}$ can be removed. According to Eq. (2.11), $\mathbf{L}$ depends only on the terms e, γ and $y\kappa$ and not on the rotation of the cross-sections θ. If the local strain terms are very small, then $\mathbf{E}$ can safely be linearized in $\mathbf{L}$ without neglecting any large rotation terms tied to the rigid-body transformation [229].

$\mathbf{E}$ is then replaced with $\tilde{\mathbf{E}}$, representing the consistent linearization of the Green-Lagrange strains where the term $\mathbf{L}^{\mathrm{T}}\mathbf{L}$ in Eq. (2.13) is removed, written as:

$$\tilde{\mathbf{E}} = \frac{1}{2}\left(\mathbf{L} + \mathbf{L}^{\mathrm{T}}\right) = \begin{bmatrix} e - y\kappa & \frac{\gamma}{2} \\ \frac{\gamma}{2} & 0 \end{bmatrix}, \tag{2.14}$$

where the intervention of the geometrical nonlinearities in the equilibrium equations is now obvious based on the definitions of the strains in Eqs. (2.12).

Stress resultants and weak form of the equations of motion As the Green-Lagrange strains $\mathbf{E}$ are energetically conjugated to the second Piola-Kirchhoff stress tensor $\mathbf{S}$, the consistent linearization $\tilde{\mathbf{E}}$ is likewise energetically conjugated to a stress tensor $\tilde{\mathbf{S}}$ and the linear constitutive law Eq. (2.5) can be applied. It has been shown that the stress resultants of $\tilde{\mathbf{S}}$ in force and moment correspond to the internal forces (axial N, shear T, and bending moment M) that are used in writing the dynamic equations of motion [115], [229], and are written when integrated over the cross-section as:

$$N = \int_A S_{xx}\,\mathrm{d}A = EAe, \tag{2.15a}$$

$$T = \int_A S_{xy}\,\mathrm{d}A = kGA\gamma, \tag{2.15b}$$

$$M = \int_A yS_{xx}\,\mathrm{d}A = EI\kappa, \tag{2.15c}$$

where A is the area of the cross-section and $\mathrm{d}A$ a differential element of it, $G = E/[2(1+\nu]$ is the shear modulus, I the second moment of area and k is the shear coefficient. A byproduct of the shear-deformable Timoshenko kinematics, k accounts for non-uniformity of the shear stresses throughout the cross-section and is usually chosen based on the geometry of the cross-section [119]. The dynamic equilibrium equations are found in the weak form found using Eq. (2.2) and (2.3) as:

$$\delta W_i = \int_V \mathbf{S} \colon \delta\mathbf{E}\,\mathrm{d}V = \int_0^L (N\delta e + T\delta\gamma + M\delta\kappa)\,\mathrm{d}x, \tag{2.16a}$$

$$\delta W_a = \int_V \rho\ddot{\mathbf{u}} \cdot \delta\mathbf{u}\,\mathrm{d}V = \int_0^L \left(\rho A\ddot{u}\delta u + \rho A\ddot{w}\delta w + \rho I\ddot{\theta}\delta\theta\right)\mathrm{d}x, \tag{2.16b}$$

$$\begin{aligned}\delta W_e &= \int_V \mathbf{f}_b \cdot \delta\mathbf{u}\,\mathrm{d}V + \int_{\partial V} \mathbf{f}_s \cdot \delta\mathbf{u}\,\mathrm{d}S \\ &= \int_0^L (n\delta u + p\delta w + q\delta\theta)\,\mathrm{d}x + [N_e\delta u]_0^L + [T_e\delta w]_0^L + [M_e\delta\theta]_0^L\,,\end{aligned} \tag{2.16c}$$

where $n(x,t)$, $p(x,t)$ and $q(x,t)$ are, respectively, the applied axial force, transverse force and moment per unit length, and N_e, T_e and M_e are, respectively, the applied axial force, traverse force and moment loadings at the extremities $x = 0$ and $x = L$. For finite element models, typically the discretization is applied directly to the beam equations in the weak form Eqs. (2.16). This is done in Chapter 3 in 2D and 5 in 3D.

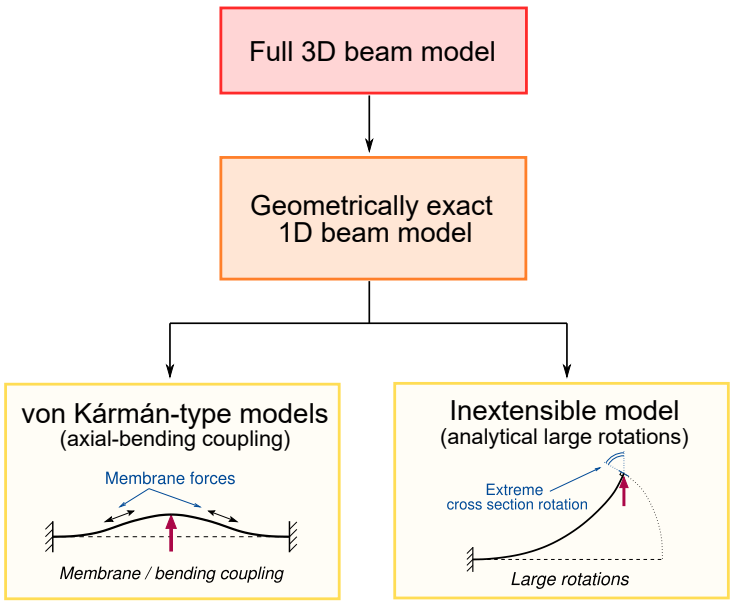

Figure 2.4: Hierarchy of beam models: particular cases as simplifications of the geometrically exact beam model.

2.1.4 Particular beam models as simplifications of the geometrically exact beam model

In this section, two simplified models are introduced, which are special cases of the geometrically exact model. In each, there are additional assumptions besides the four described in § 2.1.1 that simplify in some ways the geometrically exact model and both are based on Euler-Bernoulli kinematics, so that $\gamma = 0$. The two presented in this section (the analytical inextensible model and the von Kármán model) make appearances throughout this work in order to compare in certain cases to the geometrically exact model. A global overview of the hierarchy of the beam models is shown in Fig. 2.4.

Analytical inextensible model (truncation of the large rotation model) One model commonly used in the literature on flexible beam structures (some examples include [24], [42], [53], [54], [229]) is the so-called inextensible beam model proposed by Crespo da Silva and Glynn [46], [47]. In this model, some useful restrictions are placed on the geometrically exact model in order to derive an analytical expression for the transverse displacement of the beam. The nonlinearities are expanded in Taylor series, which enables an analytical depiction of the two nonlinear mechanisms of the beam in large rotation, the nonlinear curvature and nonlinear inertial terms. The truncation of the Taylor series expansion at order three, however, necessarily limits the accuracy of the model; unlike the geometrically exact model, which remains exact for any amplitude of the rotation, at a certain moderately large rotation amplitude the Taylor series approximation begins to break down (this is discussed later in Chapter 4 and Appendix B.3). The assumptions used in deriving the analytical inextensible model, then, are:

Crespo da Silva and Glynn (CdSG) Assumption #1

> The beam is considered to be *inextensible*, that is, the axial strain is considered to be zero ($e = 0$).

Crespo da Silva and Glynn Assumption #2

> A free end boundary condition is assumed at $x = L$, such as *e.g.* a cantilever configuration; this boundary condition is used in deriving the model of [46], [47] (see Fig. 2.4).

Crespo da Silva and Glynn Assumption #3

> The model is based on Euler-Bernoulli kinematics ($\gamma = 0$) and rotational inertia is neglected.

Crespo da Silva and Glynn Assumption #4

> The nonlinearities in the beam equation Eq. (2.21) are expanded in Taylor series and truncated at order 3 in w.

To derive the analytical model, we begin with the strong form of the dynamic equilibrium equations Eqs. (2.16), which is found directly by taking the variations of the strains Eqs. (2.12) and applying the principle of virtual work Eq. (2.2) $\forall t$, $\forall \mathbf{u}$:

$$\rho A\ddot{u} = (N\cos\theta - T\sin\theta)' + n, \tag{2.17a}$$
$$\rho A\ddot{w} = (N\sin\theta + T\cos\theta)' + p, \tag{2.17b}$$
$$\rho I\ddot{\theta} = T(1+e) - N\gamma + M' + q, \tag{2.17c}$$

associated with the boundary conditions of a cantilever beam according to CdSG Assumption #2:

$$u = w = \theta = 0, \qquad \text{at } x = 0, \tag{2.18a}$$
$$N = T = M = 0, \qquad \text{at } x = L. \tag{2.18b}$$

Integrating CdSG Assumption #1, the inextensibility condition is written:

$$e = \sqrt{(1+u')^2 + (w')^2} - 1 = 0, \tag{2.19}$$

leading to the following relationship between u' and w' [59], [229]:

$$u' = \pm\sqrt{1 - (w')^2} - 1. \tag{2.20}$$

Then, using the inextensibility relationship of Eq. (2.20), assuming no external axial load ($n = 0$) or externally applied moment ($q = 0$), applying CdSG Assumption #3 to reduce Eq. (2.17c) to $T = -M' = -EI\theta''$ and using the boundary conditions and Eq. (2.17a) to eliminate N in Eq. (2.17b), Eqs. (2.17) can be reduced to a single dynamic equation:

$$\rho A\ddot{w} + \frac{EI\kappa''}{(\cos\theta)'} - \left[\rho A\tan\theta\int_L^x \ddot{u}\mathrm{d}x\right]' = p, \tag{2.21}$$

recalling that $\kappa = \theta'$. The nonlinearities in Eq. (2.21) are expanded in Taylor series up to order 3 in w (CdSG Assumption #4), from which the model of [46], [47] is obtained:

$$\rho A\ddot{w} + EIw'''' + \underbrace{EI\left[w'\left(w''\right)^2 + w'''\left(w'\right)^2\right]'}_{\text{Nonlinear curvature}} + \underbrace{\frac{\rho A}{2}\left[w'\int_L^x \frac{\partial^2}{\partial t^2}\left(\int_0^\xi \left(w'\right)^2 \mathrm{d}\xi\right)\mathrm{d}x\right]'}_{\text{Nonlinear inertia}} = p. \tag{2.22}$$

The two nonlinear mechanisms of large rotation models (§ 1.3.2) are then easily visualized in this analytical inextensible model. As mentioned above, at a certain amplitude, the truncation at order 3 of the nonlinear terms begins to break down so that this model begins to diverge from the geometrically exact model. For this reason, this analytical model serves as an excellent way of validating *e.g.* a finite element implementation of the geometrically exact model (as done in Chapter 4), but only up to moderately large rotations.

von Kármán-type models (or moderate rotation models) Another model representing a particular case of the geometrically exact model is the von Kármán model [86], [122], [228], [229]. Recall from §1.3.2 that the von Kármán model is applicable to 1D continua in cases where the nonlinear mechanism under consideration is the axial-bending coupling (*e.g.* for beams with blocked boundary conditions in the axial direction as for a clamped-clamped beam [Fig. 2.4]). Then the displacements of the beam are on the order of the thickness of the beam and the rotation of the cross-section is considered small to (at most) moderate, beyond which the assumptions of this model break down. The von Kármán assumptions (in addition to the previous Assumptions #1-4) are:

von Kármán Assumption #1

> The rotations of the cross-sections are assumed to be small enough for the rotation terms to be linearized according to $\sin\theta \simeq \theta$ and $\cos\theta \simeq 1$ such that, in 2D, the displacement of any point P in the beam is defined by Eq. (2.23).

von Kármán Assumption #2

> Only one nonlinear term is kept in the nonlinear part of the Green-Lagrange strains $\left(\nabla^{\mathrm{T}}\mathbf{u}\nabla\mathbf{u}\right)$, the quadratic term related to the transverse displacement in the axial component of the G-L strains (see Eq. (2.26).

Based on von Kármán Assumption #1, the displacement in 2D as shown in Fig. 2.3 becomes:

$$\mathbf{u}(P) = (u - y\theta)\,\mathbf{e}_x + w\mathbf{e}_y, \tag{2.23}$$

which represents the linearization of Eq. (2.8). The gradient of the displacements $\nabla\mathbf{u}$ and the transpose of the gradient are then computed as:

$$\nabla\mathbf{u} = \begin{bmatrix} u' - y\theta' & -\theta \\ w' & 0 \end{bmatrix}, \quad \nabla^{\mathrm{T}}\mathbf{u} = \begin{bmatrix} u' - y\theta' & w' \\ -\theta & 0 \end{bmatrix}, \tag{2.24}$$

With the rotations small enough to be linearized, the linearized Green-Lagrange strains ε become:

$$\varepsilon = \frac{1}{2}\left(\nabla\mathbf{u} + \nabla^{\mathrm{T}}\mathbf{u}\right) = \begin{bmatrix} u' - y\theta' & \frac{1}{2}\left(w' - \theta\right) \\ \frac{1}{2}\left(w' - \theta\right) & 0 \end{bmatrix}, \tag{2.25}$$

where the nonlinear quadratic term has been removed from the full Green-Lagrange strains $\mathbf{E}$ [Eq. (2.4)].

In the von Kármán model, the linearized Green-Lagrange strains ε are not used alone. According to von Kármán Assumption #2, a single term of the quadratic $\nabla^{\mathrm{T}}\mathbf{u}\nabla\mathbf{u}$ term of the Green-Lagrange strains is retained in the strain measurement. Based on the linearized rotations, $\nabla^{\mathrm{T}}\mathbf{u}\nabla\mathbf{u}$ is computed as:

$$\nabla^{\mathrm{T}}\mathbf{u}\nabla\mathbf{u} = \begin{bmatrix} (u' - y\theta')^2 + (w')^2 & -\theta\,(u' - y\theta') \\ -\theta\,(u' - y\theta') & \theta^2 \end{bmatrix}, \tag{2.26}$$

with the blue font indicating the retained nonlinear term. The G-L strains then become:

$$\varepsilon = \begin{bmatrix} u' - y\theta' + \frac{1}{2}(w')^2 & \frac{1}{2}(w' - \theta) \\ \frac{1}{2}(w' - \theta) & 0 \end{bmatrix} = \begin{bmatrix} \varepsilon_{xx} & \varepsilon_{xy} \\ \varepsilon_{xy} & 0 \end{bmatrix}. \tag{2.27}$$

Based on Euler-Bernoulli kinematics, shearing of the cross-section is neglected, so that:

$$\varepsilon_{xy} = \frac{1}{2}(w' - \theta) = 0, \tag{2.28}$$

establishing the relation $\theta = w'$. Then, the Green-Lagrange strains become:

$$\varepsilon = \begin{bmatrix} \varepsilon_{xx} & \varepsilon_{xy} \\ \varepsilon_{xy} & 0 \end{bmatrix} = \begin{bmatrix} e + y\kappa & 0 \\ 0 & 0 \end{bmatrix}, \tag{2.29}$$

with:

$$\begin{cases} e = u' + \dfrac{1}{2}(w')^2, & \text{(2.30a)} \\ \kappa = \theta' = w'', & \text{(2.30b)} \end{cases}$$

where we see that the strains e and κ are much simpler than the geometrically exact model [Eqs. (2.12)] though the nonlinear term in e remains. The stress resultants in force N and moment M are defined as in Eq. (2.15a) and Eq. (2.15c) based on the definitions of the strains in Eqs. (2.30) above.

If we write the equilibrium for an infinitesimally small element in the deformed configuration while neglecting the rotation of the internal forces, considering no applied moment ($q = 0$) and neglecting the rotational inertia, then the beam equations based on the von Kármán assumptions are written as:

$$\rho A\ddot{u} - N' = n, \tag{2.31a}$$
$$\rho A\ddot{w} + M'' - \underbrace{\left(Nw'\right)'}_{} = p, \tag{2.31b}$$

with the axial force $N = EAe = EA(u' + \underbrace{\frac{1}{2}(w')^2}_{})$ and the bending moment $M = EI\kappa = EIw''$ [229]. The nonlinear axial-bending coupling term is indicated with the underline $\underbrace{(\diamond)}_{}$. Further simplifications can be brought to Eqs. (2.31) by considering no axial external loading ($n = 0$) and neglecting the axial inertia $\rho A\ddot{u}$, a step which is commonly taken to simplify the analytical equations as it reduces the axial movement to a dependence only on N [229]. In doing so, Eq. (2.31a) leads to $N' = 0$, indicating a constant axial force throughout the length of the beam. Integrating the definition of N, then, leads

to:

$$\begin{aligned}\int_0^L N\mathrm{d}x &= EA\left[\int_0^L\left(u'+\frac{1}{2}\left(w'\right)^2\right)\mathrm{d}x\right]\\ &= EA\left[u(L)-u(0)\right]+\frac{EA}{2}\int_0^L\left(w'\right)^2\mathrm{d}x\\ &= \frac{EA}{2}\int_0^L\left(w'\right)^2\mathrm{d}x,\end{aligned}\tag{2.32}$$

where the first term of the integral has been removed by recalling that the axial displacements at $x=0$ and $x=L$ are blocked. It can be seen mathematically that if both ends of the beam are not fixed, N becomes 0 and the nonlinear coupling term in Eq. (2.31b) disappears, yielding the linear beam equations. For this reason, this model was used in Chapters 3 and 5 solely for the nonlinear dynamic analysis of clamped-clamped beams. Additionally, due to the linearized rotation terms, at large displacement amplitudes the von Kármán model begins to diverge from the exact solution (see § 3.3.2).

2.2 Solving strategies

In this section, some of the common strategies for solving nonlinear systems and the specific solving strategy used in this work are presented. In general, the strategies for solving nonlinear systems are very unlike the strategies for solving linear systems. The nonlinearities in a system prevent it from having an exact, closed-form, analytical solution. Many different solving techniques have therefore been proposed in order to approximate the solutions.

We consider here nonlinear partial differential equations in the context of vibrations of mechanical systems. In some cases, analytical solving techniques are suitable. Perturbation methods (*e.g.* the Method of Multiple Scales) are one such solving strategy, where a small perturbation parameter is added to the system and the solution expanded and eventually truncated as a power series of the parameter. The books of Nayfeh are considered the references on this subject [163], [164]. These methods, however, are not typically suitable for geometrically nonlinear highly flexible systems. Instead, these systems are usually resolved with numerical strategies.

2.2.1 Spatial discretization and the Finite Element Method

To solve the nonlinear partial differential equations numerically, they first must be discretized in space. Different discretization methods can be found in the literature, such as the method of finite differences [131], [132], Galerkin techniques [69], [71] or the Finite Element Method (FEM). The FEM is the most popular strategy in the literature on slender beam structures for resolving the nonlinear equations of motion. In this method, the weak form of the beam equations [Eqs. (2.2) and (2.16)] are discretized in space into finite elements. The elementary quantities are evaluated for a single finite element, then assembled together over the entire structure to solve the full equation of motion.

The review paper of Meier, Popp and Wall [156] provides a very nice review of the literature on finite element (FE) techniques applied to very slender beams (see for example Fig. 1 of [156]). Here only some of the most common methods, including the method used in our work, are described:

- The co-rotational formulation [48], [49], [75] discretizes the beam model into 1D beam elements and decomposes the total deformation into two parts. The first part of the deformation is

governed by a rigid-body motion of the element tied to the large rotation of a local "co-rotated" reference frame from its initial position. In the local "co-rotated" frame, a small local deformation then defines the second part of the total deformation of the element, which, being small, can be approximated at first (linear) or second order.

- The Absolute Nodal Coordinate (ANC) formulation represents another method used in the literature on slender beams [81], [210], [211]. In this method, the model is not reduced to a 1D beam model as in the previous two FE methods. Instead, the 3D displacement field within the beam is interpolated in the two transverse directions in addition to the longitudinal direction. However, [21], [198] indicate a preference towards the geometrically exact FE formulation (see next) over the ANC formulation, notably based on computational difficulties and overall computational cost.
- The geometrically exact formulation directly discretizes the beam equations relating the displacement of any point in the beam cross-sections to the displacement of the centerline into 1D beam elements based on a total Lagrangian formulation. This is the discretization method employed in this thesis and is explained in more detail next.

Spatial discretization into finite elements In this work, the finite element formulation is based on a direct discretization of the geometrically exact equations into N_e Timoshenko 1D beam elements typically (but not necessarily) of equal length L^e. The discretization into finite elements is straightforward, being that only the centerline need be discretized into 1D elements to map its deformation. The discretization is applied to the weak form of the dynamic equations of motions [Eqs. (2.2) and (2.3)]. In its most basic form, the Timoshenko 1D beam elements have only 2 nodes, one at each extremity of the element, but internal nodes can be added in order to increase the interpolation order. The unknowns of the system are then found at each of the nodes and interpolated between the nodes. If the 2D geometrically exact model of the previous section is taken up again, with 2-node Timoshenko elements (no internal nodes), the three degrees of freedom u, w and θ are found at each node and gathered into the vector $\mathbf{q}^e$, where the $\diamond^e$ notation indicates an elementary quantity:

$$\mathbf{q}^e = \begin{bmatrix} u_1 & w_1 & \theta_1 & u_2 & w_2 & \theta_2 \end{bmatrix}^{\mathrm{T}}, \tag{2.33}$$

with $\diamond_1$ and $\diamond_2$ subscripts indicating the unknowns at node 1 and node 2 of the element, respectively. The displacements are then interpolated between the nodes $\forall x \in [0, L^e]$ using shape functions gathered into the matrix $\mathbf{N}(x)$:

$$\begin{bmatrix} u^e(x,t) & w^e(x,t) & \theta^e(x,t) \end{bmatrix}^{\mathrm{T}} = \mathbf{N}(x)\mathbf{q}^e(t). \tag{2.34}$$

The type of shape functions used to interpolate between the nodal values in $\mathbf{q}^e$ has been the subject of some research, notably in order to preserve the so-called objectivity of the strains (see § 2.3.2). In this work, polynomial shape functions are used; in Chapter 3 linear shape functions are used in $\mathbf{N}$ and are later extended to quadratic shape functions in Chapter 5 with the possibility of increasing the order of the polynomial via addition of internal nodes. Using the definition of the elementary displacements [Eq. (2.34)] and defining the spatial derivative as:

$$\begin{bmatrix} u^{e\prime}(x,t) & w^{e\prime}(x,t) & \theta^{e\prime}(x,t) \end{bmatrix}^{\mathrm{T}} = \mathbf{N}'(x)\mathbf{q}^e(t), \tag{2.35}$$

the discretized strains e^e, γ^e and κ^e can be found by substituting these relations into Eqs. (2.12). The variation of the elementary strains is needed in discretization of the virtual internal work [Eq. (2.16a)]

and is written in the form:

$$\delta\hat{\boldsymbol{\varepsilon}}^e = \mathbf{B}^e(x, \mathbf{q}^e)\delta\mathbf{q}^e, \tag{2.36}$$

using the notation $\hat{\boldsymbol{\varepsilon}}^e = \begin{bmatrix} e^e & \gamma^e & \kappa^e \end{bmatrix}^{\mathrm{T}}$ as the elementary strain vector and $\mathbf{B}^e$ the strain matrix. Explicit definitions of these terms are given in Chapters 3 and 5 depending on the interpolations in $\mathbf{N}$.

We are now able to proceed to discretization of the weak form of the equations of motion based on the principle of virtual work. In 2D, if the notation $\hat{\mathbf{S}}^e = \begin{bmatrix} N^e & T^e & M^e \end{bmatrix}^{\mathrm{T}}$ is introduced, this takes the form:

$$\delta W_i^e = \int_0^{L^e} (N^e\delta e^e + T^e\delta\gamma^e + M^e\delta\kappa^e)\,\mathrm{d}x = \delta\mathbf{q}^{e\mathrm{T}} \underbrace{\int_0^{L^e} \mathbf{B}^{e\mathrm{T}}\hat{\mathbf{S}}^e \mathrm{d}x}_{\mathbf{f}_{int}^e(\mathbf{q}^e)}, \tag{2.37a}$$

$$\delta W_a^e = \int_0^{L^e} \left(\rho A\ddot{u}\delta u + \rho A\ddot{w}\delta w + \rho I\ddot{\theta}\delta\theta\right)\mathrm{d}x = \delta\mathbf{q}^{e\mathrm{T}} \underbrace{\left(\int_0^{L^e} \rho\mathbf{N}^{\mathrm{T}}\mathbf{J}\mathbf{N}\mathrm{d}x\right)}_{\mathbf{M}^e} \ddot{\mathbf{q}}^e, \tag{2.37b}$$

$$\delta W_e^e = \int_0^{L^e} (n\delta u + p\delta w + q\delta\theta)\,\mathrm{d}x + [N_e\delta u]_0^L + [T_e\delta w]_0^L + [M_e\delta\theta]_0^L = \delta\mathbf{q}^{e\mathrm{T}} \underbrace{\int_0^{L^e} \mathbf{N}^{\mathrm{T}}\mathbf{f}_e^e \mathrm{d}x}_{\mathbf{f}_{ext}^e}, \tag{2.37c}$$

with:

$$\mathbf{J} = \begin{bmatrix} A & 0 & 0 \\ 0 & A & 0 \\ 0 & 0 & I \end{bmatrix}, \tag{2.38}$$

and $\mathbf{f}_e^e = \begin{bmatrix} n & p & q \end{bmatrix}^{\mathrm{T}}$. Note that any point loadings at the boundaries must be added in directly at the corresponding nodes at $x = 0$ and $x = L$.

The elementary quantities ($\mathbf{q}^e$, $\mathbf{M}^e$, $\mathbf{f}_{int}^e(\mathbf{q}^e)$ and $\mathbf{f}_{ext}^e$) are assembled over the full structure into their global counterparts and, using the definition of the principle of virtual work [Eq. (2.2)], the equation of motion becomes, $\forall\delta\mathbf{q}$:

$$\delta W_e - \delta W_i - \delta W_a = \delta\mathbf{q}^{\mathrm{T}}\left(\mathbf{f}_{ext} - \mathbf{f}_{int}(\mathbf{q}) - \mathbf{M}\ddot{\mathbf{q}}\right) = 0. \tag{2.39}$$

The finite element equation of motion can then be written in the general form of a second order ordinary differential equation:

$$\mathbf{M}\ddot{\mathbf{q}} + \mathbf{D}\dot{\mathbf{q}} + \mathbf{f}_{int}(\mathbf{q}) = \mathbf{f}_{ext}. \tag{2.40}$$

A damping term $\mathbf{D}\dot{\mathbf{q}}$ has been added in order to account for any structural damping of the system, an example of which is the linear Rayleigh damping introduced in Chapter 3.

2.2.2 Solving nonlinear differential equations: time domain strategies and frequency domain strategies

Following spatial discretization, the nonlinear ordinary differential equations are solved with numerical methods. In the context of oscillating systems, we can be interested in either a transient response or a steady-state periodic response, which affects the choice of solving method. Only some common solving methods are described here, but many others exist.

Time domain strategies For time-dependent or transient solutions, a time integration method is required to solve the nonlinear differential equations. Some commonly-used methods include the well-known Runge-Kutta method, generalized-α method, the Hilbert-Huang Transform (HHT) method and the Newmark method, among others [30], [262].

If periodic or quasi-periodic solutions are targeted, the solving strategy can also be made in the time domain (using time integration methods). In the time domain, one important strategy for finding periodic solutions is the so-called shooting method. In this method, iterations are used to correct the initial conditions by computing the response over one period until a closed periodic orbit is found (corresponding to the solution after one period returning to the initial conditions, *i.e.* a periodic solution).

Frequency domain strategies In the frequency domain, the steady-state periodic solutions are directly targeted. The Harmonic Balance Method (HBM) is frequently used for finding periodic solutions in the frequency domain. This is the solving strategy used in the work of this thesis and is detailed in the next section. In the HBM, the periodic solution is decomposed in Fourier series in order to transform the differential equation into an algebraic system of equations. The algebraic nonlinear system can then be solved using *e.g.* Netwon-Raphson iterations or continuation methods.

The solving approach of this work is *based entirely in the frequency domain*, which represents one of the main originalities of this work. Periodic solutions of the nonlinear equations of motion are expanded in Fourier series following the HBM and resolved using a continuation method called the Asymptotic Numerical Method. The remainder of this section introduces the steps of this frequency domain-based solving strategy.

2.2.3 Periodic solutions with the Harmonic Balance Method

Consider an ordinary differential equation (ODE) in the following (first order) form:

$$\dot{\mathbf{X}} = f(\mathbf{X}, t). \tag{2.41}$$

In the Harmonic Balance Method (HBM), we seek a periodic response $\mathbf{X}$ of the ODE in the form of a truncated (up to harmonic H) Fourier series as follows:

$$\mathbf{X}(t) \simeq \mathbf{X}_0 + \sum_{k=1}^{H} \left[\mathbf{X}_k^c \cos(k\omega t) + \mathbf{X}_k^s \sin(k\omega t)\right], \tag{2.42}$$

where $\mathbf{X}_0$, $\mathbf{X}_k^c$ and $\mathbf{X}_k^s$ are the Fourier coefficients and ω the angular frequency of $\mathbf{X}(t)$.

The approximation Eq. (2.42) is then substituted into the original ODE system Eq. (2.41) and the coefficients of each harmonic are balanced in order to derive an algebraic system of equations for the Fourier coefficients. In practice, the algebraic system of equations is derived by projecting the residual of the ODE onto the Fourier basis as follows:

$$\langle 1, \dot{\mathbf{X}} - f(\mathbf{X}, t)\rangle = 0 \qquad \text{(harmonic 0)}, \tag{2.43a}$$

$$\langle \cos(k\omega t), \dot{\mathbf{X}} - f(\mathbf{X}, t)\rangle = 0 \qquad \text{(harmonic } k \text{ for cosine)}, \tag{2.43b}$$

$$\langle \sin(k\omega t), \dot{\mathbf{X}} - f(\mathbf{X}, t)\rangle = 0 \qquad \text{(harmonic } k \text{ for sine)}, \tag{2.43c}$$

where the scalar product $\langle \diamond, \diamond \rangle$ is defined as:

$$\langle f, g\rangle = \frac{1}{T}\int_0^T f \cdot g \, \mathrm{d}t, \tag{2.44}$$

with $T = 1/\omega$. If the $N_f(2H+1)\times 1$ unknowns of the system are collected into a new vector $\mathbf{U} = \left[\mathbf{X}_0^{\mathrm{T}} \quad \mathbf{X}_1^{c\mathrm{T}} \quad \mathbf{X}_1^{s\mathrm{T}} \quad \mathbf{X}_2^{c\mathrm{T}} \quad \mathbf{X}_2^{s\mathrm{T}} \quad \dots \quad \mathbf{X}_H^{c\mathrm{T}} \quad \mathbf{X}_H^{s\mathrm{T}}\right]^{\mathrm{T}}$, the resulting algebraic system of $N_f(2H+1)\times 1$ equations for the Fourier coefficients resulting from Eq. (2.43) can be put in the form:

$$\mathbf{R}(\mathbf{U}) = \mathbf{0}. \tag{2.45}$$

2.2.4 The Asymptotic Numerical Method and MANLAB

The continuation method called the Asymptotic Numerical Method (ANM) useful in solving (nonlinear) algebraic systems is then used to solve the HBM equations. The ANM was developed through the work of Cochelin, Damil and Potier-Ferry [18], [37], [38], [55].

The ANM is a type of continuation method that solves an N-dimensional algebraic system of the form:

$$\mathbf{R}(\mathbf{U}) = \mathbf{0}, \tag{2.46}$$

where $\mathbf{R} \in \mathbb{R}^N$ is an algebraic system with $\mathbf{U} \in \mathbb{R}^N$. The particularity of the ANM is that it can be applied to nonlinear systems containing only *polynomial* nonlinearities of *quadratic* order or less. For this reason, a nonlinear system containing any other kind of nonlinearities must be rewritten in a procedure known as the "quadratic recast." Here the "quadratic recast" of a nonlinear system means the process by which a nonlinear system containing non-polynomial nonlinearities, or polynomial nonlinearities higher than order 2, is rewritten through the introduction of additional variables called *auxiliary variables*. While the quadratic recast procedure at first glance may seem to be a limitation of the ANM formalism, in fact many nonlinear systems can be rewritten in this way [41], [121].

In order to facilitate a basic level of understanding for the reader, a brief introduction into the steps of the ANM procedure is described in what follows.

Quadratic recast of the ODE and HBM The first step of the procedure is the quadratic recast of any nonlinearities in the system that are not polynomials of quadratic order or less (an example using a Duffing oscillator will be shown later). The result of the quadratic recast procedure is a system that can be written (in first order form) as a quadratic differential-algebraic system of equations (DAE):

$$m(\dot{\mathbf{X}}) = c + l(\mathbf{X}) + q(\mathbf{X},\mathbf{X}), \tag{2.47}$$

where $\mathbf{X} \in \mathbb{R}^{N_f}$ is the vector collecting all variables (principal and auxiliary) with $N_f = N_p + N_a$, N_p being the number of principal variables and N_a the number of auxiliary variables, and c, $l(\diamond)$ $q(\diamond,\diamond)$ are constant, linear and quadratic operators and $m(\diamond)$ is a linear operator with respect to $\dot{\mathbf{X}}$.

The HBM is then performed on the quadratic DAE [Eq. (2.47)] as described in § 2.2.3 such that, collecting the terms of each harmonic, the resulting system can be reorganized into the form:

$$\omega M(\mathbf{U}) = C + L(\mathbf{U}) + Q(\mathbf{U},\mathbf{U}), \tag{2.48}$$

where the operators $M(\diamond)$, C, $L(\diamond)$ and $Q(\diamond,\diamond)$ are related to the operators $m(\diamond)$, c, $l(\diamond)$ and $q(\diamond,\diamond)$ but now in the frequency domain. Comparing Eq. (2.48) to the pre-HBM Eq. (2.47), it can be seen that the quadratic DAE [Eq. (2.47)] has now been transformed into a quadratic algebraic system of $(2H+1)N_f$ equations with the $(2H+1)N_f$ harmonic coefficients contained in $\mathbf{U}$ and the oscillation frequency ω as variables.

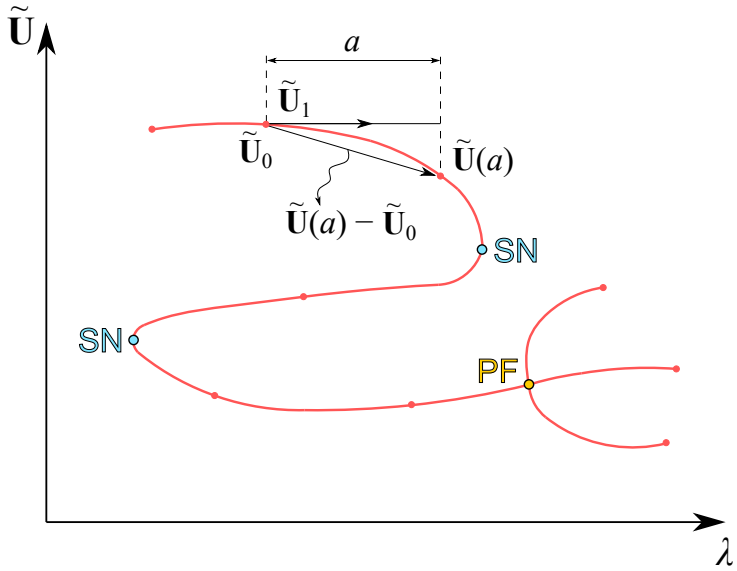

Figure 2.5: Continuation branches of solution based on pseudo-arclength path parametrization, where saddle-node (SN) and pitchfork (PF) bifurcations are marked in blue and yellow, respectively.

Asymptotic numerical method The quadratic algebraic system [Eq. (2.48)] is then solved with ANM continuation. The system must be put into the form:

$$\mathbf{R}(\mathbf{U},\lambda,\omega) = \mathbf{0}, \tag{2.49}$$

where λ is a continuation parameter that can be chosen to govern a specific variable of the system (*e.g.* $\lambda = \omega$).

To this end, if $\tilde{\mathbf{U}} = \begin{bmatrix}\mathbf{U}^{\mathrm{T}} & \lambda & \omega\end{bmatrix}^{\mathrm{T}}$, Eq. (2.48) can then be written:

$$\mathbf{R}(\tilde{\mathbf{U}}) = \mathbf{0} = \mathbf{C} + \mathbf{L}(\tilde{\mathbf{U}}) + \mathbf{Q}(\tilde{\mathbf{U}},\tilde{\mathbf{U}}), \tag{2.50}$$

where $\mathbf{R} \in \mathbb{R}^{N+1}$ and $\tilde{\mathbf{U}} \in \mathbb{R}^{N+2}$ for $N = (2H+1)N_f$, and where $\omega M(\tilde{\mathbf{U}})$ has been moved inside $\mathbf{Q}$ since ωM is quadratic. Written this way (with the inclusion of λ), the operators $\mathbf{C}$, $\mathbf{L}(\diamond)$ and $\mathbf{Q}(\diamond,\diamond)$ now also depend on λ (see [41] for details). Based on the dimensions of $\mathbf{R} \in \mathbb{R}^{N+1}$, which contains the N HBM equations and the definition of λ, we see that one equation is missing from $\mathbf{R}$ to fully define the system for $\tilde{\mathbf{U}} \in \mathbb{R}^{N+2}$ unknowns. This last equation comes from the definition of the *pseudo-arclength path parametrization*, described next.

According to the implicit function theorem, $\mathbf{U}$ can be expressed as a function of the continuation parameter λ, so that the solution branches for $\mathbf{U}$ can be computed as a function of λ. However, in the presence of certain bifurcation points, vertical tangents with respect to λ are encountered. To resolve this, a pseudo-arclength path parametrization based on the scalar a is introduced, such that $\mathbf{U} = \mathbf{U}(a)$ and $\lambda = \lambda(a)$, where a is defined as:

$$a = \left[\tilde{\mathbf{U}}(a) - \tilde{\mathbf{U}}_0\right]^{\mathrm{T}} \tilde{\mathbf{U}}_1, \tag{2.51}$$

with $\tilde{\mathbf{U}}_0 = \tilde{\mathbf{U}}(a=0)$ a known solution point and $\tilde{\mathbf{U}}_1 = \left[\frac{\partial \tilde{\mathbf{U}}}{\partial a}\right]_{a=0}$ the tangent vector at $\tilde{\mathbf{U}}_0$ as shown in Fig. 2.5. A branch of the solution is then computed through a power series expansion in a of the

unknowns $\tilde{\mathbf{U}}$ up to order n:

$$\tilde{\mathbf{U}}(a) = \tilde{\mathbf{U}}_0 + a\tilde{\mathbf{U}}_1 + a^2\tilde{\mathbf{U}}_2 + \ldots + a^n\tilde{\mathbf{U}}_n = \sum_{k=0}^{n} a^k \tilde{\mathbf{U}}_k, \tag{2.52}$$

with $\tilde{\mathbf{U}}_k = \frac{1}{k!}\left[\frac{\partial^k \tilde{\mathbf{U}}}{\partial a^k}\right]_{a=0}$ for $k = 1, \ldots, n$. The power series expansion of $\tilde{\mathbf{U}}$ [Eq. (2.52)] is then substituted into the algebraic system Eq. (2.50). Collected at each order, the resulting system is a combination of one nonlinear initial system at order 0 and n linear systems of N equations.

The final equation in $\mathbf{R}$ is found by injecting (at each order) the power series expansion of $\tilde{\mathbf{U}}$ [Eq. (2.52)] into the pseudo-arclength definition of a and likewise collecting the equations at each order $0, \ldots, n$, so that the final system is written:

$$\text{order } 0: \quad \left\{ \mathbf{R}(\tilde{\mathbf{U}}_0) = \mathbf{C} + \mathbf{L}(\tilde{\mathbf{U}}_0) + \mathbf{Q}(\tilde{\mathbf{U}}_0, \tilde{\mathbf{U}}_0) = \mathbf{0}, \right. \tag{2.53a}$$

$$\text{order } 1: \quad \begin{cases} \mathbf{L}(\tilde{\mathbf{U}}_1) + \mathbf{Q}(\tilde{\mathbf{U}}_0, \tilde{\mathbf{U}}_1) + \mathbf{Q}(\tilde{\mathbf{U}}_1, \tilde{\mathbf{U}}_0) = \mathbf{J}_0\tilde{\mathbf{U}}_1 = \mathbf{0}, \\ \tilde{\mathbf{U}}_1^{\mathrm{T}}\tilde{\mathbf{U}}_1 = 1, \end{cases} \tag{2.53b}$$

$$\text{order } 2: \quad \begin{cases} \mathbf{J}_0\tilde{\mathbf{U}}_2 + \mathbf{Q}(\tilde{\mathbf{U}}_1, \tilde{\mathbf{U}}_1) = \mathbf{0}, \\ \tilde{\mathbf{U}}_1^{\mathrm{T}}\tilde{\mathbf{U}}_2 = 0, \end{cases} \tag{2.53c}$$

$$\vdots$$

$$\text{order } 2 \leq p \leq n: \quad \begin{cases} \mathbf{J}_0\tilde{\mathbf{U}}_p + \sum_{i=1}^{p-1} \mathbf{Q}(\tilde{\mathbf{U}}_i, \tilde{\mathbf{U}}_{p-i}) = \mathbf{0}, \\ \tilde{\mathbf{U}}_1^{\mathrm{T}}\tilde{\mathbf{U}}_p = 0, \end{cases} \tag{2.53d}$$

where $\mathbf{J}_0 = \left[\frac{\partial \mathbf{R}}{\partial \tilde{\mathbf{U}}}\right]_{\tilde{\mathbf{U}}_0}$ is the Jacobian matrix of $\mathbf{R}$ evaluated at $\tilde{\mathbf{U}}_0$.

A few comments can be made on the advantages of the ANM formulation. First, in Eqs. (2.53), $\mathbf{J}_0$ needs only to be computed once to be used in all n linear systems for $n > 0$, lowering the computational cost of the method compared to methods where the Jacobian should be computed at each step. Next, the range of utility of the power series [Eq. (2.52)] is governed by a certain value of a called a_{max}, which is computed as approximately equal to the radius of convergence of the series [41]:

$$\forall a \in [0, a_{max}], \quad ||\mathbf{R}(\tilde{\mathbf{U}}(a))|| \leq \epsilon, \tag{2.54}$$

with ϵ a tolerance defined by the user. The range of utility a_{max} is automatically computed, so that one continuation branch is computed up to a_{max} and the last point of the branch is used as the starting point for the next branch. In this way, the steps a_{max} and the continuation branches of the periodic solution are all computed automatically without any special control of step size. The efficiency and robustness of this solving algorithm [41] make it an attractive method for continuation of periodic solutions.

Example using a 1 degree-of-freedom Duffing oscillator A very simple example based on a Duffing oscillator is presented here in order to show how a nonlinear differential equation can be rewritten in the form required for the ANM. The Duffing oscillator contains a cubic nonlinearity governed by the coefficient γ. The equation of motion of the Duffing oscillator (a single degree-of-freedom system) subjected to a harmonic forcing is written:

$$\ddot{u} + \mu\dot{u} + \omega_0^2 u + \gamma u^3 = F\cos\Omega t, \tag{2.55}$$

where the motion of the oscillator is governed by the unknown $u(t)$, Ω is the oscillation frequency with F the amplitude, and μ, ω_0 and γ are known coefficients. The free conservative Duffing equation can likewise be written as:

$$\ddot{u} + \omega_0^2 u + \gamma u^3 = 0, \tag{2.56}$$

where the forcing and damping terms have been removed.

Only the cubic term γu^3 prevents the system from containing only nonlinearities of quadratic order or less. To recast the system, the auxiliary variable $w = u^2$ is introduced, such that the term γu^3 can be rewritten as γuw. Next, the system is rewritten in first order state space form, necessitating a third variable $v = \dot{u}$, so that the vector containing all variables becomes $\mathbf{X} = \begin{bmatrix} u & v & w \end{bmatrix}^{\mathrm{T}}$ and the quadratically-recast forced Duffing system becomes:

$$\begin{aligned} \dot{u} &= 0 + v, \\ \dot{v} &= F\cos(\Omega t) - \omega_0^2 u - \mu v - \gamma uw, \\ 0 &= 0 + w - u^2, \end{aligned} \tag{2.57}$$

or in the free case [Eq. (2.56)]:

$$\begin{aligned} \dot{u} &= 0 + v, \\ \dot{v} &= 0 - \omega_0^2 u - \gamma uw, \\ 0 &= 0 + w - u^2. \end{aligned} \tag{2.58}$$

The Duffing system has now been put into the general form of Eq. (2.47). Many different kinds of nonlinearities can be rewritten in this way, including the geometrical nonlinearities that are at the heart of this thesis (as will be shown in Chapters 3 and 5).

Phase condition consideration in the case of autonomous systems The continuation parameter λ is added into the system to govern a specific variable of the system and its definition is used in the final system of equations. For example, returning to the forced Duffing equation [Eq. (2.55)], λ can be set as the amplitude of the forcing ($\lambda = F$, $\omega = \Omega$) by fixing the frequency Ω, or it can be set as the frequency itself, in which case $\lambda = \omega = \Omega$.

However, in the free case [Eq. (2.56)], there is no excitation, such that the time t does not enter into the equations (autonomous equations). In this case, a so-called *phase condition* (see textbook references in [41] for details on selecting the phase condition) must be imposed in order to define a unique periodic orbit or, colloquially, to "fix the phase of the periodic solution in time." In our work, this is done by imposing the condition that at time $t = 0$, the velocity of a given degree of freedom (denoted $i$phase) is set to zero, that is, $\dot{\mathbf{X}}_{i\text{phase}}(t = 0) = 0$. Based on Eq. (2.42), the phase condition can be defined explicitly as:

$$\begin{aligned} \dot{\mathbf{X}}_{i\text{phase}}(0) &= \sum_{k=1}^{H} \left[-k\omega \mathbf{X}^c_{k,i\text{phase}} \sin(0) + k\omega \mathbf{X}^s_{k,i\text{phase}} \cos(0) \right], \\ &= \sum_{k=1}^{H} k\omega \mathbf{X}^s_{k,i\text{phase}}, \\ &= \omega \sum_{k=1}^{H} k \mathbf{X}^s_{k,i\text{phase}}, \end{aligned} \tag{2.59}$$

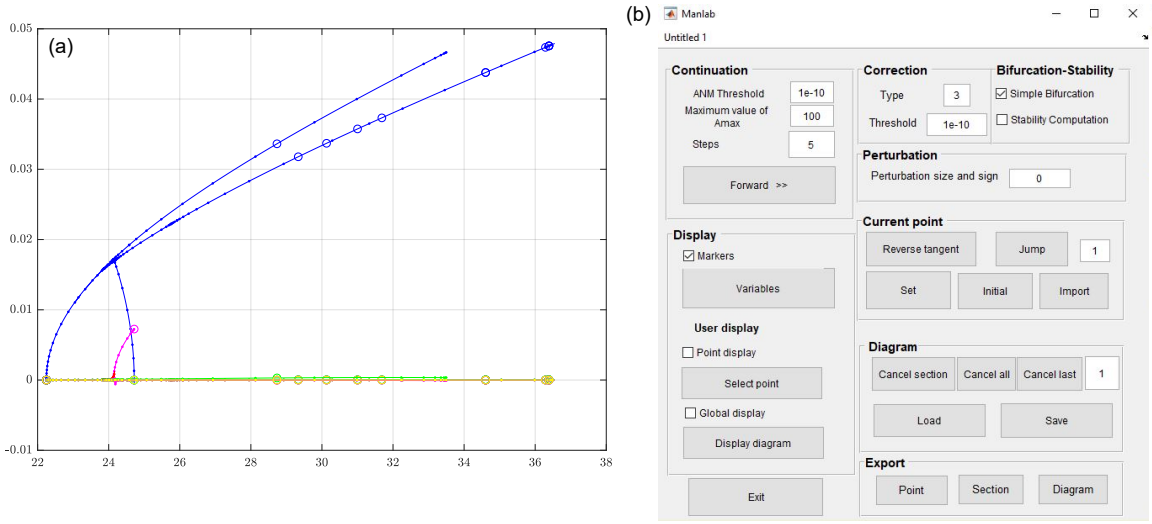

Figure 2.6: MANLAB graphical user interface (GUI) Windows, (a) continuation branches, (b) MANLAB GUI for controlling the continuation.

so that by enforcing the coefficients $\sum_{k=1}^{H} k\mathbf{X}^s_{k,i\text{phase}} = 0$, the phase of the solution is fixed. Note that in doing so, in the autonomous conservative case [Eqs. (2.56) and (2.58)], the system becomes in fact overdetermined; to resolve this, a fictitious damping $\lambda\dot{u} = \lambda v$ is added to the system with $\lambda = 0$. This topic is addressed again in § 3.2.3.

Implementation in MANLAB The details of the solving procedure described in this section are automated by the solver MANLAB. MANLAB, which is coded in MATLAB, is a frequency domain-based path-following software for continuation of periodic solutions including bifurcation and stability analysis. It has been under development by a team at the Laboratoire de Mécanique et d'Acoustique at École Centrale Marseille over the course of many years, and several works have added to its capabilities as an efficient solver for periodic systems [96]. In line with research objective #1 of § 1.2.2, one of the goals of this thesis is to integrate a large finite element model into the MANLAB solver.

The solving procedure is almost entirely automated by the MANLAB software, meaning that very little must be done on the part of the user in order to compute the periodic solutions. The procedure can be broken down intro three distinct steps:

- the quadratic recast of all nonlinear terms into polynomial nonlinearities of quadratic order or less,
- expansion of the unknowns in Fourier series up to a certain number of harmonics (H) and balancing the terms of each harmonic (known as the Harmonic Balance Method),
- application of the Asymptotic Numerical Method, a continuation method for computing periodic solutions.

The quadratic recast is the only step of the solving procedure that must be performed by the user; once a quadratically-recast system is inputted into MANLAB, the HBM and ANM are carried

out automatically by the solver. What appears to the user when MANLAB is launched is a simple graphical user interface (GUI) to control computation of the solution branches, bifurcation detection, stability analysis, *etc.* [Fig. 2.6(b)], and the solution branches solved by continuation [Fig. 2.6(a)].

As a final note, MANLAB also allows for stability analysis during continuation, but this is not addressed in the work of this thesis. For a more detailed understanding of the stability analysis automated by MANLAB, the reader is referred to the works [97] and particularly the work of Bayer and Leine [22] which notably adapted the method to large finite element systems based on a Koopman framework for the stability analysis of nonlinear periodic systems.

2.3 Numerical considerations of a FE implementation

When performing a finite element discretization of the geometrically exact beam model, there are some numerical considerations of which to be aware. The considerations that arise are purely numerical phenomena, but can affect the accuracy of the final result. In this section, we discuss some of the well-known numerical considerations that can arise.

2.3.1 Timoshenko vs. Euler-Bernoulli kinematics

There has been some discussion in the literature on flexible/geometrically exact beam models regarding the kinematic approach (Euler-Bernoulli or Timoshenko) to be taken. As mentioned briefly in § 1.2.1, 3D geometrically exact models have been derived based on both approaches, Reissner-Simo models (Timoshenko kinematics accounting for shear deformation of the cross-sections) and Kirchhoff-Love models (Euler-Bernoulli kinematics not allowing for shear deformation). When discretizing the beam model into finite elements, some considerations should be taken into account which may influence the kinematics choice.

The first consideration regards the allowance for shearing of the cross-section, or lack thereof. In Euler-Bernoulli kinematics, the no-shearing constraint is imposed, such that a relationship between the rotation of the cross-section θ and the displacements $\mathbf{u}$ (recall Eq. (1.2) noting that $\kappa = \theta'$) is derived. If polynomial functions are used in the interpolations $\mathbf{N}$ [Eq. (2.34)], the dependence of θ on $\mathbf{u}$ requires that the polynomial interpolations be at least cubic in order. With Timoshenko kinematics the interpolations need only be linear since, with the inclusion of shear deformations γ, θ is independent of $\mathbf{u}$ [74]. Furthermore, the no-shearing constraint must be incorporated into the governing equations (*e.g.* directly in the interpolations or with Lagrange multipliers or other methods [156]), which is not necessary with Timoshenko kinematics.

However, Timoshenko-style finite elements encounter the phenomenon of shear-locking, well-known in the FE literature [20], [74], [174], [189]. Shear-locking in Timoshenko beam elements is a subtle and *purely numerical* effect. It arises due to complications in the combined bending-shear rotation of the cross-section (θ in Fig. 2.3(b)) since both the rotation due to bending and the rotation due to shearing depend on the same variables. In this case, the continuity of the displacements (or their spatial derivatives) can be lost, resulting in a numerically-induced "overstiffness" [174] which even higher-order interpolations via internal nodes cannot fully resolve. A common solution, and the one used in the work of this thesis, is to perform reduced integration when determining the elementary vectors and matrices, one order below the number of nodes in the element (though other exact methods do exist, see *e.g.* [174]).

2.3.2 Objectivity of the strain measurements

Next, the topic of objectivity in finite element discretizations of the geometrically exact model is addressed, first brought to light by Crisfield and Jelenić [50]. Objectivity of material strain measurements is defined in [50] as "their inherent ability to remain unaffected by a constant motion of the configuration" or, alternately, that "strain measures are invariant under a superposed rigid-body motion." This can be understood to mean that for any rigid-body motion undergone, the strains are unchanged, which is physically logical in the sense that a rigid-body motion does not deform the body. While the strain measurements as defined in Reissner-Simo beam theory are themselves objective, certain interpolation methods during discretization into finite elements can cause the objectivity of the strains to be lost. This stems from the fact that rotations (which are not simplified in geometrically exact models - the hallmark of this method) are non-additive quantities, such that they cannot be interpolated with *e.g.* classical polynomial interpolations as additive quantities. In [50], the authors discuss the need for new interpolation strategies aimed at preserving the objectivity of the strain measurements, proposing their own strategy in [50], [116]. In [50], the authors specifically reference the early finite element formulations of [32], [112], [117], [220] as being non-objective.

If objectivity of the formulation is of primary concern, a finite element formulation involving objectivity-preserving interpolations of the rotation terms must be used [50], [83], [104], [116], [142], [156], [199]. However, these implementations can be complex and are certainly more complex than the aforementioned polynomial interpolations. In some cases, and depending on the intended use of the finite element model (*e.g.* to compute simple, efficient in-house computations versus exact reference simulations), proceeding with simpler interpolations such as with polynomials can be of interest. This is the approach taken in this thesis building on previous work [44], [225]. In this case, knowing that errors due to the non-objectivity of the formulation arise, the error is minimized by having an adequately fine mesh.

Many methods have been proposed in the last two decades appropriately accounting for objectivity or other numerical considerations tied to implementation of the geometrically exact model (see Table 2 of [156] for a systematic summary of the requirements filled by the literature). The review paper of Meier, Popp and Wall [156] systematically demonstrates the greater presence of finite element methods (as ours) based on the shear-deformable Reissner-Simo beam theory in the literature than those based on Kirchhoff-Love beam theory, describing them as having reached greater "maturity" from a numerical perspective. This is in spite of the longer "history" behind Kirchhoff-Love beam theory (developed beginning in the mid-19th century versus late 20th century for Reissner-Simo beam theory). The interested reader is referred to [156] for a more exhaustive review of the literature on finite element formulations for slender beams than what has been discussed here.

2.4 Solution types

In this section, the different types of solutions sought in this work are defined. In the context of vibrating mechanical systems, forced solutions traditionally depicted as frequency response functions can be computed, but we are also particularly interested in computing free solutions (the *nonlinear modes*) of the systems. These two solution types are described in what follows.

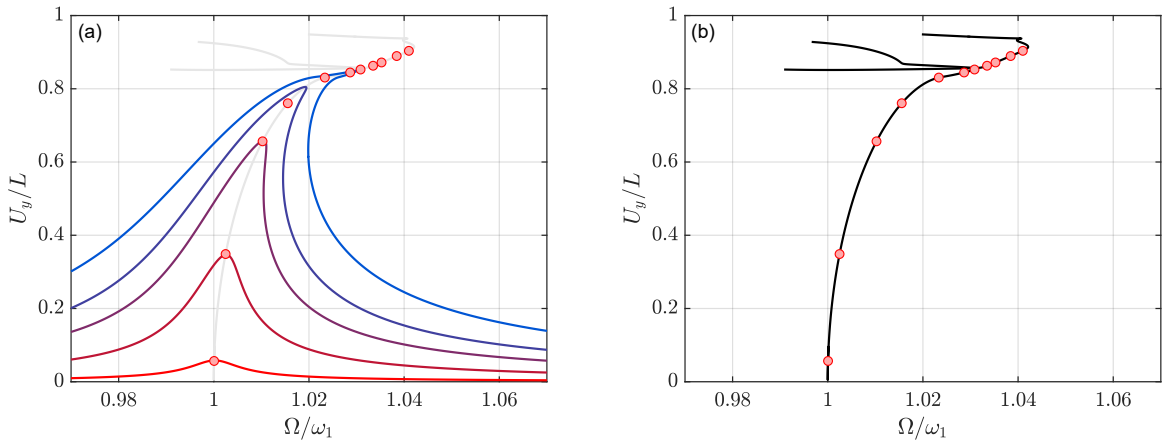

Figure 2.7: Solution types considered in this work, (a) several forced responses at different forcing amplitudes depicting the maximum transverse displacement at the free end of a cantilever beam (each curve corresponds to one FRC), (b) the backbone curve, equivalent to the first nonlinear mode. Note that the backbone of (b) is overlaid onto (a) in gray.

2.4.1 Forced solutions

We consider a *nonlinear* mechanical system of n_d degrees of freedom. The first type of solution under consideration is the forced response, the solution to the dynamic equations of motion of the form:

$$\mathbf{M}\ddot{\boldsymbol{x}} + \mathbf{D}\dot{\boldsymbol{x}} + \mathbf{K}\boldsymbol{x} + \mathbf{f}_{nl}(\boldsymbol{x}) = \mathbf{f}_e, \tag{2.60}$$

where $\boldsymbol{x}(t) \in \mathbb{R}^{n_d}$ represents the vector of degrees of freedom and $\dot{\diamond} = \partial\diamond/\partial t$ indicates the time derivative, $\mathbf{M}$ and $\mathbf{K}$ are the symmetrical $n_d \times n_d$ matrices governing the mass and stiffness, respectively, $\mathbf{D}$ governs the damping of the system (if present) and $\mathbf{f}_e(t) \in \mathbb{R}^{n_d}$ is a vector of externally-applied forces and the nonlinear term $\mathbf{f}_{nl}(\boldsymbol{x})$ indicates the nonlinear terms' dependence on $\boldsymbol{x}$.

In this thesis, the external forcing considered is periodic ($\mathbf{f}_e = \mathbf{a}\sin\Omega t + \mathbf{b}\cos\Omega t$) and the frequency response curve (FRC) of the system to a periodic forcing of a certain amplitude can be traced as shown in Fig. 2.7(a). In the FRC, the amplitude of the response $\boldsymbol{x}(t)$ is traced as a function of the oscillation frequency Ω.

2.4.2 Free solutions: nonlinear normal modes

The second type of solution considered in this work is the free solution, or the nonlinear normal mode. The concept of the nonlinear normal mode (also called simply nonlinear mode or abbreviated NNM) in the study of nonlinear dynamical systems (more specifically in our applications the nonlinear vibrations of oscillating systems) has developed extensively in recent years and it is worthwhile here to mention certain details regarding the concept for the sake of the reader's understanding. Only a brief overview of the concept and some notable works on the topic of nonlinear modes are presented here, owing principally to the fact that the nonlinear normal mode is defined in different ways (see below), often with complex or abstract demonstrations to explain them. Our interest is largely centered on the more physical interpretation of the nonlinear mode as a way of understanding and analyzing the nonlinear dynamics of the slender 1D beam systems that are the focus of the work of this thesis. In

particular, we focus on *computing* the nonlinear modes of these systems in order to gain insight into their nonlinear behavior at very large amplitudes of vibration.

Nonlinear mode as an extension of the linear mode The concept of the nonlinear normal mode originated from the idea of being able to extend the concept of the *linear* normal mode to the nonlinear regime. To better understand the nonlinear mode, then, we first recall the definition of the linear normal mode (or linear mode) [102], [113]. Linear models have long been used to describe the dynamics of mechanical systems and the concepts are generally well-known and considered the basics of dynamics and vibrations. The normal mode of a linear mechanical system represents an eigensolution of the conservative ($\mathbf{D}=\mathbf{0}$) system in free vibration ($\mathbf{f}_e=\mathbf{0}$), which is written:

$$\mathbf{M}\ddot{\boldsymbol{x}}+\mathbf{K}\boldsymbol{x}=\mathbf{0}. \tag{2.61}$$

If single harmonic responses of the form $\boldsymbol{x}(t)=\mathbf{A}_k\boldsymbol{\Phi}_k e^{i\omega_k t}$ are sought, the eigenvalue problem tied to Eq. (2.61) is written:

$$\left(\mathbf{K}-\omega_k^2\mathbf{M}\right)\boldsymbol{\Phi}_k=\mathbf{0}, \tag{2.62}$$

for $k=1,\dots,n_d$, where $\boldsymbol{\Phi}_k$ is the mode shape of mode k and ω_k its natural frequency for the n_d (eigen)modes of the system. If the response $\boldsymbol{x}(t)$ of the system is considered to be a superposition of all the modes of the system, the resulting modal superposition is written:

$$\boldsymbol{x}(t)=\sum_{k=1}^{n_d}\boldsymbol{\Phi}_k q_k(t), \tag{2.63}$$

with $q_k(t)$ the modal coordinates. Orthogonality properties between the modes are useful when projecting onto on a certain mode. They are written for the mass-normalized system:

$$\begin{cases}\Phi_i^{\mathrm{T}}\mathbf{M}\boldsymbol{\Phi}_j=\delta_{ij}, & \text{(2.64a)}\\ \boldsymbol{\Phi}_i^{\mathrm{T}}\mathbf{K}\boldsymbol{\Phi}_j=\omega_i^2\delta_{ij}, & \text{(2.64b)}\end{cases}$$

with δ_{ij} the Kronecker delta function ($\delta_{ij}=1$ for $i=j$ and $\delta_{ij}=0$ for $i\neq j$). Introducing Eqs. (2.63) and (2.64) into the linear normal mode Eq. (2.61), projecting onto mode m and multiplying all terms by $\boldsymbol{\Phi}_m^{\mathrm{T}}$ leads to the equation of motion of the oscillator in free vibration on mode m at frequency ω_m:

$$\ddot{q}_m(t)+\omega_m^2 q_m(t)=0, \tag{2.65}$$

which, notably, depends only on mode m and is therefore decoupled from all other modes. Linear modes notably have the property of *invariance*, so that when the system is excited by the initial conditions and external forcing on a certain mode, the energy remains, $\forall t$, on the excited mode and is not transferred to other modes, *i.e.*, the linear modes do not interact.

Extending the definition of the linear mode to the nonlinear regime, periodic solutions of the free conservative nonlinear system are sought:

$$\mathbf{M}\ddot{\boldsymbol{x}}+\mathbf{K}\boldsymbol{x}+\mathbf{f}_{nl}(\boldsymbol{x})=\mathbf{0}. \tag{2.66}$$

If the same development based on a modal superposition [Eq. (2.63)] as the linear mode is carried out, the equation of motion of the *nonlinear* oscillator in free vibration on mode m is written:

$$\begin{cases}\ddot{q}_m(t)+\omega_m^2 q_m(t)+g_m(q_k(t))=0, & \text{(2.67a)}\\ g_m(q_k(t))=\boldsymbol{\Phi}_m^{\mathrm{T}}\mathbf{f}_{nl}\left(\displaystyle\sum_{k=1}^{n_d}\boldsymbol{\Phi}_k q_k(t)\right), & \text{(2.67b)}\end{cases}$$

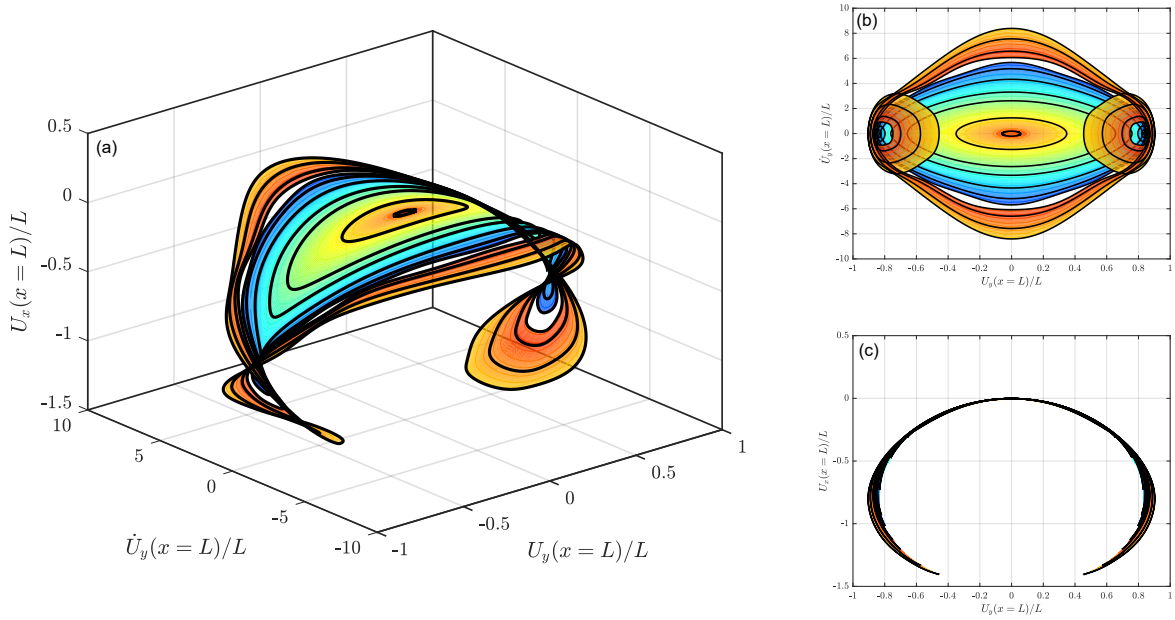

Figure 2.8: First nonlinear normal mode of a cantilever beam, invariant manifold and periodic orbits in the phase space, (a) invariant manifold (colored surface) and periodic orbits (black curves) in the phase space, (b) U_y - $\dot{U}_y$ view of (a), (c) U_y - U_x view of (a). The periodic orbits are traced for the points marked by red circles in Fig. 2.7.

where the underlined terms cannot be simplified using the orthogonality properties Eqs. (2.64) because of g_m's dependence on all $q_k(t)$. This dependence of the underlined term demonstrates some of the well-known nonlinear phenomena found in nonlinear dynamical systems, namely that, in contrast with the linear system, (1) the frequency of a certain free solution (the nonlinear mode, see formal definitions in the next section) is not simply the frequency ω_m of the associated mode but depends on the trajectory of $\boldsymbol{x}$ itself (and, therefore, evolves with it), and (2) the modes cannot be decoupled from one another and can interact via transfers of energy to other modes, leading to the phenomena known as internal resonance. This simple development has shown the fundamental ideas behind formulation of the concept of the nonlinear normal mode as an extension of the linear normal mode.

Formal definitions of the nonlinear mode In the literature on nonlinear normal modes, more precise, mathematically rigorous definitions of the nonlinear normal mode have been put forth in recent decades. These largely fall into two "families" of thought:

1. The first defines a nonlinear mode as *a family of periodic orbits in the phase space in the vicinity of a stable equilibrium point, which are solutions of the conservative nonlinear system in free vibration* [Eq. (2.66)] [124]. It was Lyapunov's work on the stability of dynamical systems that showed that, for a nonlinear conservative system of n_d degrees of freedom, there were n_d families of periodic solutions in the vicinity of a stable fixed equilibrium point [147]. Rosenberg [201], [202] then defined a nonlinear mode as a "vibration in unison" of the structure, meaning that all points of the structure vibrate at the same frequency and reach their extrema and zero amplitudes at the same time [124]. It was shown in [124] that this preliminary definition, however, is too

exclusive in cases of nonconservative systems (see [128], [133] for examples of damped NNMs), conservative systems not in unison (*e.g.* traveling waves [93]) or internal resonances, hence the generalization of the definition.

2. The second defines a nonlinear mode as *an invariant manifold of the phase space, tangent at its origin to the linear eigenspace* (represented in the phase space as a 2D horizontal plane, see *e.g.* Fig. 6 of [124] for a depiction of the phase space). The second definition was proposed by Shaw and Pierre [214]–[216] in order to extend the limited definition of Rosenberg to damped systems. Nonlinear normal modes preserve the invariance property of the linear normal mode, such that motion initiated on one manifold/nonlinear mode remains on it $\forall t$. Since the families of periodic orbits of the first definition taken together form an invariant manifold of the phase space, it can be said that the second definition is equivalent to the first.

The distinctions between the two families stem principally from the intended application. Based on the current state of the art, the concept of the nonlinear mode is often employed in two main applications, either (1) as a means of studying and characterizing the dynamics of a nonlinear system or else (2) in the development of nonlinear reduced order models. The nonlinear modes are then computed in different ways. In (1), in order to understand the complete nonlinear system, the full model is computed as periodic solutions of Eq. (2.66) using, for example, one of the strategies for finding periodic solutions described in § 2.2 (shooting methods, collocation methods, HBM, continuation methods, *etc.*). By contrast, in (2), reduced order models are sought, so that the dynamical model is reduced to a single invariant manifold representing a single nonlinear mode (single degree of freedom system). The recent review paper of Renson, Kerschen and Cochelin [195] nicely summarizes the various ways NNMs are computed numerically for applications in mechanical engineering, or the interested reader is referred to [124], [180].

Beyond what has already been cited, some notable contributors to the field are briefly mentioned, including the formative works of Rosenberg, Rand, Vakakis, Shaw and Pierre [190], [201], [202], [214]–[216], [239], [240]. The aforementioned works of Kerschen, Peeters, Golinval and Vakakis [124], [180] offer a more in-depth bibliographical timeline on the subject of the nonlinear normal mode and a summary of its features and usefulness in the field of structural dynamics. Furthermore, the recent review paper of Touzé, Vizzaccaro and Thomas [236] on model order reduction techniques for geometrically nonlinear structures includes using the invariant manifold definition of the nonlinear normal mode to derive reduced order models based on the theory of normal forms. This method has been used to compute the reduced dynamics of various structures in many works [155], [217], [237], [250], [251], both for general study and specific industrial applications (*e.g.* a MEMS micromirror [250], a fan blade [251] or a rotating twisted blade [155]).

Nonlinear modes in this work As mentioned at the beginning of this section, our interest in the nonlinear mode centers on its usefulness in understanding nonlinear dynamical systems within the scope of this thesis, that is, the nonlinear dynamics of slender 1D beam structures containing geometrical nonlinearities. To this end, in this work, the nonlinear modes are computed as solutions of the free conservative nonlinear system Eq. (2.66) and represented visually as the so-called *backbone curves* in the standard amplitude / frequency plot and as collections of snapshots of the periodic response showing the evolution of the system vibrating on one of its nonlinear modes. The backbone curves in the amplitude / frequency plot trace the frequency evolution of the nonlinear modes as a function of the amplitude of the response beginning at the linear eigenfrequency ω_m of their corresponding linear

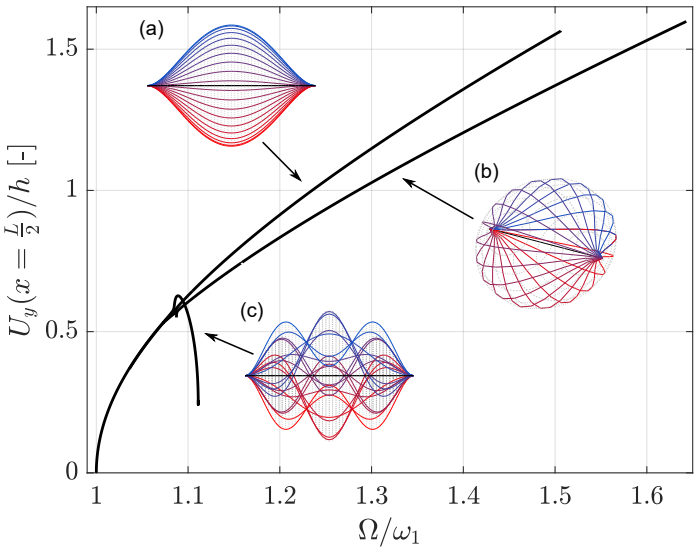

Figure 2.9: Some internal resonances of a clamped-clamped beam vibrating on its first nonlinear mode, (a) first nonlinear mode shape on the main backbone, (b) 1:1 internal resonance branch, (c) 1:5 internal resonance branch.

modes and can be thought of as collections of resonance points at different amplitudes of vibration as shown in Fig. 2.7(b). Each point along the backbone curve (marked with red circles in Fig. 2.7) of a nonlinear mode is equivalent to a periodic orbit in the phase space, as shown in Fig. 2.8(a)-(c). Figs. 2.7(b) and 2.8 demonstrate the equivalence between the different depictions and definitions of the nonlinear normal mode as either a backbone curve, periodic orbits in the phase space or invariant manifolds in the phase space: each point along the backbone curve can be alternatively represented as a periodic orbit in the phase space, which, when taken collectively, forms an invariant manifold in the phase space.

The backbone curves / nonlinear modes provide an efficient way of mapping the nonlinear dynamics of a system versus *e.g.* several frequency response functions since the nonlinear phenomena are uncovered with only a single computation. For example, the backbone curve highlights the dependence of the oscillation frequency on the oscillation amplitude through two characteristic shapes: if the backbone curves to the right, the oscillation frequency *increases* with increasing amplitude representative of a "stiffening" of the system and is known as *hardening*, while the reverse (backbone curving to the left) is known as *softening*. Both the backbone curves of Fig. 2.7(b) and Fig. 2.9 are of hardening type. The internal resonances of the system also appear as offshoots from the main backbone curve when some of the system's energy vibrating on one nonlinear mode is transferred to another mode. The first nonlinear mode of a clamped-clamped beam provides some well-known examples of internal resonances: shown in Fig. 2.9, the midline transverse displacement backbone (normalized by the thickness of the beam) is depicted where two internal resonance branches have been computed. In Fig. 2.9, a 1:5 internal resonance between the first and third bending modes of the clamped-clamped beam is shown by the deformed shape Fig. 2.9(c) and a 1:1 internal resonance between the two bending polarizations of the beam is shown in Fig. 2.9(b). The internal resonances of the clamped-clamped beam will come up again in Chapters 3 and 5 (§ 3.3.2 and § 5.5.1, respectively). More discussion on

the nonlinear phenomenon of internal resonance and how internal resonances appear on the backbone curves is presented in § 3.5 of Chapter 3. In addition to these, other well-known nonlinear phenomena such as bifurcations indicating changes in stability, unstable branches of solutions and jumps are detected automatically when computing the nonlinear solutions with MANLAB (§ 2.2.4).

Finally, the fundamental definition of the nonlinear modes as free solutions of the conservative system [Eq. (2.66)] is used to formulate methods for *experimental* measurement of the nonlinear modes [185], [186], [207], [208]. We cite in particular the work of Peeters, Kerschen and Golinval [178] proposing a methodology to perform experimental modal analysis of nonlinear vibrating structures which makes use of the invariance property of the nonlinear modes. In [178], the concept of *phase resonance* is exploited in order to demonstrate how the nonlinear modes can be extracted from a damped system under harmonic forcing. The phase resonance criterion dictates that a damped system under harmonic forcing vibrates as on one of its normal modes of the underlying conservative system if there is a phase difference of $\pi/2$ between the harmonic forcing and the response of the system. In phase resonance, it is shown in [178] that the damping of the system is exactly compensated by the harmonic forcing, such that Eq. (2.60) simplifies to Eq. (2.66), allowing the nonlinear modes to be measured. These ideas led to the development of the so-called Phase-Locked Loop, a vibration control method enabling the experimental measurement of nonlinear modes of such systems as [1], [60], [184]. The experiments of Chapter 6 investigating the large amplitude dynamics of slender beam structures are rooted deeply in these concepts.

2.5 Chapter summary: modeling and solving strategy of this work

Several different strategies for the simulation of flexible beam structures have at this point been presented. For the sake of clarity, a recap of the modeling and solving strategies of this work is provided in this section.

In this thesis, the strategy for the simulation of the dynamics of highly flexible slender beam structures is as follows:

- The *geometrically exact beam model* is used to model the deformation of the flexible slender beam structures *up to any amplitude of motion*. In our approach, the geometrically exact beam model is derived beginning from the full 3D nonlinear continuum mechanics equations and reduced to the deformation of a 1D continuum representing the centerline of the flexible beam and the rotation of the cross-sections along the centerline. The model considered in this work is based on Timoshenko kinematics, so that it is *shear-deformable*.
- A *total Langrangian finite element discretization* of the beam using Timoshenko beam elements is performed. The unknowns are described for a single finite element and assembled together for the whole structure into the the weak form of the equations of motion.
- The ODE resulting from the finite element discretization is solved *in the frequency domain* to target periodic motions. The unknowns are *expanded in Fourier series* in the Harmonic Balance Method and solved with a continuation method called the Asymptotic Numerical Method. This solving procedure is automated by the solver MANLAB.
- In the work of this thesis, we are especially interested in computing the *nonlinear modes* of the systems, both numerically and experimentally, in order to study the nonlinear dynamics of these types of systems.

This strategy is used in the next four chapters, both restricted to in-plane motions and for full motions in 3D.

Chapter 3

Nonlinear dynamics of flexible beam structures in 2D with trigonometric parametrization of rotations

In this chapter, we introduce the details of our strategy for the simulation of nonlinear dynamics of flexible slender beam structures. This chapter complements the discussions of the previous chapter by synthesizing all of the steps described in Chapter 2:

- derivation of the geometrically exact model based on Timoshenko kinematics,
- discretization into finite elements based on the geometrically exact formulation,
- solving of the equations of motion in the frequency domain using a combination of the Harmonic Balance Method (HBM) with the Asymptotic Numerical Method (ANM).

In this chapter, *the motion is fixed in the plane* such that only in-plane (2D) motions are considered (out-of-plane (3D) motions are described in Chapter 5). The 2D model is derived based on a parametrization of the rotation terms with classical rotation matrices and discretized using linear Timoshenko beam elements. The finite element model is then solved with the frequency domain-based strategy first introduced in § 2.2. The purpose of this chapter is to break down step-by-step our method in such a way as to make it accessible for the reader to understand and implement it themselves. The contents of this chapter were published in the *Journal of Sound and Vibration* in December 2022 as "Finite element computation of nonlinear modes and frequency response of geometrically exact beam structures" [58].

The summary of the chapter is as follows: in § 3.1, a review of the literature on flexible beam structures and the state of the art is provided along with common industrial applications of these structures. In § 3.2, the details of the modeling strategy based on a finite element discretization of the geometrically exact beam model (§ 3.2.1 and 3.2.2) and the solving strategy in the frequency domain based on the HBM and ANM (§ 3.2.3) are described. As recounted in § 2.2.4, the frequency domain-based solving strategy is automated by the MANLAB solver and some special considerations when implementing the model into MANLAB are discussed, such as how the geometrically exact model is recast into a quadratic system. The model is then tested using several test cases in § 3.3, both classical examples (cantilever and clamped-clamped beams) and some that are inspired by other works in the literature (flexible rings, tree-like structures and trusses). Finally, some important topics related to

the model are addressed: in § 3.4, the importance of proper convergence in the number of harmonics retained in the HBM is highlighted. In § 3.5, a discussion on the nonlinear phenomenon of internal resonance is provided, in particular on how internal resonances appear in the numerical computations using MANLAB. Final remarks and a discussion on future work in summarized in § 3.6.

Table of Contents - Chapter 3

3.1 Introduction

This work considers the numerical simulation of the dynamical behaviors of highly flexible slender beam structures subjected to geometrical nonlinearities. The geometrical nonlinearities are observed here due to the thinness of the structure, which leads to a very small stiffness in the transverse direction of deformation. Large displacements are therefore possible even for moderate external forces. This is especially true of structures with boundary conditions analogous to a cantilever (Fig. 3.1(b)), for which the main source of geometrical nonlinearities is not a membrane / bending coupling – encountered for instance in clamped-clamped beams, plates and shells (Fig. 3.1(a)) – but comes from the rotation of the cross-section, which can be very large (see *e.g.* [130], [236]). This latter case is associated with moderate nonlinear effects, which become significant for very large displacements of the structure (on the order of its characteristic length). Proper simulation of such extreme deformations of various beam structures is precisely the purpose of this work.

This field is rich with industrial engineering applications (see the introduction of [173]), for example where large amounts of wiring or cable-bundling are necessary, such as in the automotive industry. Recent work has addressed this topic in statics [45] and dynamics [30], [132], [143], [221]. Other applications of nonlinear beam models are the design of rotating blades, such as in helicopters, turbomachinery or wind turbines [108], [109], [177], [229], highly flexible structures in aerospace such as high-altitude, long endurance aircraft [182], [223], vibrating wings of nano-drones [72], [73], flexible cables for cable car systems [27], [79], [80], vibration isolation with pinched loops [246] and micro / nanosystems such as mass sensors and atomic force microscopes [23], [62], [188], [245]. Another area

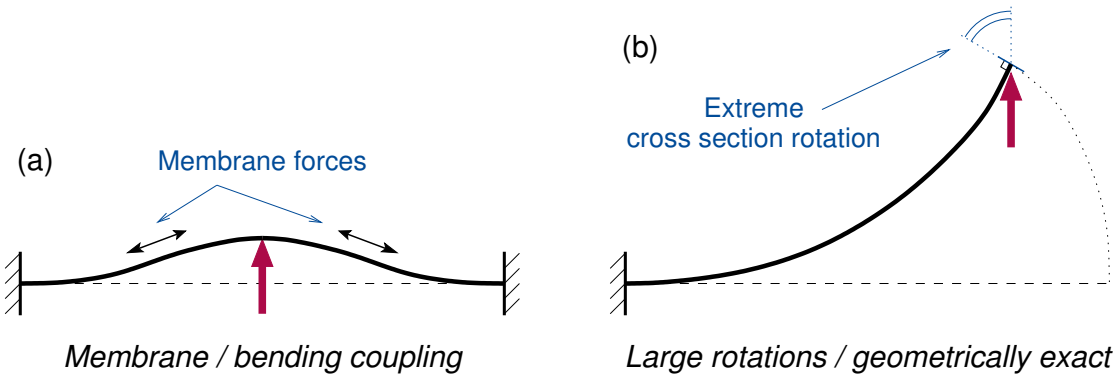

Figure 3.1: The two main mechanisms of geometrical nonlinearities in slender structures.

of interest in this vein of research is the exploitation of nonlinear cantilever beams for piezoelectric control and energy-harvesting applications, see *e.g.* [64], [99], [139], [148], [149], [257].

A common model for numerical computation related to beam structures is the so-called "inextensible beam" model of Crespo da Silva and Glynn [46], [47], [165]. In this model the length of the beam is supposed to be a constant, which allows the axial motion to be condensed into the transverse motion, thereby reducing the dynamics to a single degree of freedom partial differential equation. In addition, the geometrical nonlinearities are truncated up to the third order, retaining only cubic nonlinearities [229]. This model served as the basis for a huge number studies, but is limited to moderately large amplitudes due to the truncation of the nonlinear terms.

Highly flexible structures, however, can be subjected to deflections of extreme amplitude that necessitate richer beam models in order to be simulated appropriately. One solution is to turn to classical three dimensional finite element simulations [260], available in most commercial FE codes, which incorporate geometrical nonlinearities and do not impose restrictions on the maximum deflection that can be simulated accurately [68], [217], [236], [250]. But, in this case, an enormous number of elements (and, consequently, of degrees of freedom, leading to sometimes prohibitive computation times) is required for accurate simulation of the slender structures considered in this work, largely due to the small thickness and their flexibility in bending. This justified the development of an alternative method, the so-called geometrically exact beam model, introduced by Reissner [191], [192] and Simo [219]. This model considers beam kinematics without truncation of the nonlinear terms and, thus, does not restrict the amplitude of the rotation of the cross-section [156]. The model is therefore able to capture nonlinear behavior accurately even at extreme displacements. To reduce the computation time, reduced order models can also be used, see *e.g.* the recent review work of Touzé *et al.* [236] and some applications [145], [217], [250].

A known difficulty in putting geometrically exact beam models into practice is linked to the treatment of the rotations for three-dimensional – axial / bending / torsion – deflections of the beam. Different methods for parameterization of the rotations (rotation matrices, quaternions...) have been proposed by Simo and Vu-Quoc [220], Cardona and Géradin [32], Ibrahimbegović [111], Crisfield and Jelenić [50], [116] and Zupan *et al.* [261], among others. These studies aim to implement a numerical finite element-based discretization of the model, allowing for the simulation of structures with arbitrarily complex geometries obtained through the assembly of beam elements.

In parallel, a series of recent works targets the dynamics of a single cantilever beam in the frequency

domain, using the same geometrically exact model with an inextensibility constraint but without any trunctation of the geometrical nonlinearities. This method leads to a simple formulation in the form of partial differential equations with transverse degrees of freedom only, which are discretized by an expansion onto a normal mode basis. The strategy produces highly accurate results when compared with reference numerical FE simulations or experiments [68], [69], [71], [82], although it is restricted to the case of a single cantilever beam.

Most numerical strategies able to solve the geometrically exact beam model, available either in commercial finite-element codes or addressed in the literature, are related to time integration due to their highly nonlinear nature. However, when studying the nonlinear dynamics of such highly flexible structures, a lot of complex vibratory phenomena may be observed, including bifurcations, instabilities, bistability, qualitative changes in the nature of the solutions, quasi-periodic and chaotic responses, energy transfers between vibration modes, *etc.* [53], [97], [152], [162], [245]. In this case, simulations in the frequency domain are advantageous since they directly target the periodic steady-state vibrations under harmonic forcing and can be easily integrated into bifurcation and stability analysis tools. Moreover, the nonlinear resonance pattern of a given structure can be efficiently mapped by the so-called nonlinear normal modes [124], equivalently defined as families of periodic solutions of the conservative system or invariant manifolds of the phase space [214], [236], [237]. The nonlinear normal modes are often depicted as backbone curves in an amplitude / frequency (also known as a frequency response) plot.

This chapter proposes a novel numerical strategy to compute the nonlinear dynamics of highly flexible structures in the frequency domain. It is based on a finite element discretization of the geometrically exact beam model and computes periodic solutions using a combination of the harmonic balance method (HBM) and a numerical continuation tool based on the asymptotic numerical method (ANM). The numerical strategy is capable of calculating both the frequency response under harmonic forcing and the nonlinear normal modes of structures of arbitrary shape, as long as they can be discretized into beam elements. Due to the implementation of the continuation method for solving, both steady-state stable and unstable periodic solutions can be computed. In this chapter, only plane structures with in-plane deformations are considered; the extension to a full three-dimensional case is postponed to Chapter 5. The methodology is presented in detail in Section 3.2, including a discussion on the numerical properties and efficiency of the strategy, with several test cases gathered in Section 3.3.

3.2 Geometrically exact beam model and solution

In this section, the fundamental equations governing the motion of flexible beam structures in two dimensions (2D) are presented. Previous work derives in detail the kinematics and the equations of motion corresponding to a geometrically exact beam model [229]. For this reason, only a summary of the equations central to the argument of this chapter is presented. The interested reader may refer to Sections 2 and 4 of [229] for a more detailed derivation.

3.2.1 Kinematics

A depiction of the system under investigation is shown in Fig. 3.2. As mentioned, the geometrically exact beam model is here restricted to two dimensions, such that the centerline of any beam element lies in the $(\mathbf{e}_X, \mathbf{e}_Y)$ plane of a global basis $(\mathbf{e}_X, \mathbf{e}_Y, \mathbf{e}_Z)$ and undergoes deformations in the same plane.

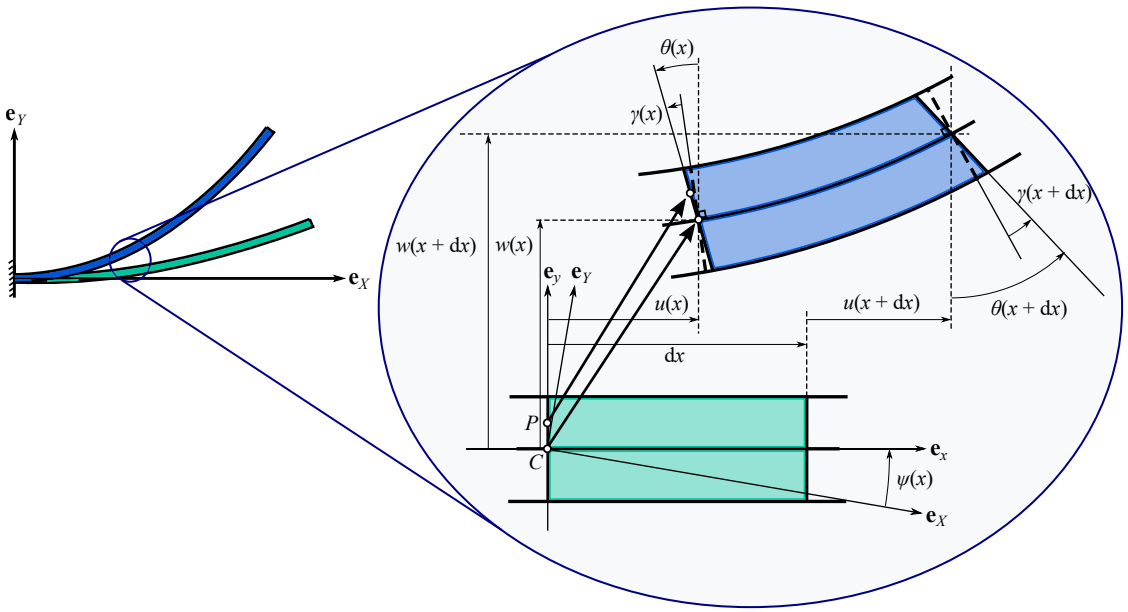

Figure 3.2: Timoshenko beam kinematics.

Based on Timoshenko kinematics for the beam, we assume that any cross-section of the beam undergoes a rigid-body motion. We consider a differential beam element of length $\mathrm{d}x$ with its centerline aligned with the $\mathbf{e}_x$ direction, where $(\mathbf{e}_x, \mathbf{e}_y, \mathbf{e}_Z)$ is a local frame that may depend (in the case of a curved structure) on x, the curvilinear coordinate that defines the location of the cross-sections. The angle $\psi(x) = (\widehat{\mathbf{e}_X, \mathbf{e}_x})$ defines its orientation. As a consequence, the displacement of any point P in the cross-section is related to the displacement field of the centerline by the following relation:

$$\begin{aligned}\mathbf{u}(x,y,t) = &[u(x,t) - y\sin\theta(x,t)]\,\mathbf{e}_x \\ &+ [w(x,t) + y\,(\cos\theta(x,t) - 1)]\,\mathbf{e}_y,\end{aligned} \tag{3.1}$$

where (x,y) are the coordinates of P in the frame $(\mathbf{e}_x, \mathbf{e}_y)$, t is the time, $u(x,t)$ and $w(x,t)$ are the axial and transverse displacements, respectively, of the corresponding point of the centerline C at axial position x and time t and $\theta(x,t)$ is the rotation of the cross-section, as shown in Fig. 3.2.

The expression for the strains, incorporating large displacements, is given by the Green-Lagrange strain tensor, denoted here $\tilde{\mathbf{E}}$, and expressed as (see *e.g.* [229]):

$$\tilde{\mathbf{E}} = \frac{1}{2}\left(\nabla\mathbf{u} + \nabla^{\mathrm{T}}\mathbf{u} + \nabla^{\mathrm{T}}\mathbf{u}\,\nabla\mathbf{u}\right). \tag{3.2}$$

For the sake of efficiency, the exact expressions of the Green-Lagrange strain tensor as a function of u, w and θ are not recopied here. Instead, a consistent linearization to the Green-Lagrange strains is computed in order to simplify the expressions without loss of accuracy. In this process, only the part of the strain terms relating purely to the local strains is linearized, maintaining the rigid-body rotation part fully exact. It is relevant so long as the the local strains remain relatively small, which is the case here, in spite of large rigid-body displacements (the latter will be assumed throughout the remainder of the chapter). The resulting simplified strain tensor, denoted $\mathbf{E}$, is then given in the basis

$(\mathbf{e}_x, \mathbf{e}_y, \mathbf{e}_Z)$, by the following [74], [101], [229]:

$$\mathbf{E} = \begin{pmatrix} e - y\kappa & \gamma/2 & 0 \\ \gamma/2 & 0 & 0 \\ 0 & 0 & 0 \end{pmatrix}, \tag{3.3}$$

where the quantities e, γ and κ represent, respectively, the axial strain, the shear strain and the beam curvature, defined as:

$$\begin{aligned} e &= (1 + u')\cos\theta + w'\sin\theta - 1, \\ \gamma &= w'\cos\theta - (1 + u')\sin\theta, \\ \kappa &= \theta', \end{aligned} \tag{3.4}$$

where $\circ' = \partial \circ / \partial x$.

The stress tensor (energetically conjugated to the Green-Lagrange strain tensor) is given by the second Piola-Kirchhoff stress tensor, denoted $\mathbf{S}$. In what follows, we consider that the material is homogeneous and isotropic and that a linear Kirchhoff-Saint-Venant constitutive relation is assumed between $\mathbf{E}$ and $\mathbf{S}$, so that the following relation holds:

$$\begin{aligned} N &= \int_A S_{xx}\,\mathrm{d}A = EAe, \\ T &= \int_A S_{xy}\,\mathrm{d}A = kGA\gamma, \\ M &= \int_A yS_{xx}\,\mathrm{d}A = EI\kappa, \end{aligned} \tag{3.5}$$

where N, T and M are the axial force, shear force and bending moment, respectively, E is the Young's modulus, G the shear modulus, A and I the area and second moment of area of the cross-section, respectively, and k the shear correction factor [110]. The generalized forces are grouped into a vector, denoted $\hat{\mathbf{S}}$:

$$\hat{\mathbf{S}} = \begin{bmatrix} N & T & M \end{bmatrix}^{\mathrm{T}}, \tag{3.6}$$

where $^{\mathrm{T}}$ defines the transpose of the vector or matrix.

The equations of motion are derived in the weak form using the principle of virtual work, which is stated in [129], [229] as, for all virtual displacement $\delta\mathbf{u}$:

$$\delta W_a + \delta W_i = \delta W_e, \tag{3.7}$$

with the inertial (δW_a), internal (δW_i) and external (δW_e) virtual work expressed as, respectively:

$$\delta W_a = \int_V \rho\ddot{\mathbf{u}} \cdot \delta\mathbf{u}\ \mathrm{d}V, \tag{3.8}$$

$$\delta W_i = \int_V \mathbf{S} \colon \delta\mathbf{E}\ \mathrm{d}V, \tag{3.9}$$

$$\delta W_e = \int_{\partial V} \mathbf{f} \cdot \delta\mathbf{u}\ \mathrm{d}A + \int_V \mathbf{b} \cdot \delta\mathbf{u}\ \mathrm{d}V, \tag{3.10}$$

where V represents the domain of the beam in the reference configuration, ∂V its frontier, ρ the density of the material, $\ddot{\mathbf{u}} = \partial^2\mathbf{u}/\partial t^2$ the acceleration of point P, $\delta\mathbf{u}$ the virtual displacement vector and $\delta\mathbf{E}$ the first variation of the strain induced by $\delta\mathbf{u}$. In addition, $\mathbf{f}$ and $\mathbf{b}$ represent, respectively, the external surface and body forces.

3.2.2 Finite element model

In this section we present the discretization used to derive the finite element equation of motion. First, the beam is discretized into N_e elements of length L^e, that may depend on x in the case of a non-uniform mesh. The element used here is the classical two-node Timoshenko beam element with linear shape functions [74]. At each node i of an element, there are three degrees of freedom (u_i, w_i, θ_i) corresponding to the axial displacement, transverse displacement and rotation of the cross-section, respectively. For a given element, we introduce the vector $\mathbf{q}^e$ containing the degrees of freedom at the two nodes of the element (denoted node 1 and node 2):

$$\mathbf{q}^e = \begin{bmatrix} u_1 & w_1 & \theta_1 & u_2 & w_2 & \theta_2 \end{bmatrix}^\mathrm{T}. \tag{3.11}$$

We then define the interpolated displacements over the element using linear shape functions as $\forall x \in [0,\, L^e]$:

$$\begin{bmatrix} u^e(x,t) \\ w^e(x,t) \\ \theta^e(x,t) \end{bmatrix} = \mathbf{N}(x)\mathbf{q}^e(t), \tag{3.12}$$

where the matrix of shape functions $\mathbf{N}$ is defined as:

$$\mathbf{N}(x) = \begin{bmatrix} N_1(x) & 0 & 0 & N_2(x) & 0 & 0 \\ 0 & N_1(x) & 0 & 0 & N_2(x) & 0 \\ 0 & 0 & N_1(x) & 0 & 0 & N_2(x) \end{bmatrix}, \tag{3.13}$$

and the linear shape functions N_1 and N_2 given by:

$$N_1(x) = 1 - \frac{x}{L^e}, \quad N_2(x) = \frac{x}{L^e}. \tag{3.14}$$

Using this interpolation, one can compute the spatial derivatives appearing in the definition of the strain measure in Eq. (3.4):

$$\begin{bmatrix} u^{e\prime}(x,t) \\ w^{e\prime}(x,t) \\ \theta^{e\prime}(x,t) \end{bmatrix} = \frac{1}{L^e} \begin{bmatrix} u_2(t) - u_1(t) \\ w_2(t) - w_1(t) \\ \theta_2(t) - \theta_1(t) \end{bmatrix}, \tag{3.15}$$

which do not depend on x because of the linearity of the shape functions.

Substituting the previous relations into Eq. (3.4) leads to the following expressions for the discretized strains over a given element:

$$\begin{aligned} e^e &= \left(1 + \frac{u_2 - u_1}{L^e}\right)\cos\theta^e + \left(\frac{w_2 - w_1}{L^e}\right)\sin\theta^e - 1, \\ \gamma^e &= \left(\frac{w_2 - w_1}{L^e}\right)\cos\theta^e - \left(1 + \frac{u_2 - u_1}{L^e}\right)\sin\theta^e, \\ \kappa^e &= \frac{\theta_2 - \theta_1}{L^e}. \end{aligned} \tag{3.16}$$

Note that at this point the function $\theta^e(x,t)$ is also discretized and should be considered as:

$$\theta^e(x,t) = \theta_1(t)N_1(x) + \theta_2(t)N_2(x), \tag{3.17}$$

which is not substituted into the equations here in order to increase their readability.

The strains in Eq. (3.16) are grouped into the elementary strain vector $\hat{\epsilon}^e$ defined by the following:

$$\hat{\epsilon}^e = \begin{bmatrix} e^e & \gamma^e & \kappa^e \end{bmatrix}^{\mathrm{T}}. \tag{3.18}$$

Then, taking the differential of Eq. (3.16), the variation of the elementary strain vector $\delta\hat{\epsilon}^e$ can be written:

$$\delta\hat{\epsilon}^e = \mathbf{B}^e(x, \mathbf{q}^e)\delta\mathbf{q}^e, \tag{3.19}$$

with $\delta\mathbf{q}^e$ the variation of the nodal displacements and:

$$\mathbf{B}^e = \frac{1}{L^e}\begin{bmatrix} -\cos\theta^e & \sin\theta^e & 0 \\ -\sin\theta^e & -\cos\theta^e & 0 \\ N_1(x)L^e\gamma^e & -N_1(x)L^e(1+e^e) & -1 \\ \cos\theta^e & -\sin\theta^e & 0 \\ \sin\theta^e & \cos\theta^e & 0 \\ N_2(x)L^e\gamma^e & -N_2(x)L^e(1+e^e) & 1 \end{bmatrix}^{\mathrm{T}}. \tag{3.20}$$

Now that the discretization is defined, it can be substituted into the principle of virtual work of Eq. (3.7) in order to obtain the finite element equations of motion. Beginning with the inertial work component, the expression of Eq. (3.8) over a single element of length L^e is first rewitten as:

$$\begin{aligned} \delta W_a^e &= \int_{V_e} \rho\ddot{\mathbf{u}}^e \cdot \delta\mathbf{u}^e \mathrm{d}V \\ &= \int_0^{L^e} \rho \begin{bmatrix} \delta u^e(x) & \delta w^e(x) & \delta\theta^e(x) \end{bmatrix} \mathbf{J} \begin{bmatrix} \ddot{u}^e(x) \\ \ddot{w}^e(x) \\ \ddot{\theta}^e(x) \end{bmatrix} \mathrm{d}x, \end{aligned} \tag{3.21}$$

with $\mathbf{J}$ defined as follows:

$$\mathbf{J} = \begin{bmatrix} A & 0 & 0 \\ 0 & A & 0 \\ 0 & 0 & I \end{bmatrix}. \tag{3.22}$$

Introducing the discretization leads to the following expression for the virtual work of the inertia forces:

$$\begin{aligned} \delta W_a^e &= \int_0^{L^e} \rho(\mathbf{N}\delta\mathbf{q}^e)^{\mathrm{T}}\mathbf{J}\mathbf{N}\ddot{\mathbf{q}}^e \mathrm{d}x \\ &= (\delta\mathbf{q}^e)^{\mathrm{T}} \underbrace{\left(\int_0^{L^e} \rho\mathbf{N}^{\mathrm{T}}\mathbf{J}\mathbf{N}\,\mathrm{d}x\right)}_{\mathbf{M}^e} \ddot{\mathbf{q}}^e. \end{aligned} \tag{3.23}$$

From equation (E.28), the elementary mass matrix is derived by evaluating the integral in parentheses, yielding:

$$\mathbf{M}^e = \frac{\rho L^e}{6}\begin{bmatrix} 2A & 0 & 0 & A & 0 & 0 \\ 0 & 2A & 0 & 0 & A & 0 \\ 0 & 0 & 2I & 0 & 0 & I \\ A & 0 & 0 & 2A & 0 & 0 \\ 0 & A & 0 & 0 & 2A & 0 \\ 0 & 0 & I & 0 & 0 & 2I \end{bmatrix}. \tag{3.24}$$

Following with the virtual work of the internal forces, the expression of Eq. (3.9) is first rewritten as follows:

$$\begin{aligned}\delta W_i^e &= -\int_{V_e} \mathbf{S}\colon \delta\mathbf{E}\,\mathrm{d}V \\ &= -\int_0^{L^e} (N^e\delta e^e + T^e\delta\gamma^e + M^e\delta\kappa^e)\,\mathrm{d}x \\ &= -\int_0^{L^e} (\delta\hat{\epsilon}^e)^{\mathrm{T}}\hat{\mathbf{S}}^e\,\mathrm{d}x.\end{aligned} \tag{3.25}$$

Introducing the discretization leads to the following expression for the virtual work of the internal forces over a given element:

$$\begin{aligned}\delta W_i^e &= -\int_0^{L^e} (\mathbf{B}^e(x,\mathbf{q}^e)\delta\mathbf{q}^e)^{\mathrm{T}}\ \hat{\mathbf{S}}^e\,\mathrm{d}x \\ &= -(\delta\mathbf{q}^e)^{\mathrm{T}}\underbrace{\int_0^{L^e} (\mathbf{B}^e(x,\mathbf{q}^e))^{\mathrm{T}}\hat{\mathbf{S}}^e\,\mathrm{d}x}_{\mathbf{f}_{\mathrm{int}}^e}.\end{aligned} \tag{3.26}$$

The elementary internal force vector is calculated by evaluating the following integral:

$$\mathbf{f}_{\mathrm{int}}^e(\mathbf{q}^e) = \int_0^{L^e} (\mathbf{B}^e)^{\mathrm{T}}\hat{\mathbf{S}}^e\,\mathrm{d}x. \tag{3.27}$$

Equation (3.27) is then readily evaluated using (3.6) and (3.20) to yield the elementary internal force vector $\mathbf{f}_{\mathrm{int}}^e$. Note that the integral is evaluated using a reduced Gauss integration (here with only a single point at $x = \frac{L^e}{2}$) to avoid the phenomenon of shear locking [20]. The elementary internal force vector $\mathbf{f}_{\mathrm{int}}^e$ is then given by:

$$\mathbf{f}_{\mathrm{int}}^e = EA\bar{e}\begin{bmatrix}-\cos\bar{\theta}\\-\sin\bar{\theta}\\\bar{\gamma}\frac{L^e}{2}\\\cos\bar{\theta}\\\sin\bar{\theta}\\\bar{\gamma}\frac{L^e}{2}\end{bmatrix} + kGA\bar{\gamma}\begin{bmatrix}\sin\bar{\theta}\\-\cos\bar{\theta}\\-\frac{L^e}{2}(1+\bar{e})\\-\sin\bar{\theta}\\\cos\bar{\theta}\\-\frac{L^e}{2}(1+\bar{e})\end{bmatrix} + EI\bar{\kappa}\begin{bmatrix}0\\0\\-1\\0\\0\\1\end{bmatrix}, \tag{3.28}$$

where $\bar{\circ}$ here denotes a quantity evaluated at $x = L^e/2$, explicitly given by:

$$\bar{\theta} = \frac{\theta_1+\theta_2}{2}, \tag{3.29}$$

$$\bar{e} = e^e(L^e/2) = \left(1+\frac{u_2-u_1}{L^e}\right)\cos\bar{\theta} + \left(\frac{w_2-w_1}{L^e}\right)\sin\bar{\theta} - 1, \tag{3.30}$$

$$\bar{\gamma} = \gamma^e(L^e/2) = \left(\frac{w_2-w_1}{L^e}\right)\cos\bar{\theta} - \left(1+\frac{u_2-u_1}{L^e}\right)\sin\bar{\theta}, \tag{3.31}$$

$$\bar{\kappa} = \kappa^e(L^e/2) = \frac{\theta_2-\theta_1}{L^e}.$$

Finally, we consider the virtual work of the external forces in Eq. (3.10) over a given element. First, it is rewritten in the form:

$$\begin{aligned}\delta W_e^e &= \int_{\partial V^e} (\delta\mathbf{u})^{\mathrm{T}}\mathbf{f}\ \mathrm{d}A + \int_{V^e} (\delta\mathbf{u})^{\mathrm{T}}\mathbf{b}\ \mathrm{d}V \\ &= \int_0^{L^e} \begin{pmatrix}\delta u & \delta w & \delta\theta\end{pmatrix} \begin{pmatrix} n \\ p \\ q \end{pmatrix} \mathrm{d}x,\end{aligned} \tag{3.32}$$

where $n(x,t)$, $p(x,t)$ and $q(x,t)$ respectively correspond to the distributed axial force, transverse force and bending moment. Introducing the discretization leads to the following expression for the virtual work of the external forces over a given element:

$$\delta W_e^e = (\delta\mathbf{q}^e)^{\mathrm{T}} \underbrace{\left(\int_0^{L^e} \mathbf{N}^{\mathrm{T}} \begin{pmatrix} n \\ p \\ q \end{pmatrix} \mathrm{d}x \right)}_{\mathbf{f}_{\mathrm{ext}}^e}, \tag{3.33}$$

from which the elementary external force vector $\mathbf{f}_{\mathrm{ext}}^e$ can be derived by evaluating the above integral in parentheses.

Gathering the expression for the various virtual works over an element in Eqs. (E.28), (E.30) and (3.33) and summing them over all elements results in the assembly procedure for the elementary matrices and force vectors. If the undeformed structure is curved, one must perform the assembly in the global frame $(\mathbf{e}_X, \mathbf{e}_Y)$ using a local rotation matrix $\mathbf{T}^e(\psi)$ applied to all elementary quantities $\mathbf{q}^e$, $\mathbf{M}^e$, $\mathbf{f}_{\mathrm{int}}^e$ and $\mathbf{f}_{\mathrm{ext}}^e$, as explained in Appendix A.1. After assembly, the discretized nonlinear finite element model falls into the following general form:

$$\mathbf{M}\ddot{\mathbf{q}} + \mathbf{D}\dot{\mathbf{q}} + \mathbf{f}_{\mathrm{int}}(\mathbf{q}) = \mathbf{f}_{\mathrm{ext}}, \tag{3.34}$$

where $\mathbf{q}$ is the column vector of the degrees of freedom expressed in the global frame of the structure, containing all variables U_{xi}, U_{yi} and θ_i for all the $N \in \mathbb{N}$ nodes, $i \in [1,\ N]$, where the displacement vector of the centerline at position x_i is $\mathbf{U}(x_i,t) = U_{xi}\,\mathbf{e}_X + U_{yi}\,\mathbf{e}_Y$. $\mathbf{M}$ is the mass matrix of size $3N \times 3N$, $\mathbf{f}_{\mathrm{int}}(\mathbf{q})$ is the internal force vector and $\mathbf{f}_{\mathrm{ext}}$ is the vector of externally-applied forces, both of size $3N \times 1$. Note that the geometrical nonlinearities are housed within $\mathbf{f}_{\mathrm{int}}(\mathbf{q})$, appearing as sine and cosine functions of the rotation degrees of freedom θ_i, as shown in Eq. (E.31). Moreover, in some cases $\mathbf{f}_{\mathrm{ext}}$ can also depend on $\mathbf{q}$, as in the case of external forces that depend on the deformed geometry of the structure, like follower forces. This case is not explicitly treated in the present study. At this stage, we also define the stiffness matrix of the problem as the tangent stiffness at the equilibrium configuration ($\mathbf{q} = \mathbf{0}$):

$$\mathbf{K} = \left.\frac{\partial \mathbf{f}_{\mathrm{int}}}{\partial \mathbf{q}}\right|_{\mathbf{q}=\mathbf{0}}. \tag{3.35}$$

Note that in Eq. (3.34), a damping matrix $\mathbf{D}$ has been introduced *a posteriori* after the FEM discretization. In the test cases that follow, a linear Rayleigh damping model will be considered, where the damping matrix is proportional to the mass matrix:

$$\mathbf{D} = \alpha\mathbf{M}, \tag{3.36}$$

with $\alpha \in \mathbb{R}$. This kind of damping was chosen here since it is the simplest damping condition to be implemented in the present finite element context and also because this study focuses primarily on the conservative nonlinear modes, as explained in Section 3.2.3.

A full Rayleigh damping model (*i.e.* $\mathbf{D} = \alpha\mathbf{M} + \beta\mathbf{K}$ with $\beta \in \mathbb{R}$) could also have been selected. However, the stiffness-proportional term creates a modal damping that increases linearly with the frequency, introducing a very heavy damping on the high-frequency modes, which can become overdamped and can subsequently influence the forced responses, likely in a non-physical way (see *e.g.* [251]). A Kelvin-Voigt damping model could also have been selected, as in [6], [69], [71]. Since this damping model is coupled to the geometrical nonlinearities, its implementation in our finite element context is not as straightforward as adding a linear damping matrix and is left for upcoming studies. This latter model seems closer to the physics since it perfectly matches measurements in a vacuum [71]. In real, open-air situations, the damping arising from air-structure interactions would be dominant over any structural damping [42], which is even more complex to include in the finite element model and is consequently left for further studies.

3.2.3 Periodic solutions computation and numerical continuation

We turn now to the determination of the solution of Eq. (3.34). Since we are interested in solutions in the frequency domain, we restrict ourselves to periodic solutions, in free oscillation or related to a forced response under harmonic forcing.

Numerically, the harmonic balance method (HBM) is used with the asymptotic numerical method (ANM [37], [55]) to compute the nonlinear modes or the forced response of the nonlinear finite element model. The MANLAB software [41], [97], which combines both the HBM and the ANM, is used to carry out the computations of the applications. A key point of the ANM is the *quadratic recast* [41], [120], which is needed to input the equation of motion into MANLAB and which guarantees faster computations and implementations. In this section, each step of the resolution method is presented briefly before moving to the presentation of the test cases.

Quadratic recast for solving with MANLAB In the remainder of the chapter, the ANM is used in conjunction with the HBM to follow periodic solutions (using the MANLAB package). In order to develop an efficient algorithm for the ANM, the HBM is not applied directly onto Eq. (3.34). Instead, the equation of motion is rewritten in the form of a differential-algebraic system of equations (DAE) with at most quadratic nonlinearities, a process known as the so-called *quadratic recast* [18], [37], [39]. This step is necessary in order for the resulting DAE system to be of quadratic order, allowing efficient computation of the Fourier coefficients of the nonlinear terms using convolution products. Another advantage of this formalism is that the definition of the Jacobian can be "hard-coded" as it only depends on the coefficients of the linear and quadratic parts of the equation. Furthermore, the MANLAB formalism requires that the dynamical system be written in first-order form, in order to be as generic as possible.

The transformation of the FE equation (3.34) into a quadratic DAE involves the definition of new variables, called *auxiliary variables*. This operation is not unique and several options are possible. Here, we introduce the quadratic recast that leads to the minimum computation time, although it is not the one which introduces the minimum number of auxiliary variables. This is a consequence of the fact that all the auxilary variables are condensed during computation of the series, such that the number of auxiliary variables has little influence on the computation time. By contrast, the number of product operations of the variables (computing $x \times y$ for variables x and y) increases the computation

time and therefore must be minimized, by introducing more auxilary variables where necessary (see [94] for details on the condensation procedure in MANLAB). Outlined below is the quadratic recast that leads to the minimum computation time. Other possible recasts are given in Appendix A.2 along with an analysis of the computation time for each of them.

We first define the following variables:

$$\bar{\theta} = (\theta_1 + \theta_2)/2, \tag{3.37a}$$

$$u_p = \frac{1}{2L^e}(u_2 - u_1), \tag{3.37b}$$

$$w_p = \frac{1}{2L^e}(w_2 - w_1), \tag{3.37c}$$

$$\theta_p = \frac{1}{2L^e}(\theta_2 - \theta_1). \tag{3.37d}$$

In addition, the sine and cosine variables c and s are introduced, defined as:

$$c = \cos\bar{\theta}, \quad s = \sin\bar{\theta}. \tag{3.38}$$

To render their evaluation quadratic, they are redefined in terms of differentials, given by:

$$\mathrm{d}c = -s\,\mathrm{d}\bar{\theta}, \quad \mathrm{d}s = c\,\mathrm{d}\bar{\theta}, \tag{3.39}$$

which are quadratic w.r.t. the variables s, c, $\mathrm{d}s$, $\mathrm{d}c$ and $\mathrm{d}\bar{\theta}$. In order to have Eqs. (3.39) fully equivalent to Eqs. (3.38), initial conditions must be added, such as:

$$c(0) = \cos[\bar{\theta}(0)], \quad s(0) = \sin[\bar{\theta}(0)], \tag{3.40}$$

as explained in [94], [95], [121] and detailed on a simple example in Appendix A.4. Notice that this process is hard-coded in the MANLAB software.

Next, the following additional auxiliary variables are introduced:

$$e = (1 + u_p)\,c + w_p s - 1, \tag{3.41a}$$

$$\gamma = w_p c - (1 + u_p)\,s, \tag{3.41b}$$

$$F_x = EAec - kGA\gamma s, \tag{3.41c}$$

$$F_y = EAes + kGA\gamma c, \tag{3.41d}$$

$$M = EI\theta_p, \tag{3.41e}$$

$$T_2 = EAe\gamma - kGA\gamma(1 + e). \tag{3.41f}$$

Note that all of the additional auxiliary variables ($\bar{\theta}$, u_p, w_p, θ_p, e, γ, F_x, F_y, M and T_2) are quadratic w.r.t. the variables u_1, u_2, w_1, w_2, θ_1, θ_2, c and s. Having defined these additional variables, the elementary internal force vector is then rewritten in a quadratic form as a function of the primary and auxiliary variables, as shown below in equation (3.45).

To summarize, the full quadratic first order DAE is given explicitly for a single finite element. For each element, the following variables are present:

1. Twelve primary variables:

   - Six positions:

$$\mathbf{q}^e = \begin{bmatrix} u_1 & w_1 & \theta_1 & u_2 & w_2 & \theta_2 \end{bmatrix}^{\mathrm{T}}, \tag{3.42}$$

- Six velocities:

$$\mathbf{V}^e = \begin{bmatrix} V_{u1} & V_{w1} & V_{\theta 1} & V_{u2} & V_{w2} & V_{\theta 2} \end{bmatrix}^{\mathrm{T}}, \tag{3.43}$$

2. Twelve auxiliary variables:

$$\mathbf{X}^e_{\mathrm{aux}} = \begin{bmatrix} \bar{\theta}\ u_p\ w_p\ \theta_p\ c\ s\ e\ \gamma\ F_x\ F_y\ M\ T_2 \end{bmatrix}^{\mathrm{T}}, \tag{3.44}$$

yielding the following quadratic first order DAE:

$$\dot{\mathbf{q}}^e = \mathbf{V}^e, \tag{3.45a}$$

$$\mathbf{M}^e\dot{\mathbf{V}}^e = \mathbf{f}^e_{\mathrm{ext}} - \mathbf{D}^e\mathbf{V}^e - \underbrace{\begin{bmatrix} -F_x \\ -F_y \\ -M + T_2 L^e/2 \\ F_x \\ F_y \\ M + T_2 L^e/2 \end{bmatrix}}_{\mathbf{f}^e_{\mathrm{int}}}, \tag{3.45b}$$

$$0 = \bar{\theta} - (\theta_1 + \theta_2)/2, \tag{3.45c}$$

$$0 = u_p - \frac{1}{2L^e}(u_2 - u_1), \tag{3.45d}$$

$$0 = w_p - \frac{1}{2L^e}(w_2 - w_1), \tag{3.45e}$$

$$0 = \theta_p - \frac{1}{2L^e}(\theta_2 - \theta_1), \tag{3.45f}$$

$$0 = \mathrm{d}c + s\mathrm{d}\bar{\theta}, \quad c = \cos\bar{\theta}, \tag{3.45g}$$

$$0 = \mathrm{d}s - c\mathrm{d}\bar{\theta}, \quad s = \sin\bar{\theta}, \tag{3.45h}$$

$$0 = e - (1 + u_p)\, c - w_p s + 1, \tag{3.45i}$$

$$0 = \gamma - w_p c + (1 + u_p)\, s, \tag{3.45j}$$

$$0 = F_x - (EAec - kGA\gamma s), \tag{3.45k}$$

$$0 = F_y - (EAes + kGA\gamma c), \tag{3.45l}$$

$$0 = M - EI\theta_p, \tag{3.45m}$$

$$0 = T_2 - (EAe\gamma - kGA\gamma(1+e))\,. \tag{3.45n}$$

In this version of the quadratic recast, there are 6 variables per node and 12 auxiliary variables per element. When considering the full mesh of N nodes and N_{e} elements, the total number of degrees of freedom of the quadratic first order DAE is then $N_{\mathrm{dof}} = 6N + 12N_{\mathrm{e}}$.

Harmonic balance method Now that the system of equations is in the form of a quadratic first order DAE, the next step is to apply the harmonic balance method (HBM). Each variable x of the N_{dof} variables of the DAE (primary and auxiliary variables) is assumed periodic of period $2\pi/\omega$, ω being the angular frequency. The variable x is expanded in the form of a truncated Fourier series (up to harmonic $H \in \mathbb{N}$):

$$x(t) = x_0 + \sum_{k=1}^{H} (x_k^c \cos k\omega t + x_k^s \sin k\omega t), \tag{3.46}$$

where x_0, x_k^c and x_k^s are the Fourier coefficients of the variable x.

In the HBM, the ansatz in Eq. (3.46) is substituted into the quadratic DAE in Eqs. (3.45) and the residual is projected orthogonally onto the (truncated) Fourier basis. This leads to an algebraic set of equations that may depend on one or several parameters (excitation frequency, forcing amplitude, *etc.*). From a general point of view, the system of (quadratic) algebraic equations resulting from the application of the HBM can be written as:

$$\mathbf{R}(\mathbf{X},\omega,\lambda) = \mathbf{R}(\tilde{\mathbf{X}}) = 0, \tag{3.47}$$

where $\mathbf{X} \in \mathbb{R}_{\mathrm{t}}^N$ is the vector containing the Fourier coefficients of all of the variables (primary and auxiliary), of size:

$$N_{\mathrm{t}} = N_{\mathrm{dof}}(2H+1) = (12N + 4N_{\mathrm{e}})(2H+1), \tag{3.48}$$

λ is a continuation parameter, $\tilde{\mathbf{X}} = \begin{bmatrix}\mathbf{X}^{\mathrm{T}} & \omega & \lambda\end{bmatrix}^{\mathrm{T}} \in \mathbb{R}^{N_{\mathrm{t}}+2}$ and $\mathbf{R} : \mathbb{R}^{N_{\mathrm{t}}+2} \to \mathbb{R}_{\mathrm{t}}^N$ is the function defining the residual of the HBM. The solutions to Eq. (3.47) will be obtained using the asymptotic numerical method (ANM) described hereafter, after describing the two main cases of computations.

Nonlinear modes and forced response In the applications presented in Section 3.3, two kinds of solutions will be computed, namely, the periodic response of the system under harmonic forcing (forced response) and the periodic response of the free and undamped system (nonlinear modes).

In the forced response case, the FE equation (3.34) to be solved is as follows:

$$\mathbf{M}\ddot{\mathbf{q}}(t) + \mathbf{D}\dot{\mathbf{q}}(t) + \mathbf{f}_{\mathrm{int}}[\mathbf{q}(t)] = \mathbf{F}\sin\Omega t, \tag{3.49}$$

where $\mathbf{F}$ is the vector of applied harmonic forcing amplitude and Ω is the angular frequency of the forcing. The computation of the forced response is quite straightforward: the user inputs the DAE Eqs. (3.45) and the angular frequency of the periodic solution is chosen equal to that of the forcing. The continuation parameter λ is also set equal to the value of the frequency, such that $\lambda = \omega = \Omega$. The equation $\lambda = \omega$ is thus added to the residual Eq. (3.47). The continuation of the periodic solution can then be carried out for several constant forcing amplitudes to reveal the effect of the nonlinearity on the dynamic behavior of the system.

In the free response case, the FE equation (3.34) to be solved is initially written as follows:

$$\mathbf{M}\ddot{\mathbf{q}}(t) + \mathbf{f}_{\mathrm{int}}[\mathbf{q}(t)] = \mathbf{0}, \tag{3.50}$$

where the damping and forcing terms have been canceled. The main differences with the forced response case are that now the system is (a) autonomous and (b) conservative. Due to (a), there is no explicit phase information in the system, so if a periodic orbit of period $2\pi/\omega$ is a solution of (3.50), any periodic orbit identical in amplitude and period, but with a different phase, is likewise a solution. This can lead to numerical instabilities and is traditionally solved with the addition of a phase condition (Eq. (3.51b)). Futhermore, because of (b), there is an additional variable – the energy of the system – which is implicit and which plays the role of the bifurcation parameter λ. However, because this variable is implicit, the system is overdetermined with the addition of the phase condition. To solve this problem, following [16], [158], a fictitious bifurcation parameter λ is introduced and Eq. (3.50) is replaced with:

$$\begin{cases} \mathbf{M}\ddot{\mathbf{q}}(t) + \lambda\dot{\mathbf{q}}(t) + \mathbf{f}_{\mathrm{int}}[\mathbf{q}(t)] = 0, & \text{(3.51a)} \\ \dot{\mathbf{q}}_i(0) = 0. & \text{(3.51b)} \end{cases}$$

Note that the above system has the form of a classical dissipative autonomous system, well posed for numerical continuation. However, since periodic solutions are computed, the only solution to problem (3.51) is undamped, and thus the solution computed by the algorithm is $\lambda \simeq 0$ [97]. The resulting branches of solution can be plotted in an amplitude / frequency plot in order to visualize the backbone curve of the system.

Asymptotic numerical method and MANLAB Due to the implicit functions theorem, the solution of Eq. (3.47) with the additional equation ($\lambda = \omega$ in the forced case or the phase equation (3.51b) in the free conservative case) defines a one-dimensional manifold in the $\mathbb{R}^{N_t+2}$ space mapped by $(\mathbf{X}, \lambda, \omega)$ that can be followed through continuation given an initial point. In this work, the asymptotic numerical method (ANM), first presented in [55] and derived at length in [37], [41], [95], is used to carry out the continuation procedure.

The ANM basically relies on a high order predictor. The solution is sought in a parametrized form along with a Taylor series expansion, up to degree P:

$$\tilde{\mathbf{X}}(a) = \tilde{\mathbf{X}}_0 + a\tilde{\mathbf{X}}_1 + a^2\tilde{\mathbf{X}}_2 + a^3\tilde{\mathbf{X}}_3 + ... + a^P\tilde{\mathbf{X}}_P, \tag{3.52}$$

where a is a pseudo arc-length and P typically chosen equal to 20. In order to obtain the coefficients of this expansion, the ansatz in Eqs. (3.52) is substituted into the HBM residual Eq. (3.47) and terms are gathered relative to the power of the parameter (zero-th order $a^0 = 1$, first order $a^1 = a$, second order a^2, ...). Balancing the coefficients of a^p for each order $p \in [0,\ P]$ and injecting the definition of a results in [41]:

1. A nonlinear algebraic system $\mathbf{R}(\tilde{\mathbf{X}}_0) = \mathbf{0}$ at zero-th order,
2. A cascade of linear systems for the higher orders, which enables the computation of $\tilde{\mathbf{X}}_p$ at order $p \geq 1$ as a function of all of the previous orders $\tilde{\mathbf{X}}_i$, $i < p$.

Using this procedure, all $\tilde{\mathbf{X}}_p$, $p \in \{0, \dots P\}$ are computed and a branch of solution is obtained as a continuous function of a. This branch has a radius of convergence a_m, automatically computed, such that $\forall a < a_\mathrm{m}\ ||\mathbf{R}(\tilde{\mathbf{X}}_p(a), \lambda_p(a))|| < \epsilon$, with ϵ a tolerance chosen by the user. A numerical continuation process consists then in computing several continuous branches, such that the first point of a given branch $\tilde{\mathbf{X}}(a = 0) = \tilde{\mathbf{X}}_0$ is taken as the final point of the previous one, thus identically verifying the zero-th order $\mathbf{R}(\tilde{\mathbf{X}}_0) = \mathbf{0}$ up to the chosen tolerance ϵ. The value of $\tilde{\mathbf{X}}_0$ for the first branch is computed by a Newton-Raphson algorithm, initiated by an initial guess defined by the user. This latter operation will be called the *initialization* step in the following section.

In practice, the MANLAB package [96], implemented in the MATLAB environment, is used to carry out the numerical continuation. In addition, it also offers tools to detect bifurcation points [40], to compute bifurcated branches and to evaluate the stability of periodic solutions [97].

Initialization Proper initialization of the calculation (*i.e.,* the computation of $\tilde{\mathbf{X}}_0$ for the first branch of the continuation) is crucial, as the accuracy of the computation of $\tilde{\mathbf{X}}_0$ guarantees the accuracy of all of the branches computed thereafter. Since resonant systems are under investigation here, a preliminary computation of the low frequency eigenmodes is necessary. One solves:

$$(\mathbf{K} - \omega^2\mathbf{M})\mathbf{\Phi} = \mathbf{0}, \tag{3.53}$$

to obtain the natural frequencies ω_i and mode shapes $\mathbf{\Phi}_i$ for $i = 1, 2, \dots$

When performing forced computations, initializing the Newton-Raphson algorithm with a zero solution far from a resonance works in most cases. Restated more precisely, one prescribes ($\mathbf{X} = \mathbf{0}$, Ω far from ω_i) as the initial guess.

When investigating the nonlinear modes, however, the initialization of a given backbone curve computation is more delicate. Two different options are presented. The first method initializes the algorithm on a linear single-mode solution; namely, for the i-th nonlinear mode $\mathbf{q}(t) = \beta\boldsymbol{\Phi}_i \cos\omega_i t$, with $\beta \in \mathbb{R}$ small so that the amplitude $||\beta\boldsymbol{\Phi}_i||$ of the vibration pattern is small enough not to activate the geometrical nonlinearities. The second option, which is the one used in the simulations of the test cases shown in Section 3.3, is to compute first a harmonically-forced solution branch and then pick a solution $(\mathbf{X},\omega)$ close to the i-th phase resonance point, where the displacement is in phase quadrature with the forcing (as done in experimental continuation [60]).

Scaling of the equations To improve the numerical conditioning of the residual $\mathbf{R}$, it can be useful to scale the parameters such that the equations are rendered dimensionless. Following [169], we define the dimensionless variables (denoted by $\hat{\circ}$):

$$\hat{U}_x, \hat{U}_y = \frac{U_x, U_y}{L}, \quad \hat{x} = \frac{x}{L}, \quad \hat{t} = \frac{t}{L^2}\sqrt{\frac{EI}{\rho A}}, \tag{3.54a}$$

$$\hat{N}, \hat{T}, \hat{q} = \frac{L^2}{EI}(N, T, q), \quad \hat{M} = \frac{L}{EI}M, \quad \hat{n}, \hat{p} = \frac{L^3}{EI}(n, p), \tag{3.54b}$$

where L is a characteristic length of the structure (*e.g.* the length of a beam, the diameter of a ring, see examples in Section 3.3). Rewritten in this way, it can be shown (see Appendix A.3) that the dimensionless equations of motion of a geometrically exact beam based on Euler-Bernoulli kinematics with uniform cross-section depend on only one parameter, the slenderness ratio:

$$\eta = I/(AL^2). \tag{3.55}$$

In the present case of Timoshenko kinematics, the slenderness ratio depends also on the shear parameter μ defined in Appendix A.3. The highly flexible structures considered in this work naturally have a very small η, underlining their slenderness. This indicates that there will be very little effect of shearing of the cross-section even at extreme amplitudes of deformation, meaning that there is virtually no difference between Timoshenko and Euler-Bernoulli kinematics.

Furthermore, introducing dimensionless parameters brings more universality to the results of this work. The dynamical behavior of any structure with the same shape and parameter η as the test cases of Section 3.3 can be quantitatively recovered using the change of variable of Eqs. (3.54).

In practice, for a beam structure with uniform cross-section and homogeneous material, the dimensionless version of system (3.34) can be obtained simply by setting $EI = 1$, $\rho A = 1$, $\rho I = \eta$, $L = 1$, $EA = 1/\eta$ and $kGA = k/[2(1+\nu)\eta]$ with ν the Poisson's ratio of the material.

3.3 Test cases

In this section, the numerical strategy developed in Section 2 is used in the simulation of various flexible beam structures. To highlight the capabilities of the method, different test cases are selected: a simple cantilever beam, a beam clamped at both ends, a circular ring, a truss structure and an idealized model of a tree, as shown in Fig. 3.3. In each case, the nonlinear modes of the system are

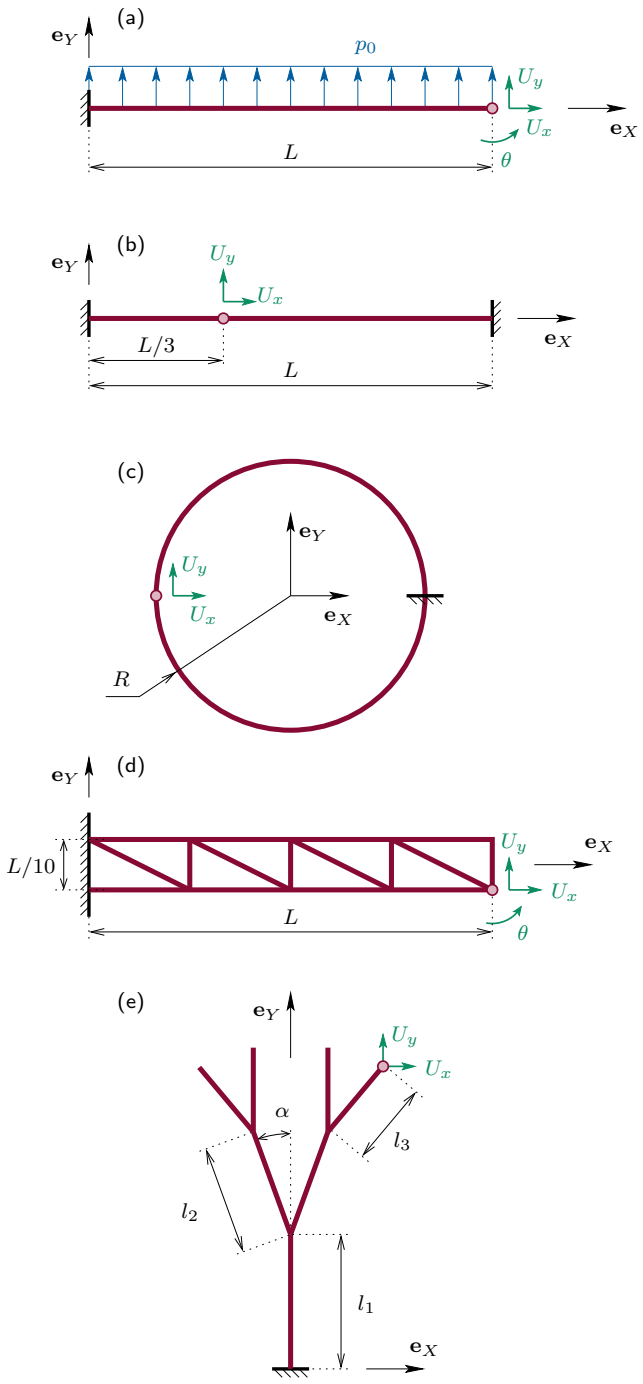

Figure 3.3: Sketches of the test cases. The red bullet shows for each test case the selected node and the associated displacement / rotation components where backbone curves are plotted.

computed with Eq. (3.51). The forced responses, however, are only shown for the cantilever beam test case for the sake of efficiency, although they can be easily calculated for each structure.

Table 3.1: Material properties of flexible beam structures, all structures.

Structure	Density ρ [kg/m^3]	Young's modulus E [GPa]
Cantilever	7800	210
CC	7800	210
Ring	4400	104
Truss	7800	210
Tree	600	13

In all computations, $k = 1$ and $G = E/[2(1+\nu)]$ with $\nu = 0.3$.

Table 3.2: Number of discrete elements per structure and corresponding number of FE nodes.

Structure	Mode	Elements N_e	Nodes N	Harmonics H
Cantilever	1	20	21	20
	2	25	26	20
	3	30	31	20
CC	1	50	51	10
Ring	1	30	30	10
	2	40	40	10
Truss	1	85	78	20
	2	85	78	10
Tree	1	54	55	20
	2	54	55	20
	3	54	55	10

The nonlinear modes are graphically represented in two ways. Firstly, we show the backbone curve, representing the evolution of the amplitude of the motion as a function of the free oscillation frequency. Precisely, the maximum value of the absolute value over one period of oscillation of the rotation of the cross-section ($\theta(t)$) and/or the displacement components of a selected point of the structure ($U_x(t), U_y(t)$) are depicted. Examples are Figs. 3.4(a,b,c) for the fundamental nonlinear mode of the cantilever beam. An alternative would have been to show some of the harmonics of these quantities instead of the maximum over a period, in order to investigate the harmonic content of the oscillation. This is addressed with the inclusion of several bar diagrams, mainly in Section 3.4.

The second graphical representation of the nonlinear modes is their deformed shapes, shown for selected points along the backbone. They are plotted here as several snapshots of the deformed configuration of the structure taken at fixed time over one half period of the periodic motion. Examples are Figs. 3.4(d,e,f) for the fundamental nonlinear modes of the cantilever beam. The deformed configurations are useful in order to understand more deeply the complex nonlinear dynamics that are observed.

3.3.1 Cantilever beam

We first consider a cantilever beam, with one end fixed and the other free, shown in Fig. 3.3(a). This configuration allows for very large deformations under small transverse loading conditions, manifesting

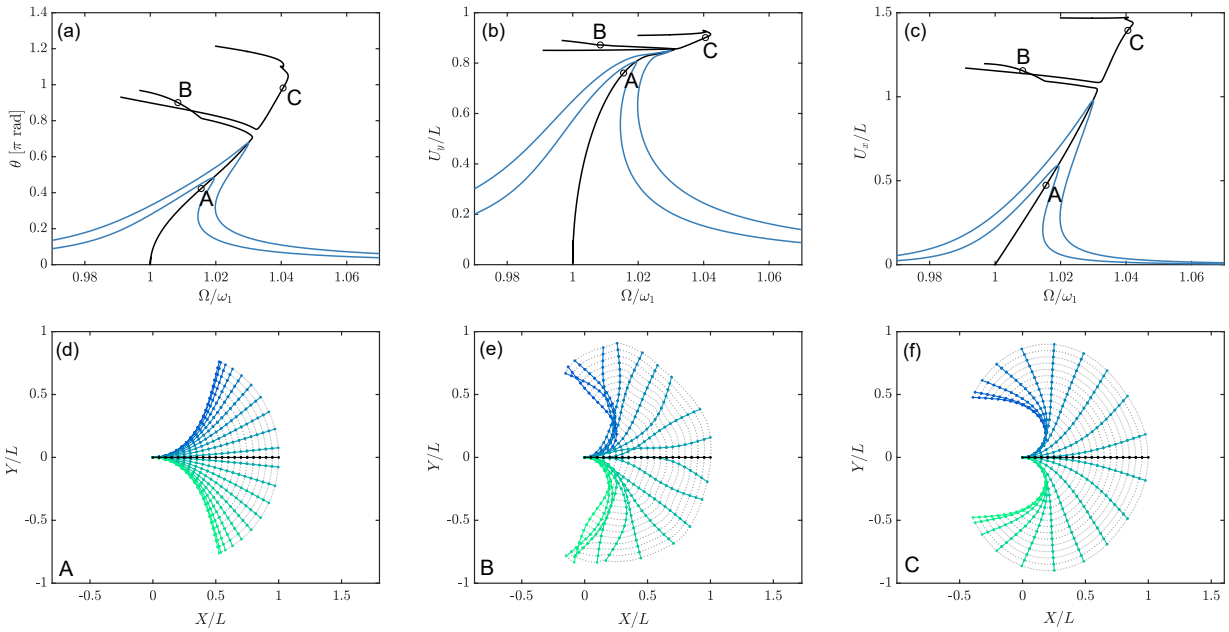

Figure 3.4: First nonlinear mode of the cantilever beam of Fig. 3.3(a). Top row: forced responses ($\hat{F}_0 = 0.05$ and $\hat{F}_0 = 0.08$) and backbone curve of (a) the cross-section rotation θ, (b) the scaled transverse displacement U_y/L, (c) the scaled axial displacement U_x/L at the tip of the cantilever. Maximum amplitude over one period of oscillation. Bottom row: nonlinear deformed shape at (a) low amplitude (point A), (b) internal resonance (point B) and (c) high amplitude (point C); 20 snapshots per half period.

extreme changes in shape of the structure. The extreme deformation sometimes even reaches the point of "bending backwards," where the free end of the cantilever achieves a displacement behind the opposite fixed end. For this reason, the geometrically exact beam model is a necessity in order to properly capture the geometrically nonlinear behavior. Additionally, the cantilever beam is the simplest example that can be selected in order to validate the numerical strategy proposed in this chapter. Many works have been published in the past on nonlinear vibrations of cantilever beams and the interested reader can refer to [229] for an overview, as well as the recent numerical contributions [68], [69], [217], [250].

A mesh corresponding to a cantilever beam of length $L = 1$ m, width $b = 0.05$ m and thickness $h = 0.001$ m, with material properties as shown in Table 3.1, is generated. Its slenderness ratio is $\eta = 8.33 \cdot 10^{-8}$, implying a very slender beam. Details on the mesh/system properties, such as the number of discrete elements, are collected in Table 3.2 for all test cases. For the simulations, as explained in Section 3.2.3, the system's geometry is normalized such that the characteristic length L is the length of the beam.

For simulation of the forced response of this system, a uniformly distributed transverse loading $p(x,t) = p_0 \sin \Omega t$, as defined in Eq. (3.33), is prescribed, with p_0 its amplitude, in [N/m]. It is equivalent to a transverse support motion, in which case the transverse loading becomes $p_0 = -\rho A \ddot{w}_0$, where $\ddot{w}_0$ is the base acceleration. In the finite element context, this load appears as an external force $\mathbf{f}_{\text{ext}}(t)$ in Eq. (3.49) of the form $\mathbf{f}_{\text{ext}}(t) = \mathbf{F} \sin \Omega t$, with the components associated to the transverse displacement

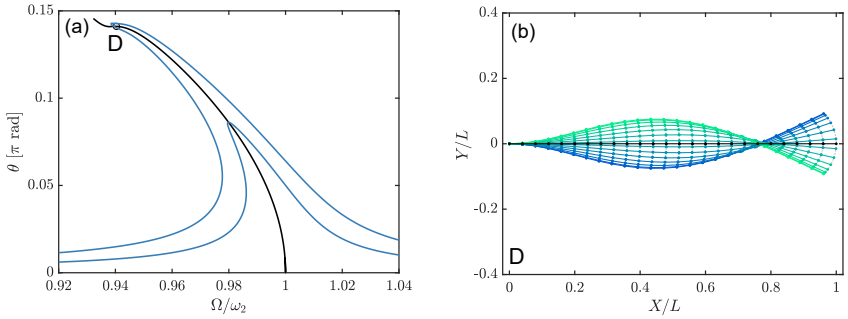

Figure 3.5: Second nonlinear mode of the cantilever beam. Left: forced responses ($F_0 = 0.16$ and $F_0 = 0.3$) and backbone curve of θ rotation of the cross-section at free end of beam. Right: deformed configuration of the cantilever at point D; 14 snapshots per half period.

in $\mathbf{F}$ of the form $F_0 \left[\frac{1}{2} \quad 1 \ldots 1 \quad \frac{1}{2}\right]^{\mathrm{T}}$ and the others being zero. Note that this is valid if the elements are of constant length L^e, in which case $F_0 = p_0 L^e$. In Fig. 3.4, we indicated its dimensionless value: $\hat{F}_0 = L^2 p_0 L^e/(EI)$.

The linear damping coefficient α of Eq. (3.36) is chosen to be $\alpha = 2\xi\omega_i$ with $\xi = 0.005$ and ω_i the (linear) natural frequency of the considered mode.

Figs. 3.4, 3.5 and 3.6 depict typical results of our computations for the first three nonlinear modes of the cantilever. Some frequency responses under forced excitation for a given value of the forcing amplitude $\hat{F}_0$ are shown in blue with the backbone curves added in black. Many interesting nonlinear dynamic phenomena, as were described in Section 3.1, are uncovered.

Beginning with the first nonlinear mode, shown in Fig. 3.4(a)-(c), it can be seen that it manifests a slightly hardening behavior, meaning that the resonant frequency Ω increases as the vibration amplitude increases, a characteristic well documented in the literature, see [68], [175], [229]. Point A represents a point of moderate amplitude of displacement along the backbone curve and point C a point of high amplitude. The solving method introduced in this chapter is capable of pushing the cantilever simulation to very extreme amplitudes, as evidenced by the deformed shape at point C. At this point, the cantilever has fully bent backwards, with the free end of the beam vibrating well beyond the location of the fixed end. Note that even though the maximum of the absolute value is shown in Fig. 3.4(c), the U_x displacement is always negative in value as the tip of the beam is always deformed "backwards" relative to its initial position.

Point B represents an instance of an internal resonance, wherein some of the energy is transferred to another vibration mode. Typically, in order to characterize the type of internal resonance, one must look at the spatial pattern depicted by each harmonic and compare it to the mode shapes of the structure in order to conclude the type of internal resonance involved, as explained in Section 3.3.2. In the present case, because this internal resonance is less clear and lacks convergence within the number of retained harmonics, the discussion is left for Section 3.4.

The second and third nonlinear modes of the cantilever are shown in Figs. 3.5 and 3.6, respectively. The forced responses and nonlinear modes are shown in θ for both modes as the rotation of the cross-section θ gives a good idea of the extent of the beam's deformation. Both the second and third modes of the cantilever beam exhibit a softening trend, wherein Ω decreases with increasing amplitude of vibration, a fact also well documented (see [175], [229]). The amplitude of deformation U_y of the

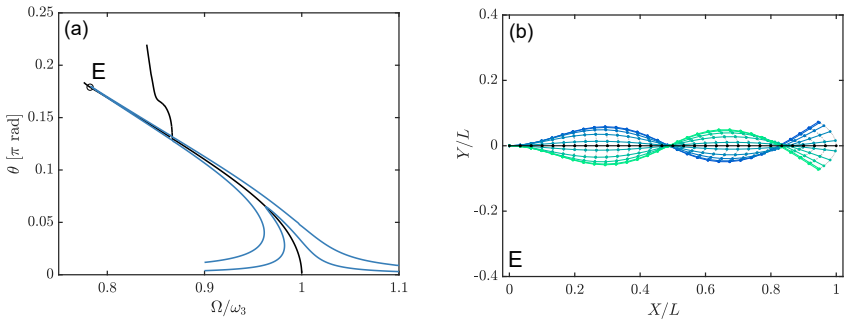

Figure 3.6: Third nonlinear mode of the cantilever beam. Left: forced responses ($F_0 = 1$ and $F_0 = 3$) and backbone curve of θ rotation of the cross-section at free end of beam. Right: deformed configuration of the cantilever at point E; 10 snapshots per half period.

beam is less pronounced on the second and third modes than on the first, due to the presence of node points in the deformed shape. Expressed more concretely, due to the particular geometry of the nonlinear mode shapes, a certain maximum rotation amplitude θ of the cross-section observed at the tip of the beam is obtained for an amplitude U_y of transverse displacement, which decreases as the index of the considered mode increases. Since the mechanism of geometrical nonlinearities is linked to the amplitude of the rotations of the cross-sections, the effect of the geometrical nonlinearities is associated with a certain θ and thus to a U_y that decreases with the index of the modes. Another internal resonance point, however, was captured in the simulation of the third mode and appears as an offshoot of the primary backbone curve. This particular internal resonance was not investigated, but a discussion on these internal resonance offshoots appears in Section 3.5.

3.3.2 Clamped-clamped beam

A second classical type of beam structure is the clamped-clamped (CC) beam. This example is considered here since the mechanism of geometrical nonlinearities is different. For all the other test cases considered in this chapter, the physical source of geometrical nonlinearities is the large rotation of the cross-sections, but in the case of the CC beam it is the bending / axial coupling (see Fig. 3.1 and *e.g.* [130]). Due to the presence of boundary conditions that restrain axial motion, a bending deformation induces an increase in the axial tension that increases the bending stiffness and creates a strong nonlinear hardening effect.

We consider the same beam as in the previous section, but fixed now at its two ends. For the computations, like the cantilever, the CC beam is normalized by its length. The fundamental nonlinear mode is computed with the geometrically exact model. Fig. 3.7(a) shows the corresponding backbone curve for U_y/h at the node located at $x = 0.3L$ from the left end of the beam (see Fig. 3.3(b)). Fig. 3.7(a) depicts this backbone curve, with a decidedly strong hardening behavior, classical of all flat structures subjected to bending / axial coupling [227]. This coupling is responsible for the stronger geometrically nonlinear effects than were seen with the cantilever beam. The hardening / softening behavior in particular is significant for much lower amplitudes of transverse displacement when comparing on the order of the thickness h of the CC beam and not of the length of the beam.

The deformed shape of the beam is also shown at two points of the backbone curve. Point F

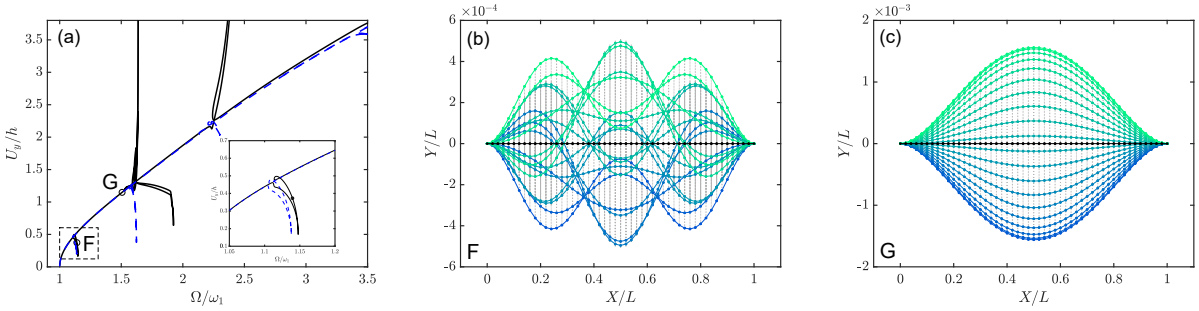

Figure 3.7: First nonlinear mode of a beam fixed on both ends (clamped-clamped beam). Left: backbone curve of U_y/h displacement at a distance $x = 0.3$ [m] from left end of beam (in blue: von Kármán solution). Center: deformed configuration at internal resonance point F. Right: deformed configuration at point G; 20 snapshots per half period.

(Fig. 3.7(b)) represents the classical 1:5 internal resonance (IR) of the first mode with the third mode (see [86]). The IR is responsible for a strong coupling between these two modes, which is clearly seen in the deformed configuration at this point. The deformed shape exhibits a mix of the first mode shape oscillating at frequency Ω and the third mode shape oscillating at 5Ω, a pattern visible in Fig. 3.7(b) as well as in Fig. 3.13(c). Point G (Fig. 3.7(c)) is characterized by the deformed shape of the first mode at a high amplitude of displacement, very close to the linear mode shape of mode 1 even for this oscillating frequency (1.5 times higher than the linear natural frequency ω_1 of the structure). Other internal resonances are also computed on the main backbone curve, a 1:9 with mode 5 around $\Omega/\omega_1 = 1.56$ and a 1:7 with mode 5 around $\Omega/\omega_1 = 2.15$.

The results of the geometrically exact model and solving method proposed in this chapter were compared against the nonlinear von Kármán (VK) analytical model, provided in [86]. It is solved in [86] by a modal expansion on the first 8 natural mode shapes of the beam and a numerical continuation of the obtained dynamical system, solved with MANLAB with $H = 10$ harmonics retained in the HBM. The results of this comparison are shown in Fig. 3.7(a), where the dashed blue line represents the nonlinear VK solution. It can be seen that the geometrically exact model perfectly agrees with the VK model, including the detection of internal resonances during simulation. However, it is noted that the internal resonance "offshoots" (known also as internal resonance "tongues" [124]) are predicted slightly differently in the two models, departing from the central backbone at slightly shifted locations and sometimes in different directions. This can be explained by the different spatial discretizations used in the two models. For the VK model, an analytical modal basis is used with exact natural frequencies, whose ratios to the first natural frequency are:

$$\omega_i^{\mathrm{VK}}/\omega_1^{VK} \in \{1; 2.76; 5.40; 8.93; 13.34\}.$$

In the FE model, they are:

$$\omega_i^{\mathrm{FE}}/\omega_1^{FE} \in \{1; 2.79; 5.58; 9.47; 14.64\},$$

for $i = 1, \ldots 5$. Considering that the internal resonance stems from the coincidence of one harmonic of the oscillation with the (nonlinear) frequency of a given nonlinear mode (see [86] for examples), the slight differences between the values of the natural frequencies in the two models explains the

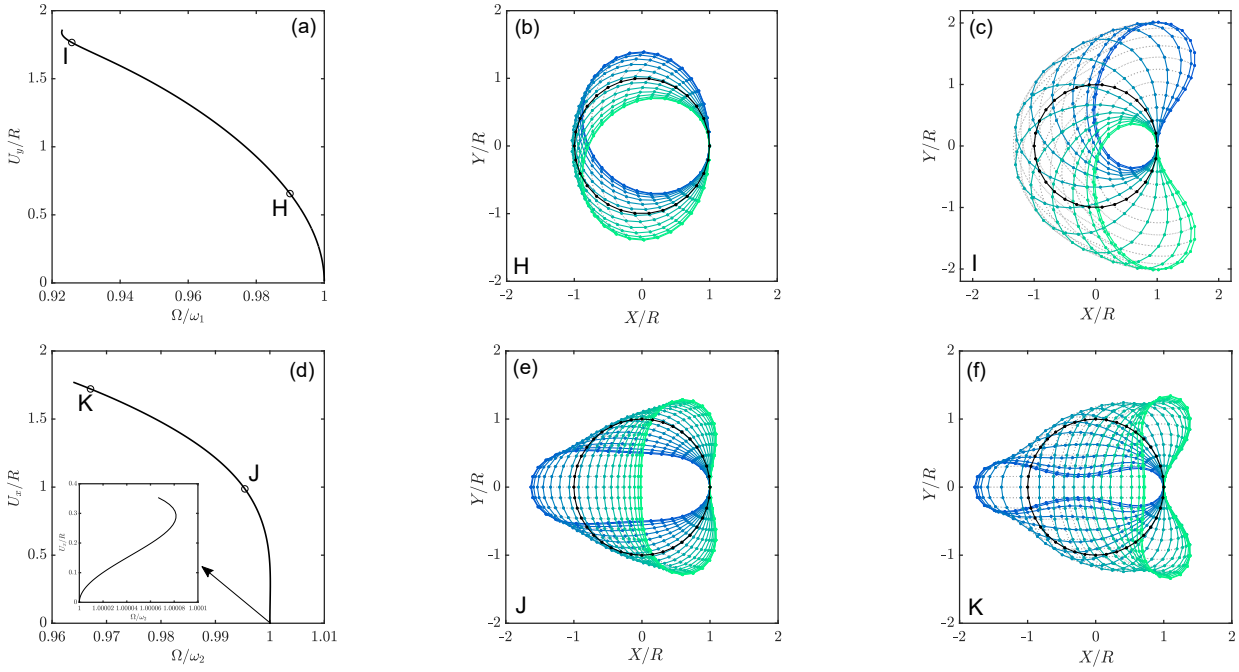

Figure 3.8: First and second nonlinear modes of a clamped circular ring. Top row: (left) mode 1 backbone curve of $U_y : R$ displacement at node opposite the clamp, (center) deformed configuration of the ring at point H, (right) at point I; 14 snapshots per half period. Bottom row: (left) mode 2 backbone curve of U_x/R displacement at node opposite the clamp, (center) deformed configuration at point J, (right) at point K; 20 snapshots per half period.

discrepancies between the two models. This is illustrated in the inset of Fig. 3.7(a), in which the shape of the 1:5 IR tongue is computed identically in both models, but with a slight shift in frequency.

Fig. 3.7(a) is also useful to quantify the limitations on the validity of the VK model, since it is based on a truncation of the beam's cross-sectional rotations and is thus valid only for moderate amplitude of vibration. By contrast, the FE geometrically exact model introduced in this chapter has no limit of validity. Looking at Fig. 3.7(a), the backbone computed from the VK model begins to depart from the geometrically exact backbone around $U_y \simeq 3h$.

3.3.3 Circular ring

Another interesting structure that was tested is the flexible ring. Previous studies have investigated the dynamics of ring structures, notably the studies of Santillan, Virgin and Plaut [205], [246] and, more recently, Lu *et al.* [144], which were the inspiration for the circular ring structure considered here. The ring of radius $R = 1$ m is discretized into beam elements of circular (radius $r = 10$ mm) cross-section with material properties shown in Table 3.1 and mesh properties shown in Table 3.2. Prior to solving, this system is normalized by its characteristic length, which in this case is chosen as the radius R. The circular ring is clamped on the rightmost node (see Fig. 3.3(c)).

The resulting dynamical response is shown for the first two nonlinear modes of vibration in Fig. 3.8. It is readily seen that the first nonlinear mode is a transverse mode, while the second represents an

axial mode of vibration. The backbone curves representing the nonlinear modes of the system are traced for the U_y/R (for mode 1) and U_x/R (for mode 2) displacements at the node directly opposite the fixed node (see Fig. 3.3(c)).

The first nonlinear mode of vibration is obviously softening (Fig. 3.8(a)). However, an interesting feature is observed in its deformed shape (Figs. 3.8(b,c)). Typically, if the amplitude of the modal motion were small, related to a linear oscillation, the displacement could be written $\mathbf{u}(t) = a\boldsymbol{\Phi}\cos\Omega t$, where $\boldsymbol{\Phi}$ is the eigenvector and $a \in \mathbb{R}$ the amplitude of the motion. Once in the period of oscillation ($t = 0, 2\pi/\Omega, 3\pi/\Omega, \ldots$ here), the structure would recover exactly its undeformed shape at this particular time, no matter the extent of the deformation, since $\mathbf{u}(0) = 0\,\forall a$. In other words, when looking at the deformed configurations of the ring in Fig. 3.8 at points H, I, J and K, the colored lines should pass exactly through the (undeformed) black line. However, at high amplitudes of vibration, the deformed shape of the ring vibrating on its first mode does not return to its initial configuration. Looking at the deformed shape of the ring at point I in Fig. 3.8(c), the ring does not pass through its initial circular shape, instead maintaining a distorted and slightly elongated oval shape. This is surely linked to a centrifugal effect gaining importance at extreme amplitudes of vibration, due to a "swinging" effect of the ring. At lower amplitude (traced at point H), the centrifugal effect is less pronounced, since the ring nearly passes back through its initial circular shape. A second interesting feature is observed in the second mode. Although its backbone curve is globally softening, at low forcing amplitude, the curve is initially of the hardening type, before bending in a softening trend at a higher amplitude. Whereas a switching from softening to hardening behavior as the amplitude increases is classical for slightly curved structures (some examples include shallow shells in [234] and shallow arches in [153], [250]), this reversed phenomenon has never been encountered previously, to the knowledge of the authors.

3.3.4 Truss structure

A fourth structure, that of a cantilever-style truss structure, is here considered (see Fig. 3.3(d)). The analysis of this style of beam was inspired by the work of Guillot, Cochelin and Vergez [94] on similar beams. The truss is of length $L = 1$ m and height $L/10$ and is composed of beams of rectangular cross-section of width $b = 0.1$ m and height $h = 0.1$ m with material properties as shown in Table 3.1. The truss is divided into four frames of $L/4$, with a diagonal beam connecting the upper left and lower right corners of each frame. The construction of the asymmetrical truss can be seen in Fig. 3.9, where the solid black lines shown at points L, M and N outline the undeformed configuration of the structure. The nodes making up the left edge of the structure are fixed, while all other nodes are free. Like the cantilever, this structure was also normalized by its characteristic length, considered here the length of the structure.

Results of the dynamic simulations are shown for the first two nonlinear modes in Fig. 3.9. The backbone curves trace the rotation of the cross-section θ at the lower, right-most node (the bottom right corner of the truss, see Fig. 3.3(d)). The deformed shapes of the truss are shown at points L and M for the first mode, and N for the second mode. The behavior of the truss mirrors the behavior of the cantilever beam, since the first two nonlinear modes of the truss have the same global shape as the first two nonlinear modes of the cantilever. At higher amplitudes, it was observed during simulations (not reproduced here) that some local "buckling"-like modes, involving single beam members, appeared in the deformed shape. Moreover, one can notice the asymmetrical shape of the deformed shape of the truss, especially visible in Fig. 3.9(e), for which the maximum (blue) and minimum (green) position of the truss are not symmetrical with respect to the horizontal axis. This is due to the asymmetry in the structure, brought by the four inclined beams that cross the frames.

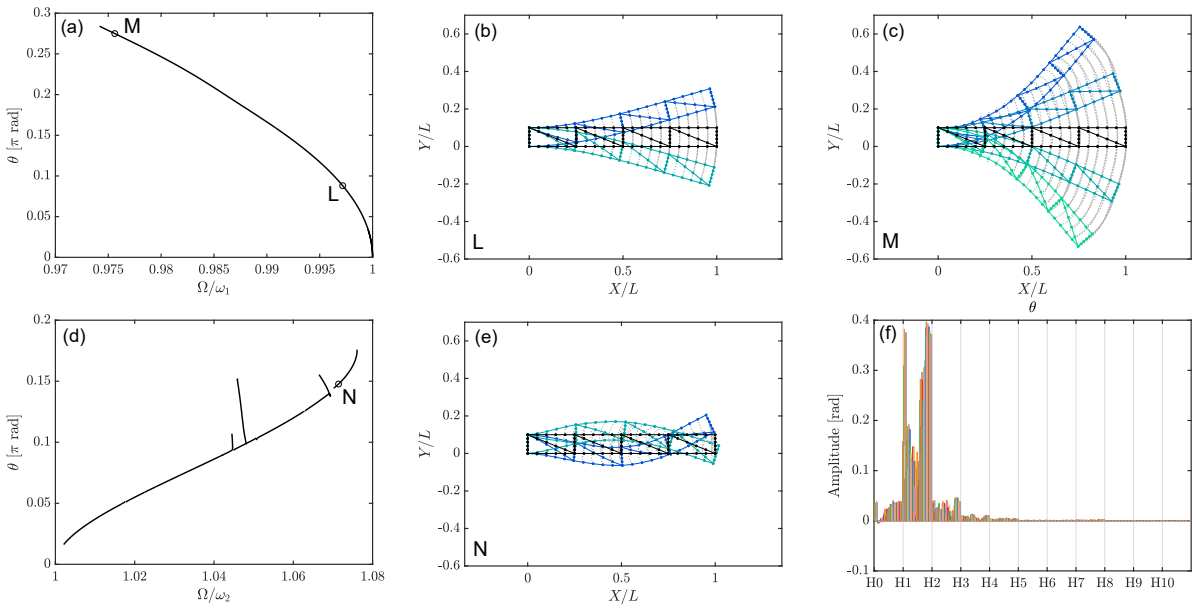

Figure 3.9: First and second nonlinear modes of a truss structure. Top row: (left) mode 1 backbone curve of θ rotation of the cross-section at top right corner of free end, (center) deformed configuration of the truss at point L; 2 snapshots per half period, (right) at point M; 4 snapshots per half period. Bottom row: (left) mode 2 backbone curve of θ rotation of the cross-section at top right corner of free end, (center) deformed configuration at point N; 4 snapshots per half period, (right) harmonic convergence of θ at point N.

It is noted that despite the global resemblance between the cantilever beam and the cantilever truss structure, the trend of the backbone curves is reversed: mode 1 of the truss manifests a softening nonlinear behavior, while it is hardening for the cantilever beam; mode 2 of the truss is hardening, whereas it is softening for the cantilever beam. Furthermore, the convergence in harmonics of θ at point N, shown in Fig. 3.9(f), is included in order to confirm that, even at the relatively high deformation shown at point N, the solution remains converged with only 10 harmonics included (see Section 3.4 for more on convergence studies).

3.3.5 Symmetrical tree model

A fifth and final structure is considered in order to confirm that the numerical method outlined in this chapter for the nonlinear dynamical simulation of flexible structures is applicable to any finite element structure. For this, a simple finite element model of a tree is introduced. The tree is represented as a collection of several branching beams connected to a central "trunk." The tree simulations were inspired by the work of Kovačić *et al.* [126], [127] on the dynamic analysis of tree-like structures based on beam models. The work of Kovačić *et al.* takes into account in the model many biological inspirations from real trees, such as the diameter, length and mass ratios of branches at each branching point, slenderness coefficient and branching angle. Some of these features are taken into account here to obtain the structure of Fig. 3.3(e), in particular constant branching angle $\alpha = \pi/9$ and length ratio $l_2/l_1 = l_3/l_2 = 0.79$, as used in [126]. The "trunk" of the tree is of length $l_1 = 0.5$ m. The tree structure

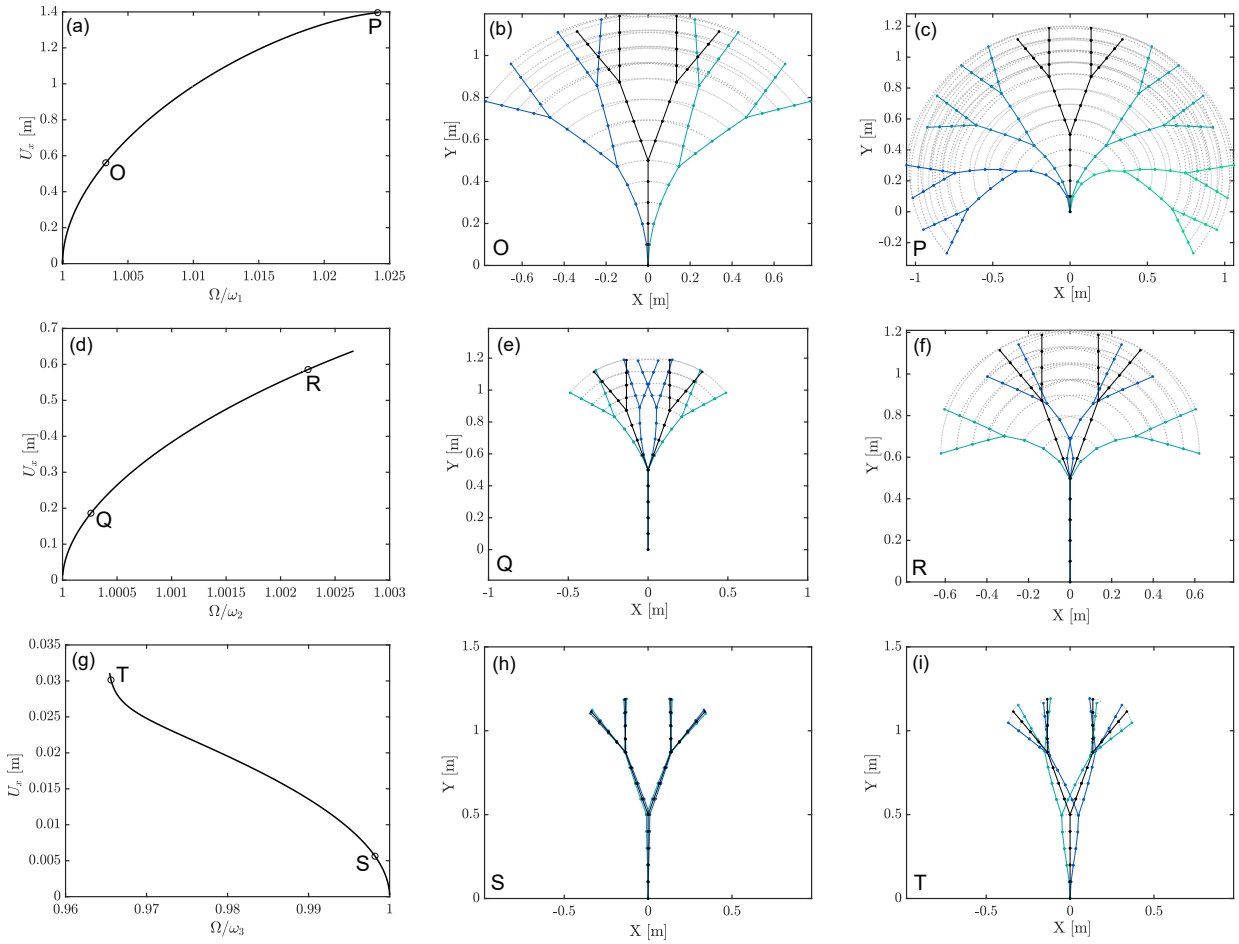

Figure 3.10: First, second and third nonlinear modes of a tree-like structure. Top row: (left) mode 1 backbone curve of U_x displacement at top rightmost node, (center) deformed configuration of the tree at point O; 2 snapshots per half period, (right) at point P; 4 snapshots per half period. Center row: (left) mode 2 backbone curve of U_x displacement at top rightmost node, (center) deformed configuration at point Q, (right) at point R; 2 snapshots per half period. Bottom row: (left) mode 3 backbone curve of U_x displacement at top rightmost node, (center) deformed configuration at point S, (right) at point T; 2 snapshots per half period.

is constructed of beam elements with constant material properties (see Table 3.1) and circular cross-section with constant diameter $d = 0.1$ m, simplifying the pattern of decreasing cross-section area of each branch used by Kovačić *et al.* Unlike the previous four test cases, this model was not normalized by any characteristic length for the simulations. Finally, the bottom-most node is considered fixed in this model, to represent the trunk of the tree being fixed to the ground.

The backbone curves representing the nonlinear modes are traced for the first three nonlinear modes at the tip of the rightmost branch, considered as a point that experiences extreme amplitudes of vibration. The deformed shapes of the tree on its first three nonlinear modes are shown at both low and high amplitudes of vibration. Interestingly, the deformed configurations of the first three

nonlinear modes of the tree share some similarities with the cantilever beam. The first mode shape of the tree closely resembles the first mode shape of the cantilever. Similarly, the two primary branches of the tree resemble the first mode shape of the cantilever when the tree vibrates on its second mode. The backbone curves of these two modes also manifest hardening behaviors, the same trend as the cantilever's first mode.

By contrast, the third nonlinear mode of the tree mirrors the second nonlinear mode of the cantilever. The deformed configuration of the tree's third mode reveals a set of nodes at the secondary branching points where little to no vibration occurs, which is very similar to the node that appears on the cantilever's second mode. The backbone curve of the tree's third mode also exhibits a softening trend, the same as the cantilever's second mode, furthering the similarities between the two structures.

3.4 Convergence studies

An investigation into the convergence of the solutions is here presented based on the harmonic spectra of the variables at various points throughout the simulations. The convergence is presented for the primary variables U_x, U_y and θ and the auxiliary variables defined in Eqs. (3.37), (3.38) and (3.41). For the solution to be considered accurate, the amplitude of the higher harmonic terms should converge to zero within H, the number of harmonics retained during the HBM in Eq. (3.46). Table 3.2 tabulates the number of retained harmonics in each test case.

Fig. 3.11 depicts the harmonic spectra of $\hat{U}_x$, $\hat{U}_y$ and θ and the auxiliary variables at two points, points A and B, on the backbone of the cantilever beam's first nonlinear mode (see Fig. 3.4). Due to the geometrical symmetry of the structure in the transverse direction ($\mathbf{e}_Y$), the harmonic content of the transverse displacement $\hat{U}_y$ and the rotation θ is odd, whereas that of the axial displacement $\hat{U}_x$ is even. The spectrum at point A demonstrates an example of a converged solution. In this simulation, $H = 20$ and it is easily seen that the solution has converged within approximately 5 harmonics.

Also in Fig. 3.11, it is noted that the convergence of the auxiliary variables closely mirrors the convergence of θ, which makes sense as the critical auxiliary variables are those that govern the rotation, c and s, which are based on θ as shown in Eq. (3.38). U_x and U_y converge "faster" than θ, meaning fewer harmonics are needed. This is confirmed in Fig. 3.12, showing the convergence in H at point L on the backbone calculation of the first mode of the truss structure. For this reason, a general and simple rule for checking convergence of a given computation would be to *focus on the convergence of* θ. The convergence in H is shown for the second nonlinear mode of the truss in Fig. 3.9(f), where even at the higher amplitude of vibration, point N on the backbone, the simulation has converged within $H = 10$. Fig. 3.13 illustrates the harmonic convergence of θ for two additional points, point C on the backbone of the cantilever's first nonlinear mode, at very high amplitude, and point F, the location of the first internal resonance detected on the backbone of the clamped-clamped beam's first nonlinear mode. Point B's θ convergence is recopied for comparison.

Throughout all of the calculations, the harmonic content increases as a function of the amplitude of the motion, since the oscillations become more complex and require more harmonics to be properly reconstructed. An example of this trend is visible when comparing the θ convergence at point A (Fig. 3.11) on the cantilever's first mode backbone and point C (Fig. 3.13) further up the backbone: point A converges more rapidly than point C. Beyond point C, convergence is no longer assured within $H = 20$. Care must be taken to ensure that each solution is properly converged. For this reason, the simulations presented in this work are only presented up to the point where convergence is lost.

A final point to consider is the convergence of the internal resonance tongues, more demanding

than the main backbone curve because of the strong coupling with higher harmonics. This point is addressed in the next section and in Appendix A.5.

3.5 Internal resonances

As already explained and illustrated for instance in [86], [236], an internal resonance (IR) is observed when there is a coincidence between some harmonics of the oscillation frequency of a given mode and the nonlinear frequency of other nonlinear modes. This results in a strong coupling and a radical change of the topology of the backbone curve, giving rise to offshoots, often called IR "tongues." We do not consider here the case in which there exists a particular tuning between the (linear) natural frequencies, in which case the backbone curves are completely changed (see *e.g* [87], [89] for 1:1 and 1:2 internal resonances).

From our experience and as shown in [97], [141], there are three topologies for the connections between the IR tongues and the main backbone curve, as illustrated in Fig. 3.14:

1. In type 1, the tongue is connected to the backbone by several bifurcation points that are merged in the plane (amplitude / frequency). The interested reader can refer to [141], which shows nice plots of the unfolding of such bifucation points. This case appears in particular when there are symmetries in the system, such as in the case of the 1:3 IR between modes 1 and 2 of a hinged-hinged beam (see [97], [141]).

2. In type 2, there are no bifurcations and, during the continuation, the IR tongue appears smoothly by an increase of the harmonics involved in the IR and a sudden bend of the backbone curve. An example of this type is the 1:5 IR of point F in Fig. 3.7.

3. In type 3, the IR tongue is obtained after symmetry-breaking bifurcations, usually in the case of even IRs such as a 1:2 (see examples in [97]).

In practice, computing the IR tongues is often tedious and one usually prefers to avoid it since the main backbone is often the primary concern. In this context, IR types 1 and 3 are interesting in practice, since a basic continuation driver follows the main backbone and the user has the choice to compute the IR tongue or not, using in the former case a bifurcation detector and a branching algorithm (such as the one implemented in MANLAB [40]). The case of type 2 IR tongues is more tricky since the user must compute *a priori* the whole loop of the tongue before returning to the main backbone. In such circumstances, the MANLAB solver gives us the capability to "jump" over the birth point of the internal resonance on the backbone, from 1 to 2 in Fig. 3.14. A tangent prediction is used, followed by several Newton-Raphson corrections to converge back to the main branch.

In the test cases presented in Section 3.3, many type 1 or 3 IRs were detected but not indicated in the figures. Moreover, several type 2 IRs were also detected and, rather than computing the tongues, we chose to "jump" over them using the "jump" tool of MANLAB. They appear in the figures only with the bottom of their connection to the main backbone curve, so as not to overload the figures and to focus on the main backbone curve.

An unusual case was discovered for the first nonlinear mode of the cantilever beam around $\Omega/\omega_1 = 1.031$. At this point a strong internal resonance of type 2 was detected, with a particularly large gap between the two connections of the tongue with the main backbone. Moreover, we noticed the smooth apparition of even harmonics in the spectrum, without symmetry-breaking bifurcation (compare points C and B in Fig. 3.13). Then, following this IR tongue, it was impossible to obtain proper convergence

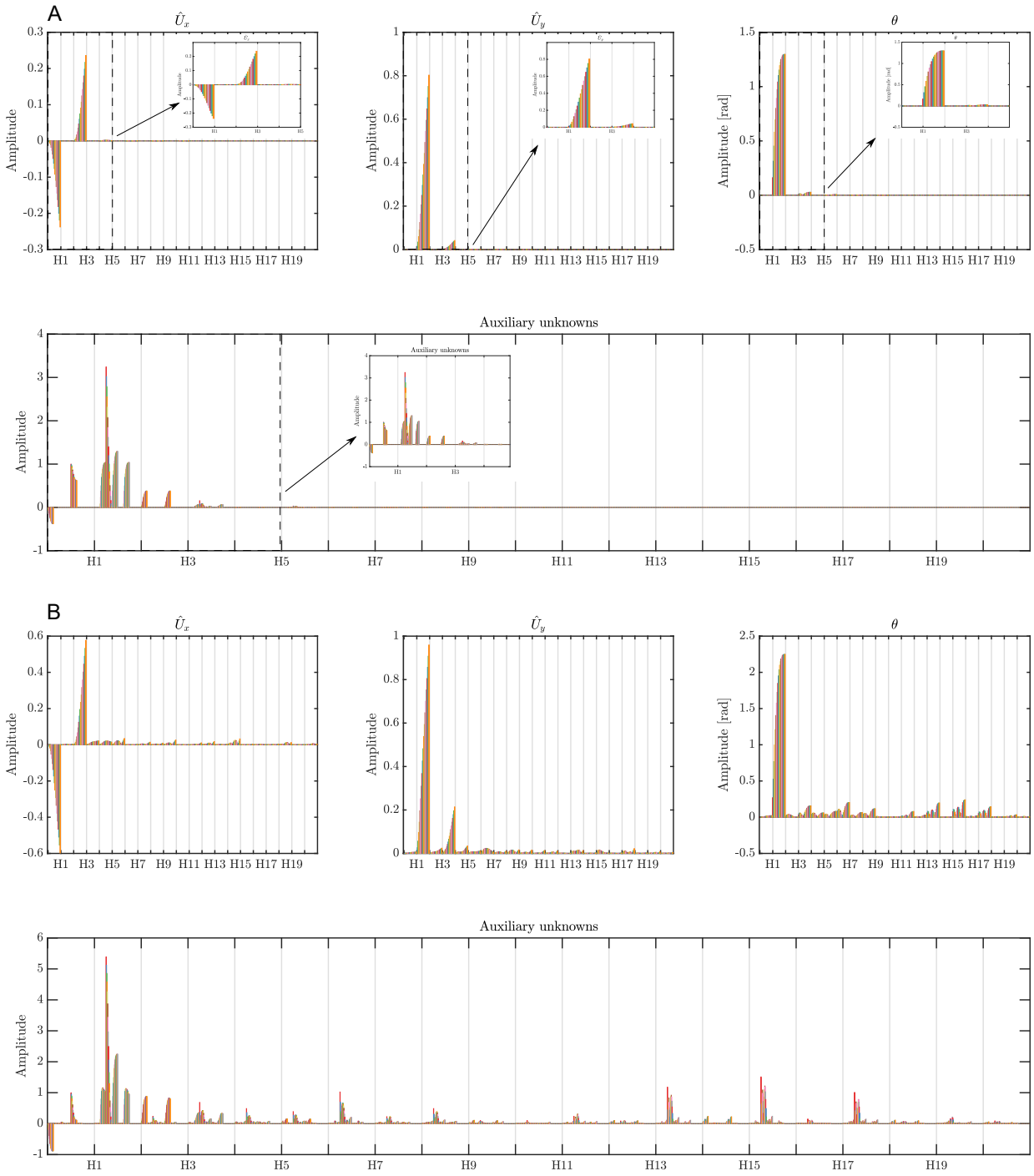

Figure 3.11: Convergence in number of retained harmonics H for U_x, U_y, θ and auxiliary variables at point A (top) and internal resonance point B (bottom) of cantilever simulation vibrating on its first nonlinear mode.

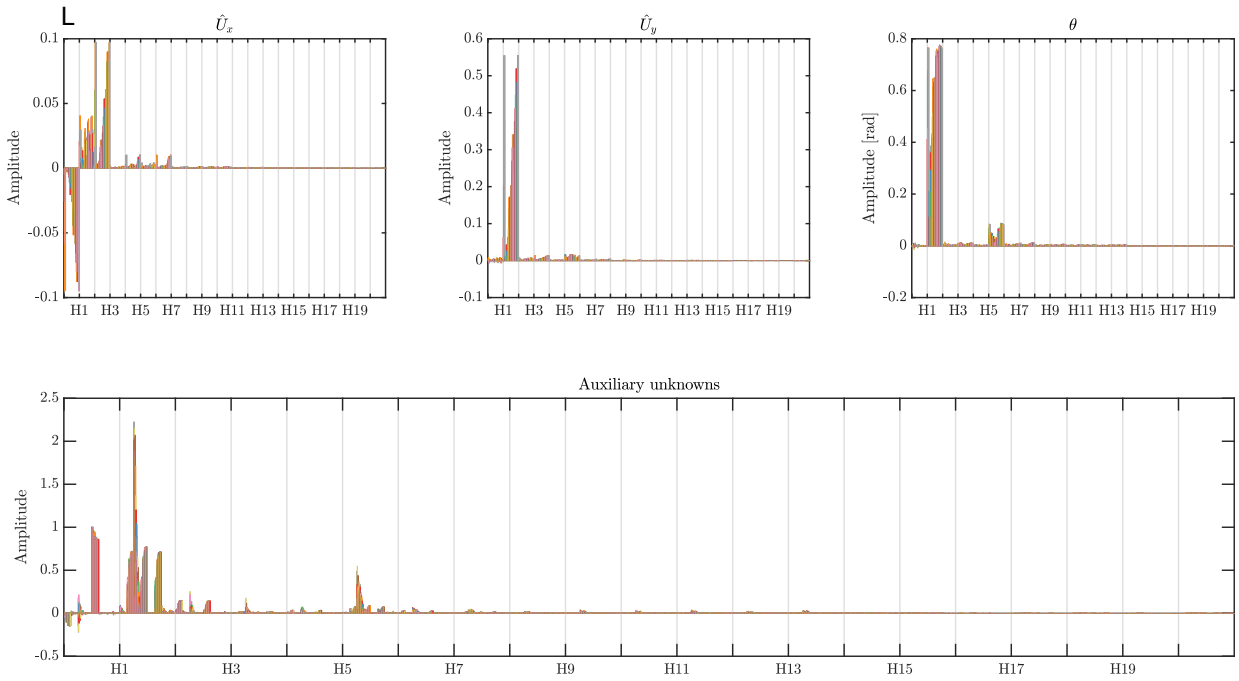

Figure 3.12: Convergence in number of retained harmonics H for U_x, U_y, θ and auxiliary variables at point L of truss simulation vibrating on its first nonlinear mode.

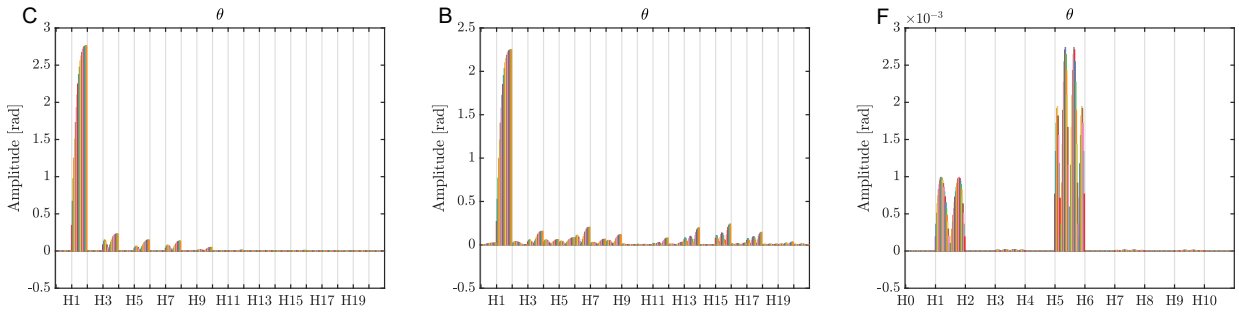

Figure 3.13: Convergence in number of retained harmonics H for θ variable at point C (left) and internal resonance point B (center) of cantilever simulation vibrating on its first mode, and at point F (left) of clamped-clamped beam simulation vibrating on its first nonlinear mode.

of the number of harmonics within $H = 20$, as seen for Point B in Fig. 3.13. Looking at the spatial pattern of the harmonics, it seems that a 1:6:15 IR with modes 2 and 3 would be at hand, with some energy spread over several harmonics (3 to 9, including even, and 13, 15, 17). The cantilever's IR is much less clear than the 1:5 IR, Point F of Fig. 3.13, for which the pattern of the third mode is clearly visible at the fifth harmonic, the energy being largely concentrated in this harmonic. Complete understanding of this particular internal resonance, not measured in the forced regime in [68] likely due to damping of the higher modes, is left for further studies.

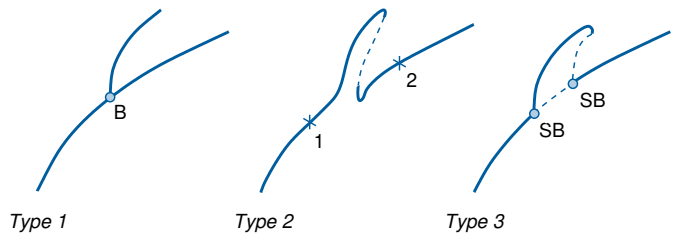

Figure 3.14: Types of connections between the internal resonance tongues and the main backbone curve. B indicates a "bifurcation" and SB indicates "symmetry-breaking." Dashed lines represent unstable parts of the branches.

3.6 Conclusion

This chapter presented a novel method for the simulation of highly flexible beam structures, based on geometrically exact beam theory and solved using a numerical strategy rooted entirely in the frequency domain. An analytical derivation of the geometrically exact finite element beam model is outlined in the first parts of Section 3.2. Section 3.2.3 introduces the solving method. The solver combines principles of the harmonic balance method (HBM) with a continuation method called the asymptotic numerical method (ANM), based in the frequency domain and automated in the MANLAB package.

In order to demonstrate the capabilities of the proposed method, the forced responses and/or nonlinear modes of several test cases were shown in Section 3.3, including a discussion of the nonlinear phenomena observed in each system and a convergence analysis with respect to the number of harmonics in Section 3.4. The model is able to capture various nonlinear phenomena, including the classical frequency-dependence on the amplitude of vibration (*i.e.* hardening and softening trends), bifurcations and instabilities, energy transfers between different modes of vibration, *etc.* The results of the test cases highlight the power of the method proposed in this chapter for the simulation of flexible structures across a variety of applications.

Many advances in the proposed model are planned for the near future in order to better capture the behavior of the flexible structures at extreme amplitudes of vibration. In particular, two main topics will be addressed. First, a stability analysis will be carried out for the free and forced solution, and, second, the model (currently restricted to two dimensions) will be generalized to three dimensions in order to allow for out-of-plane and torsional motion. Finally, future work will aim to validate the proposed model using experimental results and develop a novel nonlinear reduced-order model to reduce computation time.

The authors would like to note also that the finite element model presented in this work is open access and freely available to download in a user-friendly format along with extensive supporting documentation from GitHub [57].

Chapter 4

Influence of slenderness and gravity on nonlinear beam dynamics

In this chapter, we demonstrate with one test case how the model of Chapter 3 can be used to study the nonlinear dynamics of slender beam structures. The system of interest in this chapter is the cantilever beam in very large amplitude vibration, but distinct from the example of § 3.3.1 since here the effect of gravity is included into the equations of motion. We consider here vertical cantilever beams placed within a gravitational field. In this configuration, two orientations can be considered, a *standing* configuration, where the cantilever is fixed upright such that gravity acts to compress the beam, and a *hanging* configuration, where the cantilever hangs downward such that gravity acts to stretch the beam. This distinction is shown in Fig. 4.1. In large part inspired by the experiments of Chapter 6 involving vertical flexible cantilever beams, we are interested in determining the influence of gravity on the nonlinear dynamics of slender beams with a focus on the nonlinear modes. The contents of this chapter were published in the journal *Nonlinear Dynamics* in June 2023 as "Extreme nonlinear dynamics of cantilever beams: effect of gravity and slenderness on the nonlinear modes" [59].

The chapter is summarized as follows: § 4.1 introduces the study and reviews the state of the art with particular focus on the effect of gravity on cantilever beam structures in both statics and dynamics. Much of the literature is dedicated to the effect of gravity on the linear natural frequencies of the cantilevers, but we seek to extend the analysis to the nonlinear regime by studying the dynamics at very large amplitude. To do so, the 2D finite element model of Chapter 3 is used, into which is incorporated the effect of gravity in § 4.2. Gravity enters into the governing equations as either a compressive or tensile axial force depending on the configuration of the beam (standing or hanging) and the system is normalized as in § 3.2.3. Whereas the dimensionless system of Chapter 3 is found to depend on only a single dimensionless parameter (the "slenderness" parameter η), it is found to depend on a second dimensionless parameter after incorporating gravity into the equations of motion, called here α, the "gravity" parameter (in Timoshenko kinematics, the third dimensionless parameter μ is omitted from the study due to its negligible influence on slender beams, which is discussed in Appendix B.1). Note that for $\alpha > 0$, the force of gravity on the beam is negative (acting in compression) and therefore signifies the standing configuration; $\alpha < 0$ by extension indicates the hanging configuration and $\alpha = 0$ indicates the "no gravity" condition.

In § 4.3, the effect of both dimensionless parameters η and α on the (first three) linear eigenfrequencies of the vertical cantilever is studied and compared to other studies in the literature. Globally, gravity is found to decrease the natural frequencies when in a standing configuration and increase

the natural frequencies in a hanging configuration, which matches the studies found in the literature. Beginning in § 4.4, the analysis focuses on the nonlinear large amplitude dynamics of the cantilever. In § 4.4, the effect of the two dimensionless parameters on the (first three) nonlinear modes of the system (represented as backbone curves) is investigated and comparisons are made to two models of the literature: a comparison to the analytical Crespo da Silva model (first presented in § 2.1.4 but derived in more detail in Appendix B.3), valid up to moderate amplitudes of rotation, and to the backbone models of [204] and [146]. Next, in § 4.5, the effect of the slenderness and gravity parameters on the (first) nonlinear mode shape (§ 4.5.1) and an evolution of the mode shape as a function of the motion amplitude (§ 4.5.2) are described. Finally, an analogy to an inverted pendulum system under the influence of gravity is presented in § 4.6 and concluding remarks made in § 4.7.

Table of Contents - Chapter 4

4.1 Introduction

This work considers the extreme amplitude vibrations of cantilever beams with a focus on two particular effects: the influence of a gravitational field and that of the geometry of the cantilever, namely, its slenderness. Slender beam structures are particularly susceptible to large amplitude vibrations because of the thinness of their cross-section, which leads to a low bending stiffness and occasions large amplitude transverse vibrations for only moderate input forces. Moreover, in the special case of clamped-free boundary conditions, there is no restriction of the in-plane displacements (as in the case of a clamped-clamped beam, for instance) and, therefore, the oscillations can be extreme, especially near the first resonance of the structure. For example, the free end of the beam can be easily subjected to more than half of a complete turn, even reaching a state of bending "backwards" beyond the fixed end (see Fig. 4.4(a) and [58], [69], [71], [82]). At large amplitudes of vibration, so-called geometrical nonlinearities (trigonometric terms related to the cross-section rotation) become consequential. Although at first glance the oscillations in such cases may seem highly complex, using the concept of

nonlinear modes, it is possible to characterize the vibrations very easily in terms of oscillation frequency and mode shapes. The purpose of this work, then, is to address the effect of both gravity and the beam geometry on the nonlinear modes of cantilever beams, up to extreme amplitudes of vibration.

Past works in the literature on cantilever beam mechanics have investigated the effect of gravity on their static and dynamic behavior. In statics, Greenhill analyzed more than a century ago in [91] the point at which a tree, modeled as a "heavy column" cantilever, would buckle under its own weight, a phenomenon known as self-buckling. In dynamics, additional studies have investigated the influence of gravity on the free vibration of vertical cantilevers. An early study on the topic is found in the work of Paidoussis and Des Trois Maisons [176], who studied the influence of gravity on the free vibration of damped vertical cantilevers and recovered the self-buckling behavior described in [91]. In [206], Schäfer computed the effect of gravity on the eigenfrequencies of the first five modes of hanging Euler-Bernoulli cantilevers using a closed-form approximation based on the Ritz-Galerkin method for aerospace applications. The results of [206] were confirmed by the work of Yokoyama [258], where the eigenvalues were computed based on a finite element discretization of vertically hanging Timoshenko beams. Other studies on the free vibration of gravity-loaded beams include the work of Naguleswaran [160], [161] and Bokaian [28], [29] for Euler-Bernoulli-type cantilever beams, Abramovich [2] for composite Timoshenko-style hanging cantilevers and Xi *et al.* [255] for Rayleigh-type cantilevers. Naguleswaran, Bokaian and Xi *et al.* derived closed-form approximations of the natural frequencies of gravity-loaded cantilevers, while Abramovich estimated the eigenproblem using a Galerkin approach. In addition to these, Hijmissen and van Horssen [106] derived a closed-form approximation of the eigenfrequencies based on the linearized equations of motion of a vertical uniform Timoshenko cantilever using the method of multiple scales. This linear approximation is valid in particular for small effects of gravity. Furthermore, Virgin *et al.* experimentally investigated the influence of gravity on vertical cantilevers in [247], [248] and, most importantly, validated experimentally in [248] the influence of gravity on the eigenfrequencies (*e.g.* Fig. 2 in [255]) of the first four modes.

In all of these works, the primary interest was to investigate the influence of gravity on the linear eigenfrequencies of the vertical cantilevers. However, very little investigation has been done to date on the effect of gravity on the *nonlinear* dynamics of vertical cantilevers, especially at extreme amplitudes of vibration, which is the present aim of this chapter. Santillan *et al.* derived an analytical perturbation approximation based on the elastica model for the first nonlinear mode of a standing cantilever including self-weight and compared the results with numerical finite difference results [204]. In [204], the authors also compared their backbone approximations to the analytical expression for the amplitude-vs-frequency relationship of cantilever beams derived by Luongo *et al.* [146], though this work did not include the effect of gravity. Finally, the recent work of Farokhi *et al.* [70] on the parametric response of cantilever beams at very large amplitudes of displacement discussed the strong influence of gravity on the nonlinear dynamic response of the system.

An appropriate beam model should be selected in order to properly capture the geometrical nonlinearities at very large amplitudes of vibration. Here, a finite element discretization of the geometrically exact beam model (also known as the Reissner-Simo beam model [138], [156], [191], [192], [219]), based on Timoshenko kinematics of the cross-section, is used. The advantage of this model is that the geometrical nonlinearities are kept exact without any truncation or linearization, a strong advantage over other nonlinear models that break down at high amplitudes when the rotation of the cross-section becomes large. An example of the latter is the widely-used inextensible beam model of Crespo da Silva *et al.* [46], [47], where the nonlinearities expanded in Taylor series were truncated at order three;

this truncation begins to break down when the rotation of the cross-section nears or exceeds $\pi/4$ rad. By contrast, the geometrically exact model remains exact at any amplitude of rotation, even beyond π rad, which is extreme in a standard vibration test.

The discretized geometrically exact beam model is then solved in the frequency domain using a combination of the harmonic balance method (HBM) and numerical continuation based on the asymptotic numerical method (ANM) to compute periodic solutions, a process developed in many previous works [37], [41], [55], [97], [120]. Although many works on the modeling of flexible beam structures using the geometrically exact model involve time domain strategies to solve the system [30], [132], [142], [200], [221] (as in commercial finite element codes), a solving technique based in the frequency domain has certain advantages. Solving in the frequency domain targets the steady-state of the periodic oscillations under harmonic forcing without needing to manage time steps or transient oscillations, and also allows for easy bifurcation detection and stability analysis [97], [236]. In this way, frequency domain strategies can target various complex nonlinear vibratory phenomena such as bifurcations, instabilities, energy transfer between modes (internal resonances) [162], quasi-periodic or chaotic responses [98], [212], *etc.* that enrich the overall nonlinear dynamic analysis. Another set of works in the literature also used the geometrically exact model solved in the frequency domain to compute the dynamics of flexible cantilever beams [68], [69] and later validated this model with experimental results, notably with the weight of the cantilever incorporated into the equations of motion in [68].

In this chapter, we investigate the effects of gravity in both the linear and nonlinear regimes. For the latter, we are particularly interested in the effect of gravity on the nonlinear modes. Nonlinear modes provide a useful framework for understanding nonlinear vibrations as they constitute the skeleton of the nonlinear resonance pattern and can be useful in obtaining accurate reduced order models. Nonlinear modes are explicitly defined as families of periodic solutions of the system in free and undamped vibration [124], or as invariant manifolds of the phase space [236], both definitions being equivalent. In a way analogous to the eigenfrequencies and mode shapes in the linear regime, nonlinear modes are characterized by oscillation frequencies and mode shapes, which are dependent on the amplitude of the motion due to the presence of the nonlinearities, a point on which this work especially focuses in order to investigate the effect of gravity.

This chapter is divided into five sections: in § 4.2, the governing equations of motion are presented, including details on incorporation of the gravity terms. § 4.3 discusses the effects of the gravity on the linear eignefrequencies, including a comparison to the work of Hijmissen and van Horssen [106]. The nonlinear effects are treated in § 4.4 and 4.5, with emphasis on computation of the nonlinear modes. Finally, the chapter ends in § 4.6 with an analogy to a simple pendulum system in order to provide a more physical interpretation of the effect of gravity on the cantilever system.

4.2 Governing equations

In this section, the equations of motion and their finite element discretization are presented. Based on a previous work [229], the equations are here adapted to the case of a weighted cantilever. Within this framework, we begin by considering a straight cantilever beam of length L oriented vertically with respect to the direction of gravity, as shown in Fig. 4.1. Two orientations of the cantilever beam are equally considered: that of a *standing* cantilever, with the free end at the top of the beam (Fig. 4.1(a)), and that of a *hanging* cantilever, with the free end at the bottom (Fig. 4.1(b)).

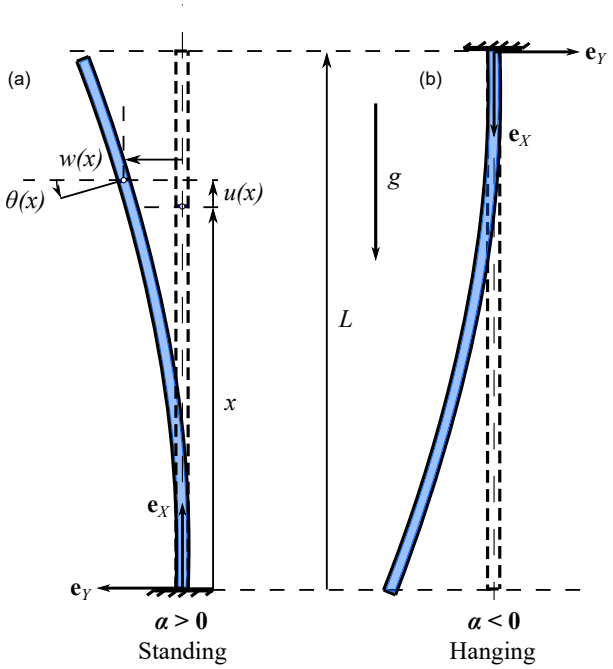

Figure 4.1: Cantilever beam orientations with rectangular cross-section: (a) standing configuration, (b) hanging configuration.

4.2.1 Beam model

Based on Timoshenko beam kinematics, it is assumed that any cross-section undergoes a rigid-body transformation that may be arbitrarily large. Considering that the undeformed centerline of the beam is aligned with the $\mathbf{e}_X$-direction and that the motion of the beam is restricted to the plane $(\mathbf{e}_X, \mathbf{e}_Y)$ of a global basis $(\mathbf{e}_X, \mathbf{e}_Y, \mathbf{e}_Z)$, the displacement field of any point in the cross-section at location x along the beam in the reference (undeformed) configuration is written [229]:

$$\begin{aligned}\mathbf{u}(x,y,t) = &[u(x,t) - y\sin\theta(x,t)]\,\mathbf{e}_X \\ &+ [w(x,t) + y\,(\cos\theta(x,t) - 1)]\,\mathbf{e}_Y,\end{aligned} \tag{4.1}$$

where (x,y) are the coordinates of the point of the beam in the reference configuration, t is the time, $u(x,t)$ and $w(x,t)$ represent, respectively, the axial and transverse displacements fields and $\theta(x,t)$ is the total rotation of the cross-section, including any shearing (see Fig. 4.1).

The strains are defined by the Green-Lagrange strain tensor, to which a consistent linearization is applied; in this process, the part of the strains relating to local strains is linearized while the part relating to rigid-body rotation is kept exact (see [229] for more details). It is appropriate in cases where the local strains remain fairly small, as is true for our case of a very thin, slender beam structure, even for extremely large rotations of the cross-section. The strains can then be written:

$$e = (1+u')\cos\theta + w'\sin\theta - 1, \tag{4.2a}$$
$$\gamma = w'\cos\theta - (1+u')\sin\theta, \tag{4.2b}$$
$$\kappa = \theta', \tag{4.2c}$$

with e and γ the axial and shear strains, respectively, and κ the beam curvature, and where $\circ' = \partial \circ / \partial x$.

Following the derivations in [229], the strong form of the equations of motion are written:

$$\begin{cases} \rho A \ddot{u} = (N\cos\theta - T\sin\theta)' + n, & \text{(4.3a)} \\ \rho A \ddot{w} = (N\sin\theta + T\cos\theta)' + p, & \text{(4.3b)} \\ \rho I \ddot{\theta} = T(1+e) - N\gamma + M' + q, & \text{(4.3c)} \end{cases}$$

with the generalized constitutive laws:

$$N = EAe, \quad T = kGA\gamma, \quad M = EI\theta', \tag{4.4}$$

where ρ, E, G are the density, Young's modulus and Coulomb's (shear) modulus, respectively, of the material, assumed homogeneous and isotropic, A and I are, respectively, the area and second moment of area of the cross-section and k is the shear correction factor that accounts for the non-uniformity of shear stresses in the cross-section. The internal forces are denoted by N, T and M, the axial force, shear force and bending moment, respectively. They are linearly-related to the strains according to a linear Kirchhoff-Saint-Venant constitutive law [170], which remains valid as long as the strains are small. The external forcing appears within n, p and q, which are, respectively, the axial force, transverse force and bending moment per unit length. Notice in Eqs. (4.3) the geometrical nonlinearities $\sin\theta$ and $\cos\theta$ governing the rotation of the cross-section, which are kept fully exact in the geometrically exact beam model.

For the cantilever beam under consideration, the boundary conditions are such that one end of the beam (at $x = 0$) is fixed and the other free (at $x = L$), written explicitly as:

$$u = w = \theta = 0, \qquad \text{at } x = 0, \tag{4.5a}$$
$$N = T = M = 0, \qquad \text{at } x = L. \tag{4.5b}$$

4.2.2 Dimensionless equations and independent parameters

The weight of the beam intervenes as a constant force in the direction of the gravitational acceleration vector. For the sake of this derivation, we choose as our reference configuration the standing beam (Fig. 4.1(a)), and thus the gravitational acceleration is written $\mathbf{g} = -g\mathbf{e}_X$. Since n, p and q are expressed in material coordinates, gravity simply leads to an axial force $n = -\rho A g$.

To better understand the influence of the gravitational field on the beam equations [Eqs. (4.3)] and to obtain independent parameters of the problem, it is convenient to render the system dimensionless. To do so, the system is normalized by injecting the following dimensionless parameters into the equations:

$$\bar{u}, \bar{w} = \frac{1}{L}(u, w), \quad \bar{x} = \frac{x}{L}, \quad \bar{t} = \frac{t}{L^2}\sqrt{\frac{EI}{\rho A}}, \quad \bar{\omega} = L^2\sqrt{\frac{\rho A}{EI}}\omega, \tag{4.6a}$$

$$\bar{N}, \bar{T}, \bar{q} = \frac{L^2}{EI}(N, T, q), \quad \bar{n}, \bar{p} = \frac{L^3}{EI}(n, p), \quad \bar{M} = \frac{L}{EI}M, \tag{4.6b}$$

where $\bar{(\,)}$ indicates a dimensionless parameter and L is a characteristic length, chosen here as the length of the cantilever. Injecting these dimensionless parameters into Eqs. (4.3) and (4.4) results in

the following dimensionless equations of motion:

$$\begin{cases} \ddot{\bar{u}} = (\bar{N}\cos\theta - \bar{T}\sin\theta)' - \alpha, & (4.7a) \\ \ddot{\bar{w}} = (\bar{N}\sin\theta + \bar{T}\cos\theta)' + \bar{p}, & (4.7b) \\ \eta\ddot{\theta} = \bar{T}(1+e) - \bar{N}\gamma + \bar{M}' + \bar{q}, & (4.7c) \end{cases}$$

with:

$$\bar{N} = e/\eta, \quad \bar{T} = \gamma/\mu, \quad \bar{M} = \theta'. \tag{4.8}$$

It can be seen in the above equations that the system depends only on three independent parameters: η, μ and α, defined as:

$$\eta = \frac{I}{AL^2}, \qquad \mu = \frac{EI}{kGAL^2} = \frac{2(1+\nu)\eta}{k}, \qquad \alpha = \frac{\rho g A L^3}{EI} = \frac{\rho g L}{E\eta}, \tag{4.9}$$

where ν represents the material Poisson's ratio, with, for a homogeneous isotropic material, $G = E/[2(1+\nu)]$. Rewriting η for the case of a rectangular cross-section as:

$$\eta = \frac{I}{AL^2} = \frac{bh^3/12}{bhL^2} = \frac{1}{12}\left(\frac{h}{L}\right)^2, \tag{4.10}$$

with h the thickness of the cross-section and b the width, η can be more easily interpreted as a slenderness parameter: the thinner the beam, *i.e.* the smaller the thickness-to-length ratio h/L, the smaller the η. The second parameter, μ, represents the ratio between the bending stiffness of the beam and its shear stiffness, and is entirely related to the Timoshenko kinematics. In the case of Euler-Bernoulli kinematics, the shear stiffness would be infinite, leading to $\mu = 0$ and $\gamma = 0$. For a homogeneous and isotropic material, μ is a function of η, as shown above. For the special case of slender beams, both η and μ are very small (see Tab. 4.1).

Table 4.1: Thickness to length (h/L) ratio corresponding to different values of η for a rectangular cross section and $\mu = 2(1+\nu)\eta/k$, with $k = 5/6$ and $\nu = 0.3$.

$\eta = \frac{1}{12}\left(\frac{h}{L}\right)^2$	h/L	μ
$2\cdot10^{-4}$	$0.0490 \simeq 1/20.4$	$6.24\cdot10^{-4}$
$1\cdot10^{-4}$	$0.0346 \simeq 1/28.9$	$3.12\cdot10^{-4}$
$5\cdot10^{-5}$	$0.0245 \simeq 1/40.8$	$1.56\cdot10^{-4}$
$1\cdot10^{-5}$	$0.0110 \simeq 1/91.3$	$3.12\cdot10^{-5}$
$1\cdot10^{-6}$	$0.0035 \simeq 1/289$	$3.12\cdot10^{-6}$
$1\cdot10^{-7}$	$0.0011 \simeq 1/913$	$3.12\cdot10^{-7}$
$1\cdot10^{-8}$	$0.0003 \simeq 1/2887$	$3.12\cdot10^{-8}$

Whereas parameters η and μ are common to any structure modeled as an assembly of beams (see *e.g.* [58]), the effect of gravity appears solely in the equations through a new parameter, α, that can be interpreted as the ratio between the effect of the restoring force due to gravity and the one due to the bending stiffness. This parameter was previously introduced in the literature to explain the buckling of a standing cantilever under its own weight when exceeding the critical value $\alpha_{\text{crit}} = 7.837$, as shown in [91].

Referring back to the definition of the gravitational acceleration vector $\mathbf{g}$ and Fig. 4.1, it can be seen that Eqs. (4.7) apply also to the hanging beam configuration simply by changing the sign of g and, thus, the sign of α. Consequently, a standing cantilever configuration is obtained when $\alpha > 0$ and a hanging cantilever when $\alpha < 0$ as shown in Fig. 4.1; both cases will be considered in §4.3, 4.4 and 4.5.

Since the effect of gravity on the mechanics of the beam depends solely on the magnitude of α, it is worth analyzing in more detail the parameters that govern it. Returning to its definition in Eq. (4.9), it can be seen that α naturally increases linearly with the gravitational acceleration g. It also depends on the material characteristics of the beam through ρ and E, which is logical since α is related to the ratio between the weight of the beam and its bending stiffness. Finally, α depends on the geometry of the beam through L and η, indicating that the effect of gravity increases as the beam becomes more slender (*i.e.* as η decreases). For this reason, it is important to investigate both the effects of gravity (through α) and the slenderness (through η) on the beam mechanics. In this study, only slender beams will be considered, *i.e.* with very small η. We consider a maximum threshold ratio h/L of around $1/20$ for the beam to be considered very slender, meaning that $\eta \leq 2 \cdot 10^{-4}$ (see Tab. 4.1). The values of η selected are chosen accordingly, ranging between $\eta \in [10^{-8}, 2 \cdot 10^{-4}]$.

As seen above, μ conditions the shear stiffness of the beam and is very small for slender beams, being proportional to η. Apart from η, its value is governed by the Poisson's ratio $0 \leq \nu \leq 0.5$ and the shear coefficient k. The value of k itself depends on ν along with the geometry of the cross-section. It may be computed based on an energetic equivalence and roughly takes values between 0.8 and 0.9 (for rectangular cross-sections, $k = 5/6 \simeq 0.833$) [76], [119], [196]. However, since only slender beams are considered here, the effect of shearing is, in fact, negligible and therefore virtually no difference between Timoshenko and Euler-Bernoulli kinematics is noticed. Consequently, the effect of variations in μ are not considered in what follows (values of $\nu = 0.3$ and $k = 1$ have been used in the simulations). Instead, we consider that the principal parameters governing the behavior of the weighted cantilever are simply η and α. Additional analysis justifying this choice and further highlighting the minimal influence of shearing for the case of very slender beams is presented in Appendix B.1.

4.2.3 Finite element geometrically exact formulation

The problem under consideration here has been fully defined by Eqs. (4.3), (4.4) and (4.5). It is highly nonlinear due to the geometrical nonlinearities (the $\sin\theta$ and $\cos\theta$ terms) and has no closed-form solution in nonlinear dynamics. An approximate analytical solution, valid up to moderate rotations of the cross-section, can be derived based on Euler-Bernoulli kinematics and assuming the condition of inextensibility and a third-order truncation of the nonlinearities (see Appendix B.3). However, as we concern ourselves more with extreme amplitude vibrations, we rely instead on a finite element (FE) method to discretize the spatial part of the problem. An alternate approach would have been to keep the model of Appendix B.3 exact (*i.e.* without the third-order truncation), rewriting it solely as a function of the rotation of the cross-section $\theta(x,t)$ and solving it via discretization on a mode shape basis, as done in [69], [71].

The problem is discretized using standard finite elements with linear shape functions, as done previously in [58], [229] without incorporating the effect of gravity, which is here added in. The beam is discretized into N^e two-node Timoshenko beam elements [74], each of length L^e, which could depend on x if the mesh is not uniform. The $(\,)^e$ superscript is used to differentiate quantities related to the individual elements from their global counterparts. For each node of the mesh, there are three degrees of freedom (u_i, w_i, θ_i), representative of the axial displacement, transverse displacement and rotation

of the cross-section, respectively. For each element, the degrees of freedom at each of the two nodes are gathered in the vector $\mathbf{q}^e$:

$$\mathbf{q}^e = \begin{bmatrix} u_1 & w_1 & \theta_1 & u_2 & w_2 & \theta_2 \end{bmatrix}^{\mathrm{T}}, \tag{4.11}$$

which relates to the displacements interpolated over the element $\forall x \in [0, L^e]$ according to:

$$\begin{bmatrix} u^e(x,t) \\ w^e(x,t) \\ \theta^e(x,t) \end{bmatrix} = \mathbf{N}(x)\mathbf{q}^e(t), \tag{4.12}$$

where $\mathbf{N}$ is the matrix of shape functions for each element, defined as:

$$\mathbf{N}(x) = \begin{bmatrix} N_1(x) & 0 & 0 & N_2(x) & 0 & 0 \\ 0 & N_1(x) & 0 & 0 & N_2(x) & 0 \\ 0 & 0 & N_1(x) & 0 & 0 & N_2(x) \end{bmatrix}. \tag{4.13}$$

Since linear shape functions are used, N_1 and N_2 take the form:

$$N_1(x) = 1 - \frac{x}{L^e}, \quad N_2(x) = \frac{x}{L^e}. \tag{4.14}$$

The equations of motion of the finite element model are derived from the principle of virtual work, which is written, for all virtual displacement $\delta\mathbf{u}$:

$$\delta W_a + \delta W_i = \delta W_e, \tag{4.15}$$

with δW_a the inertial, δW_i the internal and δW_e the external virtual works. Integrating Eq. (4.12), the virtual work terms are discretized in order to define the elementary mass matrix, the internal and external force vectors and any other elementary quantities for a single element (the explicit details of which, omitted here, are outlined in Chapter 3).

The effect of gravity is introduced as an applied force in the external virtual work component δW_e, which is written:

$$\delta W_e^e = \int_{V^e} (\delta\mathbf{u})^{\mathrm{T}}\mathbf{b}\ \mathrm{d}V = \int_0^{L^e} \begin{pmatrix} \delta u & \delta w & \delta\theta \end{pmatrix} \begin{pmatrix} n \\ p \\ q \end{pmatrix} \mathrm{d}x, \tag{4.16}$$

where $n(x,t)$, $p(x,t)$ and $q(x,t)$ correspond to the distributed axial force, transverse force and bending moment, respectively, as in Eqs. (4.3), and where $\mathbf{b}$ is the vector of body forces. As explained in § 4.2.2, gravity appears in the axial direction as $n = -\rho A g$, $p = q = 0$, which, integrating Eq. (4.12) into (4.16), leads to:

$$\delta W_e^e = (\delta\mathbf{q}^e)^{\mathrm{T}} \underbrace{\left(-\rho A g \int_0^{L^e} \mathbf{N}^{\mathrm{T}} \begin{bmatrix} 1 \\ 0 \\ 0 \end{bmatrix} \mathrm{d}x \right)}_{\mathbf{f}_{\mathrm{g}}^e}, \tag{4.17}$$

with:

$$\mathbf{f}_{\mathrm{g}}^e = -\frac{1}{2}\rho A g L^e \begin{bmatrix} 1 & 0 & 0 & 1 & 0 & 0 \end{bmatrix}^{\mathrm{T}}. \tag{4.18}$$

Following this, the expressions for the elementary quantities are assembled for the entire structure according to traditional finite element assembly procedures. Formally, the problem can be written:

$$\mathbf{M}\ddot{\mathbf{q}} + \mathbf{D}\dot{\mathbf{q}} + \mathbf{f}_{\text{int}}(\mathbf{q}) = \mathbf{f}_{\text{g}} + \mathbf{f}_{\text{ext}}, \tag{4.19}$$

where $\mathbf{q}$ is the column vector containing all degrees of freedom u_i, w_i and θ_i, $i \in [1,\ N]$ with $N \in \mathbb{N}$ the number of nodes, $\mathbf{M}$ is the mass matrix of size $3N \times 3N$, $\mathbf{f}_{\text{int}}(\mathbf{q})$ is the internal force vector, $\mathbf{f}_{\text{g}}$ is the gravitational force vector and $\mathbf{f}_{\text{ext}}$ is the external force vector (housing all external forces except gravity), all three of size $3N \times 1$. The geometrical nonlinearities $\sin\theta_i$ and $\cos\theta_i$ appear in the internal force vector $\mathbf{f}_{\text{int}}$, the full expression of which is found in Chapter 3. A linear damping term, with the damping matrix $\mathbf{D}$ of size $3N \times 3N$, is also introduced for the sake of generality, although this term is not used in what follows since we focus on free, undamped vibrations. Finally, considering the fixed-free boundary conditions defined by Eqs. (4.5), a null value for degrees of freedom (u, w, θ) is enforced at the node located at $x = 0$.

4.2.4 Numerical solving and type of problems considered

As explained in the introduction, in this study we focus primarily on computation of the nonlinear modes of the system under the influence of gravity. Consequently, we consider the free and undamped problem associated with Eq. (4.19), namely:

$$\mathbf{M}\ddot{\mathbf{q}} + \mathbf{f}_{\text{int}}(\mathbf{q}) - \mathbf{f}_{\text{g}} = \mathbf{0}. \tag{4.20}$$

The nonlinear modes are here computed by continuation of periodic solutions as the families of periodic orbits that emerge from the equilibrium position of the system in the phase space. They are identical to the invariant manifolds of the system, as explained *e.g.* in [236]. In practice, the Harmonic Balance Method (HBM) is used to compute the periodic solutions of the problem as Fourier series of $\mathbf{q}(t)$. The HBM transforms Eq. (4.20) into an algebraic system, which is then solved by the Asymptotic Numerical Method (ANM) in a process extensively documented in previous works [58], [97]. Solving the system yields the evolution of the Fourier components of $\mathbf{q}(t)$ as a function of the frequency Ω of the oscillations, leading to the frequency / amplitude relations of the nonlinear modes, well known as the so-called "backbone" curves, as well as the nonlinear mode shapes. These are investigated in § 4.4 and 4.5. As a final detail, it should be mentioned that since Eq. (4.20) is autonomous, a phase condition and a fictitious damping term are added for numerical purposes, as fully explained in Chapter 3.

Due to the presence of gravity, the equilibrium (static) configuration of the system is not $\mathbf{q}_{\text{s}} = \mathbf{0}$ but the solution of:

$$\mathbf{f}_{\text{int}}(\mathbf{q}_{\text{s}}) - \mathbf{f}_{\text{g}} = \mathbf{0}, \tag{4.21}$$

which is representative of an axial compression of the cantilever in the standing equilibrium configuration and to a stretching in the hanging configuration. The static solution is used in two different computations, either as the starting point for computation of the nonlinear modes or in computation of the evolution of the (linear) eigenmodes of the problem.

Since we are interested in vibrations of the system, it is convenient to consider its oscillations around the equilibrium configuration $\tilde{\mathbf{q}}(t)$, defined by:

$$\tilde{\mathbf{q}}(t) = \mathbf{q}(t) - \mathbf{q}_{\text{s}}. \tag{4.22}$$

Introducing this equation into Eq. (4.20), the problem is rewritten for $\tilde{\mathbf{q}}(t)$:

$$\mathbf{M}\ddot{\tilde{\mathbf{q}}} + \mathbf{f}_{\text{int}}(\tilde{\mathbf{q}} + \mathbf{q}_{\text{s}}) - \mathbf{f}_{\text{g}} = \mathbf{0}. \tag{4.23}$$

Eq. (4.23) can be linearized using the Taylor expansion of $\mathbf{f}_{\text{int}}(\mathbf{q})$ around $\mathbf{q}_{\text{s}}$, yielding:

$$\mathbf{f}_{\text{int}}(\mathbf{q}) \simeq \mathbf{f}_{\text{int}}(\mathbf{q}_{\text{s}}) + \mathbf{K}_{\text{t}}(\mathbf{q}_{\text{s}})\tilde{\mathbf{q}}, \qquad \mathbf{K}_{\text{t}}(\mathbf{q}_{\text{s}}) = \left.\frac{\partial \mathbf{f}_{\text{int}}}{\partial \mathbf{q}}\right|_{\mathbf{q}=\mathbf{q}_{\text{s}}}, \tag{4.24}$$

where the nonlinear terms in the Taylor expansion have been neglected and with $\mathbf{K}_{\text{t}}$ the tangent stiffness matrix. Introducing Eq. (4.24) into Eq. (4.20) and using Eq. (4.21), the following relation is obtained:

$$\mathbf{M}\ddot{\tilde{\mathbf{q}}} + \mathbf{K}_{\text{t}}(\mathbf{q}_{\text{s}})\tilde{\mathbf{q}} = \mathbf{0}. \tag{4.25}$$

This problem defines the small (linearized) oscillations of the system around its equilibrium (weighted) position, which leads to the eigenvalue problem:

$$\left[\mathbf{K}_{\text{t}}(\mathbf{q}_{\text{s}}) - \omega^2\mathbf{M}\right]\boldsymbol{\Phi} = \mathbf{0}. \tag{4.26}$$

The solutions of Eq. (4.26) are the (linear) eigenmodes $(\omega_m, \boldsymbol{\Phi}_m)$, $m = 1, \dots N$ of the system. Since $\mathbf{q}_{\text{s}}$ is directly tied to gravity (Eq. (4.21)), the effect of the weight of the cantilever beam on its own eigenmodes can be analyzed by solving this eigenvalue problem. The results of this analysis are described in § 4.3. In practice, the tangent stiffness matrix $\mathbf{K}_{\text{t}}$ is computed according to standard FE assembly procedures, a process explained in Appendix B.2.

Two different methods for computing $\mathbf{q}_{\text{s}}$ are implemented and compared. The first method computes the solution of the full nonlinear problem directly using a Newton-Raphson iteration algorithm to solve the nonlinear Eq. (4.21). A second method computes $\mathbf{q}_{\text{s}}$, which is assumed very small since the beams under consideration are very stiff in the axial direction, with the linearized version of Eq. (4.21), written:

$$\mathbf{K}_{\text{t}}(\mathbf{0})\mathbf{q}_{\text{s}} = \mathbf{f}_{\text{g}}. \tag{4.27}$$

It is noted that since $\mathbf{q}_{\text{s}}$ is typically small, the results of the two methods are virtually identical; however, some inconsistencies are uncovered when computing $\mathbf{q}_{\text{s}}$ for very small values of η (*i.e.* $\eta \leq 10^{-8}$), which is discussed in the next section (§4.3).

Moreover, recall from § 4.2.2 that the system can be normalized by introducing the dimensionless parameters defined in Eqs. (4.6). For better conditioning of the numerical problem and to bring more universality to the results, the normalized system is used in practice, simply by selecting the following values for the material and geometrical parameters of the system: $L = 1$, $EI = 1$, $\rho A = 1$, $\rho I = \eta$, $EA = 1/\eta$, $kGA = 1/\mu = k/[2(1+\nu)\eta]$ and $g = \alpha$. Since, as explained before, variations of μ are not investigated, values of $\nu = 0.3$ and $k = 1$ are selected in the simulations. Finally, all numerical computations presented in this work are carried out on a finite element mesh of $N = 50$ nodes (*i.e.* 49 elements) and with $H = 20$ harmonics in the HBM computations.

4.3 Effect of (α, η) on the natural frequencies

In this section, the effect of gravity on the (linear) natural frequencies of the (dimensionless) system is investigated. Following the discussion of § 4.2.2, only two independent parameters condition the

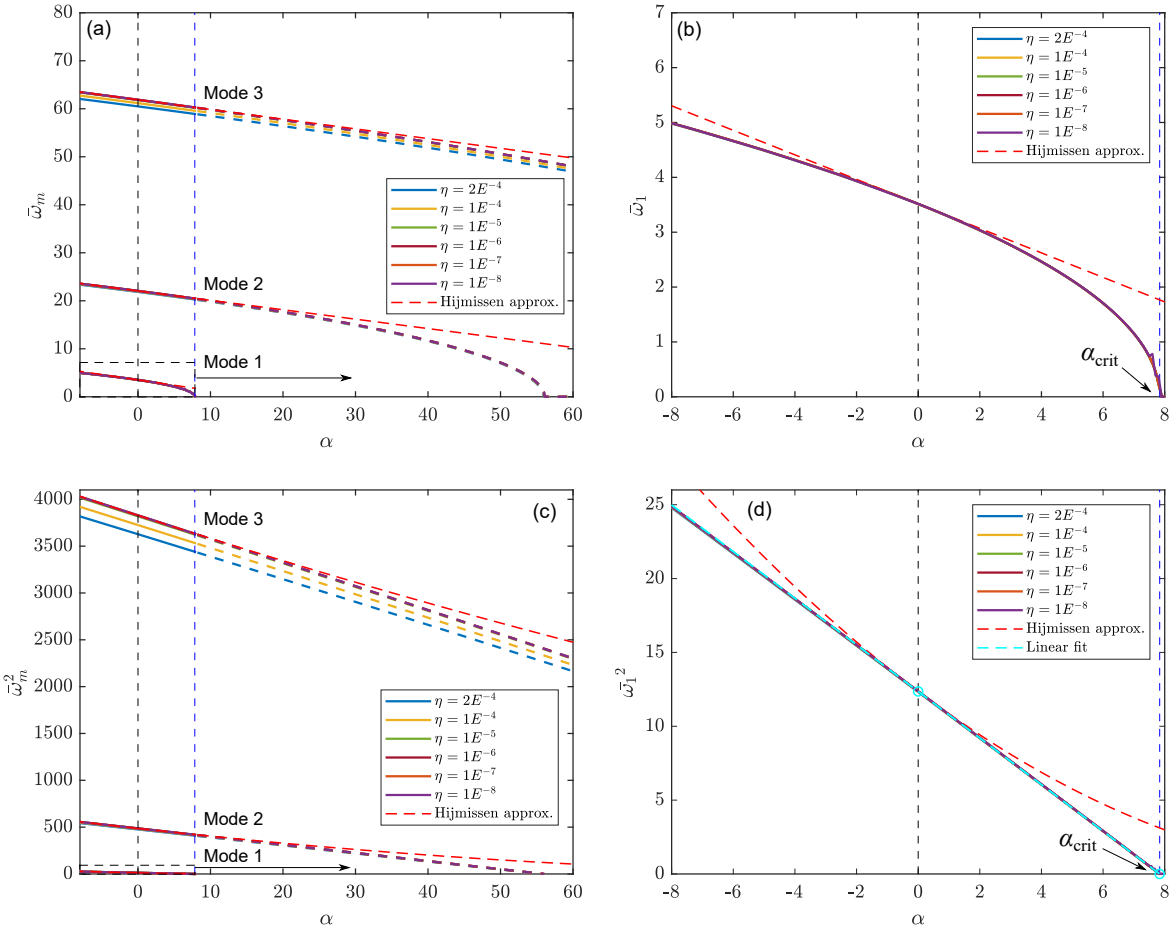

Figure 4.2: Effect of gravity on the dimensionless natural frequencies $\bar{\omega}_m$: (a) for the first three bending modes of the cantilever beam, (b) zoom of (a) onto the first bending mode, (c) the same as (a) but depicting $\bar{\omega}_m^2 = f(\alpha)$, (d) zoom of (c) onto the first bending mode. Several values of the slenderness parameter η as well as approximations based on [106] are depicted, as specified in the legend. The vertical blue dashed lines indicate the self-buckling point at α_{crit}. A linear fit based on the two points indicated with circles in (d) is shown in cyan

.

mechanics of the beam: the slenderness parameter η and the gravity parameter α. In order to investigate first the effect of (α, η) on the natural frequencies, the beam's parameters are chosen as explained at the end of § 4.2.4 and the modes of the beam $(\bar{\omega}_m, \mathbf{\Phi}_m)$ are computed by numerically solving Eq. (4.26) for several values of (α, η). Throughout this work, we choose to concentrate on the first three bending modes of the cantilever beam, $m = 1, 2, 3$.

The results of the effect of (α, η) on $\bar{\omega}_m$ are summarized in Fig. 4.2(a) for the first three bending modes. For reference, the deformed shape of the first bending mode is depicted in Fig. 4.3(a), while the second and third bending modes are depicted in Figs. 4.3(b) and (c). The linear natural frequencies $\bar{\omega}_m$ for $m = 1, 2, 3$ are solved for a range of α values for six different η values (six different beam

geometries). The black dashed line at $\alpha = 0$ indicates the location of zero gravity (*i.e.* where the weight of the beam is not taken into account), with negative α to the left indicating a "hanging" beam configuration and positive α to the right indicating a "standing" beam. At the point of "no gravity" ($\alpha = 0$), the value of $\bar{\omega}_m$ for each mode matches its classical dimensionless natural frequency for a uniform cantilever beam [102] ($\bar{\omega}_m = [3.516, 22.034, 61.701]$ for $m = 1, 2, 3$). In addition, Fig. 4.2(b) shows a zoom of Fig. 4.2(a) onto the first bending mode.

First, consider the effect of η on $\bar{\omega}_m$. The computation of $\bar{\omega}_m = f(\alpha)$ is performed for six different values of η ranging from $2 \cdot 10^{-4}$ to 10^{-8}, *i.e.* from a rather thick beam to a very thin one (see Table 4.1 for the values of h/L corresponding to η in the case of a rectangular cross section). In Fig. 4.2(a), it is readily seen that, for all three modes, $\bar{\omega}_m = f(\alpha)$ varies little for different values of η. In fact, there is virtually no difference in the curves apart from on the third bending mode, where an $\eta = 2 \cdot 10^{-4}$ or 10^{-4} reduces $\bar{\omega}_3$ slightly compared to other η (some discussion on the larger effect of η on mode 3 is presented at the end of § 4.4.1). It can be said, then, that the effect of η for $\eta \leq 10^{-5}$ on the natural frequencies $\bar{\omega}_m$ is negligible.

The same cannot be said for the influence of α on $\bar{\omega}_m$. Particularly on the first mode of vibration, $\bar{\omega}_1$ changes significantly for different values of α. In general, for all three modes, a negative α increases the natural frequency, while a positive α decreases it. The effect of gravity on a standing (resp. hanging) cantilever is to add a restoring force in the system which acts qualitatively in the same way as a pre-compression (pre-tension). This pre-compression (pre-tension) of the beam results in a decrease (increase) of the bending stiffness and, thus, decreases (increases) the natural frequencies. A more physical interpretation of this effect can be described using a simple pendulum system, which is explained in detail in § 4.6. In the case of the standing cantilever ($\alpha > 0$), the gravity decreases the global bending stiffness of the cantilever until it is completely canceled, which occurs at a critical value of the gravity parameter $\alpha = \alpha_{\text{crit}} = 7.837$. In statics, α_{crit} corresponds to the point of self-buckling, well-known in the literature [91], at which the standing beam buckles under its own weight. In dynamics, α_{crit} corresponds to the first natural frequency $\bar{\omega}_1$ tending to zero [167]–[169], as seen in Fig. 4.2(b). Beyond the point of self-buckling, the compressed, straight and vertical equilibrium configuration of the beam is no longer stable, indicated by the dashed portions of the mode 2 and 3 curves in Fig. 4.2(a). The dashed blue line in Fig. 4.2 indicates the location of failure due to self-buckling at α_{crit}.

Note, however, that as α approaches α_{crit}, the linearized tangent stiffness matrix $\mathbf{K}_{\text{t}}$ approaches a singularity, which occurs exactly at the self-buckling point (at $\alpha = \alpha_{\text{crit}} \Leftrightarrow \bar{\omega}_1 = 0$). This effect is explained since the terms in $\mathbf{K}_{\text{t}}$ related to the bending stiffness are decreased (and canceled at $\alpha = \alpha_{\text{crit}}$) due to the influence of gravity. This effect is magnified when η is very small, which explains the numerical noise observed in the $\bar{\omega}_1 = f(\alpha)$ curve of Fig. 4.2(b) close to the buckling point when $\eta = 10^{-8}$. For very small values of η (observed in our case only for $\eta = 10^{-8}$), the linear computation of $\mathbf{q}_{\text{s}}$ using Eq. (4.27) is not considered sufficiently accurate due to the existence of this numerical noise in the $\bar{\omega}_1 = f(\alpha)$ curve. To avoid this, the nonlinear computation of Eq. (4.21) is used, although some numerical noise remains very close to α_{crit}.

In the stable equilibrium region $\alpha < \alpha_{\text{crit}}$, it can be seen that α does not have as strong of a relative influence on $\bar{\omega}_m$ for $m > 1$. To describe this effect quantitatively, compare the values of $\bar{\omega}_m$ at $\alpha = 0$ and $\alpha = 7$ for all three modes: at $\alpha = 0$, $\bar{\omega}_m = [3.51, 21.93, 61.03]$ and at $\alpha = 7$, $\bar{\omega}_m = [1.18, 20.64, 60.44]$ for $m = 1, 2, 3$, respectively. On modes 2 and 3, $\bar{\omega}_m$ decreases by less than 6% and 1%, respectively, while on mode 1, it decreases by more than 66% between $\alpha = 0$ and $\alpha = 7$. This simple comparison highlights the large influence of the gravity parameter α on the natural frequency of the first bending mode

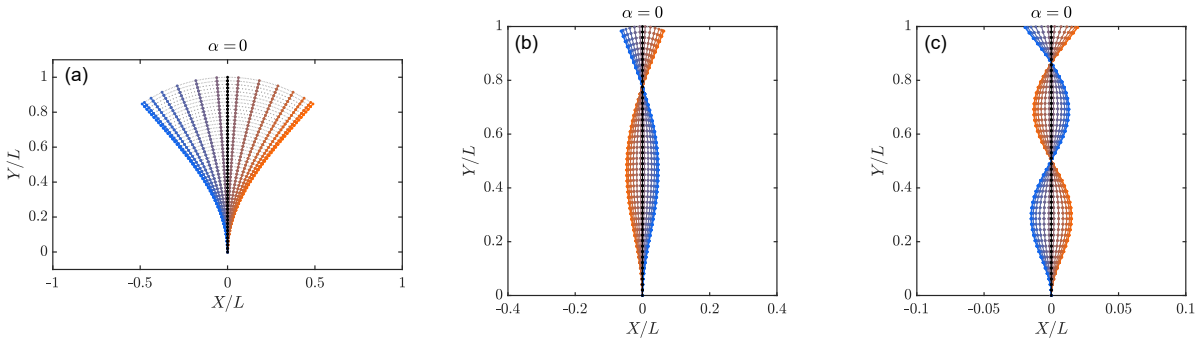

Figure 4.3: Snapshots of the cantilever beam vibrating on its first three nonlinear modes at moderate amplitude: (a) first mode, (b) second mode, (c) third mode. The locations on the backbones at which the snapshots are taken are marked with black circles in Figs. 4.5, 4.6, 4.8(a) and 4.9.

of vibration of the cantilever beam, while its influence remains relatively small on higher-frequency bending modes. The same was found in the work of Hijmissen and van Horssen in [106]; computing their linear estimation of $\bar{\omega}_m = f(\alpha)$ for $m = 1,2,3$ revealed a weaker α influence on the higher-frequency modes. The linear estimations provided by Hijmissen and van Horssen [106] are given by the red dashed lines in Fig. 4.2(a) for comparison, again with a zoom on the first mode in Fig. 4.2(b). Our results are in good agreement with the estimation of [106] (particularly close to $\alpha = 0$), once again highlighting the strong influence of α on $\bar{\omega}_1$.

An interesting feature can be seen when plotting $\bar{\omega}_m^2$ as a function of α, as done in Figs. 4.2(c) and (d): it is observed that an almost linear relationship exists between the square of the natural frequencies and α, a trend likewise noticed in [248]. A linear fit through the two known points $\left(0,\bar{\omega}_{0,1}^2\right)$ and $(\alpha_{\text{crit}},0)$ is overlaid onto Fig. 4.2(d) to further highlight this, where $\bar{\omega}_{0,m} = \bar{\omega}_m(\alpha = 0)$. By consequence, a good approximation of the α dependence of the natural frequencies can be written as a square root relationship:

$$\bar{\omega}_m = \bar{\omega}_{0,m}\sqrt{1-\alpha/\alpha_{\text{cr},m}}, \tag{4.28}$$

where $\alpha_{\text{cr},m}$ is the m-th buckling point, with of course $\alpha_{\text{cr},1} = \alpha_{\text{crit}} = 7.837$. This relationship explains why α has a stronger influence on $\bar{\omega}_1$ than on the higher-frequency modes: considering the particular shape of the square root, each curve $\bar{\omega}_m = f(\alpha)$ is a scaled version of the same overall shape, with a breakdown at $\alpha = \alpha_{\text{cr},m}$ (see Fig. 4.2(a)). Consequently, $\bar{\omega}_1 = f(\alpha)$ decreases more in the range $\alpha \in [0\ \alpha_{\text{cr},1}]$ than the higher natural frequencies $\bar{\omega}_m$, $m > 1$, justifying the stronger effect of α on $\bar{\omega}_1$.

4.4 Effect of (α,η) on nonlinear backbone curves

Next, we turn to the effects of gravity on the *nonlinear* dynamics of the slender cantilever beam. When the displacement of the beam becomes sufficiently large, the geometrical nonlinearities (recall Eqs. (4.2) and (4.3)) are activated. As explained in the introduction, we here choose to focus on the nonlinear modes of the cantilever, represented here by their backbone curves and nonlinear mode shapes. The nonlinear modes are defined as the particular solutions of the undamped and free oscillation problem, defined here by Eqs. (4.20) or (4.23). Note that they share this definition with the standard (linear) eigenmodes of a linear system, the difference being the nonlinearities in the equations of motion. They

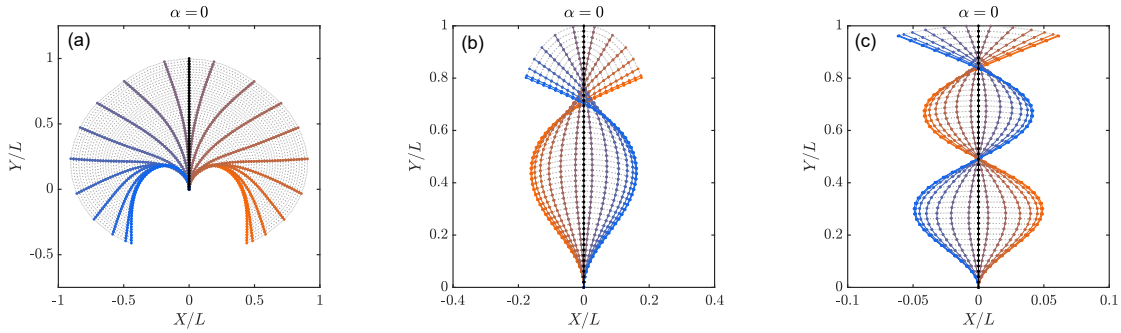

Figure 4.4: Snapshots of the cantilever beam vibrating on its first three nonlinear modes at high amplitude: (a) first mode, where the cantilever has "bent backwards" beyond its fixed end, (b) second mode, (c) third mode. The locations on the backbones at which the snapshots are taken are marked with blue circles in Figs. 4.5, 4.6, 4.8(a) and 4.9.

correspond equivalently to invariant manifolds of the phase space or to families of periodic solutions (see *e.g.* [236]). The latter (families of periodic solutions) definition is used here to compute the nonlinear modes with the HBM-ANM strategy. The main difference with linear modes is that the free oscillation frequency and the shape of the motion on the mth nonlinear mode – the extension of the natural frequencies ω_m and the mode shape $\mathbf{\Phi}_m$ to the nonlinear regime – now depend on the amplitude (or energy) of the motion. The former is represented here in a classical amplitude / frequency plot called the *backbone curve*. The latter, the nonlinear mode shape, depends on the amplitude and is illustrated by plotting snapshots of the beam oscillations over a half period, at a given energy. Examples for the first mode are shown in Figs. 4.3(a) and 4.12 for low-to-moderate amplitudes of vibration and in Fig. 4.4(a) at very large amplitude. The second and third mode shapes are shown in Figs. 4.3(b) and (c) at moderate amplitude and in Figs. 4.4(b) and (c) at a higher amplitude. In this section, we focus on the effect of (α,η) on the backbone curves; the effect on the nonlinear mode shapes is addressed in § 4.5.

As before, the influences of the two dimensionless parameters α and η are studied separately. To this end, the backbone curves are computed by solving Eq. (4.20) with the HBM-ANM method for several values of (α,η). Results are presented in § 4.4.1 for constant α and in § 4.4.2 for constant η. Here, the backbone curves trace the evolution of the amplitude of the first harmonic (H1) of either the cross-section rotation at the free end of the cantilever $\theta(L,t)$ or the transverse displacement $w(L,t)$ as a function of the frequency of oscillation Ω ($\Omega = 2\pi/T$ with T the period of the motion) in Figs. 4.5, 4.6, 4.8 and 4.9. Based on the results of [58], [71], it was found that showing only H1 gives an excellent image of the amplitude of the periodic solution since this harmonic is heavily dominant up to very large amplitudes of displacement. Moreover, the backbone curves tied to the cross-section rotation $\theta(L,t)$ are considered more readable than those of the transverse amplitude $w(L,t)$ since they increase monotonically, whereas the latter fold at large amplitude, *i.e.* beyond $\theta(L,t) > \pi/2$ when the beam bends backwards (compare Figs. 4.5(a) and (b)). For this reason, mostly $\theta(L,t)$ backbones are depicted in this work, instead of $w(L,t)$. Note also that all backbone curves have been normalized by the (linear) natural frequency $\omega_m(\alpha)$, which depends on gravity, as analyzed in § 4.3.

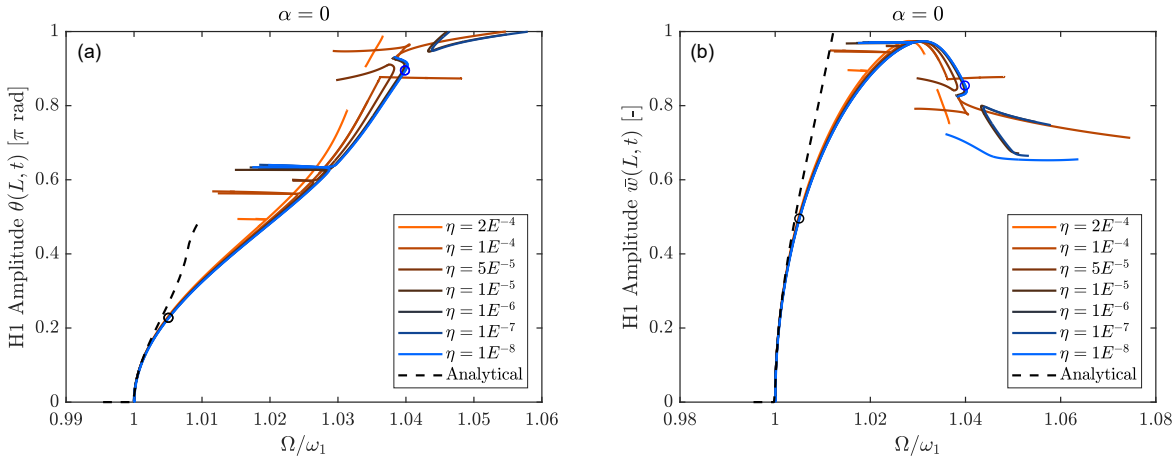

Figure 4.5: Effect of the slenderness parameter η on the first nonlinear mode: (a) amplitude of the first harmonic H1 of θ at the free end of the beam for different values of η and comparison with inextensible (analytical) beam model [46], [47], (b) amplitude of the first harmonic H1 of $\bar{w}$ at the free end of the beam for different values of η. Case with no gravity ($\alpha = 0$).

4.4.1 Effect of η

First, we study the isolated effect of the dimensionless slenderness parameter η on the first three nonlinear modes. In this case, the effect of gravity is removed, *i.e.* α is fixed at 0. The amplitude of the first harmonic H1 backbone curve is traced for the rotation degree of freedom θ at the free end of the cantilever, *i.e.* the location of maximum displacement on a cantilever beam, for several values of η. The θ backbone curve is shown for nonlinear modes one, two and three in Figs. 4.5(a) and 4.6. To these is also added the backbone curve of the first nonlinear mode for the transverse displacement degree of freedom $\bar{w}$ at the tip of the beam in Fig. 4.5(b).

Beginning with the first nonlinear mode, the shape of the backbone curves in Fig. 4.5 highlights several classical phenomena in the field of nonlinear dynamics. First, it is seen that as the displacement amplitude of the vibrating cantilever increases, the oscillating frequency Ω/ω_1 likewise increases. This behavior is known as frequency dependence on the vibration amplitude, and is strictly a nonlinear effect (a linear "backbone" curve would be a straight vertical line at the resonant frequency). If the frequency increases with increasing amplitude, the trend is referred to as *hardening* (versus *softening* if reversed). All backbone curves in Fig. 4.5 for different values of η depict this hardening trend, which validates the known hardening of the first nonlinear mode of the cantilever beam [68], [69], [165], [229]. Another classical nonlinear effect is seen in the jumps and branches or "offshoots" from the main backbone curve. Such instances represent locations of internal resonance (IR), when some energy is transferred from one mode to another one because of a frequency locking between the harmonics of the oscillating mode and the nonlinear frequencies of other modes (see *e.g* [86], [124], [236]).

The appearance of internal resonance points along the backbone curve can take different forms and can sometimes be challenging to compute numerically. For the present case of a cantilever beam, this was discussed in Chapter 3. Furthermore, since the focus in this chapter centers on the main backbone curves, the IR branches are not computed entirely, leading in some cases to interruptions in the curve shown (as explained in § 3.5). Note that the shape of the backbone curves in Fig. 4.5 is

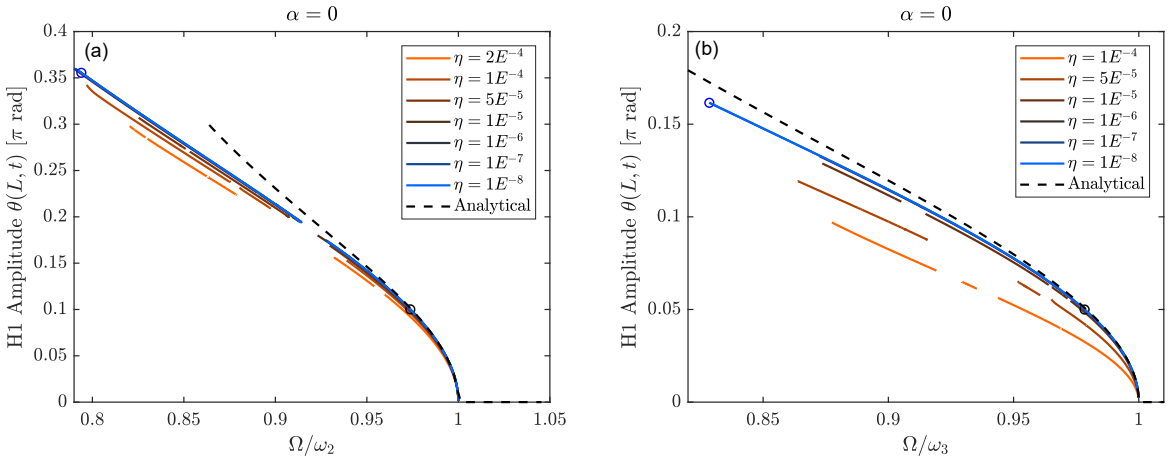

Figure 4.6: Effect of the slenderness parameter η on the second and third nonlinear modes: (a) amplitude of the first harmonic H1 of θ at the free end of the beam for different values of η (mode 2) and comparison with inextensible (analytical) beam model [46], [47], (b) the same as (a) for mode 3. Case with no gravity ($\alpha = 0$). Note that some curves (particularly for small η) overlap others and therefore some curves may not be visible.

slightly different from those shown in § 3.3.1, especially in the vicinity of the IRs as well as at large amplitude. This is due to the fact that in § 3.3.1, the maximum amplitude over one period of oscillation – thereby including the effect of all harmonics – was shown, whereas, here, only the amplitude of the first harmonic is depicted. However, the difference between the maximum amplitude and the first harmonic of θ is, in this case, slight; as mentioned earlier, the first harmonic greatly dominates the higher harmonics, which become consequential only at higher amplitude. This is illustrated in Fig. 4.7, which superimposes the backbone curve in terms of the maximum amplitude of $\theta(L,t)$ over one period onto the backbone curves of the first three odd harmonics H1, H3 and H5, and in which the dominance of H1 is clearly visible. Moreover, since the oscillations of the structure are symmetrical, $\theta(x,t)$ is an odd function of t and its even harmonics are zero (and, thus, are not included in Fig. 4.7). Some differences between Chapter 3 and this chapter can also be explained by the differences in the number of finite elements (FEs) and harmonics H. The number of FEs greatly influences the values of the natural frequencies of the higher modes and thus the locations of the IRs on the main branch, which is itself much less affected. A greater number of FEs also increases the number of IRs since it increases the number of natural modes and therefore the number of possible frequency lockings, which is also influenced by the number of harmonics H retained in the HBM. We use 50 FEs in this chapter, whereas between 20 and 30 (depending on the mode) were used in § 3.3.1, with the same number ($H = 20$) of harmonics in both cases. In practice, the IR branches are avoided during the continuation process by manually jumping across their zone of appearance using an initial guess in frequency after the critical region and a Newton-Raphson algorithm to initiate the computation on the next branch. In the present case of a cantilever beam, this process is found to be delicate because some unusually large frequency ranges for the IR branches are uncovered: notice the IRs around $\Omega \simeq 1.04\omega_1$ for the first mode and $\Omega \simeq 0.92\omega_2$ for the second mode in Figs. 4.7(a, b). For the latter case, as seen in Fig. 4.7(b), it is even more unusual that the branch of the first harmonic (dark blue) is virtually unaffected by

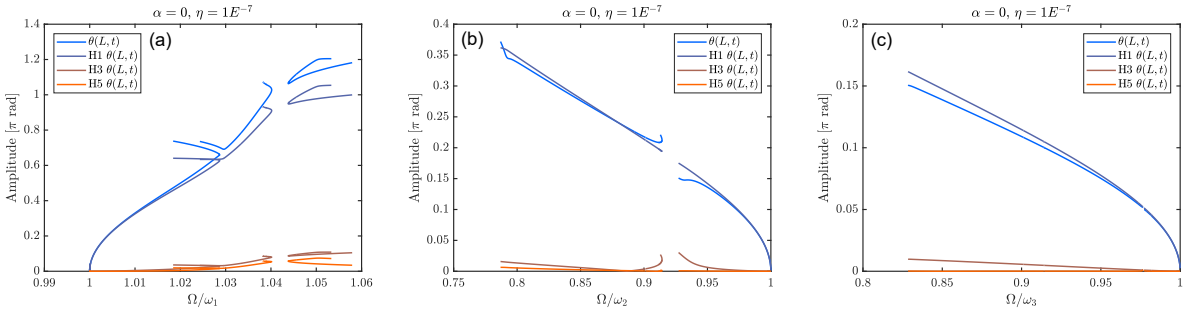

Figure 4.7: Comparison of the maximum amplitude of $\theta(L,t)$ over one period of oscillation on the first three nonlinear modes with the amplitudes of the first three odd harmonics H1, H3 and H5. Note that the H1 curves are the same as those shown in Figs. 4.5 and 4.6 for $\alpha = 0, \eta = 10^{-7}$: (a) first nonlinear mode, (b) second, (c) third.

the presence of the IR, meaning it can go undetected during continuation unless the third harmonic (brown) or the maximum amplitude of the periodic solution (light blue) is also monitored.

As in §4.3 for the natural frequencies, it can be seen that the effect of η on the mode 1 backbone curves (Fig. 4.5) is very slight, almost indistinguishable, so long as η remains small ($\eta \leq 10^{-5}$). The effect of η on the backbone curves becomes apparent only for larger values of η, *i.e.* when the beam is less slender. In this case, the location of the internal resonances shifts slightly due to changes in the frequencies of the higher modes that are affected by the change in η, thus moving the frequency locking. An analytical computation of the backbone curves is also included in Fig. 4.5, depicted with the dashed black curve, based on the approximate inextensible beam model of [46], [47] restricted to the first bending mode (see Appendix B.3 for details on this model). In this model, the geometrical nonlinearities are truncated in the Taylor series expansions at order 3 in w/L, leading to this model being valid only up to moderate amplitudes of vibration and diverging from the numerical (*i.e.* geometrically exact) backbone curves (around $\theta = 0.2\pi$ rad and $w = 0.5L$ at the beam's tip). This model is included in order to validate the finite element discretization of the geometrically exact model used here at low to moderate amplitudes.

For the second nonlinear mode, the same two observations as for mode 1 are made, as seen in Fig. 4.6(a): the influence of η on the backbone curve is negligible, so long as η remains small ($\eta \leq 10^{-5}$), and also the backbone curve is validated at low amplitudes by the mode 2 inextensible model of Crespo da Silva *et al.* (Appendix B.3). The same cannot be said for the third nonlinear mode. As shown in Fig. 4.6(b), the global trend of η's influence diminishing for small values of η holds, but only for *very* small η, around $\eta \leq 10^{-6}$. The influence of the slenderness of the beam seems to be quite large on the third nonlinear mode for "larger" η, *e.g.* $\eta > 10^{-5}$, even greater than on the first nonlinear mode. The mode 3 backbones for small $\eta \leq 10^{-6}$ are again validated by the inextensible analytical backbone, but these results seem to suggest a greater influence of the h/L ratio on the third nonlinear mode than on either of the first two. This trend seems logical when considering the mode shapes of the structure (see Fig. 4.3); an "improved" definition of the slenderness ratio η would consider instead h/λ_m, with λ_m a fraction of L representing the wavelength of the mode. Referring to Fig. 4.3 and according to the "improved" definition, as the mode number m increases, λ_m decreases, thereby suggesting a greater influence of η on the backbone curves of the higher modes. It is for this reason also that only η in the range of $[10^{-8}, 10^{-4}]$ is plotted for mode 3 in Fig. 4.6(b).

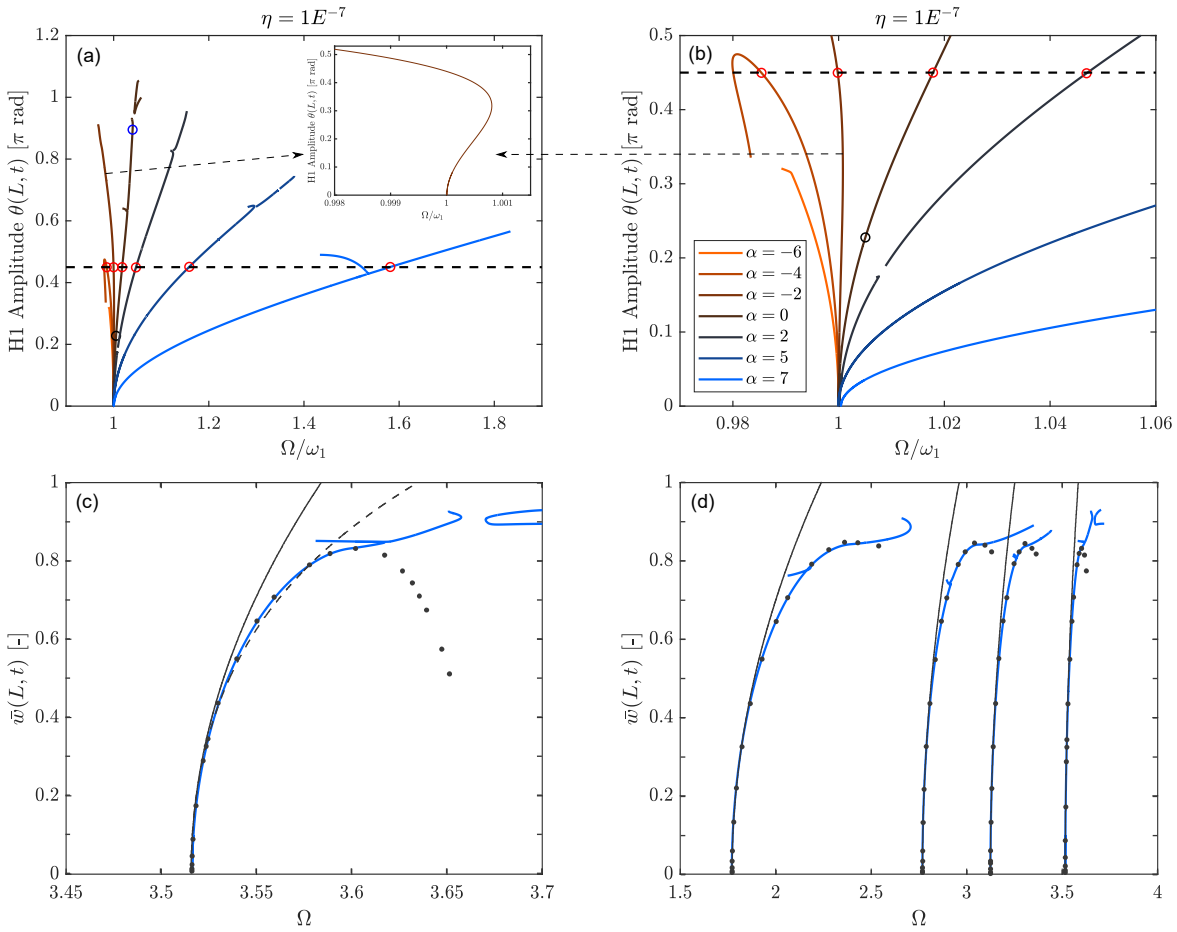

Figure 4.8: Effect of dimensionless parameters on first nonlinear mode, isolation of the effect of α: (a) amplitude of the first harmonic H1 of θ at the free end of the beam for different values of α with inset zoom onto hardening-to-softening behavior for $\alpha = -2$, (b) a zoom of (a) at low amplitudes. Comparison ($\eta = 10^{-7}$) with results of Santillan *et al.* [204] and Luongo *et al.* [146]: (c) maximum transverse displacement of the free end over one period of oscillation for $\alpha = 0$ (solid black curve: perturbation approximation [204], dashed curve: finite differences [204], dots: analytical approximation [146], solid blue curve: $\eta = 10^{-7}$ backbone curve of Fig. 4.5), (d) the same as (c) but for (from left to right) $\alpha = 5.859, 2.989, 1.655, 0$.

4.4.2 Effect of α

Next, we investigate the influence of the dimensionless gravity parameter α on the first three nonlinear modes / backbone curves of the cantilever. A constant $\eta = 10^{-7}$ is selected and the H1 backbones for the rotation degree of freedom θ at the free end of the beam (analogous to the backbones in the previous section) are shown as a function of the normalized frequency Ω/ω_m for different values of α. The results are summarized for mode 1 in Fig. 4.8 and for modes 2 and 3 in Fig. 4.9. Note that the mode 1 backbone for $(\alpha, \eta) = (0, 10^{-7})$ is the same in both Fig. 4.5(a) and Fig. 4.8.

Beginning with the first nonlinear mode, as in § 4.3, it can be seen that the dimensionless gravity

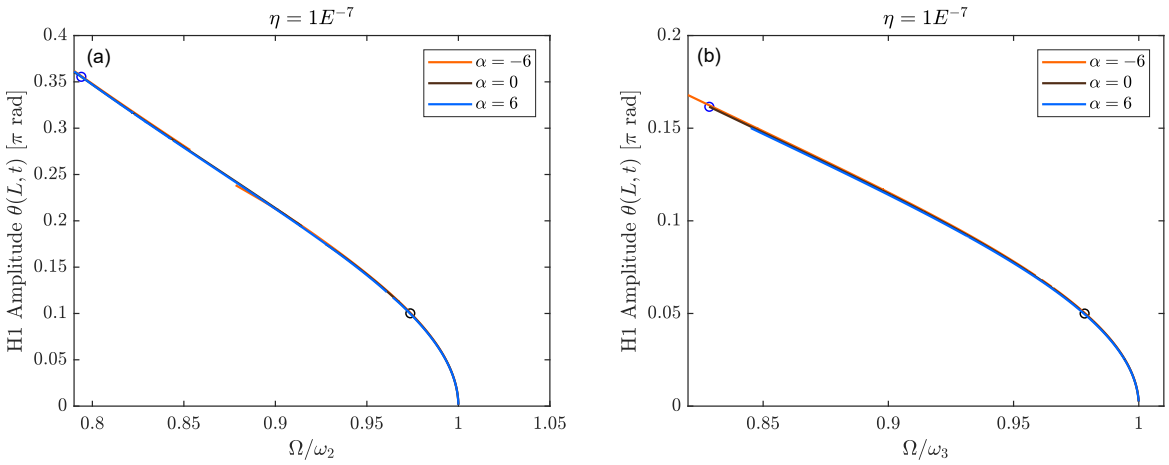

Figure 4.9: Effect of dimensionless parameters on second and third nonlinear modes, isolation of the effect of α: (a) amplitude of the first harmonic H1 of θ at the free end of the beam for different values of α (mode 2), (b) the same as (a) for mode 3.

parameter α has a significant effect on the backbone curve, much more of an effect than η in § 4.4.1. It can be seen that, noting that the $\alpha = 0$ backbone is already of hardening type, increasing α in a standing configuration (*i.e.* increasing positive α) drastically hardens the backbone curve. In a similar way, decreasing α in a hanging configuration (*i.e.* decreasing negative α), softens the backbone curve, until it eventually becomes a globally softening backbone instead of the classical hardening mode 1 backbone. Notice in the inset of Fig. 4.8(a) that the backbone curve for $\alpha = -2$, which is globally of softening type, is initially of hardening type, before switching direction around $\theta = 0.35\pi$ rad. A softening-to-hardening transition of the backbone curve is classical for initially curved structures (see *e.g.* [31], [233] for shallow shells, [153], [187], [250] for shallow arches or [224] for curved cantilevers). However, an example of the hardening-to-softening transition like that of the $\alpha = -2$ backbone in Fig. 4.8 is much more uncommon, but was observed on the second nonlinear mode of a flexible ring structure in § 3.3.3. In addition, a comparison is made to the backbone approximations of Santillan *et al.* [204] and Luongo *et al.* [146] as shown in [204] for cantilever boundary conditions. In Fig. 4.8(c), the maximum transverse displacement at the free end of the beam over one period for the $\eta = 10^{-7}$ backbone of Fig. 4.5 is computed and compared to Fig. 5 of [204]. Likewise, the same comparison is carried out for Fig. 7 of [204] for three nonzero values of $\alpha = [1.655, 2.989, 5.859]$ in Fig. 4.8(d). Up to very high amplitudes, it can be seen that there is excellent agreement between our results and the finite differences computation of [204]. The differences at high amplitude are probably due to the time integration method used in [204], which did not enforce periodicity of the response (or invariance), the property used here to compute the nonlinear modes.

With regard to the second and third nonlinear modes, the H1 backbone curves for the same θ degree of freedom at the free end of the beam as for mode 1 are shown for several values of α in Fig. 4.9(a) for mode 2 and 4.9(b) for mode 3. It can be seen that gravity has only a very minor influence on the backbone curves, almost unnoticeable. It is for this reason that only a few very different values of $\alpha \in \{-6, 0, 6\}$ are selected for modes 2 and 3 prior to the self-buckling occurring at $\alpha_{\text{crit}} = 7.837$, where $\alpha = 6$ can be considered as a "large" effect of gravity on a physical standing cantilever.

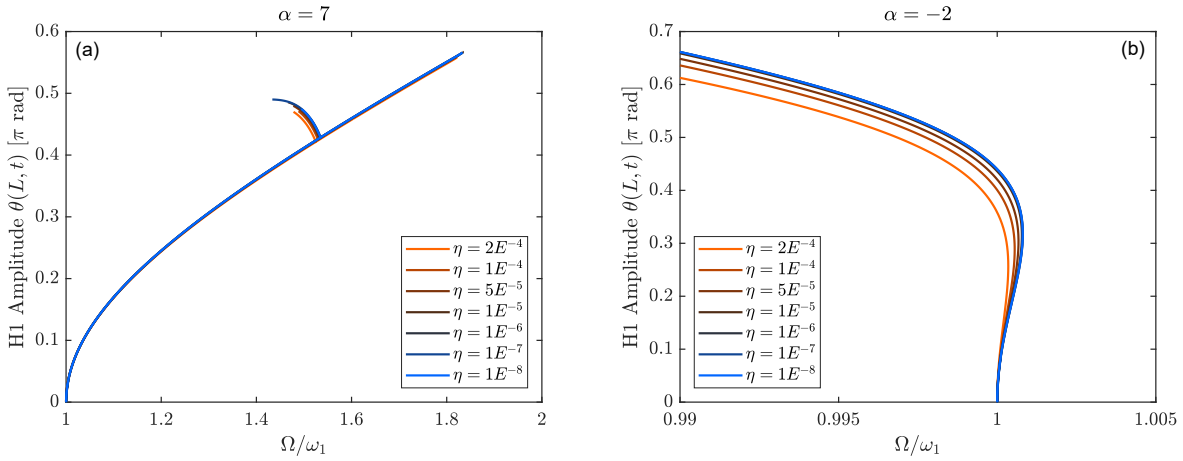

Figure 4.10: Effect of dimensionless parameters on the first nonlinear mode, isolation of the effect of η for $\alpha \neq 0$: (a) amplitude of the first harmonic H1 of θ at the free end of the beam for different values of η in the standing configuration ($\alpha = 7$), (b) the same as (a) but in the hanging configuration ($\alpha = -2$).

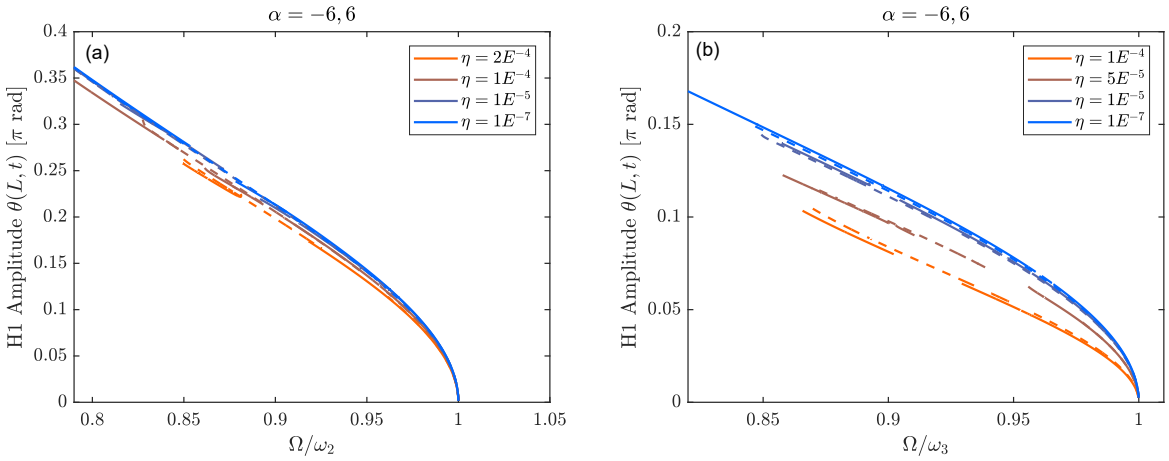

Figure 4.11: Effect of dimensionless parameters on the second and third nonlinear modes, isolation of the effect of η for $\alpha \neq 0$: (a) amplitude of the first harmonic H1 of θ at the free end of the beam for different values of η (solid curve: $\alpha = -6$, dotted curve: $\alpha = 6$), (b) the same as (a) but on the third nonlinear mode.

Finally, the joint effect of η and α on the nonlinear modes is studied, where η is varied while including the effect of gravity, *i.e.* $\alpha \neq 0$. On the first nonlinear mode, η is varied as in Fig. 4.5 for $\alpha = 7$ and $\alpha = -2$, this latter case being selected in particular due to the unique hardening-to-softening transition of the backbone curve observed in Fig. 4.8. On the second and third nonlinear modes, η is varied for $\alpha = 6$ and $\alpha = -6$ in order to be consistent with Fig. 4.9. The results are summarized in Fig. 4.10 for the first nonlinear mode and in Fig. 4.11 for the second and third nonlinear modes. In general, the main conclusions already established for the ranges of η and α studied in this work hold

also for $\eta, \alpha \neq 0$, namely that η does not have a strong influence on the backbone curves no matter the value of α so long as η is small, and that α has a strong influence only on the first nonlinear mode. Interestingly, however, larger values of η ($\eta > 10^{-5}$) appear to have a greater influence on the first nonlinear mode as α decreases: comparing Figs. 4.5 and 4.10, large η (such as $\eta = 2 \cdot 10^{-4}$) has the least influence when $\alpha = 7$ and the greatest influence when $\alpha = -2$.

To summarize, it can be said that the effect of gravity on the nonlinear modes of the system is significant on the first nonlinear mode, but comparably insignificant on higher-frequency modes. On the first nonlinear mode, it is observed that in a standing configuration ($\alpha > 0$), increasing the effect of gravity serves to *increase* the hardening trend of the backbone, meaning that the global backbone becomes more hardening when taking into account the gravitational field. In a hanging configuration ($\alpha < 0$), the effect is reversed. Interestingly, gravity has an opposite effect on the first *nonlinear* mode as compared to the *linear* one: in the standing configuration, gravity has a hardening effect on the backbone curve of the first nonlinear mode, whereas it has a softening effect on the (linear) natural frequencies, since they decrease as α increases, as described in § 4.3. A more physical interpretation of these effects is outlined in § 4.6 using a simple pendulum system.

Finally, it is noted that the case of the hanging configuration is very similar to the case of a rotating cantilever beam, in which the beam is subjected to a centrifugal axial field. In this case, the effect of the centrifugal force is hardening for the (linear) natural frequencies and softening for the backbone curves (see *e.g.* [155], [229]). The similarity between the two cases can be linked to the axial preload condition, with the only difference being that the load is not uniform (it increases with x) in the case of the rotating beam.

4.5 Nonlinear mode shapes

4.5.1 Effect of α on the first nonlinear mode shape

In addition to the effect of (α, η) on the nonlinear backbone curves, it is also of interest to study the effect of gravity on the deformed shape in the nonlinear region. Based on the results of § 4.4, we choose to concentrate the investigation primarily on the influence of α for a chosen $\eta = 10^{-7}$ on the first nonlinear mode, since it is shown in § 4.3 and 4.4 that both η (when small) and α do not have a strong influence on the higher-frequency modes up to α_{crit}.

First, we investigate the effect of α on the deformed shape of the beam at moderate-to-high cross-section rotations, around a maximum H1 amplitude of 0.45π rad, considering this region to be representative of moderate-to-high amplitudes of vibration (and, therefore, judiciously considered as nonlinear behavior). This is justified since the analytical backbone computation based on the third-order inextensible beam model of Crespo da Silva *et al.*, recalling the black dashed line in Fig. 4.5(a), begins to diverge from the geometrically exact model around $\theta = 0.2\pi$ rad.

To study the effect of the gravity parameter α on the deformed shape of the beam, the deformed shape is traced at points of (nearly) constant amplitudes along each of the $\alpha \in \{-4, -2, 0, 2, 5, 7\}$ backbones, shown as red circles in Fig. 4.8(a). Since the continuation points are different for each numerical computation, it is not possible to select an exact amplitude of 0.45π rad in all simulations, the closest continuation point being selected instead. The coordinates of the red circles in Fig. 4.8(a) for each backbone curve are tabulated in Table 4.2.

The deformed shapes of the cantilever beam at these points along the backbone curves are gathered in Fig. 4.12. The deformed shapes are taken as a certain number of snapshots over a fixed time interval

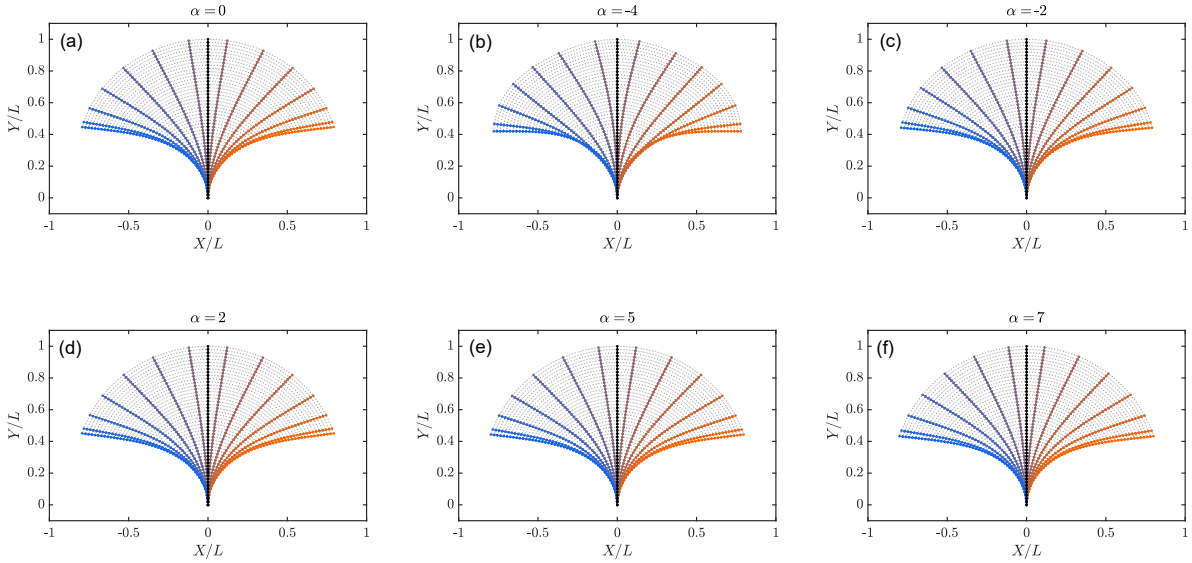

Figure 4.12: Snapshots of the cantilever beam vibrating on its first nonlinear mode for different values of α. The locations on the corresponding backbones at which the snapshots are taken are marked by red circles in Fig. 4.8(a).

Table 4.2: Coordinates at which the deformed shapes in Fig. 4.12 are taken, as shown by the red circles in Fig. 4.8(a).

α	Ω/ω_1	Amp. H1 θ [π rad]
-4	0.9854	0.4497
-2	0.9998	0.4497
0	1.0179	0.4500
2	1.0469	0.4491
5	1.1590	0.4511
7	1.5814	0.4505

equal to half of the period of the periodic motion. Over the half period, the individual snapshots of the deformed shapes appear as the colored curves, the initial reference (undeformed) configuration is the black curve, and the dashed light gray curves joining the colored curves represent the trajectory of the nodes (see Fig. 4.12). In addition, the individual snapshots of Fig. 4.12 are gathered together in a single plot in Fig. 4.13.

It is immediately observed that the deformed shapes of the beam in Figs. 4.12 and 4.13 are nearly indistinguishable despite the points being taken at very different frequencies. For example, the $\alpha = 0$ deformed shape (Fig. 4.12(a)) is traced for a frequency of $\Omega/\omega_1 = 1.0179$, while the $\alpha = 7$ deformed shape (Fig. 4.12(f)) is traced for a frequency of $\Omega/\omega_1 = 1.5814$, 1.61 times larger, yet the deformed shapes are nearly identical. Between Figs. 4.12(a)-(f), only the effect of α, *i.e.* of gravity, changes; comparing Figs. 4.8 and 4.12 proves that, although changing α bends the backbone curve either more

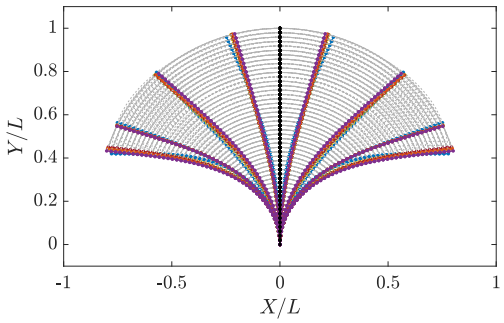

Figure 4.13: Snapshots Fig. 4.12(a)-(f) condensed into one figure: — $\alpha = 0$, — $\alpha = -4$, — $\alpha = -2$, — $\alpha = 2$, — $\alpha = 5$, — $\alpha = 7$.

hardening or more softening depending on the sign of α (and, therefore, shifts the frequency higher or lower), *the deformed shape of the nonlinear mode is essentially not influenced by gravity.*

4.5.2 Evolution of mode shape as a function of the amplitude

The surface plots in Fig. 4.14 provide another useful visualization for understanding the development of the nonlinear deformed shape of the cantilever for different values of α. Each surface plot corresponds to a backbone curve of Fig. 4.8(a) for $\alpha \in \{-2, 0, 5\}$, $\eta = 10^{-7}$. The surfaces depict the amplitude of the first harmonic H1 of the rotation $\theta(x,t)$, normalized by its value at $x = L$, as a function of (1) the cross-section positions $\bar{x} = x/L$ and (2) the amplitude of the first harmonic H1 of the rotation $\theta(L,t)$ at the free end. Consequently, at $x = L$, the amplitude of the surface is exactly 1. The curves are plotted, for each α, for the same range of amplitudes H1 of $\theta(L,t)$ as their backbone counterparts in Fig. 4.8.

These surface plots can be interpreted as the evolution of the first mode shape of the beam as a function of the amplitude of the motion. To understand this, consider first the case of the linearized model, valid for small amplitude. In this case, the motion on the first mode would be exactly $\theta(x,t) = w'(x,t) = \Phi_1'(x)\cos\Omega t$, with:

$$\Phi_i'(x) = \beta_i \left[\sin\beta_i x + \sinh\beta_i x + a_i(\cos\beta_i x - \cosh\beta_i x)\right], \quad i \in \mathbb{N}^*, \tag{4.29}$$

obtained by differentiating Eq. (B.13), showing naturally that the deformed shape $\Phi_1'(x)$ of the motion does not depend on the amplitude. The first mode shape $\Phi_1(\bar{x})$ and its derivative $\Phi_1'(\bar{x})$, normalized by their values at $x = L$, are overlaid on top of the surfaces in Fig. 4.14.

Analyzing Fig. 4.14, it can be concluded that, similar to a linear system, *the deformed shape of the first (leading) harmonic of the cross-section rotation $\theta(x,t)$ motion on the first nonlinear mode is nearly independent of the motion amplitude*, since the surfaces are almost flat as a function of H1 of $\theta(L,t)$. Since the first harmonic is leading up to large amplitude, this conclusion indicates that the

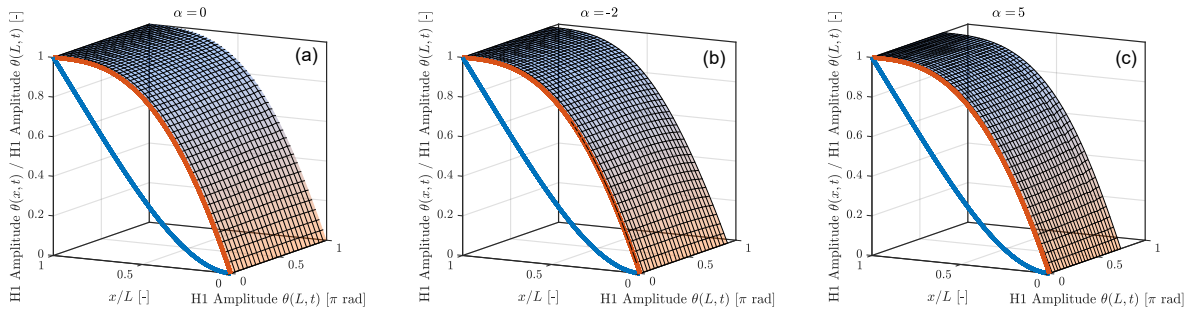

Figure 4.14: Surface plots depicting the (normalized) amplitude of H1 of $\theta(x,t)$ as a function of the position $\bar{x} = x/L$ and of the amplitude of H1 of $\theta(L,t)$, for several values of α. These surface plots correspond to the backbones shown in Fig. 4.8(a). In addition, the linear mode shapes $\Phi_1(\bar{x})/\Phi_1(L)$ and $\Phi_1'(\bar{x})/\Phi_1'(L)$ are shown in blue and orange, respectively.

motion can be approximated by:

$$\theta(x,t) = \sum_{i=1}^{+\infty} \Phi_i'(x) q_i(t), \tag{4.30a}$$

$$= \Phi_1'(x) a_1^{(1)}(\Omega) \cos \Omega t + \left[\sum_{i=1}^{+\infty} \Phi_i'(x) a_i^{(3)}(\Omega) \right] \cos 3\Omega t + \left[\sum_{i=1}^{+\infty} \Phi_i'(x) a_i^{(5)}(\Omega) \right] \cos 5\Omega t + \text{HH}, \tag{4.30b}$$

$$\simeq \Phi_1'(x) a_1^{(1)}(\Omega) \cos \Omega t, \tag{4.30c}$$

where $a_i^{(h)}(\Omega)$ is the amplitude of the hth harmonic of the ith modal coordinate $q_i(t)$ and HH stands for "higher harmonics." Above, Eq. (4.30a) is a standard modal expansion, Eq. (4.30b) represents a Fourier series decomposition explicitly enforcing the aforementioned conclusion that the deformed shape of the first harmonic is independent of the amplitude, and Eq. (4.30c) neglects the higher harmonics. This result seems astonishing at first sight since the motion of the beam at high amplitude appears very complex, as observed in Figs. 4.4(a) and 4.12. However, if the motion characterized by $\theta(x,t)$ is *a priori* very simple, the geometrical nonlinearities appear strongly in the displacement fields (u,w) of the points on the centerline of the beam through the kinematics relations (B.9) (valid if the beam is inextensible), written:

$$w(x,t) = \int_0^x \sin \theta(\xi,t) \, \mathrm{d}\xi \simeq \int_0^x \sin \left[\Phi_1'(\xi) \cos \Omega t \right] \mathrm{d}\xi, \tag{4.31a}$$

$$u(x,t) = \int_0^x \left(\cos \theta(\xi,t) - 1 \right) \mathrm{d}\xi \simeq \int_0^x \left(\cos \left[\Phi_1'(\xi) \cos \Omega t \right] - 1 \right) \mathrm{d}\xi, \tag{4.31b}$$

or, in other words, knowing $\theta(x,t)$, it is possible to reconstruct the full two-dimensional motion using Eqs. (4.31).

Then, in order to analyze the effect of the higher harmonics, Figs. 4.15 and 4.16 are traced as surfaces depicting the evolution of H3 and H5 on the first nonlinear mode backbone curves in a way analogous to what was done for H1 in Fig. 4.14(a) for $\alpha = 0$. In Fig. 4.15, H3 and H5 are normalized by (H3, H5) and by H1 in Fig. 4.16. Fig. 4.16 explicitly shows that the amplitudes of H3 and H5 are small compared to the amplitude of H1 (a result also visible in Fig. 4.7), since their amplitudes remain at 10% the amplitude of H1 or below on the entire backbone curve. Moreover, Fig. 4.15 reveals that

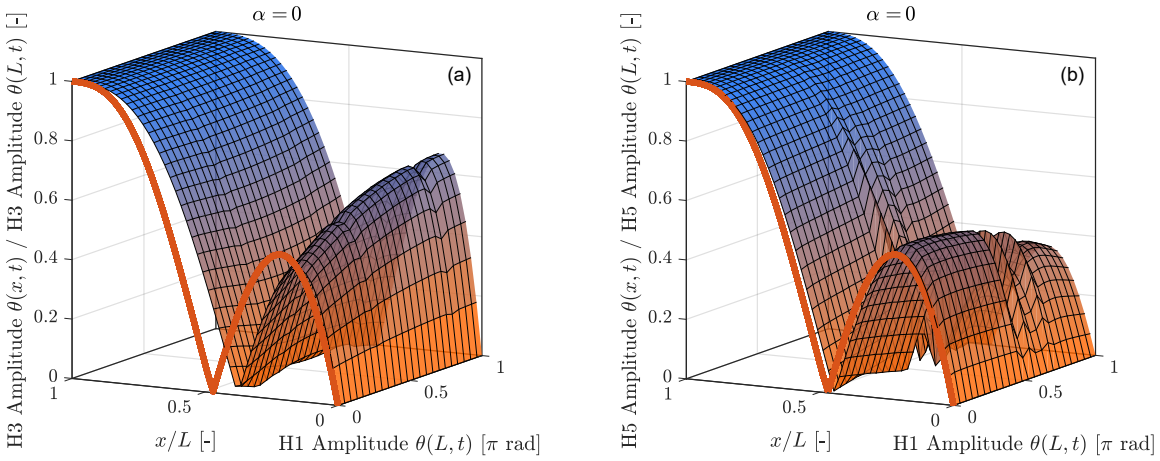

Figure 4.15: Surface plots depicting the (normalized) amplitude of H3 or H5 of $\theta(x,t)$ as a function of the position $\bar{x} = x/L$ and of the amplitude of H1 of $\theta(L,t)$: (a) H3, (b) H5. The linear mode shape $\Phi_2'(\bar{x})/\Phi_2'(L)$ is shown in orange.

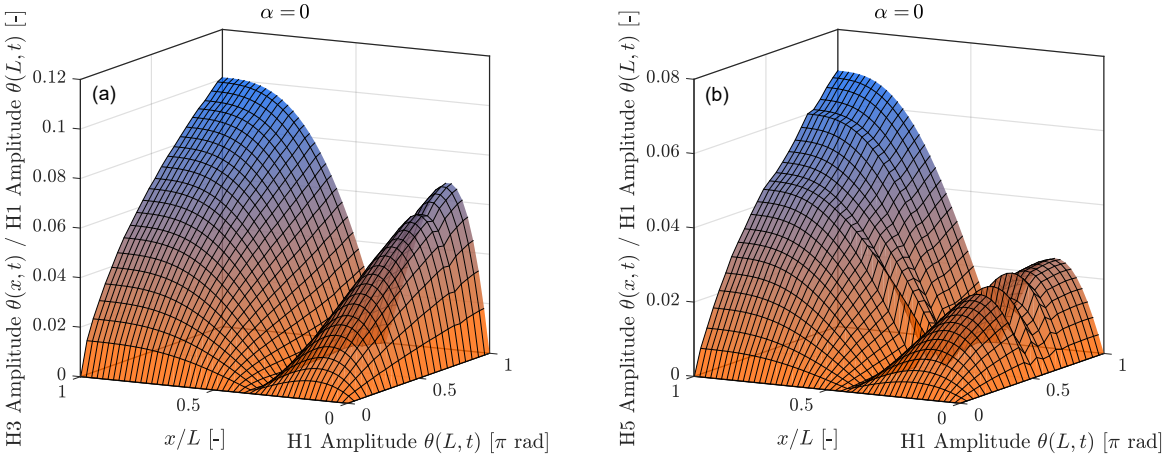

Figure 4.16: Surface plots depicting the amplitude of H3 or H5 of $\theta(x,t)$ *normalized by H1* as a function of the position $\bar{x} = x/L$ and of the amplitude of H1 of $\theta(L,t)$: (a) H3, (b) H5.

although the shapes of harmonics H3 and H5 depend slightly on the amplitude of the motion, the overall shape is close to the second mode shape of the beam, leading to an approximation of $\theta(x,t)$ based on Eq. (4.30b) as:

$$\theta(x,t) \simeq \Phi_1'(x) a_1^{(1)}(\Omega)\cos\Omega t + \Phi_2'(x)\left(a_2^{(3)}(\Omega)\cos 3\Omega t + a_2^{(5)}(\Omega)\right). \tag{4.32}$$

Note that the local discontinuities in the H3 and H5 surfaces in Figs. 4.15 and 4.16 are related to some internal resonance "offshoots," mentioned in § 4.4.1. The results presented in this section enable a more deep characterization of the motion on the first nonlinear mode while also laying the groundwork for reduced order modeling of the beam. From this perspective, choosing $\theta(x,t)$ as the principle variable to investigate seems an excellent idea, already pursued in a series of articles [69], [71], [82].

Lastly, it is noted that Fig. 4.14 also demonstrates the independence of the first harmonic of the deformed shape of the beam from gravity, since the shape of Figs. 4.14(a-c) remain identical regardless of the value of α.

4.6 Analogy with a pendulum system

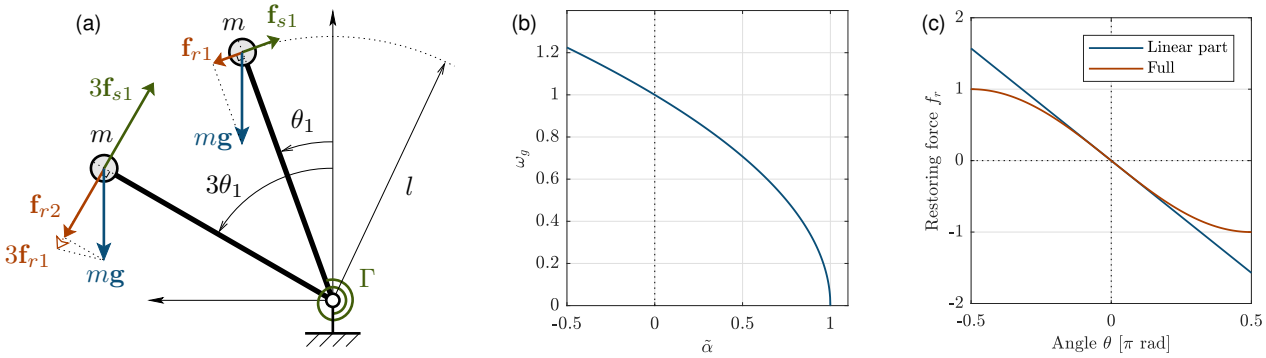

Figure 4.17: (a) Pendulum shown in two positions along with restoring force $\mathbf{f}_r$, (b) graph of the natural frequency ω_g of the pendulum as a function of the gravity parameter $\tilde{\alpha}$ (normalized), and (c) graph of the restoring force f_r as a function of angle θ (normalized).

In order to offer a more physical insight into the effect of gravity on both the linear and nonlinear frequencies of the first mode of the cantilever, consider the inverted pendulum of Fig. 4.17(a). The pendulum is of length l, with all of its inertia m concentrated at its tip, and is subjected to a gravitational acceleration $\mathbf{g}$ and a linear torsional spring of stiffness Γ. The spring is at rest when the pendulum is vertical. For this system, the equation of motion governing the angle θ of the pendulum with respect to the positive vertical axis can be written:

$$\ddot{\theta} + \frac{\Gamma}{ml^2}\theta - \frac{g}{l}\sin\theta = 0 \quad \Rightarrow \quad \ddot{\theta} + \omega_0^2(1-\tilde{\alpha})\theta + f_{\mathrm{nl}}(\theta) = 0, \quad \omega_0 = \sqrt{\frac{\Gamma}{ml^2}}, \tag{4.33}$$

where ω_0 is the natural frequency of the pendulum without gravity. In Eq. (4.33), it is clear that the spring creates a linear restoring force $f_s = \frac{\Gamma}{ml^2}\theta$ while gravity creates a restoring force $f_r = -\frac{g}{l}\sin\theta$ of opposite sign, which works to counteract the restoring force generated by the spring.

Separating the linear part of f_r and denoting by $f_{\mathrm{nl}}(\theta)$ the remaining part, the gravity parameter $\tilde{\alpha}$ and the natural frequency of the pendulum with gravity $\omega_g(\tilde{\alpha})$ can be defined such that:

$$\tilde{\alpha} = \frac{mlg}{\Gamma}, \quad \omega_g = \omega_0\sqrt{1-\tilde{\alpha}}. \tag{4.34}$$

In tracing $\omega_g(\tilde{\alpha})$ shown in Fig. 4.17(b), the graph is found to be very similar to that of $\bar{\omega}_1(\alpha)$ for the first mode of the cantilever, shown in Fig. 4.2(b). In the present case of the pendulum, the critical value for self-buckling of the pendulum is $\tilde{\alpha} = 1$. The effect of gravity on the pendulum's natural frequency ω_g is then clear: ω_g decreases as the gravity parameter $\tilde{\alpha}$ increases since it creates a restoring force *opposed to that of the spring*, thereby decreasing the overall stiffness of the pendulum. Gravity, thus, has a *softening linear effect*.

Considering the nonlinear part of the restoring force $f_{\text{nl}} = \omega_0^2\tilde{\alpha}(\theta - \sin\theta)$, it appears to add a *positive* nonlinear part to the linear restoring force $-\omega_0^2\tilde{\alpha}\theta$, which explains why gravity has a *hardening nonlinear effect*; it is responsible for a nonlinear frequency that increases with the amplitude of the motion. From a physical point of view, this can be explained by a projection effect of the gravity force $m\mathbf{g}$ in the tangent direction (the direction of the restoring force $\mathbf{f}_s$ of the spring, see Fig. 4.17(a)). As θ increases, the "full" $f_r(\theta)$ increases less in absolute value than its "linear part", thus creating a nonlinear effect of opposite nature (hardening) with respect to the linear one (softening). This is illustrated by the graph of Fig. 4.17(c), where the "full" restoring force curve $f_r(\theta)$ is above its "linear part" $-\omega_0^2\tilde{\alpha}\theta$ for $\theta > 0$ and below if $\theta < 0$.

Returning to the case of the cantilever, it can be imagined that the distributed force due to gravity has the same projection effect in each infinitesimal part of the cantilever beam. Since the curvature of the first mode shape is constant along the beam as evidenced in §4.5, the analogy to the pendulum system holds. In the case of modes 2 and 3 of the cantilever, a double or triple pendulum would likely lead to analogous results.

4.7 Conclusion

In this work, the influence of gravity on the dynamics of flexible slender cantilevers is studied. The cantilevers are considered to be vertically-oriented in either a standing or hanging configuration and are subjected to a gravitational acceleration g. It is found that by normalizing the system by the length of the cantilever, only two dimensionless parameters, a "slenderness" parameter η and a "gravity" parameter α, primarily govern the dynamics of the beam. In the linear region, shown in § 4.3, it is found that, globally, η holds little influence over the linear natural frequencies $\bar{\omega}_m$ of the first three bending modes $m = 1, 2, 3$, while α holds a much greater influence, particularly on the first mode. In a hanging configuration (represented by $\alpha < 0$), increasing the magnitude of α increases $\bar{\omega}_m$, while increasing the magnitude of α in a standing configuration ($\alpha > 0$) decreases $\bar{\omega}_m$ up to a value of α_{crit}, at which the standing cantilever buckles under its own weight.

At larger amplitudes of vibration, the dynamics of the slender cantilever become nonlinear due to the influence of the geometrical nonlinearities tied to the rotation of the cross-sections. In particular, the nonlinear modes, visually represented as backbone curves in a traditional amplitude / frequency plot and as deformed "snapshots" of the structure at high amplitude, are studied, the results of which are shown in § 4.4 and 4.5. In the nonlinear region, it is found that, as in the linear region, η globally holds little influence over the first three nonlinear modes, so long as η remains small ($\eta \leq 10^{-5}$ for modes 1 and 2 or $\eta \leq 10^{-6}$ for mode 3). The backbone curves are also validated by an analytical backbone computation based on the inextensible beam model of Crespo da Silva *et al.*, valid up to moderate amplitudes of vibration. Regarding the influence of α, it is found that α has a very large effect on the first nonlinear mode in particular, with much less effect on modes 2 and 3. Increasing the magnitude of α in a standing configuration hardens the backbone of the first nonlinear mode, while increasing the magnitude of α in a hanging configuration softens the backbone. Interestingly, however, the different values of α do not influence the deformed shape of the first nonlinear mode. Finally, α is shown to have very little influence on the higher nonlinear modes 2 and 3. The behavior of the first nonlinear mode under the influence of gravity is interpreted in another context through an analogy to a simple pendulum system in § 4.6. It is noted, however, that significant difficulties were encountered during computation of some of the backbone curves, particularly on the higher modes, due to the detection of many complex internal resonances (see § 4.4.1). Further investigation of these internal

resonances is required to better understand the nonlinear behavior of the system at these locations.

The results of this work highlight the importance of incorporating gravity in any dynamical simulations, particularly when investigating the first mode of a cantilever beam within a gravitational field. Future studies will aim to compare numerical simulations including consideration of gravity to experimental measurements, in particular of the nonlinear modes, in addition to studying the effects of gravity on different beam orientations (such as a "horizontal" cantilever with gravity perpendicular to the axis of the beam) and types of systems.

Chapter 5

Nonlinear dynamics of flexible beam structures in 3D with quaternion parametrization of rotations

In Chapter 3, we derived and implemented a finite element discretization of the geometrically exact beam model restricted to in-plane motions in two dimensions (2D). The logical next step, then, is to develop the model so as to extend the 2D motions to three dimensions (3D). In 2D, the rotations are parametrized with classical rotation matrices, but these become rather complex when extending the motion to 3D as the beam is able to rotate in three ways (rotations about the two transverse directions and torsion about the longitudinal direction of the beam) compared to only a single rotation in 2D. Many different methods have therefore been proposed in the literature for the parametrization of rotations in 3D, some of which were introduced in § 1.2.1: Euler angles, Rodrigues parameters, unit quaternions, Lie groups, *etc.* In this chapter, we choose to parameterize the rotations in 3D using quaternions, 4-dimensional complex numbers that exactly represent the rotation terms. Quaternions have long been used in the modeling of flexible structures [45], [100], [132], [197], [261], [263], but advances in the implementation of quaternions for the dynamic simulation of highly flexible structures based on the geometrically exact beam model have only recently been made [253]. Of particular interest (and which has not been done in the literature to the knowledge of the authors) is solving a quaternion-based formulation of the geometrically exact beam model in the frequency domain in order to target periodic solutions of the equations of motion. This is precisely the aim of this chapter.

Recall that the kinematics and governing equations of the geometrically exact beam model were derived in Chapters 2 and 3 only for motions restricted to 2D. The first part of this chapter, then, is dedicated to extending the derivations to general 3D motions. The derivation presented here is based on the formulation of Géradin and Cardona [101] and represents an extension to dynamics of the work of Cottanceau *et al.* [45]. The general derivation of the governing equations is given in § 5.1 similar to the derivations of Chapters 2 and 3. Some of the details are omitted from § 5.1 for the sake of efficiency, but the reader is referred to [101] wherever appropriate. The method of rotation parametrization using quaternions is then introduced in § 5.2 and the beam equations are rewritten using quaternions in place of the trigonometric nonlinearities of Chapter 3. Quaternions possess a special algebra that has many specific properties; only the most important of these are addressed in § 5.2, but the interested reader is referred to [45], [100], [101] and the references cited therein for more details. Once the governing equations have been derived, they are discretized into finite elements in

§ 5.3 in a process very similar to that described in § 2.2.1 and § 3.2.2.

For the sake of direct comparison to the 2D formulation of Chapter 3, the general 3D beam equations with quaternions are restricted to 2D motions in the plane in § 5.4 by setting the appropriate degrees of freedom (*i.e.* displacements and rotations out of the plane) to zero. The 3D FE model of § 5.3 and the 2D FE model of § 5.4 are then tested using two test cases found in the literature: a cantilever (clamped-free) beam [244] and a clamped-clamped beam [217] in one-to-one (1:1) internal resonance. The test cases (in 2D) are also compared to the 2D test cases of § 3.3 since the latter model has been extensively validated with numerous comparisons to other models in the literature in Chapters 3 and 4. Final thoughts and the limitations of the current 3D model are summarized in § 5.6.

Table of Contents - Chapter 5

5.1 Beam equations in 3D

In this section, the geometrically exact beam equations are derived for motions in 3D in a way analogous to the derivations in Chapters 2 and 3 for plane motions.

5.1.1 Beam kinematics in 3D

We begin by recovering the kinematics description of Chapters 2 and 3 but removing the restriction to in-plane motions. Recall that the beam model is reduced from the full nonlinear 3D continuum to a 1D continuum and is described by the series of cross-sections through whose centroids passes

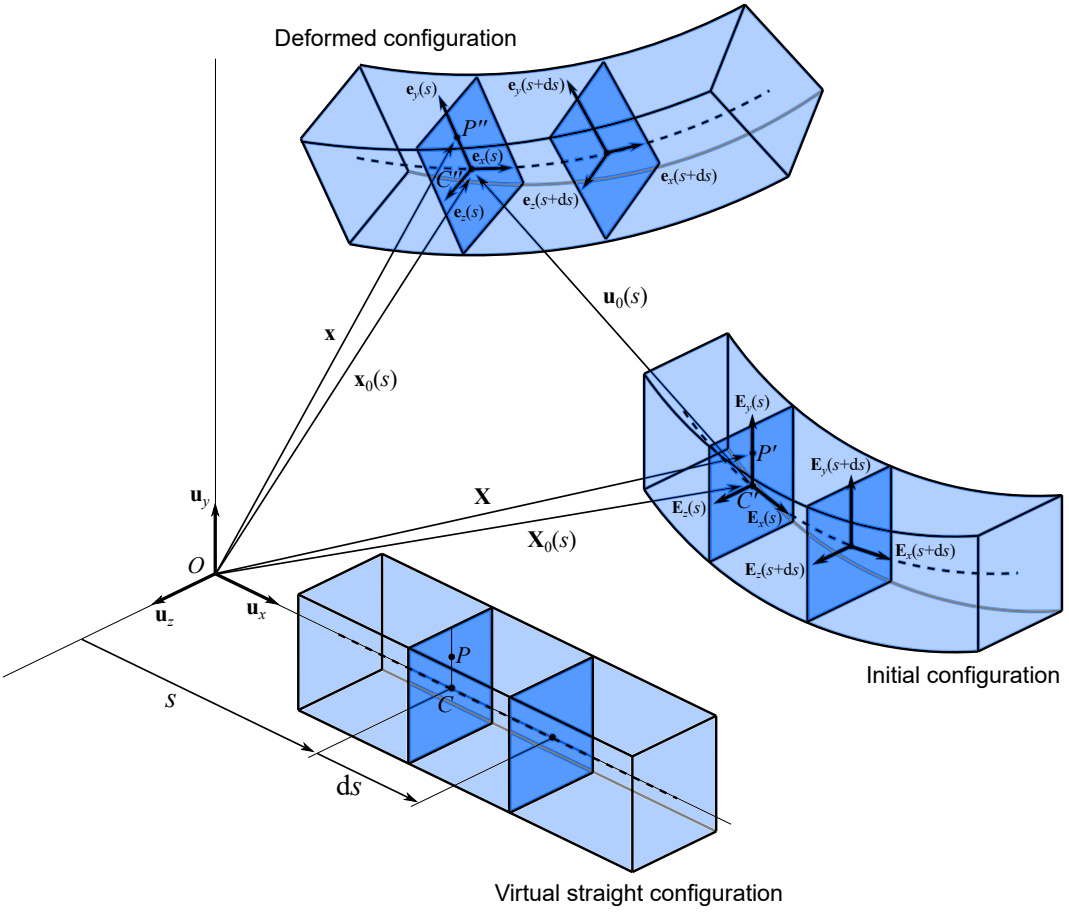

Figure 5.1: 3D beam kinematics

a curve termed the "centerline" of the beam. In this one-dimensional model, the displacement of any point in the cross-section is computed based on the displacement of the centroid falling along the centerline of the beam in that same cross-section [Eq. (2.6)]. In three dimensions, 6 degrees of freedom are considered: 3 displacements or positions of the centerline in the 3 directions considered (the longitudinal direction and the two perpendicular transverse directions) and 3 rotations governing the orientation of the cross-sections around these directions.

To begin describing the beam kinematics in 3D, the following assumptions are made:

Assumption #1

> Deformation of the cross-sections is not considered, so that they remain plane throughout deformation of the beam (only rigid body motions are considered for the cross-sections).

Assumption #2

> Timoshenko kinematics are adopted, so that the effect of shearing is taken into account.

Assumption #3

> Rotational kinetic energy of the cross-sections is neglected. Note: the choice to neglect rotational kinetic energy/rotational inertia is justified in this case because the cross-section is very thin and the contribution of these terms is negligible. An example comparison using the cantilever test case of § 3.3.1 in Chapter 3 is shown in Appendix C.1.

Consider an elementary portion of a beam illustrated in Fig. 5.1 for which the initial (undeformed and unstressed, reference) configuration can be curved (its centerline is not straight). Its geometry is defined by the position vector $\mathbf{X}_0(s) = \mathbf{OC}'$ of the points C' of the centerline, $s \in \mathbb{R}$ being a curvilinear parameter, and O the origin of a fixed (right-handed orthonormal) *global frame* $(O, \mathbf{u}_x, \mathbf{u}_y, \mathbf{u}_z)$. Each cross-section is orthogonal to the centerline such that a (right-handed orthonormal) local basis $(\mathbf{E}_x(s), \mathbf{E}_y(s), \mathbf{E}_z(s))$ is defined, with $\mathbf{E}_x(s)$ tangent to the centerline in $C'(s)$. Then, the position of any point P' of the cross-section is defined by the vector $\mathbf{C'P'} = y\mathbf{E}_y + z\mathbf{E}_z$, $(y, z) \in \mathcal{S} \subset \mathbb{R}^2$ being the coordinates of P' in the cross-section of domain $\mathcal{S}$.

The possibly-curved geometry of the initial configuration is defined by the orientation of the basis $(\mathbf{E}_x(s), \mathbf{E}_y(s), \mathbf{E}_z(s))$ with respect to the global basis $(\mathbf{u}_x, \mathbf{u}_y, \mathbf{u}_z)$, defined by a rotation operator $\mathbf{R}_0(s)$ such that $(\mathbf{E}_x(s), \mathbf{E}_y(s), \mathbf{E}_z(s)) = \mathbf{R}_0(s)\,(\mathbf{u}_x, \mathbf{u}_y, \mathbf{u}_z)$. By consequence, $\mathbf{C'P'} = \mathbf{R}_0\mathbf{CP}$ and:

$$\mathbf{X}(s, y, z) = \mathbf{X}_0(s) + \mathbf{R}_0(s)\mathbf{CP}. \tag{5.1}$$

Because any cross-section of the beam undergoes a rigid-body motion during deformation, the same logic is kept for defining the deformed (current) configuration of the beam. The deformed centerline is defined by the vector $\mathbf{x}_0(s) = \mathbf{OC}''$. The orientation of the cross-section is defined by a (right-handed orthonormal) *material basis* $(\mathbf{e}_x(s), \mathbf{e}_y(s), \mathbf{e}_z(s))$, with $\mathbf{e}_x$ normal to the deformed cross-section at point C''. Note that $\mathbf{e}_x$ is not necessarily tangent to the deformed centerline at C'' because of the Timoshenko kinematics that allows for transverse shearing. The orientation of this basis is defined with respect to the virtual straight configuration by the rotation operator $\mathbf{R}(s)$ such that $(\mathbf{e}_x(s), \mathbf{e}_y(s), \mathbf{e}_z(s)) = \mathbf{R}(s)\,(\mathbf{u}_x, \mathbf{u}_y, \mathbf{u}_z)$. The position of any point P'' of the deformed configuration is then:

$$\mathbf{x}(s, y, z) = \mathbf{x}_0(s) + \mathbf{R}(s)\mathbf{CP}. \tag{5.2}$$

The position of any point in the deformed configuration is governed by the two fields $\mathbf{x}_0(s)$ and $\mathbf{R}(s)$. The 3 positions in $\mathbf{x}_0(s)$ and the 3 rotations governed by $\mathbf{R}(s)$, then, constitute the 6 aforementioned degrees of freedom of the 1D beam model. Furthermore, the displacement field of the centerline between the initial and deformed configurations is defined as:

$$\mathbf{u}_0 = \mathbf{x}_0 - \mathbf{X}_0. \tag{5.3}$$

Note that in the 2D model of Chapters 2 and 3, the displacements are used as the degrees of freedom in the governing equations, while in [45], the positions are used in the derivation of the governing equations. In order to remain consistent with the formulation of Cottanceau *et al.* [45], the equations are derived in what follows based on the positions $\mathbf{x}_0$, but they can be easily rewritten in terms of the displacements $\mathbf{u}_0$ using the relation Eq. (5.3) (see also [101] for derivations of the equations based on both $\mathbf{x}_0$ and $\mathbf{u}_0$).

5.1.2 Beam deformations

Next, the deformation of the beam is measured by computing the position gradients before and after deformation with respect to the curvilinear parameter $s \in [0, L]$, which governs the current position along the neutral axis of the beam. For a general initial configuration, the deformation expressed in the material frame can be decomposed into two parts, the material measure of deformation of the neutral axis, denoted $\mathbf{\Gamma} = \begin{bmatrix} \Gamma_x & \Gamma_y & \Gamma_z \end{bmatrix}^{\mathrm{T}}$, and the material measure of curvature related to rotations of the cross-section, denoted $\mathbf{K} = \begin{bmatrix} \kappa_x & \kappa_y & \kappa_z \end{bmatrix}^{\mathrm{T}}$. Contained in $\mathbf{\Gamma}$ are the axial strain Γ_x and the two polarizations of shear strain Γ_y and Γ_z since the Timoshenko kinematics include the effects of shearing (Assumption #2). In $\mathbf{K}$ are the torsional curvature κ_x and likewise the two polarizations of bending curvature κ_y and κ_z. Based on the full derivation of the position and rotation gradients as shown in [101], $\mathbf{\Gamma}$ and $\mathbf{K}$ are written, for any initial reference configuration [45], [101]:

$$\mathbf{\Gamma} = \mathbf{R}^{\mathrm{T}}\mathbf{x}_0' - \mathbf{R}_0^{\mathrm{T}}\mathbf{X}_0' = \mathbf{R}^{\mathrm{T}}\mathbf{x}_0' - \mathbf{\Gamma}_0, \tag{5.4a}$$

$$\mathbf{K} = \mathrm{vect}\left(\mathbf{R}^{\mathrm{T}}\mathbf{R}' - \mathbf{R}_0^{\mathrm{T}}\mathbf{R}_0'\right) = \mathrm{vect}\left(\mathbf{R}^{\mathrm{T}}\mathbf{R}'\right) - \mathbf{K}_0, \tag{5.4b}$$

where $\diamond' = \frac{\mathrm{d}\diamond}{\mathrm{d}s}$. The vect($\diamond$) operation indicates a transformation from a 3×3 skew-symmetric matrix to a 3-element vector, such that, for a skew-symmetric matrix $\mathbf{a}$ defined as:

$$\mathbf{a} = \begin{bmatrix} 0 & -a_3 & a_2 \\ a_3 & 0 & -a_1 \\ -a_2 & a_1 & 0 \end{bmatrix}, \tag{5.5}$$

then:

$$\mathrm{vect}(\mathbf{a}) = \begin{bmatrix} a_1 \\ a_2 \\ a_3 \end{bmatrix}. \tag{5.6}$$

In Eqs. (5.4), $\mathbf{\Gamma}_0$ and $\mathbf{K}_0$ represent, respectively, the initial deformation and curvatures. In general, these are computed for any initial reference configuration by computing $\mathbf{\Gamma}_0$ and $\mathbf{K}_0$ according to Eqs. (5.4). For the sake of simplicity, moving forward only initially straight beams whose centerlines are aligned in the initial configuration with the $\mathbf{u}_x$ axis are considered, which introduces two more assumptions in order to evaluate $\mathbf{\Gamma}_0$ and $\mathbf{K}_0$:

Assumption #4

> The beam is assumed to be straight in the reference configuration (no initial curvature), so that $\mathbf{R}_0 = \mathbf{I}$ and $\mathbf{K}_0 = \mathbf{0}$ $((\mathbf{E}_x(s), \mathbf{E}_y(s), \mathbf{E}_z(s)) = (\mathbf{u}_x, \mathbf{u}_y, \mathbf{u}_z))$.

Assumption #5

> The centerline of the reference configuration lies along the x-axis, so that $\mathbf{\Gamma}_0 = \mathbf{u}_1 = \begin{bmatrix} 1 & 0 & 0 \end{bmatrix}$.

Finally, recall that in the 2D derivations, a consistent linearization of the Green-Lagrange strains is used, versus the position gradient method used here following [45], [101]. In the full Green-Lagrange

strains [Eq. (2.4)], there are additional quadratic terms that do not appear in the position gradient deformations [101]. When the consistent linearization is performed, however, these quadratic terms in the Green-Lagrange strains missing from the position gradient deformations are removed, so that the two measures of deformation are equivalent.

5.1.3 Constitutive law

Next, the strains are related to the stress resultants according to the same linear Kirchhoff-Saint-Venant constitutive law for elastic, homogeneous and isotropic materials as in Chapters 2 and 3. After integration over the cross-section, the material forces $\mathbf{N}$ and moments $\mathbf{M}$ are related linearly to the strains $\mathbf{\Gamma}$ and $\mathbf{K}$, respectively, according to:

$$\begin{bmatrix}\mathbf{N}\\ \mathbf{M}\end{bmatrix} = \begin{bmatrix}\mathbf{C}_N & 0\\ 0 & \mathbf{C}_M\end{bmatrix}\begin{bmatrix}\mathbf{\Gamma}\\ \mathbf{K}\end{bmatrix}, \tag{5.7}$$

where $\mathbf{C}_N = \text{diag}\Big(EA, \quad k_yGA, \quad k_zGA\Big)$ and $\mathbf{C}_M = \text{diag}\Big(GJ, \quad EI_y, \quad EI_z\Big)$. In $\mathbf{C}_N$, E is the Young's modulus and A the area of the cross-section, $G = \frac{E}{2(1+\nu)}$ is the shear modulus with ν the Poisson's ratio and k_y and k_z are the shear coefficients in directions $\mathbf{e}_y$ and $\mathbf{e}_z$, respectively. In $\mathbf{C}_M$, J is the polar second moment of area and I_y and I_z the second moments of area again in $\mathbf{e}_y$ and $\mathbf{e}_z$, respectively. The components of $\mathbf{N}$ and $\mathbf{M}$ can therefore be defined as $\mathbf{N} = \begin{bmatrix}N & T_y & T_z\end{bmatrix}^{\mathrm{T}}$ with $N = EA\Gamma_x$ the axial force in direction $\mathbf{e}_x$, $T_y = k_yGA\Gamma_y$ and $T_z = k_zGA\Gamma_z$ the shear forces in directions $\mathbf{e}_y$ and $\mathbf{e}_z$, respectively, and $\mathbf{M} = \begin{bmatrix}T_x & M_y & M_z\end{bmatrix}^{\mathrm{T}}$ with $T_x = GJ\kappa_x$ the torsion around $\mathbf{e}_x$, $M_y = EI_y\kappa_y$ and $M_z = EI_z\kappa_z$ the bending moments around $\mathbf{e}_y$ and $\mathbf{e}_z$, respectively.

The beam equations are derived in the weak form by making use of the principle of virtual work, written explicitly as, $\forall\delta\mathbf{x}_0$:

$$\delta W_a + \delta W_i = \delta W_e, \tag{5.8}$$

with δW_a the virtual work of the inertial forces, δW_i that of the internal forces and δW_e that of the external forces, which take the forms [101]:

$$\delta W_a = \int_0^L \Big(\rho\ddot{\mathbf{x}}_0^{\mathrm{T}}\mathbf{A}\delta\mathbf{x}_0\Big)\,\mathrm{d}s + \int_0^L \Big((\mathbf{J}\dot{\mathbf{\Omega}} + \tilde{\mathbf{\Omega}}\mathbf{J}\mathbf{\Omega})^{\mathrm{T}}\delta\mathbf{\Theta}\Big)\,\mathrm{d}s, \tag{5.9a}$$

$$\delta W_i = \int_0^L \Big(\mathbf{N}^{\mathrm{T}}\delta\mathbf{\Gamma} + \mathbf{M}^{\mathrm{T}}\delta\mathbf{K}\Big)\,\mathrm{d}s, \tag{5.9b}$$

$$\delta W_e = \int_0^L \Big(\mathbf{n}_e^{\mathrm{T}}\delta\mathbf{x}_0 + \mathbf{m}_e^{\mathrm{T}}\delta\boldsymbol{\theta}\Big)\,\mathrm{d}s + \Big[\mathbf{N}_e^{\mathrm{T}}\delta\mathbf{x}_0\Big]_0^L + \Big[\mathbf{M}_e^{\mathrm{T}}\delta\boldsymbol{\theta}\Big]_0^L, \tag{5.9c}$$

with $\mathbf{A} = A\mathbf{I}_3$ where $\mathbf{I}_3$ represents the 3×3 identity matrix, ρ the density, $\mathbf{J}$ the inertia tensor of the cross-section in the material frame, $\mathbf{\Omega}$ and $\dot{\mathbf{\Omega}}$ the angular velocity and acceleration in the material frame, $\mathbf{n}_e$ and $\mathbf{m}_e$, respectively, the external applied forces and moments per unit length and $\mathbf{N}_e$ and $\mathbf{M}_e$ the external applied force and moment loadings at the extremities $s = 0$ and $s = L$. In addition, $\delta\boldsymbol{\theta}$ represents the infinitesimal angular displacements and $\delta\mathbf{\Theta}$ the *material* infinitesimal angular displacements, related by $\delta\mathbf{\Theta} = \mathbf{R}^T\delta\boldsymbol{\theta}$ [101]. However, since Assumption #3 of the kinematic assumptions is to neglect the rotational kinetic energy of the cross-sections, the second term of Eq. (5.9a) is neglected in what follows.

5.2 Rotation parametrization with quaternions

Next we proceed to introducing the selected method for parametrization of rotations in 3D. Rather than expanding the classical parametrization with trigonometric functions used in developing the 2D in-plane dynamics of Chapters 2 and 3 to 3D, a new method of rotation parametrization is proposed which makes use of unit quaternions.

5.2.1 General definitions using quaternions

The quaternion represents an alternate way to describe finite rotations akin, albeit in a different manner, to using Euler parameters [101]. The quaternion represents a 4-dimensional complex number, the sum of a scalar term (a_0) and a 3-element vector ($\mathbf{a}$):

$$\hat{\mathbf{a}} = a_0 + \mathbf{a} = a_0 + a_1 i + a_2 j + a_3 k, \tag{5.10}$$

where $\hat{\mathbf{a}} \in \mathbb{R}^4$ and the $\hat{\diamond}$ notation is used to indicate a quaternion, a_0, a_1, a_2 and a_3 are scalar values and i, j, k are imaginary numbers such that $i^2 = j^2 = k^2 = -1$, $jk = -kh = i$, $ki = -ik = j$, and $ij = -ji = k$. [100]. In practice, the four elements of a general quaternion $\hat{\mathbf{a}}$ can be stored in a 4-element vector, *e.g.* as $\hat{\mathbf{a}} = \begin{bmatrix} a_0 & a_1 & a_2 & a_3 \end{bmatrix}^{\mathrm{T}}$. In the special case where the scalar term $a_0 = 0$, $\hat{\mathbf{a}}$ is called a "pure" or "vector" quaternion and can be "reduced" from $\mathbb{R}^4$ to the three-dimensional Euclidean space $\mathbb{R}^3$ through the projection defined here as $\mathrm{vec}(\diamond) : \mathbb{R}^4 \mapsto \mathbb{R}^3$, so that $\mathrm{vec}(\hat{\mathbf{a}}) = \mathbf{a}$. Likewise, any vector $\mathbf{p}$ of the $\mathbb{R}^3$ space can be "extended" to a quaternion in the $\mathbb{R}^4$ space by considering $\hat{\mathbf{p}} = 0 + \mathbf{p}$. These properties will be used extensively in transforming quantities in the $\mathbb{R}^3$ space in the equations of motion Eqs. (5.9) to quaternions in $\mathbb{R}^4$ and vice versa.

Quaternion multiplications, denoted by the operator $\circ$ (different from the scalar product, denoted by the operator $\cdot$), can be written using the definition of the quaternion [Eq. (5.10)] [100], but practically are carried out as matrix multiplications making use of the transformations denoted Φ_L and Φ_R ("left" and "right" multiplications, respectively) in a method analogous to the vector cross product between vectors in $\mathbb{R}^3$. Introducing the notation $\tilde{\diamond}$ to indicate the transformation of a 3-element vector into a skew-symmetric matrix (*i.e.* the reverse operation of $\mathrm{vect}(\diamond)$), the Φ_L and Φ_R operations between any two quaternions $\hat{\mathbf{a}}$ and $\hat{\mathbf{b}}$ are defined as:

$$\hat{\mathbf{a}} \circ \hat{\mathbf{b}} = \Phi_L(\hat{\mathbf{a}})\hat{\mathbf{b}} = \begin{bmatrix} a_0 & -\mathbf{a}^{\mathrm{T}} \\ \mathbf{a} & a_0\mathbf{I}_3 + \tilde{\mathbf{a}} \end{bmatrix} \begin{bmatrix} b_0 \\ \mathbf{b} \end{bmatrix}$$

$$= \begin{bmatrix} a_0 & -a_1 & -a_2 & -a_3 \\ a_1 & a_0 & -a_3 & a_2 \\ a_2 & a_3 & a_0 & -a_1 \\ a_3 & -a_2 & a_1 & a_0 \end{bmatrix} \begin{bmatrix} b_0 \\ b_1 \\ b_2 \\ b_3 \end{bmatrix}, \tag{5.11a}$$

(5.11b)

$$\hat{\mathbf{a}} \circ \hat{\mathbf{b}} = \Phi_R(\hat{\mathbf{b}})\hat{\mathbf{a}} = \begin{bmatrix} b_0 & -\mathbf{b}^{\mathrm{T}} \\ \mathbf{b} & b_0\mathbf{I}_3 - \tilde{\mathbf{b}} \end{bmatrix} \begin{bmatrix} a_0 \\ \mathbf{a} \end{bmatrix}$$

$$= \begin{bmatrix} b_0 & -b_1 & -b_2 & -b_3 \\ b_1 & b_0 & b_3 & -b_2 \\ b_2 & -b_3 & b_0 & b_1 \\ b_3 & b_2 & -b_1 & b_0 \end{bmatrix} \begin{bmatrix} a_0 \\ a_1 \\ a_2 \\ a_3 \end{bmatrix}. \tag{5.11c}$$

A "conjugate" to a quaternion is also defined, indicated with the asterisk $\diamond^*$, such that $\hat{\mathbf{a}}^* = a_0 - \mathbf{a}$ for any general quaternion $\hat{\mathbf{a}}$.

5.2.2 Rotations written with quaternions

Quaternions possess a special 3D sub-group algebra that is convenient for parametrizing the rotation operators $\mathbf{R}$ and $\mathbf{R}_0$, in particular due to the ability to describe the rotations with only 4 elements (versus the 9 elements of a classical rotation matrix) while remaining exactly equivalent to it. This ability can lead to greater computational efficiency in computing the rotations, since far fewer operations (multiplications and additions) are needed [203]. To describe the rotation, the quaternion $\hat{\mathbf{q}}$ is used, which takes the form:

$$\hat{\mathbf{q}} = \cos\left(\frac{\theta}{2}\right) + \sin\left(\frac{\theta}{2}\right)\mathbf{n} = \begin{bmatrix} q_0 & q_1 & q_2 & q_3 \end{bmatrix}^{\mathrm{T}}, \tag{5.12}$$

with $\mathbf{n}$ the unit vector describing the axis of rotation and θ the rotation angle around the axis defined by $\mathbf{n}$. Note that Eq. (5.12) represents a so-called *unit quaternion*, such that $|\hat{\mathbf{q}}| = \hat{\mathbf{q}} \cdot \hat{\mathbf{q}} = 1$. This observation introduces a unity constraint tied to $\hat{\mathbf{q}}$, since the four elements of $\hat{\mathbf{q}}$ are not independent. With $\hat{\mathbf{q}}$ defined in Eq. (5.12), the rotation operation $\mathbf{R}$ to rotate a vector $\mathbf{p}$ into the vector $\mathbf{p}_r$ such that $\mathbf{p}_r = \mathbf{R}\mathbf{p}$ is rewritten in the quaternion algebra as:

$$\hat{\mathbf{p}}_r = \hat{\mathbf{q}} \circ \hat{\mathbf{p}} \circ \hat{\mathbf{q}}^*, \tag{5.13}$$

where $\circ$ is used to indicate a quaternion multiplication between two quaternions. A key observation is made at this point: if $\hat{\mathbf{p}}$ is a pure quaternion ($p_0 = 0$) and $\hat{\mathbf{q}}$ a unit quaternion, then $\hat{\mathbf{p}}_r$ is also a pure quaternion and $\mathrm{vec}(\hat{\mathbf{p}}_r) = \mathbf{p}_r$ is the rotated vector beginning from $\mathbf{p} = \mathrm{vec}(\hat{\mathbf{p}})$. This observation will be useful in the next section when the variables defined as vectors in § 5.1 are rewritten as pure quaternions in the governing equations.

Along the same logic, an opposite rotation to rotate $\mathbf{p}_r$ back into $\mathbf{p}$, or $\mathbf{p} = \mathbf{R}^{\mathrm{T}}\mathbf{p}_r$ is written in the quaternion algebra as:

$$\hat{\mathbf{p}} = \hat{\mathbf{q}}^* \circ \hat{\mathbf{p}}_r \circ \hat{\mathbf{q}}. \tag{5.14}$$

The rotation operations in the quaternion formulation as defined in Eqs. (5.13) and (5.14) can then be rewritten as matrix multiplications in the form:

$$\hat{\mathbf{p}}_r = \hat{\mathbf{q}} \circ \hat{\mathbf{p}} \circ \hat{\mathbf{q}}^* = \underbrace{\Phi_R(\hat{\mathbf{q}}^*)\Phi_L(\hat{\mathbf{q}})}_{\mathbf{R}}\hat{\mathbf{p}}, \tag{5.15a}$$

$$\hat{\mathbf{p}} = \hat{\mathbf{q}}^* \circ \hat{\mathbf{p}}_r \circ \hat{\mathbf{q}} = \underbrace{\Phi_R(\hat{\mathbf{q}})\Phi_L(\hat{\mathbf{q}}^*)}_{\mathbf{R}^T}\hat{\mathbf{p}}_r. \tag{5.15b}$$

Based on the 4 elements of the unit quaternion $\hat{\mathbf{q}}$ [Eq. (5.12)] and using the operations $\Phi_L(\hat{\mathbf{q}})$ and $\Phi_R(\hat{\mathbf{q}}^*)$, it is shown in [203] that the equivalent 9 elements of $\mathbf{R}$ as a 3D rotation matrix can be written:

$$\mathbf{R} = \begin{bmatrix} q_0^2 + q_1^2 - q_2^2 - q_3^2 & 2(-q_0q_3 + q_1q_2) & 2(q_0q_2 + q_1q_3) \\ 2(q_0q_3 + q_2q_1) & q_0^2 - q_1^2 + q_2^2 - q_3^2 & 2(-q_0q_1 + q_2q_3) \\ 2(-q_0q_2 + q_3q_1) & 2(q_0q_1 + q_3q_2) & q_0^2 - q_1^2 - q_2^2 + q_3^2 \end{bmatrix}, \tag{5.16}$$

which underscores the storage efficiency of the 4-element quaternion [Eq. (5.12)] by comparison.

There are many useful properties of quaternions and the quaternion algebra that are utilized in rewriting the beam kinematics and equations of motion in the quaternion formulation. Since the most important of these have already been outlined in previous work [45] to rewrite the static equations of motion, they are not recopied here for the sake of brevity. The interested reader is referred to [45] for detailed derivations and [100], [101], [203], [261] (and the references cited therein) for more discussion on the mathematics of the quaternion algebra. Instead, only the main equations are shown and the static equations of [45] are extended to dynamics.

5.2.3 Beam equations rewritten with quaternions

Now all vector quantities of § 5.1 are replaced with their pure quaternion counterparts. Using the rotation operations as shown in Eqs. (5.13), (5.14) and (E.44), the strains $\hat{\mathbf{\Gamma}} = \begin{bmatrix} 0 & \Gamma_x & \Gamma_y & \Gamma_z \end{bmatrix}^{\mathrm{T}}$ and curvatures $\hat{\mathbf{K}} = \begin{bmatrix} 0 & \kappa_x & \kappa_y & \kappa_z \end{bmatrix}^{\mathrm{T}}$ are written:

$$\hat{\mathbf{\Gamma}} = \hat{\mathbf{q}}^* \circ \hat{\mathbf{x}}_0' \circ \hat{\mathbf{q}} - \hat{\mathbf{\Gamma}}_0, \tag{5.17a}$$

$$\hat{\mathbf{K}} = 2\hat{\mathbf{q}}^* \circ \hat{\mathbf{q}}' - \hat{\mathbf{K}}_0, \tag{5.17b}$$

recalling that for an initially straight beam $\hat{\mathbf{\Gamma}}_0 = \hat{\mathbf{q}}_0^* \circ \hat{\mathbf{X}}_0' \circ \hat{\mathbf{q}}_0 = \hat{\mathbf{u}}_1$ and $\hat{\mathbf{K}}_0 = 2\hat{\mathbf{q}}_0^* \circ \hat{\mathbf{q}}_0' = \mathbf{0}$ ($\hat{\mathbf{K}}$ and $\hat{\mathbf{K}}_0$ need some special manipulation to derive in the quaternion formulation, see Appendix A of [45]). The variation of Eqs. (5.17) is then written:

$$\delta\hat{\mathbf{\Gamma}} = \delta\hat{\mathbf{q}}^* \circ \hat{\mathbf{x}}_0' \circ \hat{\mathbf{q}} + \hat{\mathbf{q}}^* \circ \delta\hat{\mathbf{x}}_0' \circ \hat{\mathbf{q}} + \hat{\mathbf{q}}^* \circ \hat{\mathbf{x}}_0' \circ \delta\hat{\mathbf{q}}, \tag{5.18a}$$

$$\delta\hat{\mathbf{K}} = 2\delta\hat{\mathbf{q}}^* \circ \hat{\mathbf{q}}' + 2\hat{\mathbf{q}}^* \circ \delta\hat{\mathbf{q}}', \tag{5.18b}$$

which can be arranged in the form:

$$\begin{bmatrix} \delta\hat{\mathbf{\Gamma}} \\ \delta\hat{\mathbf{K}} \end{bmatrix} = \begin{bmatrix} \mathbf{R}^{\mathrm{T}} & 0 & \widetilde{\mathbf{R}^{\mathrm{T}}\mathbf{x}_0'}\mathbf{T} \\ 0 & \mathbf{T} & \widetilde{\hat{\mathbf{K}}}\mathbf{T} + \mathbf{T}' \end{bmatrix} \begin{bmatrix} \delta\mathbf{x}_0' \\ \delta\hat{\mathbf{q}}' \\ \delta\hat{\mathbf{q}} \end{bmatrix}, \tag{5.19}$$

as shown in [101] with $\mathbf{T} = 2\Phi_L(\hat{\mathbf{q}}^*)$ and $\mathbf{T}' = 2\Phi_L(\hat{\mathbf{q}}^{*\prime})$, and making use of the relation $\delta\hat{\boldsymbol{\theta}} = 2\hat{\mathbf{q}}^* \circ \delta\hat{\mathbf{q}}$ as derived in [45] in order to relate the variation of the rotations $\hat{\boldsymbol{\theta}}$ to the variation in quaternions. Besides in the expression of the internal virtual work, the variation of the strains in Eqs. (5.18) is needed to derive the tangent stiffness obtained from linearization of the internal forces, which is used in the eigenanalysis to find the natural frequencies of the system. The equations are rearranged using quaternion algebra to derive the tangent stiffness in Appendix C.2.

The constitutive relation Eq. (5.7) can likewise be rewritten with quaternion parameters as:

$$\begin{bmatrix} \hat{\mathbf{N}} \\ \hat{\mathbf{M}} \end{bmatrix} = \begin{bmatrix} \hat{\mathbf{C}}_N & 0 \\ 0 & \hat{\mathbf{C}}_M \end{bmatrix} \begin{bmatrix} \hat{\mathbf{\Gamma}} \\ \hat{\mathbf{K}} \end{bmatrix}, \tag{5.20}$$

where $\hat{\mathbf{N}}$ and $\hat{\mathbf{M}}$ are the pure quaternion extensions of the material forces and moments, respectively, and $\hat{\mathbf{C}}_N$ and $\hat{\mathbf{C}}_M$ represent the extension of the linear constitutive relations to the quaternion space such that $\hat{\mathbf{C}}_N = \mathrm{diag}\begin{pmatrix} 1, & EA, & k_yGA, & k_zGA \end{pmatrix}$ and $\hat{\mathbf{C}}_M = \mathrm{diag}\begin{pmatrix} 1, & GJ, & EI_y, & EI_z \end{pmatrix}$.

Having redefined all of the terms using quaternion parameters, the equations of motion in the weak form [Eqs. (5.8) and (5.9)] can be rewritten as:

$$\delta W_a = \int_0^L \rho \ddot{\hat{\mathbf{x}}}_0^{\mathrm{T}} \hat{\mathbf{A}} \delta \hat{\mathbf{x}}_0 \mathrm{d}s, \tag{5.21a}$$

$$\delta W_i = \int_0^L \left(\hat{\mathbf{N}}^{\mathrm{T}} \delta \hat{\mathbf{\Gamma}} + \hat{\mathbf{M}}^{\mathrm{T}} \delta \hat{\mathbf{K}} \right) \mathrm{d}s, \tag{5.21b}$$

$$\delta W_e = \int_0^L \left(\hat{\mathbf{n}}_e^{\mathrm{T}} \delta \hat{\mathbf{x}}_0 + \left(2\hat{\mathbf{q}} \circ \hat{\mathbf{m}}_e\right)^{\mathrm{T}} \delta \hat{\mathbf{q}} \right) \mathrm{d}s + \left[\hat{\mathbf{N}}_e^{\mathrm{T}} \delta \hat{\mathbf{x}}_0 \right]_0^L + \left[\left(2\hat{\mathbf{q}} \circ \hat{\mathbf{M}}_e\right)^{\mathrm{T}} \delta \hat{\mathbf{q}} \right]_0^L, \tag{5.21c}$$

where $\hat{\mathbf{A}} = \mathrm{diag}\,(1, A\mathbf{I}_3)$ and again using the relation $\delta\hat{\boldsymbol{\theta}} = 2\hat{\mathbf{q}}^* \circ \delta\hat{\mathbf{q}}$ to find the final version of Eq. (5.21c) [45]. Recall that the rotational inertia term in Eq. (5.9a) has been neglected here and in what follows (Assumption #3). Recall also from the definition of $\hat{\mathbf{q}}$ in Eq. (5.12) that the quaternion $\hat{\mathbf{q}}$ used to represent the rotations is subject to the constraint $|\hat{\mathbf{q}}|^2 - 1 = 0$ (the unity constraint). For this reason, an additional equation must be added to the equations of motion Eqs. (5.21) to fully define the system. This is done through the method of Lagrange multipliers [45], [261] wherein an additional parameter (that is, a Lagrange multiplier, denoted here by the scalar μ) is introduced into the equations of motion to represent the constraint relation. The additional equation is added into the principle of virtual work as the virtual work of the constraint δW_μ:

$$\delta W_\mu = \int_0^L \delta \left(\mu \left(\hat{\mathbf{q}} \cdot \hat{\mathbf{q}} - 1 \right) \right) \mathrm{d}s = \int_0^L \left(\left(\hat{\mathbf{q}} \cdot \hat{\mathbf{q}} - 1 \right) \delta\mu + 2\mu \hat{\mathbf{q}}^{\mathrm{T}} \delta\hat{\mathbf{q}} \right) \mathrm{d}s. \tag{5.22}$$

The weak form of the dynamic equations of motion rewritten in the quaternion space finally takes the form:

$$\delta W_a + \delta W_i + \delta W_\mu = \delta W_e, \tag{5.23}$$

using the definitions in Eqs. (5.21) and (5.22).

5.3 Discretization into finite elements

Next, the weak form of the equations of motion [Eqs. (5.21), (5.22) and (5.23)] is discretized into finite elements in the same method as in 2D in Chapters 2 and 3. The elements used here are analogous to the 2-node linear Timoshenko beam elements described in § 3.2.2 except that, here, 3-node quadratic Timoshenko beam elements are used (an additional internal node equally-spaced between the two end nodes of each element is added), for a total of $N_n = 2N_e + 1$ nodes for a system discretized into N_e elements of length L^e which may vary with s if the mesh is not uniform. At each node $i \in [1, N_n]$ of the mesh, there are 8 degrees of freedom (versus the 3 degrees of freedom in 2D): 3 positions $\mathbf{x}_0$ defining the absolute position of the cross-section along the centerline after deformation (related to the displacements $\mathbf{u}_0 = \mathbf{x}_0 - \mathbf{X}_0 = \begin{bmatrix} u & w & v \end{bmatrix}^T$), the 4 elements of the quaternion $\hat{\mathbf{q}}$ defining the rotation of the cross-section and the Lagrange multiplier μ governing the unity constraint. Note that since $\hat{\mathbf{x}}_0$ represents a pure quaternion, only the 3 non-zero elements are computed and stored in $\mathbf{x}_0$, from which $\hat{\mathbf{x}}_0$ is easily constructed. The degrees of freedom for each element, that is, at each of the element's end nodes (designated as nodes 1 and 3) plus the internal node at the midpoint of the element (designated node 2), can be gathered into the vector $\mathbf{z}^e$:

$$\mathbf{z}^e = [\underbrace{\mathbf{x}_{0,1}^{\mathrm{T}} \quad \hat{\mathbf{q}}_1^{\mathrm{T}} \quad \mu_1}_{\text{node 1}} \quad \underbrace{\mathbf{x}_{0,2}^{\mathrm{T}} \quad \hat{\mathbf{q}}_2^{\mathrm{T}} \quad \mu_2}_{\text{node 2}} \quad \underbrace{\mathbf{x}_{0,3}^{\mathrm{T}} \quad \hat{\mathbf{q}}_3^{\mathrm{T}} \quad \mu_3}_{\text{node 3}}]^{\mathrm{T}}, \tag{5.24}$$

where the $\diamond^e$ notation is used to indicate elementary quantities. The interpolation of the fields over an element is then written:

$$\begin{bmatrix} \mathbf{x}_0^e(s,t) \\ \hat{\mathbf{q}}^e(s,t) \\ \mu^e(s,t) \end{bmatrix} = \mathbf{P}(s)\mathbf{z}^e(t), \tag{5.25}$$

where $\mathbf{P}(s)$ is the interpolation matrix of size 8×24 collecting the quadratic interpolation functions $N_1(s)$, $N_2(s)$ and $N_3(s)$:

$$\mathbf{P}(s) = \begin{bmatrix} N_1(s)\mathbf{I}_8 & N_2(s)\mathbf{I}_8 & N_3(s)\mathbf{I}_8 \end{bmatrix}, \tag{5.26}$$

where $\mathbf{I}_8$ represents the 8×8 identity matrix. As in Chapter 3 and [45], the interpolation functions are selected as polynomial shape functions; however, unlike in Chapter 3, linear shape functions are no longer considered sufficient for interpolation of the quaternions. In general, quaternions/rotations, which are multiplicative quantities, cannot be properly interpolated additively [50]. Rather than using more complex interpolations, we instead choose *higher order* polynomial interpolations. Here, quadratic shape functions are used, so that the interpolation functions take the form:

$$N_1(s) = 2\left(\frac{s}{L^e}\right)^2 - 3\left(\frac{s}{L^e}\right) + 1, \tag{5.27a}$$

$$N_2(s) = -4\left(\frac{s}{L^e}\right)^2 + 4\left(\frac{s}{L^e}\right), \tag{5.27b}$$

$$N_3(s) = 2\left(\frac{s}{L^e}\right)^2 - \left(\frac{s}{L^e}\right). \tag{5.27c}$$

$$\tag{5.27d}$$

The spatial derivatives $\begin{bmatrix} \mathbf{x}_0^{e\prime\mathrm{T}} & \hat{\mathbf{q}}^{e\prime\mathrm{T}} & \mu^{e\prime} \end{bmatrix}^{\mathrm{T}}$ are computed based on the spatial derivatives of the shape functions:

$$\begin{bmatrix} \mathbf{x}_0^{e\prime}(s,t) \\ \hat{\mathbf{q}}^{e\prime}(s,t) \\ \mu^{e\prime}(s,t) \end{bmatrix} = \mathbf{P}'(s)\mathbf{z}^e(t) = \begin{bmatrix} N_1'(s)\mathbf{I}_8 & N_2'(s)\mathbf{I}_8 & N_3'(s)\mathbf{I}_8 \end{bmatrix} \mathbf{z}^e(t). \tag{5.28}$$

If the strains and stresses are gathered into the vectors $\mathbf{E} = \begin{bmatrix} \hat{\mathbf{\Gamma}}^{\mathrm{T}} & \hat{\mathbf{K}}^{\mathrm{T}} \end{bmatrix}^{\mathrm{T}}$ and $\mathbf{\Sigma} = \begin{bmatrix} \hat{\mathbf{N}}^{\mathrm{T}} & \hat{\mathbf{M}}^{\mathrm{T}} \end{bmatrix}^{\mathrm{T}}$, respectively, such that Eq. (5.20) is written:

$$\mathbf{\Sigma} = \begin{bmatrix} \hat{\mathbf{C}}_N & 0 \\ 0 & \hat{\mathbf{C}}_M \end{bmatrix} \mathbf{E}, \tag{5.29}$$

the relation between the variation of the element strains $\delta\mathbf{E}^e = \begin{bmatrix} \delta\hat{\mathbf{\Gamma}}^{e\mathrm{T}} & \delta\hat{\mathbf{K}}^{e\mathrm{T}} \end{bmatrix}^{\mathrm{T}}$ and the variation of the degrees of freedom $\begin{bmatrix} \delta\mathbf{x}_0^{e\prime\mathrm{T}} & \delta\hat{\mathbf{q}}^{e\prime\mathrm{T}} & \delta\hat{\mathbf{q}}^{e\mathrm{T}} & \delta\mu^e \end{bmatrix}^{\mathrm{T}}$ must be computed in order to discretize Eq. (5.21b).

To do so, a second interpolation matrix $\mathbf{Q}(s)$ of size 12×24 is introduced, making use of the same quadratic shape functions $N_1(s)$, $N_2(s)$ and $N_3(s)$ and their spatial derivatives:

$$\mathbf{Q}(s) = \begin{bmatrix} N_1'\mathbf{I}_3 & \mathbf{0} & \mathbf{0} & N_2'\mathbf{I}_3 & \mathbf{0} & \mathbf{0} & N_3'\mathbf{I}_3 & \mathbf{0} & \mathbf{0} \\ \mathbf{0} & N_1'\mathbf{I}_4 & \mathbf{0} & \mathbf{0} & N_2'\mathbf{I}_4 & \mathbf{0} & \mathbf{0} & N_3'\mathbf{I}_4 & \mathbf{0} \\ \mathbf{0} & N_1\mathbf{I}_4 & \mathbf{0} & \mathbf{0} & N_2\mathbf{I}_4 & \mathbf{0} & \mathbf{0} & N_3\mathbf{I}_4 & \mathbf{0} \\ \mathbf{0} & \mathbf{0} & N_1 & \mathbf{0} & \mathbf{0} & N_2 & \mathbf{0} & \mathbf{0} & N_3 \end{bmatrix}, \tag{5.30}$$

where $\mathbf{I}_4$ represents the 4×4 identity matrix, so that:

$$\begin{bmatrix} \delta\mathbf{x}_0^{e\prime\mathrm{T}} & \delta\hat{\mathbf{q}}^{e\prime\mathrm{T}} & \delta\hat{\mathbf{q}}^{e\mathrm{T}} & \delta\mu^e \end{bmatrix}^{\mathrm{T}} = \mathbf{Q}(s)\delta\mathbf{z}^e \tag{5.31}$$

Then, incorporating the constraint into Eq. (5.19), the relationship between the variation of the elementary strains $\delta\mathbf{E}^e$ and the variation of the nodal degrees of freedom $\delta\mathbf{z}^e$ is written:

$$\delta\mathbf{E}^e = \mathbf{B}^e\delta\mathbf{z}^e, \tag{5.32}$$

with the strain matrix [101]:

$$\mathbf{B}^e = \begin{bmatrix} \mathbf{R}^{\mathrm{T}} & 0 & \widetilde{\mathbf{R}^{\mathrm{T}}\mathbf{x}_0'}\mathbf{T} & 0 \\ 0 & \mathbf{T} & \widetilde{\hat{\mathbf{K}}}\mathbf{T} + \mathbf{T}' & 0 \end{bmatrix} \mathbf{Q}(s). \tag{5.33}$$

Taking the variation of the strains in order to derive $\mathbf{B}^e$ based on the quaternion algebra is a mathematically intensive process, so the explicit derivation of the $\mathbf{B}^e$ matrix is consigned to Appendix C.2.

5.3.1 Discretization of the dynamic equations of motion

Injecting the finite element discretization into the principle of virtual work Eqs. (5.21), (5.22) and (5.23) allows the discrete elementary vectors and matrices that are used in practice in the finite element model to be determined for a single finite element. First, discretization of the virtual work of the inertia Eq. (5.21a) is performed:

$$\delta W_a^e = \int_0^{L^e} \rho\ddot{\mathbf{x}}_0^{e\mathrm{T}}\mathbf{A}\delta\mathbf{x}_0^e \mathrm{d}s = \delta\mathbf{z}^{e\mathrm{T}} \underbrace{\left(\int_0^{L^e} \rho\mathbf{P}^{\mathrm{T}}\mathbb{J}\mathbf{P}\mathrm{d}s\right)}_{\mathbb{M}^e} \ddot{\mathbf{z}}^e, \tag{5.34}$$

where $\mathbb{J} = \mathrm{diag}\,(\mathbf{A}, 0\mathbf{I}_5, \mathbf{A}, 0\mathbf{I}_5, \mathbf{A}, 0\mathbf{I}_5)$ since the rotational inertia of the cross-sections is neglected and where $\mathbf{I}_5$ is the 5×5 identity matrix, from which the elementary mass matrix $\mathbb{M}^e$ (of size 24×24) is easily evaluated:

$$\mathbb{M}^e = \frac{\rho L^e}{30} \begin{bmatrix} 4\mathbf{A} & \mathbf{0} & \mathbf{0} & 2\mathbf{A} & \mathbf{0} & \mathbf{0} & -\mathbf{A} & \mathbf{0} & \mathbf{0} \\ \mathbf{0} & \mathbf{0} & \mathbf{0} & \mathbf{0} & \mathbf{0} & \mathbf{0} & \mathbf{0} & \mathbf{0} & \mathbf{0} \\ \mathbf{0} & \mathbf{0} & 0 & \mathbf{0} & \mathbf{0} & 0 & \mathbf{0} & \mathbf{0} & 0 \\ 2\mathbf{A} & \mathbf{0} & \mathbf{0} & 16\mathbf{A} & \mathbf{0} & \mathbf{0} & 2\mathbf{A} & \mathbf{0} & \mathbf{0} \\ \mathbf{0} & \mathbf{0} & \mathbf{0} & \mathbf{0} & \mathbf{0} & \mathbf{0} & \mathbf{0} & \mathbf{0} & \mathbf{0} \\ \mathbf{0} & \mathbf{0} & 0 & \mathbf{0} & \mathbf{0} & 0 & \mathbf{0} & \mathbf{0} & 0 \\ -\mathbf{A} & \mathbf{0} & \mathbf{0} & 2\mathbf{A} & \mathbf{0} & \mathbf{0} & 4\mathbf{A} & \mathbf{0} & \mathbf{0} \\ \mathbf{0} & \mathbf{0} & \mathbf{0} & \mathbf{0} & \mathbf{0} & \mathbf{0} & \mathbf{0} & \mathbf{0} & \mathbf{0} \\ \mathbf{0} & \mathbf{0} & 0 & \mathbf{0} & \mathbf{0} & 0 & \mathbf{0} & \mathbf{0} & 0 \end{bmatrix}. \tag{5.35}$$

Note that the Lagrange multiplier μ is only a mathematical parameter introduced to condition the constraint tied to $\hat{\mathbf{q}}$ and therefore contributes no mass. Because of the introduction of μ, the system is a differential-algebraic system of equations (DAE) and therefore has a singular mass matrix. An additional singularity is created since we neglect rotational inertia (there are empty rows and columns).

Next, discretization of the virtual internal work Eq. (5.21b) is considered, which is written:

$$\begin{aligned}\delta W_i^e &= \int_0^{L^e} \left(\hat{\mathbf{N}}^{e\mathrm{T}} \delta\hat{\mathbf{\Gamma}}^e + \hat{\mathbf{M}}^{e\mathrm{T}} \delta\hat{\mathbf{K}}^e \right) \mathrm{d}s = \int_0^{L^e} \delta\mathbf{E}^{e\mathrm{T}} \mathbf{\Sigma}^e \mathrm{d}s \\ &= \delta\mathbf{z}^{e\mathrm{T}} \int_0^{L^e} \mathbf{B}^{e\mathrm{T}} \mathbf{\Sigma}^e \mathrm{d}s = \delta\mathbf{z}^{e\mathrm{T}} \underbrace{\int_0^{L^e} \mathbf{Q}^{\mathrm{T}} \mathbf{f}_i^e(\mathbf{z}^e) \mathrm{d}s}_{\mathbf{F}_{\mathrm{int}}^e},\end{aligned} \tag{5.36}$$

making use of Eq. (5.32) and with $\mathbf{f}_i^e(\mathbf{z}^e)$ defined as [45]:

$$\mathbf{f}_i^e(\mathbf{z}^e) = \begin{bmatrix} \mathrm{vec}(\hat{\mathbf{q}}^e \circ \hat{\mathbf{N}}^e \circ \hat{\mathbf{q}}^{e*}) \\ 2\hat{\mathbf{q}}^e \circ \hat{\mathbf{M}}^e \\ 2\hat{\mathbf{q}}^e \circ \left(\hat{\mathbf{N}} \circ \left(\hat{\mathbf{\Gamma}}^e + \hat{\mathbf{\Gamma}}_0 \right) + \hat{\mathbf{M}}^e \circ \left(\hat{\mathbf{K}}^e + \hat{\mathbf{K}}_0 \right) \right) + 2\hat{\mathbf{q}}^{e\prime} \circ \hat{\mathbf{M}}^e \\ 0 \end{bmatrix}, \tag{5.37}$$

where, according to Assumptions #4 and 5, in the remainder of this chapter, $\hat{\mathbf{\Gamma}}_0 = \hat{\mathbf{u}}_1$ and $\hat{\mathbf{K}}_0 = \mathbf{0}$. We will continue to use the $\hat{\mathbf{\Gamma}}_0$ and $\hat{\mathbf{K}}_0$ notations, however, for the sake of generality.

Recall from § 2.3.1 and Chapter 3 that Timoshenko beam elements are subject to the numerical phenomenon of shear-locking. To avoid the effects of shear-locking, all integrals are evaluated using reduced Gauss integration except the elementary mass matrix $\mathbb{M}^e$, which is evaluated using exact integration. The reduced integration is evaluated one order lower than that required for exact integration [20]; here, for an element having 3 nodes, the reduced integration is carried out at 2 Gauss points located at $s = \frac{L^e}{2}\left(1 \pm \frac{1}{\sqrt{3}}\right)$.

For a general function $f(x)$, the 2-point Gauss reduced integration is written:

$$\int_a^b f(x)\mathrm{d}x \approx \frac{b-a}{2} \sum_{i=1}^{n} f(\mathrm{GP}_i), \tag{5.38}$$

where GP_i indicates the location of each i Gauss point up to n total Gauss points (here $n = 2$). The Gauss points are located at $\mathrm{GP}_i = \frac{b-a}{2}\xi_i + \frac{a+b}{2}$ with $\xi_1 = \frac{1}{\sqrt{3}}$ and $\xi_2 = -\frac{1}{\sqrt{3}}$ in 2-point reduced integration. For example, to evaluate the integral for $\mathbf{F}_{\mathrm{int}}^e$ according to Eq. (5.36), the 2-point Gauss reduced integration is written:

$$\mathbf{F}_{\mathrm{int}}^e = \int_0^{L^e} \mathbf{Q}^{\mathrm{T}} \mathbf{f}_i^e(\mathbf{z}^e) \mathrm{d}s \approx \frac{L^e}{2} \left[(\mathbf{Q}^{\mathrm{T}} \mathbf{f}_i^e)|_{\mathrm{GP}_1} + (\mathbf{Q}^{\mathrm{T}} \mathbf{f}_i^e)|_{\mathrm{GP}_2} \right], \tag{5.39}$$

evaluated at the two Gauss points. The process is carried out for all concerned integrals.

Discretization of the virtual work of the constraint follows a similar procedure and is written:

$$\delta W_\mu^e = \int_0^{L^e} \left((\hat{\mathbf{q}}^e \cdot \hat{\mathbf{q}}^e - 1)\, \delta\mu^e + 2\mu^e \hat{\mathbf{q}}^{e\mathrm{T}} \delta\hat{\mathbf{q}}^e \right) \mathrm{d}s = \delta\mathbf{z}^{e\mathrm{T}} \underbrace{\int_0^{L^e} \mathbf{Q}^{\mathrm{T}} \mathbf{f}_\mu^e \mathrm{d}s}_{\mathbf{F}_{\mathrm{cons}}^e}, \tag{5.40}$$

with $\mathbf{f}_\mu^e = \begin{bmatrix}\mathbf{0} & \mathbf{0} & 2\mu^e\hat{\mathbf{q}}^{e\mathrm{T}} & \hat{\mathbf{q}}^e\cdot\hat{\mathbf{q}}^e - 1\end{bmatrix}^{\mathrm{T}}$.

If $\mathbf{f}_i^e$ and $\mathbf{f}_\mu^e$ are taken together for convenience as done in [45], the result can be combined in a new expression $\mathbf{g}^e(\mathbf{z}^e)$, written as:

$$\mathbf{g}^e(\mathbf{z}^e) = \mathbf{f}_i^e + \mathbf{f}_\mu^e = \begin{bmatrix} \mathrm{vec}(\hat{\mathbf{q}}^e \circ \hat{\mathbf{N}}^e \circ \hat{\mathbf{q}}^{e*}) \\ 2\hat{\mathbf{q}}^e \circ \hat{\mathbf{M}}^e \\ 2\hat{\mathbf{q}}^e \circ \left(\hat{\mathbf{N}}^e \circ \left(\hat{\mathbf{\Gamma}}^e + \hat{\mathbf{\Gamma}}_0\right) + \hat{\mathbf{M}}^e \circ \left(\hat{\mathbf{K}}^e + \hat{\mathbf{K}}_0\right)\right) + 2\hat{\mathbf{q}}^{e\prime} \circ \hat{\mathbf{M}}^e + 2\mu^e\hat{\mathbf{q}}^e \\ \hat{\mathbf{q}}^e\cdot\hat{\mathbf{q}}^e - 1 \end{bmatrix}, \tag{5.41}$$

then:

$$\begin{aligned}\delta W_i^e + \delta W_\mu^e &= \delta\mathbf{z}^{e\mathrm{T}} \int_0^{L^e} \mathbf{Q}^{\mathrm{T}} \left(\mathbf{f}_i^e(\mathbf{z}^e) + \mathbf{f}_\mu^e\right) \mathrm{d}s \\ &= \delta\mathbf{z}^{e\mathrm{T}} \underbrace{\int_0^{L^e} \mathbf{Q}^{\mathrm{T}} \mathbf{g}^e(\mathbf{z}^e) \mathrm{d}s}_{\mathbf{F}_g^e},\end{aligned} \tag{5.42}$$

from which $\mathbf{F}_g^e$ is determined using (2-point) Gauss reduced integration.

Finally, the virtual external work is discretized in the same fashion:

$$\delta W_e^e = \int_0^{L^e} \left(\hat{\mathbf{n}}_e^{e\mathrm{T}} \delta\hat{\mathbf{x}}_0^e + \left(2\hat{\mathbf{q}}^e \circ \hat{\mathbf{m}}_e^e\right)^{\mathrm{T}} \delta\hat{\mathbf{q}}^e\right) \mathrm{d}s = \delta\mathbf{z}^{e\mathrm{T}} \underbrace{\int_0^{L^e} \mathbf{P}^{\mathrm{T}} \mathbf{f}_e^e \mathrm{d}s}_{\mathbf{F}_{\mathrm{ext}}^e}, \tag{5.43}$$

with $\mathbf{f}_e^e = \begin{bmatrix}\mathbf{n}_e^{e\mathrm{T}} & \left(2\hat{\mathbf{q}}^e \circ \hat{\mathbf{m}}_e^e\right)^{\mathrm{T}} & 0\end{bmatrix}^{\mathrm{T}}$. The point loads at the boundaries (*e.g.* at $s = 0$ and $s = L$) should be added into $\mathbf{F}_{\mathrm{ext}}^e$ as well, by placing the load prescriptions at the appropriate nodes [45].

Then, collecting the discretized virtual inertial, internal, external and constraint works, the elementary dynamic equations of motion in the weak form [Eq. (5.23)] are written for a single element as:

$$\delta W_e^e - \delta W_a^e - \left(\delta W_i^e + \delta W_\mu^e\right) = \delta\mathbf{z}^{e\mathrm{T}} \left(\mathbf{F}_{\mathrm{ext}}^e - \mathbf{F}_{\mathrm{iner}}^e - \mathbf{F}_g^e\right) = 0. \tag{5.44}$$

Having determined the expressions for the elementary matrices and force vectors, Eq. (5.44) is assembled over all elements in order to derive the global discrete dynamic equations for the entire structure. Considering the vector $\mathbf{z}$, which gathers all degrees of freedom of the structure:

$$\mathbf{z} = \begin{bmatrix}\mathbf{x}_{0,1}^{\mathrm{T}} & \hat{\mathbf{q}}_1^{\mathrm{T}} & \mu_1 & \mathbf{x}_{0,2}^{\mathrm{T}} & \hat{\mathbf{q}}_2^{\mathrm{T}} & \mu_2 & \dots & \mathbf{x}_{0,N_n}^{\mathrm{T}} & \hat{\mathbf{q}}_{N_n}^{\mathrm{T}} & \mu_{N_n}\end{bmatrix}^{\mathrm{T}}, \tag{5.45}$$

and considering that the principle of virtual work Eq. (5.44) is valid for any virtual displacements $\delta\mathbf{z}$, the discrete dynamic governing equations are found:

$$\mathbf{F}_{\mathrm{ext}} - \mathbf{F}_{\mathrm{iner}} - \mathbf{F}_g = 0, \tag{5.46}$$

where $\mathbf{F}_{\mathrm{ext}}$, $\mathbf{F}_{\mathrm{iner}}$, and $\mathbf{F}_g$ are the global counterparts of $\mathbf{F}_{\mathrm{ext}}^e$, $\mathbf{F}_{\mathrm{iner}}^e$ and $\mathbf{F}_g^e$, respectively. The discrete nonlinear finite element model can be written in the general form (with neglected rotational intertia):

$$\mathbb{M}\ddot{\mathbf{z}} + \mathbf{D}\dot{\mathbf{z}} + \mathbf{F}_g(\mathbf{z}) = \mathbf{F}_{\mathrm{ext}}, \tag{5.47}$$

which follows the same derivation as in Chapter 3 except that the column vector $\mathbf{z}$ housing the degrees of freedom for all nodes in the structure is now of size $8N_n \times 1$, the mass matrix $\mathbb{M}$ is of size $8N_n \times 8N_n$ (as is the linear Rayleigh damping matrix $\mathbf{D}$, which is added into the model following the same procedure as in § 3.2.2), and the internal and external force vectors $\mathbf{F}_g$ and $\mathbf{F}_{\mathrm{ext}}$, respectively, are of size $8N_n \times 1$.

5.3.2 Quadratic recast of the 3D system

The same MANLAB solving procedure for continuation of periodic solutions as is used to solve the 2D system is carried out for the 3D system, which directly computes the forced response to Eq. (5.47) or the nonlinear modes (the solution to the underlying free conservative system of Eq. (5.47)) as described in Chapters 2 and 3. Recall that in the MANLAB formalism the governing equations should be rewritten in the form of a differential-algebraic system of equations (DAE) with at most quadratic nonlinearities. To this end, auxiliary variables are next introduced into the system in the quadratic recast procedure analogous to the one described in Chapter 3. Since we use here the same quadratic recast as the one described in [45], only the main equations are recopied, notably the rewriting of Eq. (5.41) where the geometric nonlinearities of the system are apparent.

In order to render the nonlinearities of the 3D system polynomials of at most quadratic order, 17 auxiliary variables are introduced, gathered in vector $\mathbf{v}^e = \begin{bmatrix}\mathbf{v}_1^{e\mathrm{T}} & \mathbf{v}_2^{e\mathrm{T}} & \mathbf{v}_3^{e\mathrm{T}} & \hat{\mathbf{v}}_4^{e\mathrm{T}} & \hat{\mathbf{v}}_5^{e\mathrm{T}}\end{bmatrix}^{\mathrm{T}}$, where [45]:

$$\begin{cases} \mathbf{v}_1^e = \mathrm{vec}(\hat{\mathbf{\Gamma}}^e) = \mathrm{vec}(\hat{\mathbf{q}}^{e*} \circ \hat{\mathbf{x}}_0^{e\prime} \circ \hat{\mathbf{q}}^e - \hat{\mathbf{\Gamma}}_0) = \mathrm{vec}(\hat{\mathbf{v}}_4^e \circ \hat{\mathbf{q}}^e - \hat{\mathbf{\Gamma}}_0), & \text{(5.48a)} \\ \mathbf{v}_2^e = \mathrm{vec}(\hat{\mathbf{K}}^e) = \mathrm{vec}(2\hat{\mathbf{q}}^{e*} \circ \hat{\mathbf{q}}^{e\prime} - \hat{\mathbf{K}}_0), & \text{(5.48b)} \\ \mathbf{v}_3^e = \mathrm{vec}(\hat{\mathbf{N}}^e \circ (\hat{\mathbf{\Gamma}}^e + \hat{\mathbf{\Gamma}}_0) + \hat{\mathbf{M}}^e \circ (\hat{\mathbf{K}}^e + \hat{\mathbf{K}}_0)), & \text{(5.48c)} \\ \hat{\mathbf{v}}_4^e = \hat{\mathbf{q}}^{e*} \circ \hat{\mathbf{x}}_0^{e\prime}, & \text{(5.48d)} \\ \hat{\mathbf{v}}_5^e = \hat{\mathbf{q}}^e \circ \hat{\mathbf{N}}^e. & \text{(5.48e)} \end{cases}$$

Since $\mathbf{v}_1^e$, $\mathbf{v}_2^e$ and $\mathbf{v}_3^e$ are vectors and $\hat{\mathbf{v}}_4^e$ and $\hat{\mathbf{v}}_5^e$ are quaternions, the $3\times 3 + 2\times 4 = 17$ auxiliary variables are recovered. However, since the integrals are carried out using 2-point Gauss reduced integration, for each element the 17 auxiliary variables in $\mathbf{v}^e$ should be evaluated at each of the 2 Gauss points, resulting in a total of $17\times 2 = 34$ auxiliary variables per element. Substituting Eqs. (5.48) into Eq. (5.41), $\mathbf{g}^e$ is recast under the quadratic form as:

$$\mathbf{g}^e = \begin{bmatrix} \mathrm{vec}\left(\hat{\mathbf{v}}_5^e \circ \hat{\mathbf{q}}^{e*}\right) \\ 2\hat{\mathbf{q}}^e \circ \left(\hat{\mathbf{C}}_M \hat{\mathbf{v}}_2^e\right) \\ 2\hat{\mathbf{q}}^e \circ \hat{\mathbf{v}}_3^e + 2\hat{\mathbf{q}}^{e\prime} \circ \left(\hat{\mathbf{C}}_M \hat{\mathbf{v}}_2^e\right) + 2\mu^e \hat{\mathbf{q}}^e \\ \hat{\mathbf{q}}^e \cdot \hat{\mathbf{q}}^e - 1 \end{bmatrix}, \tag{5.49}$$

where the relations $\hat{\mathbf{N}}^e = \hat{\mathbf{C}}_N \hat{\mathbf{\Gamma}}^e$ and $\hat{\mathbf{M}}^e = \hat{\mathbf{C}}_M \hat{\mathbf{K}}^e$ have been used in place of $\hat{\mathbf{N}}^e$ and $\hat{\mathbf{M}}^e$. Eq. (5.49) is also evaluated at the Gauss points using the values of $\mathbf{v}^e$ at each.

The definitions of the auxiliary variables are added into the system of equations in order to characterize the full system. Therefore, the full quadratic DAE, written in first order form, is given explicitly for a single finite element in order to summarize the full system of equations. For each element having 3 nodes, there are:

1. 45 primary variables:
   - 24 "position" degrees of freedom (8 per node) contained in $\mathbf{z}^e$ [Eq. (5.24)],
   - 21 "velocity" degrees of freedom (7 per node) contained in $\mathbf{V}^e$, noting that the Lagrange multiplier μ does not have a time derivative:

$$\mathbf{V}^e = \begin{bmatrix}\mathbf{V}_{\mathbf{x}_{0,1}}^{\mathrm{T}} & \hat{\mathbf{V}}_{\hat{\mathbf{q}}_1}^{\mathrm{T}} & \mathbf{V}_{\mathbf{x}_{0,2}}^{\mathrm{T}} & \hat{\mathbf{V}}_{\hat{\mathbf{q}}_2}^{\mathrm{T}} & \mathbf{V}_{\mathbf{x}_{0,3}}^{\mathrm{T}} & \hat{\mathbf{V}}_{\hat{\mathbf{q}}_3}^{\mathrm{T}}\end{bmatrix}^{\mathrm{T}}, \tag{5.50}$$

2. 34 auxiliary variables contained in $\mathbf{v}^e$ [Eqs. (5.48)] at 2 Gauss points,

such that the first order quadratic DAE is written:

$$\dot{\mathbf{z}}^e_- = \mathbf{V}^e, \tag{5.51a}$$
$$\mathbb{M}^e\dot{\mathbf{V}}^e_+ = \mathbf{F}^e_{\text{ext}} - \mathbf{D}^e\mathbf{V}^e_+ - \mathbf{F}^e_g, \tag{5.51b}$$
$$\mathbf{0} = \mathbf{v}^e_1 - \text{vec}\left(\hat{\mathbf{v}}^e_4 \circ \hat{\mathbf{q}}^e\right) + \mathbf{\Gamma}_0, \tag{5.51c}$$
$$\mathbf{0} = \mathbf{v}^e_2 - \text{vec}\left(2\hat{\mathbf{q}}^{e*} \circ \hat{\mathbf{q}}^{e\prime}\right) + \mathbf{K}_0, \tag{5.51d}$$
$$\mathbf{0} = \mathbf{v}^e_3 - (\mathbf{C}_N\mathbf{v}^e_1) \circ \mathbf{\Gamma}_0 - (\mathbf{C}_M\mathbf{v}^e_2) \circ \mathbf{K}_0 - (\mathbf{C}_N\mathbf{v}^e_1) \circ \mathbf{v}^e_1 - (\mathbf{C}_M\mathbf{v}^e_2) \circ \mathbf{v}^e_2, \tag{5.51e}$$
$$\hat{\mathbf{0}} = \hat{\mathbf{v}}^e_4 - \hat{\mathbf{q}}^{e*} \circ \hat{\mathbf{x}}^{e\prime}_0, \tag{5.51f}$$
$$\hat{\mathbf{0}} = \hat{\mathbf{v}}^e_5 - \hat{\mathbf{q}}^e \circ \left(\hat{\mathbf{C}}_N\hat{\mathbf{v}}^e_1\right), \tag{5.51g}$$

evaluated at each of the Gauss points for a single finite element. In Eq. (5.51)(a), the $\diamond_-$ notation is used to indicate that the rows corresponding to the location of the Lagrange multiplier have been removed in order to match with $\mathbf{V}^e$, which does not contain μ. Conversely, in Eq. (5.51)(b), zeros should be added into $\mathbf{V}^e$ and $\dot{\mathbf{V}}^e$ in the locations of the Lagrange multipliers in order to match dimensions with the other quantities. This is indicated by the $\diamond_+$ notation. Summing over all the elements, for the full FE system, the total number of degrees of freedom in the first order quadratic DAE is $N_{\text{dof}} = 15N_n + 34N_e$.

5.3.3 Scaling of the equations in 3D

As in § 3.2.2, scaling the parameters in order to render the equations of motion dimensionless is useful in generalizing any results. The same dimensionless variables as in Chapters 3 and 4 are introduced here:

$$\bar{\mathbf{u}}_0 = \frac{\mathbf{u}_0}{L}, \quad \bar{\mathbf{x}}_0 = \frac{\mathbf{x}_0}{L}, \quad \bar{s} = \frac{s}{L}, \quad \bar{t} = \frac{t}{L^2}\sqrt{\frac{EI}{\rho A}}, \quad \bar{\omega} = L^2\sqrt{\frac{\rho A}{EI}}\omega, \tag{5.52a}$$
$$\bar{\mathbf{N}}, \bar{\mathbf{m}}_e = \frac{L^2}{EI}\left(\mathbf{N}, \mathbf{m}_e\right), \quad \bar{\mathbf{M}} = \frac{L}{EI}\mathbf{M}, \quad \bar{\mathbf{n}}_e = \frac{L^3}{EI}\mathbf{n}_e, \tag{5.52b}$$

where $\bar{\diamond}$ represents a dimensionless quantity and L is a characteristic length of the system, in this case the length of the beam. If these dimensionless parameters are injected into the equations of motion, the system (neglecting the effect of gravity) is found to depend on two parameters, η_y and η_z, which are analogous to the "slenderness" parameter of Chapters 3 and 4. For three-dimensional motion, however, there are two transverse polarizations, so that two "slenderness" parameters are considered:

$$\eta_y = \frac{I_y}{AL^2}, \quad \eta_z = \frac{I_z}{AL^2}. \tag{5.53}$$

As shown in Eqs. (5.52), however, only one second moment of area I is needed to normalize t, ω, $\mathbf{N}$, $\mathbf{M}$, $\mathbf{n}_e$ and $\mathbf{m}_e$. To be consistent with Chapters 3 and 4, I_z is used to normalize the parameters. This choice essentially states that, for asymmetrical cross-sections, the beam is oriented such that the low bending stiffness due to the slenderness of the beam causes large bending around $\mathbf{u}_z$; for symmetrical or near-symmetrical cross-sections, the choice is largely irrelevant. In practice, the dimensionless system

is recovered by setting $EI_z = 1$, $EA = 1/\eta_z$, $\rho A = 1$, $\rho I_z = \eta_z$, $\rho I_y = \eta_y$, $L = 1$, $k_z GA = k_z/[2(1+\nu)\eta_z]$, $k_y GA = k_y/[2(1+\nu)\eta_z]$ and $GJ = 1/[2(1+\nu)](1+\eta_y/\eta_z)$. As in Chapters 3 and 4, the dimensionless 3D beam model based on Timoshenko kinematics also depends on another dimensionless parameter tied to the effect of shearing, one shear parameter μ_y and μ_z for each direction of shearing. The shear parameters, however, have almost no effect on the nonlinear dynamics of very slender beams, based on the demonstration in Appendix B.1.

Note that, in what follows, the $\bar{\diamond}$ notation is dropped. For the test cases studied in §5.5, the normalization of each system (if applicable) is explicitly stated.

5.4 2D in-plane motions with quaternions

In this section, we introduce the process of restricting the motion in three dimensions to in-plane motions, like those of Chapters 3 and 4. Restricting the quaternion formulation of the previous sections to 2D motions is of interest as it enables (1) a method of validating the quaternion method of rotation parametrization described in this chapter, and (2) a direct comparison to the computational efficiency of the rotation matrix method of rotation parametrization (Chapter 3).

When restricting the motion to 2D in-plane motions, the definitions of the general beam deformations and dynamic equations of motion presented in §5.2.3 remain valid, but for a reduced number of degrees of freedom. In 2D, there are only two displacements in $\mathbf{u}_0(s)$, the axial displacement u and the transverse displacement w, and likewise two components in positions $\mathbf{x}_0$ and $\mathbf{X}_0$. Furthermore, based on the definition of the unit quaternion used to describe the rotation of the cross-section [Eq. (5.12)], only two components in $\hat{\mathbf{q}}$ are non-zero, q_0 and q_3. In restricting the motion from 3D to 2D, then, the degrees of freedom to consider at each location s of the continuous system decrease to only 5 (taking into account the Lagrange multiplier μ governing the unity constraint on $\hat{\mathbf{q}}$) from 8 in 3D.

In 2D, the strains and curvatures are defined then as a particular case of the general strains and curvatures in 3D [Eqs. (5.17)]. They are defined in 2D as $\hat{\mathbf{\Gamma}} = \begin{bmatrix} 0 & \Gamma_x & \Gamma_y & 0 \end{bmatrix}^{\mathrm{T}}$ and $\hat{\mathbf{K}} = \begin{bmatrix} 0 & 0 & 0 & \kappa_z \end{bmatrix}^{\mathrm{T}}$, respectively, whose components Γ_x, Γ_y and κ_z are computed using Eqs. (5.17) and can be written explicitly since the definitions are greatly simplified with the fewer degrees of freedom. For the sake of comparison to Chapter 3, the strains Γ_x and Γ_y are noted to be equivalent to the axial e and shear strains γ, respectively, while the curvature κ_3 is equivalent to κ. Moving forward, the notation of Chapter 3 will be adopted here in order to compare the two 2D methods more naturally. Additionally, in what follows the 2D equations are written based on the *displacements* $\mathbf{u}_0$ instead of the *positions* $\mathbf{x}_0$ as in the previous sections, in alignment with Chapter 3 ($\mathbf{x}_0$ can be obtained from $\mathbf{u}_0$ and vice versa using Eq. (5.3)).

With the components $q_1 = q_2 = 0$ in $\hat{\mathbf{q}}$, the $\Phi_L(\hat{\mathbf{q}})$ and $\Phi_R(\hat{\mathbf{q}})$ operations to perform the quaternion multiplication in 2D become:

$$\Phi_L(\hat{\mathbf{q}}) = \begin{bmatrix} q_0 & 0 & 0 & -q_3 \\ 0 & q_0 & -q_3 & 0 \\ 0 & q_3 & q_0 & 0 \\ q_3 & 0 & 0 & q_0 \end{bmatrix}, \quad \Phi_R(\hat{\mathbf{q}}) = \begin{bmatrix} q_0 & 0 & 0 & -q_3 \\ 0 & q_0 & q_3 & 0 \\ 0 & -q_3 & q_0 & 0 \\ q_3 & 0 & 0 & q_0 \end{bmatrix}. \tag{5.54}$$

Based on these definitions, the rotation matrix $\mathbf{R}$ as defined in Eq. (E.45) simplifies to:

$$\mathbf{R} = \begin{bmatrix} 1-2q_3^2 & -2q_0q_3 & 0 \\ 2q_0q_3 & 1-2q_3^2 & 0 \\ 0 & 0 & 1 \end{bmatrix} = \begin{bmatrix} R_{11} & -R_{21} & 0 \\ R_{21} & R_{11} & 0 \\ 0 & 0 & 1 \end{bmatrix}, \tag{5.55}$$

using the unity constraint in 2D: $\hat{\mathbf{q}}\cdot\hat{\mathbf{q}} = q_0^2 + q_3^2 = 1$. Notice that for $q_0 = \cos\left(\frac{\theta}{2}\right)$, $q_3 = \sin\left(\frac{\theta}{2}\right)$ ($\mathbf{n} = \begin{bmatrix}0 & 0 & 1\end{bmatrix}^{\mathrm{T}}$ in Eq. (5.12)) and using trigonometric double angle identities, the classical 3×3 rotation matrix $\mathbf{R}$ for rotations around the z-axis is recovered from Eq. (5.55).

Then, according to Eq. (5.17a), the strains $\hat{\mathbf{\Gamma}}$ are written explicitly as:

$$\hat{\mathbf{\Gamma}} = \begin{bmatrix}0\\ e\\ \gamma\\ 0\end{bmatrix} = \begin{bmatrix}0\\ \left(1-2q_3^2\right)(u'+1) + 2q_0q_3w' - 1\\ -2q_0q_3(u'+1) + \left(1-2q_3^2\right)w'\\ 0\end{bmatrix}. \tag{5.56}$$

In the same way, the curvatures $\hat{\mathbf{K}}$ are written:

$$\hat{\mathbf{K}} = \begin{bmatrix}0\\ 0\\ 0\\ \kappa\end{bmatrix} = \begin{bmatrix}0\\ 0\\ 0\\ 2q_0q_3' - 2q_3q_0'\end{bmatrix}. \tag{5.57}$$

The variations of Eqs. (5.56) and (5.57) $\delta\hat{\mathbf{\Gamma}}$ and $\delta\hat{\mathbf{K}}$ are likewise computed using Eq. (5.19) and reorganized into the form:

$$\begin{cases}\delta e = \left(1-2q_3^2\right)\delta u' + 2q_0q_3\delta w' - 2q_3\gamma\delta q_0 + 2q_0\gamma\delta q_3, & \text{(5.58a)}\\ \delta\gamma = -2q_0q_3\delta u' + \left(1-2q_3^2\right)\delta w' + 2q_3(e+1)\delta q_0 - 2q_0(e+1), & \text{(5.58b)}\\ \delta\kappa = -2q_3'\delta q_0 + 2q_0'\delta q_3 - 2q_3\delta q_0' + 2q_0\delta q_3'. & \text{(5.58c)}\end{cases}$$

Retaining the same constitutive relation as in Eq. (5.20), the stress resultants in force and moment restricted to 2D motions are written, respectively:

$$\hat{\mathbf{N}} = \hat{\mathbf{C}}_N\hat{\mathbf{\Gamma}} = \begin{bmatrix}0\\ N\\ T\\ 0\end{bmatrix} = \begin{bmatrix}0\\ EAe\\ k_yGA\gamma\\ 0\end{bmatrix}, \quad \hat{\mathbf{M}} = \hat{\mathbf{C}}_M\hat{\mathbf{K}} = \begin{bmatrix}0\\ 0\\ 0\\ M\end{bmatrix} = \begin{bmatrix}0\\ 0\\ 0\\ EI_z\kappa\end{bmatrix}, \tag{5.59}$$

where the only nonzero elements in 2D are the axial force N, the shear force T and the bending moment M. With these definitions, the dynamic equations in the weak form [Eqs. (5.21), (5.22) and (5.23)] can be simplified to (and rewritten in terms of the displacements $\mathbf{u}_0$ in place of the positions $\mathbf{x}_0$):

$$\delta W_a = \int_0^L \rho\ddot{\hat{\mathbf{u}}}_0^{\mathrm{T}}\hat{\mathbf{A}}\delta\hat{\mathbf{u}}_0\mathrm{d}s = \int_0^L \rho\ddot{\mathbf{u}}_0^{\mathrm{T}}\mathbf{A}\delta\mathbf{u}_0\mathrm{d}s, \tag{5.60a}$$

$$\delta W_i = \int_0^L \left(\hat{\mathbf{N}}^{\mathrm{T}}\delta\hat{\mathbf{\Gamma}} + \hat{\mathbf{M}}^{\mathrm{T}}\delta\hat{\mathbf{K}}\right)\mathrm{d}s = \int_0^L \left(N\delta e + T\delta\gamma + M\delta\kappa\right)\mathrm{d}s, \tag{5.60b}$$

$$\begin{aligned}\delta W_e &= \int_0^L \left(\hat{\mathbf{n}}_e^{\mathrm{T}}\delta\hat{\mathbf{u}}_0 + \left(2\hat{\mathbf{q}}\circ\hat{\mathbf{m}}_e\right)^{\mathrm{T}}\delta\hat{\mathbf{q}}\right)\mathrm{d}s + \left[\hat{\mathbf{N}}_e^{\mathrm{T}}\delta\hat{\mathbf{u}}_0\right]_0^L + \left[\left(2\hat{\mathbf{q}}\circ\hat{\mathbf{M}}_e\right)^{\mathrm{T}}\delta\hat{\mathbf{q}}\right]_0^L\\ &= \int_0^L \left(n(s,t)\delta u + p(s,t)\delta w + 2q(s,t)\left(-q_3\delta q_0 + q_0\delta q_3\right)\right)\mathrm{d}s + \left[\hat{\mathbf{N}}_e^{\mathrm{T}}\delta\hat{\mathbf{u}}_0\right]_0^L + \left[\left(2\hat{\mathbf{q}}\circ\hat{\mathbf{M}}_e\right)^{\mathrm{T}}\delta\hat{\mathbf{q}}\right]_0^L\end{aligned} \tag{5.60c}$$

$$\delta W_\mu = \int_0^L \left(\left(\hat{\mathbf{q}}\cdot\hat{\mathbf{q}} - 1\right)\delta\mu + 2\mu\hat{\mathbf{q}}^{\mathrm{T}}\delta\hat{\mathbf{q}}\right)\mathrm{d}s = \int_0^L \left(\left(q_0^2 + q_3^2 - 1\right)\delta\mu + 2\mu\left(q_0\delta q_0 + q_3\delta q_3\right)\right)\mathrm{d}s, \tag{5.60d}$$

where in 2D $\mathbf{A} = A\mathbf{I}_2$ with $\mathbf{I}_2$ the 2×2 identity matrix and with $n(s,t)$ and $p(s,t)$ the distributed applied axial and transverse forces ($\hat{\mathbf{n}}_e = \begin{bmatrix} 0 & n(s,t) & p(s,t) & 0 \end{bmatrix}^{\mathrm{T}}$), respectively and $q(s,t)$ the distributed applied bending moment ($\hat{\mathbf{m}}_e = \begin{bmatrix} 0 & 0 & 0 & q(s,t) \end{bmatrix}^{\mathrm{T}}$), respectively (there are also only two components in $\hat{\mathbf{N}}_e$ and $\hat{\mathbf{M}}_e$ here compared to Eqs. (5.21)). Eqs. (5.60) are related according to the principle of virtual work [Eq. (5.23)].

5.4.1 Discretization into finite elements

Discretization of the 2D system into finite elements follows much of the same procedure as in 3D except that fewer degrees of freedom are computed and stored since many of the degrees of freedom are set to zero when the motion is fixed in the plane. In § 5.3, the system is discretized using 3-node quadratic Timoshenko beam elements (2 end nodes plus an internal node at the midpoint along the element's centerline). In the 2D rotation matrix formulation of Chapter 3, 2-node linear Timoshenko beam elements are used. For the sake of a direct comparison to both models, both discretization methods have been incorporated into our FE code. The derivation that follows, however, will only be shown for the 3-node elements in line with what has been presented in this chapter thus far. Note that, in practice, the two approaches differ only in the number of nodes (and, therefore, the total degrees of freedom) involved in the computation and the order of the polynomial interpolation functions; the procedure otherwise is exactly the same.

First, the system is discretized into N_e elements of individual length L^e. At each node i of the mesh, there are 5 degrees of freedom: the 2 displacements of the centerline (u, the axial displacement, and w, the transverse displacement), contained in $\mathbf{u}_0$, the 2 non-zero elements of $\hat{\mathbf{q}}$ (q_0 and q_3) and the Lagrange multiplier μ once again governing the unity constraint. Following the same conventions established in §5.3, the degrees of freedom for a single element are gathered in the vector $\mathbf{z}^e$:

$$\mathbf{z}^e = [\underbrace{u_1 \quad w_1 \quad q_{0,1} \quad q_{3,1} \quad \mu_1}_{\text{node 1}} \quad \underbrace{u_2 \quad w_2 \quad q_{0,2} \quad q_{3,2} \quad \mu_2}_{\text{node 2}} \quad \underbrace{u_3 \quad w_3 \quad q_{0,3} \quad q_{3,3} \quad \mu_3}_{\text{node 3}}]^{\mathrm{T}}. \tag{5.61}$$

Although the 2D quaternion-based model and the 2D model using rotation matrices represent two different 2D parametrizations of the same continuous model, more degrees of freedom are involved in the computation: 5 per node in the former versus 3 per node in the latter. The interpolation to find the elementary quantities is then:

$$\begin{bmatrix} u^e \\ w^e \\ q_0^e \\ q_3^e \\ \mu^e \end{bmatrix} = \mathbf{P}(s)\mathbf{z}^e, \tag{5.62}$$

where $\mathbf{P}(s)$ is the interpolation matrix of size 5×15 with the same interpolation functions $N_1(s)$, $N_2(s)$ and $N_3(s)$ as defined in Eqs. (5.27):

$$\mathbf{P}(s) = \begin{bmatrix} N_1(s)\mathbf{I}_5 & N_2(s)\mathbf{I}_5 & N_3(s)\mathbf{I}_5 \end{bmatrix}. \tag{5.63}$$

The spatial derivatives of $\begin{bmatrix} u^{e\prime} & w^{e\prime} & q_0^{e\prime} & q_3^{e\prime} & \mu^{e\prime} \end{bmatrix}^{\mathrm{T}}$ are computed as in Eq. (5.28), so that the

interpolation matrix $\mathbf{Q}(s)$ in 2D becomes:

$$\mathbf{Q}(s) = \begin{bmatrix} N_1'\mathbf{I}_2 & \mathbf{0} & \mathbf{0} & N_2'\mathbf{I}_2 & \mathbf{0} & \mathbf{0} & N_3'\mathbf{I}_2 & \mathbf{0} & \mathbf{0} \\ \mathbf{0} & N_1'\mathbf{I}_2 & \mathbf{0} & \mathbf{0} & N_2'\mathbf{I}_2 & \mathbf{0} & \mathbf{0} & N_3'\mathbf{I}_2 & \mathbf{0} \\ \mathbf{0} & N_1\mathbf{I}_2 & \mathbf{0} & \mathbf{0} & N_2\mathbf{I}_2 & \mathbf{0} & \mathbf{0} & N_3\mathbf{I}_2 & \mathbf{0} \\ \mathbf{0} & \mathbf{0} & N_1 & \mathbf{0} & \mathbf{0} & N_2 & \mathbf{0} & \mathbf{0} & N_3 \end{bmatrix}, \tag{5.64}$$

such that $\begin{bmatrix}\delta u^{e\prime} & \delta w^{e\prime} & \delta q_0^{e\prime} & \delta q_3^{e\prime} & \delta q_0^e & \delta q_3^e & \delta\mu^{e\prime}\end{bmatrix}^{\mathrm{T}} = \mathbf{Q}(s)\delta\mathbf{z}^e$. Defining $\mathbf{E} = \begin{bmatrix} e & \gamma & \kappa \end{bmatrix}^{\mathrm{T}}$ and $\mathbf{\Sigma} = \begin{bmatrix} N & T & M \end{bmatrix}^{\mathrm{T}}$ in 2D, the strain matrix $\mathbf{B}^e$ linking the variation of the strains $\delta\mathbf{E}^e$ to the variation of the nodal degrees of freedom $\delta\mathbf{z}^e$ according to Eq. (5.32) simplifies to:

$$\mathbf{B}^e = \begin{bmatrix} 1-2q_3^{e\,2} & 2q_0^eq_3^e & 0 & 0 & -2q_3^e\gamma^e & 2q_0^e\gamma^e & 0 \\ -2q_0^eq_3^e & 1-2q_3^{e\,2} & 0 & 0 & 2q_3^e\,(e^e+1) & -2q_0^e\,(e^e+1) & 0 \\ 0 & 0 & -2q_3^e & 2q_0^e & -2q_3^{e\prime} & 2q_0^{e\prime} & 0 \end{bmatrix}\mathbf{Q}. \tag{5.65}$$

5.4.2 Discretization of the dynamic equations of motion

With all parameters now having been reduced to 2D from the general 3D motion, discretization of the dynamic equations of motion follows exactly the same procedure as presented in §5.3.1. For this reason, we focus the section on simply writing the principle vectors and matrices (notably the elementary mass matrix $\mathbb{M}^e$, the external force vector $\mathbf{F}^e_{\text{ext}}$ and the internal force vector, incorporating also the constraint as in §5.3.1, $\mathbf{F}^e_g$) for the 2D motions. Recall from § 5.3 that to avoid shear-locking, the integrals are evaluated using reduced integration: in our case, a 2-point Gauss reduced integration for 3-node elements.

We begin by discretizing the virtual inertial work (recalling that the rotational inertia is neglected), which is written:

$$\delta W_a^e = \int_0^{L^e} \rho\ddot{\mathbf{u}}_0^{e\,\mathrm{T}}\mathbf{A}\delta\mathbf{u}_0^e\mathrm{d}s = \delta\mathbf{z}^{e\,\mathrm{T}}\underbrace{\left(\int_0^{L^e}\rho\mathbf{P}^{\mathrm{T}}\mathbb{J}\mathbf{P}\mathrm{d}s\right)}_{\mathbb{M}^e}\ddot{\mathbf{z}}^e, \tag{5.66}$$

where here $\mathbb{J} = \mathrm{diag}(\mathbf{A}, 0\mathbf{I}_3, \mathbf{A}, 0\mathbf{I}_3, \mathbf{A}, 0\mathbf{I}_3)$, so that the mass matrix $\mathbb{M}^e$ in 2D matches Eq. (5.35), but simplified in size to only 15×15:

$$\mathbb{M}^e = \frac{\rho L^e}{30}\begin{bmatrix} 4\mathbf{A} & \mathbf{0} & \mathbf{0} & 2\mathbf{A} & \mathbf{0} & \mathbf{0} & -\mathbf{A} & \mathbf{0} & \mathbf{0} \\ \mathbf{0} & \mathbf{0} & \mathbf{0} & \mathbf{0} & \mathbf{0} & \mathbf{0} & \mathbf{0} & \mathbf{0} & \mathbf{0} \\ \mathbf{0} & \mathbf{0} & 0 & \mathbf{0} & \mathbf{0} & 0 & \mathbf{0} & \mathbf{0} & 0 \\ 2\mathbf{A} & \mathbf{0} & \mathbf{0} & 16\mathbf{A} & \mathbf{0} & \mathbf{0} & 2\mathbf{A} & \mathbf{0} & \mathbf{0} \\ \mathbf{0} & \mathbf{0} & \mathbf{0} & \mathbf{0} & \mathbf{0} & \mathbf{0} & \mathbf{0} & \mathbf{0} & \mathbf{0} \\ \mathbf{0} & \mathbf{0} & 0 & \mathbf{0} & \mathbf{0} & 0 & \mathbf{0} & \mathbf{0} & 0 \\ -\mathbf{A} & \mathbf{0} & \mathbf{0} & 2\mathbf{A} & \mathbf{0} & \mathbf{0} & 4\mathbf{A} & \mathbf{0} & \mathbf{0} \\ \mathbf{0} & \mathbf{0} & \mathbf{0} & \mathbf{0} & \mathbf{0} & \mathbf{0} & \mathbf{0} & \mathbf{0} & \mathbf{0} \\ \mathbf{0} & \mathbf{0} & 0 & \mathbf{0} & \mathbf{0} & 0 & \mathbf{0} & \mathbf{0} & 0 \end{bmatrix}, \tag{5.67}$$

with $\mathbf{A} = A\mathbf{I}_2$ in 2D.

Next, using the discretizations of the virtual internal work [Eq. (5.36)] and the virtual work of the constraint [Eq. (5.40)], the combined expression is written:

$$\begin{aligned}\delta W_i^e + \delta W_\mu^e &= \int_0^{L^e} \left(N^e \delta e^e + T^e \delta\gamma^e + M^e \delta\kappa^e\right) \mathrm{d}s + \int_0^{L^e} \left(\left(q_0^{e2} + q_3^{e2} - 1\right)\delta\mu^e + 2\mu^e\left(q_0^e \delta q_0^e + q_3^e \delta q_3^e\right)\right) \mathrm{d}s, \\ &= \delta\mathbf{z}^{e\mathrm{T}} \underbrace{\int_0^{L^e} \mathbf{Q}^\mathrm{T} \mathbf{g}^e(\mathbf{z}^e) \mathrm{d}s}_{\mathbf{F}_g^e},\end{aligned} \tag{5.68}$$

where the expression for $\mathbf{g}^e(\mathbf{z}^e)$ simplifies to:

$$\mathbf{g}^e = \begin{bmatrix} \left(1 - 2q_3^{e2}\right) N^e - 2q_0^e q_3^e T^e \\ 2q_0^e q_3^e N^e + \left(1 - 2q_3^{e2}\right) T^e \\ -2q_3^e M^e \\ 2q_0^e M^e \\ -2q_3^e \gamma^e N^e + 2q_3^e \left(e^e + 1\right) T^e - 2q_3^{e\prime} M^e + 2\mu^e q_0^e \\ 2q_0^e \gamma^e N^e - 2q_0^e \left(e^e + 1\right) T^e + 2q_0^{e\prime} M^e + 2\mu^e q_3^e \\ q_0^{e2} + q_3^{e2} - 1 \end{bmatrix}, \tag{5.69}$$

making use of the simplification of $\mathbf{B}^e$ [Eq. (5.65)] in 2D.

Finally, the discretization of the virtual external work in 2D takes the form:

$$\delta W_e^e = \int_0^{L^e} \left(n^e(s,t)\delta u^e + p^e(s,t)\delta w^e + 2q^e(s,t)\left(-q_3^e \delta q_0^e + q_0^e \delta q_3^e\right)\right) \mathrm{d}s = \delta\mathbf{z}^{e\mathrm{T}} \underbrace{\int_0^{L^e} \mathbf{P}^\mathrm{T} \mathbf{f}_e^e \mathrm{d}s}_{\mathbf{F}_{\mathrm{ext}}^e}, \tag{5.70}$$

with $\mathbf{f}_e^e = \begin{bmatrix} n^e(s,t) & p^e(s,t) & -2q_3^e q^e(s,t) & 2q_0^e q^e(s,t) & 0 \end{bmatrix}^\mathrm{T}$ simplified to 2D. Once again, the point loads at the boundaries must be taken into account in $\mathbf{F}_{\mathrm{ext}}^e$ as in 3D.

The elements are assembled for the entire structure and the full discrete finite element model falls into the same general form Eq. (5.47), where in 2D the vector $\mathbf{z}$ gathering all degrees of freedom reduces to:

$$\mathbf{z} = \begin{bmatrix} u_1 & w_1 & q_{0,1} & q_{3,1} & \mu_1 & u_2 & w_2 & q_{0,2} & q_{3,2} & \mu_2 & \dots & u_{N_n} & w_{N_n} & q_{0,N_n} & q_{3,N_n} & \mu_{N_n} \end{bmatrix}^\mathrm{T}, \tag{5.71}$$

of size $5N_n \times 1$. The mass $\mathbb{M}$ and damping $\mathbf{D}$ matrices likewise reduce to size $5N_n \times 5N_n$ in passing from 3D to 2D, while the internal $\mathbf{F}_g$ and external $\mathbf{F}_{\mathrm{ext}}$ force vectors reduce to size $5N_n \times 1$.

5.4.3 Quadratic recast of the 2D system

As in 3D, the 2D system should be "recast" to include only polynomial nonlinearities of at most quadratic order in order to solve it with MANLAB. Here, 6 auxiliary variables are introduced into the system, although this version of the quadratic recast is not the sole method (recall from Chapter 3 that alternate methods of writing the quadratic recast are possible, see Appendix A.2). Using the same notation as §5.3.2, the 6 auxiliary variables are introduced for each element in vector $\mathbf{v}^e = \begin{bmatrix} R_{11}^e & R_{21}^e & e^e & \gamma^e & \kappa^e & v_6^e \end{bmatrix}^\mathrm{T}$, where:

$$\begin{cases} R^e_{11} = 1 - 2q^{e2}_3, & \text{(5.72a)} \\ R^e_{21} = 2q^e_0 q^e_3, & \text{(5.72b)} \\ e^e = R^e_{11}\left(u^{e\prime}+1\right) + R^e_{21} w^{e\prime} - 1, & \text{(5.72c)} \\ \gamma^e = -R_{21}\left(u^{e\prime}+1\right) + R^e_{11} w^{e\prime}, & \text{(5.72d)} \\ \kappa^e = 2q^e_0 q^{e\prime}_3 - 2q^e_3 q^{e\prime}_0, & \text{(5.72e)} \\ v^e_6 = EAe^e\gamma^e - k_z GA\gamma^e\left(e^e+1\right). & \text{(5.72f)} \end{cases}$$

Introducing the auxiliary variables into the system, $\mathbf{g}^e$ is recast into the quadratic form:

$$\mathbf{g}^e = \begin{bmatrix} EAR^e_{11}e^e - k_y GAR_{21}\gamma^e \\ EAR^e_{21}e^e + k_y GAR_{11}\gamma^e \\ -2EI_z q^e_3 \kappa^e \\ 2EI_z q^e_0 \kappa^e \\ -2EI_z q^{e\prime}_3 \kappa^e - 2q^e_3 v^e_6 + 2\mu^e q^e_0 \\ 2EI_z q^{e\prime}_0 \kappa^e - 2q^e_0 v^e_6 + 2\mu^e q^e_3 \\ q^{e2}_0 + q^{e2}_3 - 1 \end{bmatrix}, \tag{5.73}$$

where EAe^e, $k_y GA\gamma^e$ and $EI_z\kappa^e$ have been substituted for N^e, T^e, and M^e, respectively, in Eq. (5.73). As in 3D, the auxiliary variables and $\mathbf{g}^e$ are evaluated at the 2 Gauss points, leading to a total of $6\times 2 = 12$ auxiliary variables in 2D (down from 34 in 3D).

The full first order quadratic DAE for a single finite element is written explicitly for the 2D in-plane motions. Using 3-node elements, there are:

1. 27 primary variables:
   - 15 "displacement" degrees of freedom (5 per node) contained in $\mathbf{z}^e$ Eq. (5.61),
   - 12 "velocity" degrees of freedom (4 per node) contained in $\mathbf{V}^e$, noting that the Lagrange multiplier μ does not have a time derivative:

$$\mathbf{V}^e = \begin{bmatrix} V_{u1} & V_{w1} & V_{q0,1} & V_{q3,1} & V_{u2} & V_{w2} & V_{q0,2} & V_{q3,2} & V_{u3} & V_{w3} & V_{q0,3} & V_{q3,3} \end{bmatrix}^{\mathrm{T}}, \tag{5.74}$$

2. 12 auxiliary variables contained in $\mathbf{v}^e$ [Eqs. (5.72)] at 2 Gauss points,

such that the first order quadratic DAE for a single finite element is written:

$$\begin{aligned} \dot{\mathbf{z}}^e_- &= \mathbf{V}^e, & \text{(5.75a)} \\ \mathbb{M}^e\dot{\mathbf{V}}^e_+ &= \mathbf{F}^e_{\text{ext}} - \mathbf{D}^e\mathbf{V}^e_+ - \mathbf{F}^e_g, & \text{(5.75b)} \\ 0 &= R^e_{11} - \left(1 - 2q^{e2}_3\right), & \text{(5.75c)} \\ 0 &= R^e_{21} - 2q^e_0 q^e_3, & \text{(5.75d)} \\ 0 &= e^e - R^e_{11}\left(u^{e\prime}+1\right) - R^e_{21}w^{e\prime} + 1, & \text{(5.75e)} \\ 0 &= \gamma^e + R^e_{21}\left(u^{e\prime}+1\right) - R^e_{11}w^{e\prime}, & \text{(5.75f)} \\ 0 &= \kappa^e - 2q^e_0 q^{e\prime}_3 + 2q^e_3 q^{e\prime}_0, & \text{(5.75g)} \\ 0 &= v^e_6 - EAe^e\gamma^e + k_z GA\gamma^e(e^e+1), & \text{(5.75h)} \end{aligned}$$

where, as in § 5.3, the $\diamond_-$ notation indicates that the locations of the Lagrange multipliers μ have been removed while $\diamond_+$ indicates that zeros have been added in $\mathbf{V}^e$ in the locations of the Lagrange multipliers to match dimensions.

For the full first order quadratic FE DAE, the total number of degrees of freedom is $N_{\text{dof}} = 9N_n + 12N_e$. Of course, if a 2-node element with linear interpolation functions are used, fewer degrees of freedom are involved in the full quadratic DAE.

5.5 Test cases

Next, several test cases are modeled using the FE geometrically exact quaternion-based formulation outlined above in order to validate the model with others in the literature and demonstrate the capacity of the model in simulating the nonlinear dynamics of flexible beams. In Chapter 3, several test cases were introduced, two of which are taken up again here: the classical cantilever (clamped-free) beam and the clamped-clamped beam. These two structures are selected not only for their simplicity of implementation, but also because they exhibit the two types of dominant nonlinear mechanisms found in flexible beam structures containing geometrical nonlinearities: the axial-bending coupling is the primary nonlinear mechanism of the clamped-clamped beam, while the cantilever beam represents the classic example of the beam in large rotation.

Moreover, these two classical systems are often studied in the literature on nonlinear beam dynamics [53], [71], [86], [155], [204], [229]; some of these works are used in what follows as reference simulations in order to validate the quaternion-based model of this chapter. In particular, given that in 3D the beam has two transverse directions orthogonal to the longitudinal direction, we take a special interest in the one-to-one (1:1) internal resonance (IR) phenomenon that is uncovered for beams of (near) symmetrical cross-sections. In this case, the beam has two nearly identical eigenfrequencies [124], [244] tied to a transverse bending mode in each of the two transverse directions, leading to a 1:1 coupling between the two nonlinear modes. As will be shown later, the result of the coupling is a combination in phase quadrature of the two transverse polarizations, so that the beam appears to "rotate" between the polarizations. Some examples in the literature can be found for both the cantilever [244] and the clamped-clamped beam [217]. As real manufacturing processes are imperfect and dimensions are traditionally made to certain tolerance levels instead of exact precision, a slightly asymmetrical cross-section can be reasonably expected in real-life applications. It is therefore of importance in certain industrial applications, for example in MEMS and NEMS applications [244], to characterize this 1:1 internal resonance in order to make the necessary design choices to avoid or exploit it.

5.5.1 2D and 3D motions with quaternion formulation

The two test cases under study in this section are simulated using the mesh and simulation parameters collected in Table 5.1 for elements of equal length (uniform mesh). In order to be able to compare the 2D and 3D motions exactly, the same number of elements, nodes and harmonics retained in the HBM are used in 2D as in 3D; hence, there are far fewer degrees of freedom involved in the 2D computation compared to 3D. In our models, the computational cost is generally tied to the number of degrees of freedom. In 3D, the number of degrees of freedom increases rapidly when more finite elements are used. In general, we aim to minimize the number of elements while preserving a converged solution in order to reduce computation times. The computation time of systems with many degrees of freedom,

Table 5.1: Mesh and harmonic parameters: number of discrete elements per structure used in numerical simulations, corresponding number FE nodes (+ 1 internal node per element) and harmonics retained in the HBM (see Eq. (2.42)).

Structure	**Elements** N_e	**Nodes** $N_n = 2N_e + 1$	**Harmonics** H
Cantilever	10	21	20
Clamped-clamped	12	25	10

however, represents a topic of ongoing research (see § 5.6). This serves to explain why for *e.g.* the clamped-clamped beam, only 12 elements are used in this section versus 50 in Chapter 3.

In this section, the nonlinear modes, visually depicted as the backbone curves in an amplitude / frequency plot, are the primary focus as in Chapter 4. This is primarily due to the backbone curve being a more efficient way of characterizing the system's nonlinear behavior than several forced response computations. However, it is fully possible to compute the forced response of the quaternion-based model presented in this chapter; the method is the same as in Chapter 3.

Cantilever The first system under study is the classical cantilever (initially straight) with one end fixed and the other free. With the centerline of the beam aligned with the $\mathbf{u}_x$-direction such that $(\mathbf{u}_x, \mathbf{u}_y, \mathbf{u}_z) = (\mathbf{E}_x, \mathbf{E}_y, \mathbf{E}_z)$ according to Fig. 5.1, the beam is able to deform in two orthogonal transverse directions, $\mathbf{E}_y$ and $\mathbf{E}_z$. For a beam of perfectly square cross-section ($b = h$ where b is the width of the beam (the dimension in the $\mathbf{E}_z$-direction) and h its thickness (the dimension along $\mathbf{E}_y$)), the eigenfrequencies and the motion on each bending mode are identical in each of the transverse polarizations. In order to "create" the 1:1 internal resonance coupling, a small asymmetry or "detuning" [217], [244] is imposed by breaking very slightly the symmetry between b and h. In doing so, the two transverse polarizations become slightly different, in that the eigenfrequencies and mode shapes are separated slightly. Then, when one transverse nonlinear mode is excited, at a certain amplitude of vibration (corresponding to a certain evolution of the oscillation frequency) an intersection or "overlap" between the two modes is induced such that the two resonant frequencies of the nonlinear modes intersect and the second mode (*i.e.* the twin bending mode in the other transverse direction) is excited in turn.

To visualize this phenomenon, the beam of Vincent *et al.* [244] is used, a beam of length $L = 1$ m and nearly square cross-section is modeled ($h = 0.03$ m and $b = 0.03015$ m), leading to a 0.05% detuning in the symmetry of the square cross-section. The system is normalized by its characteristic length, here the length of the beam L. The first two (dimensionless) linear resonant frequencies corresponding to the first transverse bending mode in $\mathbf{E}_y$ and $\mathbf{E}_z$ are, respectively, $\omega_1 = 3.5144$ and $\omega_2 = 3.5320$ (a 0.5% detuning between the eigenfrequencies).

Beginning with the first nonlinear mode of the cantilever, the backbone curve of the dimensionless transverse displacement in $\mathbf{E}_y$ at the free end of the cantilever $w(L,t)/L$ (computed as the maximum of the absolute value of the displacement over one period of oscillation) is shown in Fig. 5.2(a). The same nonlinear behavior as found in § 3.3.1 of Chapter 3 is recovered both in 2D and 3D: the well-known hardening trend of the first nonlinear mode of the cantilever beam [58], [59], [229] is recovered. The maximum displacement w/L at the free end of the beam is identical when using both the 2D and 3D quaternion formulations, both of which follow the same pattern as that of Fig. 4(b) in § 3.3.1 (the backbone of which is inset in Fig. 5.2(a) for reference; here the internal resonance branches that were shown in § 3.3.1 are not computed for efficiency). A direct comparison to the backbones of § 3.3 is

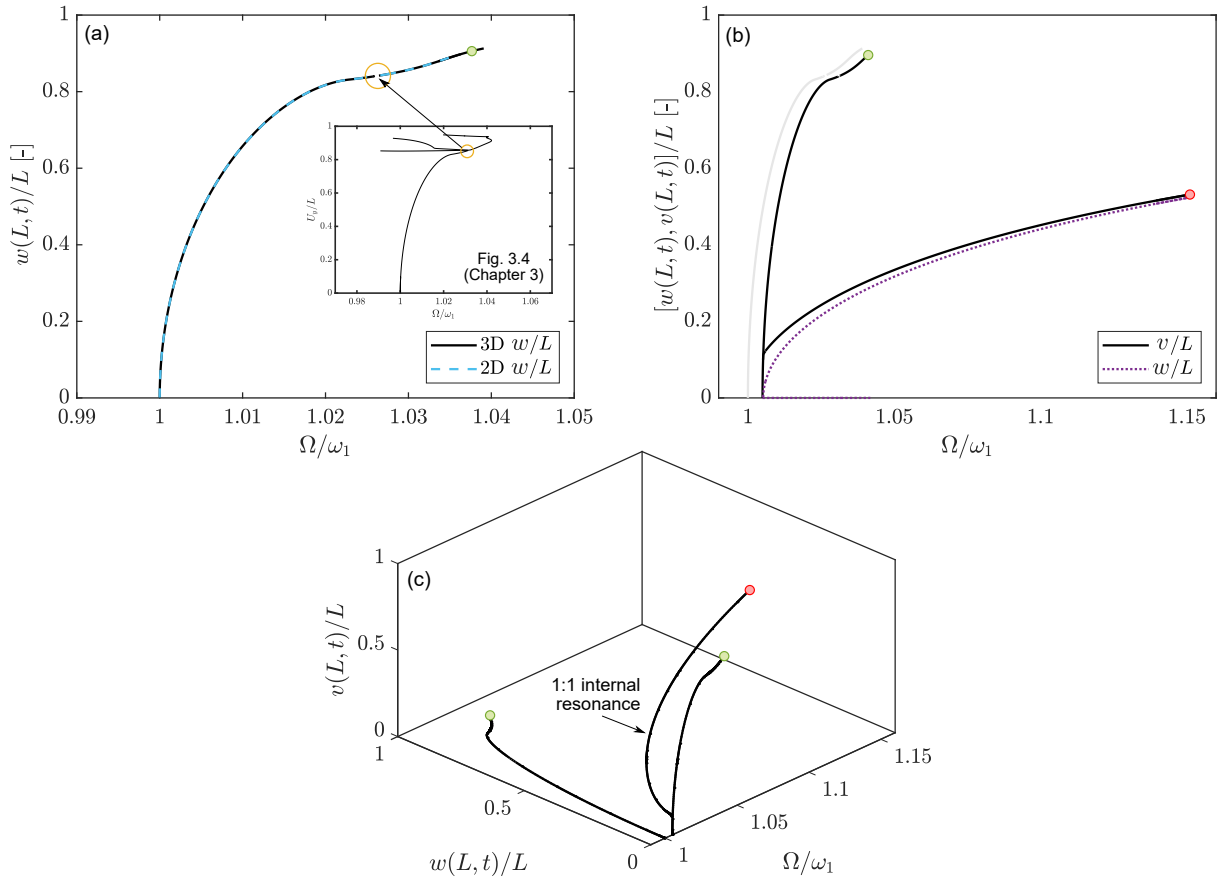

Figure 5.2: First nonlinear bending modes of the cantilever beam in the two transverse polarizations, (a) first nonlinear bending mode polarization: maximum amplitude of $w(L,t)/L$ over one period of oscillation in 2D and 3D, inset: U_y/L backbone of § 3.3.1 for comparison of the IR at high amplitude, (b) second nonlinear bending mode polarization: maximum amplitudes of $w(L,t)/L$ and $v(L,t)/L$ over one period of oscillation and 1:1 IR, (c) 3D visualization of the backbone curves.

performed in the next section.

The deformed shape of the cantilever is also traced at very large amplitude and shown in Fig. 5.3(a) and (b) for both transverse polarizations. The amplitudes along the backbone curves of Fig. 5.2 at which the deformed shapes are sketched are marked with green circles.

Of greater interest is the second nonlinear mode of the cantilever in 3D as it is on this mode that the 1:1 internal resonance manifests. The second nonlinear mode is shown in Fig. 5.2(b), where both the transverse displacement in $\mathbf{E}_y$ w/L and the transverse displacement in $\mathbf{E}_z$ v/L are depicted. It is clearly seen that at a certain amplitude in $v(L,t)$, there is a transfer of energy to the first nonlinear bending mode, exemplified by the takeoff of displacement $w(L,t)$ in the other transverse polarization. At this point, the cantilever begins to rotate in an elliptical motion, shown in Fig. 5.3(c). The amplitude at which Fig. 5.3(c) is sketched is marked by a red circle in Fig. 5.2(b). Fig. 5.3 illustrates both the deformed shape in 3D and, in Fig. 5.3(d)-(f), the projections of the deformed shape in each plane in order to better visualize the motion. In Fig. 5.2(b), the 1:1 internal resonance is located

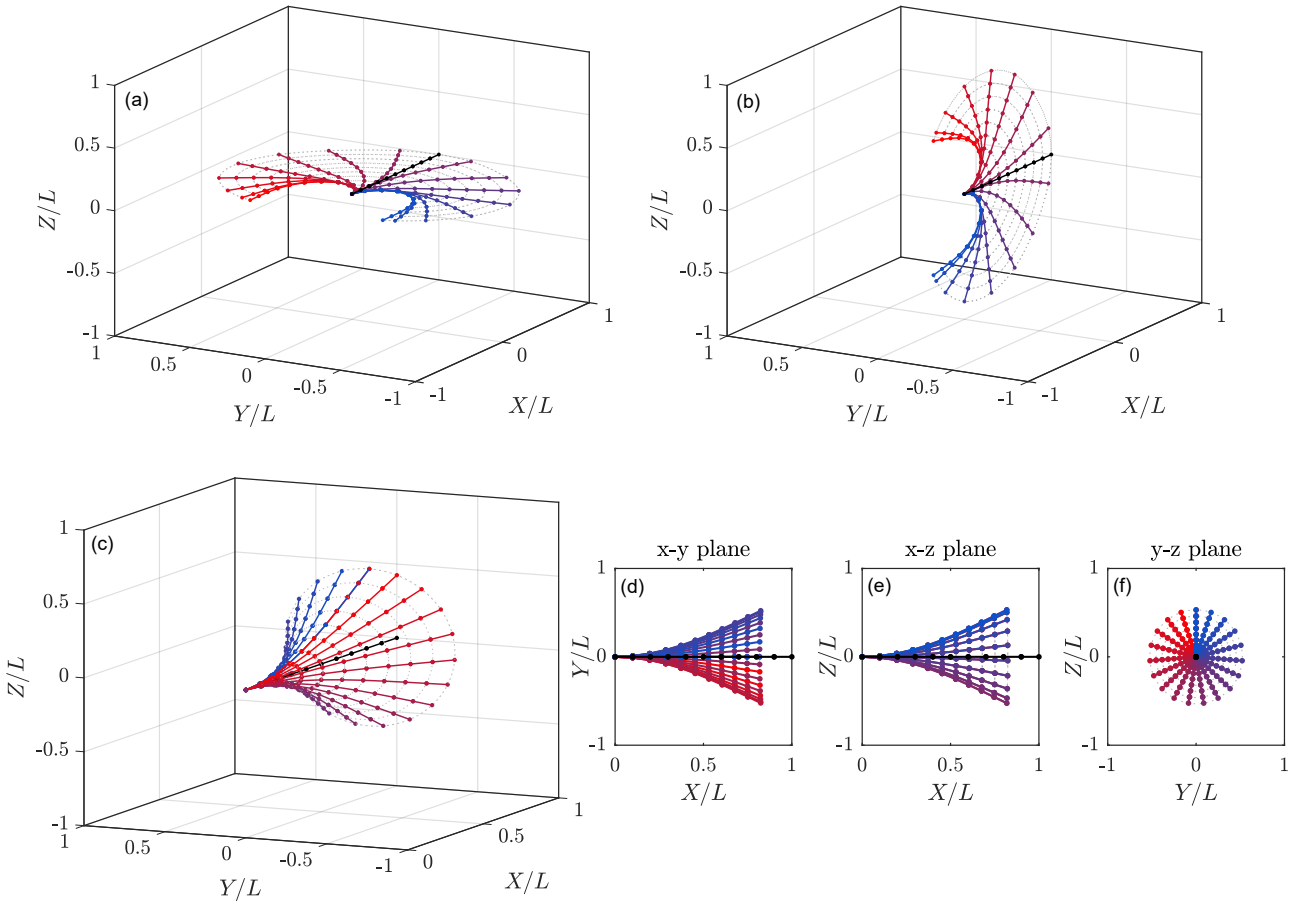

Figure 5.3: Deformed shapes of the cantilever beam, (a) high amplitude on the first polarization (green circle in Fig. 5.2(a)), (b) high amplitude on the second polarization (green circle in Fig. 5.2(b)), (c)-(f) 1:1 internal resonance between the polarizations and projections onto each plane (red circle in Fig. 5.2(b)).

at a frequency $\Omega/\omega_1 \simeq 1.005$ and at an amplitude of $v/L \simeq 0.1$, matching the results of [244]. The displacements v/L (in black) and w/L (in purple) are plotted together in Fig. 5.2(b) to demonstrate the transfer of energy from the $\mathbf{E}_z$-direction mode to the $\mathbf{E}_y$-direction mode. With only a small 0.5% difference between the eigenfrequencies of the two modes, it can be seen in Fig. 5.3(c) that the beam rotates in almost a perfect circle since the displacements w and v are almost equivalent, especially far from the birth point of the internal resonance branch.

Finally, the backbones are gathered in a 3D plot in Fig. 5.2(c) following the style of [88]. Each of the bending mode backbones are fixed in their respective planes whereas the 1:1 internal resonance branch has components in both w and v. The 3D plot clearly shows the transfer of energy from one polarization to the other.

Clamped-clamped beam Next, the 1:1 internal resonance of the (initially straight) clamped-clamped beam, with both ends of the beam blocked, is investigated following the same precedure as for the

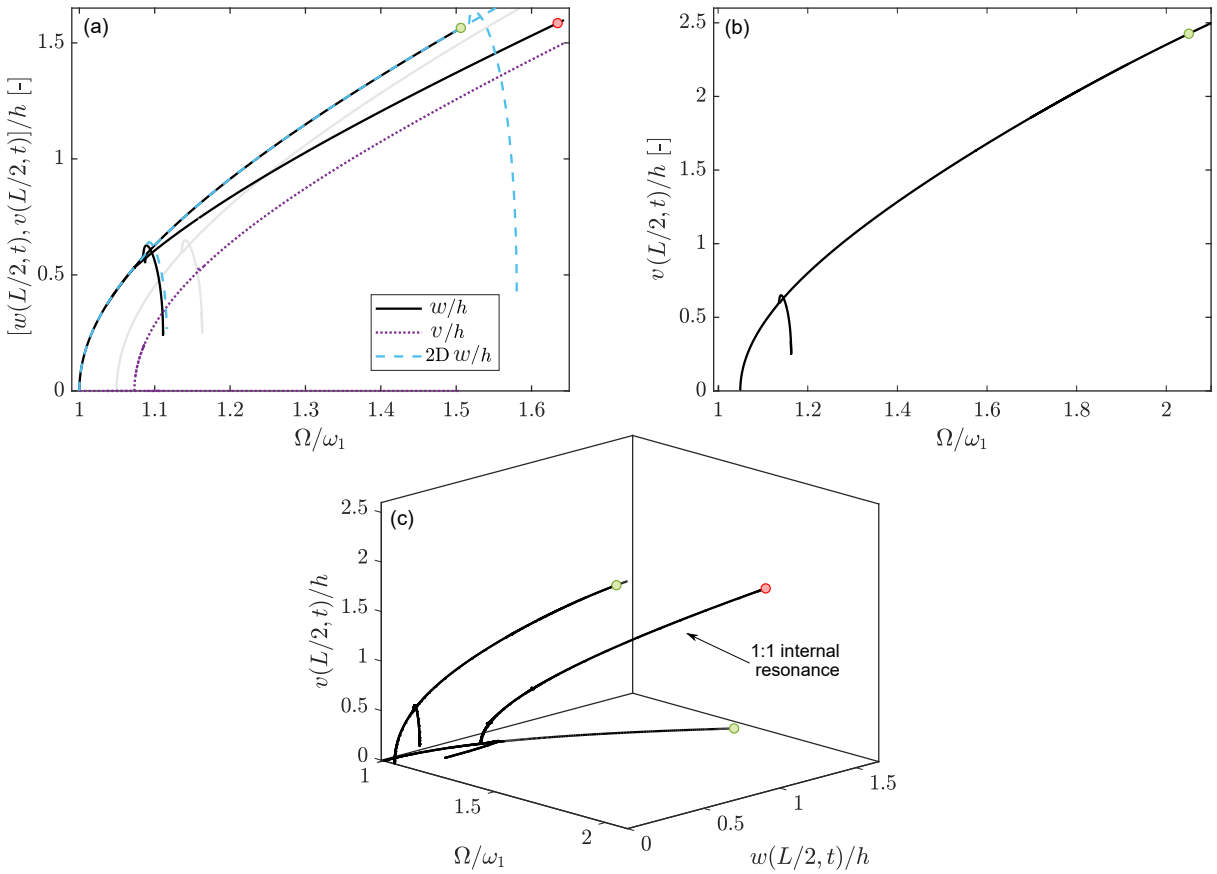

Figure 5.4: First nonlinear bending modes of the clamped-clamped beam in the two transverse polarizations, (a) first nonlinear bending mode polarization: maximum amplitude of $w(L,t)/h$ and $v(L,t)/h$ over one period of oscillation in 2D and 3D and 1:1 IR, (b) second nonlinear bending mode polarization: maximum amplitude of $v(L,t)/h$ over one period of oscillation, (c) 3D visualization of the backbone curves.

cantilever beam. The clamped-clamped beam of Shen *et al.* [217] is used ($L = 1$ m, $b = 0.0315$ m, $h = 0.03$) and normalized by L. The dimensions of the beam create a $\sim 5\%$ detuning between the first two (dimensionless) transverse bending eigenfrequencies, which are, in $\mathbf{E}_y$ and $\mathbf{E}_z$, $\omega_1 = 22.2459$ and $\omega_2 = 23.3445$, respectively.

The backbone curves of the clamped-clamped beam are depicted in the same way as for the cantilever beam. We depict w/h and v/h at the midpoint of the beam (the place of maximum displacement). The 1:1 internal resonance of the clamped-clamped beam is uncovered on the first nonlinear mode in contrast to the cantilever system (where it is uncovered on the second). The w/h backbone curve of the first nonlinear bending mode is shown in Fig. 5.4(a). As with the first nonlinear mode of the cantilever, the main backbone of the first nonlinear mode of the clamped-clamped beam, known to be hardening [58], [86], is found. The second branch depicting the 1:1 internal resonance of the clamped-clamped beam follows much of the same patterns of the cantilever beam: at a certain frequency, there is an energy transfer from the $\mathbf{E}_y$-direction polarization to the

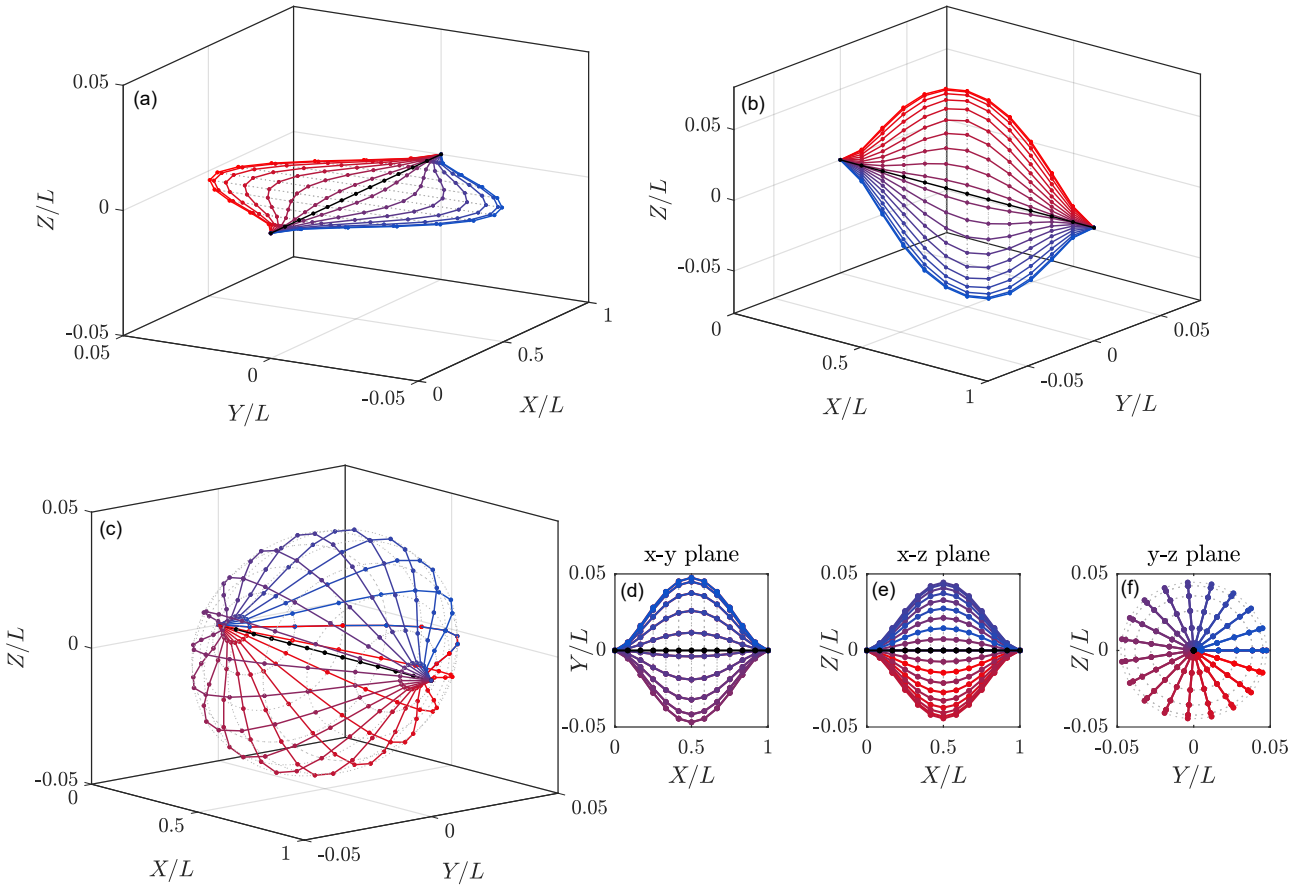

Figure 5.5: Deformed shapes of the clamped-clamped beam, (a) high amplitude on the first polarization (green circle in Fig. 5.4(a)), (b) high amplitude on the second polarization (green circle in Fig. 5.4(b)), (c)-(f) 1:1 internal resonance between the polarizations and projections onto each plane (red circle in Fig. 5.4(a)).

$\mathbf{E}_z$-direction where the displacement v/h begins to take off, resulting in the beam rotating along an elliptical trajectory. The deformed shapes of the rotating clamped-clamped beam at high amplitude and on its 1:1 internal resonance branch are shown in Fig. 5.5(a), (b) and (c), with projections onto each of the planes in Fig. 5.5(d)-(f). The coupling between the nonlinear modes occurs close to $\Omega/\omega_1 \simeq 1.073$ at an amplitude of $w/h \simeq 0.53$, which matches the reference solution of [217]. In [217], 3D beam finite elements were used in finding the 1:1 internal resonance of the clamped-clamped beam, yet our simplified 1D FE beam model is able to capture the same behavior. This could represent a significant savings in computational cost in simulating a 1D beam model in place of a full 3D beam model.

Furthermore, the w/h backbone computed in 3D is compared to the same backbone computed in 2D using the quaternion formulation, which is overlaid as the light blue dashed curve onto Fig. 5.4(a). The backbone in 2D is in perfect agreement with the backbone in 3D apart from a small shift in the location of the well-known 1:5 internal resonance of the clamped-clamped beam, found also in § 3.3.2 and in [86]. The shift in the location of the IR is due to small differences in the eigenfrequencies

between the 2D and 3D models, something which is discussed earlier in § 3.3.2. Nevertheless, the shape of the IR is exactly the same. The backbone curve of the other transverse polarization y/h is shown in Fig. 5.4(b) in order to visualize the behavior in the second bending polarization. The backbones are also once again combined in a 3D plot in Fig. 5.4(c) to more easily view the transfer of energy between the bending polarizations.

5.5.2 2D comparison with rotation matrix formulation

In the previous section, several references are made to the test cases of Chapter 3 using the 2D rotation matrix formulation. Since the rotation matrix formulation is validated by both the von Kármán model used in [86] in § 3.3.2 and the analytical model of Crespo da Silva and Glynn [24], [42], [46], [47] at low to moderate amplitudes in Chapter 4, a direct comparison between the two 2D formulations (rotation matrices vs. quaternions) serves to validate, if in agreement, the quaternion-based formulation of this chapter. Quadratic elements are used for the simulations in 5.5.1; a direct comparison, however, with the examples of Chapters 3 requires that the simulations be performed using the same type of element (in Chapters 3 and 4, they are linear). For this reason, the 2D simulations using the quaternion formulation are computed in this section using *linear* elements with the same number of variables as in Chapter 3 (number of elements, nodes and harmonics), summarized in Table 5.2. The linear elements induce an error when interpolating the quaternions terms due to them being insufficient for accurate interpolation of quaternions as mentioned in § 5.3. For this reason, a greater number of *linear* elements should be taken in the quaternion-based formulation to minimize any error.

Table 5.2: Mesh and harmonic parameters: number of discrete elements per structure used in numerical simulations, corresponding number FE nodes and harmonics retained in the HBM.

Structure	**Elements** N_e	**Nodes** $N_n = N_e + 1$	**Harmonics** H
Cantilever	20 or 30	21 or 31	20
Clamped-clamped	50	51	10

Cantilever First, we compare the first nonlinear mode of the cantilever beam computed with the quaternion formulation to the cantilever test case of § 3.3.1. The backbone curves of the rotation of the cross-section θ, the dimensionless transverse displacement at the free end of the cantilever $w(L,t)/L$ and the dimensionless axial displacement $u(L,t)/L$ (computed as the absolute value of the maximum displacement over one period of oscillation) are shown in Fig. 5.6(a), (b) and (c), respectively. In Fig. 5.6, three computations are shown: in black is the backbone curve of the rotation matrix formulation, a direct copy of the backbones of § 3.3.1, in blue is the 2D quaternion formulation with 20 elements (the same number as § 3.3.1) and in orange is the same 2D quaternion formulation with 30 elements. It is clearly seen from Fig. 5.6 that the quaternion formulation of this chapter yields exactly the same main backbone curve as the rotation matrix formulation of Chapter 3. This is a good sign, since we know from § 5.5.1 that the 2D and 3D quaternion formulations likewise yield the same results, thereby indicating that all three formulations are in agreement.

The difference between the blue (2D quat. with 20 elements) and orange (2D quat. with 30 elements) curves in Fig. 5.6(a)-(c) requires some comment, however. At higher amplitude, beginning around $\theta \simeq 0.5\pi$ [rad], the computation with only 20 elements begins to diverge from the computation

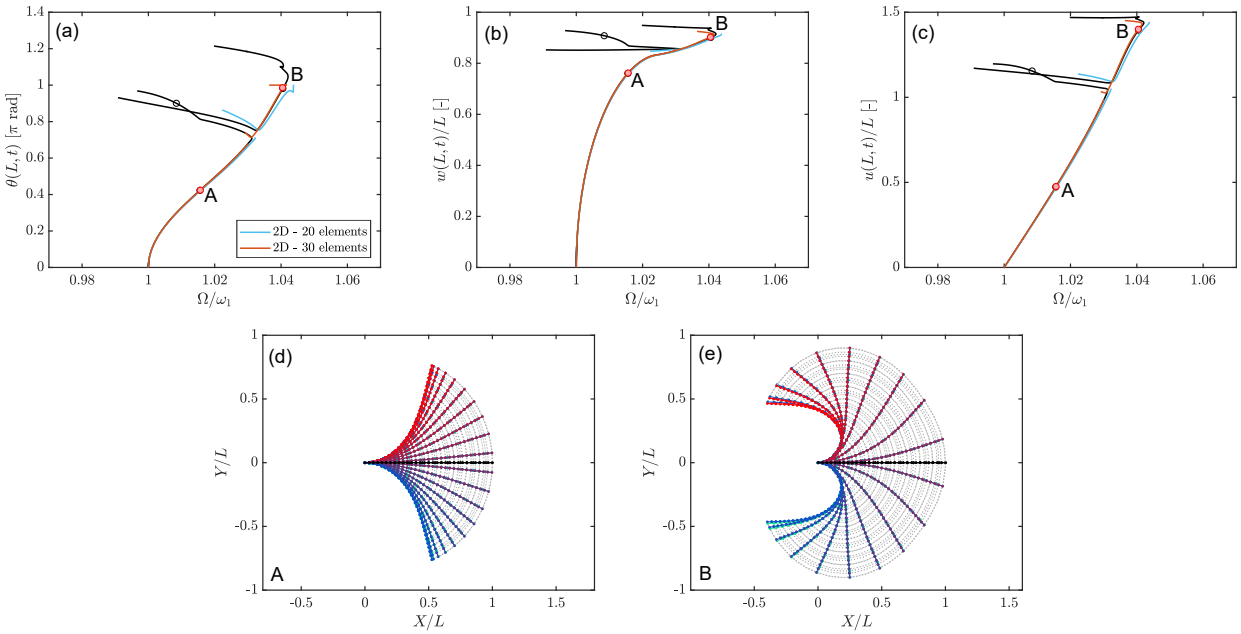

Figure 5.6: Comparison of the 2D formulations' first nonlinear mode of the cantilever beam. The backbone curve in black is a reproduction of the one shown in § 3.3.1 (2D w/ rotation matrices), (a) maximum amplitude of $\theta(L,t)$ over one period of oscillation, (b) maximum amplitude of the transverse displacement $w(L,t)/L$, (c) maximum amplitude of the axial displacement $u(L,t)/L$, (d) deformed shape at point A, representing 20 snapshots over one half period of motion, overlaid onto the deformed shapes of § 3.3.1, (e) deformed shape at point B.

with 30 elements and the backbone of Chapter 3, indicating that the finite element solution based on the quaternion formulation of the equations of motion is not fully converged with only 20 (linear) elements. This observation is interesting as it demonstrates that, for the same (linear) element, *more elements are required with the quaternion formulation for the solution to be converged.* It is shown in Appendix A.2 that the auxiliary variables do have a non-negligible influence on the numerical simulations, so that different auxiliary variable definitions may have a part in the difference between the quaternion and rotation matrix formulations. Moreover, recall from the beginning of § 5.3 that the quaternion formulation is poorly adapted to a discretization based on (linear) polynomial shape functions.

Finally, the deformed shapes at moderate (point A) and high (point B) amplitude along the backbone curve computed using the quaternion formulation (with 30 elements) are overlaid onto the deformed shapes computed using the rotation matrix formulation of § 3.3.1 in Fig. 5.6(d) and (e), respectively. Note that since the continuation branches of the two computations are not exactly identical, it is not possible to trace the deformed shape at the exact same point along the two backbone curves. Instead, the closest point of the quaternion computation with 30 elements to the deformed shapes of § 3.3.1 are selected. It is easily seen in Fig. 5.6(d) and (e) that the deformed shapes are basically identical. Since the internal resonance offshoots in Fig. 5.6(a)-(c) are not the same between the 3 computations, the deformed shape on the IR branch is not traced.

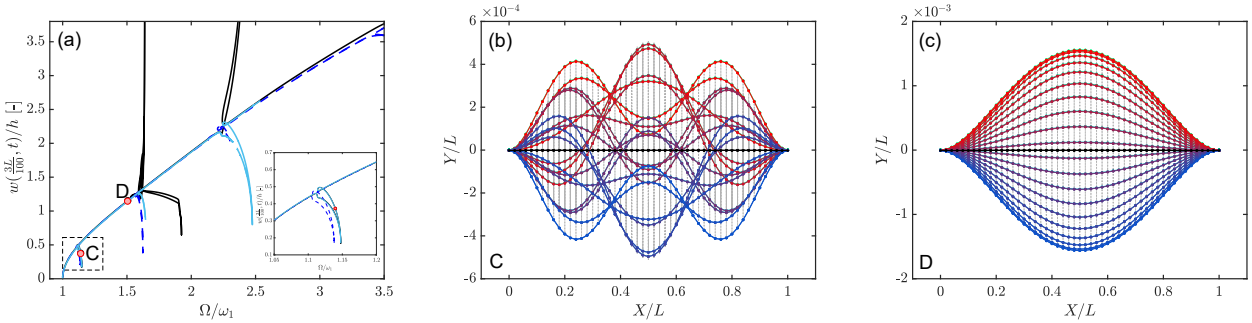

Figure 5.7: Comparison of the 2D formulations' first nonlinear mode of the clamped-clamped beam. The backbone curve in black (2D rotation matrices) and of the nonlinear von Kármán in dashed blue are a reproduction of those shown in § 3.3.2, (a) maximum amplitude of $w(\frac{3L}{100},t)/h$ over one period of oscillation, (b) deformed shape at point C, representing 20 snapshots over one half period of motion, overlaid onto the deformed shapes of § 3.3.2, (e) deformed shape at point D.

Clamped-clamped beam Another comparison is made between the two 2D formulations using the clamped-clamped beam test case of § 3.3.2. The clamped-clamped beam represents an interesting test case beyond the reasons given at the beginning of this section since, as in § 3.3.2, the geometrically exact model can be validated with the nonlinear von Kármán model. To this end, the simulation of § 3.3.2 is carried out using the 2D quaternion formulation and the results are shown in Fig. 5.7. The backbone curve of the first nonlinear mode of the clamped-clamped beam is computed as the maximum transverse displacement over one period of oscillation at the node located at $s = \frac{3L}{100}$ on the beam (normalized by the thickness h of the beam) using the quaternion formulation. The quaternion-based backbone curve is overlaid onto a copy of the rotation matrix backbone curve (Fig. 3.7(a) from § 3.3.2) in Fig. 5.7(a). Additionally, a zoom onto the 1:5 internal resonance is shown in the inset of Fig. 5.7(a).

First, it can be seen that as with the cantilever test case, the 2D computation with quaternions exactly matches the 2D computation with rotation matrices, with even the zoom onto the 1:5 internal resonance matching nearly exactly (in contrast to the 3D computation, where the 1:5 IR is slightly shifted from the 2D computation). This observation suggests that the two computations (when converged with a sufficient number of elements) are (nearly) identical, with even the eigenvalues being computed identically. As in § 3.3.2, the other branches of internal resonance are not as similar in shape as the 1:5 internal resonance (point C), but all occur at nearly identical locations. The main backbone curve, however, is nearly identical across all three models until the von Kármán model begins to diverge around a transverse displacement of $\sim w = 2.5h$. Furthermore, since 50 linear finite elements are used in the simulations of Fig. 5.7, it can be said that with 50 elements, the quaternion computation is sufficiently converged so as to exactly match the results of the rotation matrix computation.

Finally, the deformed shapes at points C and D along the backbone curve computed with the quaternion formulation are overlaid onto those recopied from § 3.3.2. Unlike for the cantilever beam, here the 1:5 IR branch is nearly identical between the 2D quaternion and rotation matrix formulations, so that the deformed shape [Fig. 5.7(b)] is nearly identical. This is likewise the case for the higher amplitude deformed shape, shown in Fig. 5.7(c).

5.6 Conclusions, limitations and future work

In this chapter, an extension of the work of Chapter 3 to three dimensions has been presented. In 3D, rather than continuing with the rotation matrix parametrization of Chapter 3, the rotations are parametrized through the use of unit quaternions, 4-dimensional complex numbers that exactly represent the three rotation degrees of freedom about $(\mathbf{E}_x, \mathbf{E}_y, \mathbf{E}_z)$. First, the geometrically exact beam model, discretized into finite elements, is expressed in 3D with quaternion parametrization of the rotations based on the quaternion algebra. The beam model is then reduced to 2D in-plane motions with the more simple equations being written explicitly for a direct comparison to the rotation matrix formulation. The cantilever beam of § 3.3.1 and the clamped-clamped beam of § 3.3.2 serve as test cases in order to validate the quaternion formulation with the results of Chapter 3 and other works in the literature.

The limitations of this method lay the foundation for future work. Firstly, due to the very large number of degrees of freedom involved in 3D computations, we are limited to a certain extent by the computation time when many nodes and harmonics are included in the simulation. Not only are there more degrees of freedom in 3D compared to plane motions, but the quaternion elements of the quaternion-based formulation mean that more nodes (and therefore degrees of freedom) are involved in the computation. Although the 3D simulations here based on a 1D geometrically exact beam model remain more efficient than full 3D simulations based on 3D beam elements using *e.g.* a FE software package, the 3D simulations shown here are limited to structures composed of ~ 15 or fewer elements unless the number of harmonics kept in the HBM is reduced (which can lead to inaccuracy if the truncation is too stringent). Ongoing research is looking to find ways to increase the computational efficiency of MANLAB, especially when many degrees of freedom are involved.

Finally, within the scope of this thesis, it was not possible to carry out a full analysis of the computational performance of the 2D quaternion formulation, especially when compared to the 2D rotation matrix formulation as mentioned at the beginning of § 5.4. Even though it can be said that the two beam models "compute the same thing," nevertheless it is still of scientific interest to compare different ways of writing the equations of motion with the aim of improving computational efficiency. A full study comparing the computational efficiency of the two approaches is envisioned, to see if the quaternion formulation is a more efficient method for computing the complex dynamics of flexible 1D systems. A method of comparing the computational speeds of the two approaches must be devised, which would take into account the method of carrying out the quadratic recast (since some ways of rewriting the system are more efficient than others), the initialization time of the system based on the number of degrees of freedom, the number of computed continuation branches, the computation time per branch, *etc.* Future work beyond this can then investigate other ways of parametrizing the rotation terms, *e.g.* based on Lie groups or other methods, and interpolating the rotation field in order to further accelerate the computation time.

Chapter 6

Phase resonance experimental testing of highly flexible structures for measurement of conservative nonlinear modes and nonlinear damping estimation

In what has been presented up to this point, the focus has been strictly on numerical simulations based on the geometrically exact beam model solved in the frequency domain (for plane motions in Chapter 3 and for full 3D motions in Chapter 5). In this chapter, we seek to validate the numerical model with experimental results. Experimental validation brings a new layer of appeal to numerical models since in this process they are confirmed to represent the true physics. In this chapter, the numerical model discussed throughout Chapters 2 - 5 for the simulation of highly flexible slender structures is validated with dedicated experiments in large amplitude vibration. The contents of this chapter are part of a pre-print currently under preparation to be submitted to the journal *Mechanical Systems and Signal Processing* as "Phase resonance testing of highly flexible structures: Measurement of conservative nonlinear modes and nonlinear damping identification."

The experiments of this chapter are carried out using techniques for the experimental measurement of the nonlinear modes (referred to in this chapter as *conservative* nonlinear modes or CNMs so as to distinguish them from dissipative nonlinear modes, a topic which is discussed in § 6.2). In particular, we make use of the concept known in the literature as *phase resonance*, which essentially indicates imposing a particular phase lag between the driving force and the system's response such that the nonlinear modes are measured. Beyond the conservative effects, phase resonance can also be used for damping estimation, which has historically been a subject given significant attention. In the experiments, the phase resonance condition is moderated using a Phase-Locked Loop, an algorithm for control of vibrating systems. The experiments are performed on very slender stainless steel cantilever beams to investigate the first three nonlinear modes. The results of the experiments are then compared to the numerical model of Chapters 3 and 4, notably with the inclusion of gravity in the model as it was shown in § 4.4.2 of Chapter 4 to have a significant effect on the first nonlinear mode of cantilever beams.

The chapter begins with a review of the current state of the art and an overview of the study, including the main originalities of our work, in § 6.1. Then, the theory behind phase resonance and its justification for the measurement of conservative nonlinear modes is presented in § 6.2. Some

discussion on current work on this topic in the literature, including the measurement of damped nonlinear modes, is also presented in this section. In § 6.3, numerical simulations are carried out using the geometrically exact finite element model of Chapter 4 to validate phase resonance for the measurement of the conservative nonlinear modes and damping estimation. Following the numerical justification of phase resonance in this context, the experiments based on Phase-Locked Loop control of cantilever beams in large amplitude vibration are described in § 6.4. The experimental results are compared to numerical simulations using the model of Chapter 4 in § 6.5. Concluding remarks and a summary of the current state of our experimental results are gathered in § 6.6.

Table of Contents - Chapter 6

6.1 Introduction

The study of highly flexible slender beam structures, where the characteristic dimension of the structure greatly exceeds the dimensions of the cross-section, has in recent years increased in popularity because of their many uses in industry. Examples include cables and cable bundles, hoses, wires, ropes and slender blades and wings and are commonly found in the automotive [45], [151], aerospace [3], [155], [223], [229] and electronic (in micro- and nano-electromechanical systems) industries or in energy harvesting with piezoelectric patches [85], [99], [139], [244], [257]. These unique structures exhibit

complex nonlinear behavior in dynamics owing to their unique geometry which induces a very low stiffness in bending that allows the structure to deform at very large amplitudes. Reliable and efficient numerical methods capable of solving these highly nonlinear systems even at very large amplitudes of motion have been developed (Chapters 3 and 4) [68], [69]. It is of great importance, however, to validate these numerical models with experimental results, which is precisely the purpose of the present work. Experimental investigations involving flexible or elastic structures have been documented in the literature [11], [12], [53], [54], [70], [71], [150], [226], but more work is still needed especially at very large amplitudes of motion.

In particular, we are concerned with the nonlinear modes of highly flexible systems, alternatively defined as periodic solutions of the conservative system in free vibration or as invariant manifolds of the phase space [124], [214], [237]. The nonlinear modes provide a useful framework for the study of nonlinear dynamics as they efficiently map the *backbone curve*, the collection of nonlinear resonances in a frequency / amplitude plot, thereby demonstrating with only a single computation the evolution of the frequency with increasing amplitude of the motion. Numerical computation of nonlinear modes has been extensively developed in recent decades [124], [180], [195], but experimental measurement of the nonlinear modes has only been investigated very recently. In [178], a method for the experimental measurement of the CNMs is outlined based on the idea of *phase resonance*. In order to measure the *conservative* nonlinear mode experimentally (where dissipative and external forces are present), a phase lag is imposed between the forcing and dissipative terms with respect to the response of the system. At this precise phase lag (*i.e.* at phase resonance), an equilibrium between the dissipative and forcing terms is created such that both terms are "canceled" from the system response and the underlying free conservative system (the nonlinear modes) is measured. Several experimental works have applied these principles to measure the experimental nonlinear modes [60], [194], [207], [252]. In particular, phase resonance is at the heart of the Phase-Locked Loop, a controller for the experimental characterization (frequency responses and nonlinear modes) of nonlinear systems [1], [60], [184]. Damped nonlinear modes also exist [128], [133], but are not the focus of the present work.

The theory behind the concept of phase resonance for the measurement of conservative nonlinear modes shows that it is valid regardless of the form of the dissipative forces. Beyond measurement of the nonlinear modes, however, the effects and form of damping become very important influences on the response of the system and must be modeled appropriately. At very small amplitudes of motion, a linear damping model such as Rayleigh damping might be appropriate. By contrast, at higher amplitudes, the damping model can take different nonlinear forms. Experimental and numerical investigations by Colin *et al.* [42] on moderate amplitude vibrations of cantilever beams found the fluid-solid interaction due to air drag led to a quadratic damping effect in open-air experiments. In the work of Farokhi *et al.* [71], a viscoelastic Kelvin-Voigt model is used to match experimental and numerical forced response curves of cantilever beams at very large amplitudes of motion in vacuum, where the effect of air is greatly reduced. Other studies by Amabili *et al.* [4], [6]–[9] further indicate that this Kelvin-Voigt model gives rise to a cubic damping effect at large amplitudes of motion due to the presence of geometrical nonlinearities.

In this chapter, we propose an experimental investigation and validation of the geometrically exact model of Chapters 3 and 4 for the simulation of highly flexible structures. We derive a technique for the experimental measurement of conservative nonlinear modes and to characterize damping effects, and extend it naturally to a large class of models, including rigid body mechanisms. The main originalities of this work include:

- a theoretical and experimental proof of the measurement of a conservative nonlinear mode using

an experimental phase resonance in case of arbitrary nonlinear damping,

- the estimation of the law of damping as function of the amplitude of motion,
- the experimental validation of a geometrically exact model on the first three nonlinear modes.

The study begins with a complete theoretical background and justification for the use of phase resonance to measure conservative nonlinear modes in § 6.2. In § 6.3, numerical simulations using phase resonance investigate the equivalence between conservative nonlinear modes computed as in Chapters 3 and 4 and with phase resonance. Then, the experiments involving vibration control of highly flexible structures and details on the Phase-Locked Loop controller are presented in § 6.4. The results of the experiments are compared to theoretical results using the numerical model in § 6.5. Finally, concluding remarks and a recap of the main results are provided in § 6.6.

6.2 Phase resonance and conservative nonlinear modes

6.2.1 Class of models

We consider a nonlinear system that is modeled by the following N-dimensional problem ($N \in \mathbb{N}$):

$$\boldsymbol{M}(\boldsymbol{x})\ddot{\boldsymbol{x}} + \boldsymbol{f}_{\mathrm{d}}(\boldsymbol{x},\dot{\boldsymbol{x}}) + \boldsymbol{f}_{\mathrm{c}}(\boldsymbol{x},\dot{\boldsymbol{x}}) = \boldsymbol{f}_{\mathrm{e}}, \tag{6.1}$$

where $\boldsymbol{x}(t)$ is the N-dimensional displacement vector, a function of time t, $\dot{\diamond} = \mathrm{d}\diamond/\mathrm{d}t$, $\boldsymbol{M}(\boldsymbol{x})$ is the $N \times N$ inertia matrix which may depend on $\boldsymbol{x}$ because of inertial nonlinearities, $\boldsymbol{f}_{\mathrm{d}}(\dot{\boldsymbol{x}},\boldsymbol{x})$ is the N-dimensional dissipative force vector that depends on the velocity $\dot{\boldsymbol{x}}$ and on the displacement $\boldsymbol{x}$, $\boldsymbol{f}_{\mathrm{c}}(\boldsymbol{x},\dot{\boldsymbol{x}})$ is the N-dimensional internal conservative force vector that depends on $\boldsymbol{x}$ and on $\dot{\boldsymbol{x}}$ in the case of inertial nonlinearities, and $\boldsymbol{f}_{\mathrm{e}}(t)$ is the N-dimensional external force vector that depends on time. Eq. (6.1) is very general and well-suited for modeling several types of systems. As shown in what follows, it can first be applied to a mechanical elastic structure subjected to geometrical nonlinearities and discretized either using a Galerkin method or a finite element (FE) method [236]. It can also be applied to model a multibody system without constraints [101]. Gyroscopic forces that lead to a skew-symmetric operator and appear in particular in rotating systems [78] are not considered in this work.

The inertia term $\boldsymbol{M}(\boldsymbol{x})\ddot{\boldsymbol{x}}$ and the force vector $\boldsymbol{f}_{\mathrm{c}}$ gather all the *conservative* contributions in the model. The latter include all elastic forces and, in some cases, nonlinear inertial forces, leading to its possible dependence on the velocity. For illustration, consider the two classical main families of geometrically nonlinear structures (see *e.g.* Chapter 2 or [236]). The first family gathers structures for which the membrane behavior is constrained, either by boundary conditions (beams with restrained ends [130], [136]) or because of 2D membrane effects (such as plates or shells [5], [230], [235]). In this case, the von Kármán family of models leads to a $\boldsymbol{f}_{\mathrm{c}}(\boldsymbol{x})$ which is a third order polynomial in $\boldsymbol{x}$ and does not depend on $\dot{\boldsymbol{x}}$. The second family of models gathers highly flexible structures such as cantilevers, rings, tree-like beam structures, ribbons, *etc.* (see Chapter 3 or [17]), for which the deformation of the centerline can reach very large amplitudes, such that the structures can be subjected to very large rotations of the cross-sections for moderate external forces. In this case, $\boldsymbol{f}_{\mathrm{c}}(\boldsymbol{x})$ includes trigonometric functions of $\boldsymbol{x}$ (as in Chapter 3). This model can be truncated to the third order in the transverse displacement and discretized with a Galerkin procedure, leading to inertial nonlinearities. These inertial nonlinearities, classical for multibody systems (see an example in Appendix D.1.1), lead to a mass matrix $\boldsymbol{M}(\boldsymbol{x})$ quadratic in $\boldsymbol{x}$ and an internal force vector $\boldsymbol{f}_{\mathrm{c}}(\boldsymbol{x},\dot{\boldsymbol{x}})$ quadratic in $\dot{\boldsymbol{x}}$, in addition

to $\boldsymbol{f}_{\rm c}(\boldsymbol{x},\dot{\boldsymbol{x}})$ being cubic in $\boldsymbol{x}$ (see [46], [229] and Appendix D.1.2). If three-dimensional finite elements are used, $\boldsymbol{f}_{\rm c}(\boldsymbol{x})$ is a third order polynomial in $\boldsymbol{x}$ in any case [249], [250]. The conservative character of $\boldsymbol{f}_{\rm c}(\boldsymbol{x})$ is a consequence of a potential energy (for the elastic forces) and a kinetic energy (for the inertial forces).

The force vector $\boldsymbol{f}_{\rm d}$ gathers all *non conservative* contributions responsible for the damping of the oscillations. In the simplest case, this term takes the form of a linear viscous damping $\boldsymbol{f}_{\rm d} = \boldsymbol{C}\dot{\boldsymbol{x}}$ with $\boldsymbol{C}$ a $N \times N$ constant matrix. However, $\boldsymbol{f}_{\rm d}$ can also be nonlinear due to several different causes. For example, friction forces lead to a nonlinear damping which can be modeled with various contact laws, the simplest being a Coulomb model, intrinsically non-smooth (see *e.g.* [241]). Aeroelastic drag forces are often modeled with quadratic terms in $\dot{\boldsymbol{x}}$ (see [42] and Appendix D.1.3). Nonlinear damping can also be caused by internal dissipation in the form of viscoelastic forces that are nonlinear because of the geometrical nonlinearities, in which case $\boldsymbol{f}_{\rm d}$ becomes $\boldsymbol{f}_{\rm d} = \boldsymbol{C}(\boldsymbol{x})\dot{\boldsymbol{x}}$ with $\boldsymbol{C}$ quadratic in $\boldsymbol{x}$ (see [7], [71] and Appendix D.1.2). Finally, special materials such as piezoelectric also manifest nonlinear dissipation forces (see [140] and Appendix D.1.4).

As described in the following sections, the present work focuses on systems that can be modeled by Eq. (6.1) where $\boldsymbol{M}(\boldsymbol{x})$, $\boldsymbol{f}_{\rm d}(\boldsymbol{x},\dot{\boldsymbol{x}})$ and $\boldsymbol{f}_{\rm c}(\boldsymbol{x},\dot{\boldsymbol{x}})$ are smooth functions of $\boldsymbol{x}$ and $\dot{\boldsymbol{x}}$. This excludes, for example, the case of dry friction forces (which are intrinsically non-smooth). The distinction between $\boldsymbol{f}_{\rm c}$ and $\boldsymbol{f}_{\rm d}$ and some important properties will be clarified in what follows.

6.2.2 Conservative nonlinear modes

Considering the nonlinear problem Eq. (6.1), it is common to define its nonlinear modes as an extension to the nonlinear range of the "linear" eigenmodes of the underlying linear and undamped system, defined by the pairs of eigenfrequencies / eigenshapes $(\omega_i, \boldsymbol{\Phi}_i)$, $i = 1, \dots N$, which are solutions of:

$$\Big[\boldsymbol{K} - \omega^2 \boldsymbol{M}(\boldsymbol{0})\Big]\boldsymbol{\Phi} = \boldsymbol{0}, \quad \boldsymbol{K} = \left.\frac{\partial \boldsymbol{f}_{\rm c}}{\partial \boldsymbol{x}}\right|_{(\boldsymbol{x},\dot{\boldsymbol{x}})=(\boldsymbol{0},\boldsymbol{0})}, \tag{6.2}$$

with $\boldsymbol{K}$ the stiffness matrix and where the equilibrium point of the system is assumed as $(\boldsymbol{x},\dot{\boldsymbol{x}}) = (\boldsymbol{0},\boldsymbol{0})$. These *conservative nonlinear modes* (CNMs)[1] are particular solutions $\boldsymbol{x}_{\rm cnm}(t)$ of the undamped nonlinear problem Eq. (6.1) in free vibration:

$$\boldsymbol{M}(\boldsymbol{x}_{\rm cnm})\ddot{\boldsymbol{x}}_{\rm cnm} + \boldsymbol{f}_{\rm c}(\boldsymbol{x}_{\rm cnm}, \dot{\boldsymbol{x}}_{\rm cnm}) = \boldsymbol{0}, \tag{6.3}$$

and have two equivalent definitions. The CNMs can be defined (i) as invariant manifolds of the phase space [214], [237] or (ii) as families of periodic solutions of Eq. (6.3) [124]. The two definitions are equivalent since any motion initiated on a periodic orbit remains in this periodic orbit and thus lies in an invariant manifold of the phase space. More theoretically, their existence is proved by a theorem of Lyapunov [147], which states that, with no internal resonance, there exist N two-dimensional CNMs in the phase space that emerge from the equilibrium point and are tangent to the N eigenplanes at this point. They are sometimes called Lyapunov Subcenter Manifolds (LSM) since their union is the center manifold [56], [123]. In the same way as for the eigenmodes of the linear underlying system,

[1] Other terminologies in the literature are Nonlinear Normal Mode (NNM) and Lyapunov Subcenter Manifold (LSM). We choose to use the CNM terminology here in order to avoid the term "normal" initially brought by Rosenberg [201] and which is sometimes synonymous with "orthogonal," which is not appropriate for a nonlinear mode. A NNM can also be a nonlinear mode of the damped system in some texts [193], [232]. We choose not to use "LSM" since we prefer to use the "Nonlinear Mode" terminology, which is closer to the perspective of a structural mechanics engineer.

a CNM is characterized by a fundamental angular frequency ω and a deformed shape $\boldsymbol{x}_{\text{cnm}}(t)$ which are functions of the amplitude of the motion. Plotting ω as a function of the amplitude leads to the backbone curve of the CNM.

It is also possible to define nonlinear modes of the damped system, *i.e.* solutions of Eq. (6.3) in free vibration (with $\boldsymbol{f}_{\text{e}} = \boldsymbol{0}$). Contrary to the CNM, several nonequivalent definitions coexist, proposed by several authors independently to fulfill a given requirement. For model reduction purposes, the invariant manifold definition still exists for the case of damping and smooth nonlinearities [103], [193], [232], [236]. For non-smooth nonlinearities, mainly for applications with friction damping, damped nonlinear modes have been defined in order to compute the skeleton of frequency responses as well as for model identification. A first definition is a family of pseudo-periodic motions, obtained with a Fourier-Galerkin expansion of the dynamics [133]. Another definition is as families of periodic solutions of the homogeneous version of Eq. (6.3), where a fictitious negative linear damping term is added [128], [207].

In practice, nonlinear modes are of great interest for the same reasons as the eigenmodes of the linear underlying system. They define the nonlinear resonances of the system, being the skeleton of its frequency response, and are thus an efficient way to summarize the main dynamical characteristic of a system [34], [124] or can be used for system identification [60]. In addition, nonlinear modes are of great importance in defining accurate reduced order models of the system [236], [237]. Here, we focus principally on CNMs as there is no ambiguity in their definition. They are useful in the study of geometrically nonlinear structures for which the damping is typically weak, such that the conservative backbone curves lie very close to the resonances of the damped and forced system [34], [56].

6.2.3 Monophase conservative nonlinear mode

If no internal resonance is activated, it is often observed and claimed in the literature that a given CNM $\boldsymbol{x}_{\text{cnm}}(t)$ is periodic and monophase [178]. It is defined as:

$$\boldsymbol{x}_{\text{cnm}}(t) \simeq \hat{\boldsymbol{x}}_0 + \sum_{h=1}^{H} \hat{\boldsymbol{x}}_h \cos(h\omega t), \tag{6.4}$$

where the above (real) Fourier series has been truncated to H harmonics and with $\hat{\boldsymbol{x}}_h \in \mathbb{R}^N$, $h \in \mathbb{N}$ defining the amplitude vector of the hth harmonic and ω the fundamental angular frequency.

This monophase property is the natural extension of the "linear" mode shape $\boldsymbol{\Phi}_i$ of the ith mode when the amplitude grows and thus when the motion on the invariant manifold moves away from the origin. Then, we can consider the motion on the ith "linear" mode shape, valid close to the equilibrium point, as:

$$\boldsymbol{x}_{\text{lm}}(t) = \boldsymbol{\Phi}_i \cos\omega_i t, \tag{6.5}$$

which is equivalent to imposing $\omega = \omega_i$, $\hat{\boldsymbol{x}}_1 = \boldsymbol{\Phi}_i$ and $\hat{\boldsymbol{x}}_h = \boldsymbol{0}$ for $h = 0, 2, 3$, in Eq. (6.4). It is assumed that the conservative force vector $\boldsymbol{f}_{\text{c}}(\boldsymbol{x}, \dot{\boldsymbol{x}})$ and the mass matrix $\boldsymbol{M}(\boldsymbol{x})$ are smooth around the equilibrium point $(\boldsymbol{x}, \dot{\boldsymbol{x}}) = (\boldsymbol{0}, \boldsymbol{0})$, and that $\boldsymbol{f}_{\text{c}}(\boldsymbol{x}, \dot{\boldsymbol{x}})$ is an even function of $\dot{\boldsymbol{x}}$ (this second property will be addressed in §6.2.4). Inserting the linear modal motion Eq. (6.5) into Eq. (6.3), it can be shown (see Appendix D.2) that the conservative forces are also monophase:

$$\boldsymbol{M}(\boldsymbol{x}_{\text{lm}})\ddot{\boldsymbol{x}}_{\text{lm}} + \boldsymbol{f}_{\text{c}}(\boldsymbol{x}_{\text{lm}}, \dot{\boldsymbol{x}}_{\text{lm}}) = \hat{\boldsymbol{f}}_{\text{c}0} + \sum_{h=1}^{H} \hat{\boldsymbol{f}}_{ch} \cos(h\omega t), \tag{6.6}$$

where $\hat{\boldsymbol{f}}_{ch} \in \mathbb{R}^N$. The nonlinearities in the conservative part of Eq. (6.1), then, naturally create harmonics that are only in phase with one another. The balancing of harmonics in Eq. (6.3) thus proves that the monophase CNM of Eq. (6.4) is an admissible and natural solution. It is the simplest form that can be obtained for a CNM and is characteristic of the main part of a backbone curve away from the internal resonances "tongues" or "offshoots" (recall § 3.5 of Chapter 3). In places of internal resonance, this solution is still admissible in some cases (in Appendix D.3, it is shown on an example that the CNM remains monophase in a 1:3 internal resonance branch, but has components in quadrature for a 1:2 branch which emanates from the main branch because of pitchfork bifurcations). In other cases, such as internal resonance at low amplitude when the "linear" natural frequencies are tuned, some phase quadrature between the components of $\boldsymbol{x}_{\text{cnm}}$ can be observed, resulting in non-monophase modes (referring to [87], [213], Appendix D.3 shows that for a 1:1 internal resonance, the "normal" coupled modes of a 1:1 internal resonance are monophase whereas the "elliptic modes" have some components in phase quadrature, as with the "parabolic modes" of a 1:2 internal resonance which have also components in phase quadrature).

The monophase form of the CNM (6.4) can be simplified further if there are symmetries in the system, such as for plate and straight beams structures for which the transverse motion is symmetrical. In this case, the components of $\boldsymbol{x}_{\text{cnm}}$ related to the bending motion have only odd harmonics whereas the ones related to the axial / membrane motion have only even harmonics (see Appendix D.5). This property is no longer valid in the case of symmetry breaking bifurcations, meaning that asymmetric responses can also be solutions to a symmetric system.

6.2.4 Separation of conservative and dissipative parts

In this section, the dependence of the two force vectors $\boldsymbol{f}_{\text{d}}(\boldsymbol{x},\dot{\boldsymbol{x}})$ and $\boldsymbol{f}_{\text{c}}(\boldsymbol{x},\dot{\boldsymbol{x}})$ of Eq. (6.1) on the velocity $\dot{\boldsymbol{x}}$ is addressed, depending on their conservative or non-conservative nature. First, the two vectors are gathered into a single internal force vector: $\boldsymbol{f} = \boldsymbol{f}_{\text{d}} + \boldsymbol{f}_{\text{c}}$. Then, following ideas from [92], [178], $\boldsymbol{f}$ is decomposed into symmetric $\boldsymbol{f}_{\text{s}}$ and antisymmetric $\boldsymbol{f}_{\text{a}}$ functions of $\dot{\boldsymbol{x}}$:

$$\boldsymbol{f} = \boldsymbol{f}_{\text{s}} + \boldsymbol{f}_{\text{a}}, \quad \text{with} \quad \left\{ \begin{array}{l} \boldsymbol{f}_{\text{s}}(\boldsymbol{x},\dot{\boldsymbol{x}}) = \boldsymbol{f}_{\text{s}}(\boldsymbol{x},-\dot{\boldsymbol{x}}) = [\boldsymbol{f}(\boldsymbol{x},\dot{\boldsymbol{x}}) + \boldsymbol{f}(\boldsymbol{x},-\dot{\boldsymbol{x}})]/2, \\ \boldsymbol{f}_{\text{a}}(\boldsymbol{x},\dot{\boldsymbol{x}}) = -\boldsymbol{f}_{\text{a}}(\boldsymbol{x},-\dot{\boldsymbol{x}}) = [\boldsymbol{f}(\boldsymbol{x},\dot{\boldsymbol{x}}) - \boldsymbol{f}(\boldsymbol{x},-\dot{\boldsymbol{x}})]/2. \end{array} \right. \tag{6.7}$$

To analyze the conservative (or non-conservative) nature of $\boldsymbol{f}$, we compute its work over one period $T = 2\pi/\omega$ of a periodic motion:

$$\mathcal{W} = \int_{-T/2}^{T/2} \mathrm{T}\dot{\boldsymbol{x}}\boldsymbol{f}(\boldsymbol{x},\dot{\boldsymbol{x}})\,\mathrm{d}t = \int_0^{T/2} \mathrm{T}\dot{\boldsymbol{x}}(t)\boldsymbol{f}[\boldsymbol{x}(t),\dot{\boldsymbol{x}}(t)]\,\mathrm{d}t - \int_0^{T/2} \mathrm{T}\dot{\boldsymbol{x}}(-t)\boldsymbol{f}[\boldsymbol{x}(-t),\dot{\boldsymbol{x}}(-t)]\,\mathrm{d}t. \tag{6.8}$$

If a monophase CNM motion is chosen for the displacement vector such $\boldsymbol{x}(t) = \boldsymbol{x}_{\text{cnm}}(t)$ of Eq. (6.4), $\boldsymbol{x}$ is an even function of t ($\boldsymbol{x}(t) = \boldsymbol{x}(-t)$) and the velocity $\dot{\boldsymbol{x}}$ is an odd function of t ($\dot{\boldsymbol{x}}(t) = -\dot{\boldsymbol{x}}(-t)$). Then, Eq. (6.8) becomes:

$$\mathcal{W} = \int_0^{T/2} \mathrm{T}\dot{\boldsymbol{x}}(t)\boldsymbol{f}[\boldsymbol{x}(t),\dot{\boldsymbol{x}}(t)]\,\mathrm{d}t - \int_0^{T/2} \mathrm{T}\dot{\boldsymbol{x}}(t)\boldsymbol{f}[\boldsymbol{x}(t),-\dot{\boldsymbol{x}}(t)]\,\mathrm{d}t. \tag{6.9}$$

Introducing the split of $\boldsymbol{f}$ according to Eq. (6.7), it can be shown that:

$$\mathcal{W} = \mathcal{W}_s + \mathcal{W}_a, \quad \text{with} \quad \left\{ \begin{array}{l} \mathcal{W}_s = 0, \\ \mathcal{W}_a = 2\int_0^{T/2} \mathrm{T}\dot{\boldsymbol{x}}(t)\boldsymbol{f}_{\text{a}}[\boldsymbol{x}(t),\dot{\boldsymbol{x}}(t)]\,\mathrm{d}t. \end{array} \right. \tag{6.10}$$

This demonstration shows that the work $\mathcal{W}_s$ of the symmetric part $\boldsymbol{f}_\mathrm{s}$ on a monophase CNM is zero, indicating that $\boldsymbol{f}_\mathrm{s}$ is a conservative force, whereas the work $\mathcal{W}_a$ is *a priori* non-zero, indicating that $\boldsymbol{f}_\mathrm{a}$ is a non-conservative force. Then, the following property can be postulated: *whatever be the* $\boldsymbol{x}$ *dependence of the internal force* $\boldsymbol{f}(\boldsymbol{x},\dot{\boldsymbol{x}})$*, its conservative part* $\boldsymbol{f}_c(\boldsymbol{x},\dot{\boldsymbol{x}})$ *is an even function of* $\dot{\boldsymbol{x}}$ *whereas its non-conservative part* $\boldsymbol{f}_d(\boldsymbol{x},\dot{\boldsymbol{x}})$ *is an odd function of* $\dot{\boldsymbol{x}}$. Consequently:

$$\begin{cases} \boldsymbol{f}_\mathrm{c}(\boldsymbol{x},\dot{\boldsymbol{x}}) = \boldsymbol{f}_\mathrm{c}(\boldsymbol{x},-\dot{\boldsymbol{x}}), \\ \boldsymbol{f}_\mathrm{d}(\boldsymbol{x},\dot{\boldsymbol{x}}) = -\boldsymbol{f}_\mathrm{d}(\boldsymbol{x},-\dot{\boldsymbol{x}}). \end{cases} \tag{6.11}$$

Even if the demonstration of this section appears restrictive, these results can be verified for most available damping models, linear or nonlinear (a selection is shown in Appendix D.1).

6.2.5 Phase resonance

Consider now the system under forced and damped conditions, where the motion is described by Eq. (6.1). If the motion is exactly the monophase CNM of Eq. (6.4), it takes the form of Eq. (6.3) such that the conservative terms of Eq. (6.1) balance each other. In this case, Eq. (6.1) reduces to:

$$\boldsymbol{f}_\mathrm{d}(\boldsymbol{x}_\mathrm{cnm},\dot{\boldsymbol{x}}_\mathrm{cnm}) = \boldsymbol{f}_\mathrm{e} = \sum_{h=1}^{H} \hat{\boldsymbol{f}}_{\mathrm{e}h} \sin(h\omega t), \tag{6.12}$$

with $\hat{\boldsymbol{f}}_{\mathrm{e}h} \in \mathbb{R}^N$. In Eq. (6.12), the second equality is a direct consequence of $\boldsymbol{f}_\mathrm{d}(\boldsymbol{x},\dot{\boldsymbol{x}})$ being an odd function of $\dot{\boldsymbol{x}}$ (see Appendix D.4). Comparing Eqs. (6.4) and (6.12), it is observed that *the external force vector associated to the motion onto a monophase CNM is also monophase and characterized by a phase lag of* $\pi/2$ *of each harmonic with respect to the displacement response, regardless of the form of the dissipative forces.*

Therefore, applying a force appropriation procedure, *i.e.* controlling the frequency ω of the external force $\boldsymbol{f}_\mathrm{e}(t)$ as well as the shapes $\hat{\boldsymbol{f}}_{\mathrm{e}h}$ for $h = 1, 2, \ldots, H$ of its harmonics such that their phases have a phase lag of $\pi/2$ with respect to the corresponding harmonic of the displacement $\boldsymbol{x}(t)$ enables *the conservative nonlinear mode* $\boldsymbol{x}_{cnm}$ *to be measured, regardless of the dissipative forces.* This conclusion, proved in [178] for the case of a linear damping law $\boldsymbol{f}_\mathrm{d} = \boldsymbol{D}\dot{\boldsymbol{x}}$ with a constant damping matrix $\boldsymbol{D}$, is the basis of experimental nonlinear force appropriation methods, used in a large number of works [1], [60], [84], [118], [157], [184], [207]. To the knowledge of the authors, the present extension to an arbitrary dissipative force $\boldsymbol{f}_\mathrm{d}(\boldsymbol{x},\dot{\boldsymbol{x}})$ was only suggested in a comment of [178], but not addressed in detail as here.

6.2.6 Imperfect space and frequency dependence for force appropriation

In practice, it is difficult to realize the exact force appropriation, meaning finding the exact vectors $\hat{\boldsymbol{f}}_{\mathrm{e}h}$ that exactly cancel the harmonics of $\boldsymbol{f}_\mathrm{d}(\boldsymbol{x}_\mathrm{cnm},\dot{\boldsymbol{x}}_\mathrm{cnm})$ according to Eq. (6.12). However, if Eq. (6.12) were perfectly respected, the motion would be on the ith nonlinear mode resonance, *i.e.* very close to the ith invariant manifold of the CNM. As shown in [60], [171] using normal form theory, because of the resonant motion, the *space repartition* of the force is not important at first order. A single harmonic forcing is often sufficient for force appropriation and used in most cases for experimental simplicity (otherwise, each harmonic of the force must be controlled independently to realize the force appropriation). It is for this reason that most experimental works on successful nonlinear phase

resonance testing in the literature involved single harmonic and single point forcing [60], [118], [179], [184]–[186], [208] or a shaker base acceleration testing [1], [125], [159].

6.2.7 The case of non-smooth nonlinearities

Although the present work is restricted to smooth nonlinearities, it is worth considering application of the concepts discussed here to non-smooth nonlinearities. A series of papers [159], [186], [207], [208] explores the use of phase resonance testing to treat the case of structures with strong non-smooth nonlinearities, such as impact and dry friction. In the case of *conservative* non-smooth nonlinearities such as impact without dissipation at the interface, the conclusions of this work hold: a phase resonance method can be used to measure the conservative backbone curve [186].

The same cannot be said for the case of dry friction. Upon first examination, dry friction forces could be considered to follow the definition of $\boldsymbol{f}_{\mathrm{d}}(\dot{\boldsymbol{x}})$ since they dissipate energy and most models define them as odd functions in $\dot{\boldsymbol{x}}$ [25], [241], [243]. Following the results of § 6.2.5, applying a phase resonance condition to a system for which the only nonlinearities are dry friction would lead to measurement of the nonlinear mode of the conservative associated system, which in this case would be purely linear. A straight backbone curve, with constant frequency (equal to the natural frequency of the mode under concern), would be obtained. However, some works [10], [159], [207], [208] show that applying a phase resonance method to such a system leads to a different result: it measures a *damped nonlinear mode*, with a non-straight backbone curve in contrast to the straight backbone curve typical of those systems. This discrepancy can be explained considering that dry friction typically includes both sticking and slipping phases during an oscillation, the first being purely conservative and the second purely dissipative. As a consequence, dry friction forces are responsible for both *conservative* and *dissipative* nonlinear effects that cannot be separated as in Eq. (6.1).

6.3 Numerical estimation of backbone curves and damping with phase resonance

To illustrate the results of § 6.2, a method is presented in this section to solve Eq. (6.1) in *phase resonance*. According to the theory of § 6.2, solving Eq. (6.1) in phase resonance computes the CNM as if they had been computed according to Eq. (6.3), which is the method used to compute them in Chapters 3 and 4. We consider here the particular case of a vertical cantilever beam subjected to gravity, the same example test case as studied in Chapter 4. The cantilever beam system is used here in order to obtain reference numerical solutions for the experimental results of the next section (§ 6.4). The numerical simulations are carried out using the same continuation method described in Chapters 2, 3 and 4 based on a combination of the Harmonic Balance Method (HBM) and the Asymptotic Numerical Method, but adapted to compute the periodic solutions of the system under a phase resonance condition.

6.3.1 Computing the backbone curves with phase resonance

As in Chapter 4, we consider a vertical cantilever beam within a gravitational field subjected to a monoharmonic base excitation with motion restricted to a plane. A geometrically exact beam model discretized using Timoshenko finite elements is used to described the motion of the system, which is written according to Eq. (4.19):

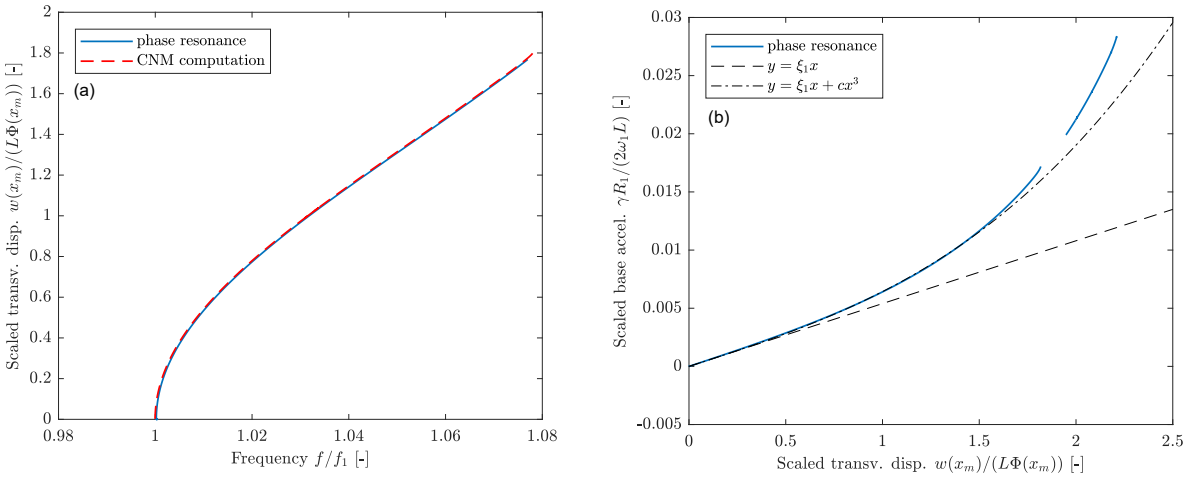

Figure 6.1: (a) Backbone curve of mode 1 computed by two numerical strategies: the classical one of Chapters 3 and 4 (red dashed line) and a phase resonance numerical continuation (blue solid line); (b) base acceleration as a function of the amplitude of beam 1 on the backbone curve computed with numerical phase resonance continuation, and several polynomial fits. The simulation is carried out with $\xi = 0.0054$ for a beam of length $L = 380$ [mm], width $b = 18.1$ [mm], and thickness $h = 0.495$ [mm] (corresponding to experimental beam 1, see Table 6.1) and with $\alpha = 1.211$ (see § 6.5.1).

$$\boldsymbol{M}\ddot{\boldsymbol{x}} + \boldsymbol{D}\dot{\boldsymbol{x}} + \boldsymbol{f}_{\mathrm{c}}(\boldsymbol{x}) = \boldsymbol{f}_{\mathrm{g}} + \boldsymbol{f}_{\mathrm{e}}(t) \tag{6.13}$$

where $\ddot{\boldsymbol{x}}$ gathers all the degrees of freedom (the axial displacement, the transverse displacement and the rotation of all the finite element nodes), $\boldsymbol{M}$ is a constant inertia matrix, $\boldsymbol{D}$ is a constant damping matrix, $\boldsymbol{f}_{\mathrm{c}}$ is the internal force vector, which is nonlinear due to the presence of geometrical nonlinearities, $\boldsymbol{f}_{\mathrm{g}}$ is a constant vector due to gravity and $\boldsymbol{f}_{\mathrm{e}}(t)$ is the external force vector.

In the HBM, $\boldsymbol{x}$ is expanded in Fourier series:

$$\boldsymbol{x}(t) \simeq \hat{\boldsymbol{x}}_0 + \sum_{h=1}^{H} \left[\hat{\boldsymbol{x}}_h^c \cos(h\omega t) + \hat{\boldsymbol{x}}_h^s \sin(h\omega t)\right]. \tag{6.14}$$

Then, introducing Eq. (6.14) into Eq. (6.13) and balancing each harmonic, the following algebraic system is obtained:

$$\boldsymbol{R}(\boldsymbol{X}, \omega, \lambda) = \boldsymbol{0}, \tag{6.15}$$

with $\boldsymbol{R} \in \mathbb{R}^{2H+1}$, $\boldsymbol{X} = [\hat{\boldsymbol{x}}_0^{\mathrm{T}}, \hat{\boldsymbol{x}}_1^{c\,\mathrm{T}}, \ldots \hat{\boldsymbol{x}}_H^{c\,\mathrm{T}}, \hat{\boldsymbol{x}}_1^{s\,\mathrm{T}}, \ldots \hat{\boldsymbol{x}}_H^{s\,\mathrm{T}}]^{\mathrm{T}} \in \mathbb{R}^{2H+1}$ and $\lambda \in \mathbb{R}$ a bifurcation parameter that is described below. Since $\boldsymbol{R}$ contains $2H+1$ equations for $2H+3$ unknowns, two more equations must be defined in order to fully dimension the continuation problem: one to define the bifurcation parameter λ and a second so-called phase condition (which has been discussed previously in Chapters 2 and 3).

To compute the conservative nonlinear modes of the system, we consider two possibilities:

- The first method (called here method A), is the method described in Chapter 3 to solve Eq. (6.13) in free vibration ($\boldsymbol{f}_{\mathrm{e}} = \boldsymbol{0}$) with a damping term corresponding to $\boldsymbol{D}\dot{\boldsymbol{x}} = \lambda\dot{\boldsymbol{x}}$, where $\lambda \in \mathbb{R}$ is

a fictitious bifurcation parameter used to avoid numerical instabilities [15]. In this case, the numerical computation will lead to a very small value of λ, such that $\lambda \simeq 0$, since the computed periodic solutions are associated to a certain *conservative* nonlinear mode. In this autonomous system, the phase condition can take several forms; the one described in § 2.2.4 and § 3.2.3 consists in setting to zero the velocity of a given component of $\dot{\boldsymbol{x}}(0)$ (*i.e.* $\dot{x}_i(t) = 0$, $i \in \{1, \dots N\}$).

- The second one (method B) is based on implementation of the phase resonance condition. To do so, the damping $\boldsymbol{D}\dot{\boldsymbol{x}}$ and external forcing $\boldsymbol{f}_{\mathrm{e}}(t)$ terms should be balanced by imposing a $\pi/2$ phase shift with the monophase displacement $\boldsymbol{x}(t)$ as described in § 6.2.

  The system is forced with a monoharmonic signal $\boldsymbol{f}_{\mathrm{e}}(t) = \lambda \hat{\boldsymbol{f}}_{\mathrm{e1}} \sin(\omega t)$, with $\hat{\boldsymbol{f}}_{\mathrm{e1}} \in \mathbb{R}^N$ a constant amplitude vector and $\lambda \in \mathbb{R}$ a scalar parameter used to modulate the forcing amplitude. The phase condition is chosen such that the sine component of the first harmonic of a given component of $\boldsymbol{x}(t)$ is set to zero ($[\hat{\boldsymbol{x}}_1^s]_i = 0$, $i \in \{1, \dots N\}$), thereby naturally imposing a $\pi/2$ phase shift between this component and the forcing vector so as to enforce the phase resonance condition. In this case, restricting to the first harmonic, the damping is written:

$$\boldsymbol{D}\dot{\boldsymbol{x}} = -\boldsymbol{D}\hat{\boldsymbol{x}}_1^c \omega \sin(\omega t), \tag{6.16}$$

  so that when the damping and external forcing are balanced:

$$\boldsymbol{f}_{\mathrm{e}} = \lambda \hat{\boldsymbol{f}}_{\mathrm{e1}} \sin(\omega t) = -\boldsymbol{D}\hat{\boldsymbol{x}}_1^c \omega \sin(\omega t), \tag{6.17}$$

  leading to a relationship between the amplitude of the response $\hat{\boldsymbol{x}}_1^c$ and the oscillation frequency ω which characterizes the backbone curve of the CNM determined using phase resonance:

$$\hat{\boldsymbol{x}}_1^c = \frac{-\lambda \hat{\boldsymbol{f}}_{\mathrm{e}}}{\boldsymbol{D}\omega}. \tag{6.18}$$

  The resonance point $(\omega, \hat{\boldsymbol{x}}_1^c)$ along the backbone curve of the CNM is found for each fixed "forcing amplitude" $\lambda \hat{\boldsymbol{f}}_{\mathrm{e}}$. Sweeping λ then enables the entire backbone curve to be traced, while ensuring that the system remains in phase resonance.

  In our simulations, the chosen ith component of $\boldsymbol{x}(t)$ for the phase condition is the transverse displacement at the node located at x_m (the location of the sensors, see § 6.4.1) and $\boldsymbol{f}_{\mathrm{e1}}$ is chosen to model the forcing due to the base acceleration. The damping matrix is chosen mass-proportional, such that $\boldsymbol{D} = 2\omega_1 \xi \boldsymbol{M}$ with ω_1 the first natural frequency and $\xi \in \mathbb{R}$ a damping ratio.

6.3.2 Numerical CNMs and damping with phase resonance

Figure 6.1(a) combines in one figure the computation of the first backbone curve of a cantilever beam both by the standard method A as well as by the phase resonance method B with the damping ratio $\xi = 0.0054$. The two curves overlap perfectly on a very large frequency range, up to very large rotation amplitudes. This comparison validates, on this example, the phase resonance method to compute a conservative nonlinear mode. In particular, for this case, it is not necessary to use an appropriate forcing vector $\boldsymbol{f}_{\mathrm{e1}}$ that exactly matches the damping vector $\boldsymbol{D}\dot{\boldsymbol{x}}$, nor to add higher harmonics than the first (recall § 6.2.6).

Then, in Fig. 6.1(b) the amplitude of the first harmonic of the scaled base acceleration is plotted as a function of the scaled transverse beam displacement. In a system containing purely linear damping,

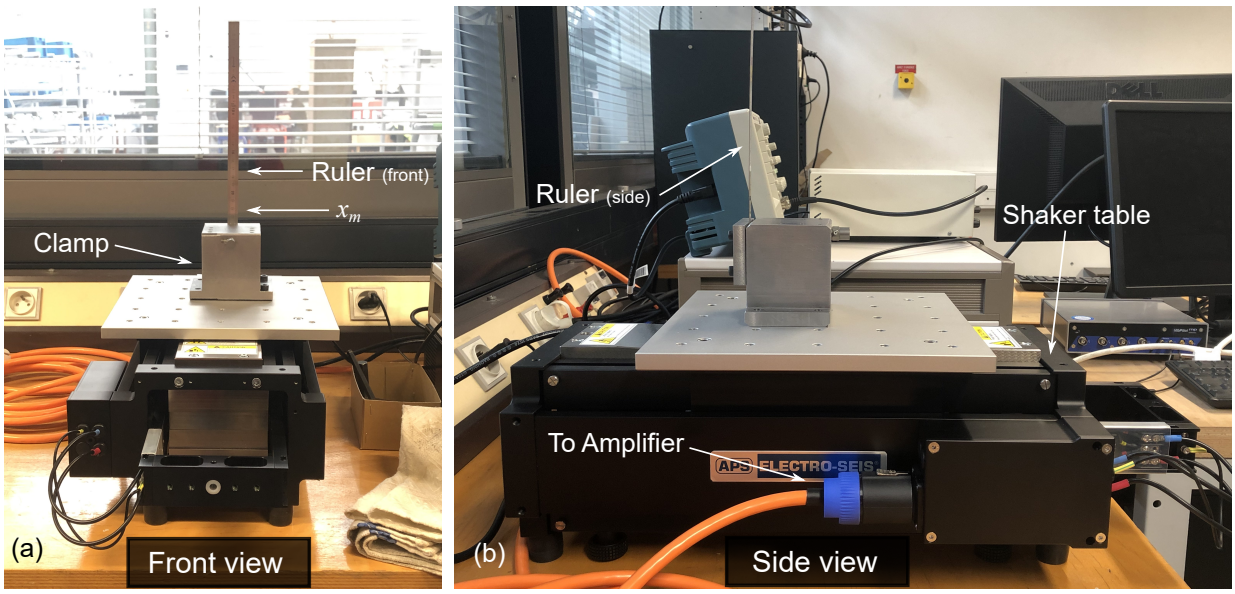

Figure 6.2: Experimental shaker table setup, (a) front view, (b) side view.

the displacement would increase proportional to the acceleration and Fig. 6.1 would show a linear relationship (the dashed line) with the slope of the line related to the linear damping coefficient (ξ in our mass-proportional damping).

In Fig. 6.1, we see that the relationship between the base acceleration and the displacement of the beam is linear only at very small amplitudes. At higher amplitudes, it follows a cubic trend (eventually turning even higher order at extreme amplitudes). This is in agreement with the findings of Amabili *et al.* [4], [6]–[9] and [71], where nonlinear damping models (*e.g.* Kelvin-Voigt in [71]) must be used to match experimental frequency response curves for large amplitude vibrations of cantilever beams in a vacuum.

6.4 Experimental measurement of conservative nonlinear modes and damping estimation

In this section, the experimental procedure for measurement of the conservative nonlinear modes using phase resonance is described. Experimental measurement of the CNMs as backbone curves with phase resonance is carried out using a Phase-Locked Loop, a vibration control algorithm that integrates the concepts of § 6.2. Using the Phase-Locked Loop of this section, both frequency response curves (FRCs) or the backbone curves can be measured experimentally. Phase-Locked Loops have been used in different applications for measurement of nonlinear modes and frequency response curves [1], [60], [184]. Here the Phase-Locked Loop is used for the experimental measurement of the CNMs of highly flexible cantilever beams *in order to validate the theory of § 6.2* and also *to validate the geometrically exact model of previous work* (Chapters 3 and 4).

The description of the experiments is broken into three sections: In § 6.4.1, the physical environment is described. Next, in § 6.4.2, the numerical environment, including the details of the

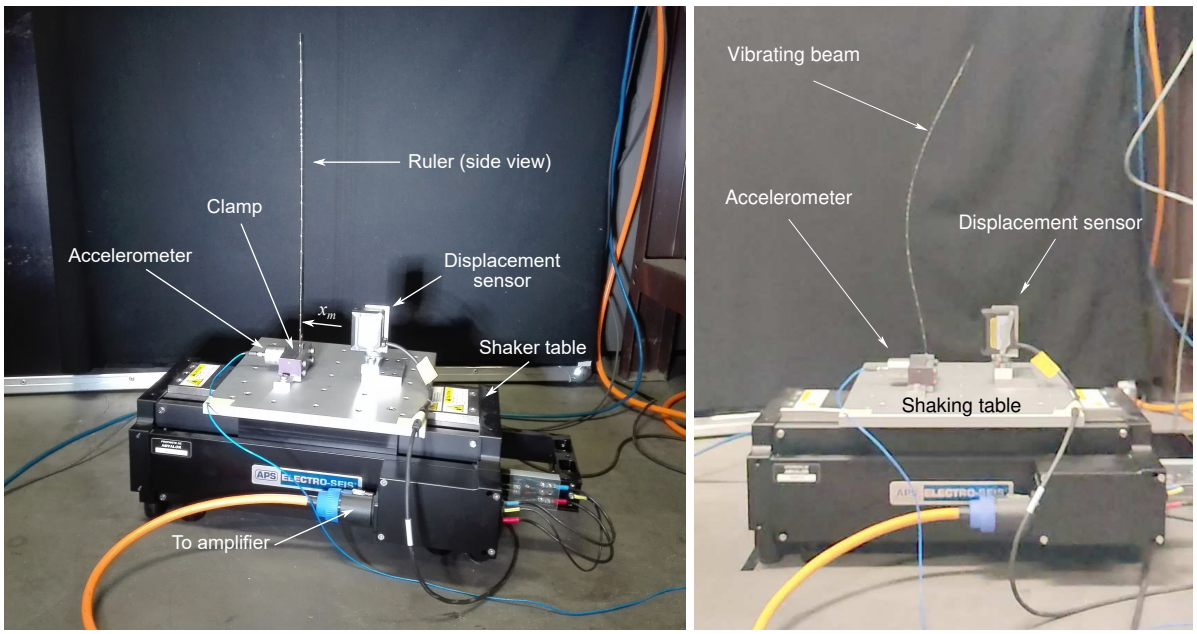

Figure 6.3: Alternate views of the experimental shaker table setup.

Phase-Locked Loop (PLL), is presented. In addition to the backbone curves, we are also interested in experimental measurement of the nonlinear mode shape. The method for tracking the deformed shape of the beam is described in § 6.4.3.

6.4.1 Experimental setup

The experimental setup is grouped into two subcategories, the physical environment and the digital environment.

Physical environment As shown in Figs. 6.2 and 6.3, in each experiment a beam is fixed to a shaker table using a clamp (the beams are described in § 6.5.1). Note that the clamp of Fig. 6.2 is an older version; the current version used for the experiments is much smaller, visible in Fig. 6.3. The shaker table is powered by a signal generated by an amplifier and provides an acceleration to the base of the cantilever. The shaker table interacts with the digital environment through three signals (depicted in Fig. 6.4):

- an input sinusoidal signal to the shaker table modulated by the digital environment and powered by the amplifier,
- two output measured signals captured with two different sensors.

Two different measurement sensors are needed for these experiments in order to isolate the motion of the beam. Since the beam is vibrating relative to the shaker table, the motion of the shaker table (relative to the ground) and the motion of the beam (relative to the ground) are measured separately so as to isolate the motion of the beam itself. In our experiments, different measurement sensors are used depending on the mode being captured, the choice of which is explained in the next paragraph.

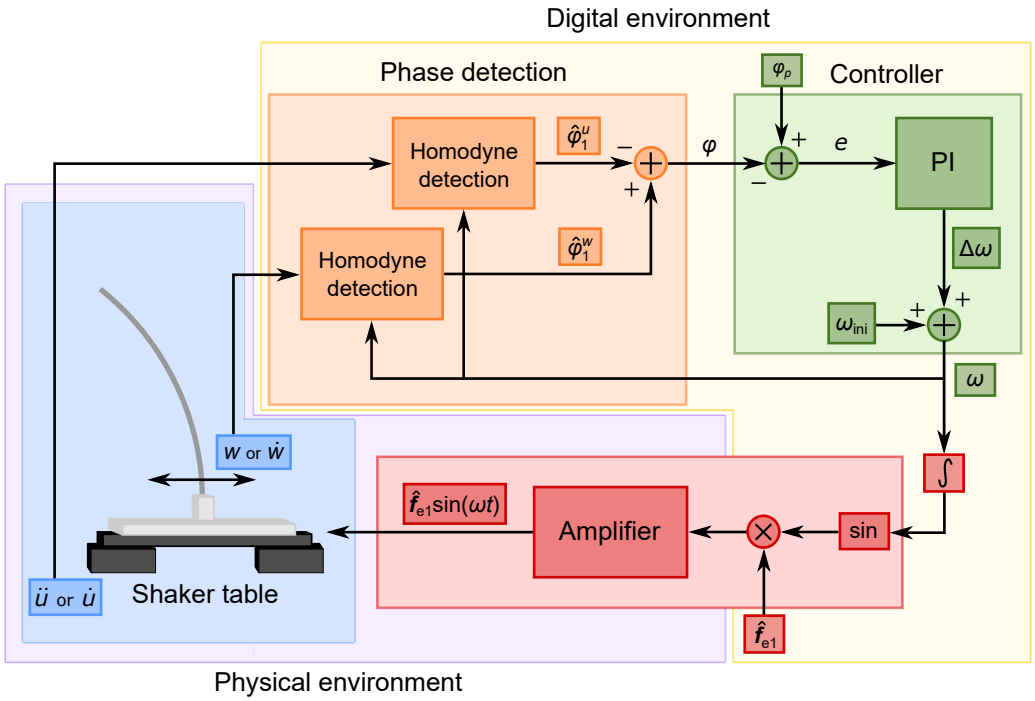

Figure 6.4: Simplified schematic of the Phase-Locked Loop vibration controller for experimental measurement of forced responses and conservative nonlinear modes using phase resonance.

In theory, the choice of whether to use accelerometers, laser vibrometers or displacement sensors to capture the motion of the physical system is open as the three quantities are related. However, some observations were made that influenced the final choice of sensors for each mode and are briefly summarized:

- If two laser vibrometers are used, the very low frequency on the first nonlinear mode (see Table 6.2) induces an error when they are related due to problems with the sampling rate at very low frequencies. In this case, a displacement sensor on the beam paired with an accelerometer at the base of the shaker table is preferred. This complication is not encountered on the higher nonlinear modes (with naturally higher frequencies).

- Conversely, the displacement sensor was found to produce a delay in the measurements that likewise induced an error in the measurements that was non-negligible on the higher frequency modes 2 and 3.

For these reasons, on mode 1, a displacement sensor and accelerometer are used to measure the motion of the beam and the table, respectively, while on the higher modes 2 and 3, two laser vibrometers measure the velocity of both the beam and the table.

The beam's sensor is placed at $x_m = 18$ [mm] from the clamp. The measurement is taken close to the base of the beam due to the very large amplitudes at other locations (which cannot be measured with *e.g.* a fixed laser vibrometer). As the beam moves, however, the exact location of the vibrometer's laser can shift slightly which leads to a small uncertainty of ~ 0.5 [mm] in x_m.

Digital environment Next, the digital environment containing the PLL is described (an overview of the PLL is provided in the next section). There are two main components of the digital environment: the Phase-Locked Loop, the control schematic of which is created in Simulink (MATLAB), and the electronic control unit it runs on (dSPACE). The two output signals of the physical environment (*i.e.* the readings of the measurement sensors) are accepted as inputs into the dSPACE. These are the inputs to the PLL control algorithm, which can be subdivided into two main parts as shown in Fig. 6.4, a "phase detection" block and the block of the controller. The phase detection is what allows the system to be maintained in phase resonance. In the controller block of the PLL, a Proportional Integral (PI) controller is used to control the oscillation frequency ω of the forcing based on the difference e between the detected phase φ and the prescribed phase φ_p. The sine of the oscillation frequency ω is then combined with a prescribed forcing amplitude $\hat{\boldsymbol{f}}_{e1}$ to define the sinuisoidal signal to be generated by the amplifier as the input signal which governs the oscillations of the shaker table.

6.4.2 The Phase-Locked Loop: an algorithm for vibration control based on the idea of phase resonance

The Phase-Locked Loop is the algorithm for vibration control that allows for experimental measurement of the nonlinear modes using phase resonance [1], [60], [184]. The PLL of the present work is largely based on the work of Denis *et al.* [60]. In [60], however, the PLL was used in experiments involving circular plate systems with frequency ranges (> 100 Hz) notably higher than the slender cantilever beam systems considered here, the first mode of which is in the range of $2-4$ Hz (see Table 6.2). At lower frequencies, a longer time is needed to reach the periodic steady-state of the response, and updates to the sampling rate and the low-pass filter (see next) must be made accordingly. Aside from these considerations, the interested reader is referred to [60] for additional details regarding the PLL.

In what follows, the two subdivisions of the PLL schematic are described. First, the method of phase detection via the technique known as *homodyne detection* is discussed. Then, the details of the control algorithm are given to indicate how the system is kept in phase resonance so as to measure the experimental CNMs through force appropriation.

Phase detection using homodyne detection In § 6.4.1, the input and output signals of the digital environment are briefly summarized. The two measured signals of the shaker table and the beam are first characterized using homodyne detection. Homodyne detection is a method for identifying the information of a signal and is used here to extract the amplitude and phase of the measured signals. The procedure is as described in Colin *et al.* [42]:

- We consider a signal of the form $x(t) = \hat{x}_0 + \sum_{h=1}^{H} a_h \cos(h\omega t + \varphi_h)$. Here, we seek to identify the phase φ_1 of the first harmonic of $x(t)$, but the procedure can be applied to any harmonic. First, $x(t) = a_1 \cos(\omega t - \varphi_1)$ is multiplied by both a sine and a cosine function at the frequency of the first harmonic, such that:

$$\begin{cases} x_s(t) = x(t)\sin(\omega t), & \text{(6.19a)} \\ x_c(t) = x(t)\cos(\omega t). & \text{(6.19b)} \end{cases}$$

  Using trigonometric identities, it can be seen that in x_s and x_c there are some higher harmonic terms that appear.

- The signals x_s and x_c then pass through low-pass filters in order to filter out these higher harmonics, *keeping only the first harmonic* H1 (recall § 6.2.6). The first harmonic is found

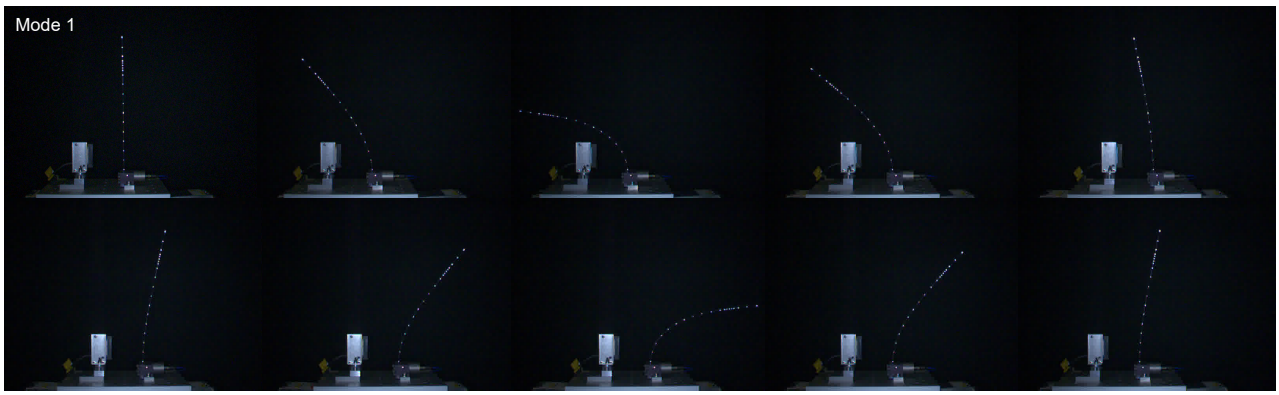

Figure 6.5: Motion of the cantilever beam excited by base acceleration on its first nonlinear mode over $\simeq 1$ period.

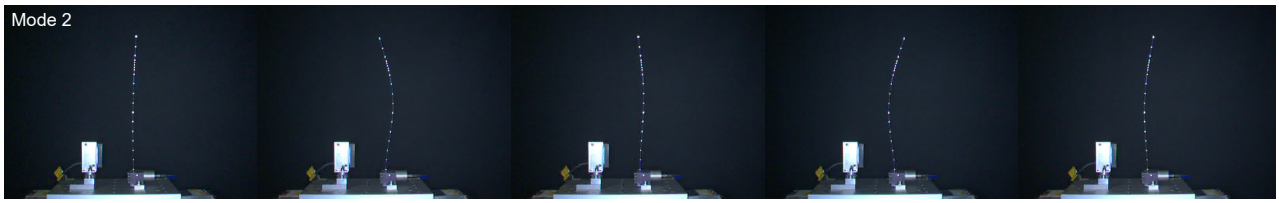

Figure 6.6: Motion of the cantilever beam excited by base acceleration on its second nonlinear mode over $\simeq 1$ period.

in Chapters 3 and 4 to be heavily dominant on the first three nonlinear modes of the slender cantilever beam up to very large amplitudes and therefore represents a good estimate of the full behavior.

- After filtering, the signals become:

$$\begin{cases} x_s(t) \approx \dfrac{a_1}{2}\sin(\varphi_1), & \text{(6.20a)} \\ x_c(t) \approx \dfrac{a_1}{2}\cos(\varphi_1). & \text{(6.20b)} \end{cases}$$

These can be related so as to approximate the amplitude and phase of the first harmonic of $x(t)$ as:

$$a_1 = 2\sqrt{(x_s(t))^2 + (x_c(t))^2}, \quad \text{(6.21a)}$$

$$\varphi_1 = \tan^{-1}\left(\frac{x_s(t)}{x_c(t)}\right). \quad \text{(6.21b)}$$

The results of the homodyne detection procedure in our experiments are the identified phases of the first harmonics of the two measured signals $\hat{\varphi}^u$ and $\hat{\varphi}^w$ (and the amplitudes of the signals, but only the phase is controlled by the PLL). These are then related as shown in Fig. 6.4 so as to subtract out the motion of the table $\hat{\varphi}^u$ and isolate the phase of the beam's motion φ.

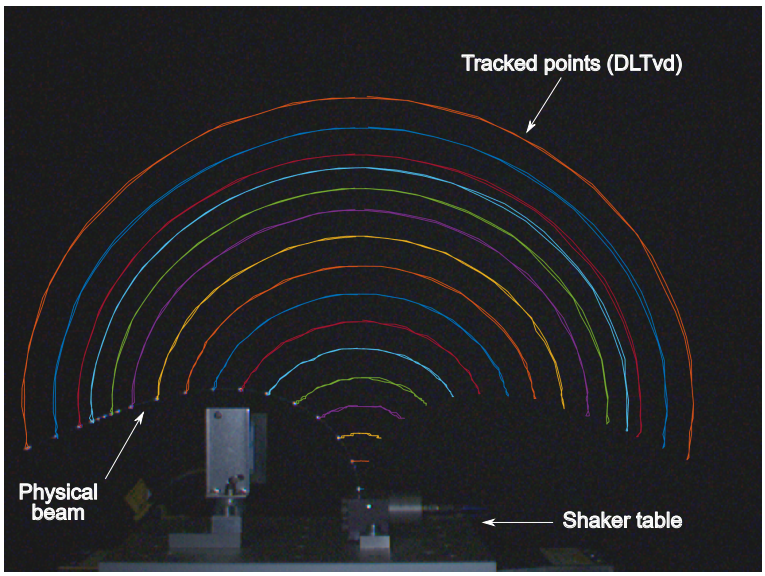

Figure 6.7: First nonlinear mode trajectories of the cantilever beam overlaid onto an example image.

Controller The phase of the beam's motion φ is then fed to the PI controller to be controlled in one of two ways depending on the desired solution. As mentioned in § 6.4.1 and shown in Fig. 6.4, two parameters are prescribed by the user, the phase φ_p and the forcing amplitude $\hat{\boldsymbol{f}}_{e1}$. Depending on their prescription, two different solutions are available [60]:

- To compute frequency responses (FRCs), a constant forcing amplitude $\hat{\boldsymbol{f}}_{e1}$ is prescribed and the prescribed phase φ_p can be swept between $[0, -\pi]$. In sweeping the phase, a positive $\Delta\omega$ is added to the starting frequency ω_{ini} and ω increases while the forcing amplitude is constant. The prescribed phase φ_p can be "swept down" in the same way with ω_{ini} high and $\Delta\omega$ negative to compute the FRC in reverse.
- To compute the CNMs using phase resonance, the $\pi/2$ phase difference between the displacement of the beam and the forcing required to maintain the phase resonance condition is prescribed for φ_p and the forcing amplitude $\hat{\boldsymbol{f}}_{e1}$ is instead swept up. In this way, the phase of the system is controlled so as to maintain the phase resonance, while sweeping of the forcing amplitude traces the backbone curve.

Note that the phase difference of $\pi/2$ to impose the phase resonance exists only between the *displacement* and the forcing terms. If φ represents the phase of a *velocity* signal, the phase lag in phase resonance between the *velocity* and the forcing terms (and therefore φ_p) becomes 0 or π (since the velocity is the time derivative of the displacement).

6.4.3 Tracking of the nonlinear mode shapes

In addition to the FRCs and CNMs measured by the PLL, the deformed mode shapes are key in characterizing the nonlinear behavior as the vibration amplitude increases. One possibility for mapping the deformed shape of periodic vibrations is via rapid motion capture using a high speed camera.

Another possibility, and the one used in our work, is to create an artificial stroboscopic effect over several periods of motion.

Mapping of the nonlinear mode shapes using a stroboscope For a periodic signal of period $T = 1/f$ [s] where f is the frequency in [Hz], an artificial stroboscope can be created by imposing a periodic capture rate on a recording device equal to n periods of motion plus a small time delay $nT + \Delta t$ where $\Delta t \ll T$. Then, the difference between the deformed shape in one image and the next is equivalent to having captured it at time t_1 and $t_2 = t_1 + \Delta t$ despite the slower overall capture rate. Examples of the types of images captured to track the deformed shape are shown for the first and second nonlinear modes in Figs. 6.5 and 6.6, respectively.

A camera (Basler) is used in conjuction with the Basler video recording software [19] to record the motion. Reflective tape is placed at locations on the beam corresponding to every other finite element node of the numerical model as shown in Figs. 6.5 and 6.6. On the higher modes, nodes in the mode shape (locations where the displacement is 0) appear, one on mode 2 and two on mode 3. Additional reflective points are added close to the known location of the mode shape nodes in order to better track the displacement close to them (this is why more reflective points are visible in Fig. 6.5 close to the mode 2 node of Fig. 6.6). Then, a light is shined onto the reflective tape (in dim surroundings), so that distinct illuminated points appear in each of the stroboscopic images (see Figs. 6.5 and 6.6).

The DLTvd digitizing tool [105], which interfaces with MATLAB, is then used for multi-point tracking between the images. This software allows the illuminated points to be tracked automatically through the series of images and returns their trajectories in space. An example of the tracked trajectories of the first nonlinear mode overlaid onto a sample image is shown in Fig. 6.7

6.5 Results for the first three nonlinear modes of a vertical cantilever

In this section, we proceed to comparing the experimental CNMs to those computed with the finite element geometrically exact numerical model of Chapters 3 and 4. The beams under study in this work are first described in § 6.5.1. The CNMs (depicted as backbone curves and nonlinear mode shapes) measured experimentally are then compared to those computed numerically for the first three CNMs in § 6.5.2 (for the backbone curves) and § 6.5.3 (for the nonlinear mode shapes). A discussion on the experimental damping estimation similar to § 6.3.2 is found in § 6.5.4.

6.5.1 Beams under study

Three different beams are used in the vibration experiments described in § 6.4, referred to as beams 1, 2 and 3. Stainless steel rulers where the length L greatly exceeds the width b and thickness h of the cross-section ($h \ll L$ and $b \ll L$) are used as the flexible slender structures. Beams 1 and 2 are of the same length L and thickness h, but have different widths b, and beam 3 is of the same thickness, but is shorter and has a width smaller than the previous two (see "**Ribbon effect**" below). The geometry and material properties of the beam specimens are summarized in Table 6.1 and their measured natural frequencies (first three modes) in Table 6.2. The measured mass and dimensions of each beam are used to determine the density ρ of each specimen. Slight differences in the thickness h were measured across the length of the beam represented by the ± 0.005 [mm] uncertainty in h, leading to a range of values for ρ. Classical tensile tests are used to determine the ratio of the Young's modulus E to ρ as shown in Appendix D.6 and the resulting E/ρ ratio of each beam is used to compute the Young's

modulus E of each material.

			Beam 1	**Beam 2**	**Beam 3**
Brand			VMADE	FACOM	FACOM
Length	L	[mm]	380	380	290
Width	b	[mm]	18.1	6.79	4.43
Thickness	h	[mm]	0.49 - 0.5	0.49 - 0.5	0.49 - 0.5
Slenderness	η	$[10^{-7}]$	1.39 - 1.44	1.39 - 1.44	2.38 - 2.48
Young's modulus / density	E/ρ	$[\mathrm{MPa}\cdot\mathrm{m}^3/\mathrm{kg}]$	21.77	24.37	24.37
Density	ρ	$[\mathrm{kg}/\mathrm{m}^3]$	7988 - 7828	7882 - 7724	7882 - 7724
Young's modulus	E	[GPa]	173.9 - 170.4	192.1 - 188.3	192.1 - 188.3
Gravity parameter	α	[-]	1.236 - 1.187	1.104 - 1.06	0.491 - 0.471

Table 6.1: Characteristics of the three tested beams.

Mode	**Beam 1**	**Beam 2**	**Beam 3**
ω_1	2.47	2.18	4.04
ω_2	16.62	14.85	26.45
ω_3	46.92	41.92	74.48

Table 6.2: Natural frequencies ω_n (in [Hz]) of the three tested beams for the first three modes.

In Chapter 4, it is shown that the equations of motion of the geometrically exact beam model depend only on three parameters η, α and μ (defined by Eqs. (4.9)) when normalized according to Eqs. (4.6). These parameters represent, respectively, a slenderness parameter, a gravity parameter and a shear parameter (tied to the Timoshenko kinematics). Neglecting the shear parameter μ (it is shown in Appendix B.1 that it has virtually no influence since the shearing is small), the values of η and α for all three beams are shown in Table 6.1.

Recall from Chapter 4 (§ 4.4.1) that the slenderness parameter η has very little effect on the first three CNMs so long as it remains small ($\eta \leq 10^{-6}$). The value of the slenderness parameter η for each beam falls in the range $\eta = 1 \cdot 10^{-7}$ and $2.5 \cdot 10^{-7}$. These values correspond to a h/L ratio between $0.0011 \simeq 1/909$ and $0.0017 \simeq 1/588.2$, indicating extreme slenderness. The ruler beam specimens of these experiments are therefore very representative of the slender structures that are the focus of our work.

Two topics related to the beams under study and which do have an effect on the CNMs are addressed next: the effect of gravity (represented by the dimensionless parameter α) and the so-called ribbon effect.

Gravity effect The first topic is the effect of gravity as represented by the dimensionless parameter α [Eq. (4.9)]. In Chapter 4, it is found that α adds a significant hardening effect to the backbone curves of the first nonlinear mode of a standing cantilever. On the second and third nonlinear modes, however, the influence of α is almost negligible.

The values of α for each of the beams are shown in Table 6.1 and range between $\alpha = 0.471 - 1.236$. For less massive beams (of a given material), there is logically less of an effect of gravity and α is smaller. Beam 1 being the most massive, it can be concluded that gravity adds the strongest hardening effect to the backbone curves of beam 1, followed by beams 2 and beam 3 ($\alpha_{\text{beam 3}} < \alpha_{\text{beam 2}} < \alpha_{\text{beam 1}}$). Without incorporating the effect of gravity into the model (*i.e.* for $\alpha = 0$), a strong discrepancy between the experimental and numerical backbone curves of the first nonlinear mode is found. This is depicted in Fig. 6.9(a) where the effect of gravity is strongest. The theoretical backbone curve without the effect of gravity ($\alpha = 0$) diverges immediately from the theoretical backbone curve including the effect of gravity. Moreover, the discrepancy between these backbone curves increases with increasing amplitude.

This simple demonstration has shown that gravity can have a significant influence on the large amplitude dynamics of flexible structures and *must be incorporated into the numerical model in order to adequately reproduce experimental results* [70].

Ribbon effect The second topic that must be addressed is the so-called "ribbon effect." In this study, we are strictly interested in structures with a geometry overwhelmingly dominant in the longitudinal direction, such that $h \ll L$ and $b \ll L$. The "ribbon effect" indicates the distinction between slender 1D structures whose width-to-thickness ratio b/h is close to 1 (rods) and those whose b/h ratio is larger, called in the literature ribbons [17], if not quite as large as slender 2D structures (plates or shells). It is important to make the distinction between rod models, ribbon models and plate models since there are differences in the models such that ribbon or plate structures cannot be accurately modeled as rods. For a given curvature, as the width of the beam increases compared to its thickness, the structure transitions from an elastic rod (1D) structure to an elastic plate or shell (2D) and changes must be made to the rod model to capture the shell behavior. Ribbons represent essentially a structure in between a rod and a shell. They can be modeled as thin elastic shells, but since shell models are more difficult to solve than rod models, 1D ribbon models are of interest [17].

It was shown in [17] that in the development of 1D ribbon models, the geometry of the structure (the ratios h/b and b/L) and the curvature $\kappa = \theta'$ are the main parameters to consider. In fact, it is the dimensionless parameter $\bar{\kappa}$, defined as:

$$\bar{\kappa} \sim \frac{\kappa b^2}{h} = \frac{(\kappa L)(b/L)}{(h/b)}, \tag{6.22}$$

that determines the appropriate model, with $\bar{\kappa} \ll 1$ tending towards rod models, $\bar{\kappa} \gg 1$ tending towards shell models or ribbon models with a large b/h ratio, and $\bar{\kappa}$ in between representative of the ribbon models of [17].

These elastic one-dimensional ribbon models, however, differ from elastic one-dimensional rod models in that they incorporate a nonlinear constitutive law derived from the underlying two-dimensional shell model [17], [134]. Since our work is based on a 1D elastic beam model with a linear constitutive law, we focus on reducing any ribbon effects by bringing specific changes to the width-to-thickness ratio rather than adapting our numerical model to incorporate the ribbon effect as is done for the gravity effect. To this end, beams 2 and 3, whose ratio b/h is significantly reduced compared to that of beam 1, are added into the study in order to investigate any potential ribbon effects. Beam 2 is of the same length as beam 1, but with a b/h ratio close to $\frac{1}{3}$ that of beam 1. Beam 3 is shorter than both beams 1 and 2 and has a b/h ratio around $\frac{1}{4}$ that of beam 1.

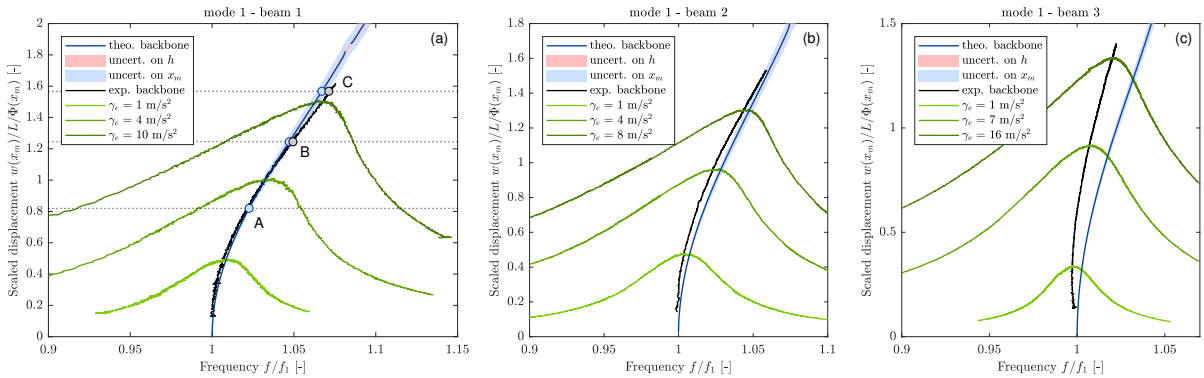

Figure 6.8: Experimental nonlinear frequency responses, for several base accelerations, and backbone curves (displacement sensor) of mode 1 compared to the theoretical backbone curve. The light blue and pink shaded area correspond to the measurement uncertainty of the theoretical backbone curve due to, respectively, the beam thickness h and the measurement position x_m (a): beam 1; (b): beam 2; (c): beam 3.

6.5.2 Backbone curves

We now proceed to comparison of the experimentally-measured backbone curves to those of the numerical model. In this section, the first three nonlinear modes of beams 1, 2 and 3 are studied in Figs. 6.8 to 6.11. The numerical simulations are carried out using beams with the same properties as beams 1, 2 and 3 discretized into 23 elements (24 nodes; 21 equally spaced nodes plus three additional nodes located at $x_m = 18$ [mm] and $x_m \pm 0.5$ [mm]. In Figs. 6.8, 6.10 and 6.11, the backbone curves representing the first harmonic (H1) of the scaled transverse displacement $w(x_m)/L/\Phi(x_m)$, measured at the point x_m along the length of the beam and normalized by the corresponding linear mode shape $\Phi(x_m)$, are plotted. Fig. 6.9 is a direct copy of Fig. 6.8, but with a zoom onto only the backbone curves.

In addition to the backbone curves, experimental nonlinear frequency responses are shown for three amplitudes of the base acceleration in these figures. Note that the exact nonlinear damping model of the system is not used in the numerical simulations; as mentioned in § 6.3, a linear damping matrix is used in our numerical model (which matches the physics less than, say, a Kelvin-Voigt damping model for the damping of flexible cantilevers in a vacuum [71]). For this reason, even though experimental FRCs are measured and shown in Figs. 6.8, 6.10 and 6.11, only the CNMs are compared since they are independent of any damping.

Nonlinear mode 1 Beginning with the first nonlinear mode of the cantilever, very good agreement is found between the experimental and numerical backbone curves for the two longer beams, beam 1 in Figs. 6.8(a) and 6.9(a) and beam 2 in Figs. 6.8(b) and 6.9(b). In the zoom of the backbone curves in Fig. 6.9, it can be seen that the experimental backbone curves of beams 1 and 2 remain within or very close to the uncertainty range of the numerical backbone (uncertainty on h and x_m, see § 6.4.1 and § 6.5.1), even up to very large amplitudes (the amplitude of the beam is more clearly visible in the snapshots of the deformed shape, see *e.g.* Fig. 6.12 for the first nonlinear mode of beam 1). The known hardening trend of the first nonlinear mode of the cantilever beam (found in Chapters 3 - 5) is

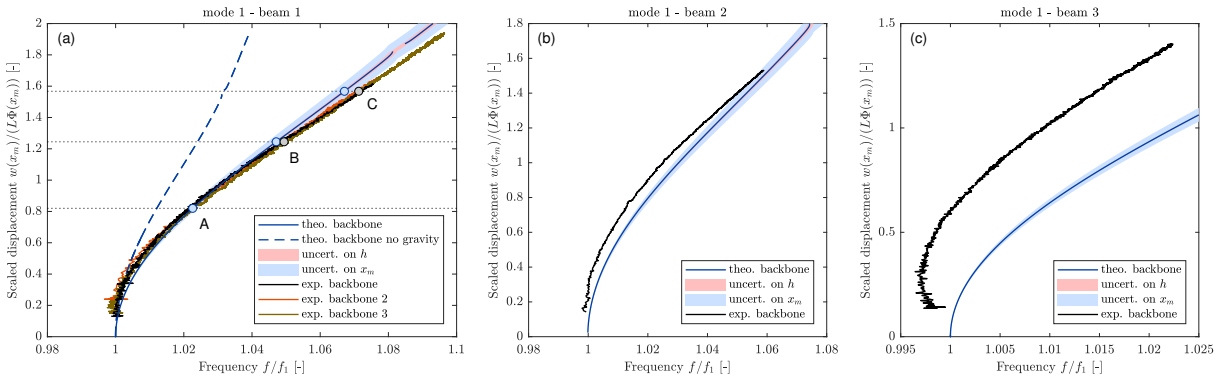

Figure 6.9: Experimental backbone curves (displacement sensor) of mode 1 compared to the theoretical one. The light blue and pink shaded area correspond to the measurement uncertainty of the theoretical backbone curve due to, respectively, the beam thickness h and the measurement position x_m. (a): beam 1; (b): beam 2; (c): beam 3.

recovered for all three beams by the experimental measurements. However, the experimental backbone curve of the shorter beam 3 in Figs. 6.8(c) and 6.9(c) does not follow the same patterns as for beams 1 and 2 and seems to be shifted in frequency from the numerical backbone with a distorted softening effect at low amplitude. This is known in the literature to be an effect of the clamp, which can lead to softening effects. This distortion also seems to appear on a smaller scale for the experimental backbone of beam 2.

Several observations can be drawn from these results. The strong effect of gravity on the first nonlinear mode as found in Chapter 4 is recovered in Fig. 6.9(a), where the $\alpha = 0$ backbone curve corresponding to the no-gravity condition departs significantly from the backbone curves including gravity where $\alpha > 0$. Fig. 6.9(a) furthermore demonstrates the repeatability of the experiments. Two additional experimental backbone curves (different tests using the same beam) are added in orange and brown to the experimental backbone curve of Fig. 6.8(a) (in black). The three experimental curves are in very good agreement, indicating that the experimental procedure of § 6.4 is robust and repeatable.

Finally, from the good agreement between the experimental and numerical backbone curves of beams 1 and 2, there appears to be weak or little "ribbon effect" on the first nonlinear mode, but this will be addressed in the next paragraphs.

Nonlinear mode 2 and ribbon effect The second nonlinear mode of beams 1, 2 and 3 is summarized in Fig. 6.10 following the same procedure as for the first nonlinear mode. The softening trend of the second nonlinear mode (see Chapters 3 and 4) of a cantilever beam is again recovered experimentally for all three beam specimens. However, unlike the first nonlinear mode, a good agreement between the numerical and experimental backbone curves is found only for the two thinner beams, beam 2 in Fig. 6.10(b) and beam 3 in Fig. 6.10(c). The experimental backbone curves of these two beams remain within or very close to the numerical backbone considering the numerical uncertainty. By contrast, the experimental backbone curve of beam 1 in Fig. 6.10(a) lies far outside the uncertainty window of the numerical backbone and, moreover, is significantly more hardening compared to even beam 2, which has the same slenderness parameter η as beam 1. Since the gravity parameter α has

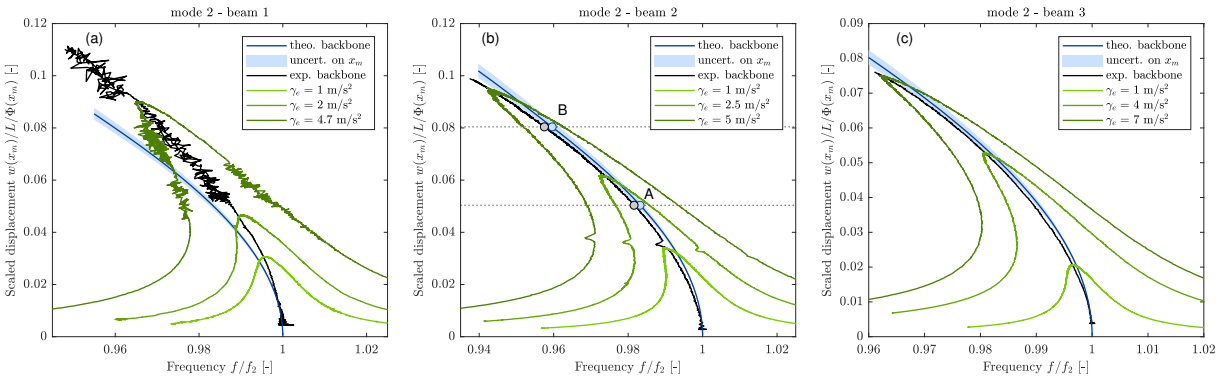

Figure 6.10: Experimental nonlinear frequency responses, for several base acceleration, and backbone curves (laser vibrometer) of mode 2 compared to the theoretical backbone curve. The light blue shaded area correspond to the measurement uncertainty of the theoretical backbone curve due to the measurement position x_m. (a): beam 1; (b): beam 2; (c): beam 3.

a negligible effect on the second nonlinear mode (§ 4.4.2), the theoretical backbone curves of beams 1 and 2 in Figs. 6.10(a) and (b) are near identical. The experimental backbone curves, however, are very different, indicating that another effect is influencing the experimental response. Note that any noise in Fig. 6.10(a) is due to a transfer of energy to mode 1. In the experiments, it was observed that on the second nonlinear mode, a low-frequency motion with the shape of mode 1 was superimposed onto the high-frequency oscillations with the shape of mode 2. Similar results have been documented in the literature, see *e.g.* the work of Nayfeh *et al.* on widely spaced modes or couplings between low- and high-frequency modes [12], [150], [166], [226].

Table 6.3: Maximum values of the curvature κ and the dimensionless ribbon parameter $\bar{\kappa} \simeq \frac{\kappa b^2}{h}$ for each beam $1-3$ on nonlinear modes $1-3$.

	Beam 1 $b = 18.1$ [mm] $h = 0.495$ [mm]	**Beam 2** $b = 6.79$ [mm] $h = 0.495$ [mm]	**Beam 3** $b = 4.43$ [mm] $h = 0.495$ [mm]
Mode 1	$\begin{cases} \kappa = 6.5126 \\ \bar{\kappa} = 4.3103 \end{cases}$	$\begin{cases} \kappa = 6.6133 \\ \bar{\kappa} = 0.6160 \end{cases}$	$\begin{cases} \kappa = 6.3813 \\ \bar{\kappa} = 0.62530 \end{cases}$
Mode 2	$\begin{cases} \kappa = 1.8483 \\ \bar{\kappa} = 1.2233 \end{cases}$	$\begin{cases} \kappa = 2.6474 \\ \bar{\kappa} = 0.2466 \end{cases}$	$\begin{cases} \kappa = 2.0593 \\ \bar{\kappa} = 0.0816 \end{cases}$
Mode 3	$\begin{cases} \kappa = 1.4207 \\ \bar{\kappa} = 0.9403 \end{cases}$	$\begin{cases} \kappa = 1.3855 \\ \bar{\kappa} = 0.1290 \end{cases}$	$\begin{cases} \kappa = 1.3320 \\ \bar{\kappa} = 0.0528 \end{cases}$

Since the beam 2 backbones are in agreement while the beam 1 backbones are not, we considered this to be an example of the ribbon effect described in § 6.5.1 as the main difference between the two beams is the width of the beam b. Recall from § 6.5.1 that the b/h ratio of beam 2 is $\sim \frac{1}{3}$ that of beam

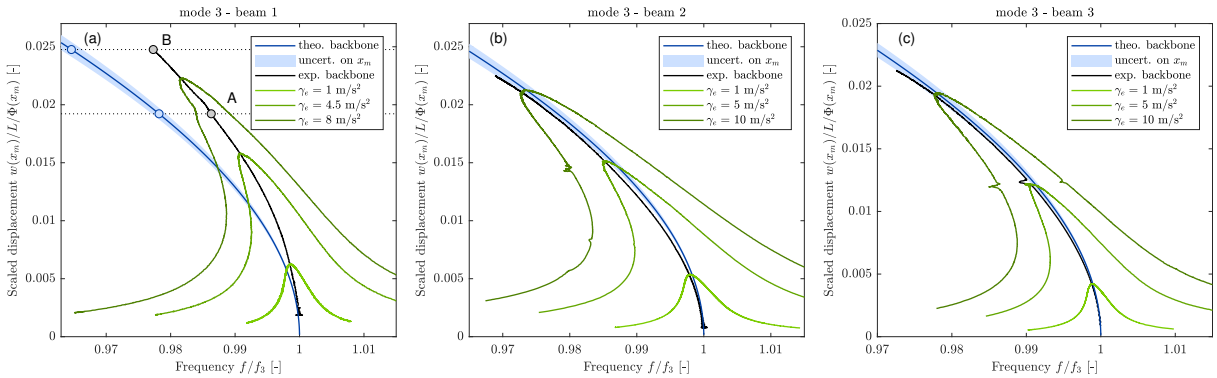

Figure 6.11: Experimental nonlinear frequency responses, for several base acceleration, and backbone curves (laser vibrometer)of mode 3 compared to the theoretical backbone curve. The light blue shaded area correspond to the measurement uncertainty of the theoretical backbone curve due to the measurement position x_m. (a): beam 1; (b): beam 2; (c): beam 3.

1 and the ribbon coefficient is computed as $\bar{\kappa} = \frac{\kappa b^2}{h}$ [Eq. (6.22)]. Looking first at the first nonlinear mode in Fig. 6.8, we see that the backbone curves of all three beams reach approximately the same scaled displacement amplitude ($\simeq 1.6$). This indicates that the maximum curvature κ attained on mode 1 remains approximately the same for all three beams as shown in the first row of Table 6.3 ($\kappa_{\text{beam 1}} \approx \kappa_{\text{beam 2}} \approx \kappa_{\text{beam 3}}$). This trend holds also on modes 2 and 3. Then, it can be concluded according to Eq. (6.22) that the ribbon coefficient $\bar{\kappa}$ changes mostly as a function of b^2/h between the beams. The ribbon coefficient $\bar{\kappa}$ is computed for all three beams on all three nonlinear modes in Table 6.3. While $\bar{\kappa}$ is reduced on beams 2 and 3 compared to beam 1 ($\bar{\kappa}_{\text{beam 3}} < \bar{\kappa}_{\text{beam 2}} < \bar{\kappa}_{\text{beam 1}}$), the largest ribbon coefficient is computed on the first nonlinear mode (of beam 1) where the curvature is highest, indicating that the strongest ribbon effect, if any, should occur on the first nonlinear mode. However, there is little difference in the backbone curves of beams 1 and 2 on the first nonlinear mode [Figs. 6.8(a) and (b)], indicating that what is being observed on the second nonlinear mode (as well as the third, see below) may not be tied to any ribbon effect.

Nonlinear mode 3 Finally, the third nonlinear mode of beams 1, 2 and 3 is shown in Fig. 6.11. The third nonlinear mode of a cantilever beam is known to be softening like the second nonlinear mode and this behavior is once again recovered by the experimental backbones of all three beams. Besides this, the trends of the third nonlinear mode globally align with the second nonlinear mode, in that beam 2 in Fig. 6.11(b) and beam 3 in Fig. 6.11(c) exhibit very good agreement between the experimentally-measured and the numerical backbone curves and beam 1 in Fig. 6.11(a) does not. The discrepancy between the mode 3 experimental and numerical backbone curves of beam 1 appears even more pronounced than for mode 2.

6.5.3 Nonlinear mode shapes

In addition to the backbone curves of the previous section, we compare the deformed shape of the cantilever on its first three nonlinear modes to the experimental deformed shape tracked as described in § 6.4.3. Numerically, the deformed shape of the beam is reconstructed directly for all degrees of

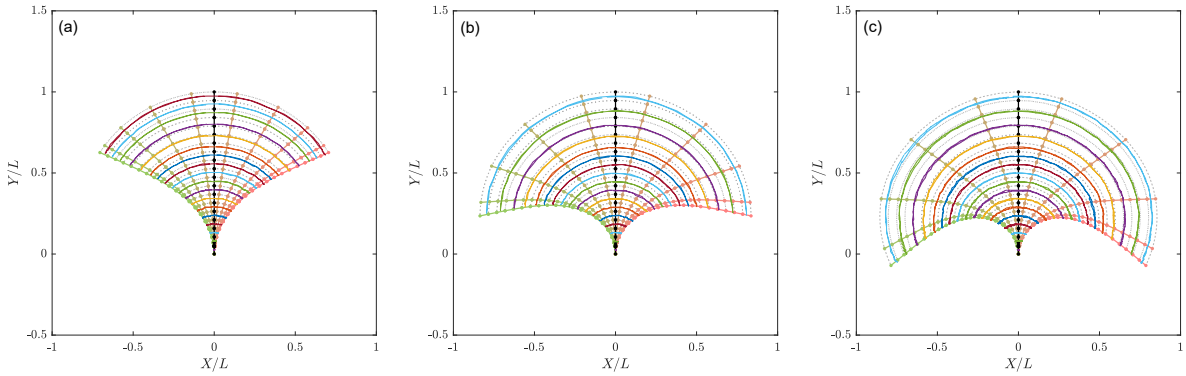

Figure 6.12: Deformed shape of the first nonlinear mode of beam 1 for several base accelerations. (a): point A of Figs. 6.8(a) and 6.9(a); (b): point B; (c): point C.

freedom from the response $\boldsymbol{x}_{\text{cnm}}$ at a certain point along the backbone curve (vibrating at a certain amplitude and frequency). The displaced beam is then traced for a number of snapshots (here, 10) over one half period of the motion, with the snapshots of the beam and the trajectory of each of the beam's nodes collected together in one figure. The point along the numerical backbone for which all the deformed shapes are drawn is selected at the same *amplitude* as the experimental deformed shapes, which may be at a different *frequency* in places where the numerical and experimental backbones do not perfectly overlap. The points at which the deformed shapes are taken are marked with circles in Figs. 6.8-6.11. The numerical deformed shape is then overlaid onto the experimental deformed shape tracked by the camera.

The deformed shape is not traced for all three beams on all three modes. Recall from § 6.5.1 that η does not have an influence on the nonlinear modes since it is very small for all three beams, and from Chapter 4 (§ 4.5.1) that α, which only affects the first nonlinear mode, does not change the nonlinear mode shape. For these reasons, it is sufficient to trace the nonlinear deformed shape for only one beam on each nonlinear mode. The following deformed shapes are compared:

- the first nonlinear mode shape of beam 1 at low, moderate and high amplitudes in Fig. 6.12,
- the second nonlinear mode shape of beam 3 at moderate and higher amplitudes in Fig. 6.13,
- the third nonlinear mode shape of beam 1 at moderate and higher amplitudes in Fig. 6.14.

Comparing these figures, globally there is very good agreement between the experimental and numerical deformed shapes. This is especially true on the first nonlinear mode in Fig. 6.12, where the experimental mode shape is nearly identical to the experimental one even at very large amplitudes. On the higher nonlinear modes 2 and 3, some points are not perfectly aligned and the mode shape is slightly off-center. Since they are not physical phenomena (*i.e.* a single point does not stick out from the global mode shape in reality), these effects are likely due to difficulties in the tracking software on the second and third nonlinear modes since the amplitudes are much smaller than on the first nonlinear mode. Overall, however, good agreement with the numerical mode shapes and an accurate representation of the known nonlinear mode shapes are found on all three nonlinear modes.

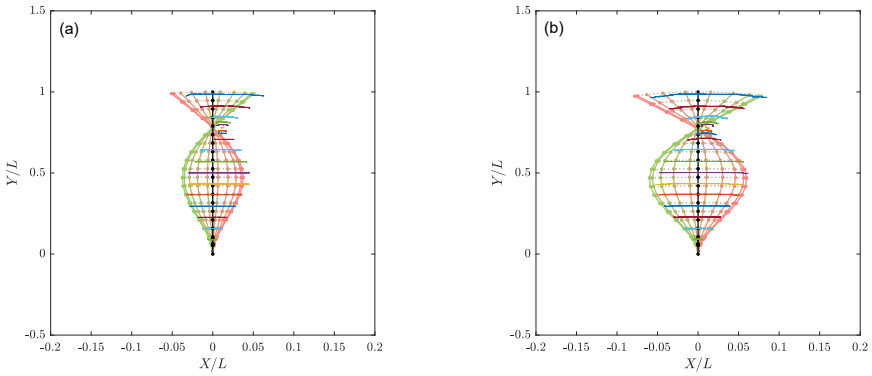

Figure 6.13: Deformed shape of the second nonlinear mode of beam 3 for several base accelerations. (a): point A of Figs. 6.10(c); (b): point B.

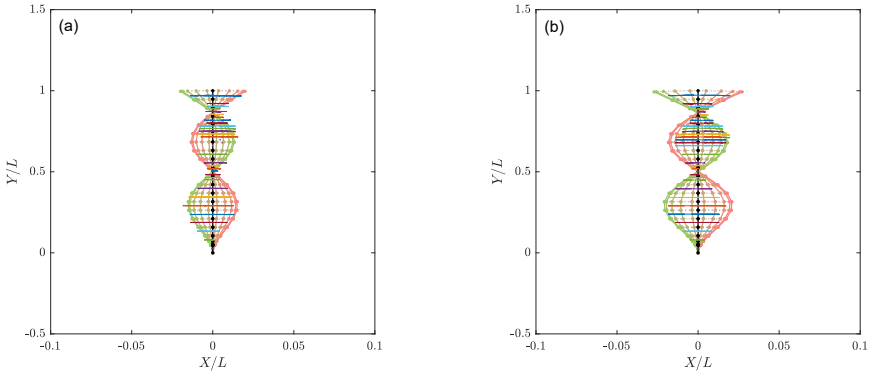

Figure 6.14: Deformed shape of the third nonlinear mode of beam 3 for several base accelerations. (a): point A of Figs. 6.11(a); (b): point B.

6.5.4 Damping estimation

In the same way as § 6.3.2, the damping of the system is investigated for the beam 1 experiments of Fig. 6.8(a), Fig. 6.10(a) and Fig. 6.11 by plotting the first harmonic of the scaled base acceleration as a function of the first harmonic of the scaled transverse displacement of the beam at x_m in Fig. 6.15. The experimental curves are shown in blue and are fitted with three polynomial models in black: linear (dotted curve), quadratic (dashed curve) and cubic (dash-dotted curve). Also included in Fig. 6.15(a) is a zoom onto lower amplitudes, where the vertical dashed line indicates the limit in amplitude of the quadratic damping model of Colin *et al.* [42].

The following observations are made:

- In the inset of Fig. 6.15(a), the quadratic damping model of [42] (in open air experiments) is recovered as the blue experimental curve follows the quadratic trend (dashed curve) in this region. This indicates the dominance of the air drag damping in this region, the topic of [42].
- At higher amplitudes of displacement, the blue experimental curve transitions from the quadratic

to the cubic trend (dash-dotted curve) up to the maximum displacement amplitude of our experiments. This agrees with the numerical trend of § 6.3.2 and indicates the dominance of cubic structural (viscoelastic) damping in this region [4], [6]–[9], [71].

- On the higher nonlinear modes 2 and 3, the blue experimental curves follow the quadratic (dashed curve) trend, which agrees with the previous observations since the amplitude of the scaled transverse displacement on these modes remains below the limit of [42].

In addition to these points, the same figures are recreated for all beams in Fig. 6.16. On each mode, the same global trends already described hold; however, on modes 1 and 3 in Figs. 6.16(a) and (c), the transition to higher orders of damping seems to occur at lower amplitudes of motion for beam 2 than for beams 1 and 3.

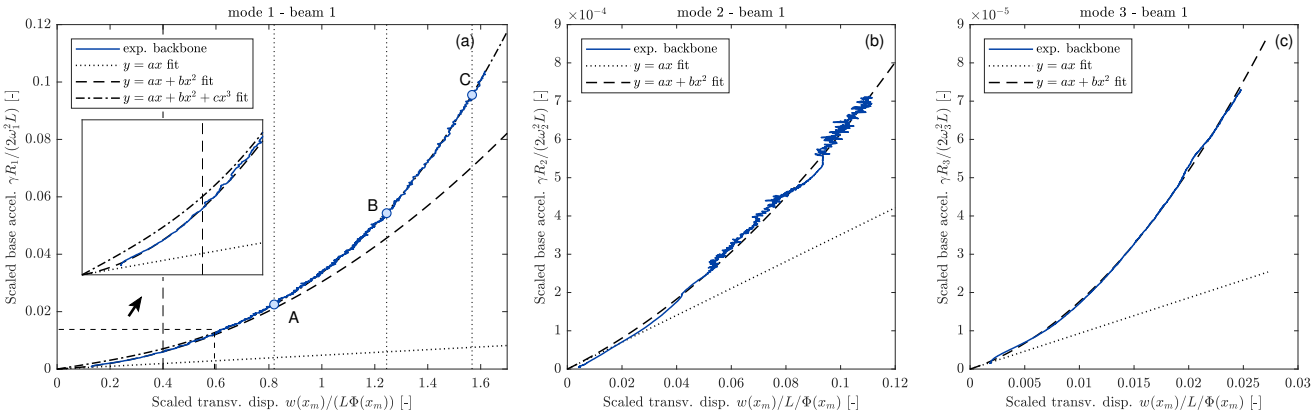

Figure 6.15: Base acceleration as a function of the amplitude of beam 1 on the backbone curve and several polynomial fits. (a): mode 1 of Fig. 6.8(a); (b): mode 2 of Fig. 6.10(a); (c): mode 3 of Fig. 6.11(a).

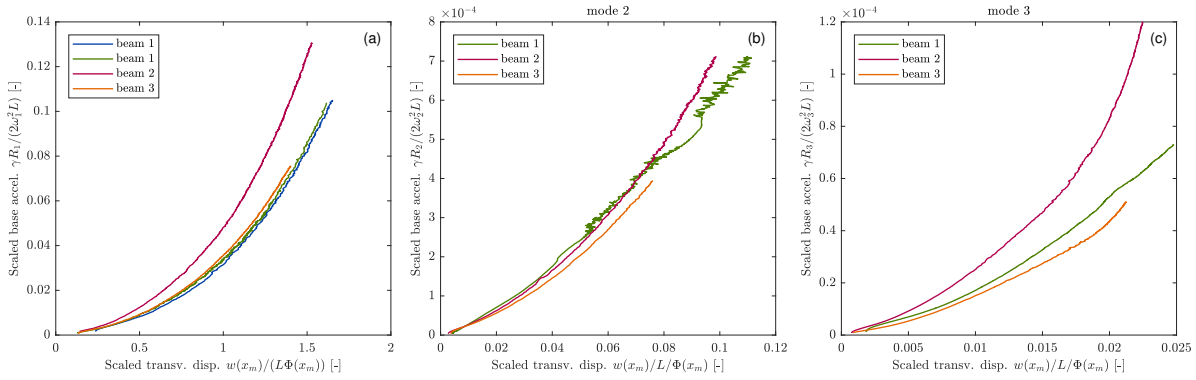

Figure 6.16: Base acceleration as a function of the amplitude of the beam on the backbone curve for modes 1, 2 and 3 of Figs. 6.8, 6.10 and 6.11 (a): mode 1; (b): mode 2; (c): mode 3.

6.6 Conclusion and future work

In this chapter, the results of phase resonance testing of highly flexible cantilevers have been presented. The results are separated into two distinct categories, conservative and dissipative effects. In the former, the idea of phase resonance has been used by way of a Phase-Locked Loop controller for the experimental measurement of conservative nonlinear modes. In particular, we are interested in measuring the experimental CNMs of highly flexible structures at very large amplitudes of vibration. To this end, the first three CNMs of slender cantilever rulers excited via base acceleration are measured and used to validate the numerical model of previous chapters (in particular Chapter 4). Globally, good agreement is found between the experimental and numerical CNMs, such that the numerical model is validated when some important considerations, such as the effect of gravity and potential ribbon effects, are also taken into account. Then, the phase resonance testing of the cantilever beams is used to estimate the nonlinear damping at very large amplitudes. It is shown numerically in § 6.3.2 and experimentally in § 6.5.4 that the damping (in open air experiments) is nonlinear, in agreement with previous work [42], [71]. Moreover, it is shown that the damping transitions from being linear at very small amplitudes to quadratic at moderate amplitudes, cubic at large amplitudes and even higher order at extreme amplitudes of motion.

In future work, we aim to continue the experiments in order to further the damping investigation; one potential option in this regard is to redo similar experiments within a vacuum as done in [71] in order to minimize the air drag of open air experiments. In addition, more work is needed in order to fully characterize the behavior of the CNMs on the second and third nonlinear modes. In particular, we seek to explain the discrepancy between the backbones of beam 1 on these modes (either through an improved understanding of the ribbon effects or by other means). Finally, the topics and experiments of this chapter can be extended to other flexible systems in future work, such as experiments involving the flexible ring of Chapter 3 or investigating the parametric behavior of flexible cantilevers [70], [82].

To assist the reader in their understanding, a short recap of the main results is summarized here:

Table 6.4: Summary of the main results of Chapter 6.

	Beam 1 $L = 380$ [mm] $b = 18.1$, $h = 0.495$ [mm]	**Beam 2** $L = 380$ [mm] $b = 6.79$, $h = 0.495$ [mm]	**Beam 3** $L = 290$ [mm] $b = 4.43$, $h = 0.495$ [mm]
Mode 1	1. CNMs → matched ✓ ∘ Must include gravity 2. Mode shape → matched ✓	1. CNMs → matched ✓ ∘ Must include gravity	1. CNMs → discrepancy ∘ Must include gravity ∘ Effect of clamp ✗
Mode 2	1. CNMs → discrepancy ∘ Gravity negligible ∘ Suspected ribbon, but open ✗	1. CNMs → matched ✓ ∘ Gravity negligible	1. CNMs → matched ✓ ∘ Gravity negligible 2. Mode shape → matched ✓ ∘ Needs improvement
Mode 3	1. CNMs → discrepancy ∘ Gravity negligible ∘ Suspected ribbon, but open ✗ 2. Mode shape → matched ✓ ∘ Needs improvement	1. CNMs → matched ✓ ∘ Gravity negligible	1. CNMs → matched ✓ ∘ Gravity negligible

Conclusion

In this work, we have developed a numerical method for the study of highly flexible slender beam structures in large amplitude vibration and demonstrated its applicability to many different types of systems. A common objective throughout our work has been to extend the computational capacity to extremely large amplitudes of motion, where the rotation of the cross-sections can reach nearly π [rad]. As has been shown in each chapter, modeling such large rotations is not straightforward and requires special considerations (especially of the rotation terms) that are typically not present at smaller amplitudes (*e.g.* if the rotations are linearized or expanded in a truncated Taylor series). We have considered only *geometrical* nonlinearities in this work, but other types of nonlinearities can also be present in flexible structures (such as in the case of geometrically nonlinear flexible 1D structures made of materials requiring nonlinear constitutive models). For these reasons (among others), research in this field is actively ongoing.

The work of this thesis is based on a total Lagrangian finite element discretization of the geometrically exact beam model (§ 2.1). The geometrically exact beam model is regularly used to model highly flexible beams since it preserves the geometrical nonlinearities at any amplitude of motion. However, it is precisely this feature - treatment of the nonlinearities/rotation terms - of the geometrically exact model that render it difficult to solve. Efficient numerical strategies are required, and to this end we have proposed our frequency domain-based solving strategy to target periodic solutions. The solving strategy is based on a Fourier series expansion of the variables in the Harmonic Balance Method and solved with continuation in the Asymptotic Numerical Method (§ 2.2). The solving strategy has been shown to be efficient, robust and useful in the study of nonlinear dynamical phenomena (nonlinear modes, internal resonances, bifurcations, stability analysis (§ 2.4)).

Our numerical model has been used in this work to simulate the nonlinear vibrations of several very different test cases, including both simple systems such as cantilever and clamped-clamped beams and complex systems such as tree models and trusses. Beyond test cases, however, it is of utmost importance that any new model be validated with existing models in the literature. To this end, we have systematically compared the results of our model to "special case" models and results found in the literature. Examples include validation of the clamped-clamped beam test case with a nonlinear Von Kármán model (§ 3.3.2 and § 5.5.2), validation at low to moderate amplitudes with the analytical inextensible beam model of [46], [47] (§ 4.4.1) and validation with works in the literature in § 4.4.2 and § 5.5. In addition to *numerical* validation, validation with *experiments* brings a new level of confidence to any numerical model. The numerical model proposed in this work has in this regard also been validated experimentally with dedicated experiments in vibration control of highly flexible beam structures (§ 6.5). By making use of the concept known as *phase resonance* for experimental measurement of nonlinear modes, we have demonstrated that our model is capable of capturing the true physics of highly flexible cantilevers even at very large amplitudes of vibration. In addition, we

are able to show almost exact equivalence between the experimental and numerical nonlinear mode shapes (particularly on the first nonlinear mode at very large amplitude). While agreement between the numerical and experimental results is found for at least one beam on the first three nonlinear modes, some experimental results do not align perfectly with numerical simulations and require further consideration. Nevertheless, we believe that these results demonstrate the usefulness of our numerical finite element model in the study of highly flexible structures.

Progression of this work Each step of the work of this thesis has followed a linear progression building off of previous work. To summarize the progression of this work, a short recap of each chapter is provided in the next paragraphs.

In Chapter 3, the model is derived beginning with motions restricted to a plane. The model is used to simulate frequency response curves and the nonlinear modes of several test structures. Details regarding some numerical considerations such as the shape and presence of internal resonances during computation, convergence studies and an investigation into formalisms of the solving strategy are presented. A version of this finite element model restricted to plane motions is made available for download at [57]. The model of Chapter 3 for plane motions is then used in Chapter 4 to study the influences of two parameters, slenderness and gravity, on the large amplitude vibrations of cantilever beams. In Chapter 4, it is shown that the dimensionless geometrically exact beam equations depend only on these two parameters (a third, a shear parameter due to the inclusion of shear in Timoshenko kinematics, is shown to be negligible for slender structures). This chapter demonstrates how the numerical strategy of our work for the simulation of flexible beam structures can be used to study the general nonlinear behavior of these structures.

The model is then extended to 3D motions in Chapter 5. This extension gives us the capacity to study nonlinear large amplitude behavior out of the 2D plane, which can occur *e.g.* during certain interactions between the nonlinear modes when energy is transferred from an in-plane mode to an out-of-plane mode. Two examples of 1:1 internal resonance between the two transverse bending polarizations illustrate this. Finally, as an extension of Chapter 4, the numerical model including gravity is used in conjunction with dedicated experiments in vibration control to validate measurement of the conservative nonlinear modes using phase resonance in Chapter 6. Many different concepts are brought together to perform these experiments. In the end, however, validation of the numerical model with experiments up to very large amplitudes of vibration brings new confidence in the capacity of our work to model highly flexible structures.

Realization of the research objectives In order to summarize how the main research objectives of this work are achieved, we recall the research objectives outlined in § 1.2.2 and indicate where they are addressed in the body of this thesis:

1. Develop a novel modeling strategy for the simulation of large amplitude nonlinear dynamics of slender 1D beam structures based in the frequency domain. The geometrically exact beam model is used in order to capture the geometrical nonlinearities of the system in large rotation and discretized into finite elements. The finite element equations of motion are solved in the frequency domain in order to directly target the steady-state periodic solutions of the system. The solving procedure consists of a Harmonic Balance (HBM) Fourier series expansion, which is then solved with a continuation strategy called the Asymptotic Numerical Method (ANM), all of which is automated by the MANLAB solver [96]. → **Achieved for plane (2D) motions in the**

work of Chapter 3 using a rotation matrix parametrization of the rotations, and later extended to 3D motions in the work of Chapter 5 using quaternions for parametrization of the rotations.

2. Validate the proposed numerical modeling strategy with dedicated vibration experiments involving flexible beam specimens subjected to periodic excitation. Experimental validation can add value to numerical models by confirming their capacity to predict physical reality. To this end, the experiments are used to investigate nonlinear phenomena predicted by the numerical model (experimentally-determined nonlinear modes, couplings between modes, instabilities, etc). $\rightarrow$ **Achieved in the work of Chapter 6 using the idea of phase resonance for experimental measurement of conservative nonlinear modes, and compared to the true conservative nonlinear modes computed as in Chapters 3 and 4.**

3. Characterize, investigate and otherwise generally explore the highly nonlinear dynamical behavior of slender 1D beam structures and the nonlinear phenomena they exhibit. $\rightarrow$ **Achieved generally throughout this work, examples of which include special investigation of nonlinear modes in the work of Chapters 3 - 6, internal resonances in Chapters 3 and 5, the nonlinear influences of slenderness and gravity in Chapter 4 and the idea of phase resonance for the measurement of nonlinear modes and nonlinear damping estimation in Chapter 6.**

Applicability of this work to industry It can be useful in highlighting the contributions of this work to the field of nonlinear dynamics to cite a few *direct* applications of our work to industrial problems. We have already presented in Chapter 1 and throughout this work the many industrial applications of flexible 1D beam structures in general. Some direct applications are now mentioned.

Since our work is adapted to target periodic oscillations, it can be used to model vibrating slender beam structures. A first application is to model the oscillations of rotating slender blades as can be found in (wind) turbines, turbo engines or rotor blades. Aircraft wings, flexible aircrafts and antenna are a natural extension of these concepts as the loads and fluid-structure interactions encountered during flight, or events such as flutter, can induce vibrations in these structures. Periodic oscillations of flexible beam structures are also prevalent in electromechanical systems (especially nano- and micro-electromechanical systems) with the use of piezoelectric patches that can be made to vibrate when exposed to electrical current. Besides simple structures such as nanotubes and microcantilevers, our model is able to simulate more complex oscillating structures assembled from the finite beam elements. Mechanical beams with piezoelectric materials can also be used for energy harvesting or to replace batteries in rotating or oscillating systems.

These few examples have shown how the work of this thesis can be *directly applied* to further research relevant to modern industry.

Future work

Finally, we conclude with some ideas for future avenues of investigation related to the work that has been presented here. The following topics are intended to serve as direct extensions of this thesis with the current state of the work here serving as a starting point for these future studies.

Numerical studies

- Improvements to both the 2D finite element model of Chapter 3 and the 3D finite element model of Chapter 5:
  - Updates of existing versions of the codes in order to allow for polynomial interpolations of any order in each formulation (rotation matrices or quaternions), or re-coding of the interpolations better suited to rotations (see § 2.3.2 and § 5.3);
  - Implementation of more physically realistic nonlinear damping conditions, such as a Kelvin-Voigt model (see § 3.2.2 or the damping aspects of Chapter 6);
  - Stability analysis for finite element systems with many degrees of freedom based on the work of [22];
  - Full comparison of the computational efficiency of the quaternion-based and rotation matrix-based 2D formulations (see § 5.5.2);
  - Development of more efficient methods in MANLAB for initialization of large systems with many degrees of freedom, particularly in order to carry out 3D simulations with more elements (and, therefore, degrees of freedom, see § 5.5.1 and § 5.6);
- Improvements specifically to the 3D finite element model of Chapter 5:
  - Inclusion of rotational inertia in the equations of motion (see § 5.1 and Appendix C.1);
  - Generalization of the model to any initial orientation (*i.e.* elimination of Assumptions #4 and 5 of Chapter 5 restricting the model to only initially straight initial configurations, see § 5.1).

Experimental studies

- Continued investigation of the cantilever beam experiments of Chapter 6 based on the main results summarized in Table 6.4 (see § 6.6);
- Extension of the cantilever beam experiments to 3D applications, *e.g.* the studies of [53], [54], and comparison with numerical simulations;
- Experimental analysis of other types of nonlinear structures based on the idea of phase resonance to measure nonlinear modes, and recreation of known nonlinear effects uncovered by the numerical model throughout this work (*e.g.* the hardening-to-softening or centrifugal effects of the circular ring in § 3.3.3 or the 1:1 internal resonances of § 5.5.1).

Works by the Author

Peer-reviewed Journal Articles

[1] Debeurre, M., Grolet, A., Cochelin, B., Thomas, O.: Finite element computation of nonlinear modes and frequency response of geometrically exact beam structures. Journal of Sound and Vibration **548**, 117534 (2023). 10.1016/j.jsv.2022.117534

[2] Debeurre, M., Grolet, A., Thomas, O.: Extreme nonlinear dynamics of cantilever beams: effect of gravity and slenderness on the nonlinear modes. Nonlinear Dynamics **111**, 12787–12815 (2023). 10.1007/s11071-023-08637-x

[3] Martin, A., Opreni, A., Vizzaccaro, A., Debeurre, M., Salles, L., Frangi, A., Thomas, O., Touzé, C.: Reduced order modeling of geometrically nonlinear rotating structures using the direct parametrisation of invariant manifolds. Journal of Theoretical, Computational and Applied Mechanics, (2023). doi:10.46298/jtcam.10430

[4] Debeurre, M., Benacchio, S., Grolet, A., Grenat, C., Giraud-Audine, C., Thomas, O.: Phase resonance testing of highly flexible structures: measurement of conservative nonlinear modes and nonlinear damping identification. *Submitted to* Mechanical Systems and Signal Processing.

[5] Debeurre, M., Grolet, A., Thomas, O.: Quaternion-based finite element computation of nonlinear modes and frequency responses of geometrically exact beam structures in three dimensions. *Submitted to* Multibody System Dynamics.

[6] Grolet, A., Vizzaccaro, A., Debeurre, M., Thomas, O.: Invariant manifold computation with a quadratic recast: a generic way of reducing the nonlinear dynamics of large models. *To be submitted to* Nonlinear Dynamics [in preparation].

Published Conference Proceedings

[7] Debeurre, M., Grolet, A., Mattei, P.-O., Cochelin, B., Thomas, O.: Nonlinear modes of cantilever beams at extreme amplitudes: Numerical computation and experiments. Conference Proceedings of the Society for Experimental Mechanics Series 40th IMAC, Orlando, Florida, 245-248 (2023). 978-3-031-04086-3_35

[8] Debeurre, M., Grolet, A., Cochelin, B., Thomas, O.: Modélisation efficace de structures élancées géométriquement non linéaires : réponses en régime forcé et modes non linéaires. Proceedings of the 15e Colloque National en Calcul des Structures, Hyères-les-Palmiers, France (2022) [in French].

Open-source Code and Documentation

[9] Debeurre, M., Grolet, A., Cochelin, B., Thomas, O.: 2D geometrically exact (nonlinear) finite element beam model solved in the frequency domain, THREAD-3-2/NL_2D_FEM (2022).

Bibliography

[1] Abeloos, G., Müller, F., Ferhatoglu, E., Scheel, M., Collette, C., Kerschen, G., Brake, M.R.W., Tiso, P., Renson, L., Krack, M.: A consistency analysis of phase-locked-loop testing and control-based continuation for a geometrically nonlinear frictional system. Mechanical Systems and Signal Processing **170**, 108820 (2022)

[2] Abramovich, H.: Free vibrations of gravity loaded composite beams. Composite Structures **23**, 17–26 (1993)

[3] Alcorta, R., Chouvion, B., Michon, G., Montagnier, O.: On the use of frictional dampers for flutter mitigation of a highly flexible wing. International Journal of Non-Linear Mechanics **156**(104515) (2023). doi:10.1016/j.ijnonlinmec.2023.104515

[4] Alijani, F., Amabili, M., Balasubramanian, P., Carra, S., Ferrari, G., Garziera, R.: Damping for large-amplitude vibrations of plates and curved panels, Part 1: Modeling and experiments. International Journal of Non-Linear Mechanics **85**, 23–40 (2016). doi:10.1016/j.ijnonlinmec.2016.05.003

[5] Amabili, M.: Nonlinear Vibrations and Stability of Shells and Plates. Cambridge University Press (2008)

[6] Amabili, M.: Nonlinear damping in large-amplitude vibrations: modelling and experiments. Nonlinear Dynamics **93**, 4–18 (2018)

[7] Amabili, M.: Nonlinear damping in nonlinear vibrations of rectangular plates: Derivation from viscoelasticity and experimental validation. Journal of the Mechanics and Physics of Solids **118**, 275–292 (2018)

[8] Amabili, M.: Derivation of nonlinear damping from viscoelasticity in case of nonlinear vibrations. Nonlinear Dynamics **97**, 1785–1797 (2019). doi:10.1007/s11071-018-4312-0

[9] Amabili, M., Alijani, F., Delannoy, J.: Damping for large-amplitude vibrations of plates and curved panels, part 2: Identification and comparisons. International Journal of Non-Linear Mechanics **85**, 226–240 (2016). doi:10.1016/j.ijnonlinmec.2016.05.004

[10] J. M. Londoño and, S.A.N., Cooper, J.E.: Identification of backbone curves of nonlinear systems from resonance decay responses. Journal ofSoundandVibration (2015)

[11] Anderson, T.J., Balachandran, B., Nayfeh, A.H.: Nonlinear resonances in a flexible cantilever beam. Journal of Vibration and Acoustics **116**(4), 480–484 (1994). doi:10.1115/1.2930452

[12] Anderson, T.J., Nayfeh, A.H., Balachandran, B.: Coupling between high-frequency modes and a low-frequency mode: Theory and experiment. Nonlinear Dynamics **11**, 17–36 (1996)

[13] Apiwattanalunggarn, P., Shaw, S., Pierre, C., Jiang, D.: Finite-element-based nonlinear modal reduction of a rotating beam with large-amplitude motion. Journal of Vibration and Control **9**(3-4), 235–263 (2003). doi:10.1177/107754603030751

[14] Argyris, J.: An excursion into large rotations. Computer Methods in Applied Mechanics and Engineering **32**, 85–155 (1982)

[15] Arquier, R., Bellizzi, S., Bouc, R., Cochelin, B.: Two methods for the computation of nonlinear modes of vibrating systems at large amplitude. Computers & Structures **84**, 1565–1576 (2006)

[16] Arquier, R., Bellizzi, S., Bouc, R., Cochelin, B.: Two methods for the computation of nonlinear modes of vibrating systems at large amplitudes. Computers and Structures **84**, 1565–1576 (2006)

[17] Audoly, B., Neukirch, S.: A one-dimensional model for elastic ribbons: A little stretching makes a big difference. Journal of the Mechanics and Physics of Solids **153**, 194457 (2021)

[18] Azrar, L., Cochelin, B., Damil, N., Potier-Ferry, M.: An asymptotic-numerical method to compute the post-buckling behavior of elastic plates and shells. International Journal for Numerical Methods in Engineering **36**, 1251–1277 (1993)

[19] Basler: Basler video recording software. `https://www2.baslerweb.com/en/downloads/software-downloads/`. Accessed: 2021-01-26

[20] Bathe, K.: Finite Element Procedures. K.J. Bathe, Watertown (2014)

[21] Bauchau, O.A., Han, S., Mikkola, A., Matikainen, M.K.: Comparison of the absolute nodal coordinate and geometrically exact formulations for beams. Multibody System Dynamics **32**, 67–85 (2014). doi:10.1007/s11044-013-9374-7

[22] Bayer, F., Leine, R.: Sorting-free Hill-based stability analysis of periodic solutions through Koopman analysis. Nonlinear Dynamics **111**, 8439–8466 (2023)

[23] Ben Shaya, N., Bucher, I., Dolev, A.: Automatic locking of a parametrically resonating, base-excited, nonlinear beam. Nonlinear Dynamics **106**, 1843–1867 (2021)

[24] Benacchio, S., Chatelain, P., Giraud-Audine, C., Thomas, O.: Mesure de résonances non linéaires et de courbes maîtresses pour des poutres excitées paramétriquement. Proceedings of the 15ème Colloque National en Calcul des Structures **Hyères-les-Palmiers, France** (May 2022)

[25] Benacchio, S., Giraud-Audine, C., Thomas, O.: Effect of dry friction on a parametric non linear oscillator. Nonlinear Dynamics **108**, 1005–1026 (2022). doi:10.1007/s11071-022-07233-9

[26] Bertails, F., Audoly, B., Cani, M.P., Querleux, B., Leroy, F., Lévêque, J.L.: Simulation of the mechanical behaviour of woven fabrics at the scale of fibers. ACM Transactions on Graphics **25**(3), 1180–1187 (2006). doi:10.1145/1141911.1142012

[27] Bertrand, C., Acary, V., Lamarque, C.H., Ture Savadkoohi, A.: A robust and efficient numerical finite element method for cables. International Journal of Numerical Methods in Engineering **121**, 4157–4186 (2020)

[28] Bokaian, A.: Natural frequencies of beams under compressive axial loads. Journal of Sound and Vibration **126**(1), 49–65 (1988)

[29] Bokaian, A.: Natural frequencies of beams under tensile axial loads. Journal of Sound and Vibration **142**(3), 481–498 (1990)

[30] Brüls, O., Cardona, A., Arnold, M.: Lie group generalized-α time integration of constrained flexible multibody systems. Mechanism and Machine Theory **48**, 121–137 (2012)

[31] Camier, C., Touzé, C., Thomas, O.: Non-linear vibrations of imperfect free-edge circular plates and shells. European Journal of Mechanics A/ Solids **28**(3), 500–515 (2009)

[32] Cardona, A., Géradin, M.: A beam finite element non-linear theory with finite rotations. International Journal for Numerical Methods in Engineering **26**, 2403–2438 (1988)

[33] Celledoni, E., Marthinsen, H., Owren, B.: An introduction to lie group integrators - basics, new developments and applications. Journal of Computational Physics **257**, 1040–1061 (2014). doi:10.1016/j.jcp.2012.12.031

[34] Cenedese, M., Haller, G.: How do conservative backbone curves perturb into forced responses? a melnikov function analysis. Proceedings of the Royal Society A **476**, 20190494 (2020)

[35] Chandrashekhara, S.K., Zupan, D.: Path following using velocity-based approach in quasi-static analysis. International Journal of Solids and Structures **275**(112292) (2023)

[36] Chu, H.N., Herrmann, G.: Influence of Large Amplitudes on Free Flexural Vibrations of Rectangular Elastic Plates. Journal of Applied Mechanics **23**(4), 532–540 (1956). doi:10.1115/1.4011396

[37] Cochelin, B., Damil, N., Potier-Ferry, M.: Asymptotic-numerical method and Padé approximations for non-linear elastic structures. International Journal for Numerical Methods in Engineering **37**, 1187–1213 (1994)

[38] Cochelin, B., Damil, N., Potier-Ferry, M.: Méthode Asymptotique Numérique. Lavoisier, Paris (2007)

[39] Cochelin, B., Damil, N., Potier-Ferry, M.: Méthode asymptotique numérique, collections méthodes numérique. Hermes Sciences Lavoisier, Paris (2007)

[40] Cochelin, B., Medale, M.: Power series analysis as a major breakthrough to improve the efficiency of asymptotic numerical method in the vicinity of bifurcations. Journal of Computational Physics **236**, 594–607 (2013)

[41] Cochelin, B., Vergez, C.: A high order purely frequency-based harmonic balance formulation for continuation of periodic solutions. Journal of Sound and Vibration **324**(1-2), 243–262 (2009)

[42] Colin, M., Thomas, O., Grondel, S., Cattan, E.: Very large amplitude vibrations of flexible structures: Experimental identification and validation of a quadratic drag damping model. Journal of Fluids and Structures **97**(103056) (2020)

[43] Cosserat, E., Cosserat, F.: Théorie des corps déformables. Hermann (1909)

[44] Cottanceau, E.: Numerical simulation of the assembly process of flexible cables under large displacements. Ph.D. thesis, Arts et Métiers ParisTech, Lille (2018)

[45] Cottanceau, E., Thomas, O., Véron, P., Alochet, M., Deligny, R.: A finite element/quaternion/asymptotic numerical method for the 3D simulation of flexible cables. Finite Elements in Analysis and Design **139**, 14–34 (2018)

[46] Crespo da Silva, M.R.M., Glynn, C.C.: Nonlinear flexural-flexural-torsional dynamics of inextensible beams. I. Equations of motion. Journal of Structural Mechanics **6**, 437–448 (1978)

[47] Crespo da Silva, M.R.M., Glynn, C.C.: Nonlinear flexural-flexural-torsional dynamics of inextensible beams. II. Forced motions. Journal of Structural Mechanics **6**, 449–461 (1978)

[48] Crisfield, M.A.: A consistent co-rotational formulation for non-linear, three-dimensional, beam-elements. Computer Methods in Applied Mechanics and Engineering **81**, 131–150 (1990)

[49] Crisfield, M.A., Galvanetto, U., Jelenić, G.: Dynamics of 3-D co-rotational beams. Computational Mechanics **20**, 507–519 (1997)

[50] Crisfield, M.A., Jelenić, G.: Objectivity of strain measures in geometrically exact 3D beam theory and its finite element implementation. Proceedings of the Royal Society of London **455**, 1125–1147 (1999)

[51] Cunff, C.L., Heurtier, J.M., Piriou, L., Berhault, C., Perdrizet, T., Teixeira, D., Ferrer, G., Gilloteaux, J.C.: Fully coupled floating wind turbine simulator based on nonlinear finite element method: Part I - Methodology. ASME 2013 32nd International Conference on Ocean, Offshore and Arctic Engineering (2013)

[52] Cunff, C.L., Ryu, S., Heurtier, J.M., Duggal, A.S.: Frequency-domain calculations of moored vessel motion including low frequency effect. 27th International Conference on Offshore Mechanics and Arctic Engineering (2008)

[53] Cusumano, J.P., Moon, F.C.: Chaotic non-planar vibrations of the thin elastica, part I: Experimental observation of planar instability. Journal of Sound and Vibration **179**(2), 185–208 (1995)

[54] Cusumano, J.P., Moon, F.C.: Chaotic non-planar vibrations of the thin elastica, part II: Derivation and analysis of a low-dimensional model. Journal of Sound and Vibration **179**(2), 209–226 (1995)

[55] Damil, N., Potier-Ferry, M.: A new method to compute perturbed bifurcation: application to the buckling of imperfect elastic structures. International Journal of Engineering Sciences **26**, 943–957 (1990)

[56] de la Llave, R., Kogelbauer, F.: Global persistence of lyapunov subcenter manifolds as spectral submanifolds under dissipative perturbations. SIAM Journal of Applied Dynamical Systems **18**(4), 2099–2142 (2019)

[57] Debeurre, M., Grolet, A., Cochelin, B., Thomas, O.: 2d geometrically exact (nonlinear) finite element beam model solved in the frequency domain. `https://github.com/THREAD-3-2/NL_2D_FEM` (2022). Accessed: 2022-12-02

[58] Debeurre, M., Grolet, A., Cochelin, B., Thomas, O.: Finite element computation of nonlinear modes and frequency response of geometrically exact beam structures. Journal of Sound and Vibration **548**(117534) (2023)

[59] Debeurre, M., Grolet, A., Thomas, O.: Extreme nonlinear dynamics of cantilever beams: effect of gravity and slenderness on the nonlinear modes. Nonlinear Dynamics **111**, 12787–12815 (2023)

[60] Denis, V., Jossic, M., Giraud-Audine, C., Chomette, B., Renault, A., Thomas, O.: Identification of nonlinear modes using phase-locked-loop experimental continuation and normal forms. Mechanical Systems and Signal Processing **106**, 430–452 (2018)

[61] Dezest, D., Thomas, O., Mathieu, F., Mazenq, L., Soyer, C., Costecalde, J., Remiens, D., Deü, J.F., Nicu, L.: Wafer-scale fabrication of self-actuated piezoelectric nanoeletromechanical resonators based on lead zirconate titanate (PZT). Journal of Micromechanics and Microengineering **25**, 035002 (2015)

[62] Dick, N., Krylov, S.: Parametric resonance and pattern selection in an array of microcantilevers interacting through fringing electrostatic fields. Nonlinear Dynamics **107**, 1703–1723 (2022)

[63] Durville, D.: Simulation of the mechanical behaviour of woven fabrics at the scale of fibers. International Journal of Material Forming **3**, 1241–1251 (2010). doi:10.1007/s12289-009-0674-7

[64] Elahi, H., Eugeni, M., Gaudenzi, P.: Piezoelectric Aeroelastic Energy Harvesting. Elsevier (2021)

[65] Escalona, J., Mohammadi, N.: Advances in the modeling and dynamic simulation of reeving systems using the arbitrary Lagrangian–Eulerian modal method. Nonlinear Dynamics **108**, 3985–4003 (2022). doi:10.1007/s11071-022-07357-y

[66] Eugster, S., Harsch, J.: A family of total Lagrangian Petrov–Galerkin Cosserat rod finite element formulations. GAMM Mitteilungen **46**(2), e202300008 (2023). doi:10.1002/gamm.202300008

[67] Fallahpasand, S., Dardel, M.: Piezoelectric energy harvesting from highly flexible cantilever beam. Journal of Multi-body Dyanmics **233**(1), 71–92 (2018). doi:10.1177/1464419318791104

[68] Farokhi, H., Erturk, A.: Three-dimensional nonlinear extreme vibrations of cantilevers based on a geometrically exact model. Journal of Sound and Vibration **510**(116295) (2021)

[69] Farokhi, H., Ghayesh, M.H.: Geometrically exact extreme vibrations of cantilevers. International Journal of Mechanical Sciences **168**, 105051 (2020)

[70] Farokhi, H., Kohtanen, E., Erturk, A.: Extreme parametric resonance oscillations of a cantilever: An exact theory and experimental validation. Mechanical Systems and Signal Processing **196**(110342) (2023)

[71] Farokhi, H., Xia, Y., Erturk, A.: Experimentally validated geometrically exact model for extreme nonlinear motions of cantilevers. Nonlinear Dynamics **107**, 457–475 (2022)

[72] Faux, D., Thomas, O., Cattan, E., Grondel, S.: Two modes resonant combined motion for insect wings kinematics reproduction and lift generation. Europhysics Letters **121**(6), 66001 (2018). doi:10.1209/0295-5075/121/66001

[73] Faux, D., Thomas, O., Grondel, S., Cattan, E.: Dynamic simulation and optimization of artificial insect-sized flapping wings for a bioinspired kinematics using a two resonant vibration modes combination. Journal of Sound and Vibration **460**, 114883 (2019). doi:10.1016/j.jsv.2019.114883

[74] Felippa, C.: Nonlinear Finite Element Methods. University of Colorado, Boulder (2001)

[75] Felippa, C.A., Haugen, B.: A unified formulation of small-strain corotational finite elements: I. Theory. Computer Methods in Applied Mechanics and Engineering **194**, 2285–2335 (2005). doi:10.1016/j.cma.2004.07.035

[76] Föppl, A.: Vorlesungen über Technische Mechanik. Dritter Band Festigkeitslehre. Druck & Verlag von B. G. Teubner, Leipzig (1897)

[77] Gazzola, M., Dudte, L.H., McCormick, A.G., Mahadevan, L.: Forward and inverse problems in the mechanics of soft filaments. Royal Society Open Science (2018). doi:10.1098/rsos.171628

[78] Genta, G.: Vibration Dynamics and Control. Springer (2009)

[79] Gerstmayr, J., Matikainen, M., Mikkola, A.: A geometrically exact beam element based on the absolute nodal coordinate formulation. Multibody System Dynamics **20**(359) (2008)

[80] Gerstmayr, J., Schöberl, J.: A 3D finite element method for flexible multibody systems. Multibody System Dynamics **15**, 305–320 (2006)

[81] Gerstmayr, J., Shabana, A.A.: Analysis of thin beams and cables using the Absolute Nodal Co-ordinate formulation. Nonlinear Dynamics **45**, 109–130 (2006)

[82] Ghayesh, M.H., Farokhi, H.: Extremely large dynamics of axially excited cantilevers. Thin Walled Structures **154**, 106275 (2020)

[83] Ghosh, S., Roy, D.: Consistent quaternion interpolation for objective finite element approximation of geometrically exact beam. Computer Methods in Applied Mechanics and Engineering **198**, 555–571 (2008)

[84] Giclais, S., Lubrina, P., Stephan, C.: Aircraft ground vibration testing at onera. Aerospace Lab Journal **12**, AL12–15 (2016). doi:10.12762/2016.AL12-05

[85] Givois, A., Deü, J.F., Thomas, O.: Dynamics of piezoelectric structures with geometric nonlinearities: A non-intrusive reduced order modelling strategy. Computers & Structures **253**(106575) (2021)

[86] Givois, A., Grolet, A., Thomas, O., Deü, J.F.: On the frequency response computation of geometrically nonlinear flat structures using reduced-order finite element models. Nonlinear Dynamics **97**(2), 1747–1781 (2019)

[87] Givois, A., Tan, J.J., Touzé, C., Thomas, O.: Backbone curves of coupled cubic oscillators in one-to-one internal resonance: bifurcation scenario, measurements and parameter identification. Meccanica **55**, 581–503 (2020). doi:10.1007/s11012-020-01132-2

[88] Givois, A., Tan, J.J., Touzé, C., Thomas, O.: Backbone curves of coupled cubic oscillators in one-to-one internal resonance: bifurcation scenario, measurements and parameter identification. Meccanica **55**(3), 481–503 (2020). doi:10.1007/s11012-020-01132-2

[89] Gobat, G., Guillot, L., Frangi, A., Cochelin, B., Touzé, C.: Backbone curves, Neimark-Sacker boundaries and appearance of quasi-periodicity in nonlinear oscillators: Application to 1:2 internal resonance and frequency combs in MEMS. Meccanica **56**(8), 1937–1969 (2021)

[90] Goyal, S., Perkins, N.C., Lee, C.L.: Nonlinear dynamics and loop formulation in Kirchhoff rods with implications to the mechanics of DNA and cables. Journal of Computational Physics **209**(1), 371–389 (2005)

[91] Greenhill, A.G.: Determination of the greatest height consistent with stability that a vertical pole or mast can be made, and the greatest height to which a tree of given proportions can grow. Proceedings of the Cambridge Philosophical Society **4**, 65–73 (1881)

[92] Grenat, C.: Nonlinear normal modes and multi-parametric continuation of bifurcations : Application to vibration absorbers and architectured MEMS sensors for mass detection. Ph.D. thesis, Lyon university, INSA, France, http://theses.insa-lyon.fr/publication/2018LYSEI078/these.pdf (2019)

[93] Grolet, A., Hoffmann, N., Thouverez, F., Schwingshackl, C.: Travelling and standing envelope solitons in discrete non-linear cyclic structures. Mechanical Systems and Signal Processing **81**, 75–87 (2016). doi:10.1016/j.ymssp.2016.02.062

[94] Guillot, L., Cochelin, B., Vergez, C.: A generic and efficient Taylor series-based continuation method using a quadratic recast of smooth nonlinear systems. International Journal for Numerical Methods in Engineering **119**, 261–280 (2019)

[95] Guillot, L., Cochelin, B., Vergez, C.: A taylor series-based continuation method for solutions of dynamical systems. Nonlinear Dynamics **98**, 2827–2845 (2019)

[96] Guillot, L., Lazarus, A., Thomas, O., Vergez, C., Cochelin, B.: Manlab 4.0: an interactive path-following and bifurcation analysis software. Tech. rep., Laboratoire de Mécanique et d'Acoustique, CNRS, http://manlab.lma.cnrs-mrs.fr (2018)

[97] Guillot, L., Lazarus, A., Thomas, O., Vergez, C., Cochelin, B.: A purely frequency based Floquet-Hill formulation for the efficient stability computation of periodic solutions of ordinary differential systems. Journal of Computational Physics **416** (2020)

[98] Guillot, L., Vigué, P., Vergez, C., Cochelin, B.: Continuation of quasi-periodic solutions with two-frequency Harmonic Balance Method. Journal of Sound and Vibration **394**, 434–450 (2017)

[99] Guillot, V., Givois, A., Colin, M., Thomas, O., Savadkoohi, A.T., Lamarque, C.H.: Theoretical and experimental investigation of a 1:3 internal resonance in a beam with piezoelectric patches. Journal of Vibration and Control **26**(13-14), 1119–1132 (2020). doi:10.1177/1077546320910536

[100] Géradin, M., Cardona, A.: Kinematics and dynamics of rigid and flexible mechanisms using finite elements and quaternion algebra. Computational Mechanics **4**, 115–135 (1989)

[101] Géradin, M., Cardona, A.: Flexible Multibody Dynamics: A Finite Element Approach. John Wiley & Sons, Ltd, Chichester (2001)

[102] Géradin, M., Rixen, D.: Mechanical Vibrations, Theory and Application to Structural Dynamics. Wiley, New York (1997)

[103] Haller, G., Ponsioen, S.: Nonlinear normal modes and spectral submanifolds: existence, uniqueness and use in model reduction. Nonlinear Dynamics **86**, 1493–1534 (2016)

[104] Harsch, J., Sailer, S., Eugster, S.: A total Lagrangian, objective and intrinsically locking-free Petrov–Galerkin SE(3) Cosserat rod finite element formulation. International Journal for Numerical Methods in Engineering **123**(13), 2965–2994 (2023). doi:10.1002/nme.7236

[105] Hendrick, T.: Dltdv digitizing tool: MATLAB tools for digitizing video files and calibrating cameras. `https://biomech.web.unc.edu/dltdv/`. Accessed: 2022-03-09

[106] Hijmissen, J., van Horssen, W.: On transverse vibrations of a vertical Timoshenko beam. Journal of Sound and Vibration **314**, 161–179 (2008)

[107] Hodges, B.: Nonlinear beam kinematics for small strains and finite rotations. Vertica **11**(3), 573–589 (1987)

[108] Hodges, B.: Geometrically-exact, intrinsic theory for dynamics of curved and twisted anisotropic beams. AIAA Journal **41**(6), 1131–1137 (2003)

[109] Hodges, B.: Nonlinear Composite Beam Theory. American Institute of Aeronautics and Astronautics, Reston (2006)

[110] Hutchinson, J.R.: Shear coefficients for Timoshenko beam theory. Journal of Applied Mechanics **68**(1), 87–92 (2001)

[111] Ibrahimbegović, A.: On finite element implementation of geometrically nonlinear Reissner's beam theory: three-dimensional curved beam elements. Computer Methods in Applied Mechanics and Engineering **122**, 11–26 (1995)

[112] Ibrahimbegović, A., Frey, F., Kožar, I.: Computational aspects of vector-like parametrization of three-dimensional finite rotations. International Journal for Numerical Methods in Engineering **38**(21), 3653–3673 (1995). doi:10.1002/nme.1620382107

[113] Inman, D.J.: Engineering Vibration. Pearson Education, Inc., Upper Saddle River (2008)

[114] Irschik, H., Gerstmayr, J.: A continuum mechanics based derivation of Reissner's large-displacement finite-strain beam theory: The case of plane deformations of originally straight Bernoulli–Euler beams. Acta Mechanica **206**, 1–21 (2009)

[115] Irschik, H., Gerstmayr, J.: A continuum-mechanics interpretation of Reissner's non-linear shear-deformable beam theory. Mathematical and Computer Modelling of Dynamical Systems **17**(1), 19–29 (2011)

[116] Jelenić, G., Crisfield, M.A.: Geometrically exact 3D beam theory: implementation of a strain-invariant finite element for statics and dynamics. Computational Methods in Applied Mechanics and Engineering **171**, 141–171 (1999)

[117] Jelenić, G., Saje, M.: A kinematically exact space finite strain beam model — finite element formulation by generalized virtual work principle. Computer Methods in Applied Mechanics and Engineering **120**(1–2), 131–161 (1995). doi:10.1016/0045-7825(94)00056-S

[118] Jossic, M., Chomette, B., Denis, V., Thomas, O., Mamou-Mani, A., Roze, D.: Effects of internal resonances in the pitch glide of chinese gongs. The Journal of the Acoustical Society of America **144**(1), 431–442 (2018). doi:10.1121/1.5038114

[119] Kaneko, T.: On timoshenko's correction for shear in vibrating beams. Journal of Physics D: Applied Physics **8**, 1927–1936 (1975)

[120] Karkar, S., Cochelin, B., Vergez, C.: A high-order, purely frequency based harmonic balance formulation for continuation of periodic solutions: The case of non-polynomial nonlinearities. Journal of Sound and Vibration **332**(4), 968–277 (2013)

[121] Karkar, S., Cochelin, B., Vergez, C.: A high-order,purely frequency based harmonic balance formulation for continuation of periodic solutions: The case of non-polynomial nonlinearities. Journal of Sound and Vibration **332**, 968–977 (2013)

[122] von Kármán, T.: Festigkeitsprobleme im maschinenbau. Encyklop adie der Mathematischen Wissenschaften **4**(4), 311–385 (1910)

[123] Kelley, A.: On the liapunov subcenter manifold. Journal of Mathematical Analysis and Applications **18**, 472–478 (1967)

[124] Kerschen, G., Peeters, M., Golinval, J., Vakakis, A.: Nonlinear normal modes, Part I: A useful framework for the structural dynamicist. Mechanical Systems and Signal Processing **23**, 170–194 (2009)

[125] Kohlmann, S.S.L., Hartung, A., Gross, J., Scheel, M., Krack, M.: Validation of a turbine blade component test with frictional contacts by phase-locked-loop and force-controlled measurements. Journal of Engineering for Gas Turbines and Power **142**, 051006 (2020)

[126] Kovacic, I., Zukovic, M., Radomirovic, D.: Sympodial tree-like structures: from small to large-amplitude vibrations. Bioinspiration and Biomimetics **13**(026002) (2018)

[127] Kovacic, I., Zukovic, M., Radomirovic, D.: Tree-like structures as hierarchical coupled oscillators. IUTAM Symposium on Exploiting Nonlinear Dynamics for Engineering Systems **37** (2018)

[128] Krack, M.: Nonlinear modal analysis of nonconservative systems: Extension of the periodic motion concept. Computers and Structures **154**, 59–71 (2015)

[129] Lacarbonara, W.: Nonlinear Structural Mechanics: Theory, Dynamical Phenomena and Modeling. Springer, New York (2013)

[130] Lacarbonara, W., Yabuno, H.: Refined models of elastic beams undergoing large in-plane motions: Theory and experiment. International Journal of Solids and Structures **43**, 5066–5084 (2006)

[131] Lang, H., Arnold, M.: Numerical aspects in the dynamic simulation of geometrically exact rods. Applied Numerical Mathematics **62**, 1411–1427 (2012)

[132] Lang, H., Linn, J., Arnold, M.: Multi-body dynamics simulation of geometrically exact Cosserat rods. Multibody System Dynamics **25**, 285–312 (2011)

[133] Laxalde, D., Thouverez, F.: Complex non-linear modal analysis for mechanical systems: Application to turbomachinery bladings with friction interfaces. Journal of Sound and Vibration **322**(4–5), 1009–1025 (2009). doi:10.1016/j.jsv.2008.11.044

[134] Laxalde, D., Thouverez, F.: "Wunderlich, Meet Kirchhoff": A general and unified description of elastic ribbons and thin rods. Journal of Elasticity **119**, 49–66 (2015). doi:10.1007/s10659-014-9487-0

[135] Lázaro, C., Monleón, S., Bessini, J., Casanova, J.: A review on geometrically exact models for very flexible rods. Proceedings of the IASS Annual Symposium **Tokyo, Japan** (2016)

[136] Lazarus, A., Thomas, O., Deü, J.F.: Finite elements reduced order models for nonlinear vibrations of piezoelectric layered beams with applications to NEMS. Finite Elements in Analysis and Design **49**(1), 35–51 (2012). doi:10.1016/j.finel.2011.08.019

[137] Lazarus, A., Thomas, O., Deü, J.F.: Finite elements reduced order models for nonlinear vibrations of piezoelectric layered beams with applications to NEMS. Finite Elements in Analysis and Design **49**(1), 35–51 (2012)

[138] Le Marrec, L., Lerbet, J., Rakotomanana, L.R.: Vibration of a timoshenko beam supporting arbitrary large predeformation. Acta Mechanica **229**, 109–132 (2018)

[139] Leadenham, S., Erturk, A.: Unified nonlinear electroelastic dynamics of a bimorph piezoelectric cantilever for energy harvesting, sensing, and actuation. Nonlinear Dynamics **79**, 1727–1743 (2015)

[140] Leadenham, S., Erturk, A.: Unified nonlinear electroelastic dynamics of a bimorph piezoelectric cantilever for energy harvesting, sensing, and actuation. Nonlinear Dynamics **79**, 1727–1743 (2015)

[141] Lewandowski, R.: Solutions with bifurcation points for free vibration of beams: an analytical approach. Journal of Sound and Vibration **177**(2), 239 – 249 (1994)

[142] Leyendecker, S., Betsch, P., Steinmann, P.: Objective energy-momentum conserving integration for the constrained dynamics of geometrically exact beams. Computer Methods in Applied Mechanics and Engineering **195**, 2313–2333 (2006)

[143] Linn, J., Hermansson, T., Andersson, F., Schneider, F.: Kinetic aspects of discrete Cosserat rods based on the difference geometry of framed curves. Proceedings of the 8th ECCOMAS Thematic Conference on Multibody Dynamics **Prague, Czech Republic** (2017)

[144] Lu, Z.Q., Gu, D.H., Ding, H., Lacarbonara, W., Chen, L.Q.: Nonlinear vibration isolation via circular ring. Mechanical Systems and Signal Processing **136**(106490) (2020)

[145] Lülf, F.A., Tran, D.M., Matthies, H.G., Ohayon, R.: An integrated method for the transient solution of reduced order models of geometrically nonlinear structures. Computational mechanics **55**, 327–344 (2015)

[146] Luongo, A., Rega, G., Vestroni, F.: On nonlinear dynamics of planar shear indeformable beams. Journal of Applied Mechanics **53**, 619–624 (1986)

[147] Lyapunov, A.M.: Problème général de la stabilité du mouvement. Annales de la faculté des sciences de Toulouse, 2e série **9**, 203–474 (1907)

[148] Mahmoodi, S.N., Jalili, N.: Non-linear vibrations and frequency response analysis of piezoelectrically driven microcantilevers. International Journal of Non-Linear Mechanics **42**, 577–587 (2007)

[149] Mahmoodi, S.N., Jalili, N., Ahmadian, M.: Subharmonics analysis of nonlinear flexural vibrations of piezoelectrically actuated microcantilevers. Nonlinear Dynamics **59**, 397–409 (2010)

[150] Malatkar, P., Nayfeh, A.H.: On the transfer of energy between widely spaced modes in structures. Nonlinear Dynamics **31**, 225–242 (2003)

[151] Manfredo, D., Dörlich, V., Linn, J., Arnold, M.: Data based constitutive modelling of rate independent inelastic effects in composite cables using Preisach hysteresis operators. Multibody System Dynamics (2023). doi:10.1007/s11044-023-09910-y

[152] Mangussi, F., Zanette, D.H.: Resonance in a vibrating beam: a zoo of nonlinear resonance peaks. PLoS ONE **11**(9), e0162365 (2016)

[153] Marconi, J., Tiso, P., Quadrelli, D.E., Braghin, F.: A higher-order parametric nonlinear reduced-order model for imperfect structures using neumann expansion. Nonlinear Dynamics **104**, 3039–3063 (2021)

[154] Marguerre, K.: Zur Theorie derGekrümmten Platte Grosser Formänderung. Proceedings of the 5th International Congress for Applied Mechanics pp. 93–101 (1938)

[155] Martin, A., Opreni, A., Vizzaccaro, A., Debeurre, M., Salles, L., Frangi, A., Thomas, O., Touzé, C.: Reduced order modeling of geometrically nonlinear rotating structures using the direct parametrisation of invariant manifolds. Journal of Theoretical, Computational and Applied Mechanics (2023). doi:10.46298/jtcam.10430

[156] Meier, C., Popp, A., Wall, W.A.: Geometrically exact finite element formulations for slender beams: Kirchhoff-Love theory versus Simo-Reissner theory. Archives of Computational Methods in Engineering **26**, 163–243 (2019)

[157] Mojrzisch, S., Wallaschek, J., Bremer, J.: An experimental method for the phase controlled frequency response measurement of nonlinear vibration systems. Proceedings in Applied Mathematics and Mechanics **12**(1), 253–254 (2012)

[158] Muñoz-Almaraz, F.J., Freire, E., Galán, J., Doedel, E., Vanderbauwhede, A.: Continuation of periodic orbits in conservative and hamiltonian systems. Physica D **181**(1-2), 1–38 (2003)

[159] Müller, F., Woiwode, L., Gross, J., Scheel, M., Krack, M.: Nonlinear damping quantification from phase-resonant tests under base excitation. Mechanical Systems and Signal Processing **177**, 109170 (2022)

[160] Naguleswaran, S.: Vibration of a vertical cantilever with and without axial freedom at clamped end. Journal of Sound and Vibration **146**(2), 191–198 (1991)

[161] Naguleswaran, S.: Transverse vibration of an uniform Euler-Bernoulli beam under linearly varying axial force. Journal of Sound and Vibration **275**, 47–57 (2004)

[162] Nayfeh, A., Mook, D.: Nonlinear Oscillations. John Wiley & Sons, Inc., New York (1995)

[163] Nayfeh, A.H.: Introduction to Perturbation Techniques. John Wiley & Sons, Inc. (1993)

[164] Nayfeh, A.H.: Perturbation Methods. John Wiley & Sons, Inc. (2000)

[165] Nayfeh, A.H., Pai, P.F.: Linear and nonlinear structural mechanics. John Wiley & sons (2004)

[166] Nayfeh, S.A., Nayfeh, A.H.: Nonlinear interactions between two widely spaced modes - External excitation. International Journal of Bifurcations and Chaos **3**(2), 417–427 (1993)

[167] Neukirch, S., Frelat, J., Goriely, A., Maurini, C.: Vibrations of post-buckled rods: The singular inextensible limit. Journal of Sound and Vibration **331**, 704–720 (2012)

[168] Neukirch, S., Goriely, A., Thomas, O.: Singular inextensible limit in the vibrations of post-buckled rods: Analytical derivation and role of boundary conditions. Journal of Sound and Vibration **333**(3), 962–970 (2014)

[169] Neukirch, S., Yavari, M., Challamel, N., Thomas, O.: Comparison of the von Kármán and kirchhoff models for the post-buckling and vibrations of elastic beams. Journal of Theoretical, Computational and Applied Mechanics (2021). doi:10.46298/jtcam.6828

[170] Ogden, R.W.: Non-Linear Elastic Deformations. Dover (1997)

[171] Opreni, A., Vizzaccaro, A., Touzé, C., Frangi, A.: High-order direct parametrisation of invariant manifolds for model order reduction of finite element structures: application to generic forcing terms and parametrically excited systems. Nonlinear Dynamics **111**, 5401–5447 (2023)

[172] Ouyang, H.: Moving-load dynamic problems: A tutorial (with a brief overview). Mechanical Systems and Signal Processing **25**(6), 2039–2060 (2011). doi:10.1016/j.ymssp.2010.12.010

[173] Pai, P.F.: Highly Flexible Structures: Modeling, Computation, and Experimentation. AIAA (2007)

[174] Pai, P.F.: Problems in geometrically exact modeling of highly flexible beams. Thin-Walled Structures **76**, 65–76 (2014)

[175] Pai, P.F., Nayfeh, A.H.: Non-linear non-planar oscillations of a cantilever beam under lateral base excitations. International Journal of Non-Linear Mechanics **25**(5), 455–474 (1990)

[176] Paidoussis, M.P., Des Trois Maisons, P.E.: Free vibration of a heavy, damped, vertical cantilever. Journal of Applied Mechanics **38**(2), 524–526 (1971)

[177] Palacios, R.: Nonlinear normal modes in an intrinsic theory of anisotropic beams. Journal of Sound and Vibration **330**(8), 1772–1792 (2011)

[178] Peeters, M., Kerschen, G., Golinval, J.: Dynamic testing of nonlinear vibrating structures using nonlinear normal modes. Journal of Sound and Vibration **330**, 486–509 (2011)

[179] Peeters, M., Kerschen, G., Golinval, J.: Modal testing of nonlinear vibrating structures based on nonlinear normal modes: Experimental demonstration. Mechanical Systems and Signal Processing **25**(4), 1227–1247 (2011)

[180] Peeters, M., Viguié, R., Sérandour, G., Kerschen, G., Golinval, J.C.: Nonlinear normal modes, Part II: Toward a practical computation using numerical continuation techniques. Mechanical Systems and Signal Processing **23**, 195–216 (2009)

[181] Perdrizet, T., Gilloteaux, J.C., Teixeira, D., Ferrer, G., Piriou, L., Cadiou, D., Heurtier, J.M., Cunff, C.L.: Fully coupled floating wind turbine simulator based on nonlinear finite element method: Part II - Validation results. ASME 2013 32nd International Conference on Ocean, Offshore and Arctic Engineering (2013)

[182] Perroni, A.P., Bussamra, F.L.S.: Effects of geometric nonlinearity on flexible wing structures. Journal of Aircraft **58**, 85–97 (2021)

[183] Pesheck, E., Pierre, C., Shaw, S.W.: Modal reduction of a nonlinear rotating beam through nonlinear normal modes. Journal of Vibration and Acoustics **124**(2), 229–236 (2002). doi:10.1115/1.1426071

[184] Peter, S., Leine, R.I.: Excitation power quantities in phase resonance testing of nonlinear systems with phase-locked-loop excitation. Mechanical Systems and Signal Processing **96**, 139–158 (2017)

[185] Peter, S., Scheel, M., Krack, M., Leine, R.I.: Synthesis of nonlinear frequency responses with experimentally extracted nonlinear modes. Mechanical Systems and Signal Processing **101**, 498–515 (2018)

[186] Peter, S., Schreyer, F., Leine, R.I.: A method for numerical and experimental nonlinear modal analysis of nonsmooth systems. Mechanical Systems and Signal Processing **120**, 193–807 (2019)

[187] Qiao, W., Guo, T., Kang, H., Zhao, Y.: Softening-hardening transition in nonlinear structures with an initial curvature: A refined asymptotic analysis. Nonlinear Dynamics **107**, 357–374 (2022)

[188] Rabenimanana, T., Walter, V., Kacem, N., Le Moal, P., Bourbon, G., Lardiès, J.: Mass sensor using mode localization in two weakly coupled mems cantilevers with different lengths: Design and experimental model validation. Sensors and Actuators A: Physical **295**, 643–652 (2019)

[189] Rakowski, J.: The interpretation of the shear locking in beam elements. Computers & Structures **37**(5), 769–776 (1990)

[190] Rand, R.: A direct method for nonlinear normal modes. International Journal of Non-Linear Mechanics **9**, 363–368 (1974)

[191] Reissner, E.: On one-dimensional finite-strain beam theory: The plane problem. Journal of Applied Mathematics and Physics **23**, 795–804 (1972)

[192] Reissner, E.: On finite deformations of space-curved beams. Journal of Applied Mathematics and Physics **32**, 734–744 (1981)

[193] Renson, L., Deliège, G., Kerschen, G.: An effective finite-element-based method for the computation of nonlinear normal modes of nonconservative systems. Meccanica **49**, 1901–1916 (2014)

[194] Renson, L., Gonzalez-Buelga, A., Barton, D.A.W., Neild, S.A.: Robust identification of backbone curves using control-based continuation. Journal of Sound and Vibration **367**, 145–158 (2016). doi:10.1016/j.jsv.2015.12.035

[195] Renson, L., Kerschen, G., Cochelin, B.: Numerical computation of nonlinear normal modes in mechanical engineering. Journal of Sound and Vibration **364**, 177–206 (2016)

[196] Renton, J.D.: Generalized beam theory applied to shear stiffness. International Journal of Solids and Structures **27**(15), 1955–1967 (1991)

[197] Romero, I.: The interpolation of rotations and its application to finite element models of geometrically exact rods. Computational Mechanics **34**, 121–133 (2004)

[198] Romero, I.: A comparison of finite elements for nonlinear beams: The absolute nodal coordinate and geometrically exact formulations. Multibody System Dynamics **20**(1), 51–68 (2008)

[199] Romero, I., Armero, F.: An objective finite element approximation of the kinematics of geometrically exact rods and its use in the formulation of an energy–momentum conserving scheme in dynamics. International Journal for Numerical Methods in Engineering **54**(12), 1683–1716 (2002). doi:10.1002/nme.486

[200] Rong, J., Wu, Z., Liu, C., Brüls, O.: Geometrically exact thin-walled beam including warping formulated on the special euclidean group se(3). Computer Methods in Applied Mechanics and Engineering **369**(113062) (2020)

[201] Rosenberg, R.: The normal modes of nonlinear n-degree-of-freedom systems. Journal of Applied Mechanics **29**(1), 7–14 (1962)

[202] Rosenberg, R.: On non-linear vibrations of systems with many degrees of freedom. Advances in Applied Mechanics **9**, 155–242 (1966)

[203] Salamin, E.: Applications of quaternions to computation with rotations. Working Paper, Stanford AI Lab (1979)

[204] Santillan, S., Plaut, R., Witelski, T., Virgin, L.: Large oscillations of beams and columns including self-weight. International Journal of Non-Linear Mechanics **43**, 761–771 (2008)

[205] Santillan, S., Virgin, L., Plaut, R.: Equilibria and vibration of a heavy pinched loop. Journal of Sound and Vibration **288**, 81–90 (2005)

[206] Schäfer, B.: Free vibrations of a gravity-loaded clamped-free beam. Ingenieur-Archiv **55**, 66–80 (1985)

[207] Scheel, M., Peter, S., Leine, R.I., Krack, M.: A phase resonance approach for modal testing of structures with nonlinear dissipation. Journal of Sound and Vibration **435**, 56–73 (2018)

[208] Scheel, M., Weigele, T., Krack, M.: Challenging an experimental nonlinear modal analysis method with a new strongly friction-damped structure. Journal of Sound and Vibration **485**, 115580 (2020)

[209] Schneider, F., Linn, J., Hermansson, T., Andersson, F.: Cable Dynamics and Fatigue Analysis for Digital Mock-Up in Vehicle Industry. Proceedings of the 8th ECCOMAS Thematic Conference on Multibody Dynamics **Prague, Czech Republic** (2017)

[210] Shabana, A.A., Hussien, H.A., Escalona, J.L.: Application of the absolute nodal coordinate formulation to large rotation and large deformation problems. Journal of Mechanical Design **120**(2), 188–195 (1998). doi:10.1115/1.2826958

[211] Shabana, A.A., Yakoub, R.Y.: Three dimensional absolute nodal coordinate formulation for beam elements: Theory. Journal of Mechanical Design **123**(4), 606–613 (2001)

[212] Shami, Z., Giraud-Audine, C., Thomas, O.: A nonlinear piezoelectric shunt absorber with a 2:1 internal resonance: Theory. Mechanical Systems and Signal Processing **170**(108768) (2022)

[213] Shami, Z.A., Shen, Y., Giraud-Audine, C., Touzé, C., Thomas, O.: Nonlinear dynamics of coupled oscillators in 1:2 internal resonance: effects of the non-resonant quadratic terms and recovery of the saturation effect. Meccanica **57**, 2701–2731 (2022). doi:10.1007/s11012-022-01566-w

[214] Shaw, S., Pierre, C.: Nonlinear normal modes and invariant manifolds. Journal of Sound and Vibration **150**(1), 170–173 (1991)

[215] Shaw, S.W., Pierre, C.: Normal modes for non-linear vibratory systems. Journal of Sound and Vibration **164**, 85–124 (1993)

[216] Shaw, S.W., Pierre, C.: Normal modes of vibration for non-linear continuous systems. Journal of Sound and Vibration **169**, 319–347 (1994)

[217] Shen, Y., Vizzaccaro, A., Kesmia, N., Yu, T., Salles, L., Thomas, O., Touzé, C.: Comparison of reduction methods for finite element geometrically nonlinear beam structures. Vibration **4**, 175–204 (2021)

[218] Shi, Y., Hearst, J.E.: The Kirchhoff elastic rod, the nonlinear Schrödinger equation, and DNA supercoiling. Journal of Chemical Physics **101**(6), 5186–5200 (1994)

[219] Simo, J.C.: A finite strain beam formulation. The three-dimensional dynamic problem. Part I. Computational Methods in Applied Mechanics and Engineering **49**, 55–70 (1985)

[220] Simo, J.C., Vu-Quoc, L.: A three-dimensional finite-strain rod model. Part II: Computational aspects. Computational Methods in Applied Mechanics and Engineering **58**, 79–116 (1986)

[221] Sonneville, V., Cardona, A., Brüls, O.: Geometrically exact beam finite element formulated on the special Euclidean group $SE(3)$. Computer Methods in Applied Mechanics and Engineering **268**, 451–474 (2014)

[222] Stavole, M., de Almagro, R.S.M., Lohk, M., Leyendecker, S.: Homogenization of the constitutive properties of composite beam cross-sections. Proceedings of the 8th European Congress on Computational Methods in Applied Sciences and Engineering (ECCOMAS) **Oslo, Norway** (2022). doi:10.23967/eccomas.2022.139

[223] Su, W., Cesnik, C.E.S.: Strain-based geometrically nonlinear beam formulation for modeling very flexible aircraft. International Journal of Solids and Structures **48**, 2349–2360 (2011)

[224] Sun, X., Kerschen, G., Cheng, L.: Geometrical nonlinearities in a curved cantilever beam: A condensation model and inertia-induced nonlinear features. Nonlinear Dynamics **111**, 6533–6556 (2023)

[225] Sénéchal, A.: Réduction de vibrations de structure complexe par shunts piézoélectriques: Applications aux turbomachines. Ph.D. thesis, CNAM, Paris (2011)

[226] Tabaddor, M., Nayfeh, A.H.: An experimental investigation of multimode responses in a cantilever beam. Transactions of the ASME **119**, 532–538 (1997)

[227] Thomas, O., Bilbao, S.: Geometrically non-linear flexural vibrations of plates: in-plane boundary conditions and some symmetry properties. Journal of Sound and Vibration **315**(3), 569–590 (2008)

[228] Thomas, O., Bilbao, S.: Geometrically nonlinear flexural vibrations of plates: In-plane boundary conditions and some symmetry properties. Journal of Sound and Vibration **315**(3), 569–590 (2008). doi:10.1016/j.jsv.2008.04.014

[229] Thomas, O., Sénéchal, A., Deü, J.F.: Hardening/softening behavior and reduced order modeling of nonlinear vibrations of rotating cantilever beams. Nonlinear Dynamics **86**, 1293–1318 (2016)

[230] Thomas, O., Touzé, C., Chaigne, A.: Non-linear vibrations of free-edge thin spherical shells: modal interaction rules and 1:1:2 internal resonance. International Journal of Solids and Structures **42**(11-12), 3339–3373 (2005). doi:10.1016/j.ijsolstr.2004.10.028

[231] Thomsen, J.J.: Vibrations and Stability, Order and Chaos. McGraw-Hill, Maidenhead (1997)

[232] Touzé, C., Amabili, M.: Nonlinear normal modes for damped geometrically nonlinear systems: Application to reduced-order modelling of harmonically forced structures. Journal of Sound and Vibration **298**(4-5), 958–981 (2006)

[233] Touzé, C., Camier, C., Favraud, G., Thomas, O.: Effect of imperfections and damping on the type of nonlinearity of circular plates and shallow spherical shells. Mathematical Problems in Engineering **2008**(678307) (2008)

[234] Touzé, C., Thomas, O.: Non-linear behaviour of free-edge shallow spherical shells: Effect of the geometry. International Journal of Non-linear Mechanics **41**(5), 678–692 (2006). doi:10.1016/j.ijnonlinmec.2005.12.004

[235] Touzé, C., Thomas, O., Chaigne, A.: Asymmetric non-linear forced vibrations of free-edge circular plates, part 1: theory. Journal of Sound and Vibration **258**(4), 649–676 (2002). doi:10.1006/jsvi.2002.5143

[236] Touzé, C., Vizzaccaro, A., Thomas, O.: Model order reduction methods for geometrically nonlinear structures: a review of nonlinear techniques. Nonlinear Dynamics **105**, 1141–1190 (2021). doi:10.1007/s11071-021-06693-9

[237] Touzé, C., Thomas, O., Chaigne, A.: Hardening/softening behaviour in non-linear oscillations of structural systems using non-linear normal modes. Journal of Sound and Vibration **273**, 77–101 (2004)

[238] Tucker, R.W., Wang, C.: An integrated model for drill-string dynamics. Journal of Sound and Vibration **224**(1), 123–165 (1999)

[239] Vakakis, A.F.: Non-linear normal modes NNMs and their applications in vibration theory: an overview. Mechanical Systems and Signal Processing **11**(1), 3–22 (1997)

[240] Vakakis, A.F., Manevitch, L.I., Mikhlin, Y.V., Philipchuk, V.N., Zevin, A.A.: Normal Modes and Localization in Nonlinear Systems. John Wiley & Sons, Inc., New York (1996)

[241] Vakilinejad, M., Grolet, A., Thomas, O.: A comparison of robustness and performance of linear and nonlinear lanchester dampers. Nonlinear dynamics **100**, 269–287 (2020). doi:10.1007/s11071-020-05512-x

[242] Vetyukov, Y., Oborin, E.: Snap-through instability during transmission of rotation by a flexible shaft with initial curvature. International Journal of Non-Linear Mechanics **154**, 104431 (2023). doi:10.1016/j.ijnonlinmec.2023.104431

[243] Viguié, P., Vergez, C., Karkar, S., Cochelin, B.: Regularized friction and continuation: Comparison with Coulomb's law. Journal of Sound and Vibration **389**, 350–363 (2017)

[244] Vincent, P., Descombin, A., Dagher, S., Seoudi, T., Lazarus, A., Thomas, O., Ayari, A., Purcell, S.T., Perisanu, S.: Nonlinear polarization coupling in freestanding nanowire/nanotube resonators. Journal of Applied Physics **125**(044302) (2019)

[245] Vincent, P., Descombin, A., Dagher, S., Seoudi, T., Lazarus, A., Thomas, O., Ayari, A., Purcell, S.T., Perisanu, S.: Nonlinear polarization coupling in freestanding nanowire/nanotube resonators. Journal of Applied Physics **125**, 044302 (2019). doi:10.1063/1.5053955

[246] Virgin, L., Santillan, S., Plaut, R.: Vibration isolation using extreme geometric nonlinearity. Journal of Sound and Vibration **315**, 721–731 (2008)

[247] Virgin, L.N., Plaut, R.H.: Postbuckling and vibration of linearly elastic and softening columns under self-weight. International Journal of Solids and Structures **41**, 4989–5001 (2004)

[248] Virgin, L.N., Santillan, S.T., Holland, D.B.: Effect of gravity on the vibration of vertical cantilevers. Mechanics Research Communications **34**, 312–317 (2007)

[249] Vizzaccaro, A., Givois, A., Longobardi, P., Shen, Y., Deü, J.F., Salles, L., Touzé, C., Thomas, O.: Non-intrusive reduced order modelling for the dynamics of geometrically nonlinear flat structures using three dimensional finite elements. Computational Mechanics **66**, 1293–1319 (2020). doi:10.1007/s00466-020-01902-5

[250] Vizzaccaro, A., Opreni, A., Salles, L., Frangi, A., Touzé, C.: High order direct parametrisation of invariant manifolds for model order reduction of finite element structures: application to large amplitude vibrations and uncovering of a folding point. Nonlinear Dynamics **110**(1), 525–571 (2022)

[251] Vizzaccaro, A., Shen, Y., Salles, L., Blahos, J., Touzé, C.: Direct computation of nonlinear mapping via normal form for reduced-order models of finite element nonlinear structures. Computer Methods in Applied Mechanics and Engineering **384**(113957) (2021)

[252] Volvert, M., Kerschen, G.: Phase resonance nonlinear modes of mechanical systems. Journal of Sound and Vibration **511**, 116355 (2021). doi:10.1016/j.jsv.2021.116355

[253] Wasmer, P., Betsch, P.: The geometrically exact beam model with a normalized quaternion discretization. Proceedings of the 11th ECCOMAS Thematic Conference on Multibody Dynamics **Lisbon, Portugal** (2023)

[254] Woodall, S.R.: On the large amplitude oscillations of a thin elastic beam. International Journal of Non-Linear Mechanics **1**, 217–238 (1966)

[255] Xi, L.Y., Li, X.F., Tang, G.J.: Free vibration of standing and hanging gravity-loaded Rayleigh cantilevers. International Journal of Mechanical Sciences **66**, 233–238 (2013)

[256] Yang, Y., Tobias, I., Olson, W.K.: Finite element analysis of DNA supercoiling. Journal of Chemical Physics **98**(2), 1673–1686 (1993)

[257] Yang, Z., Erturk, A., Zu, J.: On the efficiency of piezoelectric energy harvesters. Extreme Mechanics Letters **15**, 26–37 (2017)

[258] Yokoyama, T.: Vibrations of a hanging Timoshenko beam under gravity. Journal of Sound and Vibration **141**(2), 245–258 (1990)

[259] Zhang, X., Chan, F.K., Parthasarathy, T., Gazzola, M.: Modeling and simulation of complex dynamic musculoskeletal architectures. Nature Communications **10**(4825) (2019). doi:10.1038/s41467-019-12759-5

[260] Zienkiewicz, O.C., Taylor, R.L.: The finite element method. Volume 2: solid mechanics, 5th. edn. Butterworth-Heinemann (2000)

[261] Zupan, E., Saje, M., Zupan, D.: The quaternion-based three-dimensional beam theory. Computational Methods in Applied Mechanics and Engineering **198**, 3944–3956 (2009)

[262] Zupan, E., Saje, M., Zupan, D.: Quaternion-based dynamics of geometrically nonlinear spatial beams using the Runge–Kutta method. Finite Elements in Analysis and Design **54**, 48–60 (2012). doi:10.1016/j.finel.2012.01.007

[263] Zupan, E., Saje, M., Zupan, D.: The rotational quaternion-based beam FEM formulations. Proceedings of the European Congress on Computational Methods in Applied Sciences and Engineering (ECCOMAS) **Vienna, Austria** (2012)

[264] Zupan, E., Zupan, D.: On conservation of energy and kinematic compatibility in dynamics of nonlinear velocity-based three-dimensional beams. Nonlinear Dynamics **95**(2), 1379–1394 (2019). doi:10.1007/s11071-018-4634-y

Appendix A

Appendices to Chapter 3

A.1 Elementary quantities in the global frame

This section specifies the change of basis procedure from the local frames to the global frame prior to the finite element assembly process. The angle $\psi(x) = (\widehat{\mathbf{e}_X, \mathbf{e}_x})$ previously introduced defines the orientation of the local frame $(\mathbf{e}_x, \mathbf{e}_y)$ of a given finite element in the global frame $(\mathbf{e}_X, \mathbf{e}_X)$, as shown in Fig. 3.2.

Following discretization of the beam into finite beam elements, the assembly of the elements into the complete structure must be performed in the global frame $(\mathbf{e}_X, \mathbf{e}_Y)$ in order to properly define the deformation of the elements relative to each other. To this end, the displacement degrees of freedom $[u_i, w_i, \theta_i]^{\mathrm{T}}$, written in the local frame, must be projected in the global frame to obtain $[U_{xi}, U_{yi}, \theta_i]^{\mathrm{T}}$. This is done by using the change of basis matrix:

$$\mathbf{T^e} = \begin{bmatrix} \cos\psi & -\sin\psi & 0 \\ \sin\psi & \cos\psi & 0 \\ 0 & 0 & 1 \end{bmatrix}, \tag{A.1}$$

such that:

$$\mathbf{q}^e_{\text{global}} = \mathbf{R}^e \mathbf{q}^e, \quad \mathbf{R}^e = \begin{bmatrix} \mathbf{T}^e & 0 \\ 0 & \mathbf{T}^e \end{bmatrix}, \tag{A.2}$$

where $\mathbf{q}^e_{\text{global}} = [U_{x1}, U_{y1}, \theta_1, U_{x2}, U_{y2}, \theta_2]^{\mathrm{T}}$ gathers the degrees of freedom in the global frame. Inserting the above equation into Eqs. (E.30), (E.28), and (3.33) leads to the transformation of all elementary quantities into the global frame, as follows:

$$\begin{aligned} \mathbf{M}^e_{\text{global}} &= \mathbf{R}^e \mathbf{M}^e \mathbf{R}^{e\mathrm{T}}, \\ \mathbf{f}^e_{\text{int,global}} &= \mathbf{R}^e \mathbf{f}^e_{\text{int}}, \\ \mathbf{f}^e_{\text{ext,global}} &= \mathbf{R}^e \mathbf{f}^e_{\text{ext}}, \end{aligned} \tag{A.3}$$

prior to assembly, to obtain Eq. (3.34).

A.2 Details on the quadratic recast of the equations of motion

The transformation of the FEM Eq. (3.34) into a quadratic DAE involves the definition of new variables, called auxiliary variables. Note that the quadratic recast is not unique. In this section, two

other alternative quadratic recasts are given, with less auxiliary variables than the recast presented in Section 3.2.3.

A.2.1 Minimal quadratic recast with 4 auxiliary variables per element

In this recast, we consider the definition of 4 auxiliary variables for each element, leading to a minimal number of auxiliary variables. We first add the two sine and cosine variables:

$$c = \cos\frac{\theta_1+\theta_2}{2}, \quad s = \sin\frac{\theta_1+\theta_2}{2}. \tag{A.4}$$

The cosine and sine functions are redefined in terms of differential equations, given by:

$$\mathrm{d}c = -s(\mathrm{d}\theta_1+\mathrm{d}\theta_2)/2, \quad \mathrm{d}s = c(\mathrm{d}\theta_1+\mathrm{d}\theta_2)/2. \tag{A.5}$$

We also define the auxiliary variables e and γ related to the axial and shear strains, respectively:

$$\begin{aligned} e &= \left(1+\frac{u_2-u_1}{L^e}\right)c+\left(\frac{w_2-w_1}{L^e}\right)s-1, \\ \gamma &= \left(\frac{w_2-w_1}{L^e}\right)c-\left(1+\frac{u_2-u_1}{L^e}\right)s. \end{aligned} \tag{A.6}$$

To summarize, the full quadratic DAE for a single finite element is stated explicitly. For each element, there are:

1. Twelve primary variables:

   - Six positions:

$$\mathbf{q}^e = \begin{bmatrix} u_1 & w_1 & \theta_1 & u_2 & w_2 & \theta_2 \end{bmatrix}^{\mathrm{T}}, \tag{A.7}$$

   - Six velocities:

$$\mathbf{V}^e = \begin{bmatrix} V_{u1} & V_{w1} & V_{\theta 1} & V_{u2} & V_{w2} & V_{\theta 2} \end{bmatrix}^{\mathrm{T}}, \tag{A.8}$$

2. Four auxiliary variables:

$$\mathbf{X}_{4\_\mathrm{aux}} = \begin{bmatrix} c & s & e & \gamma \end{bmatrix}^{\mathrm{T}}, \tag{A.9}$$

so that there are $12+4=18$ variables per element. The quadratic DAE is given by (for a single element):

$$\dot{\mathbf{q}}^e = \mathbf{V}^e, \tag{A.10a}$$

$$\mathbf{M}^e\dot{\mathbf{V}}^e = \mathbf{f}^e_{\text{ext}} - \mathbf{D}^e\mathbf{V}^e - \underbrace{\left\{ EAe \begin{bmatrix} -c \\ -s \\ \gamma L^e/2 \\ c \\ s \\ \gamma L^e/2 \end{bmatrix} + kGA\gamma \begin{bmatrix} s \\ -c \\ -(1+e)L^e/2 \\ -s \\ c \\ -(1+e)L^e/2 \end{bmatrix} + EI \begin{bmatrix} 0 \\ 0 \\ (\theta_1-\theta_2)/2 \\ 0 \\ 0 \\ (\theta_2-\theta_1)/2 \end{bmatrix} \right\}}_{\mathbf{f}^e_{\text{int}}}, \tag{A.10b}$$

$$0 = \mathrm{d}c + s(\mathrm{d}\theta_1 + \mathrm{d}\theta_2)/2, \quad c = \cos[(\theta_1+\theta_2)/2], \tag{A.10c}$$

$$0 = \mathrm{d}s - c(\mathrm{d}\theta_1 + \mathrm{d}\theta_2)/2, \quad s = \sin[(\theta_1+\theta_2)/2], \tag{A.10d}$$

$$0 = e - \left(1 + \frac{u_2-u_1}{L^e}\right)c - \left(\frac{w_2-w_1}{L^e}\right)s + 1, \tag{A.10e}$$

$$0 = \gamma - \left(\frac{w_2-w_1}{L^e}\right)c + \left(1 + \frac{u_2-u_1}{L^e}\right)s. \tag{A.10f}$$

A.2.2 Quadratic recast with 8 auxiliary variables per element

In this recast, we consider the definition of 8 auxiliary variables for each element. With respect to the quadratic recast of Section 3.2.3, the terms F_x, F_y, M and T_2 are not defined as auxiliary variables. For each element, there are:

1. Twelve primary variables:

   - Six positions:

$$\mathbf{q}^e = \begin{bmatrix} u_1 & w_1 & \theta_1 & u_2 & w_2 & \theta_2 \end{bmatrix}^{\mathrm{T}}, \tag{A.11}$$

   - Six velocities:

$$\mathbf{V}^e = \begin{bmatrix} V_{u1} & V_{w1} & V_{\theta 1} & V_{u2} & V_{w2} & V_{\theta 2} \end{bmatrix}^{\mathrm{T}}, \tag{A.12}$$

2. Eight auxiliary variables:

$$\mathbf{X}_{8\_\text{aux}} = \begin{bmatrix} \bar{\theta} & u_p & w_p & \theta_p & c & s & e & \gamma \end{bmatrix}^{\mathrm{T}}, \tag{A.13}$$

so that there are $12+8=20$ variables per element. The quadratic DAE is given by (for a single

element):

$$\dot{\mathbf{q}}^e = \mathbf{V}^e, \tag{A.14a}$$

$$\mathbf{M}^e\dot{\mathbf{V}}^e = \mathbf{f}^e_{\text{ext}} - \mathbf{D}^e\mathbf{V}^e - \left[EAe \begin{bmatrix} -c \\ -s \\ \gamma L^e/2 \\ c \\ s \\ \gamma L^e/2 \end{bmatrix} + kGA\gamma \begin{bmatrix} s \\ -c \\ -(1+e)L^e/2 \\ -s \\ c \\ -(1+e)L^e/2 \end{bmatrix} + EI \begin{bmatrix} 0 \\ 0 \\ -\theta_p \\ 0 \\ 0 \\ \theta_p \end{bmatrix} \right], \tag{A.14b}$$

$$0 = \bar{\theta} - (\theta_1 + \theta_2)/2, \tag{A.14c}$$

$$0 = u_p - \frac{1}{2L^e}(u_2 - u_1), \tag{A.14d}$$

$$0 = w_p - \frac{1}{2L^e}(w_2 - w_1), \tag{A.14e}$$

$$0 = \theta_p - \frac{1}{2L^e}(\theta_2 - \theta_1), \tag{A.14f}$$

$$0 = \mathrm{d}c + s\mathrm{d}\bar{\theta}, \quad c = \cos\bar{\theta}, \tag{A.14g}$$

$$0 = \mathrm{d}s - c\mathrm{d}\bar{\theta}, \quad s = \sin\bar{\theta}, \tag{A.14h}$$

$$0 = e - (1+u_p)\,c - w_p s + 1, \tag{A.14i}$$

$$0 = \gamma - w_p c + (1+u_p)\,s. \tag{A.14j}$$

A.2.3 Comparison of computation time

In this paragraph, we illustrate the difference in computation time when using the three different formulations of the quadratic recast (resp. with 4, 8 and 12 auxiliary variables). The computations were carried out for the cantilever beam of Section 3.3.1, discretized with 20 elements and using 20 harmonics in the HBM development. In each case, 50 ANM branches are computed with an ANM threshold set to 10^{-6}. Note that for each formulation, the results are the same and only the computation time differs. Table A.1 shows the mean computation time per ANM branch for each of the three quadratic formulations presented in this paper. It can be seen that the smallest computation time is obtained when using the quadratic formulation using 12 auxiliary variables. As explained in the main text, what increases the computation time is the number of products of variables and not the addition of auxiliary variables. Looking at the proposed DAE, one finds, for each finite element, 12 products of the variables in Eqs. (3.45), 24 products in Eqs. (A.10) and 18 products in Eqs. (A.14). Table A.1 confirms that the computation time increases with the number of products.

Table A.1: Comparison of computation time for the different formulations of the quadratic recast (example of cantilever beam with 20 elements and 20 harmonics).

No. aux vars per element	4	8	12
No. of products	24	18	12
Mean time per ANM branch [s]	2.65	2.63	1.96

A.3 Dimensionless form of the equations

Following [229], the strong form of the beam equations equivalent to the weak form of Eq. (3.7) for a geometrically exact beam model with a Timoshenko kinematics is written:

$$\begin{cases} \rho A\ddot{u} = (N\cos\theta - T\sin\theta)' + n, & \text{(A.15)} \\ \rho A\ddot{w} = (N\sin\theta + T\cos\theta)' + p, & \text{(A.16)} \\ \rho I\ddot{\theta} = T(1+e) - N\gamma + M' + q, & \text{(A.17)} \\ N = EAe, \quad T = kGA\gamma, \quad M = EI\theta'. & \text{(A.18)} \end{cases}$$

Using the dimensionless variable definitions of Eqs. (3.54), one obtains:

$$\begin{cases} \hat{\ddot{u}} = (\hat{N}\cos\theta - \hat{T}\sin\theta)' + \hat{n}, & \text{(A.19)} \\ \hat{\ddot{w}} = (\hat{N}\sin\theta + \hat{T}\cos\theta)' + \hat{p}, & \text{(A.20)} \\ \eta\ddot{\theta} = \hat{T}(1+e) - \hat{N}\gamma + \hat{M}' + \hat{q}, & \text{(A.21)} \\ \hat{N} = e/\eta, \quad \hat{T} = \gamma/\mu, \quad \hat{M} = \theta', & \text{(A.22)} \end{cases}$$

where η is defined by Eq. (3.55) and:

$$\mu = \frac{EI}{kGAL^2} = \frac{2(1+\nu)\eta}{k}, \tag{A.23}$$

is the shear parameter [102], ν is the material Poisson's ratio and where the second equation is valid for a homogeneous material with $G = E/[2(1+\nu)]$. In the case of Euler-Bernoulli kinematics, $\gamma = 0$, so that μ does not appear in the equations.

A.4 Quadratic recast of transcendental function

Let us consider two time functions $x(t)$ and $y(t)$ related by a transcendental function. To better understand the ideas, consider here an exponential function:

$$y(t) = \exp[x(t)]. \tag{A.24}$$

Differentiating the above equation and adding an initial condition yields the following equivalent system:

$$\mathrm{d}y = y\,\mathrm{d}x, \tag{A.25a}$$
$$y(0) = \exp[x(0)], \tag{A.25b}$$

where the first equation is quadratic with respect to x, y, $\mathrm{d}x$ and $\mathrm{d}y$.

To illustrate the HBM treatment, we consider only two harmonics in cosine for $x(t)$ and $y(t)$:

$$x(t) = x^{(0)} + x^{(1)}\cos\omega t + x^{(2)}\cos 2\omega t, \tag{A.26}$$
$$y(t) = y^{(0)} + y^{(1)}\cos\omega t + y^{(2)}\cos 2\omega t. \tag{A.27}$$

Introducing the above equations into Eq. (A.25a), with d$\circ$ considered as a time differentiation $\mathrm{d}\circ/\mathrm{d}t$ and balancing the zero-th and first two harmonics in a standard HBM process leads to:

$$0 = 0, \tag{A.29}$$

$$y^{(1)} = x^{(1)} y^{(0)}, \tag{A.30}$$

$$y^{(2)} = x^{(2)} y^{(0)} + x^{(1)} y^{(1)}/4. \tag{A.31}$$

Because of the differentiation in Eq. (A.25a), the zero-th harmonics do not yield an equation. This is corrected by considering Eq. (A.25b) with the Fourier series expansion:

$$y^{(0)} + y^{(1)} + y^{(2)} = \exp\left(x^{(0)} + x^{(1)} + x^{(2)}\right). \tag{A.32}$$

As a preliminary conclusion, the above equation proves that the Fourier coefficients of $x(t)$ and $y(t)$ are solutions of an algebraic system that is almost quadratic, with only one of the equations (Eq. (A.32) here) incorporating the transcendental function. In the ANM process, this function is treated in the same manner, by differentiating with respect to the arclength parameter a. Namely, Eq. (A.32) is rewritten:

$$y(a) = \exp[x(a)], \tag{A.33}$$

and the two functions x and y of a are expanded in Taylor series (see Eq. (3.52)):

$$x(a) = x_0 + a x_1 + a^2 x_2, \quad y(a) = y_0 + a y_1 + a^2 y_2. \tag{A.34}$$

Then, considering Eq. (A.25a) with d$\circ$ replaced by a differentiation with respect to a ($\mathrm{d}\circ/\mathrm{d}a$) and balancing each power of a, one obtains:

$$y_1 = y_0 x_1, \tag{A.35}$$

$$y_2 = x_2 y_0 + y_1 x_1/2. \tag{A.36}$$

Again, because of the differentiation in Eq. (A.25a), one equation is lacking. This is corrected by considering Eq. (A.25b):

$$y_0 = \exp(x_0), \tag{A.37}$$

which is evaluated by computing $\mathbf{R}(\tilde{\mathbf{X}}_0)$ of the zero-th order of the first series with a Newton-Raphson.

In conclusion, it has been shown with this simple example that replacing the transcendental equation (A.24) with (A.25) leads to a quadratic ANM-HBM process enabling computation of all of the unknowns $\tilde{\mathbf{X}}_p$ of the problem. This process is hard-coded in the MANLAB software.

A.5 Effect of the number of harmonics

In this appendix, we present a quick convergence study with relation to the number of retained harmonics in the HBM development. The computations are carried out for the first nonlinear mode of the cantilever beam presented in Section 3.3.1, discretized with 20 elements and using a quadratic recast with 12 auxiliary variables. Fig. A.1 depicts the evolution of the rotation at the free end of the beam as a function of angular frequency for $H = 20$, $H = 40$ and $H = 60$ harmonics.

It can be seen that the backbone curve of the first mode is well-approximated with $H = 20$ harmonics so as long as the amplitude of the rotation is lower than 3 radians. At higher amplitudes, the harmonic content must be increased in order to obtain a converged solution.

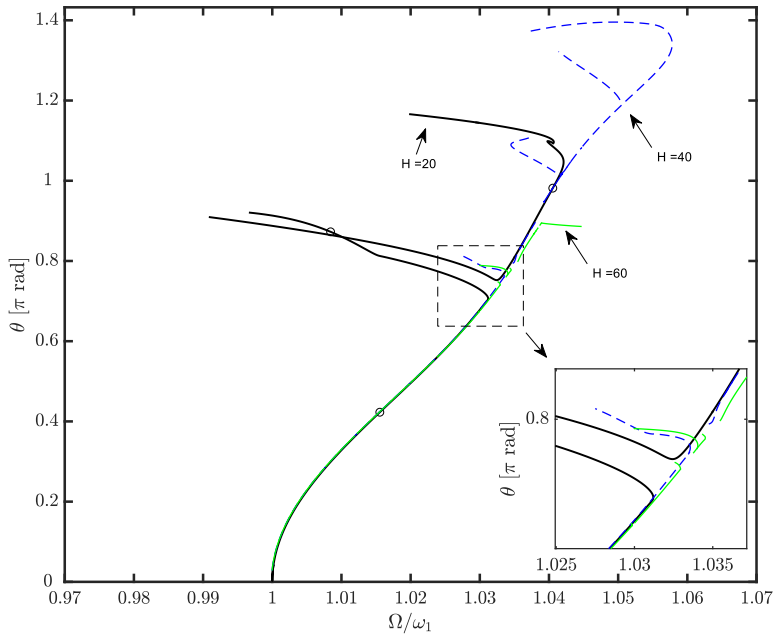

Figure A.1: Amplitude of the rotation at the free end of the cantilever beam for the first nonlinear mode as a function of the angular frequency for several numbers of retained harmonic ($H = 20$, $H = 40$ and $H = 60$).

It is also observed that the location of the internal resonance depends on the number of harmonics retained in the HBM development. The higher the number of retained harmonics, the higher the number of uncovered internal resonances, which may be disadvantageous during computation if the primary interest is in the principal resonance curve of a mode. In addition, in order to obtain a correct solution around the internal resonance, a large number of harmonics is required in the HBM development. Even with $H = 60$, the solution around the internal resonance occurring close to $\Omega/\omega_1 \approx 1.03$ is clearly not converged, as can be observed in Fig. A.2.

For information purposes, Table A.2 shows the mean computation time per ANM branch as a function of the number of retained harmonics H.

Table A.2: Comparison of computation time as a function of the harmonic number (example of cantilever beam with 20 elements, quadratic recast with 12 auxiliary variables).

No. harmonics H	20	40	60
No. unknowns in algebraic system	14022	27702	41382
Mean time per ANM branch [s]	1.96	10.15	15.23

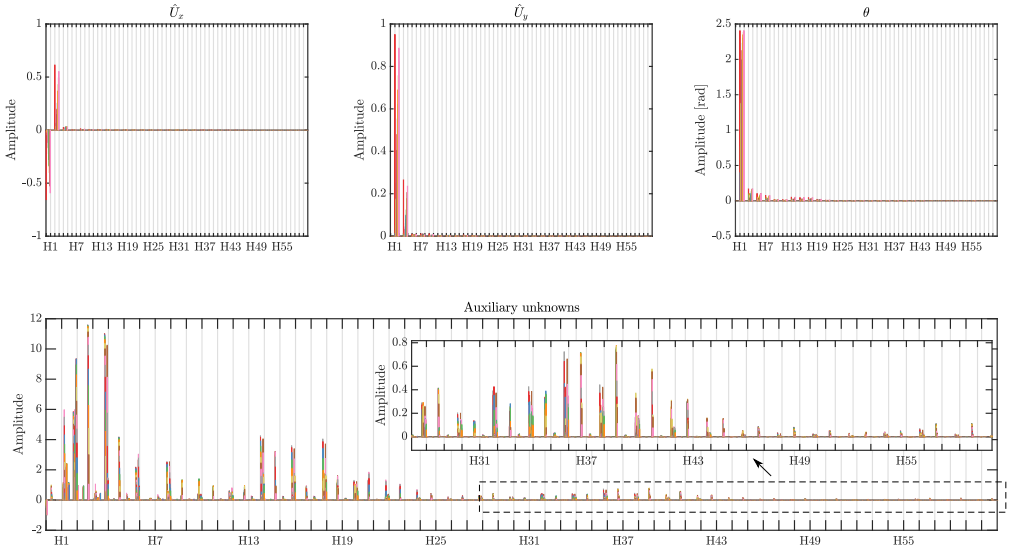

Figure A.2: Harmonic content of the solution at the internal resonance occurring close to $\Omega/\omega_1 \approx 1.03$ computed with $H = 60$ harmonics.

Appendix B

Appendices to Chapter 4

Table of Contents - Appendix B

B.1 Effect of shear parameter μ

As detailed in § 4.2, a third dimensionless parameter related to the shear stiffness of the beam (which is present exclusively in the case of Timoshenko kinematics), called μ in §4.2, appears in the equations of motion Eqs. (4.7) and (4.8). Recalling Eq. (4.6), μ is found to depend on three parameters: the shear coefficient k, the Poisson's ratio ν and the slenderness parameter η. Considering only slender beams such that η is very small ($\eta \leq 2 \cdot 10^{-4}$) , it naturally follows that μ is also very small, being proportional to η. Recalling Eq. (4.8), a very small μ tends the overall shear stiffness towards infinity, *i.e.* to the point of no shearing of the cross-section as in Euler-Bernoulli kinematics. Therefore, for very small μ, it can be considered that there is very little effect of shearing of the cross-section (even at high amplitudes of rotation) and little difference between Timoshenko and Euler-Bernoulli kinematics.

In order to confirm the minor influence of the dimensionless parameter μ, the simulations of § 4.4 were performed again with different values of k and ν while keeping η and α the same. As mentioned in § 4.2.2, typical values of k and ν are in the ranges of $0.8 \leq k \leq 0.9$ and $0 \leq \nu \leq 0.5$, respectively. The two extremities of μ within these ranges for k and ν were selected, $\mu = 2.22 \cdot 10^{-7}$ and $3.75 \cdot 10^{-7}$ for $\eta = 1 \cdot 10^{-7}$, in order to compare with the simulations of § 4.4, where $k = 1, \nu = 0.3$. The breakdown of these parameters is shown in Table B.1.

Table B.1: Values of μ for different values of k and ν, with $\eta = 1 \cdot 10^{-7}$.

$\mu = \frac{2(1+\nu)\eta}{k}$	k	ν	η
$2.22 \cdot 10^{-7}$	0.9	0.0	
$2.60 \cdot 10^{-7}$	1.0	0.3	$1 \cdot 10^{-7}$
$3.75 \cdot 10^{-7}$	0.8	0.5	

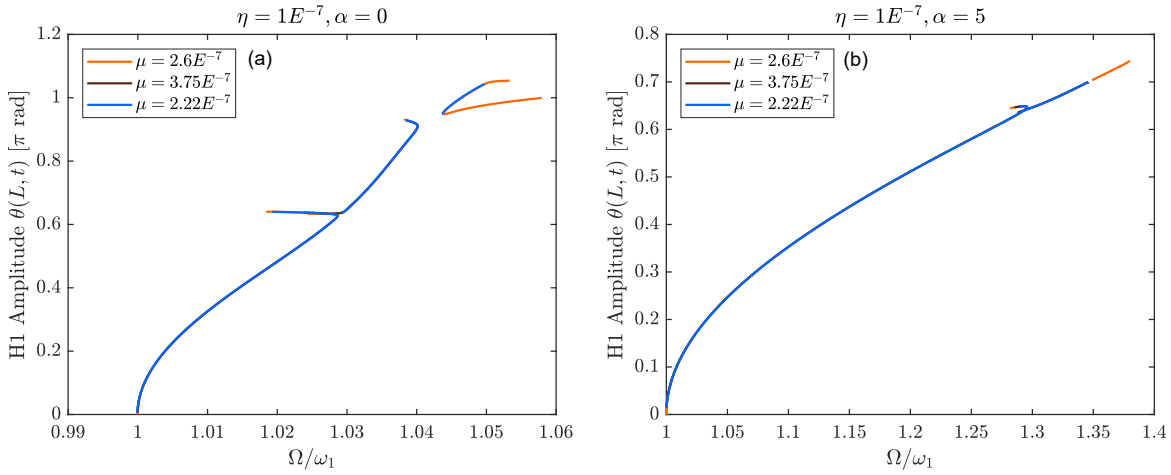

Figure B.1: Effect of dimensionless parameters on the first nonlinear mode, isolation of the effect of μ: (a) amplitude of the first harmonic H1 of θ at the free end of the beam for different values of μ, no-gravity condition ($\alpha = 0$); (b) the same as (a) but with gravity condition ($\alpha = 5$).

The simulations of § 4.4.1 and 4.4.2 (where $\mu = 2.60 \cdot 10^{-7}$ for $\eta = 10^{-7}$) are recomputed using these two additional values of μ. For the latter, $\alpha = 5$ is chosen. The results of these simulations are summarized in Fig. B.1; the orange curves in both figures are the same as their counterparts in § 4.4.

In both conditions, regardless of the presence of gravity in Fig. B.1(b), the variation in μ between its minimum and maximum values has next to no effect on the backbone curve of the first nonlinear mode; the three curves overlap to the point of being indistinguishable. These comparisons prove the negligible influence of shearing on the mechanics of very slender beams and, therefore, justify the omission of the third dimensionless parameter μ from the analyses presented in this work.

B.2 Tangent stiffness computation

According to Eq. (4.24), the tangent stiffness $\mathbf{K}_\mathrm{t}$ is defined as the first derivative of the internal force vector $\mathbf{f}_\mathrm{int}$ with respect to the vector of degrees of freedom:

$$\mathbf{K}_\mathrm{t} = \frac{\partial \mathbf{f}_\mathrm{int}}{\partial \mathbf{q}}. \tag{B.1}$$

In practice, it can be computed at the elementary level and then assembled according to standard finite element procedures.

All details having been explained in previous work [58], [229], we recall here only the main parts of the reasoning. First, the strains of Eqs. (4.2) are discretized according to Eq. (4.12), yielding the

elementary strain expressions:

$$e^e = \left(1 + \frac{u_2 - u_1}{L^e}\right)\cos\theta^e + \left(\frac{w_2 - w_1}{L^e}\right)\sin\theta^e - 1, \tag{B.2a}$$

$$\gamma^e = \left(\frac{w_2 - w_1}{L^e}\right)\cos\theta^e - \left(1 + \frac{u_2 - u_1}{L^e}\right)\sin\theta^e, \tag{B.2b}$$

$$\kappa^e = \frac{\theta_2 - \theta_1}{L^e}. \tag{B.2c}$$

Then, the elementary discretized gradient matrix is defined as:

$$\delta\boldsymbol{\varepsilon}^e = \mathbf{B}^e\delta\mathbf{q}^e \quad \Rightarrow \quad \mathbf{B}^e = \frac{1}{L_e}\begin{bmatrix} -\cos\theta^e & -\sin\theta^e & N_1(x)L^e\gamma^e & \cos\theta^e & \sin\theta^e & N_2(x)L^e\gamma^e \\ \sin\theta^e & -\cos\theta^e & -N_1(x)L^e(1+e^e) & -\sin\theta^e & \cos\theta^e & -N_2(x)L^e(1+e^e) \\ 0 & 0 & -1 & 0 & 0 & 1 \end{bmatrix}, \tag{B.3}$$

with $\boldsymbol{\varepsilon}^e = [e^e\ \gamma^e\ \kappa^e]^{\mathrm{T}}$. Considering the internal virtual work (see [58], [229]), the elementary internal force vector is written:

$$\mathbf{f}^e_{\mathrm{int}}(\mathbf{q}^e) = \int_0^{L^e} (\mathbf{B}^e)^{\mathrm{T}}\mathbf{C}\boldsymbol{\varepsilon}^e\,\mathrm{d}x, \tag{B.4}$$

with:

$$\mathbf{C} = \begin{bmatrix} EA & 0 & 0 \\ & kGA & 0 \\ & & EI \end{bmatrix}. \tag{B.5}$$

Recalling Eqs. (B.1) and (B.2), the first variation of Eq. (B.4) can be written:

$$\delta\mathbf{f}^e_{\mathrm{int}}(\mathbf{q}^e) = \left\{\int_0^{L^e} (\mathbf{B}^e)^{\mathrm{T}}\mathbf{C}\mathbf{B}^e\,\mathrm{d}x + \int_0^{L^e}\left(\frac{\partial\mathbf{B}^e}{\partial\mathbf{q}^e}\right)^{\mathrm{T}}\mathbf{C}\boldsymbol{\varepsilon}^e\,\mathrm{d}x\right\}\delta\mathbf{q}^e = \mathbf{K}^e_{\mathrm{t}}\delta\mathbf{q}^e, \tag{B.6}$$

where $\mathbf{K}^e_{\mathrm{t}}$ is the elementary tangent stiffness matrix. Finally, $\mathbf{K}^e_{\mathrm{t}}$ is computed $\mathbf{K}^e_{\mathrm{t}} = \mathbf{K}^e_e + \mathbf{K}^e_\gamma + \mathbf{K}^e_\kappa$, with:

$$\mathbf{K}^e_e = \frac{EA}{L^e}\begin{bmatrix} K_1 & K_3 & K_4 & -K_1 & -K_3 & K_4 \\ & K_2 & K_5 & -K_3 & -K_2 & K_5 \\ & & K_6 & -K_4 & -K_5 & K_6 \\ & & & K_1 & K_3 & -K_4 \\ & & & & K_2 & -K_5 \\ & & & & & K_6 \end{bmatrix}, \tag{B.7a}$$

$$\mathbf{K}^e_\gamma = \frac{kGA}{L^e}\begin{bmatrix} K_2 & -K_3 & K_7 & -K_2 & K_3 & K_7 \\ & K_1 & K_8 & K_3 & -K_1 & K_8 \\ & & K_9 & -K_7 & -K_8 & K_9 \\ & & & K_2 & -K_3 & -K_7 \\ & & & & K_1 & -K_8 \\ & & & & & K_9 \end{bmatrix}, \tag{B.7b}$$

$$\mathbf{K}^e_\kappa = \frac{EI}{L^e}\begin{bmatrix} 0 & 0 & 0 & 0 & 0 & 0 \\ & 0 & 0 & 0 & 0 & 0 \\ & & 1 & 0 & 0 & -1 \\ & & & 0 & 0 & 0 \\ & & & & 0 & 0 \\ & & & & & 1 \end{bmatrix}, \tag{B.7c}$$

and with:

$$K_1 = \cos^2\bar{\theta}, \quad K_2 = \sin^2\bar{\theta}, \quad K_3 = \cos\bar{\theta}\sin\bar{\theta}, \quad K_4 = \frac{L^e}{2}(\bar{e}^e\sin\bar{\theta} - \bar{\gamma}^e\cos\bar{\theta}),$$
$$K_5 = -\frac{L^e}{2}(\bar{e}^e\cos\bar{\theta} + \bar{\gamma}^e\sin\bar{\theta}), \quad K_6 = \frac{(L^e)^2}{4}[(\bar{\gamma}^e)^2 - \bar{e}^e(\bar{e}^e+1)], \quad K_7 = \frac{L^e}{2}[\bar{\gamma}^e\cos\bar{\theta} - \sin\bar{\theta}(\bar{e}^e+1)],$$
$$K_8 = \frac{L^e}{2}[\bar{\gamma}^e\sin\bar{\theta} + \cos\bar{\theta}(\bar{e}^e+1)], \quad K_9 = \frac{(L^e)^2}{4}[(\bar{e}^e+1)^2 - (\bar{\gamma}^e)^2].$$

In the above expressions for K_i, $i = 1,\ldots 9$, $\bar{\theta} = (\theta_1+\theta_2)/2$, $\bar{e} = e(\bar{\theta})$, and $\bar{\gamma} = \gamma(\bar{\theta})$ since the internal force vector integration is evaluated using a single-point Gaussian quadrature at $x = L^e/2$ to avoid shear locking (see [58], [74], [229]). Then, $\mathbf{K}_{\mathrm{t}}^e$ is assembly according to standard finite element procedures in order to obtain the full tangent stiffness matrix $\mathbf{K}_{\mathrm{t}}$.

Notice that $\mathbf{K}_{\mathrm{t}}^e = \mathbf{K}_{\mathrm{t}}^e(\mathbf{q}^e)$ and, by extension, $\mathbf{K}_{\mathrm{t}} = \mathbf{K}_{\mathrm{t}}(\mathbf{q})$ depend on the degrees of freedom u_i, w_i and θ_i through their presence in $\bar{\theta}$, $\bar{e}$ and $\bar{\gamma}$ (see Eq. (B.2)); in other words, due to the presence of geometrical nonlinearities, the tangent stiffness of the structure is a function of its deformed state. This serves to explain the dependence of the natural frequencies of the cantilever on the gravitational field, as seen in Eq. (4.26) and § 4.3.

As explained in § 4.2.4, the tangent stiffness matrix is also used in computing the equilibrium solution $\mathbf{q}_{\mathrm{s}}$ of the cantilever subjected to the gravitational field. In this case, the tangent stiffness is evaluated at $\mathbf{q} = \mathbf{0}$, such that the elementary tangent stiffness prior to assembly takes the form of Eq. (B.7) with $\mathbf{q}^e = \mathbf{0} \Rightarrow u_1 = u_2 = w_1 = w_2 = \theta_1 = \theta_2 = 0 \Rightarrow \bar{\theta} = e^e = \gamma^e = 0$, which is with $K_1 = 1$, $K_2 = K_3 = K_4 = K_5 = K_6 = K_7 = 0$, $K_8 = L^e/2$ and $K_9 = (L^e)^2/4$.

B.3 Analytical backbone computation with the third-order inextensible beam model

In this appendix, additional details are provided regarding the approximate inextensible cantilever beam model first introduced by Crespo da Silva *et al.* in [46], [47], serving in § 4.4 (represented as the black dashed lines in Figs. 4.5 and 4.9) as a comparison to the geometrically exact finite element model. This model is very interesting as it is both analytical and valid up to a moderate (but not inconsiderable) amplitude of vibration and has thus been used widely in the literature on nonlinear beam dynamics [42], [165]. In our case, it is advantageous to use this model for comparison since, when restricting the modal projection to a single mode and solving via a first-order harmonic balance, the computation of the backbone curve itself becomes analytical.

The derivation of the full inextensible beam model is shown in detail in §3.2 of [229], which we use as the starting point for our development. We begin with the strong form of the geometrically exact model, Eqs. (4.3), to which four assumptions are added:

1. The condition of inextensibility;

2. Euler-Bernoulli kinematics along with elimination of the rotatory inertia;

3. Truncation of the the geometrical nonlinearities up to order 3 in w;

4. A free end boundary condition.

Based on assumptions 1 and 2, $e = \gamma = 0$, so that Eq. (4.3c), taking into account the constitutive Eqs. (4.4), simplifies to $T = -M' - q = -EI\theta'' - q$. Then, eliminating N in Eq. (4.3b) using (4.3a) and assumption 4 ($N(L,t) = T(L,t) = 0\ \forall t$), the following partial differential equation is obtained:

$$\rho A\ddot{w} + \left(\frac{EI\theta'' + q}{\cos\theta}\right)' - \left[\tan\theta \int_L^x (\rho A\ddot{u} - n)\,\mathrm{d}x\right]' = p. \tag{B.8}$$

To recover the model of Crespo da Silva *et al.*, we first assume no external axial load ($n = 0$) or moment ($q = 0$). Then, the inextensibility condition, written explicitly as $\sqrt{(1+u')^2 + w'^2} - 1 = 0$ [229], is used in order to rewrite the axial displacement as a function of w in Eq. (B.8) according to $u' = \sqrt{1 - w'^2} - 1$. In addition, the geometrically exact kinematics of the beam with the inclusion of the inextensibility condition simplify to:

$$\sin\theta = w', \qquad \cos\theta = 1 + u' = \sqrt{1 - w'^2}. \tag{B.9}$$

Finally, performing a Taylor expansion up to order three in w leads to:

$$\rho A\ddot{w} + EI\left(w''' + w'w''^2 + w'''w'^2\right)' + \frac{\rho A}{2}\left[w' \int_L^x \frac{\partial^2}{\partial t^2}\left(\int_0^x w'^2 \mathrm{d}x\right)\mathrm{d}x\right]' = p. \tag{B.10}$$

The same normalization as that of § 4.2 [Eqs. (4.6)] is carried out, so that Eq. (B.10) becomes:

$$\ddot{\bar{w}} + \bar{w}'''' + \left(\bar{w}'\bar{w}''^2 + \bar{w}'''\bar{w}'^2\right)' + \frac{1}{2}\left[\bar{w}' \int_1^{\bar{x}} \frac{\partial^2}{\partial \bar{t}^2}\left(\int_0^{\bar{x}} \bar{w}'^2 \mathrm{d}\bar{x}\right)\mathrm{d}\bar{x}\right]' = \bar{p}, \tag{B.11}$$

where all terms are now dimensionless.

Next, the model is discretized via a projection of the transverse displacement w onto a single eigenmode $\Phi_k(x)$, for a given $k \in \mathbb{N}$:

$$\bar{w}(\bar{x}, t) = \Phi_k(\bar{x}) q_k(t), \tag{B.12}$$

where $q_k(t)$ are the modal coordinates and the transverse mode shapes Φ_k represent those of a cantilever beam, solutions of the linear part of the equations of motion, *i.e.* $\Phi'''' + \beta^4\Phi = 0$ with boundary conditions $\Phi(0) = \Phi'(0) = \Phi''(1) = \Phi'''(1) = 0$. Written explicitly:

$$\Phi_k(\bar{x}) = \cos\beta_k\bar{x} - \cosh\beta_k\bar{x} - a_k\left(\sin\beta_k\bar{x} - \sinh\beta_k\bar{x}\right). \tag{B.13}$$

In Eq. (B.13), the coefficients β_k are related to the dimensionless natural frequencies, such that $\bar{\omega}_k = \beta_k^2$ [102], and the coefficient a_k can be calculated by normalizing the mode shapes Φ_k such that $\int_0^1 \Phi_k^2 \mathrm{d}\bar{x} = 1$. The values of β_k and a_k for the first three bending modes are shown in Table B.2.

In a standard procedure, the modal projection (B.12) is injected into Eq. (B.11), the result is multiplied by $\Phi_k(\bar{x})$ and integrated over the length of the beam. Additionally, as we are here deriving an expression for the nonlinear modes / backbone curve (*i.e.* the *free* and *undamped* solution), the damping terms and external forcing are removed, so that Eq. (B.11) after the modal projection becomes:

$$\ddot{q}_k + \bar{\omega}_k^2 q_k + \Gamma_k q_k^3 + \Pi_k\left(\ddot{q}_k q_k + \dot{q}_k^2\right) q_k = 0, \tag{B.14}$$

Table B.2: Bending parameters of the k-th bending mode for the first three bending modes of a cantilever beam.

k-the bending mode	β_k	a_k	Γ_k	Π_k
1	1.875	0.7341	40.441	4.597
2	4.694	1.0185	13418	144.726
3	7.855	0.9992	269710	1006.43

with:

$$\begin{cases} \Gamma_k = \displaystyle\int_0^1 \left(\Phi_k'\Phi_k''\Phi_k'' + \Phi_k'''\Phi_k'\Phi_k'\right)' \Phi_k \mathrm{d}\bar{x}, & \text{(B.15a)} \\ \Pi_k = \displaystyle\int_0^1 \left[\Phi_k' \int_1^{\bar{x}} \int_0^{\bar{x}} \Phi_k'\Phi_k' \mathrm{d}\bar{x}\mathrm{d}\bar{x}\right]' \Phi_k \mathrm{d}\bar{x}, & \text{(B.15b)} \end{cases}$$

where the expressions for Γ_k and Π_k have been evaluated for the first three bending modes based on Eq. (B.13) and are shown in Table B.2.

Next, we seek to solve Eq. (B.14) using a harmonic balance (HBM) expansion truncated to a single harmonic: $q_k(t) = Q_k \cos\Omega t$ with Q_k the amplitude of the oscillation. Injecting this expression for $q_k(t)$ into Eq. (B.14) and keeping only terms in $\cos\Omega t$ leads to the analytical expression for the amplitude Q_k as a function of the frequency Ω and thus of the backbone curve:

$$Q_k = 2\sqrt{\frac{\Omega^2 - \omega_k^2}{3\Gamma_k - 2\Omega^2\Pi_k}}. \tag{B.16}$$

Finally, the dimensionless transverse displacement is recovered according to Eq. (B.12) restricted to one mode as $\bar{w}(\bar{x},t) = \Phi_k(\bar{x})Q_k\cos\Omega t$. The black dashed backbone curve in Fig. 4.5(b) is traced by sweeping its amplitude $\Phi_k(1)Q_k(\Omega)$ as a function of Ω. Then, $\bar{w}$ is used to compute the amplitudes of the cross-section rotation according to Eq. (B.9): $\theta(\bar{x},t) = \sin^{-1}[\bar{w}'(\bar{x},t)]$. To trace the analytical black dashed curves in Figs. 4.5(a) and 4.6 in θ, the first harmonic of $\theta(1,t)$ is computed as the amplitude of the first Fourier coefficient of $\sin^{-1}[\Phi_k(1)Q_k(\Omega)\cos\Omega t]$. It is noted that this Fourier coefficient necessarily has an amplitude less than $\simeq 0.4\pi$ rad due to the limitations of the inverse sine function itself, limiting in turn the maximum amplitude of $\theta(L,t)$ plotted in Figs. 4.5(a) and 4.6.

Appendix C

Appendices to Chapter 5

Table of Contents - Appendix C

C.1 Effect of rotational inertia on the backbone curves of slender beams

Assumption #3 of the 3D beam kinematics derivation (§ 5.1) neglects the rotational kinetic energy (KE) of the cross-sections of the beam. This assumption greatly simplifies the derivation of δW_a, the virtual work of the inertial forces. Recopying the full equation from Eq. (5.9a), δW_a is defined as:

$$\delta W_a = \underbrace{\int_0^L \left(\rho \mathbf{A} \ddot{\mathbf{x}}_0^{\mathrm{T}} \delta \mathbf{x}_0\right) \mathrm{d}s}_{\text{translational KE}} + \underbrace{\int_0^L \left((\mathbf{J}\dot{\boldsymbol{\Omega}} + \tilde{\boldsymbol{\Omega}}\mathbf{J}\boldsymbol{\Omega})^{\mathrm{T}} \delta \boldsymbol{\Theta}\right) \mathrm{d}s}_{\text{rotational KE}}, \tag{C.1}$$

where the translational and rotational contributions to δW_a have been identified. Assumption #3 removes the second term of δW_a and neglects rotational inertial effects in the mass matrix (as seen by the definition of the mass matrix in Eq. (5.35), where zeros are added in the place of the rotation degrees of freedom). Assumption #3 greatly simplifies the derivation of the elementary mass matrix, but it is only valid in cases where the rotational inertia contributions are indeed negligible. To confirm this, the cantilever beam test case of Chapter 3 (where the rotational kinetic energy was *kept* in the simulations) is rerun with the rotational inertial contributions removed from the simulation (*i.e.* $I = 0$ in Eq. (E.29)). We choose the cantilever as a test case since it has the largest amplitude of motion of any of the systems studied in this thesis, meaning that any rotational inertia effects should be highest for the cantilever vibrating at large amplitude. The comparison between the simulations with and without inertia is summarized in Fig. C.1.

In Fig. C.1, the black backbone curves are directly recopied from Fig. 3.4 of § 3.3.1, while the yellow backbone curve overlaid onto Fig. C.1 represents the same computation while neglecting the rotational inertia. It is clearly seen that there is no distinguishable difference between the computation with

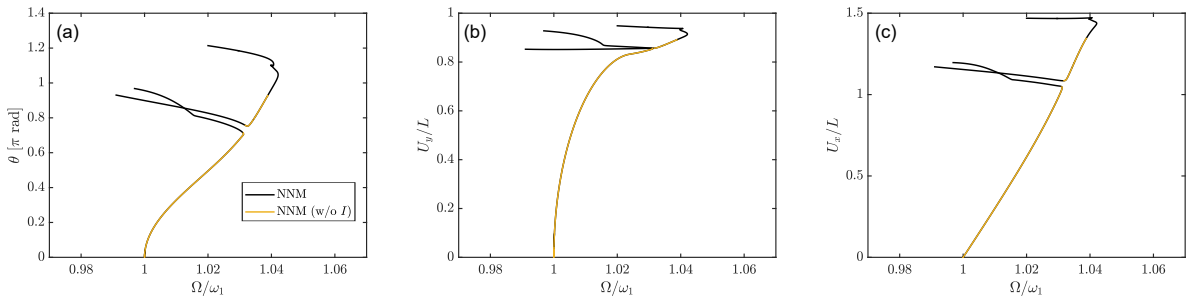

Figure C.1: Comparison of the backbone curves of the first nonlinear mode of the cantilever beam of § 3.3.1 with and without rotational inertia.

rotational inertia and without, thereby justifying the use of Assumption #3 to reduce the derivation of the 3D beam kinematics.

C.2 Derivation of the tangent stiffness matrix with quaternions

In this appendix, the process for deriving the tangent stiffness matrix used in computing the eigenvalues of the system is shown with a quaternion parametrization of the rotation terms. With this formulation, some quaternion algebra is involved in order to derive the exact expression for the tangent stiffness matrix, the details of which will be explained at each step of the derivation.

C.2.1 Variation of the strains

To begin the derivation, recall the expressions for the strains $\hat{\mathbf{\Gamma}}$ and curvatures $\hat{\mathbf{K}}$ [Eqs. (5.17)], which are discretized as shown in § 5.3 and written for a single element:

$$\hat{\mathbf{\Gamma}}^e = \hat{\mathbf{q}}^{e*} \circ \hat{\mathbf{x}}_0^{e\prime} \circ \hat{\mathbf{q}}^e - \hat{\mathbf{\Gamma}}_0^e, \tag{C.2a}$$

$$\hat{\mathbf{K}}^e = 2\hat{\mathbf{q}}^{e*} \circ \hat{\mathbf{q}}^{e\prime} - \hat{\mathbf{K}}_0^e, \tag{C.2b}$$

recalling that $\mathbf{E}^e = \left[\hat{\mathbf{\Gamma}}^{e\mathrm{T}} \quad \hat{\mathbf{K}}^{e\mathrm{T}}\right]^{\mathrm{T}}$.

As explained in [101], the tangent stiffness matrix is derived through a linearization of the internal forces ($\mathbf{F}^e_{\text{int}}$ in Eq. (5.36)) or, taking into account the effect of the unity constraint, the combined internal / constraint force $\mathbf{F}^e_g$ as shown in Eq. (5.42), such that the elemental tangent stiffness matrix $\mathbf{K}^e_t$ is derived as:

$$\delta\mathbf{F}^e_g = \mathbf{K}^e_t \delta\mathbf{z}^e, \tag{C.3}$$

with $\mathbf{z}^e$ as defined in Eq. (5.24). The procedure to be taken can be summarized as follows: according to the expression for $\mathbf{F}^e_g$ [Eq. (5.42)] which is a function of the variables $\left[\mathbf{x}_0^{e\prime\mathrm{T}} \quad \hat{\mathbf{q}}^{e\prime\mathrm{T}} \quad \hat{\mathbf{q}}^{e\mathrm{T}} \quad \mu^e\right]^{\mathrm{T}}$, we seek to relate $\delta\mathbf{F}^e_g$ to $\delta\mathbf{z}^e$ using a matrix $\mathbf{K}^e_t$.

To do so, the variations of the strains $\delta\hat{\mathbf{\Gamma}}$ and the curvatures $\delta\hat{\mathbf{K}}$ are needed. Some quaternion algebra is involved in their derivation; here we introduce three relations that are useful in deriving and

condensing the expressions found here, which are:

$$\mathbf{H} = \Phi_R(\hat{\mathbf{q}}^{e*})\Phi_L(\hat{\mathbf{q}}^e), \tag{C.4a}$$
$$\mathbf{H}^{\mathrm{T}} = \Phi_R(\hat{\mathbf{q}}^{e})\Phi_L(\hat{\mathbf{q}}^{e*}), \tag{C.4b}$$

making use of the definitions of Φ_L and Φ_R [Eqs. (5.11)] and:

$$\delta\hat{\mathbf{q}}^{e*} = -\hat{\mathbf{q}}^{e*} \circ \delta\hat{\mathbf{q}}^{e} \circ \hat{\mathbf{q}}^{e*}. \tag{C.5}$$

Recall also that based on the definition of the conjugate quaternion in § 5.2.1, $\mathbf{q}^* \circ \mathbf{q} = 1$. Then, beginning from the strain expressions above:

$$\begin{aligned}
\delta\hat{\mathbf{\Gamma}}^e &= \delta\hat{\mathbf{q}}^{e*} \circ \hat{\mathbf{x}}_0^{e\prime} \circ \hat{\mathbf{q}}^e + \hat{\mathbf{q}}^{e*} \circ \delta\hat{\mathbf{x}}_0^{e\prime} \circ \hat{\mathbf{q}}^e + \hat{\mathbf{q}}^{e*} \circ \hat{\mathbf{x}}_0^{e\prime} \circ \delta\hat{\mathbf{q}}^e, \\
&= -\hat{\mathbf{q}}^{e*} \circ \delta\hat{\mathbf{q}}^e \circ \mathbf{H}^{\mathrm{T}}\hat{\mathbf{x}}_0^{e\prime} + \mathbf{H}^{\mathrm{T}}\hat{\mathbf{x}}_0^{e\prime} \circ \hat{\mathbf{q}}^{e*} \circ \delta\hat{\mathbf{q}}^e + \mathbf{H}^{\mathrm{T}}\delta\hat{\mathbf{x}}_0^{e\prime}, \\
&= \left[\Phi_L(\mathbf{H}^{\mathrm{T}}\hat{\mathbf{x}}_0^{e\prime}) - \Phi_R(\mathbf{H}^{\mathrm{T}}\hat{\mathbf{x}}_0^{e\prime})\right] \Phi_L(\hat{\mathbf{q}}^{e*})\delta\hat{\mathbf{q}}^e + \mathbf{H}^{\mathrm{T}}\delta\hat{\mathbf{x}}_0^{e\prime},
\end{aligned} \tag{C.6}$$

and:

$$\begin{aligned}
\delta\hat{\mathbf{K}}^e &= 2\delta\hat{\mathbf{q}}^{e*} \circ \hat{\mathbf{q}}^{e\prime} + 2\hat{\mathbf{q}}^{e*} \circ \delta\hat{\mathbf{q}}^{e\prime}, \\
&= -2\Phi_R(\hat{\mathbf{q}}^{e*})\Phi_R(\hat{\mathbf{q}}^{e\prime})\Phi_L(\hat{\mathbf{q}}^{e*})\delta\hat{\mathbf{q}}^e + 2\Phi_L(\hat{\mathbf{q}}^{e*})\delta\hat{\mathbf{q}}^{e\prime}.
\end{aligned} \tag{C.7}$$

C.2.2 Variation of the internal force

The combined internal and constraint force vector for a single element $\mathbf{F}^e_{\mathrm{int}}$ is recopied from Eq. (5.42) and evaluated using the 2-point reduced Gauss integration as described by Eqs. (5.38) and (5.39):

$$\begin{aligned}
\mathbf{F}^e_g &= \int_0^{L^e} \mathbf{Q}^{\mathrm{T}}\mathbf{g}^e(\mathbf{z}^e)\mathrm{d}s, \\
&\approx \frac{L_e}{2}\left[\left(\mathbf{Q}^{\mathrm{T}}\mathbf{g}^e\right)|_{\mathrm{GP}_1} + \left(\mathbf{Q}^{\mathrm{T}}\mathbf{g}^e\right)|_{\mathrm{GP}_2}\right],
\end{aligned} \tag{C.8}$$

with $\mathbf{Q}$ as defined in Eq. (5.30).

The expression for $\mathbf{g}^e(\mathbf{z}^e)$ is recalled [Eq. (5.41)]:

$$\mathbf{g}^e(\mathbf{z}^e) = \begin{bmatrix} \mathrm{vec}(\hat{\mathbf{q}}^e \circ \hat{\mathbf{N}}^e \circ \hat{\mathbf{q}}^{e*}) \\ 2\hat{\mathbf{q}}^e \circ \hat{\mathbf{M}}^e \\ 2\hat{\mathbf{q}}^e \circ \left(\hat{\mathbf{N}}^e \circ \left(\hat{\mathbf{\Gamma}}^e + \hat{\mathbf{\Gamma}}_0\right) + \hat{\mathbf{M}}^e \circ \left(\hat{\mathbf{K}}^e + \hat{\mathbf{K}}_0\right)\right) + 2\hat{\mathbf{q}}^{e\prime} \circ \hat{\mathbf{M}}^e + 2\mu^e\hat{\mathbf{q}}^e \\ \hat{\mathbf{q}}^e \cdot \hat{\mathbf{q}}^e - 1 \end{bmatrix}, \tag{C.9}$$

so that taking the variation $\delta\mathbf{g}^e(\mathbf{z}^e)$ leads to:

$$\delta\mathbf{g}^e(\mathbf{z}^e) = \begin{bmatrix} \mathrm{vec}\left(\delta\hat{\mathbf{q}}^e \circ \hat{\mathbf{N}}^e \circ \hat{\mathbf{q}}^{e*} + \hat{\mathbf{q}}^e \circ \delta\hat{\mathbf{N}}^e \circ \hat{\mathbf{q}}^{e*} + \hat{\mathbf{q}}^e \circ \hat{\mathbf{N}}^e \circ \delta\hat{\mathbf{q}}^{e*}\right) \\ 2\delta\hat{\mathbf{q}}^e \circ \hat{\mathbf{M}}^e + 2\hat{\mathbf{q}}^e \circ \delta\hat{\mathbf{M}}^e \\ 2\delta\hat{\mathbf{q}}^e \circ [\sim] + 2\hat{\mathbf{q}}^e \circ \delta[\sim] + 2\delta\hat{\mathbf{q}}^{e\prime} \circ \hat{\mathbf{M}}^e + 2\hat{\mathbf{q}}^{e\prime} \circ \delta\hat{\mathbf{M}}^e + 2\delta\mu\hat{\mathbf{q}}^e + 2\mu^e\delta\hat{\mathbf{q}}^e \\ 2\hat{\mathbf{q}}^e \cdot \delta\hat{\mathbf{q}}^e \end{bmatrix}, \tag{C.10}$$

where $[\sim] = \left(\hat{\mathbf{N}}^e \circ (\hat{\mathbf{\Gamma}}^e + \hat{\mathbf{\Gamma}}_0^e) + \hat{\mathbf{M}}^e \circ (\hat{\mathbf{K}}^e + \hat{\mathbf{K}}_0^e)\right)$, $\delta\hat{\mathbf{N}}^e = \hat{\mathbf{C}}_N \delta\hat{\mathbf{\Gamma}}^e$ and $\delta\hat{\mathbf{M}}^e = \hat{\mathbf{C}}_M \delta\hat{\mathbf{K}}^e$. To simplify computation of the tangent stiffness matrix, the relation between $\delta\mathbf{g}^e$ and $\delta\mathbf{z}^e$ is decomposed into a matrix multiplication, such that:

$$\delta\mathbf{g}^e(\mathbf{z}^e) = \begin{bmatrix} & \\ & \mathbf{A}_1 \\ & \end{bmatrix} \begin{bmatrix} \delta\hat{\mathbf{\Gamma}}^e \\ \delta\hat{\mathbf{K}}^e \\ \delta\hat{\mathbf{q}}^{e\prime} \\ \delta\hat{\mathbf{q}}^e \\ \delta\mu^e \end{bmatrix}, \tag{C.11}$$

and:

$$\begin{bmatrix} \delta\hat{\mathbf{\Gamma}}^e \\ \delta\hat{\mathbf{K}}^e \\ \delta\hat{\mathbf{q}}^{e\prime} \\ \delta\hat{\mathbf{q}}^e \\ \delta\mu^e \end{bmatrix} = \begin{bmatrix} & \\ & \mathbf{A}_2 \\ & \end{bmatrix} \begin{bmatrix} \delta\mathbf{x}_0^{e\prime} \\ \delta\hat{\mathbf{q}}^{e\prime} \\ \delta\hat{\mathbf{q}}^e \\ \delta\mu^e \end{bmatrix}, \tag{C.12}$$

where:

$$\begin{bmatrix} \delta\mathbf{x}_0^{e\prime\mathrm{T}} & \delta\hat{\mathbf{q}}^{e\prime\mathrm{T}} & \delta\hat{\mathbf{q}}^{e\mathrm{T}} & \delta\mu^e \end{bmatrix}^{\mathrm{T}} = \mathbf{Q}(s)\delta\mathbf{z}_e, \tag{C.13}$$

so that, in the end, according to the reduced integration of $\mathbf{F}_g^e$ [Eq. (C.8)], the following relation is derived:

$$\begin{aligned} \delta\mathbf{F}_g^e &= \frac{L_e}{2}\left[\left(\mathbf{Q}^{\mathrm{T}}\delta\mathbf{g}^e\right)|_{\mathrm{GP}_1} + \left(\mathbf{Q}^{\mathrm{T}}\delta\mathbf{g}^e\right)|_{\mathrm{GP}_2}\right] \\ &= \underbrace{\frac{L_e}{2}\left[\left(\mathbf{Q}^{\mathrm{T}}[\mathbf{A}_1][\mathbf{A}_2]\mathbf{Q}\right)|_{\mathrm{GP}_1} + \left(\mathbf{Q}^{\mathrm{T}}[\mathbf{A}_1][\mathbf{A}_2]\mathbf{Q}\right)|_{\mathrm{GP}_2}\right]}_{\mathbf{K}_t^e}\delta\mathbf{z}_e. \end{aligned} \tag{C.14}$$

Next, the $[\mathbf{A}_1]$ and $[\mathbf{A}_2]$ matrices are derived explicitly. For improved readability, the rows in $\delta\mathbf{g}^e$ as they appear in Eq. (C.10) are here analyzed separately. First, the $[\mathbf{A}_1]$ matrix is derived; beginning with the first row:

$$\begin{aligned} &\mathrm{vec}\left(\delta\hat{\mathbf{q}}^e \circ \hat{\mathbf{N}}^e \circ \hat{\mathbf{q}}^{e*} + \hat{\mathbf{q}}^e \circ \delta\hat{\mathbf{N}}^e \circ \hat{\mathbf{q}}^{e*} + \hat{\mathbf{q}}^e \circ \hat{\mathbf{N}}^e \circ \delta\hat{\mathbf{q}}^{e*}\right) \\ &= \mathrm{vec}\left(\mathbf{H}\delta\hat{\mathbf{N}}^e + \Phi_R(\hat{\mathbf{q}}^{e*})\left[\Phi_R(\mathbf{H}\hat{\mathbf{N}}^e) - \Phi_L(\mathbf{H}\hat{\mathbf{N}}^e)\right]\delta\hat{\mathbf{q}}^e\right) \\ &= \mathrm{vec}\left(\mathbf{H}\hat{\mathbf{C}}_N\delta\hat{\mathbf{\Gamma}}^e + \Phi_R(\hat{\mathbf{q}}^{e*})\left[\Phi_R(\mathbf{H}\hat{\mathbf{N}}^e) - \Phi_L(\mathbf{H}\hat{\mathbf{N}}^e)\right]\delta\hat{\mathbf{q}}^e\right), \end{aligned} \tag{C.15}$$

then the second row:

$$\begin{aligned} 2\delta\hat{\mathbf{q}}^e \circ \hat{\mathbf{M}}^e + 2\hat{\mathbf{q}}^e \circ \delta\hat{\mathbf{M}}^e &= 2\Phi_R(\hat{\mathbf{M}}^e)\delta\hat{\mathbf{q}}^e + 2\hat{\mathbf{q}}^e \circ \delta\hat{\mathbf{M}}^e \\ &= 2\Phi_R(\hat{\mathbf{M}}^e)\delta\hat{\mathbf{q}}^e + \Phi_L(2\hat{\mathbf{q}}^e)\hat{\mathbf{C}}_M\delta\hat{\mathbf{K}}^e, \end{aligned} \tag{C.16}$$

the third row:

$$\begin{aligned} &2\delta\hat{\mathbf{q}}^e \circ [\sim] + 2\hat{\mathbf{q}}^e \circ \delta[\sim] + 2\delta\hat{\mathbf{q}}^{e\prime} \circ \hat{\mathbf{M}}^e + 2\hat{\mathbf{q}}^{e\prime} \circ \delta\hat{\mathbf{M}}^e + 2\delta\mu^e\hat{\mathbf{q}}^e + 2\mu^e\delta\hat{\mathbf{q}}^e \\ &= 2\Phi_R[\hat{\mathbf{N}}^e \circ (\hat{\mathbf{\Gamma}}^e + \hat{\mathbf{\Gamma}}_0^e) + \hat{\mathbf{M}}^e \circ (\hat{\mathbf{K}}^e + \hat{\mathbf{K}}_0^e)]\delta\hat{\mathbf{q}}^e + 2\hat{\mathbf{q}}^e \circ \left[\hat{\mathbf{N}}^e \circ \delta\hat{\mathbf{\Gamma}}^e - (\hat{\mathbf{\Gamma}}^e + \hat{\mathbf{\Gamma}}_0^e) \circ \delta\hat{\mathbf{N}}^e + \hat{\mathbf{M}}^e \circ \delta\hat{\mathbf{K}}^e - (\hat{\mathbf{K}}^e + \hat{\mathbf{K}}_0^e) \circ \delta\hat{\mathbf{M}}^e\right] \\ &\quad + 2\delta\hat{\mathbf{q}}^{e\prime} \circ \hat{\mathbf{M}}^e + 2\hat{\mathbf{q}}^{e\prime} \circ \delta\hat{\mathbf{M}}^e + 2\delta\mu^e\hat{\mathbf{q}}^e + 2\mu^e\delta\hat{\mathbf{q}}^e \\ &= 2\Phi_R[\Phi_L(\hat{\mathbf{N}}^e)(\hat{\mathbf{\Gamma}}^e + \hat{\mathbf{\Gamma}}_0^e) + \Phi_L(\hat{\mathbf{M}}^e)(\hat{\mathbf{K}}^e + \hat{\mathbf{K}}_0^e)]\delta\hat{\mathbf{q}}^e + \Phi_L(2\hat{\mathbf{q}}^e)\left[\Phi_L(\hat{\mathbf{N}}^e)\delta\hat{\mathbf{\Gamma}}^e - \Phi_L(\hat{\mathbf{\Gamma}}^e + \hat{\mathbf{\Gamma}}_0^e)\hat{\mathbf{C}}_N\delta\hat{\mathbf{\Gamma}}^e\right] \\ &\quad + \Phi_L(2\hat{\mathbf{q}}^e)\left[\Phi_L(\hat{\mathbf{M}}^e)\delta\hat{\mathbf{K}} - \Phi_L(\hat{\mathbf{K}} + \hat{\mathbf{K}}_0)\hat{\mathbf{C}}_M\delta\hat{\mathbf{K}}\right] + 2\Phi_R(\hat{\mathbf{M}})\delta\hat{\mathbf{q}}' + \Phi_L(2\hat{\mathbf{q}}')\hat{\mathbf{C}}_M\delta\hat{\mathbf{K}} + 2\hat{\mathbf{q}}\delta\mu + 2\mu\delta\hat{\mathbf{q}}, \end{aligned} \tag{C.17}$$

and finally the fourth row:

$$2\hat{\mathbf{q}}^e \cdot \delta\hat{\mathbf{q}}^e = 2\hat{\mathbf{q}}^{e\mathrm{T}}\delta\hat{\mathbf{q}}^e. \tag{C.18}$$

The $[\mathbf{A}_1]$ matrix can then be written explicitly:

$$[\mathbf{A}_1] = \begin{bmatrix} \mathbf{a}_{11} & \mathbf{0} & \mathbf{0} & \mathbf{a}_{14} & \mathbf{0} \\ \mathbf{0} & \mathbf{a}_{22} & \mathbf{0} & \mathbf{a}_{24} & \mathbf{0} \\ \mathbf{a}_{31} & \mathbf{a}_{32} & \mathbf{a}_{33} & \mathbf{a}_{34} & \mathbf{a}_{35} \\ \mathbf{0} & \mathbf{0} & \mathbf{0} & \mathbf{a}_{44} & \mathbf{0} \end{bmatrix}, \tag{C.19}$$

with:

$$\begin{aligned}
\mathbf{a}_{11} &= \mathbf{H}\hat{\mathbf{C}}_N, \\
\mathbf{a}_{14} &= \Phi_R(\hat{\mathbf{q}}^{e*})\left[\Phi_R(\mathbf{H}\hat{\mathbf{N}}^e) - \Phi_L(\mathbf{H}\hat{\mathbf{N}}^e)\right], \\
\mathbf{a}_{22} &= \Phi_L(2\hat{\mathbf{q}}^e)\hat{\mathbf{C}}_M, \\
\mathbf{a}_{24} &= 2\Phi_R(\hat{\mathbf{M}}^e), \\
\mathbf{a}_{31} &= \Phi_L(2\hat{\mathbf{q}}^e)\left[\Phi_L(\hat{\mathbf{N}}^e) - \Phi_L(\hat{\mathbf{\Gamma}}^e + \hat{\mathbf{\Gamma}}_0^e)\hat{\mathbf{C}}_N\right], \\
\mathbf{a}_{32} &= \Phi_L(2\hat{\mathbf{q}}^e)\left[\Phi_L(\hat{\mathbf{M}}^e) - \Phi_L(\hat{\mathbf{K}}^e + \hat{\mathbf{K}}_0^e)\hat{\mathbf{C}}_M\right] + \Phi_L(2\hat{\mathbf{q}}^{e\prime})\hat{\mathbf{C}}_M, \\
\mathbf{a}_{33} &= 2\Phi_R(\hat{\mathbf{M}}^e), \\
\mathbf{a}_{34} &= 2\Phi_R[\Phi_L(\hat{\mathbf{N}}^e)(\hat{\mathbf{\Gamma}}^e + \hat{\mathbf{\Gamma}}_0^e) + \Phi_L(\hat{\mathbf{M}}^e)(\hat{\mathbf{K}}^e + \hat{\mathbf{K}}_0^e)] + 2\mu^e, \\
\mathbf{a}_{35} &= 2\hat{\mathbf{q}}^e, \\
\mathbf{a}_{44} &= 2\hat{\mathbf{q}}^{e\mathrm{T}}.
\end{aligned}$$

Computation of the $[\mathbf{A}_2]$ matrix is more simple since we can make use of the variations of the strains $\delta\hat{\mathbf{\Gamma}}^e$ and the curvatures $\delta\hat{\mathbf{K}}^e$ derived in the previous section. Written explicitly:

$$[\mathbf{A}_2] = \begin{bmatrix} \mathbf{H}^{\mathrm{T}} & \mathbf{0} & \left[\Phi_L(\mathbf{H}^{\mathrm{T}}\hat{\mathbf{x}}_0^{e\prime}) - \Phi_R(\mathbf{H}^{\mathrm{T}}\hat{\mathbf{x}}_0^{e\prime})\right]\Phi_L(\hat{\mathbf{q}}^{e*}) & \mathbf{0} \\ \mathbf{0} & \Phi_L(2\hat{\mathbf{q}}^{e*}) & -2\Phi_R(\hat{\mathbf{q}}^{e*})\Phi_R(\hat{\mathbf{q}}^{e\prime})\Phi_L(\hat{\mathbf{q}}^{e*}) & \mathbf{0} \\ \mathbf{0} & \mathbf{I}_4 & \mathbf{0} & \mathbf{0} \\ \mathbf{0} & \mathbf{0} & \mathbf{I}_4 & \mathbf{0} \\ \mathbf{0} & \mathbf{0} & \mathbf{0} & \mathbf{I}_1 \end{bmatrix}, \tag{C.20}$$

where $\mathbf{I}$ represents the identity matrix of appropriate size (4×4 or 1×1). Care should be taken to make sure the dimensions of $[\mathbf{A}_1]$ and $[\mathbf{A}_2]$ are correct for the elements in $\delta\mathbf{z}_e$, since *e.g.* $\mathbf{x}_0^e$ is a vector (sometimes extended to a pure quaternion $\hat{\mathbf{x}}_0^e$ in the derivations above; the dimensions must be accounted for appropriately in the code).

All of the terms in the definition of $\mathbf{K}_t^e$ according to Eq. (C.14) have now been derived and $\mathbf{K}_t^e$ is computed and assembled into the global tangent stiffness matrix according to the principles of finite element analysis (in the same was as the elementary mass matrix of Chapters 3 and 5). In the solving scheme described in this work, the tangent stiffness matrix is solely used in the eigenanalysis to compute the natural frequencies of the system around the static equilibrium of the system (see § 2.4.2 of Chapter 2, Eq. (2.62)).

C.2.3 Extraction of the strain matrix $\mathbf{B}^e$

Based on relationship Eq. (C.12), the strain matrix $\mathbf{B}^e$ [Eq. (5.33)] relating $\delta\mathbf{E}^e$ and $\delta\mathbf{z}^e$ according to Eq. (5.32) can be extracted from Eq. (C.20) as:

$$\mathbf{B}^e = \begin{bmatrix} \mathbf{H}^{\mathrm{T}} & \mathbf{0} & \left[\Phi_L(\mathbf{H}^{\mathrm{T}}\hat{\mathbf{x}}_0^{e\prime}) - \Phi_R(\mathbf{H}^{\mathrm{T}}\hat{\mathbf{x}}_0^{e\prime})\right]\Phi_L(\hat{\mathbf{q}}^{e*}) & \mathbf{0} \\ \mathbf{0} & \Phi_L(2\hat{\mathbf{q}}^{e*}) & -2\Phi_R(\hat{\mathbf{q}}^{e*})\Phi_R(\hat{\mathbf{q}}^{e\prime})\Phi_L(\hat{\mathbf{q}}^{e*}) & \mathbf{0} \end{bmatrix}. \tag{C.21}$$

Eq. (C.21) can then be used to derive the internal force vector, as shown in Eq. (5.36).

Appendix D

Appendices to Chapter 6

Table of Contents - Appendix D

D.1 Some models with nonlinear damping and inertia

In this appendix, several models of the literature are recalled in order to show various forms of nonlinearities, both conservative and dissipative. In all cases, the model falls into the form of Eq. (6.1), with the conservative and dissipative vectors, respectively, odd and even functions of $\dot{\boldsymbol{x}}$, as described in § 6.2.4.

D.1.1 An elastic pendulum

Consider first the free oscillations of an elastic pendulum, composed of a mass m linked to a Galilean frame by a linear spring of stiffness k and unstretched length l_0, subjected to a plane motion in a vertical gravity field of acceleration g. Its two generalized coordinates are chosen as the angle $\theta(t)$ of the spring with the vertical and the length $\lambda(t)$ of the spring. The kinetic and potential energies are written as:

$$\mathcal{T} = \frac{1}{2} m \left(\dot{\lambda}^2 + \lambda^2 \dot{\theta}^2 \right), \quad \mathcal{V} = \frac{1}{2} k \left(\lambda - l_0 \right)^2 - m \lambda g \cos\theta, \tag{D.1}$$

The equations of motion, obtained for instance with Lagrange equations, are in the form of Eq. (6.1) with:

$$\boldsymbol{x}(t)=\begin{bmatrix}\theta(t)\\ \lambda(t)\end{bmatrix},\quad \boldsymbol{M}=\begin{bmatrix}m\lambda^2 & 0\\ 0 & m\end{bmatrix},\quad \boldsymbol{f}_{\rm c}=\begin{bmatrix}2m\dot\theta\dot\lambda\lambda+m\lambda g\sin\theta\\ -m\dot\theta^2\lambda+k(\lambda-l_0)-mg\cos\theta\end{bmatrix},\quad \boldsymbol{f}_{\rm d}=\boldsymbol{f}_{\rm e}=\boldsymbol{0}. \tag{D.2}$$

Notice the dependence of the inertia matrix on $\lambda(t)$ and the nonlinear quadratic (even) dependence of the conservative force vector $\boldsymbol{f}_c$ on $(\dot\theta,\dot\lambda)$.

D.1.2 An inextensible beam model with viscous and Kelvin-Voigt damping

As initially introduced in [46] and with the same notations as in Chapter 4 and [229], we consider the free vibrations of a slender cantilever beam of length L whose deformation is defined by the axial displacement field $u(x,t)$, the transverse displacement field $w(x,t)$ and rotation field $\theta(x,t)$ of the cross section at abscissa x and time t. The purpose of this section is to analyze the effect of damping in the equations.

With an inextensibility constraint ($(1+u')^2+w'^2=1$, with $\circ'=\partial\circ/\partial x$), Euler-Bernoulli kinematics and neglected rotational inertia, the equations of motion can be written:

$$\rho A(\ddot u+\mu\dot u)=(N\cos\theta-T\sin\theta)',\quad \rho A(\ddot w+\mu\dot u)=(N\sin\theta+T\cos\theta)',\quad T=-M', \tag{D.3}$$

where ρ is the density of the material, A the area of the cross section and (N,T,M) the generalized forces (axial force, transverse force, bending moment). Notice the *viscous damping term* introduced in both axial and transverse motion, of coefficient μ [s^{-1}].

As in [70], [71], a *Kelvin-Voigt (KV) damping model* is added in the form $\sigma=E(\varepsilon+\tau\dot\varepsilon)$, with σ the axial stress, ε the axial strain, E the Young's modulus of the material and τ a damping time constant. Considering the geometrically exact model with an inextensible centerline, $\varepsilon=-z\theta'$ with z the transverse coordinate of any point in the cross section. Then, considering the definitions of M as an integral of stress in the cross section, the following relation is obtained:

$$M=\int_A z\sigma\,\mathrm{d}A=EI(\theta'+\tau\dot\theta'), \tag{D.4}$$

with I the second moment of area of the cross section. Then, as explained in Chapter 4 and [229], the above expression is introduced into the equations of motion Eq. (D.3), in which N is eliminated, to obtain only one equation for the bending motion of the beam:

$$\rho A(\ddot w+\mu\dot w)+EI\left(\frac{\theta''}{\cos\theta}\right)'+\tau EI\left(\frac{\dot\theta''}{\cos\theta}\right)'-\rho A\left(\tan\theta\int_L^X(\ddot u+\mu\dot u)\,X\right)'=0. \tag{D.5}$$

The inextensibility condition leads to $\sin\theta=w'$, $\cos\theta=1+u'$, $u'=\sqrt{1-w'^2}-1$. Finally, eliminating u and θ as functions of w and performing Taylor expansions in w up to order three, it is possible to obtain a model cubic in $w(x,t)$:

$$\begin{aligned}&\rho A(\ddot w+\mu\dot w)+EI\left[w''''+(w'w''^2+w'''w'^2)'\right]+\\ &\tau EI\left[\dot w''''+\dot w'(w'w'''+w''^2)+2\dot w''w'w''+\dot w'''w'^2\right]'+\frac{\rho A}{2}\left[w'\int_L^x\left(\frac{\partial^2}{\partial t^2}+\mu\frac{\partial}{\partial t}\right)\int_0^x w'^2xx\right]=0.\end{aligned} \tag{D.6}$$

To analyze the effect of the damping, it is convenient to expand this partial differential equation on a given vibration mode: $w(x,t) = \Phi(x)q(t)$. Using the orthogonality of Φ, one obtains:

$$\ddot{q} + 2(\mu + \tau\omega_0^2)\dot{q} + (\mu\Lambda + \tau\Delta)q^2\dot{q} + \omega_0^2 q + \Gamma q^3 + \Pi(\dot{q}^2 + q\ddot{q})q = 0, \tag{D.7}$$

where ω_0 is the natural frequency of the considered mode and (Γ, Π) are the classical nonlinear coefficients (see *e.g.* Appendix B.3 or [229]). This equation is in the form of Eq. (6.1) with $\boldsymbol{x} = [q]$. The viscous damping (proportional to μ) adds a linear term, but also a nonlinear term proportional to the coefficient Λ because of the axial motion condensation. The KV damping (proportional to τ) further adds a linear term and also a nonlinear term proportional to coefficient Δ. These two nonlinear damping contributions are both cubic (of the form $q^2\dot{q}$) and stem from the joint contribution of the damping models, both linear, with the geometrical nonlinearities. This result has been identified and analyzed in [7] and is illustrated in Fig. 6.1. As shown in § 6.2.4, is is observed that the conservative terms have an *even* dependence in $\dot{q}$ through the term $\Pi\dot{q}^2 q$, whereas the dissipative terms are *odd* in $\dot{q}$ (they are all proportional to $\dot{q}$).

D.1.3 A cantilever beam with quadratic aeroelastic drag

It is possible to include in the model of a vibrating structure the damping effect of an aeroelastic drag, proportional to the square of the velocity as shown in [42]. In [42], a term of the form $f_{\text{ae}} = \nu\dot{q}|\dot{q}|$ is added *a posteriori* in Eq. (D.7). As described in § 6.2.4, this term is an odd function of $\dot{q}$ since $f_{\text{ae}}(-\dot{q}) = -f_{\text{ae}}(\dot{q})$ (due to the absolute value).

D.1.4 An energy harvester with material piezoelectric nonlinearities

When a mechanical structure includes a piezoelectric material, particular nonlinearities (both conservative and dissipative) due to ferroelastic hysteresis behaviour have to be taken into account. A model for such a structure, restricted to one of its vibration modes and coupled to an electric resistor R for energy harvesting applications, is considered in [140]. It can be written in the form of Eq. (6.1) with:

$$\boldsymbol{x}(t) = \begin{bmatrix} u(t) \\ Q(t) \end{bmatrix}, \quad \boldsymbol{M} = \begin{bmatrix} m & 0 \\ 0 & 0 \end{bmatrix}, \quad \boldsymbol{f}_{\text{c}} = \begin{bmatrix} k_1 u + k_2 u^2 \text{sgn}(u) - [\theta_1 + \theta_2 u \text{sgn}(u)]\, Q/C \\ Q - [\theta_1 + \theta_2 u \text{sgn}(u)/2]\, u \end{bmatrix}, \tag{D.8}$$

$$\boldsymbol{f}_{\text{d}} = \begin{bmatrix} [c_1 u \text{sgn}(u) + c_2 u^2]\, \text{sgn}(\dot{u}) \\ RC\dot{Q} \end{bmatrix}, \quad \boldsymbol{f}_{\text{e}} = \begin{bmatrix} F(t) \\ 0 \end{bmatrix}, \tag{D.9}$$

where $\text{sgn}(\circ)$ is the sign of function $\circ(t)$. The unknowns are the mechanical modal coordinate $u(t)$ and the electric charge $Q(t)$. C is the electric capacitance of the piezoelectric elements, m the modal mass, (c_1, c_2) damping coefficients, (k_1, k_2) stiffness coefficients, (θ_1, θ_2) piezoelectric coupling coefficients and $F(t)$ the external mechanical force. Here, the dissipative factor $\boldsymbol{f}_{\text{d}}$ is an odd function of $\dot{\boldsymbol{x}} = \text{T}[\dot{u}\,\dot{Q}]$.

D.2 Justification of a monophase CNM motion

We assume that the conservative force vector $\boldsymbol{f}_{\text{c}}(\boldsymbol{x}, \dot{\boldsymbol{x}})$ and the mass matrix $\boldsymbol{M}(\boldsymbol{x})$ are smooth around the equilibrium point $(\boldsymbol{x}, \dot{\boldsymbol{x}}) = (\boldsymbol{0}, \boldsymbol{0})$ and that the $\dot{\boldsymbol{x}}$ dependence is even, such that their Taylor expansions can be written, in index notation:

$$M_{ij}(\boldsymbol{x}) = M_{ij}^{(0)} + M_{ijk}^{(1)} x_k + M_{ijkl}^{(2)} x_k x_l + M_{ijklm}^{(3)} x_k x_l x_m + \dots \tag{D.10}$$

$$[\boldsymbol{f}_{\mathrm{c}}(\boldsymbol{x}, \dot{\boldsymbol{x}})]_i = K_{ij}^{(1)}(\dot{\boldsymbol{x}}) x_j + K_{ijk}^{(2)}(\dot{\boldsymbol{x}}) x_j x_k + \dots, \tag{D.11}$$

$$K_{ij}^{(1)}(\dot{\boldsymbol{x}}) = K_{ij}^{(1,0)} + K_{ijkl}^{(1,2)} \dot{x}_k \dot{x}_l + \dots \tag{D.12}$$

$$K_{ijk}^{(2)}(\dot{\boldsymbol{x}}) = K_{ijk}^{(2,0)} + K_{ijklm}^{(2,2)} \dot{x}_l \dot{x}_m + \dots, \tag{D.13}$$

where the index i, j, k, l, m are integers, $f_i = [\boldsymbol{f}]_i$ is the ith component of vector $\boldsymbol{f}$ and $M_{\bullet}^{(\bullet)}$, $K_{\bullet}^{(\bullet)}$ are the components of high order matrices corresponding to the coefficients of the Taylor expansions. Analyzing these expressions, it can be concluded that their time dependencies appear through products of the components of $\boldsymbol{x}(t)$ of arbitrary order and components of $\dot{\boldsymbol{x}}(t)$ of even order only. For the particular case of the motion onto the ith "linear" mode defined by Eq. (6.5) (we omit here the i and "lm" indices in what follows in order to simplify the writing), the following relations are found:

$$\boldsymbol{x}(t) = \boldsymbol{\Phi} \cos \omega t \quad \Rightarrow \quad \begin{cases} x_k(t) = \Phi_k \cos \omega t \\ \dot{x}_k(t) = -\omega \Phi_k \sin \omega t \end{cases} \quad \forall k = 1 \dots N. \tag{D.14}$$

Then, considering the trigonometric relations:

$$\sin^2 \theta = (1 - \cos 2\theta)/2, \quad \sin^4 \theta = (3 - 4\cos 2\theta + \cos 4\theta)/8, \tag{D.15}$$

$$\cos^2 \theta = (1 + \cos 2\theta)/2, \quad \cos^3 \theta = (3\cos \theta + \cos 3\theta)/4, \tag{D.16}$$

that contain only $\cos h\theta$ ($h \in \mathbb{N}^*$), the product of $\cos(\omega t)$, to any power, with $\sin(\omega t)$, to any even power, is found to produce only $\cos(h\omega t)$ terms in its Fourier expansion. Consequently, the conservative forces in Eq. (6.1) $\boldsymbol{M}(\boldsymbol{x})\ddot{x}$ and $\boldsymbol{f}_{\mathrm{c}}(\boldsymbol{x}, \dot{\boldsymbol{x}})$ produce only $\cos(h\omega t)$ and thus only in-phase harmonics, in the case of a given "linear" mode motion as written in Eq. (6.6).

D.3 Monophase motion and internal resonance

The monophase property of a given CNM clearly holds in the main parts of a given backbone curve, but it is worth investigating if this property is maintained in the presence of internal resonances. We first consider internal resonances which are observed far from the equilibrium point, if commensurable relationships appear between the nonlinear modal frequencies of several modes. These internal resonance often appear as "tongues" or branches that emanate from the backbone branch [124].

As an example, consider the two degree-of-freedom system considered in [124]:

$$\ddot{x}_1 + (2x_1 - x_2) + 0.5x_1^3 = 0, \quad \ddot{x}_2 + (2x_2 - x_1) = 0. \tag{D.17}$$

The first CNM of Eq. (D.17), of natural frequency $\omega_1 = 1$, is computed by numerical continuation of periodic solutions using the MANLAB software as explained in [97]. It allows for computation of the sine and cosine components of the variables, such as:

$$x(t) = \hat{x}_0 + \sum_{h=1}^{H} \left(\hat{x}_h^{\mathrm{c}} \cos \omega t + \hat{x}_h^{\mathrm{s}} \sin \omega t \right), \tag{D.18}$$

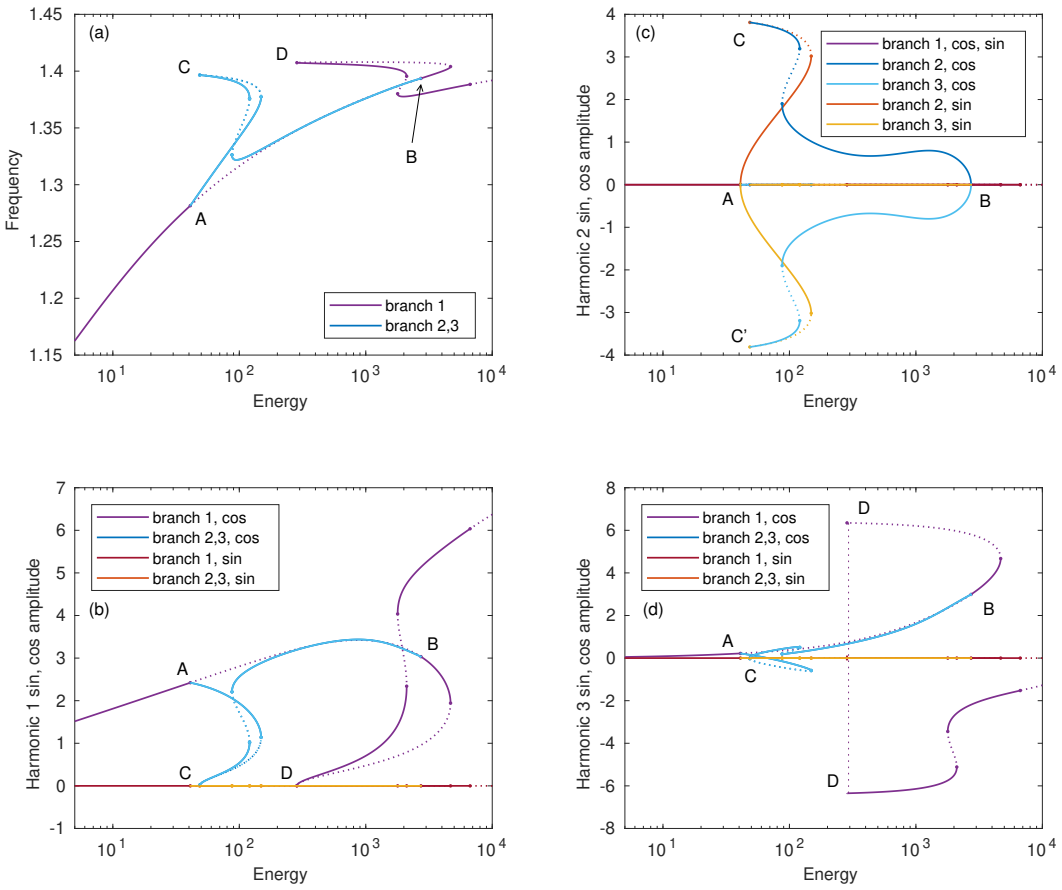

Figure D.1: Backbone curve of mode 1 of the two degrees-of-freedom system of Eq. (D.17). (a) Frequency-energy plot; (b,c,d) cosine and sine components of harmonic 1, 2, 3 of $x_1(t)$ as a function of the energy. A and B are two symmetry breaking pitchfork bifurcations, between the main branch with odd only harmonics (branch 1) and the two bifurcated branches of the 1:2 internal resonance (branch 2, 3) with even harmonics in addition. C and D are the connections between CNM 1 and CNM 2 (see [99]).

for a variable $x(t)$. In our simulations, the phase condition is prescribed as $\hat{x}_1^{\mathrm{s}} = 0$ (the sine component of the first harmonic of $x_1(t)$ is enforced to be zero). Figure D.1(a) shows the backbone curve of the first CNM in a frequency energy plot in the vicinity of the 1:2 and 1:3 internal resonances. Figs. D.1(b),(c) and (d) depict the sine and cosine of the first three harmonics of $x_1(t)$.

In Figs. D.1(b)-(d), it is first noted that the main backbone branch (called branch 1) is perfectly monophase since all sine components are zero on this branch. Analogous figures, not reported here for the sake of brevity, are obtained for $x_2(t)$. The periodic solution in branch 1 thus naturally verifies Eq. (6.4). Remarkably, this property still holds in the 1:3 internal resonance branches, which are also monophase.

The case of the 1:2 internal resonance tongue is slightly different. The corresponding branches are obtained after symmetry breaking (pitchfork) bifurcations of branch 1 (points A and B), leading to two bifurcated branches (branches 2 and 3) with additional even harmonics with respect to branch 1

(all even harmonics in branch 1 are zero since the nonlinearities in Eq. (D.17) are cubic only). In this case, the motion is monophase (it verifies Eq. 6.4) only in the right part of the branches, between points B and C. In the other part (between points A and C), the harmonic 2 sine component is nonzero with a zero cosine component, leading to a motion of the form:

$$\boldsymbol{x}_{1:2}(t) = \hat{\boldsymbol{x}}_0 + \hat{\boldsymbol{x}}_1 \cos\omega t + \hat{\boldsymbol{x}}_2 \sin 2\omega t + \hat{\boldsymbol{x}}_3 \cos 3\omega t + \hat{\boldsymbol{x}}_4 \sin 4\omega t + \dots, \tag{D.19}$$

which *is not* a monophase CNM since the even harmonics are in quadrature with respect to the odd ones.

Monophase and non-monophase CNMs with components in quadrature are also classical in the case of internal resonances that appear at low amplitude, if the commensurable relations are verified between the natural frequencies of the system. In the case of a 1:1 internal resonance between two modes of a system with cubic nonlinearities (their natural frequencies being written $\omega_1 \simeq \omega_2$), there are two possible coupled modes [87]. The former, called a "normal mode," is characterized by the two modal coordinates oscillating in phase or out of phase (see Eq. (16) of [87]); it is therefore a monophase CNM. In the latter, called an "elliptic mode," the two modal coordinates are in phase quadrature; it is therefore not a monophase CNM. Another example is found for the case of a system with quadratic nonlinearities and two modes in 1:2 internal resonance (their natural frequencies being written $\omega_2 \simeq 2\omega_1$) [213]. In this case, the coupled CNM, called "parabolic modes," are characterized by a phase quadrature, similar to Eq. (D.19) (see Eq. (21) of [213]).

D.4 Odd and even parts of the forces vectors with a monophase motion

Due to the parity of $f_{\mathrm{c}}(\boldsymbol{x},\dot{\boldsymbol{x}})$ and $f_{\mathrm{d}}(\boldsymbol{x},\dot{\boldsymbol{x}})$ as in Appendix D.2, their Taylor expansions are of the form:

$$[\boldsymbol{f}_{\mathrm{c}}(\boldsymbol{x},\dot{\boldsymbol{x}})]_i = \tilde{f}_i^{(0)}(\boldsymbol{x}) + \tilde{K}_{ijk}^{(2)}(\boldsymbol{x})\dot{x}_j\dot{x}_k + \dots, \tag{D.20}$$

$$[\boldsymbol{f}_{\mathrm{d}}(\boldsymbol{x},\dot{\boldsymbol{x}})]_i = C_{ij}^{(1)}(\boldsymbol{x})\dot{x}_j + C_{ijkl}^{(3)}(\boldsymbol{x})\dot{x}_j\dot{x}_k\dot{x}_l + \dots, \tag{D.21}$$

where $\tilde{f}_i^{(0)}(\boldsymbol{x})$, $\tilde{K}_{\bullet}^{(\bullet)}(\boldsymbol{x})$, $C_{\bullet}^{(\bullet)}(\boldsymbol{x})$ are the components of high order matrices corresponding to the coefficients of the Taylor expansions in $\dot{\boldsymbol{x}}$, all arbitrary smooth functions of $\boldsymbol{x}$. The tilde notation is used to distinguish the coefficients from those of Eq. (D.11).

We consider the particular monophase motion Eq. (6.4) of a CNM. As it contains only $\cos(h\omega t)$ components and because of the following trigonometric identity:

$$\cos(n\theta)\cos(m\theta) = (\cos[(m+n)\theta] + \cos[(m-n)\theta])/2, \quad \forall n,m \in \mathbb{N}, \tag{D.22}$$

the Fourier expansion of any product of any order $[\boldsymbol{x}_{\mathrm{cnm}}]_i[\boldsymbol{x}_{\mathrm{cnm}}]_j$, $[\boldsymbol{x}_{\mathrm{cnm}}]_i[\boldsymbol{x}_{\mathrm{cnm}}]_j[\boldsymbol{x}_{\mathrm{cnm}}]_k, \dots$ of the components of $\boldsymbol{x}_{\mathrm{cnm}}$ is monophase and contains only $\cos(h\omega t)$ components. This is also the case for the Fourier expansions of $\tilde{f}_i^{(0)}(\boldsymbol{x})$, $\tilde{K}_{\bullet}^{(\bullet)}(\boldsymbol{x})$, $C_{\bullet}^{(\bullet)}(\boldsymbol{x})$ since their Taylor expansions in $\boldsymbol{x}$ are of the form of Eq. (D.10).

In addition, $\dot{\boldsymbol{x}}_{\mathrm{cnm}}$ is monophase with only $(\sin h\omega t)$ components:

$$\dot{\boldsymbol{x}}_{\mathrm{cnm}}(t) = -\sum_{h=1}^{H} h\omega\hat{\boldsymbol{x}}_h \sin(h\omega t). \tag{D.23}$$

The Fourier expansion of *even order products* of the components of $\dot{\boldsymbol{x}}_{\text{cnm}}$ contain only $\cos(h\omega t)$ components, whereas *odd order products* of the components of $\dot{\boldsymbol{x}}_{\text{cnm}}$ contain only $\sin(h\omega t)$ components, due the following trigonometric identity, $\forall n, m \in \mathbb{N}$:

$$\sin(n\theta)\sin(m\theta) = (\cos[(m-n)\theta] - \cos[(m+n)\theta])/2, \tag{D.24}$$

$$\sin(n\theta)\cos(m\theta) = (\sin[(m+n)\theta] - \sin[(m-n)\theta])/2. \tag{D.25}$$

As a consequence, the Fourier expansion of the *conservative* force vector is monophase and contains only $\cos(h\omega t)$ components, while the Fourier expansion of the *dissipative* force vector (also monophase) contains only $\sin h\omega t$ components:

$$\boldsymbol{f}_{\text{c}}(\boldsymbol{x}, \dot{\boldsymbol{x}}) = \hat{\boldsymbol{f}}_{\text{c}0} + \sum_{h=1}^{H} \hat{\boldsymbol{f}}_{\text{c}h} \cos(h\omega t), \quad \boldsymbol{f}_{\text{d}}(\boldsymbol{x}, \dot{\boldsymbol{x}}) = \sum_{h=1}^{H} \hat{\boldsymbol{f}}_{\text{d}h} \sin(h\omega t). \tag{D.26}$$

D.5 Odd and even parts of the motion for a geometrically nonlinear straight beam

As in Appendix D.1.2, we consider the free conservative vibration of a straight beam based on a geometrically exact model with Euler-Bernoulli kinematics (Timoshenko kinematics, not investigated here for the sake of brevity, would lead to exactly the same results with the same reasoning). The equations of motion are (D.3), with $\mu = 0$ to cancel the damping and, from [229]:

$$N = EA\left[(1+u')\cos\theta + w'\sin\theta - 1\right], \quad M = EI\theta'. \tag{D.27}$$

The equations of motion can be rewritten as $\ddot{u} = f_u(u, w, \theta)$ and $\ddot{w} = f_w(u, w, \theta)$, with $\sin\theta = w'$ and $\cos\theta = 1 + u'$ because of the Euler-Bernoulli kinematics. Observing the definition of f_u and f_w with Eqs. (D.3) and (D.27), it is clear that $f_u(u, -w, -\theta) = f_u(u, w, \theta)$ is even in (w, θ) and $f_w(u, -w, -\theta) = -f_u(u, w, \theta)$ is odd in (w, θ). With the reasoning of Appendix D.2, these parity properties lead to the following Taylor expansions:

$$f_u(u,w,\theta) = f_u^{(0)}(u) + k_{uww}^{(2)}(u)w^2 + k_{uw\theta}^{(2)}(u)w\theta + k_{u\theta\theta}^{(2)}(u)\theta^2 + k_{uw\theta}^{(2)}(u)w\theta + k_{uwwww}^{(4)}(u)w^4 + \ldots, \tag{D.28}$$

$$f_w(u,w,\theta) = k_{ww}^{(1)}(u)w + k_{w\theta}^{(1)}(u)\theta + k_{wwww}^{(3)}(u)w^3 + k_{www\theta}^{(3)}(u)w^2\theta + \ldots, \tag{D.29}$$

where $f_u^{(0)}(u)$, $k_{u\bullet}^{(\bullet)}$, $k_{w\bullet}^{(\bullet)}$ are the coefficients of the Taylor expansions. Consequently, $f_u(u, w, \theta)$ is quadratic in (w, θ) whereas $f_w(u, w, \theta)$ is cubic in (w, θ).

Finally, we consider the case of the motion onto a particular bending mode of the beam:

$$\begin{bmatrix} u(x,t) \\ w(x,t) \\ \theta(x,t) \end{bmatrix} = \begin{bmatrix} 0 \\ \Phi_w(x) \\ \Phi_\theta(x) \end{bmatrix} \cos(\omega t), \tag{D.30}$$

in which there is no axial motion because the beam is straight. Introducing these equations into the Taylor expansions Eqs. (D.28) and (D.29)), it is shown using Eq. (D.16) that f_u is monophase (in the form of Eq. (6.4)) with even harmonics only, whereas f_u (also monophase) has only odd harmonics. By

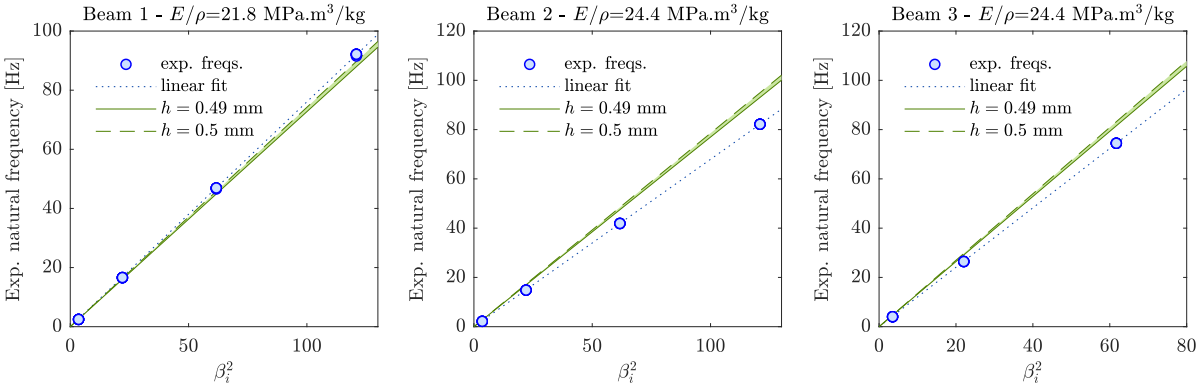

Figure D.2: Experimental natural frequencies of the three beams as a function of the theoretical frequency parameters β_i^2 of a cantilever beam. Comparisons with theoretical values with E/ρ of Tab. 6.1 and $h \in \{0.49\ 0.5\}$ mm.

consequence, an acceptable form for the axial, transverse and rotation fields of the CNM of a straight beam are:

$$u(x,t) = \hat{u}_0(x) + \hat{u}_2(x)\cos 2\omega t + \hat{u}_4(x)\cos 4\omega t + \ldots, \tag{D.31}$$
$$w(x,t) = \hat{w}_1(x)\cos\omega t + \hat{w}_3(x)\cos 3\omega t + \ldots, \qquad \theta(x,t) = \hat{\theta}_1(x)\cos\omega t + \hat{\theta}_3(x)\cos 3\omega t + \ldots.$$

This property is a direct consequence of the straight geometry of the beam and would be violated with a non-zero curvature.

D.6 Material parameters estimation

To estimate the value of the material parameters (Young's modulus E and density ρ), tensile tests are performed on two 300×13 rulers: one from the VMADE brand (the material of beam 1) and one from the FACOM brand (the material of beams 2 and 3). The traction machine enables measurement of different values of the traction force F and the resulting strain ε. With a linear fit, the value of the slope coefficient $\gamma_{F\varepsilon} = F/\varepsilon$ is estimated. The mass m of each ruler is measured with a precision scale along with the area A_{top} of its top surface and its width b. Then, the ratio E/ρ, which notably does not depend on the thickness h of the rulers (itself a source of uncertainty), is estimated as:

$$E = \frac{\gamma_{F\varepsilon}}{bh}, \quad \rho = \frac{m}{hA_{\text{top}}} \quad \Rightarrow \quad \frac{E}{\rho} = \frac{\gamma_{F\varepsilon}A_{\text{top}}}{bm}. \tag{D.32}$$

The corresponding values of E/ρ are indicated in Tab. 6.1.

Appendix E

Résumé de la thèse en français

Afin d'apporter plus de visibilité à la communauté française, certaines sections et des résultats clés du mémoire de thèse ont été résumés et traduits ci-dessous. Le résumé ci-dessous fait référence aux chapitres en anglais ; cependant l'objectif principal de cette annexe est de présenter *les parties les plus importantes* aux lectures francophones, en particulier l'état de l'art autour du travail de thèse et le modèle impliqué.

Table de matières

E.1 Introduction

Le travail de cette thèse concerne la modélisation, l'analyse et la maîtrise générale de la dynamique des structures élancées unidimensionnelles (1D) de type poutre dont les exemples incluent les fils et les câbles, les tuyaux, les cordes, les ficelles, les réglets flexibles et même dans certains cas les ailes et les pales (quelques exemples sont montrés dans les Figs. 1.1 et 1.2). Ces structures représentent des exemples de poutre mécanique, considérée comme l'une des structures fondamentales de la mécanique des solides et des structures et dont l'utilisation est très répandue dans l'aérospatiale, le génie civil, le génie biomédical, l'ingénierie électrique et la robotique. Cette thèse est réalisée dans le cadre du projet européen THREAD (THREAD-ETN) portant sur la modélisation numérique de structures hautement flexibles et financé par le programme de recherche et d'innovation Horizon 2020 de l'Union européenne (subvention Marie Skłodowska-Curie n° 860124). L'objectif du projet THREAD-ETN est de rassembler une nouvelle génération d'ingénieurs-chercheurs et de mathématiciens afin de développer des modèles et des méthodes numériques appropriés pour la conception de structures élancées hautement flexibles capables de répondre aux enjeux de l'industrie moderne. Dans ce cadre, les travaux de cette thèse en particulier se concentrent sur le développement de modèles efficaces, entièrement numériques, capables de capturer la dynamique non linéaire de ces structures flexibles 1D jusqu'à n'importe quelle amplitude de vibration, permettant ainsi une meilleure compréhension de leur comportement hautement non linéaire. Les travaux de la thèse ont été réalisés au Laboratoire d'Ingénierie des Systèmes Physiques et Numériques (LISPEN) situé sur le campus de Lille de l'École nationale supérieure d'Arts et Métiers.

Quelques sections clées du chapitre 1 sont traduites ci-dessous.

E.1.1 Contexte

Dans le contexte du projet THREAD, les travaux de cette thèse ont été inspirés par le manque perçu dans la littérature de stratégies numériques (en particulier de stratégies numériques *efficaces*) pour modéliser et caractériser la dynamique des structures de poutres 1D flexibles. Ces structures sont capables d'atteindre de très grandes amplitudes de déplacement ou de rotation en vibration avec seulement des excitations faibles à modérées en raison de leur géométrie unique. La géométrie de ces structures prend la forme d'une poutre (déformable) dont une dimension, dans ce cas la longueur de la poutre, est extrêmement grande par rapport à ses autres dimensions (d'où "unidimensionnelle"), de sorte que les dimensions de la section sont petites et la poutre peut être caractérisée comme "mince". En raison de cette géométrie particulière, la raideur en flexion *i.e.* dans les directions transverses (perpendiculaires à la direction longitudinale) est faible, alors que la raideur dans la direction axiale est quant à elle très élevée. Le résultat est une capacité de déplacement inhabituellement grande en flexion dans les directions transverses (d'où "flexible").

Ces caractéristiques rendent les structures de poutres flexibles à la fois intéressantes et uniques dans le domaine de la mécanique des solides et des structures, mais aussi très difficiles à modéliser physiquement. Le comportement ne peut pas être représenté correctement par des modèles de poutres linéaires ; des modèles non linéaires prenant en compte les non linéarités géométriques présentes dans de tels systèmes (abordés dans la section 1.3.2) sont donc nécessaires, ainsi que des stratégies numériques appropriées pour résoudre les équations dynamiques non linéaires.

E.1.2 Motivation et état de l'art

Si la modélisation et le prototypage constituent des étapes indispensables de la conception mécanique, la modélisation et le prototypage numériques ne sont devenus répandus qu'au cours des dernières décennies, à mesure que la technologie a évolué. En particulier, l'industrie en général s'appuie de plus en plus sur le prototypage virtuel, car le coût associé à la réalisation d'expériences ou à des modifications de conception peut augmenter considérablement lors du passage d'un environnement virtuel à un environnement physique. Les exemples de structures minces en forme de poutre 1D de la section 1.1 se retrouvent partout dans les systèmes d'ingénierie modernes : un système avec n'importe quel composant électrique incorpore naturellement des fils pour transporter le courant électrique ; tout système impliquant un ventilateur ou une turbine implique la présence de pales souvent élancées ; les personnes et les objets sont transportés à l'aide de systèmes suspendus ou incorporant des cordes et des câbles ; les applications industrielles de ces types de structures semblent infinies. De plus, ces composants sont souvent regroupés ou intégrés dans des systèmes d'ingénierie complexes, augmentant le coût de calcul associé, parfois jusqu'à un niveau prohibitif, d'une simulation numérique tout à fait exacte du système dans son ensemble. Pour ces raisons, le développement de modèles numériques efficaces et précis de structures de poutres flexibles représente un sujet de recherche actif.

Les exemples industriels spécifiques sont nombreux, tant en statique qu'en dynamique, couvrant de nombreuses disciplines d'ingénierie. Des exemples d'applications civiles incluent la dynamique des câbles et des systèmes de téléphériques ou des systèmes de mouflage [65], [172]. Les pales tournantes des éoliennes peuvent également être modélisées sous forme de structures de poutres minces dont la vitesse de rotation change en fonction de la vitesse du vent et, dans le cas des éoliennes offshore, des modèles appropriés pour les lignes d'amarrage et les câbles électriques sont nécessaires afin de optimiser la performance offshore [51], [52], [181]. Les structures de poutres minces sont également utilisées dans des applications biomédicales telles que des équipements médicaux flexibles comme les endoscopes [222] ou le super-enroulement de brins d'ADN [90], [218], [256], dans l'ingénierie bio-inspirée pour les applications en robotique souple [77], [259] ou des nanodrones ressemblant à des insectes [42], [72], [73], et dans la modélisation de tissus et de cheveux humains [26], [63], entre autres.

Outre ces applications (et bien d'autres encore peuvent être citées), les structures de poutres flexibles trouvent leur place dans les domaines de l'automobile, de l'aérospatiale et de l'électronique, et des études approfondies ont été financées à cet égard. Dans l'industrie automobile, une modélisation efficace des câbles et des systèmes de câbles est d'une grande importance pour trouver la disposition optimale du câblage dans les véhicules [45] et, de plus, leur importance ne fera que croître dans la transition mondiale vers les véhicules électriques. L'optimisation du placement et de la manipulation lors de la fabrication est également importante afin de maximiser la durée de vie des câbles, car une torsion excessive ou cyclique d'un câble peut entraîner une fatigue et une défaillance précoce [209]. Un autre sujet de recherche lié à l'optimisation du câblage dans les véhicules est la modélisation appropriée des lois de comportement des câbles composites (rappelons que les câbles électriques sont constitués d'un fil conducteur, souvent en cuivre, enveloppé afin de le protéger dans une coque en

élastomère ; la section est donc non homogène ni isotrope) [151]. Le câblage est également largement utilisé dans le secteur aérospatial, de sorte que les thèmes de recherche susmentionnés s'appliquent toujours, mais d'autres applications aérospatiales de structures flexibles peuvent être citées. Les pales tournantes, telles que les aubes de turbomoteur ou les pales d'hélicoptère, peuvent être modélisées sous forme de structures de poutres minces [13], [155], [183], [229]. L'antenne satellite et les ailes d'avions flexibles et de satellites [3], [182], [223] constituent tous des exemples dans lesquels la modélisation non linéaire de structures de poutres minces est essentielle à la conception et à la fonctionnalité du système. À plus petite échelle, des structures de poutres élancées peuvent également être trouvées dans de nombreuses applications électromécaniques. Elles sont largement utilisées dans les systèmes nano et microélectromécaniques (respectivement NEMS et MEMS) [61], [85], [137]. Quelques exemples de structures de poutres minces dans les NEMS et les MEMS récemment apparus dans la littérature incluent les nanotubes et les nanofils [244] et les microcantilevers [148], [149] pour diverses applications. De plus, les systèmes électromécaniques couplant des structures de poutres élancées avec des éléments piézoélectriques sont largement étudiés pour des applications en récupération d'énergie [61], [67], [85], [99], [139], [257].

Au-delà des applications strictement industrielles, il est également intéressant pour les chercheurs d'étudier le comportement des structures de poutres élancées puisqu'elles représentent une structure mécanique hautement non linéaire qui manifeste certains phénomènes caractéristiques de la dynamique non linéaire. L'étude et l'analyse générales de ces phénomènes non linéaires peuvent permettre une meilleure compréhension de ceux-ci et une éventuelle exploitation industrielle au-delà de l'état actuel de la technologie. Certains de ces phénomènes non linéaires incluent la dépendance de la fréquence d'oscillation sur l'amplitude ou l'énergie du système, les interactions entre modes non linéaires via des transferts d'énergie (résonances internes), les bifurcations, les changements de stabilité et l'existence de solutions multiples, les sauts, les discontinuités et le chaos éventuel. Beaucoup de ces phénomènes sont discutés dans les références classiques sur les vibrations non linéaires, comme *Nonlinear Oscillations* de Nayfeh et Mook [162] ou Thomsen [231] et le lecteur est renvoyé aux travaux récents de [22] pour une analyse de la stabilité compatible avec les grands systèmes contenant de nombreux degrés de liberté (tels que les grands systèmes d'éléments finis). Certains de ces phénomènes non linéaires sont rencontrés dans les travaux de cette thèse et sont examinés plus en détail dans la section 2. Enfin, l'étude des structures de poutres minces est utile dans le développement de modèles d'ordre réduit non linéaires. Dans les situations où la solution est complexe ou coûteuse en termes de calcul, où les solutions de référence doivent être calculées avec un logiciel d'éléments finis (EF), les modèles d'ordre réduit non linéaires sont particulièrement intéressants. Une revue complète des techniques de réduction d'ordre de modèle pour les structures géométriquement non linéaires se trouve dans [236], et quelques détails sur les modèles d'ordre réduit non linéaires et en particulier le mode non linéaire sont présentés dans la section 2.4.2.

Pour modéliser la dynamique non linéaire des structures de poutres élancées, des approximations analytiques peuvent être trouvées dans la littérature (*e.g.* le modèle Crespo da Silva de la section 2.1.4), mais leur utilité est souvent limitée à des rotations modérées. Des modèles entièrement numériques, particulièrement efficaces, capables de modéliser la dynamique non linéaire des structures de poutres minces 1D jusqu'à n'importe quelle amplitude de rotation sont nécessaires, car de nombreuses méthodes jusqu'à présent entraînent un coût de calcul important. Ce manque dans la littérature, couplé à la pléthore d'applications citées, constitue la motivation pour cette thèse.

État de l'art La littérature concernant la mécanique des structures de poutres représente un énorme volume de stratégies de modélisation et de résolution qui dépasse de loin le cadre de cette thèse. Même en se focalisant sur des structures de poutres en grande rotation, la littérature reste vaste. De nombreux modèles différents ont été proposés dans la littérature et en particulier différentes approches pour dériver les équations du mouvement. Les différences résident souvent dans la définition de la loi de comportement reliant la mesure de déformation aux contraintes. On préfère donc de regrouper ici quelques-unes des approches les plus courantes qui contribuent à positionner les travaux de cette thèse dans la littérature.

Dans un premier groupe sont regroupés des modèles géométriquement non linéaires dans lesquels la loi de comportement est imposée afin de relier les mesures de contrainte et de déformation. Parmi eux figurent les modèles basés sur la célèbre théorie des frères Cosserat [43] et le modèle inextensible dite "elastica" développé pour la première fois par Crespo da Silva et Glynn [46], [47]. Dans le modèle de Cosserat, en supposant qu'une direction (appelée ici axiale ou longitudinale) est beaucoup plus grande que les deux autres, la cinématique de la poutre s'écrit en fonction du déplacement de l'axe de la poutre et du mouvement des sections le long de la ligne moyenne, mouvement qui est écrit à travers un repère local appelé "directeurs" (voir Fig. 2.3)). La loi de comportement est imposée, dans certains cas ayant été déterminée expérimentalement [151], [156], afin de trouver les efforts et les moments (voir *e.g.* [132]). Le modèle de Cosserat capture les effets d'extension et de cisaillement comme une généralisation des poutres de Timoshenko, une extension du modèle de Kirchhoff, qui quant à lui capture uniquement les effets de flexion et de torsion (et éventuellement d'extension s'il s'agit du modèle *extensible* ou *inextensible* de Kirchhoff [131], [254]). Un autre modèle, initialement développé par Crespo da Silva et Glynn pour les oscillations non linéaires non planaires de poutres jusqu'à des rotations modérées [46], [47], utilise la même mesure de déformation que celle utilisée dans la théorie de Cosserat et la loi de comportement est encore une fois imposée. Dans [46], [47], l'objectif était de développer des équations du mouvement adaptées à une méthode de perturbation et ce modèle a été largement utilisé dans la littérature pour l'analyse non linéaire de la dynamique des poutres jusqu'à des rotations modérées [24], [42], [53], [54], [229].

Dans un autre groupe, des modèles géométriquement non linéaires sont rassemblés et formulés de manière naturelle selon la mécanique des milieux continus 3D, basés soit sur la cinématique d'Euler-Bernoulli, soit sur la cinématique de Timoshenko. Ici, la cinématique de la section et les équations de la mécanique des milieux continus non linéaires 3D guident la dérivation du modèle, de telle sorte que la mesure de contrainte est déterminée a priori en fonction du choix de la mesure de déformation (c'est-à-dire celle qui lui est énergétiquement conjuguée). La formulation proposée pour cette thèse suit cette logique. Dans notre cas, la formulation est basée sur une linéarisation cohérente du tenseur de déformation de Green-Lagrange, énergétiquement conjugué au deuxième tenseur de contrainte de Piola-Kirchhoff et une loi de comportement élastique linéaire. D'autres travaux utilisent les contraintes et déformations de Biot, qui sous certaines conditions (comme dans le cas de la cinématique d'Euler-Bernoulli [229] ou de la cinématique de Timoshenko avec l'hypothèse de petites déformations [107], [229]) sont équivalentes à la linéarisation cohérente des déformations de Green-Lagrange. L'article d'Irschik et Gerstmayr [114] aborde ces sujets d'une manière accessible.

Bien qu'il puisse être difficile de trier les différentes approches des modèles de grande rotation, les équations finales de chaque approche prennent la même forme. Des différences dans les approches peuvent de nouveau naître en foncton de la manière dont les équations sont résolues ou des simplifications postulées. En particulier, un modèle appelé *géométriquement exact*, ou parfois appelé modèle de poutre *Reissner-Simo* basé sur la formulation originale de Reissner [191], [192] et étendu à la 3D

par Simo et Vu -Quoc [219], [220], est mis en évidence ici. Dans le cadre des modèles géométriquement exacts, les modèles appelés *Reissner-Simo* dans la littérature incluent généralement les effets de cisaillement (basés sur une cinématique de Timoshenko), alors que les modèles connus sous le nom de *Kirchhoff-Love* ne l'incluent généralement pas (basés sur une cinématique d'Euler-Bernoulli) [131], [156], [242]. En général, dans le modèle géométriquement exact, aucune simplification n'est apportée aux non linéarités géométriques du système, de sorte que le comportement reste exact quelle que soit l'amplitude de rotation des sections de la poutre. Le modèle géométriquement exact est au cœur de nombreux travaux récents (*e.g.* [68], [69], [253] ou voir [135], [156]) concernant la dynamique des structures de poutres flexibles, et représente l'approche adoptée dans cette thèse. Puisque les rotations dans le modèle géométriquement exact sont arbitrairement grandes, un autre sujet de recherche concerne la paramétrisation des termes de rotation (c'est-à-dire comment les rotations sont représentées dans les équations du mouvement) [14], [135]. Les différentes approches peuvent être complexes ; certaines de ces approches incluent une paramétrisation via des vecteurs de rotation, des angles d'Euler, des paramètres de Rodrigues (voir *e.g.* [101]), des quaternions unitaires [35], [45], [83], [100], [101], [132], [197], [261], [263] et des groupes de Lie [30], [33], [200], [221], mais la recherche à cet égard est en cours.

Enfin, une stratégie de résolution des équations non linéaires du mouvement doit être définie. En général, les équations non linéaires pour les structures très flexibles ne peuvent pas être résolues avec une méthode analytique simple. Des stratégies numériques doivent impérativement être proposées et les approches dans la littérature peuvent encore une fois varier. Pour réaliser une discrétisation spatiale du modèle, les méthodes d'éléments finis sont courants [21], [27], [48]–[50], [66], [79]–[81], [116], [156], [198], [210], [211], ou autres techniques telles que les différences finies [131], [132] ou les techniques de Galerkin [69], [71] se trouvent dans la littérature. Des logiciels éléments finis commerciaux peuvent également être utilisés, mais pour les systèmes complexes, le coût de calcul est parfois prohibitif et des stratégies plus efficaces sont souhaitées. Différentes strategies de résolution numérique des équations discrétisées sont possibles lorsque l'on considère la résolution de systèmes dynamiques dépendants du temps (contrairement aux simulations statiques, où les équations indépendantes du temps peuvent être résolues *e.g.* avec des méthodes de continuation [45]). Les méthodes d'intégration temporelle sont souvent utilisées [30], [131], [142], [199], [200], [221], [262], mais les stratégies dans le domaine fréquentiel pour résoudre des systèmes périodiques peuvent également être avantageuses. Les stratégies dans le domaine fréquentiel ciblent directement le régime permanent de la solution périodique et peuvent donc représenter une stratégie efficace pour modéliser la dynamique non linéaire des systèmes vibrants. Certains travaux impliquant des simulations dans le domaine fréquentiel de poutres hautement flexibles ont été publiés récemment, mais ceux-ci se limitent à la dynamique des poutres encastrées-libres hautement flexibles [69]–[71], [82].

Les différentes stratégies de résolution numérique trouvées dans la littérature ont chacune leurs avantages et leurs inconvénients et le choix se fait généralement à la lumière de certaines propriétés numériques. Par exemple, en fonction de l'application éventuelle du modèle, certains "choix" numériques peuvent être faits, comme, entre autres :

- le choix des interpolations dans une méthode d'éléments finis, telles que les interpolations préservant l'objectivité [50], [83], [104], [116], [142], [199] ou les interpolations polynomiales plus simples [45], [229] (ce sujet est abordé dans la section 2.3.2),
- le choix d'un algorithme d'intégration temporelle numérique qui conserve l'énergie [50], [142], [264],

- le choix d'une méthode de résolution dans le domaine fréquentiel pour calculer des solutions périodiques [41], [97], [121].

Certaines des techniques de résolution les plus courantes sont présentées dans la section 2.2.

La nouveauté de cette thèse se trouve principalement dans la résolution des équations du mouvement géométriquement exactes discrétisées en éléments finis *entièrement dans le domaine fréquentiel*. Dans ce cas, on s'intéresse principalement aux vibrations périodiques en grande amplitude des structures de poutres élancées hautement flexibles. La stratégie en fréquentiel est automatisée par le solveur MANLAB [96] (abordé en plus de détail dans la section 2.2.4), un solveur qui est basé sur la méthode d'équilibrage harmonique (HBM) et résolu à l'aide d'une méthode de continuation de solutions périodiques appelée la méthode asymptotique numérique (MAN) [37], [38], [41], [55], [121]. La procédure de résolution implémentée dans MANLAB est efficace, peut être appliquée à une grande variété de systèmes non linéaires et permet une analyse de bifurcation et de stabilité lors de la continuation [22], [97].

En conjonction avec les simulations numériques, l'analyse expérimentale retrouve également une grande importance dans l'étude des systèmes mécaniques et en particulier des structures de poutres hautement flexibles. Les phénomènes non linéaires uniques manifestés par ces structures dans des simulations numériques peuvent être recréés et validés avec des expériences dédiées. De nombreux travaux dans la littérature ont étudié expérimentalement la dynamique des structures de poutres flexibles, dont certains incluent [11], [12], [53], [54], [70], [71], [150], [205], [226], [246]. Bien que des travaux récents aient permis de faire correspondre la dynamique expérimentale des poutres encastrées-libres en grande amplitude aux simulations numériques [70], [71], des travaux supplémentaires sont néanmoins nécessaires pour mieux comprendre le comportement non linéaire des structures flexibles. En particulier, on cherche à développer un protocole expérimental qui soit à la fois en accord avec les simulations numériques et puisse également être étendu à de nombreux systèmes flexibles. Une revue plus approfondie de la littérature est discutée dans le chapitre 6 en lien avec les concepts impliqués dans nos expériences.

E.1.3 Non linéarités géométriques en mécanique des solides

Les non linéarités géométriques regroupent les types de non linéarités considérées quand le mouvement d'un système mécanique est de grande amplitude, et représentent les principales non linéarités rencontrées dans ce travail.

Rappelons (voir la section 1.1) que la particularité des structures de poutres 1D flexibles est leur extrême capacité de déformation en flexion. Dans de tels systèmes, les non linéarités qui apparaissent sont naturellement géométriques, liées à la grande amplitude de déplacement de la transformation. Deux principaux types de mécanismes non linéaires sont généralement abordés dans l'étude des structures 1D flexibles, celui lié (i) à un couplage de *membrane-flexion*, ou (ii) aux *très grandes rotations des sections* de la poutre en raison de son déplacement important (Fig. E.1).

E.1.4 Résume de la thèse

Pour mieux aider la compréhension du lecteur, une présentation du travail qui a été réalisé est ensuite détaillée. Le travail de cette thèse est divisé en plusieurs chapitres suivant un ordre chronologique, de sorte que le travail des chapitres ultérieurs s'appuie naturellement sur le travail des chapitres précédents. Le chapitre 2 vise à décrire les outils et sujets de base nécessaires à la compréhension

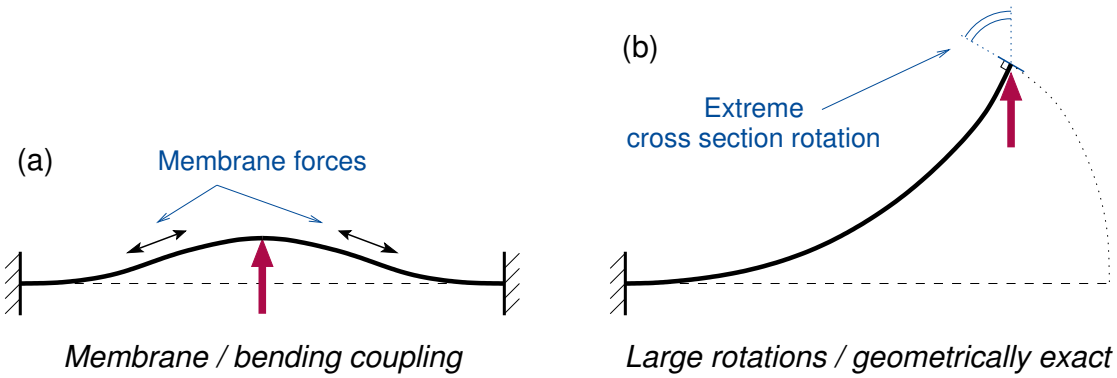

Figure E.1: Non linéarités géométriques rencontrées dans les structures de poutres flexibles, (a) couplage membrane-flexion (modèles de type von Kármán), (b) grandes rotations (modèles géométriquement exacts).

du travail de thèse ; les équations générales liées à la modélisation et à la résolution de la dynamique des poutres non linéaires sont développées et un aperçu de plusieurs modèles de poutres couramment trouvés dans la littérature est fourni ainsi que leurs hypothèses, simplifications, avantages et limites. Les idées, modèles et méthodes de résolution décrits dans le chapitre 2 apparaissent à plusieurs reprises dans les chapitres ultérieurs de cette thèse. Au-delà de cela, les chapitres 3 - 6 détaillent le parcours scientifique entrepris au cours de la thèse :

- Le chapitre 3 décrit le développement et la mise en œuvre du modèle éléments finis de poutre géométriquement exact pour la modélisation numérique de structures de poutres en grande amplitude. Dans ce chapitre, le modèle est limité aux mouvements dans le plan (2D). Les spécificités du modèle, de la discrétisation et de la procédure de résolution sont décrites et évaluées à l'aide de plusieurs cas tests.
- Le chapitre 4 représente une application du modèle 2D présenté au chapitre 3 afin d'étudier l'effet de la gravité et de l'élancement sur la dynamique de grande amplitude des poutres encastrées-libres flexibles. Le comportement non linéaire des poutres encastrées-libres est étudié avec un accent particulier sur l'utilisation des résultats pour mieux définir les expériences du chapitre 6.
- Le chapitre 5 étend le modèle 2D du chapitre 3 en trois dimensions (3D). Une méthode alternative pour la paramétrisation des termes de rotation basée sur les quaternions unitaires est présentée et testée sur des cas tests simples. De plus, la formulation 2D avec quaternions est dérivée afin de la comparer à la méthode du chapitre 3.
- Le chapitre 6 discute de la validation expérimentale du modèle numérique. Le modèle numérique d'une poutre encastrée-libre en grande amplitude vibrant sur ses trois premiers modes non linéaires est comparé à des expériences avec un réglet flexible excité avec une table vibrante. Les expériences utilisent une technique de contrôle vibratoire afin de mesurer expérimentalement les modes non linéaires.

Enfin, une synthèse des principaux résultats et des remarques finales sont présentées en conclusion ainsi que des perspectives qui s'appuient sur les travaux entrepris au cours de cette thèse.

E.2 Modélisation de structures de poutres hautement flexibles : modélisation et résolution des non linéarités géométriques

Le chapitre 1 a centré notre étude sur l'analyse dynamique non linéaire des structures de poutres élancées flexibles. Dans ce qui suit, les non linéarités rencontrées dans les structures de poutres flexibles étudiées à travers cette thèse sont les non linéarités géométriques décrites dans la section 1.3.2. D'autres types de non linéarités peuvent bien entendu être envisagés et le sont souvent dans de nombreuses applications industrielles (voir la section 1.3.1) ; ici, cependant, l'étude se limite aux matériaux élastiques isotropes où la loi de comportement est linéaire et ne prend pas en compte le contact. Ainsi, on se focalise uniquement sur les non linéarités géométriques. Des exemples des types de structures de poutres considérées dans ce travail sont présentés dans la Fig. 2.1.

L'objectif de ce chapitre est de présenter les stratégies de modélisation et de résolution les plus importantes rencontrées dans cette thèse pour la simulation de structures de poutres élancées hautement flexibles. Les thèmes de ce chapitre représentent les principaux outils pour comprendre les travaux de cette thèse.

Dans la section 1.1, la structure de poutre élancée est définie comme une poutre déformable où une dimension de sa géométrie (généralement la longueur de la poutre) est extrêmement grande par rapport aux deux autres dimensions, permettant ainsi des déplacements extrêmes. Le modèle de poutre géométriquement exact est dans ce cas le modèle le plus adapté car il n'y a pas de simplification des termes de rotation, ce qui signifie qu'il représente correctement le comportement de la poutre à n'importe quelle amplitude de déplacement. Dans la section 1.2.1, il est indiqué qu'il existe plusieurs façons de dériver les équations de poutre géométriquement exactes. Dans ce chapitre, on montrera à partir de la section 2.1 comment les équations de poutre géométriquement exactes peuvent être dérivées grâce à une réduction systématique en 1D des équations 3D de la mécanique des milieux continus non linéaire. Les distinctions cinématiques et certains modèles de "cas particuliers" dérivés de simplifications apportées au modèle géométriquement exact sont également présentés dans la section 2.1. Ensuite, les méthodes courantes utilisées pour résoudre les équations différentielles non linéaires sont discutées dans la section 2.2, et un aperçu de la procédure de résolution utilisée dans cette thèse est présenté. Certaines considérations concernant l'implémentation numérique du modèle géométriquement exact sont abordées dans la section 2.3. Les types de solutions recherchées dans les travaux de cette thèse sont décrits dans la section 2.4, y compris les principaux concepts liés aux modes non linéaires qui sont importants pour la compréhension des chapitres ultérieurs de la thèse. Enfin, une synthèse des principaux points de ce chapitre à rappeler pour la suite est fournie dans la section 2.5.

Quelques sections clées du chapitre 2 sont traduites ci-dessous.

E.2.1 Modélisation de structures de poutres : généralités et le modèle géométriquement exact

On cherche ici à poser les bases de la modélisation de structures de poutres minces très flexibles. La procédure générale pour dériver systématiquement le modèle de poutre 1D géométriquement exact à partir des équations 3D de la mécanique des milieux continus non linéaire est décrite.

Afin de dériver les équations dynamiques non linéaires du mouvement de la structure de poutre déformable, une approche basée sur la mécanique des mileux continus est adoptée, dérivant les équations de poutre après particularisation des équations pour un milieu non linéaire subissant de grands

déplacements. Cela contraste avec la méthode plutôt simple d'écrire les équations du mouvement pour un système composé d'une collection d'éléments discrets (pendules, systèmes masse-ressort, *etc.*), directement à partir *e.g.* des équations d'Euler-Lagrange.

Les hypothèses globales, compatibles à la fois avec la cinématique d'Euler-Bernoulli et celle de Timoshenko, peuvent se résumer ainsi :

Hypothèse n°1

> Les sections subissent un mouvement de corps rigide avec le déplacement $\mathbf{u}$ défini par l'Eq. (E.6).

Hypothèse n°2

> Les contraintes dans les directions perpendiculaires à la direction longitudinale (c'est-à-dire les deux directions transverses $\mathbf{u}_y$ et $\mathbf{u}_z$) sont négligées, étant considérées comme petites devant la direction principale $\mathbf{u}_x$, de sorte que :
>
> $$S_{yy} = S_{zz} = 0. \tag{E.1}$$

Hypothèse n°3

> Bien que les sections du milieu 1D soient soumises à des rotations d'une amplitude donnée, les déformations locales du milieu 1D restent faibles tout au long du mouvement.

Hypothèse n°4

> La poutre est homogène et constituée d'un matériau élastique et isotrope, de sorte qu'une loi de comportement linéaire est valable.

Équations du mouvement basées sur une formulation lagrangienne à partir de la mécanique des mileux continus 3D On cherche à dériver les équations dynamiques du mouvement sous la forme faible en utilisant le principe des travaux virtuels, qui s'écrit pour tout temps t et pour tous déplacements virtuels $\delta\mathbf{u}$:

$$\delta W_e - \delta W_i - \delta W_a = 0, \tag{E.2}$$

avec δW_i, δW_a et δW_e le travail virtuel des forces internes, inertielles et externes, respectivement, écrits :

$$\delta W_i = \int_V \mathbf{S} \colon \delta\mathbf{E} \, \mathrm{d}V, \tag{E.3a}$$

$$\delta W_a = \int_V \rho\ddot{\mathbf{u}} \cdot \delta\mathbf{u} \, \mathrm{d}V, \tag{E.3b}$$

$$\delta W_e = \int_V \mathbf{f}_b \cdot \delta\mathbf{u} \, \mathrm{d}V + \int_{\partial V} \mathbf{f}_s \cdot \delta\mathbf{u} \, \mathrm{d}S, \tag{E.3c}$$

où V représente le domaine de la configuration de référence du milieu 3D, ∂V la frontière de la surface et $\mathrm{d}V$ un volume différentiel de celle-ci, $\delta\mathbf{E}$ la variation de $\mathbf{E}$, le tenseur de déformation de Green-Lagrange, et $\mathbf{S}$ le deuxième tenseur de contraintes de Piola-Kirchhoff, énergétiquement conjugué à $\mathbf{E}$,

$\ddot{\mathbf{u}} = \partial^2\mathbf{u}/\partial t^2$ est l'accélération du point considéré, ρ la densité du matériau, dS une section différentielle de la surface, et $\mathbf{f}_b$ et $\mathbf{f}_s$ les efforts externes sur le corps et la surface, respectivement. Le choix des tenseurs lagrangiens $\mathbf{E}$ et $\mathbf{S}$ est lié à la description du mouvement par rapport à la configuration de référence initiale à $t = 0$ puisque cette configuration est connue, alors que la configuration actuelle du milieu est inconnue.

Mesure de déformation On considère que tout élément différentiel de la poutre peut se déformer de 6 manières différentes : trois déformations en translation comprenant une déformation axiale et une déformation de cisaillement dans deux polarisations, et trois déformations en rotation comprenant une courbure due à la torsion et une courbure de flexion dans deux polarisations. Pour un mouvement fixe dans le plan, le nombre de modes de déformation naturellement se réduit à trois : une déformation axiale, une déformation de cisaillement dans la polarisation dans le plan et une courbure due à la flexion dans le plan. Les autres polarisations de flexion et de cisaillement ainsi que la courbure due à la torsion impliquent une déformation hors plan et ne sont pas prises en compte dans les mouvements plans.

Le tenseur de déformation de Green-Lagrange $\mathbf{E}$ est utilisé pour décrire la déformation d'un milieu subissant de grands déplacements et s'écrit :

$$\mathbf{E} = \frac{1}{2}\left(\mathbf{F}^{\mathrm{T}}\mathbf{F} - \mathbf{I}\right) = \frac{1}{2}\left(\nabla\mathbf{u} + \nabla^{\mathrm{T}}\mathbf{u} + \nabla^{\mathrm{T}}\mathbf{u}\nabla\mathbf{u}\right), \tag{E.4}$$

où $\mathbf{F} = \mathbf{I} + \nabla\mathbf{u}$ est le tenseur du gradient de déformation, $\mathbf{I}$ la matrice d'identité, $\nabla\mathbf{u}$ le gradient des déplacements $\mathbf{u}$ et où $^{\mathrm{T}}$ indique la transposée d'un vecteur ou d'une matrice. Notez que le dernier terme de l'Eq. (E.4) $\nabla^{\mathrm{T}}\mathbf{u}\nabla\mathbf{u}$ est quadratique par rapport à $\mathbf{u}$. $\mathbf{E}$ reste valable pour toute amplitude de rotation du milieu de poutre, même quand la rotation devient très importante.

Loi de comportement La loi de comportement reliant $\mathbf{E}$ et $\mathbf{S}$ est ensuite indiquée. Puisque dans cette thèse l'étude est limitée aux milieux de matériau élastique isotrope (et homogène) (hypothèse #4), une loi de comportement linéaire de type Kirchhoff-Saint-Venant est utilisée, qui prend la forme générale :

$$\mathbf{E} = \frac{1+\nu}{E}\mathbf{S} - \frac{\nu}{E}\mathrm{tr}(\mathbf{S})\mathbf{I}, \tag{E.5}$$

avec E le module d'Young du matériau et ν le coefficient de Poisson.

E.2.1.1 Modèle géométriquement exact : réduction à la ligne moyenne

On procède maintenant à la dérivation du modèle géométriquement exact basé sur la cinématique de la ligne moyenne de la poutre. Pour simplifier, les mouvements sont limités aux mouvements 2D dans le plan afin de dériver plus facilement les équations de poutre. Le modèle géométriquement exact pour les mouvements en 3D est dérivé plus tard dans le chapitre 5.

Le modèle du milieu 3D occupant le domaine V est désormais réduit à un milieu 1D dont la cinématique est définie par (i) le déplacement de la ligne moyenne sur laquelle chaque point C est défini par l'abscisse curviligne $x \in [0, L]$ avec L la longueur de la poutre, et (ii) les orientations d'un ensemble de sections, où chaque section située en x est une surface plane (2D) dont le centroïde passe par C sur la ligne moyenne. Dans la configuration de référence, la section plane en x est orthogonale à la ligne moyenne.

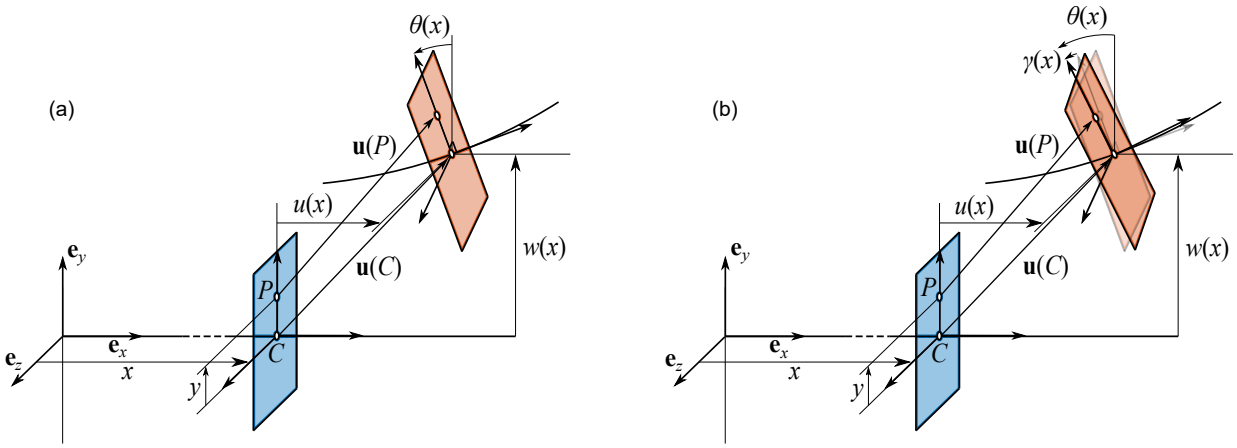

Figure E.2: Cinématique en 2D, (a) de type Euler-Bernoulli, (b) de type Timoshenko.

Dans le modèle géométriquement exact, les non linéarités géométriques liées aux grandes rotations des sections sont maintenues exactes sans aucune troncature ou simplification des non linéarités (d'où "géométriquement exact"). Ce modèle décrit donc la transformation de la poutre *quelle que soit l'amplitude de la rotation*. Même dans les cas de rotation extrême, *e.g.* une poutre encastrée-libre "se courbant vers l'arrière" au-delà de son extrémité fixe [Fig. 2.1(a)], le modèle géométriquement exact reste précis. La difficulté de ce modèle est alors liée à la manière dont les termes de rotation sont modélisés ; en 2D, la modélisation est simple puisqu'il n'y a qu'une seule rotation à prendre en compte (θ). Cependant, différentes méthodes de paramétrisation de la rotation en 3D existent et représentent l'un des principaux défis du modèle géométriquement exact (voir la section 1.2.1).

Cinématique En nous référant à la Fig. E.2, on considère une section d'une poutre de longueur L située en x. Le déplacement de tout point P de la section s'écrit :

$$\mathbf{u}(P) = \mathbf{u}(C) + [\mathbf{R}(\theta) - \mathbf{I}]\,\mathbf{CP}, \tag{E.6}$$

où C représente le point dans la section de P croisant la ligne moyenne de la poutre, $\mathbf{u}(C)$ est le déplacement de C, $\mathbf{CP}$ est le vecteur qui définit la position de P dans la section et $\mathbf{R}(\theta)$ est l'opérateur de rotation, ici donné par la matrice de rotation 2D :

$$\mathbf{R}(\theta) = \begin{bmatrix} \cos\theta & -\sin\theta \\ \sin\theta & \cos\theta \end{bmatrix}, \tag{E.7}$$

avec θ l'angle de rotation de la section. Le déplacement s'écrit alors explicitement sous la forme :

$$\mathbf{u}(P) = (u - y\sin\theta)\,\mathbf{e}_x + [w + y(\cos\theta - 1)]\,\mathbf{e}_y, \tag{E.8}$$

où $(\mathbf{e}_x, \mathbf{e}_y)$ est le repère tel que défini dans la Fig. E.2 et avec u et w les déplacements axial et transverse respectivement de C.

Linearisation cohérente des déformations de Green-Lagrange Pour le déplacement $\mathbf{u}$ de tout point P de la poutre tel que défini par l'Eq. (E.8), les déformations de Green-Lagrange $\mathbf{E}$ sont définies

selon l'Eq. (E.4) sans aucune simplification des termes non linéaires (contrairement au modèle de von Kármán, qui est présenté dans la section 2.1.4). Il est tout à fait possible de procéder avec les déformations de Green-Lagrange non linéaires complètes, mais, étant complexes, une procédure appelée la "linéarisation cohérente" des déformations de Green-Lagrange est souvent effectuée pour simplifier $\mathbf{E}$ lorsque les déformations locales sont petites sans perte de précision [74], [229]. Dans la linéarisation cohérente, le gradient de déformation $\mathbf{F}$ est décomposé en deux parties, un tenseur de rotation définissant la rotation de la section $\mathbf{R}(\theta)$ [Eq. (E.7)] et un tenseur d'étirement (noté ici $\tilde{\mathbf{U}}$) indépendant de la transformation du corps rigide :

$$\mathbf{F} = \mathbf{R}(\theta)\tilde{\mathbf{U}}, \tag{E.9}$$

avec $\mathbf{R}^{\mathrm{T}}\mathbf{R} = \mathbf{I}$ en se rappelant que $\mathbf{R}$ est orthogonal. Ensuite, $\tilde{\mathbf{U}}$ peut être réécrit :

$$\tilde{\mathbf{U}} = \mathbf{R}(-\theta)\mathbf{F} = \mathbf{I} + \mathbf{L}, \tag{E.10}$$

où :

$$\mathbf{L} = \begin{bmatrix} e - y\kappa & 0 \\ \gamma & 0, \end{bmatrix} \tag{E.11}$$

et :

$$\begin{cases} e = (1+u')\cos\theta + w'\sin\theta - 1, & \text{(E.12a)} \\ \gamma = w'\cos\theta - (1+u')\sin\theta, & \text{(E.12b)} \\ \kappa = \theta', & \text{(E.12c)} \end{cases}$$

où $\diamond' = \partial\diamond/\partial x$ est la dérivée spatiale en $\mathbf{e}_x$, e est la déformation axiale, γ la déformation de cisaillement et κ la courbure.

Selon cette définition, le tenseur de déformation de Green-Lagrange $\mathbf{E}$ défini par l'Eq. (E.4) peut être réécrit :

$$\mathbf{E} = \frac{1}{2}\left(\mathbf{F}^{\mathrm{T}}\mathbf{F} - \mathbf{I}\right) = \frac{1}{2}\left(\tilde{\mathbf{U}}^{\mathrm{T}}\tilde{\mathbf{U}} - \mathbf{I}\right) = \frac{1}{2}\left(\mathbf{L} + \mathbf{L}^{\mathrm{T}} + \mathbf{L}^{\mathrm{T}}\mathbf{L}\right). \tag{E.13}$$

La procédure de linéarisation cohérente indique essentiellement que, pour les cas où les déformations locales sont très petites, c'est-à-dire $e \ll 1$ (petite déformation axiale), $\gamma \ll 1$ (petite déformation de cisaillement) et $y\kappa \ll 1$ (petite *épaisseur*, ce qui ne veut pas dire que la courbure κ doit nécessairement être petite), la partie quadratique de $\mathbf{E}$ en fonction de $\mathbf{L}$ peut être négligée. D'après l'Eq. (E.11), $\mathbf{L}$ dépend uniquement des termes e, γ et $y\kappa$ et non de la rotation des sections θ. Si les termes de déformation locaux sont très petits, alors $\mathbf{E}$ peut être linéarisé en toute sécurité dans $\mathbf{L}$ sans négliger les grands termes de rotation liés à la transformation du corps rigide [229].

$\mathbf{E}$ est ensuite remplacé par $\tilde{\mathbf{E}}$, représentant la linéarisation cohérente des déformations de Green-Lagrange où le terme $\mathbf{L}^{\mathrm{T}}\mathbf{L}$ dans l'Eq. (E.13) est négligé, écrit :

$$\tilde{\mathbf{E}} = \frac{1}{2}\left(\mathbf{L} + \mathbf{L}^{\mathrm{T}}\right) = \begin{bmatrix} e - y\kappa & \frac{\gamma}{2} \\ \frac{\gamma}{2} & 0 \end{bmatrix}, \tag{E.14}$$

où la présence des non linéarités géométriques dans les équations du mouvement est désormais évidente en se rappelant des définitions des déformations dans les Eqs. (E.12).

Forme faible des équations du mouvement Comme les déformations de Green-Lagrange $\mathbf{E}$ sont énergétiquement conjuguées au deuxième tenseur de contraintes de Piola-Kirchhoff $\mathbf{S}$, la linéarisation cohérente $\tilde{\mathbf{E}}$ est également énergétiquement conjuguée à un tenseur de contraintes $\tilde{\mathbf{S}}$ et la loi de comportement linéaire de l'Eq. (E.5) peut être appliquée. Il a été montré que les résultantes de contrainte de $\tilde{\mathbf{S}}$ en force et moment correspondent aux efforts internes (axial N, cisaillement T et moment de flexion M) qui sont utilisés dans l'écriture des équations dynamiques du mouvement [115], [229] et s'écrivent lorsqu'ils sont intégrés sur la section sous la forme :

$$N = \int_A S_{xx}\,\mathrm{d}A = EAe, \tag{E.15a}$$

$$T = \int_A S_{xy}\,\mathrm{d}A = kGA\gamma, \tag{E.15b}$$

$$M = \int_A yS_{xx}\,\mathrm{d}A = EI\kappa, \tag{E.15c}$$

où A est l'aire de la section et $\mathrm{d}A$ un élément différentiel de celle-ci, $G = E/[2(1+\nu]$ est le module de cisaillement, I le deuxième moment de l'aire et k est le coefficient de cisaillement. Sous-produit de la cinématique de Timoshenko déformable en cisaillement, k représente la non uniformité des contraintes de cisaillement dans la section et est généralement choisi en fonction de la géométrie de la section [119]. La forme faible des équations du mouvement se trouve en utilisant l'Eq. (E.2) et (E.3) :

$$\delta W_i = \int_V \mathbf{S} \colon \delta\mathbf{E}\,\mathrm{d}V = \int_0^L (N\delta e + T\delta\gamma + M\delta\kappa)\,\mathrm{d}x, \tag{E.16a}$$

$$\delta W_a = \int_V \rho\ddot{\mathbf{u}}\cdot\delta\mathbf{u}\,\mathrm{d}V = \int_0^L \left(\rho A\ddot{u}\delta u + \rho A\ddot{w}\delta w + \rho I\ddot{\theta}\delta\theta\right)\mathrm{d}x, \tag{E.16b}$$

$$\begin{aligned}\delta W_e &= \int_V \mathbf{f}_b\cdot\delta\mathbf{u}\,\mathrm{d}V + \int_{\partial V}\mathbf{f}_s\cdot\delta\mathbf{u}\,\mathrm{d}S \\ &= \int_0^L (n\delta u + p\delta w + q\delta\theta)\,\mathrm{d}x + [N_e\delta u]_0^L + [T_e\delta w]_0^L + [M_e\delta\theta]_0^L\,,\end{aligned} \tag{E.16c}$$

où $n(x,t)$, $p(x,t)$ et $q(x,t)$ sont, respectivement, la force axiale appliquée, la force transverse et le moment par unité de longueur, et N_e, T_e et M_e sont, respectivement, la force axiale, la force transverse et les moments appliqués aux extrémités $x = 0$ et $x = L$. Pour les modèles d'éléments finis, la discrétisation est généralement appliquée directement aux équations de poutre sous la forme faible des Eqs. (E.16). Cela se fait dans les chapitres 3 en 2D et 5 en 3D.

E.2.2 Stratégies de résolution

E.2.2.1 Discrétisation spatiale avec la méthode des éléments finis

Pour résoudre numériquement les équations aux dérivées partielles non linéaires, elles doivent d'abord être discrétisées dans l'espace. Différentes méthodes de discrétisation peuvent être trouvées dans la littérature, comme la méthode des différences finies [131], [132], les techniques de Galerkin [69], [71] ou encore la méthode des éléments finis (FEM). La FEM est la stratégie la plus populaire dans la littérature sur les structures de poutres minces pour résoudre les équations de mouvement non linéaires. Dans cette méthode, la forme faible des équations de poutre [Eqs. (E.2) et (E.16)] sont discrétisées dans l'espace en éléments finis. Les grandeurs élémentaires sont évaluées pour un seul élément fini, puis assemblées sur l'ensemble de la structure pour résoudre l'équation complète du mouvement.

E.2. MODÉLISATION DE STRUCTURES DE POUTRES HAUTEMENT FLEXIBLES : MODÉLISATION ET RÉSOLUTION DES NON LINÉARITÉS GÉOMÉTRIQUES

Dans ce travail, la formulation d'éléments finis est basée sur une discrétisation directe des équations géométriquement exactes en éléments de poutre 1D de Timoshenko généralement (mais pas nécessairement) de longueur égale L^e. La discrétisation en éléments finis est simple, étant donné que seule la ligne moyenne doit être discrétisée en éléments 1D pour suivre sa déformation. Dans sa forme la plus basique, les éléments de poutre Timoshenko 1D n'ont que 2 nœuds, un à chaque extrémité de l'élément, mais des nœuds internes peuvent être ajoutés afin d'augmenter l'ordre d'interpolation. Les inconnues du système sont ensuite retrouvées à chacun des nœuds et interpolées entre les nœuds. Si l'on reprend le modèle 2D géométriquement exact de la section précédente, avec des éléments de Timoshenko à 2 nœuds (pas de nœuds internes), les trois degrés de liberté u, w et θ se retrouvent à chaque nœud et sont rassemblés dans le vecteur $\mathbf{q}^e$, où la notation $\diamond^e$ indique une quantité élémentaire :

$$\mathbf{q}^e = \begin{bmatrix} u_1 & w_1 & \theta_1 & u_2 & w_2 & \theta_2 \end{bmatrix}^{\mathrm{T}}, \tag{E.17}$$

avec les indices $\diamond_1$ et $\diamond_2$ indiquant respectivement les inconnues au nœud 1 et au nœud 2 de l'élément. Les déplacements sont ensuite interpolés entre les nœuds $\forall x \in [0, L^e]$ à l'aide des fonctions de forme regroupées dans la matrice $\mathbf{N}(x)$:

$$\begin{bmatrix} u^e(x,t) & w^e(x,t) & \theta^e(x,t) \end{bmatrix}^{\mathrm{T}} = \mathbf{N}(x)\mathbf{q}^e(t). \tag{E.18}$$

Dans cette thèse, des fonctions de forme polynomiales sont utilisées ; dans le chapitre 3 des fonctions de forme linéaire sont utilisées dans $\mathbf{N}$ et sont ensuite étendues aux fonctions de forme quadratiques dans le chapitre 5 avec la possibilité d'augmenter l'ordre des polynômes avec des nœuds internes. En utilisant la définition des déplacements élémentaires [Eq. (E.18)] et en définissant la dérivée spatiale comme :

$$\begin{bmatrix} u^{e\prime}(x,t) & w^{e\prime}(x,t) & \theta^{e\prime}(x,t) \end{bmatrix}^{\mathrm{T}} = \mathbf{N}'(x)\mathbf{q}^e(t), \tag{E.19}$$

les déformations discrétisées e^e, γ^e et κ^e peuvent être trouvées en substituant ces relations dans les Eqs. (E.12). La variation des déformations élémentaires est nécessaire pour discrétiser le travail interne virtuel [Eq. (E.16a)] et s'écrit sous la forme :

$$\delta\hat{\boldsymbol{\varepsilon}}^e = \mathbf{B}^e(x, \mathbf{q}^e)\delta\mathbf{q}^e, \tag{E.20}$$

en utilisant la notation $\hat{\boldsymbol{\varepsilon}}^e = \begin{bmatrix} e^e & \gamma^e & \kappa^e \end{bmatrix}^{\mathrm{T}}$ comme vecteur de déformation élémentaire et $\mathbf{B}^e$ la matrice de déformation. Des définitions explicites de ces termes sont données dans les chapitres 3 et 5 en fonction des interpolations dans $\mathbf{N}$.

On peut maintenant passer à la discrétisation de la forme faible des équations du mouvement basée sur le principe des travaux virtuels. En 2D, si la notation $\hat{\mathbf{S}}^e = \begin{bmatrix} N^e & T^e & M^e \end{bmatrix}^{\mathrm{T}}$ est introduite, cela

prend le forme :

$$\delta W_i^e = \int_0^{L^e} (N^e \delta e^e + T^e \delta\gamma^e + M^e \delta\kappa^e)\,\mathrm{d}x = \delta\mathbf{q}^{e\mathrm{T}} \underbrace{\int_0^{L^e} \mathbf{B}^{e\mathrm{T}} \hat{\mathbf{S}}^e \mathrm{d}x}_{\mathbf{f}_{int}^e(\mathbf{q}^e)}, \tag{E.21a}$$

$$\delta W_a^e = \int_0^{L^e} \left(\rho A \ddot{u}\delta u + \rho A \ddot{w}\delta w + \rho I \ddot{\theta}\delta\theta\right)\mathrm{d}x = \delta\mathbf{q}^{e\mathrm{T}} \underbrace{\left(\int_0^{L^e} \rho \mathbf{N}^{\mathrm{T}} \mathbf{J} \mathbf{N} \mathrm{d}x\right)}_{\mathbf{M}^e} \ddot{\mathbf{q}}^e, \tag{E.21b}$$

$$\delta W_e^e = \int_0^{L^e} (n\delta u + p\delta w + q\delta\theta)\,\mathrm{d}x + [N_e \delta u]_0^L + [T_e \delta w]_0^L + [M_e \delta\theta]_0^L = \delta\mathbf{q}^{e\mathrm{T}} \underbrace{\int_0^{L^e} \mathbf{N}^{\mathrm{T}} \mathbf{f}_e^e \mathrm{d}x}_{\mathbf{f}_{ext}^e}, \tag{E.21c}$$

avec :

$$\mathbf{J} = \begin{bmatrix} A & 0 & 0 \\ 0 & A & 0 \\ 0 & 0 & I \end{bmatrix}, \tag{E.22}$$

et $\mathbf{f}_e^e = \begin{bmatrix} n & p & q \end{bmatrix}^{\mathrm{T}}$. Toutes les conditions aux limites doivent être ajoutées directement aux nœuds correspondants à $x = 0$ et $x = L$.

Les quantités élémentaires ($\mathbf{q}^e$, $\mathbf{M}^e$, $\mathbf{f}_{int}^e(\mathbf{q}^e)$ et $\mathbf{f}_{ext}^e$) sont assemblées sur la structure complète en leurs homologues globaux et, en utilisant la définition du principe des travaux virtuels [Eq. (E.2)], l'équation du mouvement devient :

$$\delta W_e - \delta W_i - \delta W_a = \delta\mathbf{q}^{\mathrm{T}} (\mathbf{f}_{ext} - \mathbf{f}_{int}(\mathbf{q}) - \mathbf{M}\ddot{\mathbf{q}}) = 0. \tag{E.23}$$

L'équation du mouvement éléments finis peut alors s'écrire sous la forme générale d'une équation différentielle ordinaire du second ordre :

$$\mathbf{M}\ddot{\mathbf{q}} + \mathbf{D}\dot{\mathbf{q}} + \mathbf{f}_{int}(\mathbf{q}) = \mathbf{f}_{ext}. \tag{E.24}$$

Un terme d'amortissement $\mathbf{D}\dot{\mathbf{q}}$ a été ajouté afin de prendre en compte tout amortissement structurel du système, dont un exemple est l'amortissement linéaire de Rayleigh introduit dans le chapitre 3.

E.2.2.2 Résolution dans le domaine fréquentiel et types de solutions visées

Dans le domaine fréquentiel, les solutions périodiques en régime permanent sont directement ciblées. La méthode de l'équilibrage harmonique (HBM) est fréquemment utilisée pour trouver des solutions périodiques dans le domaine fréquentiel. Il s'agit de la stratégie de résolution utilisée dans les travaux de cette thèse, détaillée dans la section 2.2.3. Dans l'HBM, la solution périodique est décomposée en séries de Fourier afin de transformer l'équation différentielle en un système algébrique d'équations. Le système algébrique non linéaire peut ensuite être résolu en utilisant *e.g.* des itérations Netwon-Raphson ou des méthodes de continuation.

L'approche de résolution de cette thèse est *entièrement basée dans le domaine fréquentiel*, ce qui représente l'une des principales originalités de ce travail. Les solutions périodiques des équations non linéaires du mouvement sont développées en séries de Fourier suivant l'HBM et résolues à l'aide d'une méthode de continuation appelée la méthode asymptotique numérique (MAN). La section 2.2 présente les étapes de cette stratégie de résolution en domaine fréquentiel.

E.3 Dynamique non linéaire des structures de poutres flexibles en 2D avec paramétrisation trigonométrique des termes de rotation

On présente ici les détails de la stratégie pour simuler la dynamique non linéaire des structures flexibles de poutres élancées. Ce chapitre complète les discussions du chapitre précédent en synthétisant toutes les étapes décrites dans le chapitre 2 :

- la dérivation du modèle géométriquement exact basé sur une cinématique de type Timoshenko,
- la discretisation du modèle géométriquement exact en éléments finis,
- la résolution des équations du mouvement dans le domaine fréquentiel à travers la combinaison de la méthode d'equilibrage harmonique (HBM) avec une méthode de continuation appelée la méthode asymptotique numérique (MAN).

Dans ce chapitre, *le mouvement est fixé dans le plan* de sorte que seuls les mouvements dans le plan (2D) sont pris en compte (les mouvements hors plan (3D) sont décrits dans le chapitre 5) . Le modèle 2D est basé sur une paramétrisation des termes de rotation par matrices de rotation classiques et discrétisé avec des éléments de poutre de type Timoshenko linéaires. Le modèle éléments finis est ensuite résolu avec la stratégie dans le domaine fréquentiel introduite pour la première fois dans la section 2.2. Le contenu de ce chapitre a été publié dans la revue *Journal of Sound and Vibration* en décembre 2022 sous le titre "Finite element computation of nonlinear modes and frequency response of geometrically exact beam structures" [58].

Dans la section 3.1, une revue de la littérature sur les structures de poutres flexibles et l'état de l'art est proposée ainsi que les applications industrielles courantes de ces structures. Dans la section 3.2, les détails de la stratégie de modélisation basée sur une discrétisation par éléments finis du modèle de poutre géométriquement exact (voir sections 3.2.1 et 3.2.2) et la stratégie de résolution dans le domaine fréquentiel basée sur l'HBM et la MAN (voir la section 3.2.3) sont décrits. Comme indiqué dans la section 2.2.4, la stratégie de résolution dans le domaine fréquentiel est automatisée par le solveur MANLAB et certaines considérations particulières lors de l'implémentation du modèle dans MANLAB sont discutées, telles que la façon dont le modèle géométriquement exact est réécrit sous forme d'un système quadratique. Le modèle est ensuite testé à l'aide de plusieurs cas tests dans la section 3.3, à la fois des exemples classiques (poutres encastrées-libres et poutres bi-encastrées) et d'autres inspirés de travaux de la littérature (anneaux flexibles, poutres en forme d'arbre, *etc.*). Enfin, quelques sujets importants liés au modèle sont abordés : dans la section 3.4, l'importance d'une bonne convergence en nombre d'harmoniques retenues dans l'HBM est soulignée. Dans la section 3.5, une discussion sur le phénomène non linéaire de résonance interne est proposée, en particulier sur la façon dont les résonances internes apparaissent dans les calculs numériques dans MANLAB. Les remarques finales et les perspectives sont résumées dans la section 3.6.

Quelques sections du chapitre 3 et des résultats clés sont traduits ci-dessous.

E.3.1 Modèle géométriquement exact en 2D

En se basant sur les dérivations de la section E.2, les équations du modèle géométriquement exact sont ici détaillées.

Cinématique Le système étudié est représenté dans la Fig. E.3. Le modèle de poutre géométriquement exact est ici limité à deux dimensions, de telle sorte que la ligne moyenne de tout élément de poutre se

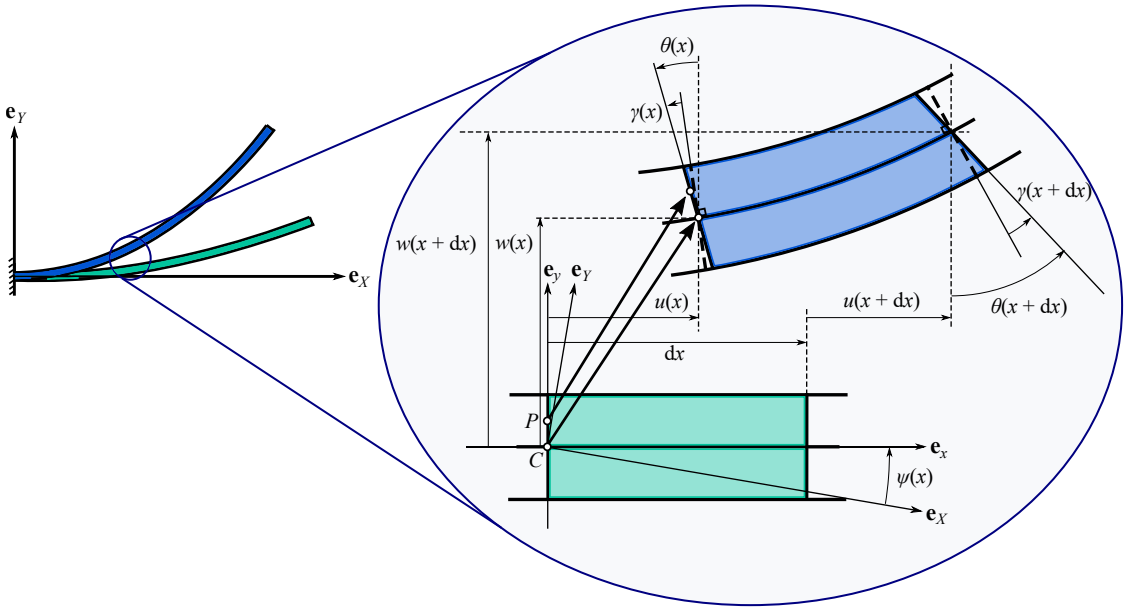

Figure E.3: Cinématique de poutre de type Timoshenko.

trouve dans le plan $(\mathbf{e}_X, \mathbf{e}_Y)$ d'une base globale $(\mathbf{e}_X, \mathbf{e}_Y, \mathbf{e}_Z)$ et subit des déformations dans le même plan.

En se basant sur une cinématique de Timoshenko, on suppose que toute section de la poutre subit un mouvement de corps rigide. On considère un élément de poutre différentiel de longueur dx avec sa ligne moyenne alignée avec la direction $\mathbf{e}_x$, où $(\mathbf{e}_x, \mathbf{e}_y, \mathbf{e}_Z)$ est un repère local qui peut dépendre (dans le cas d'une structure courbe) de x, la coordonnée curviligne qui définit l'emplacement des sections. L'angle $\psi(x) = (\widehat{\mathbf{e}_X, \mathbf{e}_x})$ définit son orientation. En conséquence, le déplacement de tout point P dans la section est lié au champ de déplacement de la ligne moyenne par la relation suivante :

$$\begin{aligned}\mathbf{u}(x,y,t) = &[u(x,t) - y\sin\theta(x,t)]\,\mathbf{e}_x \\ &+ [w(x,t) + y\,(\cos\theta(x,t) - 1)]\,\mathbf{e}_y,\end{aligned} \tag{E.25}$$

où (x,y) sont les coordonnées de P dans le repère $(\mathbf{e}_x, \mathbf{e}_y)$, t est le temps, $u(x,t)$ et $w(x,t)$ sont les déplacements axial et transverse, respectivement, du point correspondant de la ligne moyenne C à la position axiale x et au temps t, et $\theta(x,t)$ est la rotation de la section, comme montré dans la Fig. E.3.

Les déformations de Green-Lagrange, la loi de comportement et les contraintes peuvent ensuite être écrites selon la procédure détaillée dans la section E.2. La forme faible des équations du mouvement est trouvée d'abord en continu à partir du principe des travaux virtuels des Eqs. (E.16).

Discretisation en éléments finis La poutre est ensuite discrétisée en N_e éléments de longueur L^e, qui peut dépendre de x dans le cas d'un maillage non uniforme. Si on reprend le modèle discrétisé de la section E.2, la matrice $\mathbf{N}$ des fonctions de forme qui permettent d'interpoler les valeurs des degrés de

liberté entre les nœuds est écrite :

$$\mathbf{N}(x) = \begin{bmatrix} N_1(x) & 0 & 0 & N_2(x) & 0 & 0 \\ 0 & N_1(x) & 0 & 0 & N_2(x) & 0 \\ 0 & 0 & N_1(x) & 0 & 0 & N_2(x) \end{bmatrix}, \tag{E.26}$$

avec les fonctions de formes linéaires N_1 et N_2 définis par :

$$N_1(x) = 1 - \frac{x}{L^e}, \quad N_2(x) = \frac{x}{L^e}. \tag{E.27}$$

Avec cette interpolation, la discrétisation peut être substituée dans le principe des travaux virtuels des Eqs. (E.16) afin d'obtenir les équations du mouvement discrétisées (Eqs. (E.21)). En commençant par le travail virtuel des efforts inertiels, l'introduction de la discrétisation conduit à l'expression suivante (à partir de l'Eq. (E.21b) :

$$\begin{aligned} \delta W_a^e &= \int_0^{L^e} \rho (\mathbf{N}\delta\mathbf{q}^e)^{\mathrm{T}} \mathbf{J}\mathbf{N}\ddot{\mathbf{q}}^e \,\mathrm{d}x \\ &= (\delta\mathbf{q}^e)^{\mathrm{T}} \underbrace{\left(\int_0^{L^e} \rho \mathbf{N}^{\mathrm{T}}\mathbf{J}\mathbf{N} \,\mathrm{d}x \right)}_{\mathbf{M}^e} \ddot{\mathbf{q}}^e. \end{aligned} \tag{E.28}$$

La matrice de masse élémentaire est retrouvée après évaluation de l'intégrale :

$$\mathbf{M}^e = \frac{\rho L^e}{6} \begin{bmatrix} 2A & 0 & 0 & A & 0 & 0 \\ 0 & 2A & 0 & 0 & A & 0 \\ 0 & 0 & 2I & 0 & 0 & I \\ A & 0 & 0 & 2A & 0 & 0 \\ 0 & A & 0 & 0 & 2A & 0 \\ 0 & 0 & I & 0 & 0 & 2I \end{bmatrix}. \tag{E.29}$$

Ensuite, l'introduction de la discrétisation conduit à l'expression suivante (à partir de l'Eq. (E.21a)) pour le travail virtuel des efforts internes sur un élément donné :

$$\begin{aligned} \delta W_i^e &= -\int_0^{L^e} (\mathbf{B}^e(x,\mathbf{q}^e)\delta\mathbf{q}^e)^{\mathrm{T}} \, \hat{\mathbf{S}}^e \,\mathrm{d}x \\ &= -(\delta\mathbf{q}^e)^{\mathrm{T}} \underbrace{\int_0^{L^e} (\mathbf{B}^e(x,\mathbf{q}^e))^{\mathrm{T}} \hat{\mathbf{S}}^e \,\mathrm{d}x}_{\mathbf{f}_{\mathrm{int}}^e}. \end{aligned} \tag{E.30}$$

On note que l'intégrale est évaluée par une intégration réduite (intégration de Gauss, ici avec un seul point en $x = \frac{L^e}{2}$) pour éviter le phénomène de verrouillage en cisaillement [20]. Le vecteur de force interne élémentaire $\mathbf{f}_{\mathrm{int}}^e$ est alors donné par :

$$\mathbf{f}_{\mathrm{int}}^e = EA\bar{e} \begin{bmatrix} -\cos\bar{\theta} \\ -\sin\bar{\theta} \\ \bar{\gamma}\frac{L^e}{2} \\ \cos\bar{\theta} \\ \sin\bar{\theta} \\ \bar{\gamma}\frac{L^e}{2} \end{bmatrix} + kGA\bar{\gamma} \begin{bmatrix} \sin\bar{\theta} \\ -\cos\bar{\theta} \\ -\frac{L^e}{2}(1+\bar{e}) \\ -\sin\bar{\theta} \\ \cos\bar{\theta} \\ -\frac{L^e}{2}(1+\bar{e}) \end{bmatrix} + EI\bar{\kappa} \begin{bmatrix} 0 \\ 0 \\ -1 \\ 0 \\ 0 \\ 1 \end{bmatrix}, \tag{E.31}$$

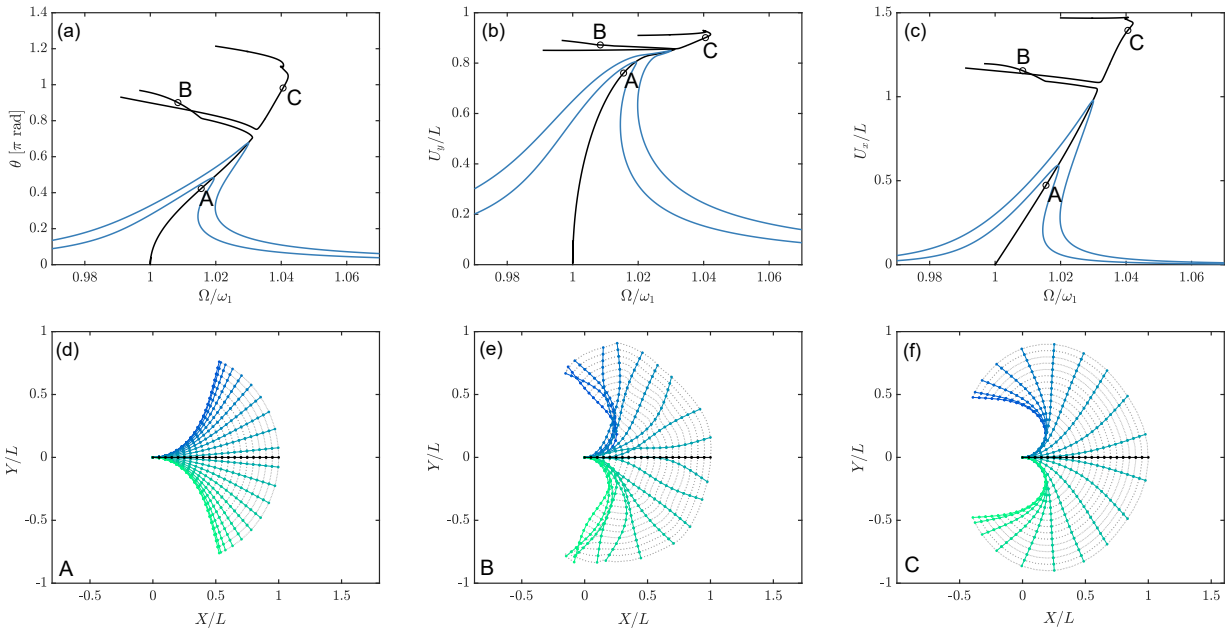

Figure E.4: Premier mode non linéaire d'une poutre encastrée-libre. Première rangée : réponses forcées ($\hat{F}_0 = 0.05$ and $\hat{F}_0 = 0.08$) et backbones en (a) rotation de la section θ, (b) déplacement transverse adimensionné U_y/L, (c) déplacement axial adimensionné U_x/L à l'extrémité de la poutre. Amplitude maximale sur une période d'oscillation. Deuxième rangée : déformée modale (a) à basse amplitude (point A), (b) à la résonance interne (point B) et (c) à grande amplitude (point C) ; 20 captures sur une demi-période.

où $\bar{\circ}$ désigne ici une quantité évaluée à $x = L^e/2$.

Enfin, l'introduction de la discrétisation conduit à l'expression suivante (à partir de l'Eq. (E.21c)) pour le travail virtuel des forces externes sur un élément donné :

$$\delta W_e^e = (\delta \mathbf{q}^e)^{\mathrm{T}} \underbrace{\left(\int_0^{L^e} \mathbf{N}^{\mathrm{T}} \begin{pmatrix} n \\ p \\ q \end{pmatrix} \mathrm{d}x \right)}_{\mathbf{f}_{\mathrm{ext}}^e}, \tag{E.32}$$

à partir duquel le vecteur de force externe élémentaire $\mathbf{f}_{\mathrm{ext}}^e$ peut être écrit en évaluant l'intégrale ci-dessus.

Rassemblant les expressions pour la matrice de masse et les vecteurs de forces interne et externe pour un seul élément et les assemblant sur l'ensemble de la structure, les équations du mouvement discrétisées peuvent être écrites sous la forme générale de l'Eq. (E.24). Le système d'équations est ensuite resolu entièrement dans le domaine fréquentiel afin de cibler les solutions périodiques.

E.3.2 Cas test : poutre encastrée-libre

Pour demontrer la capacité du modèle éléments finis à capturer la dynamique non linéaire des structures hautement flexibles, on considère une poutre encastrée-libre, avec une extrémité fixe et l'autre

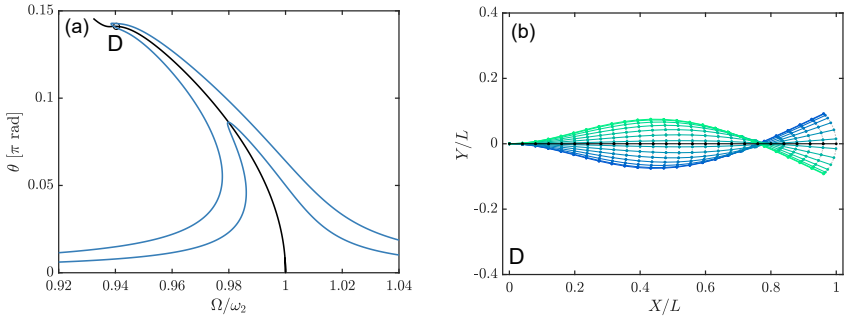

Figure E.5: Deuxième mode non linéaire d'une poutre encastrée-libre. Gauche : réponses forcées ($F_0 = 0.16$ and $F_0 = 0.3$) et backbone en θ, la rotation de la section à l'extrémité de la poutre. Droite : déformée modale au point D ; 14 captures sur une demi-période.

libre. Cette configuration subit de très grandes déformations pour seulement un faible chargement dans la direction transverse, ce qui peut mener à des déplacements et rotations importants de la structure.

À cette fin, un maillage correspondant à une poutre encastrée-libre de longueur $L = 1$ m, de largeur $b = 0.05$ m et d'épaisseur $h = 0.001$ m est généré.

Pour simuler la réponse forcée de ce système, une charge transverse uniformément répartie $p(x,t) = p_0 \sin \Omega t$, telle que définie dans l'Eq. (3.33), est prescrite, avec p_0 son amplitude en [N/m]. Cela est égal à une accélération de la base, auquel cas la charge transverse devient $p_0 = -\rho A \ddot{w}_0$, où $\ddot{w}_0$ est l'accélération de base. Dans le contexte des éléments finis, cette charge apparaît comme une force externe $\mathbf{f}_{\text{ext}}(t)$ dans l'Eq. (3.49) de la forme $\mathbf{f}_{\text{ext}}(t) = \mathbf{F} \sin \Omega t$, avec les composants associés au déplacement transverse en $\mathbf{F}$ de la forme $F_0 \left[\frac{1}{2} \quad 1 \ldots 1 \quad \frac{1}{2}\right]^{\mathrm{T}}$ et les autres étant nuls. Ce dernier est valable si les éléments sont de longueur constante L^e, auquel cas $F_0 = p_0 L^e$. Dans la Fig. E.4, la valeur adimensionnée est indiquée : $\hat{F}_0 = L^2 p_0 L^e/(EI)$. Le coefficient d'amortissement linéaire α de l'Eq.. (3.36) est choisi comme $\alpha = 2\xi\omega_i$ avec $\xi = 0.005$ et ω_i la pulsation propre (linéaire) du mode considéré.

Les figures E.4, E.5 et E.6 montrent les résultats typiques de nos calculs sur les trois premiers modes non linéaires de la poutre encastrée-libre. Certaines réponses forcées pour une valeur donnée de l'amplitude du forçage $\hat{F}_0$ sont représentées en bleu avec les backbones superposées en noir. De nombreux phénomènes dynamiques non linéaires intéressants sont découverts.

Mode 1 En commençant par le premier mode non linéaire, illustré dans la Fig. E.4(a)-(c), on peut voir qu'il manifeste un comportement légèrement raidissant, ce qui signifie que la fréquence de résonance Ω augmente avec l'amplitude de vibration, une caractéristique bien documentée dans la littérature, voir [68], [175], [229]. Le point A représente un point de déplacement d'amplitude modérée sur la backbone, tandis que le point C représente un point de grande amplitude. La méthode de résolution présentée dans cette thèse est capable de pousser la simulation à des amplitudes extrêmes, vu avec la déformée modale au point C. À ce point, la poutre encastrée-libre s'est pliée complètement vers l'arrière, l'extrémité libre de la poutre vibrant bien au-delà de l'emplacement de l'extrémité fixe. Le point B représente un exemple de résonance interne, quand une partie de l'énergie est transférée vers un autre mode de vibration.

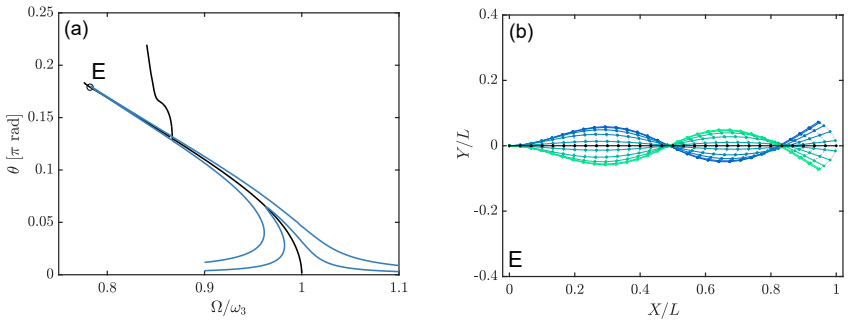

Figure E.6: Troisième mode non linéaire d'une poutre encastrée-libre. Gauche : réponses forcées ($F_0 = 1$ and $F_0 = 3$) et backbone en θ, la rotation de la section à l'extrémité de la poutre. Droite : déformée modale au point E ; 10 captures sur une demi-période.

Modes 2 et 3 Les deuxième et troisième modes non linéaires du cantilever sont représentés dans les Figs. E.5 et E.6, respectivement. Les réponses forcées et les modes non linéaires sont représentés en θ pour les deux modes vu que la rotation de la section θ donne une idée globale de la déformation de la poutre. Les deuxième et troisième modes de la poutre encastrée-libre manifestent cette fois-ci une tendance assouplissante, dans laquelle Ω diminue avec la croissance de l'amplitude de vibration, un fait également bien documenté (voir [175], [229]).

E.4 Effet de l'élancement et de la gravité sur la dynamique non linéaire des poutres

On souhaite maintenant démontrer avec un cas test dédié comment le modèle du chapitre 3 peut être appliqué pour étudier la dynamique non linéaire des structures de poutres élancées. Le système étudié ici est la poutre encastrée-libre en vibration de très grande amplitude, différente de celle de la section E.3.2 puisqu'ici l'effet de la gravité est inclus dans les équations du mouvement. On considère des poutres encastrées-libres verticales placées dans un champ gravitationnel. Dans cette configuration, deux orientations peuvent être considérées : une configuration *debout*, où la poutre est fixée de telle sorte que la gravité agisse pour compresser la poutre (effet de compression), et une configuration *suspendue*, où la poutre pend vers le bas de telle sorte que la gravité agisse pour étirer la poutre (effet de tension). En grande partie inspiré par les expériences du chapitre 6, on souhaite étudier l'influence de la gravité sur la dynamique non linéaire des ces poutres élancées et notamment sur les modes non linéaires.

La section 4.1 introduit l'étude et une revue sur l'état de l'art concernant l'effet de la gravité sur les structures de poutres encastrées-libres en statique et en dynamique. Une grande partie de la littérature est consacrée à l'effet de la gravité sur les pulsations propres linéaires de la poutre encastrée-libre, mais on cherche à étendre cet analyse au régime non linéaire en étudiant la dynamique à très grande amplitude. À cette fin, on utilise le modèle éléments finis 2D du chapitre 3 auquel est incorporé l'effet de la gravité dans la section 4.2. La gravité se présente dans les équations du mouvement sous la forme d'une force axiale en compression ou en traction en fonction de la configuration de la poutre (debout ou suspendue), puis le système est normalisé comme dans la section 3.2.3. Alors que le système adimensionné du chapitre 3 ne dépend d'un seul paramètre adimensionné (le paramètre "élancement" η), un deuxième paramètre adimensionné intervient dans le système après l'ajout de la gravité dans les équations du mouvement, appelé ici α, le paramètre "gravité" (avec une cinématique de Timoshenko, le troisième paramètre adimensionné μ est omis en raison de son influence négligeable sur les poutres élancées, demontrée dans l'annexe B.1). Notons que pour $\alpha > 0$, l'effort lié à la gravité est négatif (agissant en compression) et signifie donc la configuration debout ; $\alpha < 0$ par conséquence indique la configuration suspendue alors que $\alpha = 0$ indique la condition "sans gravité".

Dans la section 4.3, l'effet des deux paramètres adimensionnés η et α sur les (trois premières) pulsations propres linéaires de la poutre encastrée-libre est étudié et comparé à d'autres études de la littérature. Globalement, la gravité diminue les pulsations propres en configuration debout et augmente les pulsations propres en configuration suspendue, ce qui correspond aux études de la littérature. À partir de la section 4.4, l'analyse se concentre sur la dynamique non linéaire de la poutre encastrée-libre en grand amplitude. Dans la section 4.4, l'effet des deux paramètres adimensionnés sur les (trois premiers) modes non linéaires du système (représentés sous forme de courbes de maîtresse / backbones) est étudié et des comparaisons sont faites avec deux modèles de la littérature : une première comparaison au modèle analytique de Crespo da Silva (présenté pour la première fois dans la section 2.1.4 mais dérivé plus en détail dans l'annexe B.3), valable jusqu'à des amplitudes de rotation modérées, et aux modèles de base de [204] et [146]. Ensuite, dans la section 4.5, l'effet des paramètres d'élancement et de gravité sur la (première) déformée modale non linéaire (section 4.5.1) et sur l'évolution de la déformée modale en fonction de l'amplitude du mouvement (section 4.5.2) est démontré. Enfin, une analogie avec un système de pendule inversé sous l'influence de la gravité est présentée dans la section 4.6 et des remarques finales sont détailées dans la section 4.7.

Quelques sections du chapitre 4 et des résultats clés sont traduits ci-dessous.

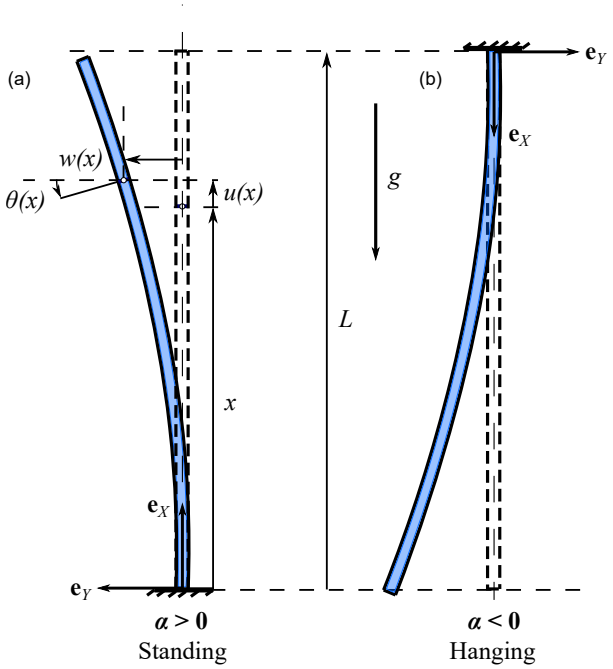

Figure E.7: Configurations de la poutre encastrée-libre à section rectangulaire : (a) configuration suspendue, (b) configuration debout.

E.4.1 Équations du modèle de poutre avec gravité

En se basant sur la cinématique du chapitre précédent avec les notations de la Fig. E.7, la forme forte des équations du mouvement est écrite :

$$\begin{cases} \rho A\ddot{u} = (N\cos\theta - T\sin\theta)' + n, & \text{(E.33a)} \\ \rho A\ddot{w} = (N\sin\theta + T\cos\theta)' + p, & \text{(E.33b)} \\ \rho I\ddot{\theta} = T(1+e) - N\gamma + M' + q, & \text{(E.33c)} \end{cases}$$

avec la même loi de comportement menant à :

$$N = EAe, \quad T = kGA\gamma, \quad M = EI\theta'. \tag{E.34}$$

Le poids de la poutre intervient comme une force constante dans la direction de l'accélération gravitationnelle. Pour faciliter la démonstration, on choisit comme configuration de référence la poutre debout (Fig. E.7(a)) ; l'accélération gravitationnelle s'écrit donc $\mathbf{g} = -g\mathbf{e}_X$. Puisque n, p et q sont exprimés en coordonnées matérielles, la gravité conduit simplement à une force axiale $n = -\rho Ag$.

Afin de mieux comprendre l'influence de la gravité sur les équations du mouvement, celles-ci sont normalisées. Le système adimensionné est écrit :

$$\begin{cases} \ddot{\bar{u}} = (\bar{N}\cos\theta - \bar{T}\sin\theta)' - \alpha, & \text{(E.35a)} \\ \ddot{\bar{w}} = (\bar{N}\sin\theta + \bar{T}\cos\theta)' + \bar{p}, & \text{(E.35b)} \\ \eta\ddot{\theta} = \bar{T}(1+e) - \bar{N}\gamma + \bar{M}' + \bar{q}, & \text{(E.35c)} \end{cases}$$

avec :

$$\bar{N} = e/\eta, \quad \bar{T} = \gamma/\mu, \quad \bar{M} = \theta'. \tag{E.36}$$

On peut voir dans les équations ci-dessus que le système ne dépend que de trois paramètres indépendants, η, μ et α, définis comme :

$$\eta = \frac{I}{AL^2}, \qquad \mu = \frac{EI}{kGAL^2} = \frac{2(1+\nu)\eta}{k}, \qquad \alpha = \frac{\rho g A L^3}{EI} = \frac{\rho g L}{E\eta}, \tag{E.37}$$

où ν représente le coefficient de Poisson du matériau, avec, pour un matériau isotrope homogène, $G = E/[2(1+\nu)]$. Pour une section rectangulaire, η peut être réécrit :

$$\eta = \frac{I}{AL^2} = \frac{bh^3/12}{bhL^2} = \frac{1}{12}\left(\frac{h}{L}\right)^2, \tag{E.38}$$

avec h l'épaisseur de la section et b la largeur. η peut être plus facilement interprété comme un paramètre d'élancement : plus la poutre est fine, c'est-à-dire plus le rapport épaisseur/longueur h/L est petit, plus η est petit. Le deuxième paramètre, μ, représente le rapport entre la raideur de la poutre en flexion et sa raideur en cisaillement et est entièrement lié à la cinématique de Timoshenko. Si une cinématique d'Euler-Bernoulli avait été utilisée, la raideur en cisaillement serait infinie, conduisant à $\mu = 0$ et $\gamma = 0$.

En revenant à la définition du vecteur d'accélération gravitationnelle $\mathbf{g}$ et à la Fig. E.7, on peut voir que les Eqs. (E.35) s'appliquent également à la configuration suspendue simplement en changeant le signe de g et, donc, le signe de α. Par conséquent, une configuration debout est obtenue lorsque $\alpha > 0$ et une configuration suspendue lorsque $\alpha < 0$, comme montré dans la Fig. E.7.

E.4.2 Effet de (α, η) sur les backbones non linéaires

On se tourne maintenant vers les effets de l'élancement et de la gravité sur la dynamique *non linéaire* de la poutre encastré-libre élancée. Lorsque le déplacement de la poutre devient suffisamment grand, les non linéarités géométriques sont activées. On choisit ici de se concentrer sur les *modes non linéaires* de la poutre encastrée-libre, représentés ici par les backbones et les déformées modales non linéaires.

Effet du paramètre adimensionné η Tout d'abord, on étudie l'effet isolé du paramètre d'élancement adimensionné η sur le premier mode non linéaire. L'effet de la gravité est donc négligé, c'est-à-dire α est fixé à 0. L'amplitude de la première harmonique H1 est tracée pour le degré de liberté de rotation θ à l'extrémité de la poutre, c'est-à-dire l'emplacement du déplacement maximal sur une poutre encastrée-libre, pour plusieurs valeurs de η. La backbone en θ est représentée pour le premier mode non linéaire dans la Fig. E.8(a). À celle-ci s'ajoute également la backbone du premier mode non linéaire pour le degré de liberté de déplacement transverse $\bar{w}$ à l'extrémité de la poutre dans la Fig. E.8(b).

On peut voir que l'effet de η sur les backbones du mode 1 (Fig. E.8) est très léger, presque impossible à distinguer tant que η reste petit ($\eta \leq 10^{-5}$). L'effet de η sur les backbones n'apparaît que pour des valeurs plus grandes de η, c'est-à-dire lorsque la poutre devient moins élancée. Un calcul analytique des backbones est également inclus dans la Fig. E.8, représenté par la courbe en pointillés noirs et basé sur le modèle approximatif de poutre inextensible de [46], [47] restreint au premier mode de flexion. (voir annexe B.3 pour plus de détails sur ce modèle). Dans ce modèle, les non linéarités géométriques sont tronquées dans les développements de la série de Taylor à l'ordre 3 en w/L, ce qui fait que ce

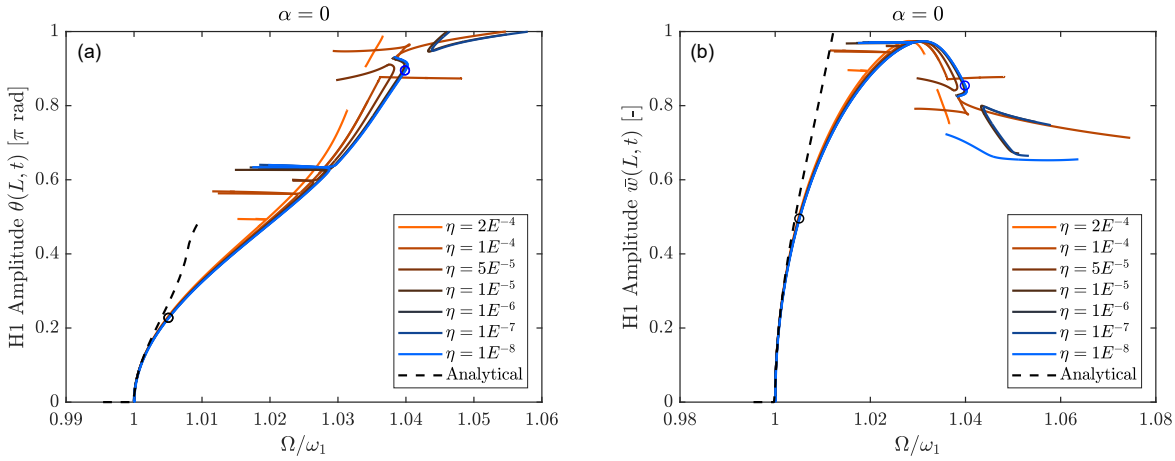

Figure E.8: Effet du paramètre d'élancement η sur le premier mode non linéaire : (a) amplitude de la première harmonique de θ à l'extrémité de la poutre pour différentes valeurs de η et comparaison au modèle de poutre inextensible (analytique) [46], [47], (b) amplitude de la première harmonique de $\bar{w}$ à l'extrémité de la poutre pour différentes valeurs de η. Cas sans gravité ($\alpha = 0$).

modèle n'est valable qu'à des amplitudes de vibration modérées et s'écarte de la courbe numérique géométriquement exacte (autour de $\theta = 0.2\pi$ rad et $w = 0.5L$ à l'extrémité de la poutre). Ce modèle est inclus afin de valider le modèle géométriquement exact à faibles amplitudes de mouvement.

Effet du paramètre adimensionné α Ensuite, on étudie l'influence du paramètre de gravité adimensionné α sur les trois premiers modes non linéaires de la poutre encastrée-libre. Un $\eta = 10^{-7}$ constant est sélectionné et les backcones H1 pour le degré de liberté de rotation θ à l'extrémité de la poutre (analogues aux backbones de la section précédente) sont représentées pour différentes valeurs de α. Les résultats sont résumés pour le mode 1 dans la Fig. E.9. La backbone du mode 1 pour $(\alpha, \eta) = (0, 10^{-7})$ est la même dans les deux Figs. E.8 (a) et E.9.

On peut voir sur le premier mode non linéaire que le paramètre de gravité sans dimension α a un effet important sur la backbone, bien plus que η dans la section précédente. On peut voir que, en notant que la backbone $\alpha = 0$ est déjà de type raidissant, l'augmentation de α dans une configuration debout augmente la tendance raidissante de la backbone de manière considérable. De la même manière, diminuer α dans une configuration suspendue (c'est-à-dire diminuer α négatif) diminue cette tendance (la backbone devient plus assouplissante), jusqu'à ce que la backbone devienne finalement globalement assouplissante au lieu de la backbone raidissante classique du mode 1. De plus, une comparaison est faite avec les approximations de Santillan *et al.* [204] et Luongo *et al.* [146] comme indiqué dans [204] pour la poutre encastrée-libre. Dans la Fig. E.9(c), le déplacement transverse maximal à l'extrémité de la poutre sur une période pour $\eta = 10^{-7}$ est calculé et comparé à la Fig. 5 de [204]. La même comparaison est effectuée pour la Fig. 7 de [204] pour trois valeurs non nulles de $\alpha = [1.655, 2.989, 5.859]$ dans la Fig. E.9(d). Jusqu'à de très grandes amplitudes, on peut voir qu'il y a un excellent accord entre nos résultats et le calcul différences finies de [204]. Les différences à haute amplitude sont probablement dues à la méthode d'intégration temporelle utilisée dans [204], qui n'imposait pas la périodicité de la réponse (ou l'invariance), propriété utilisée ici pour calculer les modes non linéaires.

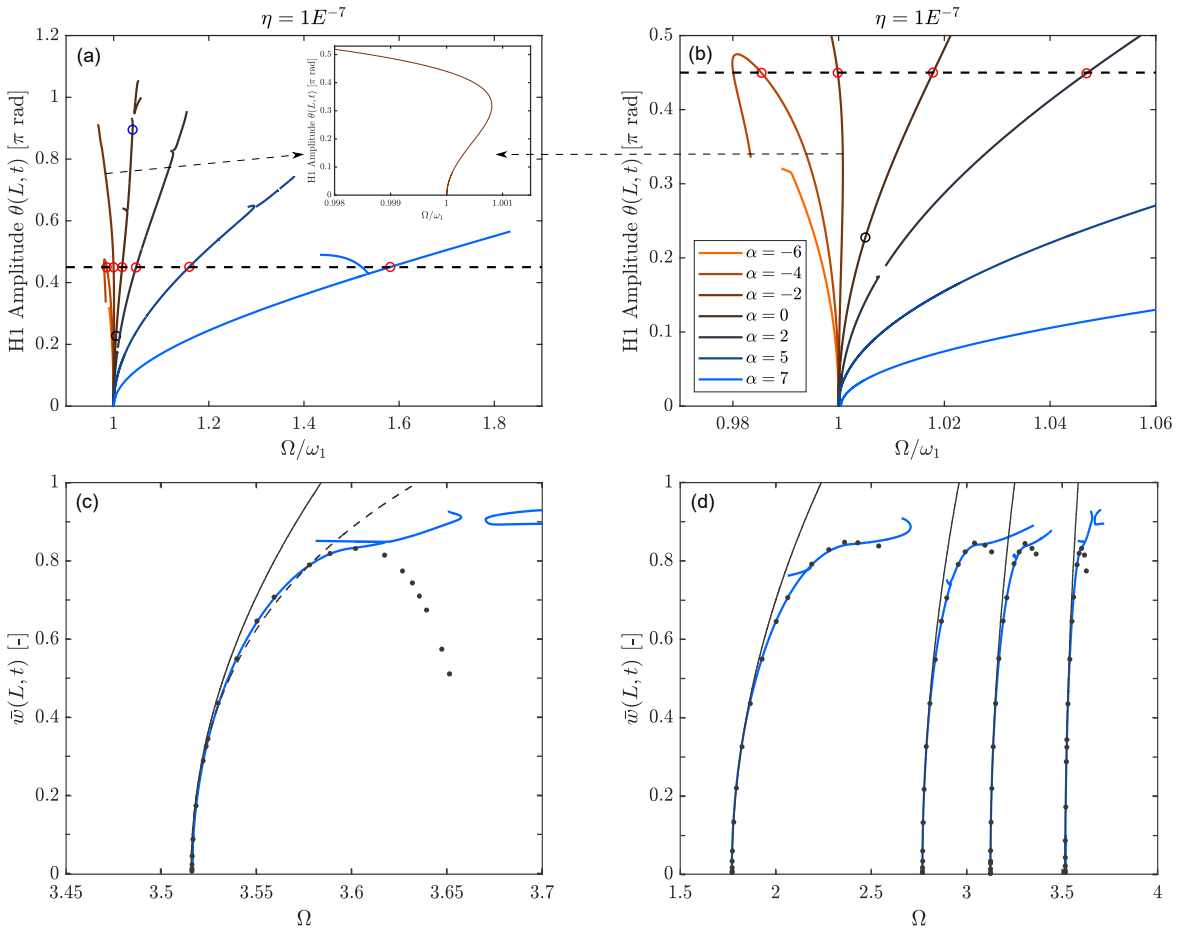

Figure E.9: Effet du paramètre de gravité α sur le premier mode non linéaire : (a) amplitude de la première harmonique H1 de θ à l'extrémité de la poutre pour différentes valeurs de α avec zoom sur l'effet raidissant-assouplissant pour $\alpha = -2$, (b) zoom sur (a) à basses amplitudes. Comparaison ($\eta = 10^{-7}$) aux résultats de Santillan *et al.* [204] et Luongo *et al.* [146]: (c) déplacement transverse maximal à l'extrémité sur une période d'oscillation pour $\alpha = 0$ (courbe noire : approximation avec une méthode de perturbation [204], courbe pointillée : différences finies [204], courbe en ronds : approximation analytique [146], courbe bleue : $\eta = 10^{-7}$ backbone de la Fig. E.8), (d) pareil que (c) mais pour (de gauche à droite) $\alpha = 5.859, 2.989, 1.655, 0$.

E.4.3 Effet de α sur la déformée modale non linéaire

Il est également intéressant d'étudier l'effet de la gravité sur la déformée modale non linéaire de la poutre. Vu les résultats des sections précédentes, on choisit de se concentrer ici principalement sur l'influence de α sur le premier mode non linéaire pour un $\eta = 10^{-7}$ donné.

Pour étudier l'effet du paramètre de gravité α sur la déformée modale de la poutre, la déformée est tracée pour un point à amplitude (presque) constante (autour d'une amplitude H1 maximale de 0.45 π rad) à travers toutes les backbones $\alpha \in \{-4, -2, 0, 2, 5, 7\}$; les points choisis sont représentés par des cercles rouges dans la Fig. E.9(a). Toutes les déformées sont rassemblées dans la Fig. E.10.

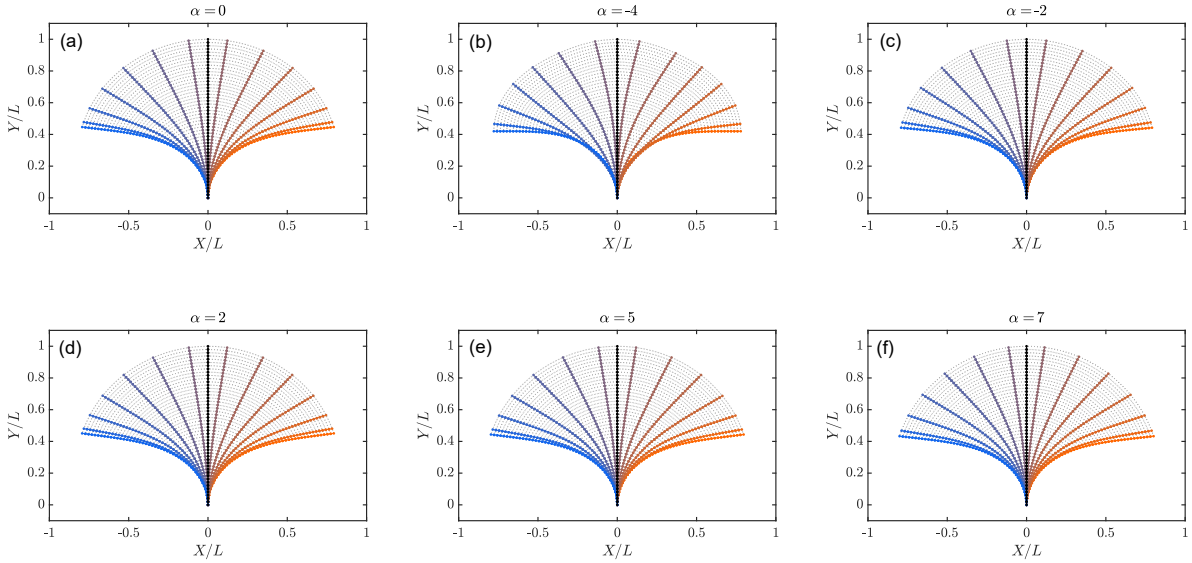

Figure E.10: Déformées modales de la poutre encastrée-libre vibrant sur son premier mode non linéaire pour différentes valeurs de α. Les emplacements sur les backbones correspondantes où les déformées modales sont tracées sont marqués par des cercles rouges dans la Fig. E.9(a).

On observe tout de suite que les déformations de la poutre dans la Fig. E.10 sont presque impossibles à distinguer malgré les points pris à des fréquences très différentes. Par exemple, la déformée modale pour $\alpha = 0$ (Fig. E.10(a)) est tracée à une fréquence de $\Omega/\omega_1 = 1.0179$, tandis que la déformée modale pour $\alpha = 7$ (Fig. E.10(f)) est tracée à une fréquence de $\Omega/\omega_1 = 1.5814$, 1.61 fois plus grande, mais les déformées modales restent presque identiques. Entre les Figs. E.10(a)-(f), seul l'effet de α, *i.e.* de la gravité, change ; comparer les Figs. E.9 et E.10 prouve que, bien que l'effet de changer α influence la backbone, *la déformée modale du mode non linéaire n'est essentiellement pas influencée par la gravité.*

E.5 Dynamique non linéaire des structures de poutres flexibles en 3D avec paramétrisation par quaternions des termes de rotation

Dans le chapitre 3, on a dérivé et implémenté une discrétisation par éléments finis du modèle de poutre géométriquement exact limité aux mouvements dans le plan en deux dimensions (2D). La prochaine étape consiste donc à développer le modèle de manière à étendre les mouvements 2D à trois dimensions (3D). En 2D, les rotations sont paramétrées avec des matrices de rotation classiques, mais celles-ci deviennent assez complexes lorsqu'on étend le mouvement en 3D car la poutre est capable de tourner de trois manières (rotations autour des deux directions transverses et torsion autour de la direction longitudinale de la poutre) contre une seule rotation en 2D. De nombreuses méthodes différentes ont donc été proposées dans la littérature pour la paramétrisation des rotations en 3D, dont certaines ont été introduites dans la section 1.2.1 : angles d'Euler, paramètres de Rodrigues, quaternions unitaires, groupes de Lie, *etc.* Dans ce chapitre, on choisit de paramétrer les rotations en 3D avec quaternions, nombres complexes à 4 dimensions qui représentent exactement les termes de rotation. Les quaternions sont souvent employés dans la modélisation de structures flexibles [45], [100], [132], [197], [261], [263], mais leur mise en œuvre pour la simulation dynamique de structures hautement flexibles basée sur le modèle de poutre géométriquement exact n'a été faite que récemment [253]. Il est particulièrement intéressant (et n'a pas été fait dans la littérature à la connaissance des auteurs) de résoudre cette formulation géométriquement exacte basée sur les quaternions dans le domaine fréquentiel afin de cibler des solutions périodiques des équations du mouvement. Ce dernier est précisément le principal objectif de ce chapitre.

La première partie de ce chapitre est consacrée à la dérivation des équations du mouvement pour des mouvements 3D généraux. La dérivation présentée ici est basée sur la formulation de Géradin et Cardona [101] et représente une extension à la dynamique des travaux de Cottanceau *et al.* [45]. La dérivation générale des équations est donnée dans la section 5.1 analogue aux dérivations des chapitres 2 et 3. Certains détails sont omis de la section 5.1 pour simplifier, mais le lecteur est renvoyé à [101] pour en savoir plus. La paramétrisation de la rotation par quaternions est ensuite introduite dans la section 5.2 et les équations de poutre sont réécrites en utilisant les quaternions. Les quaternions manifestent une algèbre spéciale possédant de nombreuses propriétés spécifiques ; seuls les plus importants d'entre eux sont abordés dans la section 5.2, mais le lecteur intéressé peut se référer à [45], [100], [101] et aux références qui y sont citées pour plus de détails. Une fois les équations dérivées, elles sont discrétisées en éléments finis dans la section 5.3 suivant un processus très similaire à celui décrit dans la section 2.2.1 et la section 3.2.2.

Afin de pouvoir comparer à la formulation 2D du chapitre 3, les équations du mouvement 3D avec quaternions sont réduites aux mouvements 2D dans le plan dans la section 5.4 en fixant les degrés de liberté appropriés (c'est-à-dire déplacements et rotations hors du plan) à zéro. Le modèle EF 3D de la section 5.3 et le modèle EF 2D de la section 5.4 sont ensuite testés à l'aide de deux cas tests trouvés dans la littérature : une poutre encastrée-libre [244] et une poutre bi-encastrée [217] en résonance interne "one-to-one" (1:1). Les cas tests (en 2D) sont également comparés aux cas tests 2D de la section 3.3 puisque ce modèle a été largement validé avec de nombreuses comparaisons à la littérature dans les chapitres 3 et 4. Les réflexions finales et les limites du modèle 3D actuel sont résumées dans la section 5.6.

Quelques sections du chapitre 5 et des résultats clés sont traduits ci-dessous.

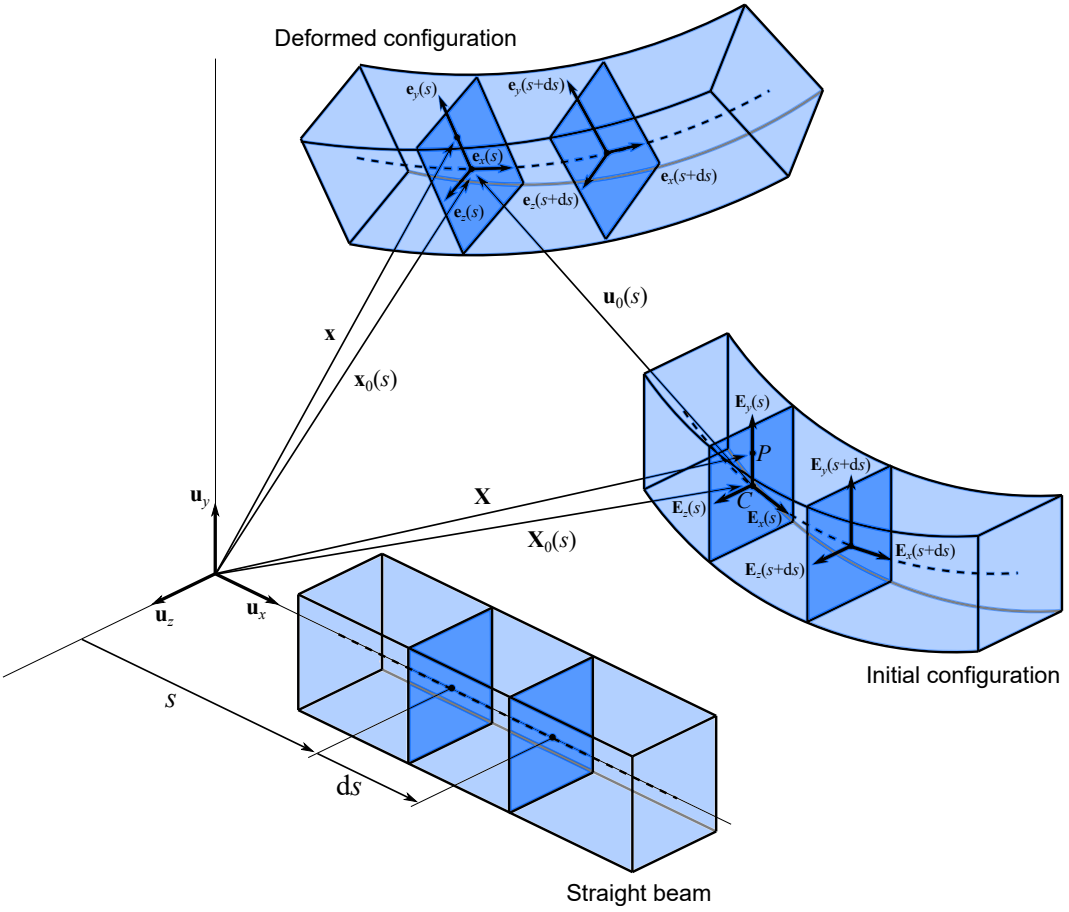

Figure E.11: Cinématique en 3D.

E.5.1 Paramétrisation des rotations avec quaternions

On étend ici la cinématique des chapitres précédents en trois dimensions (3D), représentée dans la Fig. E.11. En se basant sur le même modèle géométriquement exact, on peut procéder directement à la paramétrisation des rotations en 3D. Plutôt que d'étendre en 3D la paramétrisation classique avec matrices de rotations utilisée dans le modèle 2D des sections E.2 et E.3, une nouvelle méthode pour réaliser la paramétrisation des rotations est proposée basée sur les quaternions unitaires.

E.5.1.1 Définitions générales avec quaternions

Le quaternion représente une manière alternative de décrire les rotations finies, semblable à l'utilisation des paramètres d'Euler [101]. Le quaternion peut être défini comme un nombre complexe à 4 dimensions, la somme d'un terme scalaire (a_0) et d'un vecteur à 3 éléments ($\mathbf{a}$) :

$$\hat{\mathbf{a}} = a_0 + \mathbf{a} = a_0 + a_1 i + a_2 j + a_3 k, \tag{E.39}$$

où $\hat{\mathbf{a}} \in \mathbb{R}^4$ (et, de manière générale, la notation $\hat{\diamond}$) est utilisé pour indiquer un quaternion, a_0, a_1, a_2 et a_3 sont des valeurs scalaires et i, j, k sont des nombres imaginaires tels que $i^2 = j^2 = k^2 = -1$, $jk = -kh = i$, $ki = -ik = j$ et $ij = -ji = k$. [100]. En pratique, les quatre éléments d'un quaternion

donné $\hat{\mathbf{a}}$ peuvent être stockés dans un vecteur à 4 éléments, *e.g.* sous la forme $\hat{\mathbf{a}} = \begin{bmatrix} a_0 & a_1 & a_2 & a_3 \end{bmatrix}^{\mathrm{T}}$. Dans le cas particulier où le terme scalaire $a_0 = 0$, $\hat{\mathbf{a}}$ est appelé un quaternion "pur" ou "vectoriel" et peut être "réduit" de $\mathbb{R}^4$ à l'espace euclidien tridimensionnel $\mathbb{R}^3$ à travers la projection défini ici comme $\mathrm{vec}(\diamond) : \mathbb{R}^4 \mapsto \mathbb{R}^3$, de sorte que $\mathrm{vec}(\hat{\mathbf{a}}) = \mathbf{a}$. De même, tout vecteur $\mathbf{p}$ de l'espace $\mathbb{R}^3$ peut être "étendu" à un quaternion dans l'espace $\mathbb{R}^4$ en considérant $\hat{\mathbf{p}} = 0 + \mathbf{p}$. Ces propriétés seront largement utilisées pour transformer des quantités dans l'espace $\mathbb{R}^3$ dans les équations du mouvement Eqs. (5.9) en quaternions dans $\mathbb{R}^4$ et vice versa.

Les multiplications de quaternions, notées par l'opérateur $\circ$ (différentes du produit scalaire, noté par l'opérateur $\cdot$), peuvent être écrites en utilisant la définition du quaternion [Eq. (E.39)] [100], mais sont réalisées en pratique sous forme de multiplications matricielles en utilisant les transformations notées Φ_L et Φ_R (multiplications "gauche" et "droite", respectivement) dans une méthode analogue au produit vectoriel entre les vecteurs dans $\mathbb{R}^3$. Introduisant la notation $\tilde{\diamond}$ pour indiquer la transformation d'un vecteur à 3 éléments en une matrice asymétrique (c'est-à-dire l'opération inverse de $\mathrm{vect}(\diamond)$), les opérations Φ_L et Φ_R entre deux quaternions $\hat{\mathbf{a}}$ et $\hat{\mathbf{b}}$ sont définies comme :

$$\begin{aligned} \hat{\mathbf{a}} \circ \hat{\mathbf{b}} = \Phi_L(\hat{\mathbf{a}})\hat{\mathbf{b}} &= \begin{bmatrix} a_0 & -\mathbf{a}^{\mathrm{T}} \\ \mathbf{a} & a_0\mathbf{I}_3 + \tilde{\mathbf{a}} \end{bmatrix} \begin{bmatrix} b_0 \\ \mathbf{b} \end{bmatrix} \\ &= \begin{bmatrix} a_0 & -a_1 & -a_2 & -a_3 \\ a_1 & a_0 & -a_3 & a_2 \\ a_2 & a_3 & a_0 & -a_1 \\ a_3 & -a_2 & a_1 & a_0 \end{bmatrix} \begin{bmatrix} b_0 \\ b_1 \\ b_2 \\ b_3 \end{bmatrix}, \end{aligned} \tag{E.40a}$$

(E.40b)

$$\begin{aligned} \hat{\mathbf{a}} \circ \hat{\mathbf{b}} = \Phi_R(\hat{\mathbf{b}})\hat{\mathbf{a}} &= \begin{bmatrix} b_0 & -\mathbf{b}^{\mathrm{T}} \\ \mathbf{b} & b_0\mathbf{I}_3 - \tilde{\mathbf{b}} \end{bmatrix} \begin{bmatrix} a_0 \\ \mathbf{a} \end{bmatrix} \\ &= \begin{bmatrix} b_0 & -b_1 & -b_2 & -b_3 \\ b_1 & b_0 & b_3 & -b_2 \\ b_2 & -b_3 & b_0 & b_1 \\ b_3 & b_2 & -b_1 & b_0 \end{bmatrix} \begin{bmatrix} a_0 \\ a_1 \\ a_2 \\ a_3 \end{bmatrix}. \end{aligned} \tag{E.40c}$$

Un "conjugué" à un quaternion est également défini, indiqué par l'astérisque $\diamond^*$, tel que $\hat{\mathbf{a}}^* = a_0 - \mathbf{a}$ pour tout quaternion général $\hat{\mathbf{a}}$.

E.5.1.2 Rotations écrites avec quaternions

Les quaternions possèdent un sous-groupe unitaire pratique pour paramétrer les opérateurs de rotation $\mathbf{R}$ et $\mathbf{R}_0$, notamment grâce à la possibilité de décrire les rotations avec seulement 4 éléments (contre les 9 éléments d'une matrice de rotation classique) tout en lui restant exactement équivalent. Cette capacité peut conduire à une plus grande efficacité de calcul des rotations, puisque beaucoup moins d'opérations (multiplications et additions) sont nécessaires [203]. Pour décrire la rotation, on utilise le quaternion $\hat{\mathbf{q}}$, qui prend la forme :

$$\hat{\mathbf{q}} = \cos\left(\frac{\theta}{2}\right) + \sin\left(\frac{\theta}{2}\right)\mathbf{n} = \begin{bmatrix} q_0 & q_1 & q_2 & q_3 \end{bmatrix}^{\mathrm{T}}, \tag{E.41}$$

avec $\mathbf{n}$ le vecteur unitaire décrivant l'axe de rotation et θ l'angle de rotation autour de l'axe défini par $\mathbf{n}$. Notez que l'Eq. (E.41) représente ce qu'on appelle un *quaternion unitaire*, tel que $|\hat{\mathbf{q}}| = \hat{\mathbf{q}} \cdot \hat{\mathbf{q}} = 1$.

Cette observation introduit une contrainte d'unité liée à $\hat{\mathbf{q}}$, puisque les quatre éléments de $\hat{\mathbf{q}}$ ne sont pas indépendants. Avec $\hat{\mathbf{q}}$ défini dans l'Eq. (E.41), l'opération de rotation $\mathbf{R}$ pour faire pivoter un vecteur $\mathbf{p}$ dans le vecteur $\mathbf{p}_r$ tel que $\mathbf{p}_r = \mathbf{R}\mathbf{p}$ est réécrite dans l'algèbre des quaternions :

$$\hat{\mathbf{p}}_r = \hat{\mathbf{q}} \circ \hat{\mathbf{p}} \circ \hat{\mathbf{q}}^*, \tag{E.42}$$

où $\circ$ est utilisé pour indiquer une multiplication entre deux quaternions. Une observation clé est faite à ce stade : si $\hat{\mathbf{p}}$ est un quaternion pur ($p_0 = 0$) et $\hat{\mathbf{q}}$ un quaternion unitaire, alors $\hat{\mathbf{p}}_r$ est également un quaternion pur et $\text{vec}(\hat{\mathbf{p}}_r) = \mathbf{p}_r$ est le vecteur pivoté à partir de $\mathbf{p} = \text{vec}(\hat{\mathbf{p}})$.

Dans la même logique, une rotation opposée pour faire pivoter $\mathbf{p}_r$ vers $\mathbf{p}$, ou $\mathbf{p} = \mathbf{R}^{\mathrm{T}}\mathbf{p}_r$ s'écrit dans l'algèbre des quaternions sous la forme :

$$\hat{\mathbf{p}} = \hat{\mathbf{q}}^* \circ \hat{\mathbf{p}}_r \circ \hat{\mathbf{q}}. \tag{E.43}$$

Les opérations de rotation dans la formulation quaternion telles que définies dans les Eqs. (E.42) et (E.43) peuvent ensuite être réécrites sous forme de multiplications matricielles :

$$\hat{\mathbf{p}}_r = \hat{\mathbf{q}} \circ \hat{\mathbf{p}} \circ \hat{\mathbf{q}}^* = \underbrace{\Phi_R(\hat{\mathbf{q}}^*)\Phi_L(\hat{\mathbf{q}})}_{\mathbf{R}}\hat{\mathbf{p}}, \tag{E.44a}$$

$$\hat{\mathbf{p}} = \hat{\mathbf{q}}^* \circ \hat{\mathbf{p}}_r \circ \hat{\mathbf{q}} = \underbrace{\Phi_R(\hat{\mathbf{q}})\Phi_L(\hat{\mathbf{q}}^*)}_{\mathbf{R}^T}\hat{\mathbf{p}}_r. \tag{E.44b}$$

En se basant sur les 4 éléments du quaternion unitaire $\hat{\mathbf{q}}$ [Eq. (E.41)] et en utilisant les opérations $\Phi_L(\hat{\mathbf{q}})$ et $\Phi_R(\hat{\mathbf{q}}^*)$, il est montré dans [203] que les 9 éléments équivalents de $\mathbf{R}$ sous forme de matrice de rotation 3D peuvent s'écrire :

$$\mathbf{R} = \begin{bmatrix} q_0^2+q_1^2-q_2^2-q_3^2 & 2(-q_0q_3+q_1q_2) & 2(q_0q_2+q_1q_3) \\ 2(q_0q_3+q_2q_1) & q_0^2-q_1^2+q_2^2-q_3^2 & 2(-q_0q_1+q_2q_3) \\ 2(-q_0q_2+q_3q_1) & 2(q_0q_1+q_3q_2) & q_0^2-q_1^2-q_2^2+q_3^2 \end{bmatrix}, \tag{E.45}$$

ce qui souligne l'efficacité de stockage du quaternion à 4 éléments [Eq. (E.41)] par comparaison.

E.5.2 Cas test : modes elliptiques d'une poutre encastrée-libre

Le système étudié est la poutre encastrée-libre classique (initialement droite) avec une extrémité fixe et l'autre libre. Avec la ligne moyenne de la poutre alignée avec la direction $\mathbf{u}_x$ telle que $(\mathbf{u}_x, \mathbf{u}_y, \mathbf{u}_z) = (\mathbf{E}_x, \mathbf{E}_y, \mathbf{E}_z)$ selon la Fig. E.11, la poutre est capable de se déformer dans deux directions transverses orthogonales, $\mathbf{E}_y$ et $\mathbf{E}_z$. Pour une poutre de section parfaitement carrée ($b = h$ où b est la largeur de la poutre (la dimension dans la direction $\mathbf{E}_z$) et h son épaisseur (la dimension le long de $\mathbf{E}_y$)), les pulsations propres et le mouvement sur chaque mode de flexion sont identiques dans chacune des polarisations transverses. Afin de "créer" le couplage de résonance interne 1:1, une petite asymétrie [217], [244] est imposée en brisant très légèrement la symétrie entre b et h. Ce faisant, les deux polarisations transverses deviennent légèrement éloignées, dans la mesure où les pulsations propres et les déformées modales sont légèrement séparées. Ensuite, lorsqu'un mode transverse non linéaire est excité, à une certaine amplitude de vibration (correspondant à une certaine évolution de la fréquence d'oscillation) une intersection ou "detuning" entre les deux modes est induit de telle sorte que les deux fréquences de résonance des modes non linéaires se croisent et le deuxième mode (c'est-à-dire le mode de flexion jumeau dans l'autre direction transverse) est excité à son tour.

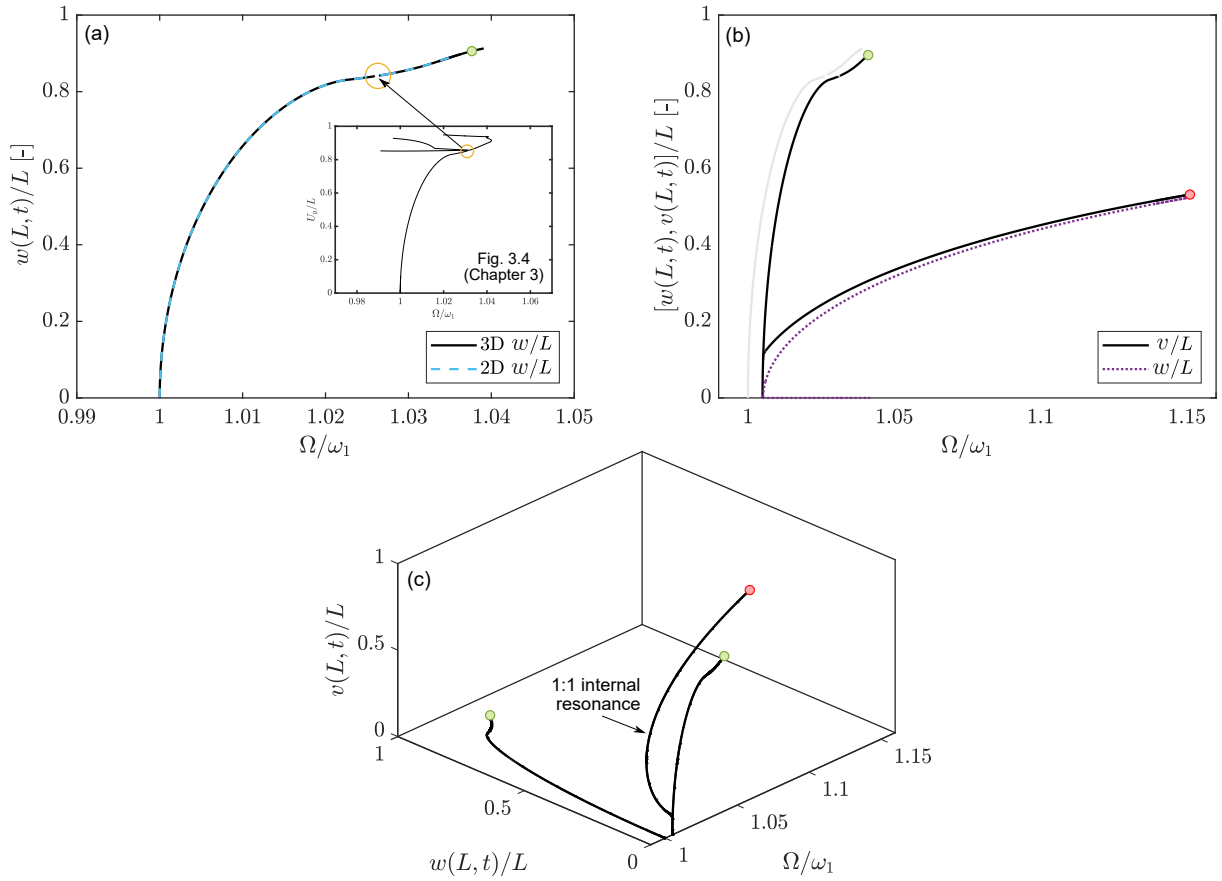

Figure E.12: Premiers modes de flexion non linéaires d'une poutre encastrée-libre dans les deux polarisations transverses, (a) premier mode de flexion dans une polarisation : amplitude maximale de $w(L,t)/L$ sur une période d'oscillation en 2D et en 3D, zoom : backbone U_y/L de la section 3.3.1 pour comparer la résonance interne à grande amplitude, (b) deuxième polarisation du mode de flexion : amplitudes maximales de $w(L,t)/L$ et $v(L,t)/L$ sur une période d'oscillation et résonance interne 1:1, (c) visualisation 3D des backbones.

Pour visualiser ce phénomène, la poutre de Vincent *et al.* [244] est utilisée, une poutre de longueur $L = 1$ m avec section presque carrée est modélisée ($h = 0.03$ m et $b = 0.03015$ m), conduisant à un désaccord de 0.05% dans la symétrie de la section carrée. Le système est normalisé par sa longueur caractéristique, ici la longueur de la poutre L. Les deux premières pulsations propres linéaires (sans dimension) correspondant au premier mode de flexion transverse dans $\mathbf{E}_y$ et $\mathbf{E}_z$ sont respectivement $\omega_1 = 3.5144$ et $\omega_2 = 3.5320$ (un désaccord de 0.5% entre les pulsations propres).

En commençant par le premier mode non linéaire, la backbone en déplacement transverse adimensionné en $\mathbf{E}_y$ à l'extrémité de la poutre $w(L,t)/L$ (calculée comme le maximum de la valeur absolue du déplacement sur une période d'oscillation) est indiquée dans la Fig. E.12(a). Le même comportement non linéaire que celui trouvé dans la section 3.3.1 du chapitre 3 est récupéré à la fois en 2D et en 3D : la tendance raidissante bien connue du premier mode non linéaire de la poutre encastrée-libre [58], [59], [229] est récupérée.

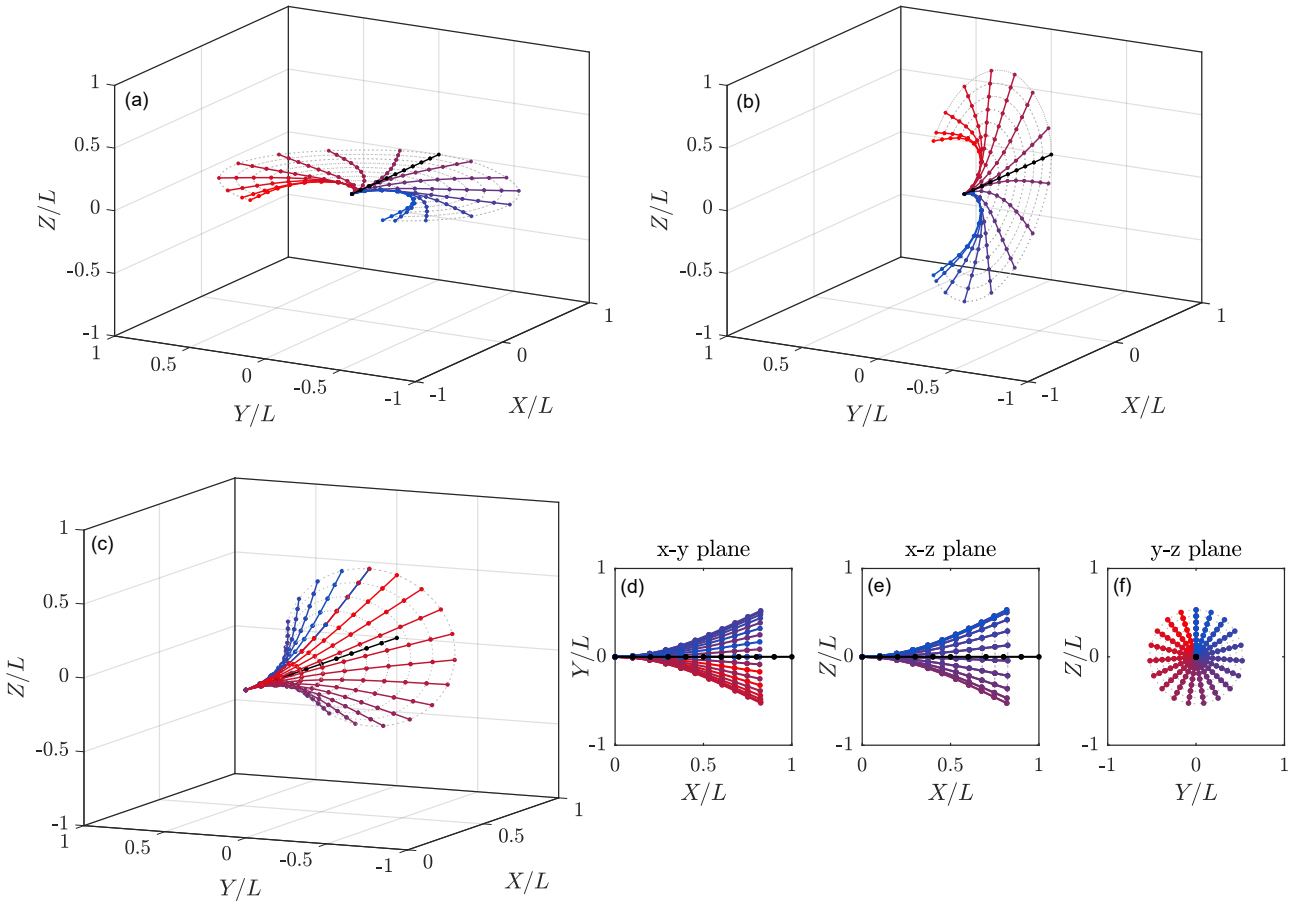

Figure E.13: Déformées modales de la poutre encastrée-libre, (a) à grande amplitude sur la première polarisation (cercle vert dans la Fig. E.12(a)), (b) à grande amplitude sur la deuxième polarisation (cercle vert dans la Fig. E.12(b)), (c)-(f) résonance interne 1:1 entre les polarisations et projections dans les plans (cercle rouge dans la Fig. E.12(b)).

La déformée modale de la poutre encastrée-libre est également tracée à très grande amplitude et représentée dans la Fig. E.13(a) et (b) pour les deux polarisations transverses. Les amplitudes le long des backbones de la Fig. E.12 auxquelles les déformées modales sont prises sont marquées par des cercles verts.

Le deuxième mode non linéaire de la poutre encastrée-libre en 3D est plus intéressant car c'est sur ce mode que se manifeste la résonance interne 1:1. Le deuxième mode non linéaire est représenté dans la Fig. E.12(b), où à la fois le déplacement transverse en $\mathbf{E}_y$ w/L et le déplacement transverse en $\mathbf{E}_z$ v/L sont représentés. On voit bien qu'à une certaine amplitude dans $v(L,t)$, il y a un transfert d'énergie vers le premier mode de flexion non linéaire, illustré par le décollage de déplacement $w(L,t)$ dans l'autre polarisation. À ce stade, la poutre encastrée-libre commence à tourner selon un mouvement elliptique, illustré dans la Fig. E.13(c). L'amplitude à laquelle la Fig. E.13(c) est tracée est marquée par un cercle rouge dans la Fig. E.12(b). La Fig. E.13 illustre à la fois la déformée en 3D et, en Fig. E.13(d)-(f), les projections de la déformée dans chaque plan afin de mieux visualiser le mouvement. Dans la

Fig. E.12(b), la résonance interne 1:1 est située à une fréquence de $\Omega/\omega_1 \simeq 1.005$ et à une amplitude de $v/L \simeq 0.1$, correspondant aux résultats de [244]. Les déplacements v/L (en noir) et w/L (en violet) sont tracés ensemble dans la Fig. E.12(b) pour démontrer le transfert d'énergie du mode de direction $\mathbf{E}_z$ vers le mode de direction $\mathbf{E}_y$. Avec seulement une petite différence de 0.5% entre les pulsations propres des deux modes, on peut voir dans la Fig. E.13(c) que la poutre tourne dans un cercle presque parfait puisque les déplacements w et v sont presque équivalents, surtout loin du point de départ de la branche de résonance interne.

Enfin, les backbones sont rassemblées dans une figure 3D dans la Fig. E.12(c) suivant le style de [88]. Chacune des backbones des modes de flexion est fixée dans son plan respectif tandis que la branche de résonance interne 1:1 a des composants à la fois en w et en v. La figure 3D montre clairement le transfert d'énergie d'une polarisation à l'autre.

E.6 Expériences en résonance de phase réalisées sur structures hautement flexibles pour la mesure des modes non linéaires conservatifs et estimation de l'amortissement non linéaire

Jusqu'à présent, on a présenté uniquement les aspects numériques du modèle de poutre géométriquement exact résolu dans le domaine fréquentiel. On cherche maintenant à valider ce modèle numérique avec des résultats expérimentaux. La validation expérimentale apporte un nouveau niveau ce certitude aux modèles numériques puisqu'elle confirme de manière incontestable qu'ils représentent la vraie physique. Dans ce chapitre, le modèle numérique présenté dans les chapitres 2 - 5 pour la simulation de structures élancées hautement flexibles est validé avec des expériences dédiées en vibrations de grande amplitude.

Les expériences de ce chapitre sont réalisées en utilisant des techniques de mesure expérimentale des modes non linéaires (appelés dans ce chapitre modes non linéaires *conservatifs* ou CNM afin de les distinguer des modes non linéaires dissipatifs, un sujet qui est abordé dans la section 6.2). En particulier, nous utilisons le concept connu dans la littérature sous le nom de *résonance de phase*, qui indique essentiellement l'imposition d'un décalage de phase particulier entre le forçage appliqué et la réponse du système afin que les modes non linéaires soient mesurés. Au-delà des effets conservatifs, la résonance de phase peut également être utilisée pour une estimation de l'amortissement, qui historiquement a fait l'objet d'une grande attention. Dans les expériences, la condition de résonance de phase est controllée à l'aide d'une boucle à verrouillage de phase, un algorithme de contrôle vibratoire. Les expériences sont réalisées avec des poutres encastrées-libres élancées en acier inoxydable et les trois premiers modes non linéaires sont étudiés. Les résultats des expériences sont ensuite comparés au modèle numérique des chapitres 3 et 4, notamment avec l'inclusion de la gravité dans le modèle, qui a un effet important sur le premier mode non linéaire comme a été montré dans le chapitre 4.

Le chapitre commence par une revue de l'état actuel de l'art et un aperçu de l'étude incluant les principales originalités de ce travail dans la section 6.1. La théorie derrière la résonance de phase et sa justification pour la mesure des modes non linéaires conservatifs est ensuite présentée dans la section 6.2. Une discussion sur les travaux actuels à ce sujet dans la littérature, y compris la mesure des modes non linéaires amortis, est également présentée dans cette section. Dans la section 6.3, des simulations numériques sont effectuées en utilisant le modèle éléments finis géométriquement exact du chapitre 4 pour valider la résonance de phase pour la mesure des modes non linéaires conservatifs et l'estimation de l'amortissement. Suite à la justification numérique de la résonance de phase dans ce contexte, les expériences réalisées par boucle à verrouillage de phase en vibration de grande amplitude sont décrites dans la section 6.4. Les résultats expérimentaux sont comparés aux simulations numériques en utilisant le modèle du chapitre 4 dans la section 6.5. Les remarques finales et un résumé de l'état actuel des résultats expérimentaux sont rassemblés dans la section 6.6.

Quelques sections du chapitre 6 et des résultats clés sont traduits ci-dessous.

E.6.1 Résonance de phase et le mode non linéaire conservatif

On considère un système non linéaire modélisé par le problème N-dimensionnel ($N \in \mathbb{N}$) suivant :

$$\boldsymbol{M}(\boldsymbol{x})\ddot{\boldsymbol{x}} + \boldsymbol{f}_{\mathrm{d}}(\boldsymbol{x}, \dot{\boldsymbol{x}}) + \boldsymbol{f}_{\mathrm{c}}(\boldsymbol{x}, \dot{\boldsymbol{x}}) = \boldsymbol{f}_{\mathrm{e}}, \tag{E.46}$$

où $\boldsymbol{x}(t)$ est le vecteur de déplacement N-dimensionnel, fonction du temps t, $\dot{\diamond} = \mathrm{d}\diamond/\mathrm{d}t$, $\boldsymbol{M}(\boldsymbol{x})$ est la matrice d'inertie $N \times N$ qui peut dépendre de $\boldsymbol{x}$ en raison des non linéarités inertielles, $\boldsymbol{f}_{\mathrm{d}}(\dot{\boldsymbol{x}}, \boldsymbol{x})$

est le vecteur de force dissipative N-dimensionnel qui dépend de la vitesse $\dot{\boldsymbol{x}}$ et du déplacement $\boldsymbol{x}$, $\boldsymbol{f}_{\mathrm{c}}(\boldsymbol{x},\dot{\boldsymbol{x}})$ est le vecteur de force conservative N-dimensionnel qui dépend de $\boldsymbol{x}$ et de $\dot{\boldsymbol{x}}$ dans le cas des non linéarités inertielles, et $\boldsymbol{f}_{\mathrm{e}}(t)$ est le vecteur de force externe de dimension N qui dépend du temps.

Ces *modes non linéaires conservatifs* (CNM) sont des solutions particulières $\boldsymbol{x}_{\mathrm{cnm}}(t)$ du problème non amorti non linéaire de l'Eq. (E.46) en vibration libre :

$$\boldsymbol{M}(\boldsymbol{x}_{\mathrm{cnm}})\ddot{\boldsymbol{x}}_{\mathrm{cnm}} + \boldsymbol{f}_{\mathrm{c}}(\boldsymbol{x}_{\mathrm{cnm}},\dot{\boldsymbol{x}}_{\mathrm{cnm}}) = \boldsymbol{0}. \tag{E.47}$$

Un CNM donné $\boldsymbol{x}_{\mathrm{cnm}}(t)$ est périodique et monophase [178] et peut être défini comme :

$$\boldsymbol{x}_{\mathrm{cnm}}(t) \simeq \hat{\boldsymbol{x}}_0 + \sum_{h=1}^{H} \hat{\boldsymbol{x}}_h \cos(h\omega t), \tag{E.48}$$

où la série de Fourier ci-dessus a été tronquée en harmoniques H et avec $\hat{\boldsymbol{x}}_h \in \mathbb{R}^N$, $h \in \mathbb{N}$ définissant le vecteur de l'amplitude de la $h$ème harmonique et ω la fréquence angulaire fondamentale.

Si le mouvement est exactement le CNM monophase de l'Eq. (E.48), il prend la forme de l'Eq. (E.47) tel que les termes conservatifs de l'Eq. (E.46) s'équilibrent. Dans ce cas, l'Eq. (E.46) se réduit à :

$$\boldsymbol{f}_{\mathrm{d}}(\boldsymbol{x}_{\mathrm{cnm}},\dot{\boldsymbol{x}}_{\mathrm{cnm}}) = \boldsymbol{f}_{\mathrm{e}} = \sum_{h=1}^{H} \hat{\boldsymbol{f}}_{\mathrm{e}h} \sin(h\omega t), \tag{E.49}$$

avec $\hat{\boldsymbol{f}}_{\mathrm{e}h} \in \mathbb{R}^N$. Dans l'Eq. (E.49), la deuxième égalité est une conséquence directe de $\boldsymbol{f}_{\mathrm{d}}(\boldsymbol{x},\dot{\boldsymbol{x}})$ étant une fonction impaire de $\dot{\boldsymbol{x}}$ (voir annexe D.4). En comparant les Eqs. (E.48) et (E.49), on observe que *le vecteur de force externe associé au mouvement sur un CNM monophasé est également monophase et caractérisé par un décalage de phase de $\pi/2$ de chaque harmonique par rapport à la réponse en déplacement, quelle que soit la forme des forces dissipatives.*

E.6.2 Calcul de la backbone en résonance de phase

Pour calculer les modes non linéaires conservatifs du système, on considère deux possibilités :

- La première méthode (appelée ici méthode A), est la méthode décrite dans le chapitre 3 pour résoudre l'Eq. (6.13) en vibration libre ($\boldsymbol{f}_{\mathrm{e}} = \boldsymbol{0}$) avec un terme d'amortissement correspondant à $\boldsymbol{D}\dot{\boldsymbol{x}} = \lambda\dot{\boldsymbol{x}}$, où $\lambda \in \mathbb{R}$ est un paramètre de bifurcation fictif utilisé pour éviter les instabilités numériques [15]. Dans ce cas, le calcul numérique conduira à une très petite valeur de λ, telle que $\lambda \simeq 0$, puisque les solutions périodiques calculées sont associées à un certain mode non linéaire *conservatif*. Dans ce système autonome, la condition de phase peut prendre plusieurs formes ; celle décrite dans la section 2.2.4 et la section 3.2.3 consiste à mettre à zéro la vitesse d'une composante donnée de $\dot{\boldsymbol{x}}(0)$ (c'est-à-dire $\dot{x}_i(t) = 0$, $i \in \{1,\dots N\}$).
- La deuxième (méthode B) est basée sur la mise en œuvre de la condition de résonance de phase. Pour ce faire, les termes d'amortissement $\boldsymbol{D}\dot{\boldsymbol{x}}$ et de forçage externe $\boldsymbol{f}_{\mathrm{e}}(t)$ doivent être équilibrés en imposant un déphasage de $\pi/2$ avec le déplacement monophase $\boldsymbol{x}(t)$ comme décrit dans la section 6.2. Le système est forcé avec un signal monoharmonique $\boldsymbol{f}_{\mathrm{e}}(t) = \lambda\hat{\boldsymbol{f}}_{\mathrm{e}1}\sin(\omega t)$, avec $\hat{\boldsymbol{f}}_{\mathrm{e}1} \in \mathbb{R}^N$ un vecteur d'amplitude constante et $\lambda \in \mathbb{R}$ un paramètre scalaire utilisé pour moduler l'amplitude du forçage. La condition de phase est choisie telle que la composante sinus de la première harmonique d'une composante donnée de $\boldsymbol{x}(t)$ est fixée à zéro ($[\hat{\boldsymbol{x}}_1^s]_i = 0$, $i \in \{1,\dots N\}$), imposant ainsi naturellement un déphasage $\pi/2$ entre cette composante et le vecteur de forçage de manière à faire respecter la condition de résonance de phase.

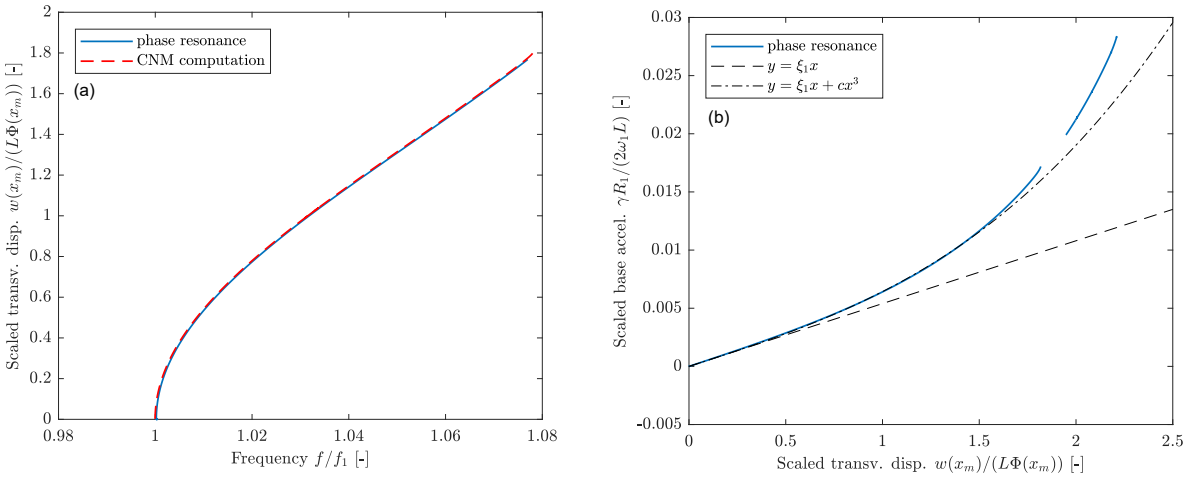

Figure E.14: (a) Backbone du mode 1 calculée par deux stratégies différentes : la stratégie classique des chapitres 3 et 4 (courbe rouge pointillée) et en résonance de phase numérique (courbe bleue) ; (b) accélération de la base en fonction de l'amplitude du déplacement de la poutre obtenue lors du calcul en résonance de phase, et plusieurs fits polynomiaux. La simulation est faite avec $\xi = 0.0054$ pour une poutre de longueur $L = 380$ [mm], largeur $b = 18.1$ [mm], et épaisseur $h = 0.495$ [mm] (corréspondant à la poutre 1 expérimentale) et avec $\alpha = 1.211$.

La Fig. E.14(a) combine en une seule figure le calcul de la backbone d'une poutre encastrée-libre à la fois par la méthode standard A ainsi que par la méthode de résonance de phase B. Les deux courbes se superposent parfaitment l'une sur l'autre sur une très large gamme de fréquences, jusqu'à de très grandes amplitudes de rotation. Cette comparaison valide, sur cet exemple, la méthode de résonance de phase pour calculer un mode non linéaire conservatif.

Dans la Fig. E.14(b), l'amplitude de la première harmonique de l'accélération de la base est tracée en fonction du déplacement transverse de la poutre. Dans un système contenant un amortissement purement linéaire, le déplacement augmenterait proportionnellement à l'accélération et la Fig. E.14 montrerait une relation linéaire (la ligne pointillée) avec la pente de la ligne liée au coefficient d'amortissement linéaire (ξ dans notre amortissement proportionnel à la masse). Dans la Fig. E.14, on voit par contre que cette relation entre l'accélération de la base et le déplacement de la poutre n'est linéaire qu'à très faible amplitude. À des amplitudes plus élevées, elle suit une tendance cubique (devenant finalement un ordre encore plus élevé à des amplitudes extrêmes). Ceci est en accord avec les résultats d'Amabili *et al.* [4], [6]–[9] et [71], où les modèles d'amortissement non linéaires (*e.g.* Kelvin-Voigt dans [71]) doit être utilisés pour faire correspondre les courbes de réponse forcée expérimentales.

E.6.3 Mesure expérimentale des modes non linéaires conservatifs

La mesure expérimentale des CNM en tant que backbones avec résonance de phase est réalisée à l'aide d'une boucle à verrouillage de phase, un algorithme de contrôle vibratoire. En utilisant la boucle à verrouillage de phase, les courbes de réponse forcée ou les backbones peuvent être mesurées expérimentalement. Ici, la boucle à verrouillage de phase est utilisée pour la mesure expérimentale

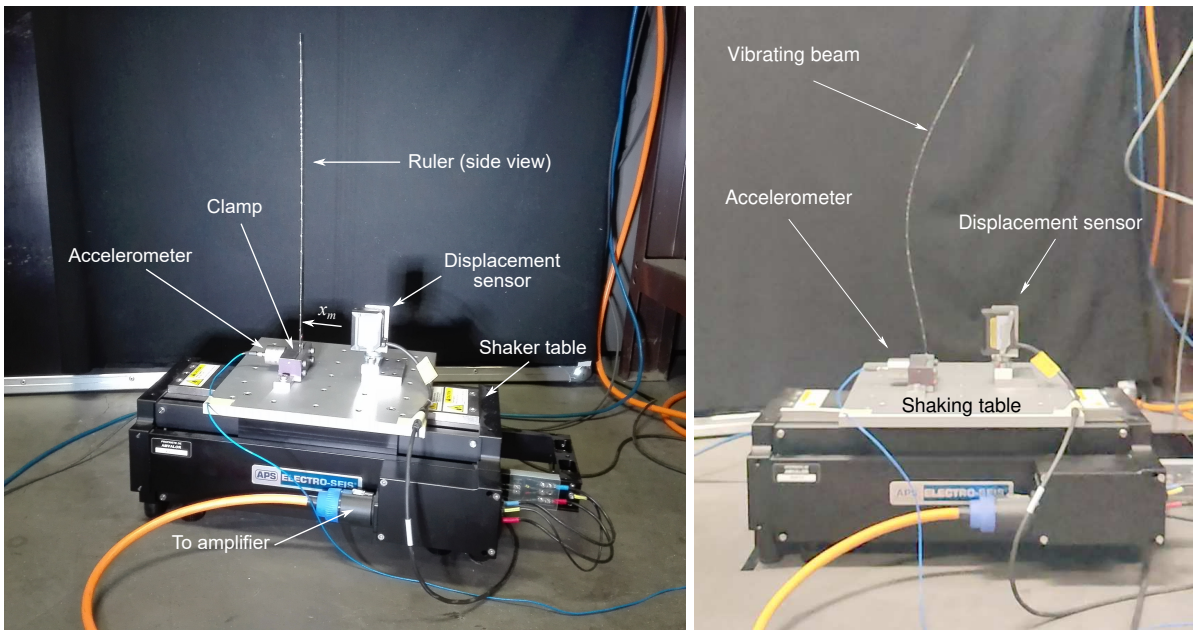

Figure E.15: Vues du dispositif expérimental.

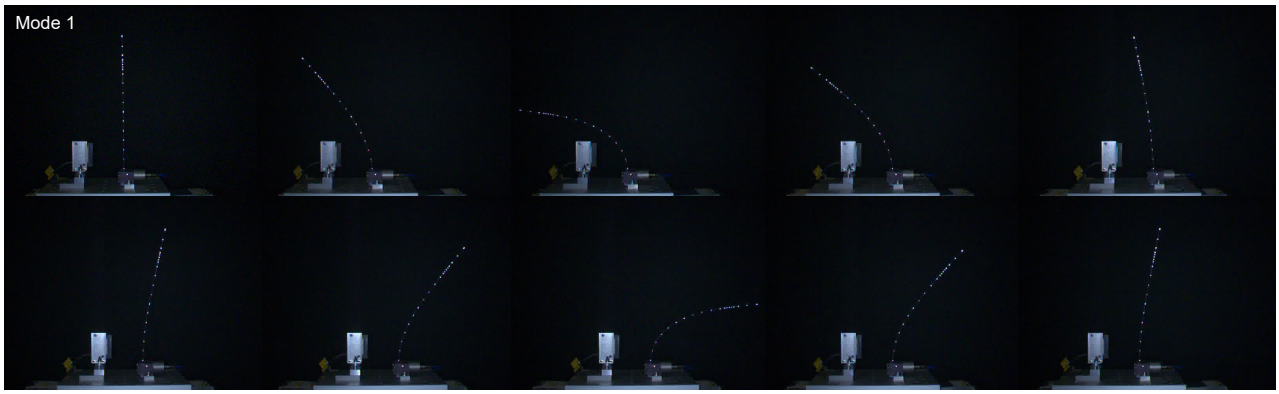

Figure E.16: Mouvement de la poutre encastrée-libre excité par accélération de la base sur son premier mode non linéaire sur $\simeq 1$ période.

des CNM de poutres encastrées-libres hautement flexibles *afin de valider la théorie de la section 6.2* et également *de valider le modèle géométriquement exact des travaux antérieurs* (chapitres 3 et 4). Les expériences sont réalisées avec trois poutres de géométrie différente.

Le montage expérimental ainsi que quelques exemples d'expériences en cours sont visibles dans les Figs. E.15 et E.16.

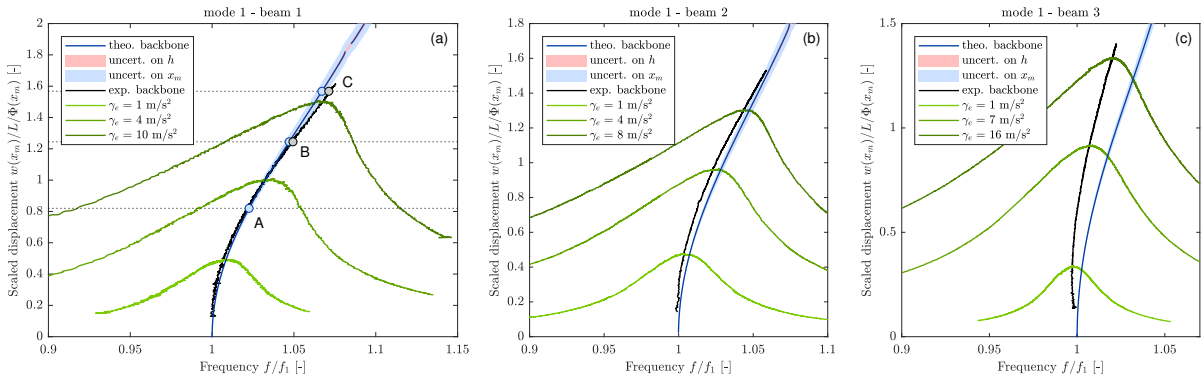

Figure E.17: Réponses forcées non linéaires expérimentales, pour plusieurs accélérations de la base, et backbones du premier mode non linéaire comparées à la backbone théorique : (a) poutre 1, (b) poutre 2, (c) poutre 3.

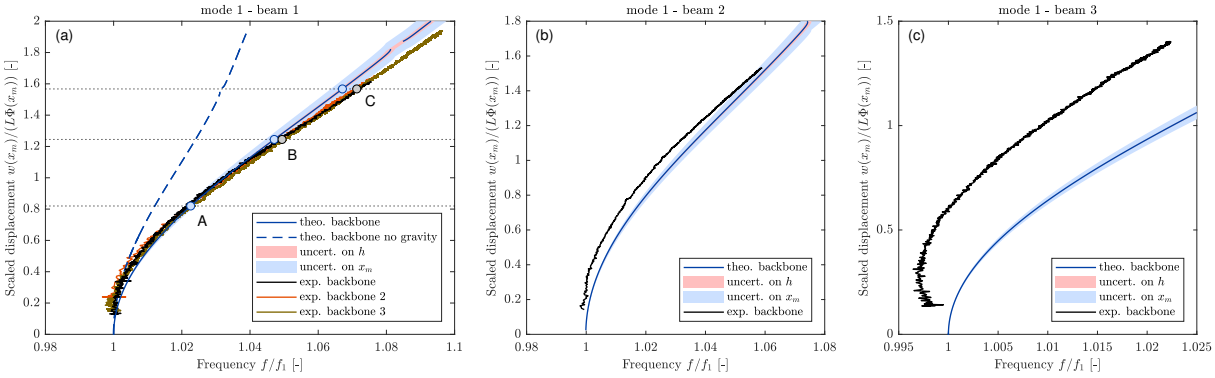

Figure E.18: Backbones expérimentales du premier mode non linéaire comparées à la backbone théorique : (a) poutre 1, (b) poutre 2, (c) poutre 3.

E.6.4 Résultats pour le premier mode non linéaire de la poutre encastrée-libre

Dans cette section, on procède à la comparaison des CNM expérimentaux à ceux calculés avec le modèle numérique géométriquement exact éléments finis des chapitres 3 et 4.

E.6.4.1 Backbones

Dans la Fig. E.17, les backbones de la première harmonique (H1) du déplacement transverse $w(x_m)/L/\Phi(x_m)$, mesuré au point x_m sur la poutre et normalisé par la déformée modale linéaire correspondante $\Phi(x_m)$, sont tracées.

Un très bon accord est trouvé entre les backbones expérimentales et numériques sur le premier mode non linéaire de la poutre encastrée-libre pour les deux poutres plus longues, la poutre 1 dans les Figs. E.17(a) et E.18(a) et la poutre 2 dans les Figs. E.17(b) et E.18(b). Dans la Fig. E.18, on peut voir que les backbones expérimentales des poutres 1 et 2 restent dans ou très proches de la plage d'incertitude des backbones numériques, même jusqu'à de très grandes amplitudes (l'amplitude

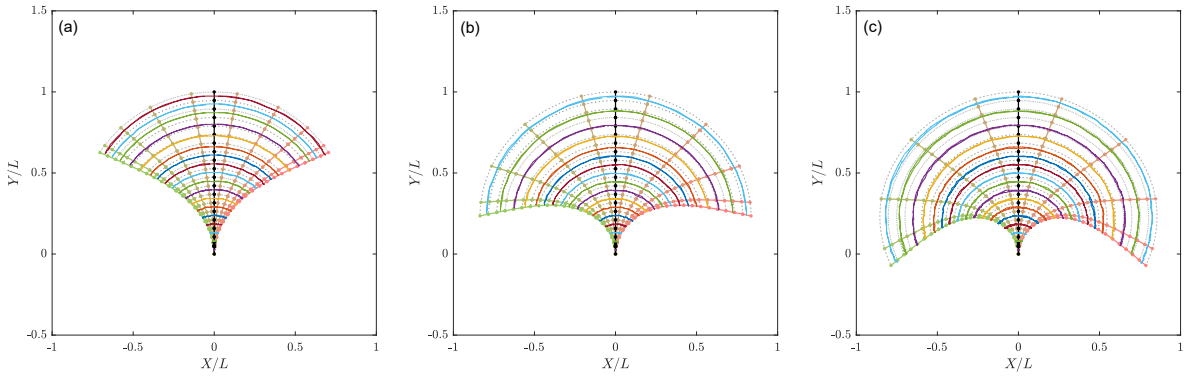

Figure E.19: Déformée modale du premier mode non linéaire de la poutre 1 pour plusieurs accélérations : (a) point A des Figs. E.17(a) et E.18(a), (b) point B, (c) point C.

de la poutre est plus clairement visible dans la Fig. E.19 pour le premier mode non linéaire de la poutre 1). La tendance raidissante connue du premier mode non linéaire de la poutre encastrée-libre (trouvée dans les chapitres 3 - 5) est récupérée pour les trois poutres par les mesures expérimentales. Cependant, la backbone de la poutre la plus courte 3 dans les Figs. E.17(c) et E.18(c) ne suit pas les mêmes tendances que pour les poutres 1 et 2 et semble être décalée en fréquence par rapport à la backbone numérique avec un effet assouplissant à faible amplitude. Ceci est connu dans la littérature comme étant un effet dû à l'encastrement de la poutre, qui peut conduire à des effets assouplissants.

Plusieurs observations peuvent être tirées de ces résultats. Le fort effet de la gravité sur le premier mode non linéaire tel que trouvé dans le chapitre 4 est récupéré dans la Fig. E.18(a), où la backbone $\alpha = 0$ correspondant à l'absence de gravité s'écarte considérablement des autres courbes où $\alpha > 0$. La Fig. E.18(a) démontre en outre la répétabilité des expériences. Deux backbones expérimentales supplémentaires (différents tests utilisant la même poutre) sont ajoutées en orange et marron à la backbone expérimentale de la Fig. E.17(a) (en noir). Les trois courbes expérimentales sont en très bon accord, indiquant que la procédure expérimentale de la section 6.4 est robuste et répétable.

E.6.4.2 Déformées modales

Outre les backbones de la section précédente, on s'intéresse aussi à la déformée modale expérimentale de la poutre encastrée-libre sur son premier mode non linéaire suivie comme décrit dans la section 6.4.3. Numériquement, la déformée modale de la poutre est reconstruite directement pour tous les degrés de liberté à partir de la réponse $\boldsymbol{x}_{\text{cnm}}$ en un certain point sur la backbone. Les points auxquels les déformées modales sont prises sont marqués par des cercles dans la Fig. E.17. La déformée numérique est ensuite superposée à la déformée expérimentale.

En comparant ces figures, il existe globalement un très bon accord entre les déformées expérimentales et numériques sur le premier mode non linéaire de la Fig. E.19, où on voit que la déformee expérimentale est presque identique à la numérique même à très grandes amplitudes.

E.7 Conclusion

Dans cette thèse, on a développé une méthode numérique pour l'étude des structures de poutres élancées hautement flexibles en vibration de grande amplitude, et on a démontré son applicabilité à de nombreux types de systèmes différents. Un objectif commun à tous ces travaux a été de pousser le calcul à des amplitudes de mouvement extrêmement grandes, où la rotation des sections pouvait atteindre près de π [rad]. Comme on l'a montré à travers cette thèse, la modélisation de ces grandes rotations n'est pas simple et nécessite des considérations spéciales (en particulier les termes de rotation) qui ne sont généralement pas présentes à des amplitudes plus faibles (par exemple, si les rotations sont linéarisées ou développées dans une série de Taylor tronquée). On n'a considéré que les non linéarités *géométriques* dans ce travail, mais d'autres types de non linéarités peuvent également être présents dans les structures flexibles (comme dans le cas des structures 1D flexibles non linéaires géométriques composées de matériaux nécessitant des lois de comportement non linéaires). Pour ces raisons (entre autres), la recherche à ce sujet se poursuit activement.

Le travail de cette thèse est basé sur une discrétisation lagrangienne totale par éléments finis du modèle de poutre géométriquement exact (section 2.1). Le modèle de poutre géométriquement exact est régulièrement utilisé pour modéliser des poutres très flexibles car il préserve les non linéarités géométriques quelle que soit l'amplitude du mouvement. Cependant, c'est précisément cette caractéristique - le traitement des non linéarités/termes de rotation - du modèle géométriquement exact qui le rend difficile à résoudre. Des stratégies numériques efficaces sont nécessaires et, à cette fin, on a proposé une stratégie de résolution entièrement basée dans le domaine fréquentiel pour cibler les solutions périodiques. La stratégie de résolution est basée sur une expansion en série de Fourier des variables dans la méthode d'équilibrage harmonique et résolue avec une méthode de continuation appelée la méthode asymptotique numérique (section 2.2). La stratégie de résolution s'est avérée efficace, robuste et utile dans l'étude des phénomènes dynamiques non linéaires (modes non linéaires, résonances internes, bifurcations, analyse de stabilité (section 2.4)).

Notre modèle numérique a été utilisé dans ce travail pour simuler les vibrations non linéaires de plusieurs cas tests très différents, y compris des systèmes simples tels que des poutres encastrées-libres et des poutres bi-encastrées et des systèmes complexes tels qu'un modèle d'arbre et de treillis. Au-delà des cas tests, cependant, il est de la plus haute importance que tout modèle soit validé par rapport aux modèles existants dans la littérature. À cette fin, on a systématiquement comparé les résultats de notre modèle aux modèles de "cas particuliers" et aux résultats trouvés dans la littérature. Les exemples incluent la validation du cas test de la poutre bi-encastrée avec un modèle non linéaire de Von Kármán (section 3.3.2 et section 5.5.2), la validation à faible amplitude avec le modèle analytique de poutre inextensible de [46], [47] (section 4.4.1) et des validations avec les travaux de la littérature dans la section 4.4.2 et la section 5.5. Outre la validation *numérique*, la validation avec *expériences* apporte davantage de confiance à tout modèle numérique. À cet égard, le modèle numérique proposé dans ce travail a également été validé expérimentalement par des expériences dédiées en contrôle vibratoire des structures de poutres hautement flexibles (section 6.5). En utilisant le concept de la *résonance de phase* pour la mesure expérimentale des modes non linéaires, on a démontré que notre modèle est capable de capturer la vraie physique des poutres encastrées-libres hautement flexibles, même à très grandes amplitudes de vibration. En outre, on a montré une équivalence presque exacte entre les déformées modales non linéaires expérimentales et numériques (en particulier pour le premier mode non linéaire à très grande amplitude).

E.7.1 Perspectives

Enfin, on conclut par quelques perspectives de recherche liées au travail présenté dans ce mémoire de thèse. Les sujets suivants sont destinés à servir de prolongements directs à cette thèse, l'état actuel des travaux servant de point de départ à ces études futures.

Études numériques

- Améliorations apportées au modèle éléments finis 2D du chapitre 3 et au modèle éléments finis 3D du chapitre 5 :
  - Mise à jour des versions existantes du code afin de permettre des interpolations polynomiales de n'importe quel ordre dans chaque formulation (matrices de rotation ou quaternions), ou recodage des interpolations mieux adaptées aux rotations (voir la section 2.3.2 and la section 5.3) ;
  - Réalisation de conditions d'amortissement non linéaires plus adaptées, telles qu'un modèle Kelvin-Voigt (voir la section 3.2.2 ou la discussion concernant l'amortissement du chapitre 6) ;
  - Analyse de stabilité pour les systèmes à éléments finis avec de nombreux degrés de liberté basée sur les travaux de [22] ;
  - Comparaison approfondie de l'efficacité de calcul des formulations 2D avec quaternions et avec matrices de rotation (voir la section 5.5.2) ;
  - Développement de méthodes plus efficaces dans MANLAB pour l'initialisation de grands systèmes contenant de nombreux degrés de liberté, en particulier pour réaliser des simulations en 3D avec davantage d'éléments (et ainsi de degrés de liberté, voir la section 5.5.1 et la section 5.6) ;
- Améliorations apportées en particulier au modèle éléments finis 3D du chapitre 5 :
  - Inclusion de l'inertie de rotation dans les équations du mouvement (voir la section 5.1 et l'annexe C.1) ;
  - Généralisation du modèle à toute orientation initiale (*e.g.* poutres initialement courbées, voir la section 5.1).

Études expérimentales

- Poursuite des expériences du chapitre 6 avec poutres encastrées-libres à partir des résultats résumés dans le tableau 6.4 (voir la section 6.6) ;
- Extension des expériences avec poutres encastrées-libres à des applications 3D (*e.g.* les études de [53], [54]) et comparaison aux simulations numériques ;
- Analyse expérimentale d'autres types de structures non linéaires en résonance de phase pour mesurer les modes non linéaires et reproduction des effets non linéaires connus découverts par le modèle numérique à travers ce travail de thèse (*e.g.* les effets raidissant-assouplissant ou centrifuge démontrés par l'anneau flexible de la section 3.3.3 ou les resonances internes de type 1:1 du chapitre 5).

Marielle DEBEURRE

Nonlinear dynamics of highly flexible slender beams: efficient numerical strategies in the frequency domain

Résumé : L'étude des structures de poutres élancées hautement flexibles telles que les câbles, les fils, les tuyaux, les pales de turbine, de moteur et de rotor, les cordes, les règles flexibles et les ailes a suscité un grand intérêt récemment en raison de leur utilisation répandue dans l'industrie moderne. Ces structures flexibles sont répandues dans la fabrication automobile et aérospatiale, les transports publics, la robotique, les systèmes micro et nano-électromécaniques (MEMS/NEMS) et même la mécanique bio-inspirée et la biomécanique. La géométrie unique de ces structures prend la forme d'une poutre dont une dimension, généralement la longueur, est extrêmement grande par rapport aux deux autres. Cette géométrie conduit à une raideur en flexion très faible tandis que la raideur axiale reste relativement élevée, de sorte que ces poutres élancées dites hautement flexibles sont capables d'atteindre des amplitudes de déplacement extrêmes. À très grande amplitude, les non linéarités géométriques liées aux rotations des sections de la poutre entrent dans les équations du mouvement sans qu'il soit possible de les simplifier. Dans ces cas, le modèle de poutre géométriquement exact est souvent utilisé pour modéliser la mécanique de la structure car il préserve exactement les non linéarités géométriques quelle que soit l'amplitude du mouvement. Dans ce travail de thèse, nous nous intéressons aux oscillations périodiques de ces systèmes fortement non linéaires à des amplitudes de vibration extrêmes. Une discrétisation par éléments finis du modèle de poutre géométriquement exact est réalisée. Le modèle éléments finis est entièrement résolu dans le domaine fréquentiel pour cibler des solutions périodiques en mettant fortement la priorité sur l'efficacité des calculs. La stratégie numérique présentée dans ce travail est capable de modéliser des structures de poutres hautement flexibles à la fois en 2D comme en 3D. Ce travail est clôturé par une validation expérimentale de la stratégie numérique impliquant des expériences dédiées en contrôle des vibrations.

Mots clés : Dynamique non linéaire, Poutres élancées, Stratégies numériques, Modèle de poutre géométriquement exact, Non linéarités géométriques, Méthode des éléments finis, Solutions Périodiques.

Abstract: The study of highly flexible slender beam structures such as cables, wires, hoses, turbine, engine and rotor blades, ropes, flexible rulers and wings has been of great interest in recent years due to their widespread use in modern industry. These flexible structures are found extensively in automotive and aerospace manufacturing, public transportation, robotics, micro- and nano-electromechanical systems (MEMS/NEMS) and even bio-inspired and biomechanics. The unique geometry of these structures takes the form of a beam where one dimension, typically the length, is exceedingly large compared to the two others. This geometry leads to a very low bending stiffness while the axial stiffness remains relatively high, so that these so-called highly flexible beams are capable of reaching extreme amplitudes of displacement. At very large amplitudes, so-called geometrical nonlinearities tied to the rotations of the cross-sections of the beam enter into the equations of motion, nonlinearities that cannot be simplified with any accuracy at such large amplitudes. In such cases, the geometrically exact beam model is often used to model the mechanics of the structure since it exactly preserves the geometrical nonlinearities up to any amplitude of motion. In this work, we are interested in studying the periodic oscillations of these highly nonlinear systems at extreme amplitudes of vibration. To this end, a finite element discretization of the geometrically exact beam model is realized. The finite element model is solved entirely in the frequency domain to target periodic solutions with a strong focus on computational efficiency. The numerical strategy presented in this work is capable of modeling highly flexible beam structures both in 2D and in 3D. Also included in this work is an experimental validation of the numerical strategy involving dedicated experiments in vibration control.

Keywords: Nonlinear dynamics, Slender beams, Numerical strategies, Geometrically exact beam model, Geometrical nonlinearities, Finite element method, Periodic solutions.